

ISSN 2071-4726  
2071-0305

# Инженерно-строительный журнал

НАУЧНОЕ ИЗДАНИЕ

№5(89) 2019





**ПОЛИТЕХ**  
Санкт-Петербургский  
политехнический университет  
Петра Великого

**Инженерно-строительный институт**  
Центр дополнительных профессиональных программ  
195251, г. Санкт-Петербург, Политехническая ул., 29,  
тел/факс: 552-94-60, [www.stroikursi.spbstu.ru](http://www.stroikursi.spbstu.ru),  
[stroikursi@mail.ru](mailto:stroikursi@mail.ru)

**Приглашает специалистов организаций, вступающих в СРО,  
на курсы повышения квалификации (72 часа)**

Код	Наименование программы	Виды работ*
<b>Курсы по строительству</b>		
БС-01-04	«Безопасность и качество выполнения общестроительных работ»	п.1,2, 3, 5, 6, 7, 9, 10, 11, 12, 13, 14
БС-01	«Безопасность и качество выполнения геодезических, подготовительных и земляных работ, устройства оснований и фундаментов»	1,2,3,5
БС-02	«Безопасность и качество возведения бетонных и железобетонных конструкций»	6,7
БС-03	«Безопасность и качество возведения металлических, каменных и деревянных конструкций»	9,10,11
БС-04	«Безопасность и качество выполнения фасадных работ, устройства кровель, защиты строительных конструкций, трубопроводов и оборудования»	12,13,14
БС-05	«Безопасность и качество устройства инженерных сетей и систем»	15,16,17,18,19
БС-06	«Безопасность и качество устройства электрических сетей и линий связи»	20,21
БС-08	«Безопасность и качество выполнения монтажных и пусконаладочных работ»	23,24
БС-12	«Безопасность и качество устройства мостов, эстакад и путепроводов»	29
БС-13	«Безопасность и качество выполнения гидротехнических, водолазных работ»	30
БС-14	«Безопасность и качество устройства промышленных печей и дымовых труб»	31
БС-15	«Осуществление строительного контроля»	32
БС-16	«Организация строительства, реконструкции и капитального ремонта. Выполнение функций технического заказчика и генерального подрядчика»	33
<b>Курсы по проектированию</b>		
БП-01	«Разработка схемы планировочной организации земельного участка, архитектурных решений, мероприятий по обеспечению доступа маломобильных групп населения»	1,2,11
БП-02	«Разработка конструктивных и объемно-планировочных решений зданий и сооружений»	3
БП-03	«Проектирование внутренних сетей инженерно-технического обеспечения»	4
БП-04	«Проектирование наружных сетей инженерно-технического обеспечения»	5
БП-05	«Разработка технологических решений при проектировании зданий и сооружений»	6
БП-06	«Разработка специальных разделов проектной документации»	7
БП-07	«Разработка проектов организации строительства»	8
БП-08	«Проектные решения по охране окружающей среды»	9
БП-09	«Проектные решения по обеспечению пожарной безопасности»	10
БП-10	«Обследование строительных конструкций и грунтов основания зданий и сооружений»	12
БП-11	«Организация проектных работ. Выполнение функций генерального проектировщика»	13
Э-01	«Проведение энергетических обследований с целью повышения энергетической эффективности и энергосбережения»	
<b>Курсы по инженерным изысканиям</b>		
И-01	«Инженерно-геодезические изыскания в строительстве»	1
И-02	«Инженерно-геологические изыскания в строительстве»	2,5
И-03	«Инженерно-гидрометеорологические изыскания в строительстве»	3
И-04	«Инженерно-экологические изыскания в строительстве»	4
И-05	«Организация работ по инженерным изысканиям»	7

\*(согласно приказам Минрегионразвития РФ N 624 от 30 декабря 2009 г.)

**По окончании курса слушателю выдается удостоверение о краткосрочном повышении  
квалификации установленного образца (72 ак. часа)**

Для регистрации на курс необходимо выслать заявку на участие, и копию диплома об образовании по телефону/факсу: 8(812) 552-94-60, 535-79-92, , e-mail: [stroikursi@mail.ru](mailto:stroikursi@mail.ru).

**Инженерно-строительный журнал**

НАУЧНОЕ ИЗДАНИЕ

ISSN 2071-4726, 2071-0305

Свидетельство о государственной регистрации: ПИ №ФС77-38070, выдано Роскомнадзором

Специализированный научный журнал. Выходит с 09.2008.

Включен в Перечень ведущих периодических изданий ВАК РФ

Периодичность: 8 раз в год

**Учредитель и издатель:**

Санкт-Петербургский политехнический университет Петра Великого

**Адрес редакции:**

195251, СПб, ул. Политехническая, д. 29, Гидрокорпус-2, ауд. 245

**Главный редактор:**

Екатерина Александровна Линник

**Научный редактор:**

Николай Иванович Ватин

**Выпускающий редактор:**

Анастасия Крупина

**Редакционная коллегия:**

д.ф.-м.н., доцент Р.А. Абдикаримов;  
 д.т.н., проф. В.В. Бабков;  
 к.т.н., проф. А.И. Боровков;  
 д.т.н., проф. А. Бородинец;  
 д.т.н., проф. Н.И. Ватин;  
 PhD, проф. М. Вельжкович;  
 к.т.н., М.Р. Гарифуллин;  
 д.т.н., проф. Э.К. Завадскас;  
 д.ф.-м.н., проф. М.Н. Кирсанов;  
 D.Sc., проф. М. Кнежевич;  
 д.т.н., проф. В.В. Лалин;  
 д.т.н., проф. Б.Е. Мельников;  
 д.т.н., академик М.М. Мирсаидов;  
 д.т.н., проф. Р.Б. Орлович;  
 Dr. Sc. Ing., professor  
 Л. Пакрастиньш;  
 Dr.-Ing. Habil., professor  
 Х. Пастернак;  
 д.т.н., проф. А.В. Перельмутер;  
 д.т.н., проф. М.Р. Петриченко;  
 д.т.н., проф. В.В. Сергеев;  
 д.ф.-м.н., проф. М.Х. Стрелец;  
 д.т.н., проф. О.В. Тараканов;  
 д.т.н., проф. Б.Б. Телтаев;  
 д.т.н., проф. В.И. Травуш;  
 д.т.н., проф. Д. Унгерман;  
 д.т.н., проф. С.В. Федосов

Дата выхода: 19.09.2019

**Содержание**

Мирсаидов М.М., Тошматов Э.С. Пространственное напряженное состояние и динамические характеристики грунтовых плотин	3
Орищук Р.Н. Глиноцементобетонная диафрагма, расчётное обоснование новых конструкций	16
Абделгадер Х., Федюк Р.С., Курпинска М., Хатиб Д., Мурали Г., Баранов А.В., Тимохин Р.А. Физико-механические свойства каркасного бетона, модифицированного кремнеземом	26
Лалин В.В., Дмитриев А.Н., Дьяков С.Ф. Геометрически нелинейное деформирование и устойчивость упругих арок	39
Иванов К.С. Оптимизация структуры и свойств пеностеклокерамики	52
Тюкалов Ю.Я. Конечно-элементная модель в напряжениях для пластин Рейснера	61
Лалин В.В., Рыбаков В.А., Иванов С.С., Азаров А.А. Смешанный метод конечных элементов в полусдвиговой теории тонкостенных стержней В.И. Сливкера	79
Миах, М.Д., Миах М.С., Алам В.Б., Ло Монте Ф., Ли Й.. Усиление железобетонных балок ферроцементом	94
Джун Ф., Юэ Ф., Джабин Й. Моделирование водопроницаемости газобетонных блоков методом решёточных уравнений Больцмана	106
Рыбаков В.А., Лалин В.В., Иванов С.С., Азаров А.А. Квадратичная аппроксимация функций форм в полусдвиговой теории устойчивости В.И. Сливкера	115
Шеховцова С.Ю., Королев Е.В., Иноземцев С.С., Ю Д., Ю Х. Методика прогнозирования прочности и термочувствительности асфальтобетона	129
Иконин С.В., Сухотерин А.В. Влияние конструктивного исполнения на взаимодействие фундаментных плит с основанием	141
Нгуен Ч.Ч., Анискин Н.А. Температурный режим возводимого бетонного массива с трубным охлаждением	156
Лукашевич А.А. Моделирование контактного взаимодействия конструкций с основанием при динамическом нагружении	167
Иноземцев А.С., Королев Е.В., Зыонг Т. Физико-механические свойства цементного камня с раствором суперабсорбирующих полиакрилатов	179

© ФГАОУ ВО СПбГУ, 2019

© Иллюстрация на обложке: Илья Смагин

**Контакты:**

E-mail: mce@spbstu.ru

Web: <http://www.engstroy.spbstu.ru>

*Magazine of Civil Engineering*

SCHOLAR JOURNAL

ISSN 2071-4726, 2071-0305

Peer-reviewed scientific journal

Start date: 2008/09

8 issues per year

**Publisher:**Peter the Great St. Petersburg  
Polytechnic University**Indexing:**Scopus, Russian Science Citation  
Index (WoS), Compendex, DOAJ,  
EBSCO, Google Academia, Index  
Copernicus, ProQuest, Ulrich's Serials  
Analysis System**Corresponding address:**245 Hydro Building, 29  
Polytechnicheskaya st., Saint-  
Petersburg, 195251, Russia**Editor-in-chief:**

Ekaterina A. Linnik

**Science editor:**

Nikolay I. Vatin

**Technical editor:**

Anastasia Krupina

**Editorial board:**R.A. Abdikarimov, D.Sc., associate  
professor

V.V. Babkov, D.Sc., professor

A.I. Borovkov, PhD, professor

A. Borodinecs, Dr.Sc.Ing., professor

M. Veljkovic, PhD, professor

M. Garifullin, PhD, postdoctorant

E.K. Zavadskas, D.Sc., professor

M.N. Kirsanov, D.Sc., professor

M. Knezevic, D.Sc., professor

V.V. Lalin, D.Sc., professor

B.E. Melnikov, D.Sc., professor

M.M. Mirsaidov, D.Sc., professor

R.B. Orlovich, D.Sc., professor

L. Pakrastinsh, Dr.Sc.Ing., professor

H. Pasternak, Dr.-Ing.habil.,  
professor

A.V. Perelmuter, D.Sc., professor

M.R. Petrichenko, D.Sc., professor

V.V. Sergeev, D.Sc., professor

M.Kh. Strelets, D.Sc., professor

O.V. Tarakanov, D.Sc., professor

B.B. Teltayev, D.Sc., professor

V.I. Travush, D.Sc., professor

S.V. Fedosov, D.Sc., professor

Date of issue: 19.09.2019

## Contents

Mirsaidov, M.M., Toshmatov, E.S. Spatial stress state and dynamic characteristics of earth dams	3
Orishchuk, R.N. Clay-cement-concrete diaphragm – justifying calculation for new-built constructions	16
Abdelgader, H.S., Fediuk, R.S., Kurpinska, M., Khatib, J., Murali, G., Baranov, A.V., Timokhin, R.A. Mechanical properties of two-stage concrete modified by silica fume	26
Lalin, V.V., Dmitriev, A.N., Diakov, S.F. Nonlinear deformation and stability of geometrically exact elastic arches	39
Ivanov, K.S. Optimization of the structure and properties of foam-glass ceramics	52
Tyukalov, Yu.Ya. Finite element model of Reisner's plates in stresses	61
Lalin, V.V., Rybakov, V.A., Ivanov, S.S., Azarov, A.A. Mixed finite-element method in V.I. Slivker's semi-shear thin-walled bar theory	79
Miah, M.J., Miah, M.S., Alam, W.B., Lo Monte, F., Li, Y. Strengthening of RC beams by ferrocement made with unconventional concrete	94
Jun, F., Yue, Y., JiaBin, Y. Water permeation simulation of autoclaved aerated concrete blocks using the Lattice Boltzmann method	106
Rybakov, V.A., Lalin, V.V., Ivanov, S.S., Azarov, A.A. Coordinate functions quadratic approximation in V.I. Slivker's semi-shear stability theory	115
Shekhovtsova, S.Yu., Korolev, E.V., Inozemtcev, S.S., Yu, J., Yu, H. Method of forecasting the strength and thermal sensitive asphalt concrete	129
Ikonin, S.V., Sukhoterin, A.V. The effect of design on interaction of foundation slabs with the base	141
Nguyen, C.T., Aniskin, N.A. Temperature regime during the construction massive concrete with pipe cooling	156
Lukashevich, A.A. Modelling of contact interaction of structures with the base under dynamic loading	167
Inozemtcev, A.S., Korolev, E.V., Duong, T.Q. Physical and mechanical properties of cement stone with superabsorbent polyacrylate solutions	179

© Peter the Great St. Petersburg Polytechnic University. All rights reserved.

© Illustration – Ilya Smagin

E-mail: [mce@spbstu.ru](mailto:mce@spbstu.ru)Web: <http://www.engstroy.spbstu.ru/eng/index.html>



DOI: 10.18720/MCE.89.1

## Spatial stress state and dynamic characteristics of earth dams

**M.M. Mirsaidov\*, E.S. Toshmatov**

*Tashkent Institute of Irrigation and Agricultural Mechanization Engineers, Tashkent, Uzbekistan*

\* E-mail: [theormir@mail.ru](mailto:theormir@mail.ru)

**Keywords:** spatial system, three-dimensional (spatial) model, inhomogeneity, earth dam, stress-strain state, dynamic characteristic, natural frequency, modes of oscillations

**Abstract.** Strength assessment of earth dams is mainly conducted using a plane design scheme, which does not always lead to adequate results. In this paper, it is proposed to assess the stress state of earth dams in a three-dimensional statement. Consequently, to assess the stress-strain state and dynamic characteristics of earth dams, appropriate mathematical models, methods and algorithms are built. The basis of the developed methods for solving specific problems for a spatial structure is a finite element method, the Gauss method (or the square root method) and the Muller method. Reliability of results is proved by solving a series of test problems. With the developed methods, the stress-strain state and dynamic characteristics of the Gissarak and Sokh earth dams were investigated. Based on the results of the study, it has been shown that for some types of earth dams, at preliminary assessment of the stress state and dynamic characteristics of structures, it is possible to use a plane-deformable model of calculation. Studies have shown that to ensure the required accuracy in assessing the stress state and dynamic characteristics of complex inhomogeneous spatial systems (such as earth dams), it is necessary to make calculations using a three-dimensional model. The data obtained as a result of research allowed to reveal some features of the stress state in a spatial case, indicating dangerous areas with the greatest stresses, as well as to study the pattern of natural oscillations that cannot be described using a plane model.

### 1. Introduction

Correct definition of the stress-strain state (SSS) and dynamic characteristics of the object under consideration is a major factor in assessing the strength of structures. Reliable definition of these parameters, in turn, depends on the chosen design scheme of structure, used mathematical models describing the processes occurring in the object under consideration, the equations of material state and the solution methods of considered problems [1–5].

Recently several papers [6–14] have been published, where static and dynamic stress-strain states of various earth dams are considered in plane and spatial statements, taking into account various factors, such as design features of structure, moisture-content properties of soil, structure interaction with water reservoir and hydro-mechanical phenomena.

Along with that, it is necessary to mention separately the following papers devoted to the solution of various topical issues related to the state assessment of earth structures.

In [10], the state of the dam was analyzed by numerical simulation taking into account water-saturated soil and hydro-mechanical phenomena. Material selection for the design of the dam was discussed.

Using the ABAQUS software package the state of the dam was analyzed in [11], taking into account the interaction of the dam with water of the reservoir. Obtained results have shown that the neglect of this factor leads to an overestimated value of stability and, as a result, to structure damage. The effect of clay and rock bases on the cracks propagation in the dam body was considered.

---

Mirsaidov, M.M., Toshmatov, E.S. Spatial stress state and dynamic characteristics of earth dams. Magazine of Civil Engineering. 2019. 89(5). Pp. 3–15. DOI: 10.18720/MCE.89.1

Мирсаидов М.М., Тошматов Э.С. Пространственное напряженное состояние и динамические характеристики грунтовых плотин // Инженерно-строительный журнал. 2019. № 5(89). С. 3–15. DOI: 10.18720/MCE.89.1



This open access article is licensed under CC BY 4.0 (<https://creativecommons.org/licenses/by/4.0/>)

Reliability indices and safety factors of dams [12] were evaluated for various heights and slopes. It was stated that the values of safety factors for high dams in normal conditions should be no less than 1.70 and in seismic conditions no less than 1.40.

In [13, 14], the effect of hydrodynamic pressure on dam state during earthquakes was considered in a plane statement. The results obtained showed that the neglect of rigid body-water interaction effect led not only to an overestimation of the acceleration reaction in the rock-fill material, but also to an overestimation of dynamic stresses in a structure.

Dynamic characteristics of the dam with filled reservoir were studied experimentally and numerically in [14]. It was stated that the acceleration gain factors varied with the height of the dam depending on natural frequency, modes of structure oscillations, depth of the reservoir, and other factors. It was recommended to take these factors into consideration when designing a structure.

In [15], static and dynamic elastic-plastic analysis of the dam state by the finite element method was carried out during the Wenchuan earthquake. To describe the properties of rock-fill material, an elastoplastic model was used, taking into account the destruction of particles. Numerical calculations obtained corresponded to a great extent to field measurements during construction and after the Wenchuan earthquake.

Bending strain of the dam was investigated in [16], since bending often led to structure destruction. Using special programs and the finite element method, numerical modeling of dam bending rate was carried out. The results of numerical simulation and statistical analysis have shown that an increase in elastic modulus, Poisson's ratio, internal friction angle and the ratio of core thickness to filter thickness would result in a decrease in bending.

Hydro-mechanical properties of traditional and unconventional materials (i.e. clay material, masonry) used in the construction of dams were analyzed in [17]. The use of unconventional material (soil and stone mixtures) for reasons of ensuring dam stability was analyzed in more detail.

The above review of published papers shows that the problem of earth dam spatial calculation is studied insufficiently [18–24] and therefore is of great interest.

Usually, when evaluating the stress-strain state of dams located in wide dam sites, it is sufficient to use plane strain conditions, however, the use of plane design schemes for earth dams located in narrow dam sites still requires more careful checking of the accuracy of the SSS estimation of structures.

The state of earth dam under various effects is also determined by its length. As noted in [25, 26] for extended dams (with a ratio of the crest length —  $L_{cr}$  to the dam height  $H$  equal to  $L_{cr}/H \geq 6$ ), calculations can be made according to the plane strain scheme; in this case, it is possible to assess not the entire structure, but only its central section. If the given ratio is violated, then the spatial nature of the dam is revealed. At the same time, as studies in [6, 18, 19, 24–26] show, the accuracy of dam calculation changes not only under static load, but under dynamic effect as well.

Brief review presented here shows that obtaining of reliable results in the SSS calculation and assessment of dynamic characteristics of earth dams are quite serious problems, since the task to develop sound quantitative estimates of structure strength with account of actual geometric dimensions of earth dams dictates the need to take into account spatial nature of structure operation [4, 6, 7].

Therefore, at present, it is necessary to give primary recommendations to assess the stress-strain state and dynamic characteristics of earth dams by adequate design models that describe the actual features of a structure.

This paper is devoted to the solution of the following issues:

- to assess the stress-strain state and dynamic characteristics of earth dams, a three-dimensional (spatial) model is proposed that takes into account inhomogeneous and geometric features of a structure;
- a variation statement of the problem is given taking into account spatial strain state of earth dams under consideration;
- the methods to solve specific tasks for real structures using spatial finite elements are proposed;
- the stress-strain state and dynamic characteristics of real earth dams are studied using spatial (that is, three-dimensional) models and the models of plane strain;
- plane (plane-strain) and three-dimensional (spatial) models;
- primary conclusions on the use of three-dimensional models in assessment of the SSS and dynamic characteristics of specific earth dams are given, based on the analysis of the results obtained.

## 2. Methods

Dynamic characteristics, that is, natural frequencies, oscillation modes and damping coefficients of structures are determined by studying natural oscillations of structures. Dynamic characteristics of a structure are the passport of the considered structure, allowing evaluating in advance dynamic properties of a structure as a whole.

### 2.1. Mathematical model

To assess the stress-strain state (SSS) and dynamic characteristics of earth dams, an inhomogeneous three-dimensional model of the system, Figure 1, is considered, in which the base surfaces and side slopes  $\Sigma_0, \Sigma_{S_1}, \Sigma_{S_2}$  are rigidly fixed, the surface of the downstream  $\Sigma_3$  is stress-free, the hydrostatic pressure of water acts on surface  $\Sigma_1$  (on the part of upstream slope which is lower than the BSL line,  $S_p$ ), and an external load is applied to a part of crest surface  $\Sigma_2$  of the site  $\Sigma_p$ .

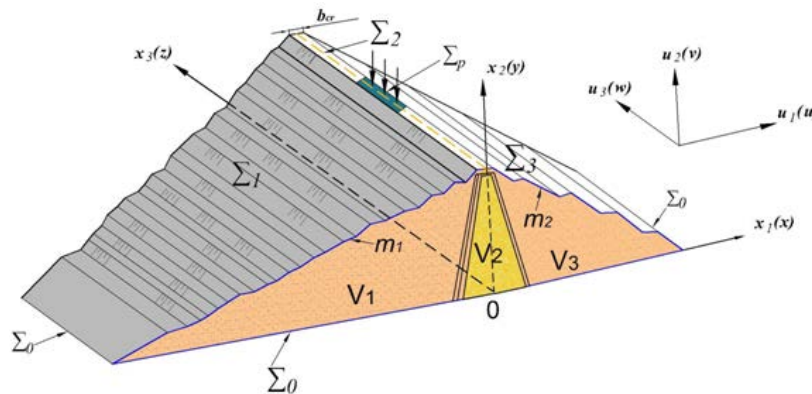


**Figure 1. Three-dimensional model of inhomogeneous system.**

Here  $V = V_1 + V_2 + V_3$  is the capacity of the dam body ( $V_1, V_3$  are the capacities of the upper and lower retaining prisms,  $V_2$  is the capacity of the core);  $\Sigma_{S_1}, \Sigma_{S_2}$  are the surfaces of the coastal slopes,  $\Sigma_0$  is the surface of the base along the bottom, and  $\Sigma_1, \Sigma_2, \Sigma_3$  are the surfaces of the retaining prisms and the crest.

System material is considered to be elastic. In calculations the mass forces  $\vec{f}$  acting on the system and hydrostatic pressure of water  $\vec{p}$  are taken into account [4].

The aim is to determine the fields of displacements, stresses and dynamic characteristics of an earth dam of  $V = V_1 + V_2 + V_3$  capacity (Figure 1).

To simulate the process of strain and to assess dynamic characteristics of earth dams (Figure 1) in a three-dimensional statement, the Lagrange variation equation, based on the d'Alembert principle for inhomogeneous deformable bodies is used:

$$\begin{aligned}
 & - \int_{V_1} \sigma_{ij} \delta \varepsilon_{ij} dV - \int_{V_2} \sigma_{ij} \delta \varepsilon_{ij} dV - \int_{V_3} \sigma_{ij} \delta \varepsilon_{ij} dV - \\
 & - \int_{V_1} \rho_1 \ddot{u} \delta \bar{u} dV - \int_{V_2} \rho_2 \ddot{u} \delta \bar{u} dV - \int_{V_3} \rho_3 \ddot{u} \delta \bar{u} dV + \\
 & + \int_V \vec{f} \delta \bar{u} dV + \int_{S_p} \vec{p} \delta \bar{u} dS + \int_{\Sigma_p} \vec{P}_1 \delta \bar{u} d\Sigma = 0.
 \end{aligned} \tag{1}$$

Physical properties of system material are described by the relations between stresses  $\sigma_{ij}$  and strains  $\varepsilon_{ij}$  in the form [27]:

$$\sigma_{ij} = \lambda_n \varepsilon_{kk} \delta_{ij} + 2\mu_n \varepsilon_{ij} \tag{2}$$

the relationship between the components of the strain tensor and the displacement vector is described by the linear Cauchy relations [27]

$$\varepsilon_{ij} = \frac{1}{2} \left( \frac{\partial u_i}{\partial x_j} + \frac{\partial u_j}{\partial x_i} \right). \quad (3)$$

Further, when building mathematical models, uniform kinematic boundary conditions are taken into account:

$$\bar{x} \in \sum_0: \bar{u} = 0. \quad (4)$$

Here  $\bar{u}$ ,  $\varepsilon_{ij}$ ,  $\sigma_{ij}$  are the displacement vector, the strain and stress tensors, respectively;

$\delta\bar{u}$ ,  $\delta\varepsilon_{ij}$  are the isochronous variations of displacements and strains;

$\rho_n$  is the material density of the system elements under consideration (index  $n = 1, 2, 3$  means different parts of the dam to which this quantity relates);

$\bar{f}$  is the vector of mass forces;

$\bar{P}_1$  is the vector of external forces applied to area  $\Sigma_p$ ;

$\bar{p}$  is the hydrostatic pressure of water.

In all the problems considered, the displacement vector in spatial coordinate system  $\bar{x} = \{x_1, x_2, x_3\} = \{x, y, z\}$  has three components  $\bar{u} = \{u_1, u_2, u_3\} = \{u, v, w\}$  in all relations  $i, j, k = 1, 2, 3$ .

Now, the variation problem to assess the stress-strain state of an earth dam can be formulated as follows: it is necessary to determine (without taking into account the inertial forces) fields of displacements  $\bar{u}(\bar{x}, t)$ , strains  $\varepsilon_{ij}(\bar{x}, t)$  and stresses  $\sigma_{ij}(\bar{x}, t)$  in an inhomogeneous three-dimensional system (Figure 1) arising under mass forces ( $\bar{f}$ ), external forces ( $\bar{P}_1$ ) and hydrostatic pressure of water ( $\bar{p}$ ), satisfying equations (1), (2), (3) and corresponding to kinematic conditions (4) at any possible displacement  $\delta\bar{u}$ .

In the case of determining dynamic characteristics of an earth dam, the variation problem under consideration can be formulated as follows: it is necessary to determine the most ordered movements of the system point, occurring according to a harmonic law at different amplitudes in the absence of external influences, i.e. ( $\bar{f}$ ), ( $\bar{P}_1$ ), ( $\bar{p}$ ), satisfying the equations (1), (2), (3) and corresponding to boundary conditions (4) at any possible displacement  $\delta\bar{u}$ .

## 2.2. Method and algorithm

Variation problem set above (1)–(4) of the SSS assessment of inhomogeneous systems (Figure 1), under the effect of hydrostatic pressure and mass forces, taking into account spatial factors, with the use of a finite element (in the form of a hexahedral parallelepiped with 24 degrees of freedom) is reduced to the resolving system of algebraic equations of  $N$ -th order:

$$[K]\{u\} = \{P\}, \quad (5)$$

where the element stiffness matrix  $[K]$  of the system (Figure 1) is constant and depends on elastic physicommechanical parameters of the system;

$\{u\}$  is the sought for vector of nodal displacements;

$\{P\}$  is the vector of external load (mass forces and hydrostatic pressure of water).

When deriving equation (5), the stiffness matrix  $[K]$  and nodal forces  $\{P\}$  are formed automatically using the algorithm given in [4, 20].

Kinematic boundary conditions (4) are taken into account when forming the system of equations (5), restricting its order only to equations that do not contain zero displacements. The order of the formed systems of algebraic equations (5) in some calculations exceeded 4000.

Solution of the obtained system of algebraic equations (5) was performed by the Gauss method and the square root method [29, 30], taking into account the tape structure of the stiffness matrix. Solving the system of equations (5), the components of displacements ( $u_1, u_2, u_3$ ) at each point of the system (i.e. displacement fields) are determined; then using these data the components of strain (3) and stress (2) tensors are determined, taking into account inhomogeneous structural features of systems.

When determining the natural frequencies and modes of oscillation, the considered variation problem (1)–(4), with the use of a finite element (in the form of a hexahedral parallelepiped with 24 degrees of freedom), is reduced to an algebraic eigenvalue problem for a homogeneous system of algebraic equations of  $N$ -th order:

$$\{[K] - \omega^2[M]\}\{u\} = 0. \quad (6)$$

Here  $[K]$ ,  $[M]$  are the stiffness and mass matrices, and  $\omega$ ,  $\{u\}$  are the sought for eigenfrequency and eigenvector of the system under consideration (Figure 1). The elements of stiffness matrix  $[K]$  are constant and depend only on elastic physicomaterial parameters of structure material.

Solution of equations (6), (i.e. determination of eigenfrequencies) is carried out by the Muller method [4, 31], and determination of eigenvector – by the Gauss method or the square root method [29, 30].

The order of the systems of algebraic equations (6) in some calculations reached 3000.

The algorithm to determine the eigenfrequencies and vectors of algebraic problems on eigenvalue is described in detail in [4]. The essence of this algorithm is as follows:

1. With the iterative procedure of the Muller method, a sequence of eigenvalues of algebraic equations (6)  $\lambda_1, \lambda_2, \dots, \lambda_n$  is determined.

2. Then, using expression ( $\lambda = \omega^2$ ), the eigenfrequencies  $\omega_1, \omega_2, \dots, \omega_n$  of algebraic equations (6) are calculated.

3. By substituting the found values  $\omega_1, \omega_2, \dots, \omega_n$  in equation (6), eigenvectors in (6) (i.e., oscillation modes)  $\{u_1\}, \{u_2\}, \dots, \{u_n\}$  are obtained by the Gauss method or the square root method [29, 30].

The program for determining eigenfrequencies and modes of oscillations of inhomogeneous spatial systems is protected by the copyright certificate of the Patent Agency of the Republic of Uzbekistan.

### 2.3. Test problems to check the accuracy of the methods and computing algorithms

This section verifies the accuracy of the developed methods and algorithms solving test problems for which the exact or numerical solution is known.

**Problem 1.** Consider elastic spatial structure in the form of a long rectangular parallelepiped under uniform pressure  $P$  acting on the upper surface.

The parallelepiped rests on an absolutely rigid and smooth base, i.e.

$$x_2 = 0: u_2 = 0; \sigma_{12} = 0; \sigma_{13} = 0. \quad (7)$$

Surface load is applied on the upper surface in the form of uniform pressure

$$x_2 = a: \sigma_{22} = -P. \quad (8)$$

The side surface of the parallelepiped is stress-free.

It is required to determine displacements and stresses at various points of the parallelepiped under pressure  $P$  using plane-deformable and spatial models. For the plane problem, the exact solution is known [34]. In a specific calculation, the following geometrical parameters of the parallelepiped and mechanical characteristics of material were used:  $P = 1 \text{ tf/m}^2$ ; cross-sectional dimensions  $a = b = 2.0 \text{ m}$ ; the modulus of material elasticity  $E = 1.0 \text{ tf/m}^2$  and the Poisson's ratio  $\mu = 0.3$ .

Comparison of exact results (Table 1) with numerical solutions (Table 2) for the same points of the parallelepiped shows good agreement of the values obtained both in terms of the displacement components and in stress tensor components.

**Problem 2.** Natural oscillations of a body (height  $H = 8.0 \text{ m}$ ) of rectangular cross sections ( $b = 0.5 \text{ m}$ ;  $h = 0.5 \text{ m}$ ), rigidly fixed along the base ( $x_2 = 0$ ) and with free upper end ( $x_2 = H$ ) are considered in the problem.

**Table 1. Exact solution of plane problem for section ( $x_3 = 0.0$  m) of the parallelepiped.**

Coordinates, $x_2$ (m)	$x_1 = -1.0$ m					$x_1 = 1.0$ m				
	$u_1$	$u_2$	$\sigma_{11}$	$\sigma_{22}$	$\sigma_{12}$	$u_1$	$u_2$	$\sigma_{11}$	$\sigma_{22}$	$\sigma_{12}$
0.0	-0.39	0.0	0	-1	0	0.39	0.0	0	-1	0
0.5	-0.39	-0.455	0	-1	0	0.39	-0.455	0	-1	0
1.0	-0.39	-0.910	0	-1	0	0.39	-0.910	0	-1	0
1.5	-0.39	-1.365	0	-1	0	0.39	-1.365	0	-1	0
2.0	-0.39	-1.820	0	-1	0	0.39	-1.820	0	-1	0

**Table 2. Solution of spatial problem for section ( $x_3 = 0.0$  m) of the parallelepiped.**

Coordinate, $x_2$ (m)	$x_1 = -1.0$ m								
	$u_1$	$u_2$	$u_3$	$\sigma_{11}$	$\sigma_{22}$	$\sigma_{33}$	$\sigma_{12}$	$\sigma_{13}$	$\sigma_{23}$
0.0	-0.3889	0.0	-0.0	-0.2996	-0.9983	-0.41e <sup>-3</sup>	0.131e <sup>-12</sup>	0.157e <sup>-10</sup>	0.797e <sup>-4</sup>
0.5	-0.3886	-0.4541	-0.417e <sup>-14</sup>	-0.2966	-0.9980	0.258e <sup>-3</sup>	0.202e <sup>-14</sup>	0.246e <sup>-11</sup>	0.600e <sup>-4</sup>
1.0	-0.3883	-0.9091	-0.617e <sup>-14</sup>	-0.2947	-0.9989	0.245e <sup>-3</sup>	-0.139e <sup>-13</sup>	0.629e <sup>-11</sup>	0.235e <sup>-4</sup>
1.5	-0.3881	-1.3648	-0.727e <sup>-14</sup>	-0.2935	-0.9994	0.257e <sup>-3</sup>	-0.122e <sup>-13</sup>	0.509e <sup>-11</sup>	0.360e <sup>-6</sup>
2.0	-0.3880	-1.8207	-0.947e <sup>-14</sup>	-0.2930	-0.9996	0.227e <sup>-3</sup>	0.556e <sup>-14</sup>	0.29e <sup>-11</sup>	-0.607e <sup>-15</sup>

Natural frequencies and oscillation modes of this body are determined using one-dimensional and spatial models.

In one-dimensional statement, this problem has an exact solution [35] for the eigenfrequencies  $\omega_i$ .

Solving this problem, the following mechanical parameters of material were used: specific weight of material  $\gamma = 1.0$  tf/m<sup>3</sup>; elastic modulus  $E = 1.0$  tf/m<sup>2</sup> and Poisson's ratio  $\mu = 0.25$ .

Exact solution of the body, obtained by one-dimensional model is compared in Table 3 with numerical results obtained by three-dimensional models (using spatial finite elements) with developed computer program.

**Table 3. Table of eigenfrequencies.**

Number of eigenfrequency	Eigenfrequencies of a body, rad/sec			
	Exact solution by one-dimensional model			Numerical solution obtained by the FEM with three-dimensional model
	Bending	Longitudinal	Torsional	
1	2	3	4	5
1	<b>0.0248*</b>	<b>0.6150**</b>	0.1459	<b>0.0248*</b>
2	<b>0.1556*</b>	<b>1.8450**</b>	0.4376	<b>0.1531*</b>
3	0.4358	3.0749	0.7294	0.3536
4	0.8494	4.3049	1.0211	0.4174
5	1.4117	5.5349	1.3129	<b>0.6159**</b>
6	2.1089	6.7648	1.6047	0.7895
7	2.9455	7.9948	1.8964	1.0606
8	3.9215	9.2248	2.1882	1.2521
9	5.0370	10.4550	<b>2.4799***</b>	1.2522
10	6.2919	11.6851	2.7717	1.7670
11				1.7869
12				<b>1.8447**</b>
13				2.3778
14				2.3779
15				<b>2.4725***</b>

In Table 3 one asterisk indicates the frequencies corresponding to the bending modes of oscillations, two asterisks — the longitudinal modes and three asterisks — the torsional modes of the body, obtained by spatial model.

Comparison of the exact value of natural frequencies of one-dimensional model with numerical values obtained by the FEM with spatial model

Partial coincidence of corresponding frequencies with results of one-dimensional model exact solution and with results obtained using the developed computer programs with three-dimensional model proves the reliability of the developed methods, algorithms and the calculation program when determining natural frequencies and oscillation modes of a spatial body.

Analyzing the obtained eigenmodes of body oscillations using spatial model, the spatial nature should be noted: only the first two are the bending modes, the fifth is a longitudinal mode, and in the others, that is, in the 3<sup>rd</sup>, 4<sup>th</sup>, 6<sup>th</sup>, 7<sup>th</sup>, 8<sup>th</sup> and 9<sup>th</sup> modes of oscillations the strain has a spatial character. This shows that one-dimensional model is not able to fully describe the real strain under natural oscillations even of a thin bar.

### 3. Results and Discussion

Using the developed methods and algorithms the stress-strain state of Gissarak and Sokh earth dams are studied in spatial statement, taking into account the actual geometric dimensions of the structure and uniform and non-uniform structural features of a dam, arising under gravitational forces (own weight) and hydrostatic pressure of water.

#### 3.1. Assessment of the stress-strain state

As specific examples we have considered

– **the Gissarak earth dam:** height  $H = 138.5$  m; base width  $B_w = 634.0$  m; crest width  $b_{cr} = 16.0$  m; inclination coefficients of upstream and downstream slopes  $m_1 = 2.2$ ,  $m_2 = 1.9$ ; longitudinal dimensions: base length  $L_b = 140.0$  m, crest length  $L_{cr} = 660.0$  m. Mechanical characteristics of material of different sections of the dam are: volume weight  $\gamma$  — kgf/cm<sup>3</sup>, Poisson's ratio —  $\mu$ , shear modulus  $G$  — kgf/cm<sup>2</sup>: core —  $\gamma = 0.0017$  kgf/cm<sup>3</sup>,  $\mu = 0.37$ ,  $G = 2780$  kgf/cm<sup>2</sup>; transition zones —  $\gamma = 0.00215$  kgf/cm<sup>3</sup>,  $\mu = 0.35$ ,  $G = 3500$  kgf/cm<sup>2</sup>; retaining prisms —  $\gamma = 0.0024$  kgf/cm<sup>3</sup>,  $\mu = 0.25$ ,  $G = 3210$  kgf/cm<sup>2</sup>; slope strengthening —  $\gamma = 0.0017$  kgf/cm<sup>3</sup>,  $\mu = 0.37$ ,  $G = 84000$  kgf/cm<sup>2</sup>;

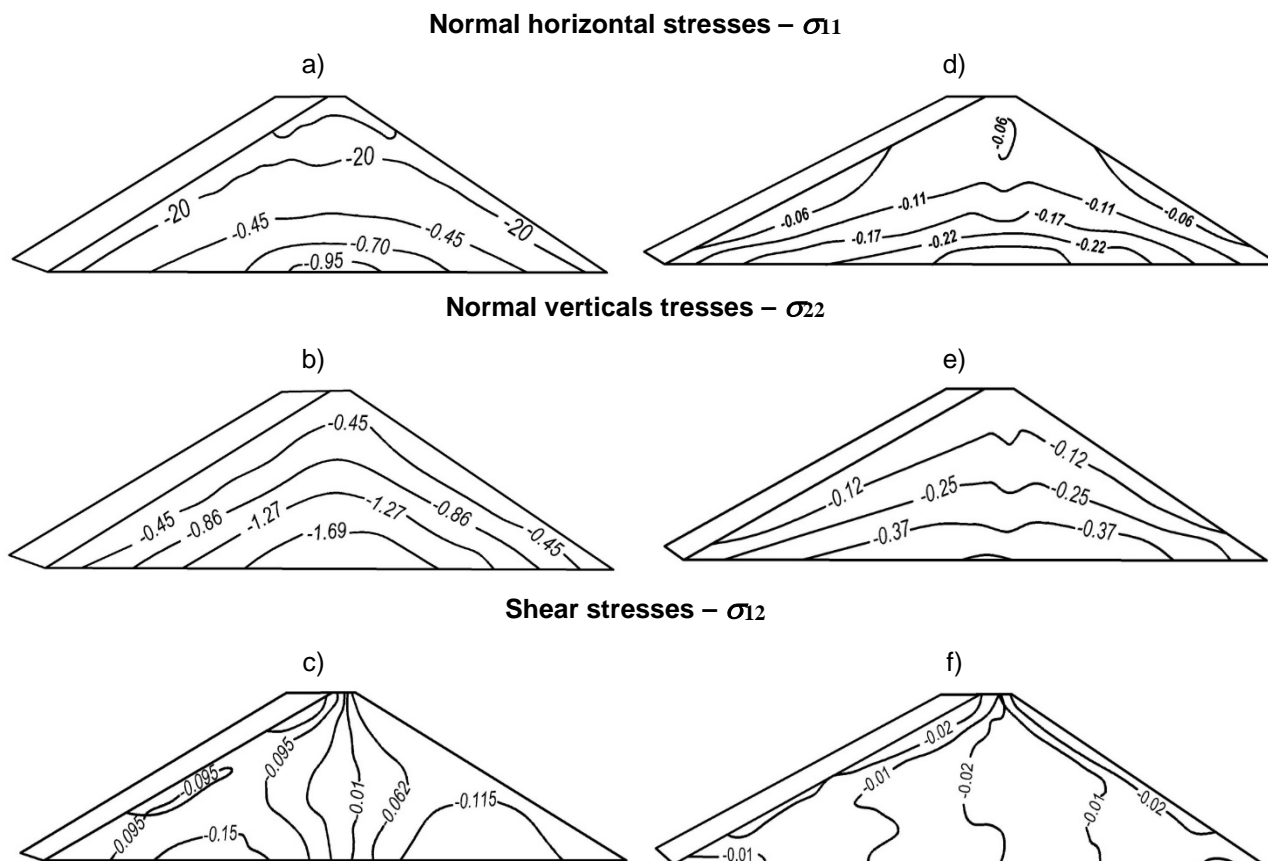
– **the Sokh earth dam:** height  $H = 87.3$  m; base width  $B_w = 530.0$  m; crest width  $b_{cr} = 10.0$  m; inclination coefficients of upstream and downstream slopes  $m_1 = 2.5$ ,  $m_2 = 2.2$ ; longitudinal dimensions: base length  $L_b = 21.0$  m, crest length  $L_{cr} = 48.75$  m. Mechanical characteristics of material of different sections of the dam are: volume weight —  $\gamma$ , Poisson's ratio —  $\mu$ , shear modulus —  $G$ : core —  $\gamma = 0.0017$  kgf/cm<sup>3</sup>,  $\mu = 0.40$ ,  $G = 2820$  kgf/cm<sup>2</sup>; retaining prisms —  $\gamma = 0.0021$  kgf/cm<sup>3</sup>,  $\mu = 0.35$ ,  $G = 3160$  kgf/cm<sup>2</sup>; slope strengthening —  $\gamma = 0.00185$  kgf/cm<sup>3</sup>,  $\mu = 0.35$ ,  $G = 3100$  kgf/cm<sup>2</sup>.

Figure 2 shows the isolines of the stress tensor components distribution for the central section of the Gissarak (Figure 2a, b, c) and Sokh (Figure 2d, e, f) dams under their own weight, obtained using a spatial model of structures. Stress magnitudes in all figures are indicated in MPa.

Coordinate axes shown in Figure 1 have the following directions: the axes  $x_1$  (horizontal) and  $x_2$  (vertical) are in the plane of the central section; the  $x_3$  axis is perpendicular to this plane.

Comparison of the results obtained using spatial model (Figure 2a, b, c) for the Gissarak dam with plane-deformable model shows almost the same pattern of stress distribution and their close values, i.e. under vertical gravitational load acting on the dam, the patterns of stress components distribution ( $\sigma_{11}$ ,  $\sigma_{12}$ ,  $\sigma_{22}$ ) in the central section of the dam are identical. The maximum values of horizontal  $\sigma_{11}$  and vertical  $\sigma_{22}$  stresses are observed at the bottom of the central — the highest — part of the dam (Figure 2a, b), and shear stresses  $\sigma_{12}$  — along the slopes (Figure 2c). At the same time, the distribution of stresses (Figure 2a, b, c) relative to the  $x_2$  axis is almost symmetrical, since the structure itself is also almost symmetrical with a slight difference in inclination coefficients of the slopes ( $m_1 = 2.2$ ,  $m_2 = 1.9$ ).

When obtaining results in the vicinity of the onshore zones of the structure in contact with mountain slopes, the condition of rigid fixation was set. The results obtained with spatial model have no plane analogues. Therefore, when calculating this zone, it is necessary to use a spatial model.



**Figure 2. Isolines of distribution of stress tensor components in the central section of the Gissarak (a, b, c) and the Sokh (d, e, f) dams obtained using spatial model under own weight.**

The ratios of geometric dimensions for the Gissarak dam (the length of the crest to the height —  $L_{cr}/H$ , the length of the base to the height —  $L_0/H$  and the width of the base to the height —  $B_w/H$ ) are:  $L_{cr}/H = 4.78$ ,  $L_0/H = 1.01$ ,  $B_w/H = 4.57$ , respectively. Therefore, the use of plane and spatial models for this dam gives almost identical results, so, it is possible to use plane models in static calculations of such dams.

Isolines of stress components distribution of the Sokh dam, obtained with spatial model (Figure 2d, e, f) shows a significant difference from the results obtained using plane-deformable models. The maximum values of normal horizontal stresses —  $\sigma_{11}$  and vertical stresses —  $\sigma_{22}$  (Figure 2c, d) occur at the bottom of the central — the highest — part of the dam, and shear stresses  $\sigma_{12}$  — along the slopes (Figure 2e) and in upstream retaining prism. The analysis of the results obtained shows that the calculation of this dam using a plane-deformable model does not provide necessary accuracy at estimating the stress state of the dams of such dimensions. This, apparently, is explained by the small ratios of the horizontal dimensions of the dam to its height, which are  $L_{cr}/H = 0.56$ ,  $L_0/H = 0.24$ ,  $B_w/H = 6.07$ . In this case, the structure is not extended and does not meet the condition to choose a model of plane strain. It should be considered as a three-dimensional body.

The analysis of stress state of the Gissarak dam under its own weight, by plane and spatial models, shows a qualitative and quantitative identity of stresses across the section.

Thus, the stress state of dams, geometrically similar to the Gissarak dam under gravitation forces, with satisfactory accuracy can be described by a model of plane strain. As for the evaluation of stresses in the plane of dam site, the study is possible with a spatial model, while the stress state of the Sokh dam and the ones similar in geometry, must be estimated with a spatial model.

Analysis of the stress state of the above dams has shown that the maximum shear stresses  $\sigma_{23}$  under vertical gravitational load arise along the lateral boundaries of the dam site and can cause shear and cracks at the sides. Vertical normal stresses  $\sigma_{22}$  occur in the central part of the dam base. Maximal (in the modulus) horizontal stresses  $\sigma_{11}$  appear at the base along the crest; their negative values in the central part indicate the compression of the central part under the crest, and positive values indicate the heaving of the lower side of the side slopes at the dam body settlement under its own weight. Positive values of horizontal stresses  $\sigma_{33}$  in the upper part of the sides indicate the possibility of fractures and cracks on the side slopes.

Thus, a spatial model allows estimating the stress-strain state not only in the cross section, but also in the dam junction with the gorge, where the danger zones appear.

Further, the possibility of using the models of plane strain for solving specific problems for real dams should be proved by studying the stress state, taking into account geometric dimensions, structural features and spatial factors of the structures under consideration.

### 3.2. Assessment of dynamic characteristics of a dam

Spatial eigenfrequencies and oscillation modes of earth dams considered above, have been studied further, taking into account the non-uniform structural features.

Figure 3 shows natural modes of oscillations of the Gissarak dam, corresponding to the eigenfrequencies obtained.

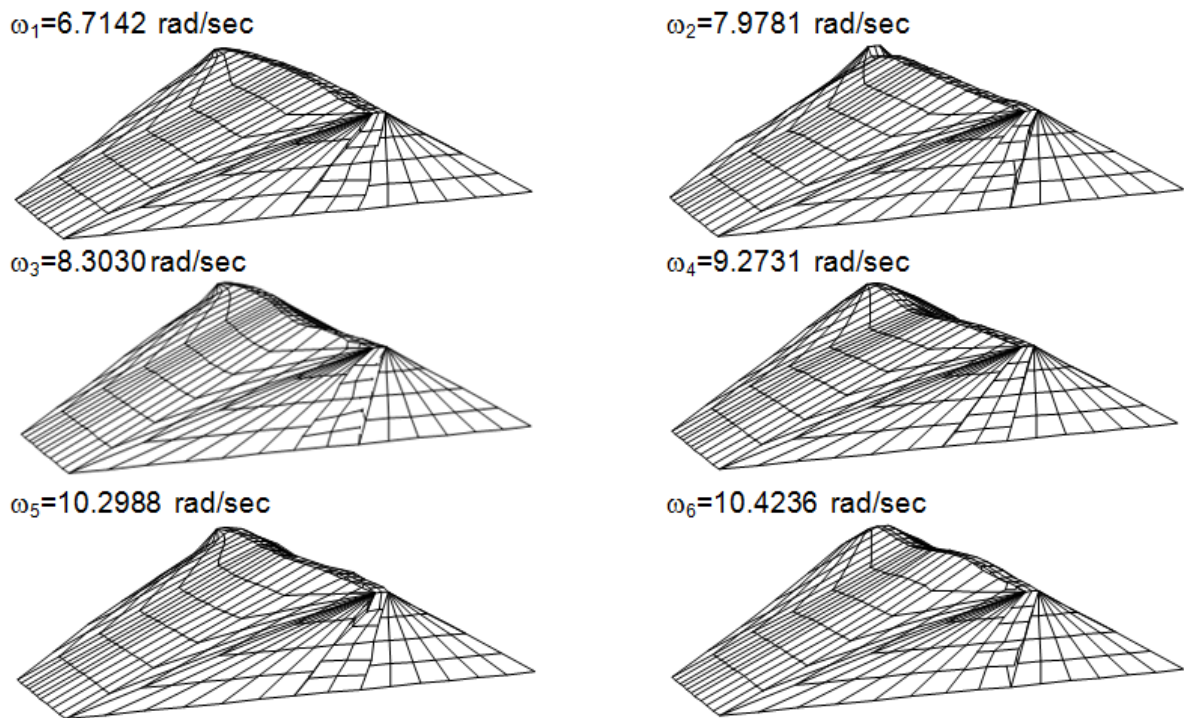


**Figure 3. Natural modes of oscillations of the Gissarak dam, obtained using the spatial model.**

An analysis of spatial eigenfrequencies distribution of the dam indicates the existence of more dense spectrum in a wider range, that is:  $\omega_1 = 6.7142$  rad/sec;  $\omega_2 = 7.9781$  rad/sec;  $\omega_3 = 8.3030$  rad/sec;  $\omega_4 = 9.2731$  rad/sec;  $\omega_5 = 10.2988$  rad/sec;  $\omega_6 = 10.4236$  rad/sec;  $\omega_7 = 10.8966$  rad/sec;  $\omega_8 = 11.0334$  rad/sec;  $\omega_9 = 11.1865$  rad/sec;  $\omega_{10} = 11.8026$  rad/sec;  $\omega_{11} = 12.0947$  rad/sec;  $\omega_{12} = 12.3554$  rad/sec;  $\omega_{13} = 12.4357$  rad/sec;  $\omega_{14} = 12.7373$  rad/sec;  $\omega_{15} = 12.9691$  rad/sec;  $\omega_{16} = 13.1138$  rad/sec;  $\omega_{17} = 13.3937$  rad/sec;  $\omega_{18} = 13.4548$  rad/sec;  $\omega_{19} = 14.2052$  rad/sec;  $\omega_{20} = 14.3668$  rad/sec.

This is explained by the fact that different models have different number of degrees of freedom, each of which makes an additional contribution to the spectrum of fundamental frequencies of natural vibrations. The frequencies obtained for this dam, reflecting shear and vertical oscillations of the central cross section, are almost identical in spatial and plane models.

For a spatial model, the shift of the central cross section is the bending of the longitudinal axis of the model ( $x_3$ ). Subsequent oscillation frequencies of spatial model are the highest forms of bending of longitudinal axis ( $x_3$ ), not considered by plane model. Therefore, the frequency spectrum in spatial case is denser, since between the main frequencies there are intermediate ones, reflecting higher modes of bending vibrations of the longitudinal axis of model ( $x_3$ ).

As for the pattern of oscillations modes, we can note the following. Fundamental modes, reflected by spatial and plane models, are: the shear of the central section (the first mode); vertical displacements of the central section (for the plane model this is the second mode); complex deformations of the central section slope (for the plane model, this is the third and subsequent modes). For a spatial model, all modes, including mentioned above, are accompanied by a bending in longitudinal axis of the model (a crest) along the horizontal and vertical axes. For the above modes – these are the main modes of bending, for the subsequent ones – this is a bending with nodes. The bending of the crest (main one and with nodes) is accompanied by complex

deformations of the structure slopes, and not only in their central part (central section), but also over the entire surface. These additional modes, and corresponding frequencies, are not reflected by plane model but fully reflected by spatial one. However, its use, as noted above, is quite laborious. The choice of a particular model when considering specific structures should be substantiated not only by the geometry of the object, but also by the estimated load, its direction and frequency spectrum, which can cause structure oscillations not only of fundamental mode but also in higher modes not reflected by plane model [32, 33].

The question of how great the longitudinal strain along the axis ( $x_3$ ) is, remains the priority, since the validity of using a plane model depends on it. If longitudinal displacements under a certain effect are large, then in this case the use of a plane model is unacceptable, since the possibility of transverse cracks formation is not taken into account.

To answer the question, it is necessary to consider the problem of unsteady forced oscillations of the dam under different (in directions) kinematic effects using plane and spatial models and to compare the results obtained.

#### 4. Conclusions

1. A mathematical model, methods and algorithm for estimating the stress-strain state and dynamic characteristics of inhomogeneous spatial systems using a spatial model are presented.

2. The stress-strain state and dynamic characteristics of two different earth dams using three-dimensional models is estimated taking into account actual geometric dimensions and inhomogeneous features of a structure.

3. An analysis of obtained results on the stress-strain state assessment of earth dams with spatial models has shown that for some types of dams it is possible to use plane strained models to obtain results with acceptable accuracy. Nevertheless, in each case, for specific structures, in assessing the stress state of dams, it is necessary to check the stress state using a spatial model.

4. The use of spatial model makes it possible to identify dangerous zones of the structure (where higher stresses occur compared to other areas), which could not be identified using a plane model.

5. Analysis of dynamic characteristics of dams with a plane model has revealed a rather dense spectrum of spatial eigenfrequencies and the identity of fundamental modes of natural oscillations over the cross section of a dam.

6. The first three fundamental modes for the Gissarak dam are: the displacement of the central section (the first mode); vertical compression of the section (the second mode); complex deformations of the slopes of central section (the third mode), etc.

7. For a spatial model, all modes are accompanied by a bending in longitudinal axis (a crest) in different planes. The bending of the crest is accompanied by complex deformations of the structure slopes, not reflected by plane model. The eigenfrequencies corresponding to these modes make an additional contribution to the frequency spectrum, condensing and expanding its range.

#### References

- Zaretsky, Yu.K., Lombardo, V.N. Statika i dinamika gruntovykh plotin [Statics and dynamics of earth dams]. Moscow: Energoizdat. 1983. 256 p. (rus)
- Krasnikov, N.D. Seysmostoykost gidrotekhnicheskikh sooruzheniy iz gruntovykh materialov [Seismic stability of hydrotechnical structures built of earth material]. Moscow: Energoizdat. 1981. 240 p. (rus)
- Lyakhter, V.M., Ivashenko, I.N. Seysmostoykost gruntovykh plotin [Earthquake resistance of earth dams]. Moscow: Nauka, 1986. 233 p. (rus)
- Mirsaidov, M.M., Sultanov, T.Z. Theory and methods of strength assessment of earth dams. Lambert Academic Publishing. Saarbrücken/Germany, 2015. 341 p.
- Akhmedov, M.A., Salyamova, K.J. Analiz i otsenka povrezhdeniy gidrotekhnicheskikh sooruzheniy [Analysis and assessment of damage to hydraulic structures]. Tashkent: Fan va texnologiya. 2016. 160 p. (rus)
- Sultanov, T., Yuldoshev, B., Toshmatov, E., Yarashov, J., Ergashev, R., Mirsaidov, M. Strength assessment of earth dams. MATEC Web of Conferences. 2019. Vol. 265. No. 04015.
- Mirsaidov, M.M., Sultanov, T.Z., Abdikarimov, R.A., Ishmatov, A.N., Yuldoshev, B.Sh., Toshmatov, E.S., Jurayev, D.P. Strength parameters of earth dams under various dynamic effects. Magazine of Civil Engineering. 2018. No. 77(1). Pp. 101–111. doi: 10.18720/MCE.77.9
- Mirsaidov, M.M., Sultanov, T.Z. Assessment of stress-strain state of earth dams with allowance for non-linear strain of material and large strains. Magazine of Civil Engineering. 2014. 49(5). Pp. 73–82. (rus). DOI: 10.5862/MCE.49.8
- Sultanov, T.Z., Khodzhaev, D.A., Mirsaidov, M.M. The assessment of dynamic behavior of heterogeneous systems taking into account non-linear viscoelastic properties of soil. Magazine of Civil Engineering. 2014. 45(1). Pp. 80–89. (rus). DOI: 10.5862/MCE.45.9
- Pinyol, N.M., Alonso, E.E. Earth dam, spatial model, stress-strain state, dynamic characteristic, natural frequency, modes of oscillations. International Journal of Civil Engineering. 2019. Vol. 17. No. 4. Pp. 501–513.
- Nariman, N.A., Lahmer, T., Karampour, P. Uncertainty quantification of stability and damage detection parameters of coupled hydrodynamic-ground motion in concrete gravity dams. Frontiers of Structural and Civil Engineering. 2019. Vol. 13. No. 2. Pp. 303–323.

12. Li, Y., Li, K., Wen, L., Li, B., Liu, Y. Safety standard for slopes of ultra-high earth and rock-fill dams in china based on reliability analysis. *International Journal of Civil Engineering*. 2019. Vol. 17. Pp. 1–16.
13. Fu, Z., Chen, S., Li, G. Hydrodynamic pressure on concrete face rockfill dams subjected to earthquakes. *Journal of Hydrodynamics*. 2019. Vol. 31. No. 1. Pp. 152–168.
14. Wang, M., Chen, J., Xiao, W. Experimental and numerical comparative study on gravity dam-reservoir coupling system. *KSCE Journal of Civil Engineering*. 2018. Vol. 22. No. 10. Pp. 3980–3987.
15. Kong, X., Liu, J., Zou, D. Numerical simulation of the separation between concrete face slabs and cushion layer of Zipingpu dam during the Wenchuan earthquake. *Science China Technological Sciences*. 2016. Vol. 59. No. 4. Pp. 531–539.
16. Esmaeilzadeh, M., Talkhablou, M., Ganjalipour, K. Arching parametric study on earth dams by numerical modeling. *Indian Geotechnical Journal*. 2018. Vol. 48. No. 4. Pp. 728–745.
17. Alonso, E.E., Cardoso, R. Behavior of materials for earth and rockfill dams. *Frontiers of Structural and Civil Engineering*. 2010. Vol. 4. No. 1. Pp. 1–39.
18. Abarin, A.M. Seysmostoykost gruntovykh plotin (prostranstvennaya postanovka) [Seismic resistance of earth dams (spatial statement)]. Diss ... Cand. techn. sciences: 05.23.07. Moscow, 1999. 228 p. (rus)
19. Tao Tuan An. Prostranstvennoye napryazhenno-deformirovannoye sostoyaniye gruntovykh plotin s tonkim protivofiltratsionnym elementom [The spatial stress-strain state of earth dams with a thin anti-filtration element]. Diss. ... Cand. techn. sciences: 05.23.07. Moscow, 2002. 259 p. (rus)
20. Orekhov, V.V. Prognoznoye matematicheskoye modelirovaniye napryazhenno-deformirovannogo sostoyaniya gruntovykh plotin i skalnykh massivov [Predictive mathematical modeling of the stress-strain state of earth dams and rock massifs]. Dis. ... Doctor of techn. sciences: 05.23.07. Moscow, 2003. 306 p. (rus)
21. Nguyen Phuong Lam. Napryazhenno-deformirovannoye sostoyaniye kamenno-zemlyanykh plotin pri seysmicheskikh vozdeystviyakh [Stress-strain state of stone-earth dams under seismic effects]. Diss. ... Cand. tech. sciences: 05.23.07. Moscow, 2010. 183 p. (rus)
22. Bestuzheva, A.S., Nguyen Phuong Lam. Dinamicheskii i spektralnyy metody opredeleniya seysmicheskoy nagruzki, deystvuyushchey na sooruzheniye pri zemletryasenii [Dynamic and spectral methods for determining the seismic load acting on the structure during an earthquake]. *Vestnik MGSU*. 2010. No. 1. Pp. 155–168. (rus)
23. Rasskazov, L.N., Bestuzheva, A.S., Nguyen Phuong Lam. Uchet «begushchey volny» v prostranstvennykh zadachakh seysmoustoychivosti gruntovykh plotin [Accounting for the "traveling wave" in the spatial problems of seismic stability of earth dams]. *Hydrotechnical Engineering*. 2010. No. 11. Pp. 47–53. (rus)
24. Rasskazov, L.N., Bestuzheva, A.S., Nguyen Phuong Lam. Seysmostoykost gruntovykh plotin v prostranstvennoy postanovke [Earthquake resistance of earth dams in spatial statement] [Online]. 2010. URL: [www.mirexpo.ru/exhibitions/gidrostroy/files/gidrostroymgsu.doc](http://www.mirexpo.ru/exhibitions/gidrostroy/files/gidrostroymgsu.doc) (rus)
25. Natarius, Ya.I. Uchet ogranichennosti dliny plotin iz gruntovykh materialov v raschetakh ikh seysmostoykosti [Account of the limited length of dams built of earth material in the calculations of their seismic resistance]. *Hydrotechnical Engineering*. 1978. No. 10. Pp. 30–33. (rus)
26. Natarius, Ya.I. Povysheniye seysmostoykosti plotin iz gruntovykh materialov [Increase of seismic resistance of dams built of earth material]. Moscow: Energoatomizdat, 1984. 88 p. (rus)
27. Koltunov, M.A., Kravchuk, A.S., Mayboroda, V.P. Prikladnaya mekhanika deformiruyemogo tverdogo tela [Applied mechanics of a deformable rigid body]. Moscow: High School, 1983. 349 p. (rus)
28. Bathe, K.-J., Wilson, E.L. Numerical methods in finite element analysis. Prentice-Hall, 1976. 544 p.
29. Berezin, I.S., Zhidkov, N.P. Metody vychisleniy [Calculation methods]. Moscow: Nauka, 1969. Vol. 2. 640 p. (rus)
30. Fadeev, D.K., Fadeeva, V.N. Vychislitelnyye metody lineynoy algebry [Computational methods of linear algebra]. Moscow: Fizmatgiz, 1960. 655 p. (rus)
31. Muller, D.E. A method for solving algebraic equations using an automatic computer. *Mathematical Table and Other Aids to Computation*. 1956. Vol. 10. No. 3. Pp. 208–215.
32. Khudayarov, B.A., Turaev, F.Z. Mathematical simulation of oscillations of viscoelastic pipelines conveying fluid. *Applied Mathematical Modeling*. 2019. Vol. 66. Pp. 662–679.
33. Khudayarov, B.A., Turaev, F.Z. Nonlinear supersonic flutter for the viscoelastic orthotropic cylindrical shells in supersonic flow. *Aerospace Science and Technology*. 2019. Vol. 84. Pp. 120–130.
34. Rekach, V.G. Rukovodstvo k resheniyu zadach po teorii uprugosti [Guide to solving problems in the theory of elasticity]. Moscow: High School. 1977. 215 p. (rus)
35. *Vibrasii v tekhnike [Vibration in technology]: a Handbook in 6 vol.* Moscow: Mashinostroyeni, 1978. Vol. 1. Kolebaniya lineynykh sistem [Oscillations of linear systems]. 1978. 352 p. (rus)

### **Contacts:**

*Mirziyod Mirsaidov, +7(987)2370981; эл. почта: theormir@mail.ru*

*Elyor Toshmatov, +7(987)2372267; эл. почта: toshmatov.elyor@bk.ru*



DOI: 10.18720/MCE.89.1

## Пространственное напряженное состояние и динамические характеристики грунтовых плотин

**М.М. Мирсаидов\*, Э.С. Тошматов**

*Ташкентский институт инженеров ирригации и механизации сельского хозяйства,  
г. Ташкент, Узбекистан*

\* E-mail: [theormir@mail.ru](mailto:theormir@mail.ru)

**Ключевые слова:** пространственная система, трехмерная (пространственная) модель, неоднородность, грунтовая плотина, напряженно-деформированное состояние, динамическая характеристика, собственная частота и форма колебаний

**Аннотация.** Оценка прочности грунтовых плотин, в основном, производится с использованием плоской расчетной схемы, которая не всегда приводит к адекватным результатам. В данной работе предлагается провести оценку напряженного состояния грунтовых плотин в трехмерной постановке. Следовательно, для оценки напряженно-деформированного состояния и динамических характеристик грунтовых плотин строятся соответствующие математические модели, методика и алгоритм. В основу разработанной методики при решении конкретных задач для пространственного сооружения заложен метод конечных элементов, метод Гаусса (или метод квадратного корня) и метод Мюллера. Достоверность полученных результатов проверена решением ряда тестовых задач. С помощью разработанной методики исследованы напряженно-деформированное состояние и динамические характеристики Гиссаракской и Сохской грунтовых плотин. На основе результатов исследования показано, что для некоторых типов грунтовых плотин, при предварительной оценке напряженного состояния и динамических характеристик сооружений, возможно использование плоско-деформируемой модели расчета. Проведенные исследования показали, что для обеспечения требуемой точности при оценке напряженного состояния и динамических характеристик сложных неоднородных пространственных систем (т.е. грунтовых плотин) необходимо проводить расчеты с использованием трехмерной модели. Полученные в результате исследований данные позволили выявить некоторые особенности напряженного состояния в пространственном случае, указывающие на возникающие опасные участки с наибольшими напряжениями, а также изучить характер собственных колебаний, которые невозможно описать использованием плоской модели.

### Литература

1. Зарецкий Ю.К., Ломбардо В.Н. Статика и динамика грунтовых плотин. М.: Энергоиздат, 1983. 256 с.
2. Красников Н.Д. Сейсмостойкость гидротехнических сооружений из грунтовых материалов. М.: Энергоиздат, 1981. 240 с.
3. Ляхтер В.М., Ивашенко И.Н. Сейсмостойкость грунтовых плотин. М.: Наука, 1986. 233 с.
4. Mirsaidov M.M., Sultanov T.Z. Theory and methods of strength assessment of earths dams. Lambert Academic Publishing, Saarbrucken/Germany, 2015. 341 p.
5. Ахмедов М.А., Саяямова К.Дж. Анализ и оценка повреждений гидротехнических сооружений. Ташкент: Фан ва технология, 2016. 160 с.
6. Sultanov T., Yuldoshev B., Toshmatov E., Yarashov J., Ergashev R., Mirsaidov M. Strength assessment of earth dams // MATEC Web of Conferences. 2019. Vol. 265. No. 04015.
7. Мирсаидов М.М., Султанов Т.З., Абдикаримов Р.А., Ишматов А.Н., Юлдошев Б.Ш., Тошматов Э.С., Жураев Д.П. Прочностные параметры грунтовых плотин при различных динамических воздействиях // Инженерно-строительный журнал. 2018. № 1(77). С. 101–111. doi: 10.18720/MCE.77.9
8. Мирсаидов М.М., Султанов Т.З. Оценка напряженно-деформированного состояния грунтовых плотин с учетом нелинейного деформирования материала и конечных деформаций // Инженерно-строительный журнал. 2014. № 5(49). С. 73–82. DOI: 10.5862/MCE.49.8
9. Султанов Т.З., Ходжаев Д.А., Мирсаидов М.М. Оценка динамического поведения неоднородных систем с учетом нелинейно-вязкоупругих свойств грунта // Инженерно-строительный журнал. 2014. №1(45). С. 80–89. DOI: 10.5862/MCE.45.9
10. Pinyol N.M., Alonso E.E. Earth dam, spatial model, stress-strain state, dynamic characteristic, natural frequency, modes of oscillations // International Journal of Civil Engineering. 2019. Vol. 17. No. 4. Pp. 501–513.

11. Nariman N.A., Lahmer T., Karampour P. Uncertainty quantification of stability and damage detection parameters of coupled hydrodynamic-ground motion in concrete gravity dams // *Frontiers of Structural and Civil Engineering*. 2019. Vol. 13. No. 2. Pp. 303–323.
12. Li Y., Li K., Wen L., Li B., Liu Y. Safety standard for slopes of ultra-high earth and rock-fill dams in china based on reliability analysis // *International Journal of Civil Engineering*. 2019. Vol. 17. Pp. 1–16.
13. Fu Z., Chen S., Li G. Hydrodynamic pressure on concrete face rockfill dams subjected to earthquakes // *Journal of Hydrodynamics*. 2019. Vol. 31. No. 1. Pp. 152–168.
14. Wang M., Chen J., Xiao W. Experimental and numerical comparative study on gravity dam-reservoir coupling system // *KSCE Journal of Civil Engineering*. 2018. Vol. 22. No. 10. Pp. 3980–3987.
15. Kong X., Liu J., Zou D. Numerical simulation of the separation between concrete face slabs and cushion layer of Zipingpu dam during the Wenchuan earthquake // *Science China Technological Sciences*. 2016. Vol. 59. No. 4. Pp. 531–539.
16. Esmaeilzadeh M., Talkhablou M., Ganjalipour K. Arching parametric study on earth dams by numerical modeling // *Indian Geotechnical Journal*. 2018. Vol. 48. No. 4. Pp. 728–745.
17. Alonso E.E., Cardoso R. Behavior of materials for earth and rockfill dams // *Frontiers of Structural and Civil Engineering*. 2010. Vol. 4. No. 1. Pp. 1–39.
18. Абарин А.М. Сейсмостойкость грунтовых плотин (пространственная постановка): дис... канд. техн. наук: 05.23.07. М., 1999. 228 с.
19. Дао Туан Ань. Пространственное напряжённо-деформированное состояние грунтовых плотин с тонким противодиффузионным элементом: дис. ... канд. техн. наук: 05.23.07. М., 2002. 259 с.
20. Орехов В.В. Прогнозное математическое моделирование напряженно-деформированного состояния грунтовых плотин и скальных массивов: дис. ... д-ра техн. наук: 05.23.07. М., 2003. 306 с.
21. Нгуен Фьонг Лам. Напряженно-деформированное состояние каменно-земляных плотин при сейсмических воздействиях: дис. ... канд. техн. наук: 05.23.07. М., 2010. 183 с.
22. Бестужева А.С., Нгуен Фьонг Лам. Динамический и спектральный методы определения сейсмической нагрузки, действующей на сооружение при землетрясении // *Вестник МГСУ*. 2000. № 1. С. 155–168.
23. Рассказов Л.Н., Бестужева А.С., Нгуен Фьонг Лам. Учет «бегущей волны» в пространственных задачах сейсмоустойчивости грунтовых плотин // *Гидротехническое строительство*. 2000. № 11. С. 47–53.
24. Рассказов Л.Н., Бестужева А.С., Нгуен Фьонг Лам. Сейсмостойкость грунтовых плотин в пространственной постановке [Электронный ресурс]. 2010. URL: [www.mirexpo.ru/exhibitions/gidrostroy/files/gidrostroymgisu.doc](http://www.mirexpo.ru/exhibitions/gidrostroy/files/gidrostroymgisu.doc)
25. Натариус Я.И. Учет ограниченности длины плотин из грунтовых материалов в расчетах их сейсмостойкости // *Гидротехническое строительство*. 1978. № 10. С. 30–33.
26. Натариус Я.И. Повышение сейсмостойкости плотин из грунтовых материалов. М.: Энергоатомиздат, 1984. 88 с.
27. Колтунов М.А., Кравчук А.С., Майборода В.П. Прикладная механика деформируемого твердого тела. М.: Высшая школа, 1983. 349 с.
28. Бате К., Вилсон Е. Численные методы анализа и метод конечных элементов. М.: Стройиздат, 1982. 448 с.
29. Березин И.С., Жидков Н.П. Методы вычислений. М.: Наука, 1969. Т. 2. 640 с.
30. Фадеев Д.К., Фадеева В.Н. Вычислительные методы линейной алгебры. М.: Физматгиз, 1960. 655 с.
31. Muller D.E. A method for solving algebraic equations using an automatic computer // *Mathematical Table and Other Aids to Computation*. 1956. Vol. 10. No. 3. Pp. 208–215.
32. Khudayarov B.A., Turaev F.Z. Mathematical simulation of oscillations of viscoelastic pipelines conveying fluid // *Applied Mathematical Modeling*. 2019. Vol. 66. Pp. 662–679.
33. Khudayarov B.A., Turaev F.Z. Nonlinear supersonic flutter for the viscoelastic orthotropic cylindrical shells in supersonic flow // *Aerospace Science and Technology*. 2019. Vol. 84. Pp. 120–130.
34. Рекач В.Г. Руководство к решению задач по теории упругости. М.: Высшая школа, 1977. 215 с.
35. Вибрация в технике: Справочник. В 6-ти т. М.: Машиностроении, 1978. Т. 1. Колебания линейных систем. 1978. 352 с.

#### **Контактные данные:**

*Мирзиёд Мирсаидович Мирсаидов, +7(987)2370981; эл. почта: [theormir@mail.ru](mailto:theormir@mail.ru)*

*Элёр Собирович Тошматов, +7(987)2372267; эл. почта: [toshmatov.elyor@bk.ru](mailto:toshmatov.elyor@bk.ru)*



DOI: 10.18720/MCE.89.2

## Clay-cement-concrete diaphragm — justifying calculation for new-built constructions

**R.N. Orishchuk**

*B.E. Vedeneev VNIIG, JSC, St. Petersburg, Russia*

**Keywords:** embankment dam, clay-cement concrete diaphragm, bored-secant piles, strain-stress state, soil/structure interaction, numerical modeling, cut-of wall, strength

**Abstract.** Due to the observed improvement of machines and mechanisms and the process equipment thereof used during the construction of clay-cement concrete slurry walls by means of bored-secant piles, the author proposes to extend the range of considered designs of impervious elements of embankment dams by adding modifications with an arch diaphragm and an inclined diaphragm. Performed surveys and comparisons with the traditional design (vertical wall) allowed to identify the main trends of the influence of using the effect of clay-cement concrete diaphragms inclination and the arch effect on the change in the strain-stress state of the embankment dam — diaphragm system. Consideration of the clay-cement concrete diaphragm designs proposed by the author in designing embankment dams will allow extending the range of possible application of this technical solution. It was established that there is a possibility to optimize the existing technical solutions for the clay-cement concrete diaphragm embankment dams if they are designed with due consideration of not only the assignment of clay-cement concrete strength and strain-stress properties, but also taking into account the change in configuration of the diaphragm itself.

### 1. Introduction

The distinguishing features of hydraulic power facilities defined by high investment costs of construction have justified the need for research aimed at finding the new and improving the existing technical and process solutions for the construction of hydraulic power facilities, ensuring application of modern machines and mechanisms and use of new materials.

One of the ways to reduce the time for a dam construction is to replace the classic impervious element, for example, an asphalt-concrete one, with a clay-cement-concrete cut-off wall constructed by means of using bored-secant piles.

Paragraph [1–5] contains data on hydraulic engineering structures with thin impervious elements of various designs built around the globe, including those built using clay-cement concrete; the same paragraph also specifies the peculiarities of operation of such structures.

Surveys and works related to the above-mentioned field have also been carried out in Russia. Paragraph [6–10] contains a description and analysis of the Russian experience of building an impervious element for embankment dams represented by clay-cement-concrete diaphragms in the course of design, repair and construction of hydraulic structures.

In Russia, this technical solution was first applied in 2017 during the construction of the Nizhne-Bureyskaya HPP located in Amurskaya Oblast. The structures of the Nizhne-Bureyskaya HPP waterfront include: the spillway, the HPP building, the left-bank embankment dam with the length of 400.0 m and maximum height of 38.0 m. The embankment dam features an impervious element, which is a thin clay-cement-concrete diaphragm created after the erection of the embankment dam body to the design elevations during one construction season.

---

Orishchuk, R.N. Clay-cement-concrete diaphragm – justifying calculation for new-built constructions. Magazine of Civil Engineering. 2019. 89(5). Pp. 16–25. DOI: 10.18720/MCE.89.2.

Орищук Р.Н. Глиноцементобетонная диафрагма, расчётное обоснование новых конструкций // Инженерно-строительный журнал. 2019. № 5(89). С. 16–25. DOI: 10.18720/MCE.89.2.



This open access article is licensed under CC BY 4.0 (<https://creativecommons.org/licenses/by/4.0/>)

This solution was applied at hydraulic power facilities with such height parameters and productive head pressures for the first time in the world (Figure 1).

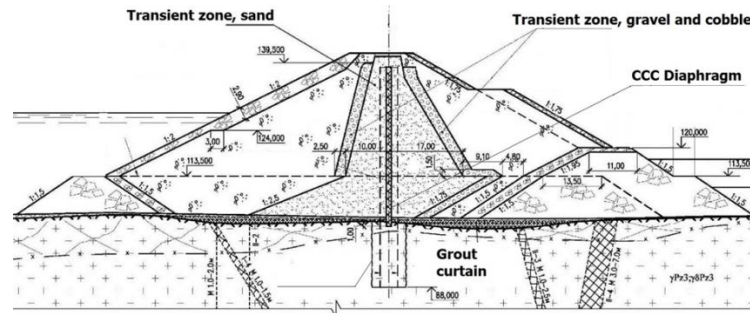


**Figure 1. Cross section of Nizhne-Bureyskaya HPP embankment dam.**

The experience of construction and operation of the Nizhne-Bureyskaya HPP embankment dam has demonstrated high efficiency of the proposed technical solution. With a comparable cost of construction of an embankment dam with an option involving core erection using local cohesive soils, the implemented technical solution allowed to reduce the dam construction time from 22 to 14 months. The scientific and technical justification of reliability and safety of such impervious elements and the development of design and process solutions was performed by the JSC "Vedeneev VNIIG" and JSC "Lenhydroproject".

Previously at the Gotsatlinskaya HPP located in the Republic of Dagestan (Russian Federation), during the preliminary design stage a solution involving the installation of an impervious clay-cement concrete diaphragm using the bored-secant piles method was considered as one of the possible technical solutions for the installation of an impervious element in the embankment dam body (Figure 2).

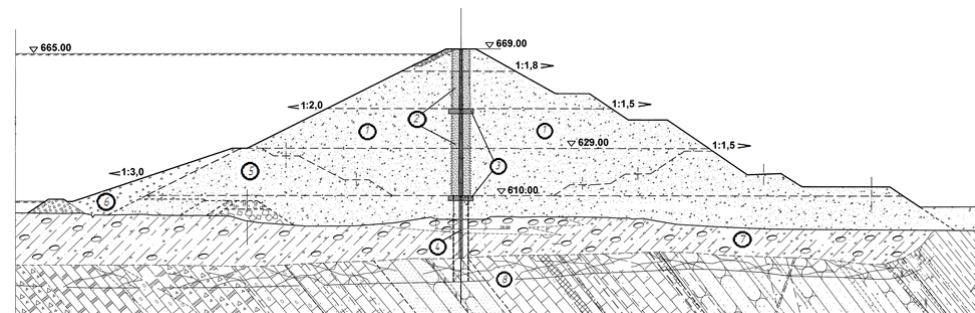


**Figure 2. Design cross section of Gotsatlinskaya HPP embankment dam: 1 — downstream and upstream shells; 2 — stages (layers) of diaphragm construction; 3 — joint of connection between diaphragm layers and foundation (foreshaft); 4 — impervious element; 5 — upstream cofferdam; 6 — impervious screen; 7 — alluvial base; 8 — bedrock base.**

The set of calculations performed in ABAQUS 2016 specialized software aimed at justification of the possibility of constructing a clay-cement-concrete diaphragm embankment dam by means of bored-secant piles method using the Gotsatlinskaya HPP as an example has shown that the calculated diaphragm compressive stresses are close to the maximum allowed values for clay-cement concrete and amount approximately to 1.65–1.80 MPa. In addition to that, calculations revealed extensive areas of diaphragm tensile stresses confined to the side abutments with maximum tensile stresses in the crest part of the dam equal to 0.33 MPa (0.21 MPa [11] along the board).

Tensile stresses significantly reduce the reliability of WTE operation, especially for the clay-cement concrete diaphragm constructed by means of bored-secant piles which is characterized by vertical split seams presence; movement along such seams can lead to their opening and blowout piping, both along the seams and in contact with the side abutments. Due to the lack of scientific and technical justification of the possibility of reliable clay-cement-concrete diaphragms operation at the start of the dam body backfill (2012–2013) and taking into account the high seismic activity of the hydraulic power station area, a decision was taken to abandon the clay-cement-concrete diaphragms design in favor of the classical option involving an impervious element made of asphalt concrete.

At present, considering the accumulated practical experience gained during Nizhne-Bureyskaya HPP construction as well as the performed set of research works aimed at finding solutions to ensure reliable operation of this type of impervious element, it can be stated that its widespread use is justified (if the relevant justification is available) in the design of an embankment dam with the height of up to 100 m. It should be noted that the equipment that has appeared in the arsenal of construction companies (inclined drilling machines) as well as the accumulated practical experience could significantly extend the range of designs available with this type of an impervious element, including construction of diaphragms in the form of arches or erection of flat diaphragms at predetermined slope angles [12].

No solutions similar to the one proposed by the author exist anywhere else in the world. The survey results contained in this article may allow for using them both for structures elaboration at the design stage and for construction of embankment dams not only in Russia but also when implementing hydraulic engineering projects worldwide.

Based on the necessity of ensuring the required embankment dams reliability and safety level with the proposed impervious element type and the reduction of tensile stresses risk in the diaphragm body, the author has carried out a set of calculations in order to assess the change in the strain-stress state of the diaphragm when its configuration is changed.

This survey was aimed at analyzing the influence of changes in the configuration of the clay-cement-concrete diaphragm of an embankment dam on its strain-stress state.

The following tasks were set and then solved in order to achieve this goal:

1. To elaborate a numerical model of an embankment dam (taking as an example the Gotsatlinskaya HPP embankment dam site) based on the ABAQUS 2016 finite-element software package;
2. To elaborate a plan for calculation experiments and perform the relative calculations regarding the two possible technical solutions aiming at establishing the conditions for a more favorable strain-stress state of clay-cement-concrete diaphragms: the option with an arch outline diaphragm and the other option with an inclined diaphragm.
3. To compare the results of the strain-stress state calculations performed with the results of previous calculations of the strain-stress state of an embankment dam having a traditional vertical clay-cement-concrete diaphragm regarding the values of horizontal displacement, maximum settlement, tensile stress and compressive stress.

## 2. Methods

The author has elaborated a numerical model of an embankment dam (taking as an example the Gotsatlinskaya HPP embankment dam site) based on the ABAQUS 2016 finite-element software package; all the embankment dam material properties and clay-cement concrete properties were assumed to be identical in order to allow for a correct comparison of calculation results. The diameter of the bored-secant piles of the clay-cement-concrete diaphragm was assumed as 1.2 m for all options.

A model of a dam with an inclined flat clay-cement-concrete diaphragm with a vertical deviation of  $15^\circ$  towards the tail race is shown in Figure 3a. A simulation model of an embankment dam with a vertical arch clay-cement-concrete diaphragm is shown in Figure 3b. The dam body is represented by a part of an arch-shaped shell with the radial section coinciding with the dam cross section. In this case, the clay-cement-concrete diaphragm is an arch integrated into the side abutments with a horizontal curve radius of 90 m.

The following materials were used in the numerical simulation: [12–18].

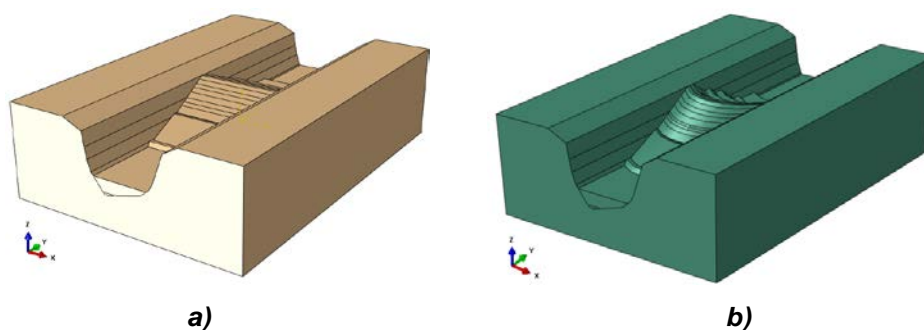


**Figure 3. Overall view of «Gotsatlinskaya HPP — foundation system» three-dimensional model: a) a flat vertical or inclined diaphragm dam; b) an arch diaphragm dam.**

A three-dimensional model of the studied impervious elements is shown in Figure 4.

Calculation experiments planning was performed with consideration of such factors as compliance with the absolutely identical boundary conditions in order to ensure the possibility of comparing the obtained results and with two options considered according to the conditions for filling the reservoir and the possibilities of establishing the conditions for a more favorable strain-stress state of clay-cement-concrete diaphragms for the proposed options with an arch outline diaphragm and the other option with an inclined diaphragm.

Two reservoir filling cases were considered for the options of a soil embankment with various clay-cement-concrete diaphragms:

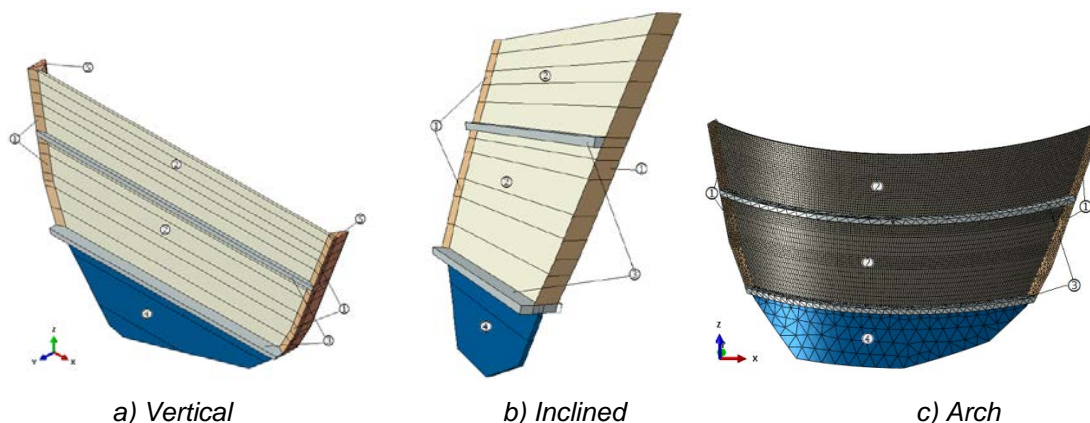


**Figure 4. Three-dimensional model of dam non-soil impervious elements:**

**1 — CCC cushions; 2 — diaphragm layers; 3 — foreshaft; 4 — cut-off wall; 5 — rock abutment.**

First option includes filling the reservoir in two steps:

A) After the construction of the upstream cofferdam and the cut-off wall, the water level in the reservoir rises from the elevation of 602.0 to 628.0;

B) After the construction is complete, the water in the reservoir rises from the elevation of 628.0 to the elevation of 665.0, which corresponds to the normal flood control storage level.

Second option includes filling the reservoir in three steps:

A) After the construction of the upstream cofferdam and the cut-off wall, the water level in the reservoir rises from the elevation of 602.0 to 628.0;

B) After the installation of the first diaphragm layer, the reservoir is filled from the elevation of 628.0 to the intermediate elevation of 643.0;

C) After the construction is complete, the level rises from the elevation of 643.0 to the flood control storage level of 665.0.

The consolidated plan developed for calculating strain-stress state of the options is presented in Table 1.

**Table 1. Plan of Options for Calculating Strain-Stress State of Gotsatlinskaya HPP Embankment Dam Site with a Flat Vertical, Flat Inclined and Arch Clay-Cement-Concrete Diaphragm.**

Number of layers	Number of filling stages	Clay-cement-concrete diaphragm design		
		Flat vertical	Flat inclined	Arch vertical
One layer of bored-secant clay-cement-concrete piles	3	+	–	–
Two layers of bored-secant clay-cement-concrete piles	2	+	+	+
	3	+	+	+

### 3. Results and Discussion

The results have been compared with the results of calculations for the vertical clay-cement-concrete diaphragm previously performed by the author and presented in [11]. The following parameters describing the clay-cement-concrete diaphragm working conditions for all the options considered have been compared: values of horizontal displacement, maximum settlement, tensile stress and compressive stress.

The results of diaphragm displacement calculation for the considered configurations for the two-layer diaphragm options with 2 and 3 stages of reservoir filling are given in Table 2.

**Table 2. Displacement Calculation Results for an Embankment Dam with a Flat Vertical, Flat Inclined and Arch Vertical clay-cement-concrete diaphragm.**

Number of layers	Reservoir filling mode	Clay-cement-concrete diaphragm design	Maximum diaphragm displacement towards tail race, cm	Percentage of area of clay-cement-concrete diaphragm displacement towards tail race, (by more than 20 cm) from total area, %	Deviation of crest part towards the headrace, cm
Two layers	2 stages	Flat vertical	33	22	8
		Flat inclined	25	15	5
		Arch vertical	25	20	9
Two layers	3 stages	Flat vertical	32	18	4
		Flat inclined	22	5	1
		Arch vertical	22	15	4

When analyzing the obtained results, it can be noted that the maximum horizontal displacements for the proposed alternative configurations almost coincide and fall within the range of 22–25 cm, the highest values of the maximum displacement correspond to the vertical diaphragm option while these displacements are essentially independent from the phasing of reservoir filling and equal 32–33 cm.

It is also apparent when comparing the area of the diaphragm sections with displacements exceeding 20 cm that movements are mostly specific to the option with a flat inclined diaphragm which are 0.7 times less than those of the classical vertical diaphragm option in the case of 2-stage filling and 3.6 times less in the case of 3-stage filling. The change in the reservoir filling mode produces the maximum positive effect on the option with a flat inclined diaphragm as the area of the maximum displacement zone reduces by exactly 3.0 times. This pattern is also observed in horizontal displacements of tilting towards the headrace of the clay-cement-concrete diaphragm crest part.

All the considered configuration options in the setting of almost equal maximum horizontal displacements are generally in more favorable conditions characterized by a smaller overall displacement of the whole diaphragm body and a lesser tilt towards the headrace in case of a three-stage filling as compared to the two-stage filling mode. The change in the filling mode has the most significant effect on the inclined diaphragm option that, for the case being considered, has the smallest areas of maximum horizontal displacements.

The results of maximum settlement calculations for all the clay-cement-concrete diaphragm configurations considered are given in Table 3.

**Table 3. Maximum Settlement Calculation Results for an Embankment Dam with a Flat Vertical, Flat Inclined and Arch Vertical Clay-Cement-Concrete Diaphragm.**

Number of layers	Reservoir filling mode	Clay-cement-concrete diaphragm design	Maximum diaphragm settlement values, cm
Two layers	2 stages	Flat vertical	45
		Flat inclined	36
		Arch vertical	42
Two layers	3 stages	Flat vertical	40
		Flat inclined	30
		Arch vertical	32

Table 3 shows that for all the clay-cement-concrete diaphragm configuration options and reservoir filling modes in 2 and 3 stages the spread in maximum settlement values is relatively small and ranges from 30 to 45 cm. At the same time, for all considered stages of reservoir filling, the inclined diaphragm option shows minimum settlement with values 0.75–0.80 times less than the classical option with a vertical diaphragm.

In general, it can be noted that the more favorable case having the lowest values of the maximum vertical settlement is the one with a three-stage reservoir filling characterized by a decrease in their values by (11–24) % in relation to the two-stage filling; same is noted for the maximum horizontal displacements. In general, the settlement has a value of approximately (0.5–0.7) % of the dam height and are permissible.

The analysis of the results of strain-stress state calculation for different options of the clay-cement-concrete diaphragm configurations with tensile stresses considered is given in Table 4. The resulting values are also compared in terms of various design cases of reservoir filling – filling in 2 and 3 stages. The table contains maximum tensile stress values for the side abutments of the embankment dam first and second layers and in the upper crest belt.

**Table 4. Results of Calculations of Tensile Areas of an Embankment Dam Design with a Flat Vertical, Flat Inclined and Arch Vertical Clay-Cement-Concrete Diaphragm.**

Number of layers	Reservoir filling mode	Design clay-cement-concrete diaphragms	Maximum tensile stresses, MPa	Tensile stresses in side abutments (b is strip width)		Tensile stresses of the upper crest belt (b is strip width)
				1 <sup>st</sup> layer	2 <sup>st</sup> layer	
Two layers	2 stages	Flat vertical	0.33	Up to 0.2 MPa at $b \leq 2-3$ m	Up to 0.2–0.3 MPa at $b \leq 3-5$ m	Up to 0.15 MPa at $b \leq 3-4$ m
		Flat inclined	0.33	Up to 0.2 MPa at $b \leq 2$ m	Up to 0.2–0.3 MPa at $b \leq 1-3$ m	Up to 0.06 MPa at $b \leq 4-6$ m
		Arch vertical	0.33	Very low	Up to 0.15 MPa at $b \leq 1-3$ m	Up to 0.03 MPa at $b \leq 2-3$ m
Two layers	3 stages	Flat vertical	0.30	Up to 0.15 MPa at $b \leq 3$ m	Up to 0.24 MPa at $b \leq 2$ m	Up to 0.06 MPa at $b \leq 2$ m
		Flat inclined	0.20	Very low	Up to 0.15 MPa at $b \leq 1$ m	Very low
		Arch vertical	0.27	Very low	Up to 0.12 MPa at $b \leq 0.5$ m	Up to 0.03 MPa at $b \leq 1-1.5$ m

The resulting stress values for the considered clay-cement-concrete diaphragm configurations shall be compared according to the ones previously determined for clay-cement-concrete [11]. The adopted Mohr-Coulomb yield criteria,  $\operatorname{tg} \varphi = 0.78$  and  $c = 0.32$  MPa, correspond to the ultimate tensile strength  $R_t = 0.31$  MPa and the ultimate compressive strength  $R_c = 1.35$  MPa. These values conform to the average values of the clay-cement-concrete strength characteristics for the formulae previously applied and studied.

It should be noted that the maximum tensile stresses for these design cases are within the range of 0.33–0.20 MPa, and their upper value exceeds the maximum allowable values for clay-cement-concrete. At the same time, these maximum stresses occur in the local crest zone of the dam confined to the side abutments above the flood control storage level elevations and, accordingly, in general do not have any significant effect on the reliability of its operation.

The calculation option with reservoir filling in 2 stages is characterized by the maximum tensile stresses. When the pattern of reservoir filling is changed, a significant decrease is observed in tensile stresses for the arch and inclined diaphragm configurations by 0.8 and 0.6 times, respectively, while for the flat vertical diaphragm this decrease is not so significant.

It should be noted that the values of side abutments tensile stresses for the flat vertical diaphragm option (in the second layer) are close to the maximum allowable ones for all considered stages of reservoir filling. For the rest of the considered options, the tensile stress values in case of the 3-stage reservoir filling do not exceed 0.15 MPa, which ensures reliable diaphragm operation.

Tensile stresses in the upper crest belt for all the cases considered are small and do not exceed the allowable values.

Minimum tensile stresses in side abutments have been obtained for the arch configuration diaphragm with the option of 3-stage reservoir filling.

Table 5 contains the strain-stress state calculation results for a clay-cement-concrete diaphragm determining the compressive stresses. The table shows the values of maximum compressive stresses in clay-cement-concrete diaphragm sides and body for the first and second layers and in various reservoir filling modes.

**Table 5. Compressive Stress Calculation Results for an Embankment Dam with a Flat Vertical, Flat Inclined and Arch Vertical Clay-Cement-Concrete Diaphragm.**

Number of layers	Reservoir filling mode	Design clay-cement-concrete diaphragms	Maximum compressive stresses, MPa			
			Layer 1		Layer 2	
			Side	Body	Side	Body
Two layers	2 stages	Flat vertical	1.65	1.1	0.6	0.3
		Flat inclined	1.67	1.0	0.4	0.4
		Arch vertical	1.85	1.1	0.8	0.4
Two layers	3 stages	Flat vertical	1.65	1.0	0.5	0.3
		Flat inclined	1.26	0.9	0.3	0.4
		Arch vertical	1.71	0.9	0.6	0.5

The maximum compressive stresses are confined to the first layer side abutments and fall within the range between 1.26 MPa and 1.85 MPa. The bigger values are as follows: 1.65 MPa for the flat vertical design, 1.67 MPa for the flat inclined design and 1.85 MPa for the arch vertical design corresponding to the option of 2-stage reservoir filling. The resulting calculated values of compressive stresses in the side abutments for all considered cases exceed or are close to the maximum allowable values for the adopted ultimate compression strength of clay-cement-concrete  $R_c = 1.35$  MPa. At the same time, these stresses are confined to narrow areas with a width not exceeding 0.5–1.0 m and, probably, they will require only some adjustment of the applied clay-cement-concrete composition in order to ensure that the maximum allowable values of clay-cement-concrete compressive strength are not exceeded. This statement is particularly true in relation to the inclined flat diaphragm option where a more favorable pattern of compressive stresses distribution is observed.

Maximum compressive stresses of the first layer of the clay-cement-concrete diaphragm body for all configurations, regardless of the phasing of reservoir filling, have little difference and are about 1.0 MPa. For the second layer of all the considered clay-cement-concrete diaphragm structures, the compressive stress values are 2.0–2.5 times smaller.

In general, it can be noted that the calculated maximum compressive stresses in all considered clay-cement-concrete diaphragm designs (flat vertical, flat inclined, arch vertical) mostly do not exceed the maximum allowable values of clay-cement-concrete compressive strength. The exception is the narrow areas of increased compressive stresses resulting from the calculations of these diaphragms, which are located in

the first layer along the line of side abutment on the tail race end. However, these areas do not pose any danger to the structure since they do not extend into the depth of the diaphragm, but are localized in the outer layer with the thickness of not more than 1.0 m.

The complex numerical simulation performed allowed to identify the main trends of the influence of using the effect of the clay-cement-concrete diaphragm inclination and the influence of the arch effect on the strain-stress state of an embankment dam with a clay-cement-concrete diaphragm.

Based on the results of the analysis of the three-dimensional model performed using the example of the Gotsatinskaya HPP embankment dam with a clay-cement-concrete diaphragm, an extremely complex strain-stress state pattern was obtained describing the connections of the strain-stress state both with the design features of the diaphragm itself and the embankment dam installation procedure, and with reservoir filling mode, that is, creating the pressure head of the structure.

It has been determined that settlement and displacements causing dangerous tensile stresses that may lead to clay-cement-concrete diaphragm cracking occur in the following sections:

- in the upper clay-cement-concrete diaphragm belt, however, they do not spread deep inside the impervious element and are localized within the first 2–3 m from the clay-cement-concrete diaphragm crest. They may potentially lead to the opening of a rhythmic sub-vertical joint system;

- in the side abutments, observed along the entire abutment length, potentially forming sub-vertical displacement cracks, with the nature of the deformations and the presence of clay-cement-concrete cushions in the abutments to the rock sides and concrete abutments considered, without crack opening;

- in contact with the foundation, observed along the entire length of the abutment to the foundation, potentially forming sub-horizontal displacement cracks, with the nature of deformations and the presence of foreshaft in the foundation abutment considered, without crack opening;

- in the lower third of the central clay-cement-concrete diaphragm part due to the nature of displacement towards the tail race under water pressure, an area of maximum deformations is formed in the clay-cement-concrete diaphragm, with the potential possibility of opening of a radial sub-horizontal and sub-vertical cracks.

To ensure reliable functioning of a clay-cement-concrete diaphragm during the entire period of the embankment dam operation, special attention should be paid to these areas when designing protective or remedial measures during supervision at construction and operation stages; at the same time, in the design special attention should be paid to the issues of reservoir filling mode assignment, and actual compliance therewith should be ensured. It is necessary to ensure the required quality of construction and installation works, availability of construction and technical supervision over construction works. The research results also confirm the potential possibility of cracks opening in the clay-cement-concrete diaphragm body for all considered configurations, which confirms the relevance of development of a clay-cement-concrete diaphragm design with an obligatory mending layer in the transition zone from the headrace side [19–21].

The performed numerical simulation and detailed analysis of the strain-stress state calculation results for different configurations of a two-layer clay-cement-concrete diaphragm (with the specified foundation properties), dam body and clay-cement-concrete have revealed that for the inclined flat diaphragm option the minimum horizontal displacements and vertical settlement were obtained; the strain-stress state pattern is more favorable as well. This option can be recommended for further elaboration and preparation of justification materials for the application thereof as an impervious element in an embankment dam with a height exceeding 70 meters, for which using the classical option with a vertical clay-cement-concrete diaphragm is already significantly difficult.

When designing an embankment dam with a clay-cement-concrete diaphragm in the future, it is generally reasonable to account for technical and process possibilities of erecting diaphragms both with the effect of inclination and the arch effect, and to consider these options taking into account the identified trends in the influence of these effects on the strain-stress state of an embankment dam with a clay-cement-concrete diaphragm.

An important condition ensuring the following reliable and safe operation of an embankment dam with this type of impervious element is the development of the process flow-charts for dam construction providing exhaustive information on the process flow of work performance and controlled parameters within the construction arrangement design.

#### *4. Conclusions*

1. For purposes of analyzing the influence of changes in the clay-cement-concrete diaphragm configuration of an embankment dam on its strain-stress state a numerical model of an embankment dam (taking as an example the Gotsatinskaya HPP embankment dam site) based on the ABAQUS 2016 finite-element software package has been elaborated;

2. A plan for calculation experiments has been elaborated and mathematic simulation has been performed in relation to the technical solutions aiming at establishing the conditions for a more favorable strain-

stress state of clay-cement-concrete diaphragms proposed by the author: the option with an arch outline diaphragm and the other option with an inclined diaphragm.

3. The results of the strain-stress state calculations performed have been analyzed and compared with the results of previous calculations of the strain-stress state that showed the main trends of the influence of clay-cement-concrete diaphragm configurations as compared to a traditional vertical clay-cement-concrete diaphragm regarding the values of horizontal displacement, maximum settlement, tensile stress and compressive stress.

## References

1. Radchenko, V.G., Lopatina, M.G., Nikolaichuk, Ye.V., Radchenko, S.V. Opyt vozvedeniya protivofiltracionnykh ustrojstv iz gruntocementnykh smesey [Experience in construction of water seals from soil-cement mixtures]. *Gidrotekhnicheskoe Stroitel'stvo*. 2012. No. 6. Pp. 46–54. (rus)
2. Fedoseyev, V.I., Shishov, I.N., Pekhtin, V.A., Krivonogova, N.F., Kagan, A.A. Protivofiltracionnye zavesy gidrotekhnicheskikh sooruzhenij na mnogoletnej merzlobe [Grout curtains of hydraulic structures on permafrost]. Experience in Design and Work Performance In 2 volumes. Saint Petersburg: JSC «Vedeneev VNIIG». 2009. Vol. 2. Pp. 303–316. (rus)
3. Argal, E.S., Korolev, V.M. On some properties of clay-cement concrete and features of cutoff wall in dam body. *Gidrotekhnicheskoe Stroitel'stvo*. 2019. No. 5. Pp. 10–19.
4. ICOLD. Soil-cement for embankment dams. *Bulletin* № 54. 1986.
5. Lorenz, W., List, F. Application of the trench diaphragm method in constructing the impervious core of dams consisting in part of low-grade fill material. 12-th ICOLD Congress. 1976. Q. 44, R. 6. Mexico. Pp. 93–104.
6. Orishchuk, R.N. Problemy proektirovaniya, stroitelstva i ekspluatatsii glinocementobetonnykh diafragm gruntovykh plotin, vozvodimyykh metodom buresekushchihsya svaj [Design, construction and operation issues of clay-cement-concrete diaphragms of soil dams mounted by means of bored-secant piles]. *Izvestia of B.E. Vedeneev VNIIG, JSC*. 2018. Vol. 287. Pp. 3–13. (rus)
7. Radzinskiy, A.V., Rasskazov, L.N., Sainov, M.P. Plotina stometrovoy vysoty s glinotsementobetonnoy diafragmoy po tipu «stena v grunte» [Clay-cement Concrete Diaphragm of the Type «Slurry Wall» in the 100 Meter High Dam]. *Vestnik MGSU [Proceedings of Moscow State University of Civil Engineering]*. 2014. No. 9. Pp. 106–115. DOI 10.22227/1997-0935.2014.9.106-115 (rus)
8. Miltsin, V.L., Orishchuk, R.N., Solskiy, S.V. Rekomendatsii po proektirovaniyu, raschetam i vozvedeniyu protivofiltracionnogo elementa iz glinocementobetonnykh buresekushchihsya svaj [Recommendations on design, calculations and erection of a watertight element from clay-cement-concrete bored-secant piles]. *Company Standard*. – STP 310.02.NT-2017. St. Petersburg: B.E. Vedeneev VNIIG, JSC, 2017. 117 p. (rus)
9. Sainov, M.P., Soroka, V.B. Ultra-high rockfill dam with combination of the reinforced concrete face and clay-cement diaphragm. *Magazine of Civil Engineering*. 2018. 81(5). Pp. 135–148. DOI 10.18720/MCE.81.14
10. Borzunov, V.V., Denisov, G.V., Kadushkina, E.A., Nikolaeva, E.A., Fedorov, A.V. Experience in design and construction of the Nizhne-Bureyskaya HPP embankment dam using a bored-secant piles diaphragm as an impervious element. *Gidrotekhnicheskoe Stroitel'stvo*. 2019. No. 6. Pp. 2–11.
11. Prokopovich, V.S., Velichko, A.S., Orishchuk, R.N. Napryazhenno-deformirovannoye sostoyaniye zemlyanoy plotiny s glinotsementobetonnoy diafragmoy na primere zemlyanoy plotiny Gotsatlinskoy GES [Analysis of stress-strain state of embankment dam with CCCD]. *Izvestia of B.E. Vedeneev VNIIG, JSC*. 2016. Vol. 282. Pp. 87–98. (rus)
12. Orishchuk, R.N. Novye konstrukcii gruntovykh plotin s glinocementobetonnyimi diafragmami [New designs of soil dams with clay-cement-concrete diaphragms]. *Izvestia of B.E. Vedeneev VNIIG, JSC*. 2019. Vol. 292. Pp. 21–30. (rus)
13. Kang, F.E.I., Han-Long, L. Secondary development of ABAQUS and its application to static and dynamic analyses of earth-rockfill dam. *Rock and Soil Mechanics*. 2010. Vol. 31. No. 3. Pp. 881–890.
14. Rasskazov, L.N., Radzinsky, A.V., Sainov, M.P. Plotiny s glinotsementobetonnoy diafragmoy: napryazhenno-deformirovannoye sostoyaniye i prochnost [Dams with clay-cement concrete diaphragm stress-strain state and strength]. *Gidrotekhnicheskoe Stroitel'stvo*. 2014. No. 9. Pp. 37–44. (rus)
15. Rekomendatsii po raschetu napryazhenno-deformirovannogo sostoyaniya i ustojchivosti vysokikh plotin iz gruntovykh materialov pri staticheskikh i seismicheskikh vozdeystviyah P 824-85 [Recommendations on calculation of the strain-stress state and stability of high dams of soil materials under static and seismic influences P 824-85]. Moscow: Hydroproject. 1985. Pp. 112. (rus)
16. Sainov, M.P. Osobennosti chislennogo modelirovaniya napryazhenno-deformirovannogo sostoyaniya gruntovykh plotin s tonkimi zhestkimi protivofil'tratsionnyimi elementami [Numerical Modeling of the Stress-Strain State of Earth Dams That Have Thin Rigid Seepage Control Elements]. *Vestnik MGSU [Proceedings of Moscow State University of Civil Engineering]*. 2012. No. 10. Pp. 102–108. DOI 10.22227/1997-0935.2012.10.102-108. (rus)
17. Sainov, M.P. Priblizhnyy prognoz prochnosti protivofiltracionnoy steny v osnovanii plotiny [Approximate prognosis of the strength of the anti-seepage wall at the base of the dam]. *Nauchnoe obozrenie*. 2017. No. 4. Pp. 34–38. (rus)
18. Luo, Z.J., Zhang, Y.Y., Wu, Y.X. Finite element numerical simulation of three-dimensional seepage control for deep foundation pit dewatering. *Journal of Hydrodynamics*. 2008. Vol. 20. No. 5. Pp. 596–602. DOI 10.1016/S1001-6058(08)60100-6
19. Solskiy, S.V., Orishchuk, R.N., Lopatina, M.G., Orlova, N.L. Issledovaniye samozalechivaniya treshchin v glinotsementobetonnykh diafragmakh (na primere zemlyanoy plotiny Gotsatlinskoy GES). [Study of crack self-healing in clay-cement concrete diaphragms (using the example of Gotsatlinskaya HPP)]. *Izvestia of B.E. Vedeneev VNIIG, JSC*. 2017. Vol. 283. Pp. 19–29. (rus)
20. Solskiy, S.V., Orishchuk, R.N., Orlova, N.L. Model of crack self-healing in clay-cement concrete diaphragm of embankment dam. *Budowle piętrzące eksploatacja i monitoring*. Warszawa: Instytut Meteorologii i Gospodarki Wodnej. Państwowy Instytut Badawczy. 2017. Pp. 341–349
21. Solskiy, S.V., Lopatina, M.G., Bolshakova, O.A. Vodoneproniaemoe sopryazhenie betonnoy oblicovki bortovogo primykaniya s glinocementnymi blokami [Watertight sidewall of concrete encasement of side abutment with clay-cement blocks]. Patent RF, No. 127088, 2013. (rus)

## Contacts:

Roman Orishchuk, +7(812)4939338; OrishchukRN@vniig.ru

© Orishchuk, R.N., 2019



DOI: 10.18720/MCE.89.2

## Глиноцементобетонная диафрагма, расчётное обоснование новых конструкций

**Р.Н. Орищук**

АО «ВНИИГ им. Б.Е. Веденеева», Санкт-Петербург, Россия

**Ключевые слова:** грунтовая плотина, глиноцементобетонная диафрагма, бурсекущиеся сваи, напряженно-деформированное состояние.

**Аннотация.** В связи с совершенствованием машин и механизмов, технического оснащения и технологических приемов, применяющихся при производстве работ по устройству глиноцементобетонных «стен в грунте» методом бурсекущихся свай, автор предлагает расширить диапазон рассматриваемых конструкций противофильтрационного элемента грунтовых плотин, добавив к ним модификации с арочной и наклонной диафрагмой. Проведенные исследования позволили выявить основные тенденции влияния использования эффекта наклона глиноцементобетонных диафрагм и арочного эффекта на изменение напряженно-деформированного состояния системы грунтовая плотина — диафрагма в сравнении с традиционной конструкцией (вертикальная стена). Учёт предложенных автором конструкций глиноцементобетонных диафрагм при проектировании грунтовых плотин позволит расширить диапазон возможного применения данного технического решения. Установлено, что имеется возможность оптимизации существующих технических решений грунтовых плотин с глиноцементобетонной диафрагмой при их проектировании с учётом не только назначения прочностных и деформативных характеристик глиноцементобетона, но и с учётом изменения конфигурации самой диафрагмы.

### Литература

1. Радченко В.Г., Лопатина М.Г., Николайчук Е.В., Радченко С.В. Опыт возведения противофильтрационных устройств из грунтоцементных смесей // Гидротехническое строительство. 2012. № 6. С. 46–54.
2. Федосеев В.И., Шишов И.Н., Пехтин В.А., Кривоногова Н.Ф., Каган А.А. Противофильтрационные завесы гидротехнических сооружений на многолетней мерзлоте // Опыт проектирования и производства работ. В 2 т. Т. 2. СПб.: ВНИИГ им. Б.Е. Веденеева, 2009. С. 303–316.
3. Аргал Э.С., Королев В.М. О некоторых свойствах глиноцементобетона и особенностях работы стены в грунте в теле плотины // Гидротехническое строительство. 2019. № 5. С. 10–19.
4. ICOLD. Soil-cement for embankment dams // Bulletin № 54. 1986.
5. Lorenz W., List F. Application of the trench diaphragm method in constructing the impervious core of dams consisting in part of low-grade fill material // 12-th ICOLD Congress. 1976. Q. 44, R. 6, Mexico. Pp. 93–104.
6. Орищук Р.Н. Проблемы проектирования, строительства и эксплуатации глиноцементобетонных диафрагм грунтовых плотин, возводимых методом бурсекущихся свай // Известия ВНИИГ им. Б.Е. Веденеева. 2018. Т. 287. С. 3–13.
7. Радзинский А.В., Рассказов Л.Н., Саинов М.П. Плотина стометровой высоты с глиноцементобетонной диафрагмой по типу «стена в грунте» // Вестник МГСУ. 2014. № 9. С. 106–115. DOI 10.22227/1997-0935.2014.9.106-115
8. Мильцин В.Л., Орищук Р.Н., Сольский С.В. Рекомендации по проектированию, расчетам и возведению противофильтрационного элемента из глиноцементобетонных бурсекущихся свай // Стандарт предприятия. – СТП 310.02.НТ-2017. СПб. изд. АО «ВНИИГ им. Б.Е. Веденеева», 2017. 117 с.
9. Саинов М.П., Сорока В.Б. Сверхвысокая каменно-набросная плотина с комбинацией железобетонного экрана и глиноцементобетонной диафрагмы // Инженерно-строительный журнал. 2018. № 5(81). С. 135–148. DOI 10.18720/MCE.81.14
10. Борзунов В.В., Денисов Г.В., Кадушкина Е.А., Николаева Е.А., Федоров А.В. Опыт проектирования и строительства грунтовой плотины Нижне-Бурейской ГЭС с применением в качестве противофильтрационного устройства диафрагмы из бурсекущихся свай // Гидротехническое строительство. 2019. № 6. С. 2–11.
11. Прокопович В.С., Величко А.С., Орищук Р.Н. Напряженно-деформационное состояние земляной плотины с глиноцементобетонной диафрагмой (на примере земляной плотины Гоцатлинской ГЭС) // Известия ВНИИГ им. Б.Е. Веденеева. 2016. Т. 282. С. 87–98.
12. Орищук Р.Н. Новые конструкции грунтовых плотин с глиноцементобетонными диафрагмами // Известия ВНИИГ им. Б.Е. Веденеева. 2019. Т. 292. С. 21–30.
13. Kang F.E.I., Han-Long L. Secondary development of ABAQUS and its application to static and dynamic analyses of earth-rockfill dam // Rock and Soil Mechanics. 2010. No. 3.
14. Рассказов Л.Н., Радзинский А.В., Саинов М.П. Плотины с глиноцементобетонной диафрагмой. Напряженно-деформированное состояние и прочность // Гидротехническое строительство. 2014. № 9. С. 37–44.

15. Рекомендации по расчету напряженно-деформированного состояния и устойчивости высоких плотин из грунтовых материалов при статических и сейсмических воздействиях. П 824-85. М.: Гидропроект, 1985. 112 с.
16. Саинов М.П. Особенности численного моделирования напряженно-деформированного состояния грунтовых плотин с тонкими противифльтрационными элементами // Вестник МГСУ. 2012. № 10. С. 102–108. DOI 10.22227/1997-0935.2012.10.102-108
17. Саинов М.П. Приближенный прогноз прочности противифльтрационной стены в основании плотины // Научное обозрение. 2017. № 4. С. 34–38.
18. Luo Z.J., Zhang Y.Y., Wu Y.X. Finite element numerical simulation of three-dimensional seepage control for deep foundation pit dewatering // Journal of Hydrodynamics. 2008. Vol. 20. No. 5. Pp. 596–602. DOI 10.1016/S1001-6058(08)60100-6
19. Сольский С.В., Орищук Р.Н., Лопатина М.Г., Орлова Н.Л. Исследование самозалечивания трещин в глиноцементнобетонных диафрагмах (на примере земляной плотины Гоцатлинской ГЭС) // Известия ВНИИГ им. Б.Е. Веденеева. 2017. Т. 283. С. 19–29.
20. Solskyi S.V., Orischuk R.N., Orlova N.L. Model of crack self-healing in clay-cement concrete diaphragm of embankment dam // Budowle piętrzące eksploatacja i monitoring. Warszawa: Instytut Meteorologii i Gospodarki Wodnej. Państwowy Instytut Badawczy. 2017. Pp. 341–349
21. Сольский С.В., Лопатина М.Г., Большакова О.А., Водонепроницаемое сопряжение бетонной облицовки бортового примыкания с глиноцементными блоками. Патент РФ № 127088, 2013.

**Контактные данные:**

*Роман Николаевич Орищук, +7(812)4939338; эл. почта: OrischukRN@vniig.ru*

© Орищук Р.Н., 2019



DOI: 10.18720/MCE.89.3

## Mechanical properties of two-stage concrete modified by silica fume

**H.S. Abdelgader<sup>a</sup>, R.S. Fediuk<sup>b,\*</sup>, M. Kurpinska<sup>a</sup>, J. Khatib<sup>c</sup>, G. Murali<sup>d</sup>, A.V. Baranov<sup>b</sup>, R.A. Timokhin<sup>b</sup>**

<sup>a</sup> Gdańsk University of Technology, Gdańsk, Poland

<sup>b</sup> Far Eastern Federal University, Vladivostok, Russia

<sup>c</sup> Beirut Arab University, Beirut, Lebanon

<sup>d</sup> SASTRA Deemed To Be University, Thanjavur, India

\* E-mail: roman44@yandex.ru

**Keywords:** two-stage concrete, silica fume, mechanical properties, cement, coarse aggregate

**Abstract.** Two-stage concretes, despite the fact that they have proven themselves in various types of construction, have not been studied to the same extent as traditional heavy concretes. Therefore, the article developed the composition of frame concrete with various additives in the composition of the cement-sand mortar. A comparison of the mechanical characteristics of the developed compositions with the addition of silica fume (SF) and superplasticizer (SP) in various combinations. In addition, test specimens were prepared with combinations of water/cement ratios of 0.45, 0.55, and 0.85, and cement/sand ratios of 0.5, 1, and 1.5. A total of 36 mixtures were prepared, silica fume was introduced as a partial replacement of cement in the amount of 6 wt.%. And a superplasticizer equal to 1.2 % of the cement content was added to the water. Compressive strength tests on two-stage concrete cylinders were carried out in accordance with ASTM-C873 and ASTM-C943. Tensile strength was also tested on 3 samples of each composition in accordance with the procedure described in ASTM-C496/C496M. As a result, the development of the strength of two-stage concrete for 7, 28 and 120 days was studied. It was found that the overall compressive strength of the two-stage concrete based on SF, SP and SF + SP was higher than in concrete without any additives. At the same time, the modified concrete has higher strength properties, because it provides better contact due to expansion, as well as by reducing the water-cement ratio in grout. The results obtained allow to design a cement-sand mortar capable of filling all the voids between the coarse aggregate, thereby creating a dense structure of two-stage concrete.

### 1. Introduction

Concretes obtained from high-tech self-compacting concrete mixtures based on modern superplasticizers, along with a number of technological advantages, in terms of structural properties, have a number of disadvantages due to the increased concentration of the mortar component, which leads to decrease in the initial modulus of elasticity [1], increased shrinkage [2] and creep [3]. To improve deformation indicators of concrete quality, it needs minimizing the capacity of the mortar component, which ideally should be equal to the volume of coarse aggregate voids [4].

Two-stage concretes (TSC) of the frame structure are produced according to separate technology by injecting a low-viscosity mortar component into the voids between of coarse aggregates, fixed in volume, or by immersion in the low-viscous mortar component of coarse aggregate. This casting method is beneficial in construction work, where there are difficult concreting conditions and limited access to the site [5–7]. It is widely used in various construction applications, for example, concrete for restoration works, hydraulic structures and massive concrete structures [8–17]. TSC's special concreting technology leads to several

---

Abdelgader, H.S., Fediuk, R.S., Kurpinska, M., Khatib, J., Murali, G., Baranov, A.V., Timokhin, R.A. Mechanical properties of two-stage concrete modified by silica fume. Magazine of Civil Engineering. 2019. 89(5). Pp. 26–38. DOI: 10.18720/MCE.89.3.

Абделгадер Х., Федюк Р.С., Курпинска М., Хатиб Д., Мурали Г., Баранов А.В., Тимохин Р.А. Физико-механические свойства каркасного бетона, модифицированного кремнеземом // Инженерно-строительный журнал. 2019. № 5(89). С. 26–38. DOI: 10.18720/MCE.89.3.



advantages [18–23]. Recycled concrete aggregates, which usually cause poor performance and serious problems with pumping due to their higher water absorption, will not contribute to problems with concreting in TSC technology [24, 25]. Production of two-stage concrete has a fairly simple technology, because the same raw materials are used as for conventional concrete: cement, crushed stone, fine-grained aggregate, water, and the necessary modifiers. Differences are only at the production stage. First, the wet cleaned coarse aggregate is accommodated into a timbering in place. Then a specially grout is injected into a timbering from below by pressure of injection and gravitation to fill all the voids, cementing the units to the monolith, as shown in Figure 1. When grout goes up via aggregates, all air and water are discharged. As a result, a dense material is obtained with reduced porosity. Thanks to this simple technology, concrete is maximally compacted without the use of additional equipment [26–30]. Various additives can be selected as needed to improve strength, adhesion and physico-mechanical properties [31–37]. The main difference in materials compared to conventional concrete is that only fine sand (less than 2 mm fraction) and coarse aggregate (usually more than 20 mm) are used as aggregates, which eliminates the need for expensive gravel materials. Nonstandardly a lot of rubble in TSC (up to 70 %) in combination with the use of sand, leads to minimization of the cement component, respectively, reduces total shrinkage and increases efficiency compared to conventional concrete [38–43]. TSC cement mix must be manufactured with high workability so that grout can spread through coarse aggregates. However, due to the uniqueness of the preparation technology of two-stage concrete, it is necessary to modify a grout by various additives. Unfortunately, information in this regard is currently very limited.

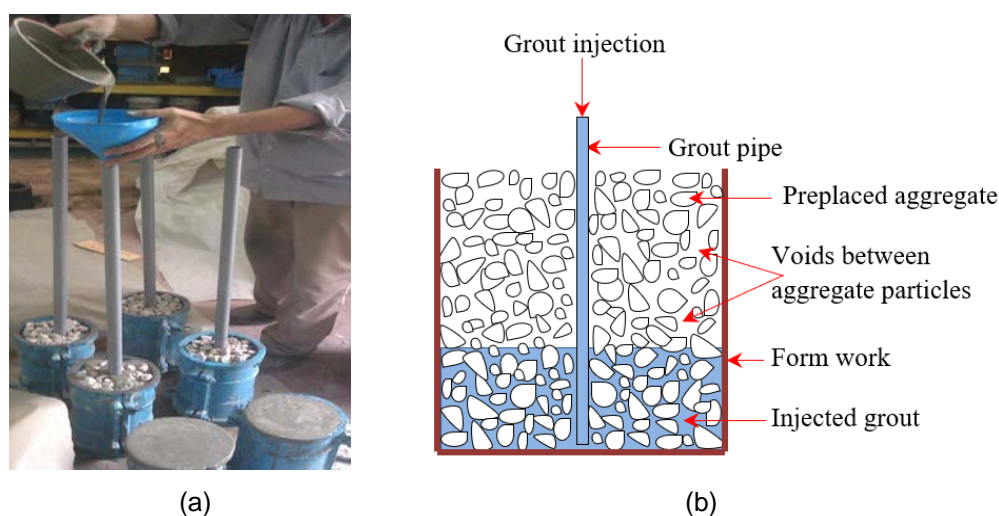


**Figure 1. Casting a two-stage concrete: (a) making the samples; (b) scheme of pumping a grout through a pipe.**

In particular, Co and Pheeraphan [44] studied the use of fly ash and limestone as cement grout fillers. The effect of some active additives on a grout investigated by Nesvetaev [46]. Abdelgader [1] and Najjar [40] investigated the effect of superplasticizers on the properties of cement grout. At the same time, it is known that silica fume and superplasticizer have well reputation for established in more studied types of concrete.

So, the aim of the paper was to study the effect of silica fume and superplasticizer additives in various combinations to strength properties of two-stage concrete.

## 2. Materials and methods

### 2.1. Materials

The two main components in the manufacture of two-stage concretes are coarse aggregate and grout [22, 48]. Accordingly, the selection of coarse aggregates is of paramount importance. In the study, crushed dolomitic limestone with a maximum size of 37.5 mm, a specific gravity of 2.68, a crush strength value of 18.83 %, an abrasion value of 23.81 %, and an absorption value of 1.66 % was used as a «frame» of concrete. Both coarse aggregate and fine aggregate evaluation is crucial in terms of the workability of grout. Natural quartz sand with a specific weight of 2.68 and a maximum size of 2 mm was used in the production of cement grout. The particle sizes of small and coarse aggregates used in this study are shown in Figure 2 [20, 27]. Ordinary Portland cement (OPC) CEM I 42.5 N (Libyan Cement Company) was used for manufacturing of grout (Table 1). In the study, two types of additives were used: superplasticizer (SP) and silica fume (SF). The SP used was ViscoCrete-10 (Sika, Switzerland) and it was applied at a measuring of 1.2 % (by weight of OPC). Silica fume powder, containing 95 % SiO<sub>2</sub> (specific surface area of 20,000 m<sup>2</sup>/kg), was the only mineral additive applied. SF was used in dried form as an additive in the amount of 6 % (by OPC wt.).

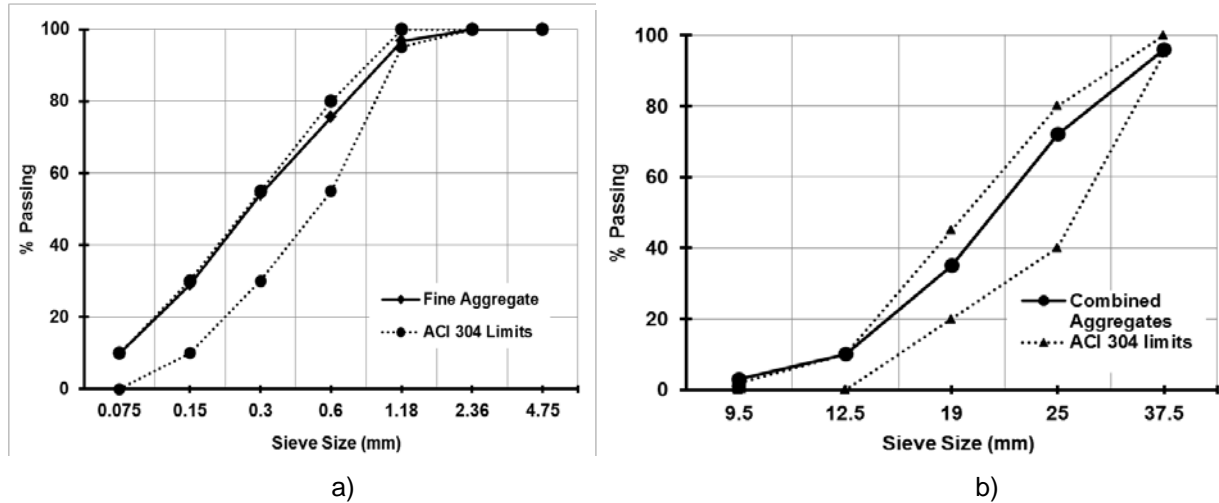


Figure 2. Particle sizes of fine (a) and combined (b) aggregates.

Table 1. Chemical analysis of OPC and SF.

Component	OPC (%)	SF (%)
SiO <sub>2</sub>	21.22	95.30
Al <sub>2</sub> O <sub>3</sub>	4.45	0.17
Fe <sub>2</sub> O <sub>3</sub>	4.08	0.08
CaO	62.98	0.49
SO <sub>3</sub>	1.98	0.24
Na <sub>2</sub> O	0.33	0.19
L.O.I	0.67	4.7

## 2.2. Grout Mix Preparation

Cement-based groutings are a mixture of cement, water, silica-containing component, superplasticizer, and fine aggregate. Constancy of properties, which is the adhesion of a liquid solution and it no delamination, is a significant characteristic for liquid grouting of coarse aggregates. If the grout is prone to delamination, it cannot be guaranteed uniform when filling a formwork. When segregation and water separation occur after pouring the cement mix, the connection with a «frame» may be broken. The main characteristic, on which the strength properties depend, as well as the rate of water separation and plasticity, is the water/cement ratio ( $w/c$ ). Here, the principle of designing traditional concrete, which states that with a decrease in  $w/c$ , the complex of strength characteristics (compression, adhesion, tensile) of a grout obtained is raised. However, at lower ratios of water and cement, the grout loses its fluidity, which means that the mixture has become too thick because cannot seep between of coarse aggregate particles. Although the cement/sand ratio does not significantly affect the strength properties of cement mixture or TSC manufactured, it does have a significant effect on flowability, air removal speed and mixture constancy. Silica fume affects the characteristics of the grout by different itineraries. This is a very pozzolanic material with high reaction potential. Consequently, addition of a silica-containing component into the composition of the binder leads to a change in the rheological properties of the grout, and, then, in the mechanical properties of the cured composite. As a rule, mixtures with SF are more binded and have raised need for mixing by water. Therefore, using of superplasticizers is necessary to maintain the workability of the grout [35, 49–50]. Fine aggregate (i.e. sand) is a significant unit in the rheological planning of grout. Ideally, fine sand without gaps in its gradation is preferred. When using sand with coarse particles larger than 3 mm, the segregation risk of is higher than with smaller sand, where constancy can be supported with reduced water content [27, 51].

The choice of the  $w/c/s$  ratio is extremely important in two-stage concrete, since the amount of water and sand controls the pumpability and distribution of the mixture [9, 27]. The absolute volume method was applied for the study to make proportions of self-compacting grout mixes, followed by adjusting the components of the mixture to characterize mixtures by filling, throughput, and segregation resistance [1]. The voids content between the coarse aggregates was nearly 50 %, and it bulk density was 1,430 kg/m<sup>3</sup>. In total, the study used 36 mixtures, apportioned in 4 series. Each group consisted of a combination of 9 mixtures with permanent indicators:  $w/c$  — 0.45, 0.55, and 0.85 and  $c/s$  — 0.5, 1, and 1.5. The 1<sup>st</sup> series was developed with additives free and was designated in the paper as (no additives). SP was applied only for the 2<sup>nd</sup> series at constant content of 1.2 % by OPC wt. SF was used only in the third group as a mineral additive at a dosage of 6 % by weight of cement. The combination of both SF and SP was used in the fourth group with the same dosages as in the other groups, and is referred to in the text as (SP + SF), the mixing code in the table is also used. Grout was prepared by mixing the starting components by an electric mixer for about two minutes in a

dry form, followed by three minutes stirring with water to make the required homogeneity substance. Table 2 lists the proportions of everything tested two-stage concrete mixtures.

**Table 2. Tested mixes ratios.**

Mix ID	Water/Cement ratio	Cement /Sand ratio	Quantity (kg/m <sup>3</sup> )			
			Cement	Silica Fume	Water	Sand
1		1/0.5	524	31.4	236	262
2	0.45	1/1	438	26.3	198	438
3		1/1.5	377	22.6	170	565
4		1/0.5	474	28.5	261	237
5	0.55	1/1	403	24.2	222	403
6		1/1.5	350	21.	193	526
7		1/0.5	369	22.2	314	185
8	0.85	1/1	325	19.5	276	325
9		1/1.5	290	17.4	246	434

### 2.3. Manufacturing and testing of samples

During the production of two-stage concrete, the grouting of aggregates can be carried out either by gravity or by pumping a grout at the base of the formwork so that it can move up through the voids between the parts of the aggregates. The grout components were weighed separately before mixing. Mixing components is performed in a dry form. This is due to the fact that SF, if it is added to the wet mixture, begins to accumulate in certain places, forming miniature feeble balls. The cement-sand mixture was shifted out the mixer into the cylinder sample with a size of 150×300 mm using a pipe diameter of 20 mm and a length of 1.5 m using a funnel. The pipe was placed in the center of the cylinder before adding a large aggregate in order to most accurately model an authentic manufacturing technology. When the grout rises through crushed stone, only its end remained below the grout. All samples were cured until the day of testing in water at 20°C. A series of tests for compressive and tensile strengths was performed for different mixes, cured during 7, 28 and 120 days (3 samples for each test). Tests on compressive strength on TSC cylinders were made in accordance with ASTM-C873 [52] and ASTM-C943 [53]. Tensile strength was also tested on 3 samples of each composition according to the procedure described in ASTM-C496/C496M [54].

## 3. Results and Discussion

### 3.1 Characteristics of Grout

Figure 3 shows a microstructure of new growths of OPC and SF.

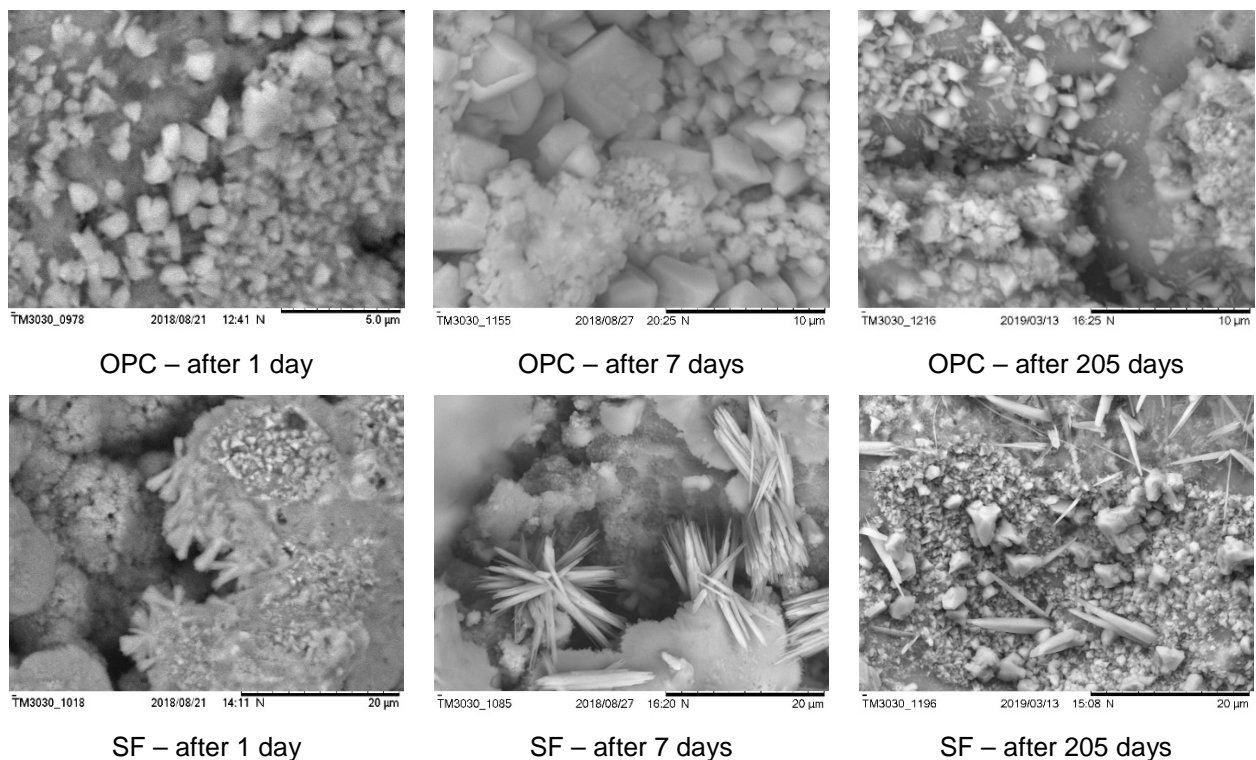


**Figure 3. Microstructure of new growths in cement stone with OPC and SF.**

The grout must have basic properties such as flow characteristics (consistency of the mortar) and sedimentation, which is suitable for use in two-stage concrete. It was investigated that raising  $w/s$  at permanent  $c/s$  content leads to an increase in fluidity. Increasing the amount of water reduces the mixture's cohesion and internal shear forces, which allows the grout to pass by and above each other loosely. At superior ratios of cement and sand, the internal flowability of the mortar is likely to be due to the higher ratio of superplasticizer to sand. The fluidity of cement-sand mixtures with excellent  $w/c$  ratios may increase due to the low stability in these mixtures. During mixing in the laboratory, it was observed that in mixes with a higher ratio of water to cement, fine aggregate grains drown almost at once since ceasing the blender. This may indicate potential problems with this particle size of fine aggregates for two-stage concretes. The cement-sand mixture should be able to move loosely through the large-grained crushed stones so that after they are applied, everything is coated. Naturally, this was complicated at decreased cement/sand ratios ( $c/s = 0.5$ ), as shown in Figure 4, where the grout could not fill all voids. Grout prepared from these composite ratios cannot be used to produce TSC due to the large volume of voids between coarse aggregates, thus potentially weak areas. It was found that large volumes of voids are a problem in only two of the «driest» mixtures; water/cement = 0.42 with cement/sand = 0.5 and water/cement = 0.42 with cement/sand = 1. However, other mixtures have enough flowability to infiltrate into the «frame» of the aggregates.

It was either proved that with a permanent  $c/s$  ratio, higher in the water leads to a steady increase in the sedimentation speed, while higher  $c/s$  ratios are liable to a more expressed sedimentation speed. The predominance of smaller particles in the mixture at increased  $c/s$  ratios, where rateably more binder in volume, reason the formation of gaps in the cement mortar as a whole. To maintain stability, it is recommended that fine grained aggregate and cement material be well sorted. According to the general empirical equations given by Abdelgader [1], sedimentation and fluidity can be calculated.

### 3.2 Compressive Strength

It has been found that the main rule of conventional concrete, that states that increasing the  $w/c$  ratio will drive to a decrease in strength properties, is also true for TSC samples. Table 3 lists the compressive strengths for the developed two-stage concretes with different ratios of water/cement, cement/sand and various chemical and mineral impurities. However, the results of compressive strength for the most dense mixtures with  $w/c = 0.42$  at  $c/s = 0.5$  and  $c/s = 1$  were not included in Table 3, due to the fact that in paragraph 3.1 their inefficiency is proved. The previous articles [2, 10] show that the strength of the grout is most tender to modifications in the  $w/c$  ratio than concrete. This creates meaning in that case it takes into account, how two-stage concrete transfers compression tension. In case if outer energies are attached to the two-stage concrete, the inner large-grained «frame» mainly transfers the load through a dot hookup of particles. When crushed stones are destroyed and deformed, the solution draws it down. It should be assumed that most of the supporting capacitance in concrete is provided afore the onset of cracking in coarse aggregates, which may explain why a significantly more durable solution does not allow one to obtain concrete of proportional strength. The results showed in general that TSC mixtures showed a similar strength properties tendency with regard to the style of additives. As a rule, at the same age and proportions, it was observed that an increase in the heat transfer coefficient slightly decreases the strength properties of the two-stage concrete, that is apparently associated with a decrease in the fluidity and permeability of the solution, which leads to the formation of a two-stage concrete microstructure with a cellular internal structure with local fastening of the aggregates «frame». The use of superplasticizer improves fluidity and permeability of solution and drives to improved strength properties. In addition, using of only silica fume, or it together with superplasticizer showed desirable results in strength properties by comparison to mixtures with no additives as well as only with superplasticizer, and this fact can be explained by the because:

a) higher flowability of the solution is with using superplasticizer, which allows cement mortar fill entirely hollows among crushed stones;

b) pozzolanic reactivity of the silica fume leads speed-up of the hydration, which, thereafter, cause to an increase in the package solidity of the particles of concrete microstructure. For instance, when the cement/sand relation is 1: 0.5, the use of a combination of SF and SP leads to growth of strength after 28 days of curing on a par of 40 % for all the considered water/cement relations. Contrariwise, growth a cement/sand value for the similar  $w/c$  value results in middle decline of strength properties of 12 % at the age of 28 days, this is not an important result.

Other significant result which apparent in Table 3, is the lower compressive strength of the TSC. This decrease is due to water separation and a lower connection among the cement-sand mixture and crushed stones inside of sample. However, the level of strength characteristics will bond on the aptness of the grout to oppose to water separation [8, 55, 56]. The sediment of mix components usually takes place on the bottom of the crushed stones, which leads to the creation of hollows. These hollows form feeble transition areas of aggregate and grout in TSC, preventing the solution from binding to coarse aggregates [29, 32]. In addition,

TSC blends, both without impurities and with SF, create hollows (great capillary pores), that are roots of feebleness in concrete. Figure 5 shows image obtained using a scanning electron microscope (SEM) illustrating a TSC sample. These hollows were created as a result of the surplus water which stayed as spare water in the grout of the two-stage concrete. The capacity of capillary pores rised depends on growth spare water and relies on the grade of hydration of the binder. Conversely, a TSC blend with less spare water formed fewer hollows than another two-stage concrete blends, so reach a better strength properties of two-stage concrete.

**Table 3. Average Compressive Strength Outcomes of two-stage concretes.**

w/c	Additives	Curing Time (days)			Curing Time (days)			Curing Time (days)		
		7	28	120	7	28	120	7	28	120
		c/s = 1: 0.5 (MPa)			c/s = 1:1 (MPa)			c/s = 1:1.5 (MPa)		
0.45	SF	16.79	18.49	26.59	16.60	17.35	25.65	13.58	16.22	25.09
	SP	12.07	18.67	20.18	13.00	17.35	19.05	15.40	15.47	17.17
	SF+SP	17.35	25.65	28.29	16.79	22.63	26.03	13.95	22.26	25.65
	No additives	11.13	15.28	20.37	11.13	14.15	18.11	9.24	13.00	16.03
0.55	SF	13.29	15.85	24.89	11.88	15.10	20.56	10.75	13.58	19.81
	SP	14.34	16.79	20.75	12.64	16.03	20.56	11.32	14.52	18.49
	SF+SP	13.20	21.32	26.88	12.83	19.24	21.50	11.70	15.00	21.87
	No additives	8.67	12.45	15.85	8.49	9.05	13.58	7.73	8.49	12.07
0.85	SF	7.36	10.56	13.58	5.28	9.43	12.07	4.90	9.43	11.69
	SP	6.98	13.20	16.22	8.11	11.51	15.47	8.86	10.94	14.52
	SF+SP	9.05	14.71	16.98	9.81	11.70	15.85	10.19	11.32	15.47
	No additives	6.60	8.29	11.69	4.53	7.36	10.19	3.96	5.66	9.81



**Figure 4. The grout was not able to fill all the voids between coarse aggregates.**

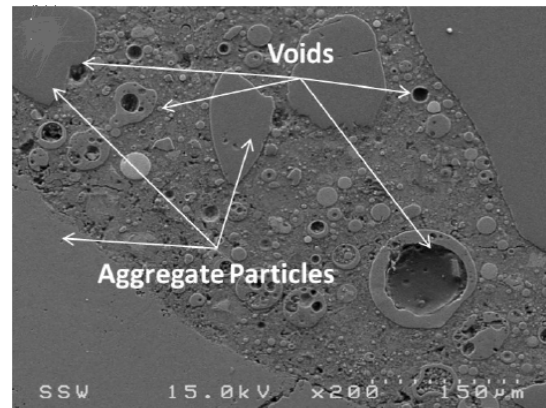


**Figure 5. SEM of specimen of TSC.**

The results can be described by the proposed formula:

$$f'_c = A + B \times w/c + C \times (w/c)^D + E \times (c/s), \quad (1)$$

here  $f'_c$  is the calculated compressive strength of two-stage concrete at 120 day (MPa). Table 4 lists the values of the regression factors.

**Table 4. Regression Factors for Equation 1.**

Additives	Regression Constants					Correlation coefficients
	A	B	C	D	E	
Silica fume	23.838	-19.641	7.022	-0.815	-2.715	0.975
Superplasticizer	-110.44	-172.456	291.909	0.418	-3.823	0.947
Silica fume + Superplasticizer	8.73	7.265	2.399	-2.456	-2.395	0.977
No additives	7.34	5.278	1.427	-2.647	-3.357	0.979

The correlation coefficients close to 1 confirm the reliability of the results obtained for all the compositions developed.

### 3.3 Tensile Strength

Splitting tensile strength is generally applied for appreciate one of important TSC property. Table 5 lists the results of the TSC tensile experiment for various mixes. It was found that the tensile strength of a two-stage concrete becomes higher with decreasing  $c/s$ . A decrease in the water/cement value below 0.42 resulted in the appearance of a cellular structure, which partially binds coarse aggregates, which leads to a decrease in tensile strength. Tensile strength at splitting after 7 days was poor, notably for no additive mixes, but furthers its progress speed growth over time. For example, tensile strength at 7 days for a mixture that does not contain additives was 20 % worse than that of a mixture with silica fume and superplasticizer additives. As a rule, the higher the compressive strength of the TSC, a higher the tensile strength of the TSC, this is consistent with previous studies [1, 9, 13, 17]. In addition, better mechanical adhesion between particles lead to higher tensile strength in TSC.

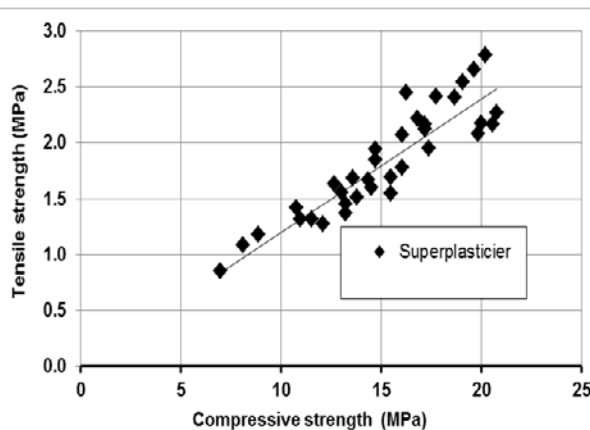
**Table 5. Average Tensile Strength Outcomes of two-stage concrete.**

$w/c$	Additives	Curing Time (days)			Curing Time (days)			Curing Time (days)		
		7	28	120	7	28	120	7	28	120
		$c/s = 1: 0.5$ (MPa)			$c/s = 1:1$ (MPa)			$c/s = 1:1.5$ (MPa)		
0.45	SF	2.075	2.428	2.785	1.933	2.357	2.738	1.789	1.982	2.547
	SP	1.873	2.405	2.783	1.655	1.950	2.542	1.137	1.693	2.167
	SF+SP	2.452	2.972	3.772	1.982	2.765	2.207	1.796	2.363	3.111
	No additives	1.745	1.837	2.547	1.604	1.673	2.406	1.507	1.603	1.984
0.55	SF	1.620	1.626	2.359	1.677	1.653	2.078	1.430	1.510	1.698
	SP	1.666	2.213	2.266	1.636	2.071	2.165	1.415	1.688	2.075
	SF+SP	1.716	2.122	2.265	1.691	1.839	2.170	1.603	1.608	2.124
	No additives	1.424	1.522	1.768	1.383	1.518	1.628	1.180	1.190	1.579
0.85	SF	1.226	1.508	1.603	1.037	1.340	1.536	0.713	1.320	1.483
	SP	0.852	1.450	2.452	1.084	1.320	1.549	1.179	1.320	1.601
	SF+SP	0.943	1.674	2.304	1.226	1.406	1.699	0.943	1.264	1.625
	No additives	0.884	1.461	1.529	0.870	1.320	1.622	0.578	1.226	1.447

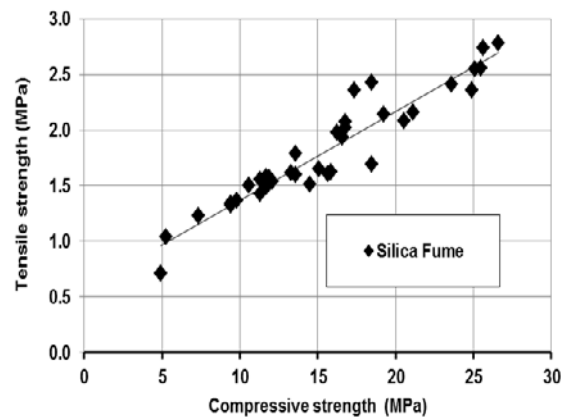
### 3.4 The ratio of strengths of compressive and tensile

The outcomes of this research represent that there is a nice depend among both strengths. When a compressive strength increases, a tensile strength is growth in a similar way. In this paper the Equation 2, was created using regression analysis to relate the tensile strength at 120 days ( $f_t$ ) to compressive strength at 120 days ( $f_c$ ).

$$f_t = a + b \times f_c' + c \times (f_c')^d \quad (2)$$



**Figure 6. Dependence among compressive strength and tensile strength for created mixes.**



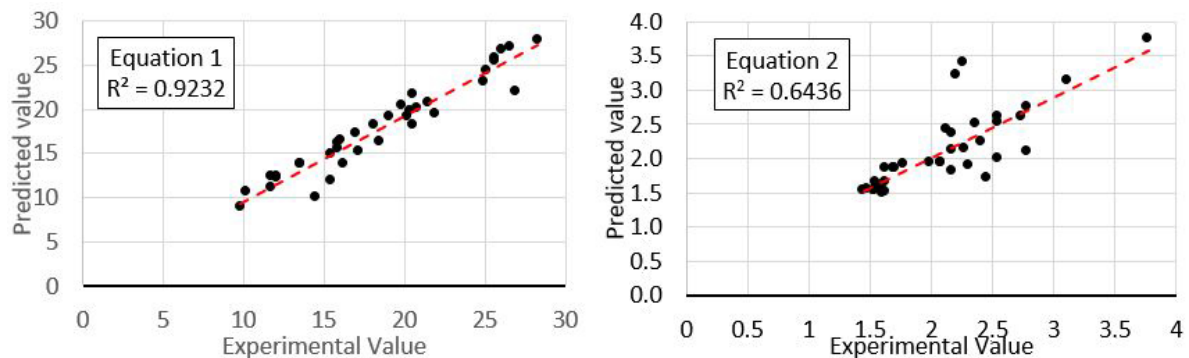
**Figure 7 shows the graphical presentation of this relationship.**

Table 6 shows the values of the regression factors.

**Table 6. Regression Coefficients for Equation 2.**

Additives	Regression constants				Correlation Factors
	<i>a</i>	<i>b</i>	<i>c</i>	<i>d</i>	
SF	-6.048	0.223	26.158	-0.674	0.943
SP	-78.020	-0.003	75.050	0.022	0.901
SF+SP	66.074	0.584	-52.448	0.122	0.907
No additives	-4.197	0.249	24.023	-0.871	0.936

Compressive and tensile strengths calculated by equations 1 and 2, respectively, are shown in Figure 7. Compressive strength has a smaller deviation between the experimental value and the predicted ones, and  $R^2$  reaches 0.9, which shows the accuracy of equation 1. In the case of tensile strength, obtained from Equation 2, the deflection among the empirical and predicted values is significantly less when the value of  $R^2$  is 0.6436. Many points fall off the line, indicating the need for more tests and data.

**Figure 7. Comparison of experimental values with predicted ones.**

### 3.5. Strength properties of partially bound concrete

The strength results for concrete samples obtained with a water/cement value of 0.42 were not presented in the main analysis. At the same time, 2 specimens were tested for compressive strength and tensile strength with 28-day curing, and the results are shown in Table 7. Although the grout did not completely fill the cylindrical specimens, the 28-day strengths showed a fairly high value. This notice also confirms that the coarse aggregate framework is important for both TSC strengths.

**Table 7. Compressive and tensile strength of partially bound concrete ( $w/c = 0.42$ ).**

Compressive strength at 28 day (MPa)		Tensile strength at 28 day (MPa)	
Specimen	Average	Specimen	Average
21.1	23.2	2.21	1.8
25.3		1.32	

## 4. Conclusion

1. The lower limit of the water-cement ratio of a grout (0.42) is established, upon reaching which dense structure of two-stage concrete cannot be ensured.
2. A formula is proposed for calculating the compressive strength of TSC with various combinations of silica fume and superplasticizer, as well as with various water-cement and cement-sand ratios.
3. Tensile strength of a two-stage concrete becomes higher with decreasing  $c/s$ . In addition, better mechanical adhesion between particles leads to higher tensile strength in TSC.
4. Conducting a correlation between compressive strength and tensile strength of the developed concrete, it shows that with an increase in one type of strength, the other also increases. Considering a small amount of work on these concretes in world literature (and the structure differs significantly from traditional heavy concrete), obtaining reliable results (as indicated by almost all coefficients of correlation) is a definite contribution to the study of two-stage concrete.
5. Even with a low water-cement ratio, when the grout did not completely fill the cylindrical specimens, the 28-day strength showed a rather high value. This notice also confirms that the coarse aggregate structure is important for both TSC strengths.

## References

1. Abdelgader, H.S. How to design concrete produced by a two-stage concreting method. *Cement and Concrete Research*. 1999. 29(3). Pp. 331–337. DOI 10.1016/S0008-8846(98)00215-4
2. Fediuk, R.S., Yevdokimova, Y.G., Smoliakov, A.K., Stoyushko, N.Y., Lesovik, V.S. Use of geonics scientific positions for designing of building composites for protective (fortification) structures. *IOP Conference Series: Materials Science and Engineering*. 2017. No. 221. Pp. 012011.
3. O'Malley, J., Abdelgader, H.S. Investigation into viability of using two stage (preplaced aggregate) concrete in an Irish setting. *Front. Archit. Civ. Eng. China*. 2010. 4(1). Pp. 127–132.
4. Fediuk, R., Timokhin, R., Mochalov, A., Otsokov, K., Lashina, I. Performance properties of high-density impermeable cementitious paste. *Journal of Materials in Civil Engineering*. 2019. 31(4).
5. Abdelgader, H.S., Najjar, M.F. Advances in concreting methods, *Proceed. 1st Int. Conf. Sust. Built. Env. Infrastruct. Devel. Countr., Oran, Algeria*. 2009. Pp. 315–324.
6. Abirami, T., Loganaganandan, M., Gunasekaran, M., Fediuk, R., Vickhram Sreekrishna, R., Vignesh, T., Kothandapani, K. T. Experimental research on impact response of novel steel fibrous concretes under falling mass impact. *Construction and Building Material*. 2019. No. 222. Pp. 447–457.
7. Loganina, V., Skachkov, Yu.P., Ryzhov, A.D. Additive based on aluminosilicates for lime dry mortar mixes. *IOP Conference Series: Mater. Sci. Eng.* 2018. 441. 012028.
8. Svintsov, A.P., Nikolenko, Yu.V., Kharun, M.I., Kazakov, A.S. Effect of viscosity of petroleum products on deformation properties of concrete. *Magazine of Civil Engineering*. 2014. 51(7). Pp. 16–22. (rus). DOI: 10.5862/MCE.51.2.
9. Abdelgader, H.S., Elgalhud, A.A. Effect of grout proportions on strength of two-stage concrete. *Struct. Concr.* 2008. 9(3). Pp. 163–170.
10. Najjar, M.F., Ahmed, M.S., Mancef, L.N. Critical overview of two-stage concrete: properties and applications. *Construction and Building Materials*. 2014. No. 62. Pp. 47–58. DOI 10.1016/j.conbuildmat.2014.03.021
11. Volodchenko, A.A., Lesovik, V.S., Zagorodnjuk, L.H., Volodchenko, A.N. Influence of the inorganic modifier structure on structural composite properties. *Int. J. Appl. Eng. Res.* 2015. 19(10). Pp. 40617–40622.
12. Ghasan Fahim Huseien, Abdul Rahman Mohd.Sam, Shah Kwok Wei, Asaad, M.A., Tahir, M.Md., Mirza, J. Properties of ceramic tile waste based alkali-activated mortars incorporating GBFS and fly ash. *Construction and Building Materials*. 2019. No. 214. Pp. 355–368. DOI: 10.1016/j.cemconres.2016.08.007
13. Abdelgader, H.S., Górski, J. Concrete repair using two-stage concrete method. *Materiały Budowlane*. 2015. No. 8. Pp. 66–67. DOI: 10.15199/33.2015.08.17
14. Lesovik, V.S., Alfimova, N.I., Trunov, P.V. Reduction of energy consumption in manufacturing the fine ground cement. *Res. J. Appl. Sci.* 2014. 11(9). Pp. 745–748.
15. Najjar, M.F., Soliman, A.M., Azabi, T.M., Nehdi, M.L. Green sidewalks using sustainable two-stage concrete, *Proceed. CSCE Annual Conf. 2016. Resilient Infrastructure, London, Ontario, Canada*.
16. Volodchenko, A.A., Lesovik, V.S., Volodchenko, A.N., Zagorodnjuk, L.H., Pukharenko, Y.V. Composite performance improvement based on non-conventional natural and technogenic raw materials. *Int. J. Pharm. Technol.* 2016. 8(3). Pp. 18856–18867.
17. Abdelgader, H.S., Najjar, M.F., Azabi, T.M. Study of underwater concrete using two-stage (pre-placed aggregate) concrete in Libya. *J. Struct. Concr.* 2010. 11(3). Pp. 161–165.
18. Mosaberpanah, M.A., Eren O. Effect of Different Ingredients of Ultra High Performance Asphalt Concrete Pavement on Modulus of Elasticity Using Response Surface Modelling. *Solid State Phenomena*. 2019. No. 292. DOI: 10.1016/j.cemconres.2017.04.007
19. Dauji, S., Bhargava, K. Comparison of concrete strength from cube and core records by bootstrap. *J. Asian Concr. Fed.* 2014. 4(1). Pp. 35–46.
20. ACI 304.1, Guide for the use of preplaced aggregate concrete for structural and mass concrete applications. American Concrete Institute, Farmington Hills, Michigan, USA. 2005. Pp. 19–24.
21. Klemm, A.J., Sikora, K.S. The effect of Superabsorbent Polymers (SAP) on microstructure and mechanical properties of fly ash cementitious mortars. *Construction and Building Materials*. 2013. No. 49. Pp. 134–143.
22. Mohammadhosseini, H., Awal, A.S.M.A., Sam, A.R.M. Mechanical and thermal properties of prepacked aggregate concrete. *Sadhana-Springer*. 2016. 41(10). Pp. 1235–1244.
23. Ibrahim, M., Issa, M.A. Evaluation of chloride and water penetration in concrete with cement containing limestone and IPA. *Construction and Building Materials* 2016. No. 129. Pp. 279–288.
24. Prentice, D.P., Walkley, B., Bernal, S.A., Bankhead, M., Hayes, M., Provis, J. Thermodynamic modelling of BFS-PC cements under temperature conditions relevant to the geological disposal of nuclear wastes. *Cement and Concrete Research*. 2019. No. 119. Pp. 21–35. DOI: 10.1016/j.cemconres.2019.02.005
25. Morohashi, N., Meyer, C., Abdelgader, H.S. Concrete with recycled aggregate produced by the two-stage method. *Concr. Plant Intl.* 2013. No. 4. Pp. 34–41.
26. Niyigena, C., Amziane, S., Chateaneuf, A. Assessing the impact of calculation methods on the variability of Young's modulus for hemp concrete material. *Construction and Building Materials*. 2018. No. 198. Pp. 332–344.
27. Abdelgader, H.S. Effect of the quantity of sand on the compressive strength of two-stage concrete. *Magazine of Concrete Research*. 1996. No. 48(177). Pp. 353–360.
28. Choi, W.-C., Picornell, M., Hamoush, S.A. Performance of 90-year-old concrete in a historical structure. *Construction and Building Materials*. 2016. No. 105. Pp. 595–602.
29. Abdelgader, H.S., Ben-Zeitun, A.E. Effect of grout proportions on tensile strength of two-stage concrete measured by split and double-punch tests. *Struct. Concr.* 2004. 5(4). Pp. 173–177.
30. Macie, Z., Skocek, J., Bullerjahn, F., Lothenbach, B., Scrivener, K.L., Ben Haha, M. Early hydration of ye'elimite: Insights from thermodynamic modeling. *Cement and Concrete Research*. 2019. No. 120. Pp. 152–163. DOI: 10.1016/j.cemconres.2019.03.024
31. Shamsuddoha, Md., Hüsken, G., Schmidt, W., Kühne, H.-C., Baeßler M. Ternary mix design of grout material for structural repair using statistical tools. *Construction and Building Materials*. 2018. No. 189. Pp. 170–180.
32. Najjar, M., Soliman, A., Nehdi, M. Two-stage concrete made with single, binary and ternary binders. *Mater. Struct. Concr. J.* 2014. No. 62. Pp. 47–58.

33. Mariak, A., Kurpińska, M., Wilde, K. Maturity curve for estimating the in-place strength of high performance concrete. 64 Scient. Conf. Committee Civ. Eng. Polish Acad. Sciences and the Science Committee of the Polish Assoc. Civ. Eng. (PZITB). 2019. KRYNICA. Pp. 1–7.
34. Horszczaruk, E., Brzozowski, P., Adamczewski, G. Influence of Hydrostatic Pressure on Compressive Strength of Self-Consolidating Underwater Concrete. Fifth North Americ. Conf. Des. Use of Self-Consolid. Concr., Chicago. 2013.
35. Abdelgader, H.S., Górski, J., Khatib, J., El-Baden, A.S. Two-stage concrete: effect of silica fume and superplasticizers on strength. Concr. Plant Precast Technol. 2016. 82(3). Pp. 38–47.
36. Lukutsova, N.P., Pykin, A.A. Stability of nanodisperse additives based on metakaolin. Glass and Ceramics. 2015. 71(11-12). Pp. 383–386.
37. Hunger, M., Brouwers, H.J.H. Flow analysis of water–powder mixtures: application to specific surface area and shape factor. Cement and Concrete Composites. 2009. 31(1). Pp. 39–59.
38. Co, M., Pheeraphan, T. Effect of sand, fly ash, and coarse aggregate gradation on preplaced aggregate concrete studied through factorial design. Construction and Building Materials. 2015. No. 93. Pp. 812–821.
39. Yoon, J.Y., Kim, J.H., Hwang, Y.Y., Shin, D.K. Lightweight Concrete Produced Using a Two-Stage Casting Process. Mater. 2015. No. 8. Pp. 1384–1397. DOI: 10.3390/ma8041384
40. Najjar, M.F. Innovating Two-Stage Concrete with Improved Rheological, Mechanical and Durability Properties, Electronic Thesis and Dissertation Repository. 2016. No. 4118 [Online]. URL: <https://ir.lib.uwo.ca/etd/4118>
41. Lukutsova, N., Kolomatskiy, A., Pykin, A., Nikolaenko, A., Kalugin, A., Tugicova, M. Environmentally safe schungite-based nano-dispersion additive to concrete. Int. J. Appl. Eng. Res. 2014. 22(9). Pp. 15801.
42. Da Silva, W.R., Stemberk, P. Optimized fuzzy logic model for predicting selfcompacting concrete shrinkage. Mechanika. 2013. 19(1). Pp. 67–72.
43. Najjar, M., Soliman, A., Nehdi, M. Two-Stage Concrete Made With Single, Binary and Ternary Binders. Mater. Struct. 2016. 49(1). Pp. 317–327.
44. Co, M., Pheeraphan, T. Effect of sand, fly ash and limestone powder on preplaced aggregate concrete mechanical properties and reinforced beam shear capacity. Construction and Building Materials. 2016. No. 120. Pp. 581–592.
45. Nesvetaev, G.V., Koryanova, Y.I., Zhilnikova, T.N. Coefficients for calculation of deformation-strength characteristic of concrete for injection with two-stage expansion. Solid State Phenomena. 2018. No. 284. Pp. 922–928
46. Kristowski, A., Grzyl, B., Kurpińska, M., Pszczoła, M. The rigid and flexible road pavements in terms of life cycle costs. Creative Construction Conference 2018, CCC 2018, 30 June – 3 July 2018, Ljubljana, Slovenia. Pp. 226–233. DOI 10.3311/CCC2018-030
47. Abdelgader, H.S., Górski, J. Influence of grout proportions on modulus of elasticity of two-stage concrete. Magazine of Concrete Research. 2002. 5(4). Pp. 251–255.
48. Rajabi, A.M., Omid, M.F. Simple empirical formula to estimate the main geomechanical parameters of preplaced aggregate concrete and conventional concrete. Construction and Building Materials. 2017. No. 146. Pp. 485–492. DOI 10.1016/j.conbuildmat.2017.04.089
49. Telford, T. Condensed Silica Fume in Concrete. FIP Commission on Concrete, State of the Art Report. 1988.
50. Horszczaruk, E., Sikora, P., Cendrowski, K., Mijowska, E. The effect of elevated temperature on the properties of cement mortars containing nanosilica and heavyweight aggregates. Construction and Building Materials. 2017. No. 137. Pp. 420–431.
51. Raposeiro da Silva, P., de Brito, J. Fresh-state Properties of Self-compacting Mortar and Concrete with Combined Use of Limestone Filler and Fly Ash. Mater. Res. 2015. 18(5). DOI 10.1590/1516-1439.028715
52. ASTM C873, Standard test method for compressive strength of concrete cylinders cast in place in cylinder molds, American Society for Testing and Materials, Philadelphia, 9, USA. 2010.
53. ASTM C496/C496M, Standard test method for splitting tensile strength of cylindrical concrete specimens, American Society for Testing and Materials, West Conshohocken, PA, USA. 2011.
54. ASTM C943, Standard practice for making test cylinders and prisms for determining strength and density of preplaced-aggregate concrete in the laboratory, American Society for Testing and Materials, West Conshohocken, PA, USA. 2010.
55. Najjar, M.F., Soliman, A.M., Nehdi, M.L. Sustainable high-volume fly ash grouts for two-stage concrete. Proceed. CSCE Annual Conf.: Resilient Infrastructure. 2016. London, Ontario, Canada.
56. Omid, M.F., Rajabi, A.M., Abdelgader, H.S., Kurpińska, M., Wilde, K. Effect of coarse grain aggregate on strength parameters of two-stage concrete. Materiały Budowlane. 2019. No. 559. DOI: 10.15199/33.2019.03 [Online]. URL: <http://www.materiaלבudowlane.info.pl/pl/11885>
57. Klyuev, S.V., Klyuev, A.V., Vatin, N.I. Fiber concrete for the construction industry. Magazine of Civil Engineering. 2018. 84(8). Pp. 41–47. DOI: 10.18720/MCE.84.4.

### Contacts:

*Hakim Abdelgader, +79502817945; hakimsa@poczta.onet.pl*

*Roman Fediuk, +79502817945; roman44@yandex.ru*

*Marzena Kurpinska, +79502817945; marzena.kurpinska@pg.edu.pl*

*Jamal Khatib, +79502817945; j.khatib@bau.edu.ib*

*Gunasekaran Murali, +919944224485; murali\_220984@yahoo.co.in*

*Andrey Baranov, +79502817945; de\_montgomery@mail.ru*

*Roman Timokhin, +79502817945; gera210307@yandex.ru*

© Abdelgader, H.S., Fediuk, R.S., Kurpinska, M., Khatib, J., Murali, G., Baranov, A.V., Timokhin, R.A., 2019



DOI: 10.18720/MCE.89.3

## Физико-механические свойства каркасного бетона, модифицированного кремнеземом

**Х. Абделгадер<sup>а</sup>, Р.С. Федюк<sup>б\*</sup>, М. Курпинска<sup>а</sup>, Д. Хатиб<sup>с</sup>, Г. Мурали<sup>д</sup>, А.В. Баранов<sup>б</sup>, Р.А. Тимохин<sup>б</sup>**

<sup>а</sup> Гданьский политехнический университет, Гданьск, Польша

<sup>б</sup> Дальневосточный Федеральный Университет, г. Владивосток, Россия

<sup>с</sup> Бейрутский арабский университет, Бейрут, Ливан

<sup>д</sup> Университет САСТРА, Танджавур, Индия

\* E-mail: [roman44@yandex.ru](mailto:roman44@yandex.ru)

**Ключевые слова:** каркасный бетон, кремнезем, физико-механические свойства, цемент, крупный заполнитель

**Аннотация.** Каркасные бетоны, несмотря на то, что хорошо зарекомендовали себя в различных видах строительства, изучены не в такой степени, как традиционные тяжелые бетоны. Поэтому в статье разработаны составы каркасных бетонов с различными добавками в составе цементно-песчаного раствора. Проведено сравнение механических характеристик разработанных композиций с добавлением кремнезема (SF) и суперпластификатора (SP) в различных комбинациях. Кроме того, образцы для испытаний готовили с комбинациями соотношений вода/цемент 0,45, 0,55 и 0,85 и соотношений цемент/песок 0,5, 1 и 1,5. Всего было приготовлено 36 смесей, в качестве частичной замены цемента в количестве 6 мас.% вводили кремнезем, а в воду добавляли суперпластификатор, равный 1,2 % содержания цемента в воде. Испытания прочности на сжатие на двухступенчатых бетонных цилиндрах были проведены в соответствии с ASTM-C873 и ASTM-C943. Прочность на растяжение также тестировали на 3 образцах каждой композиции в соответствии с процедурой, описанной в ASTM-C496/C496M. В результате, было изучено развитие прочности каркасного бетона за 7, 28 и 120 дней. При этом было обнаружено, что общая прочность на сжатие каркасного бетона на основе SF, SP и SF + SP была выше, чем в бетоне без каких-либо добавок. При этом, модифицированный бетон обладает более высокими прочностными свойствами, поскольку обеспечивает лучший контакт за счет расширения, а также за счет снижения водоцементного соотношения в цементном растворе. Полученные результаты позволяют проектировать цементно-песчаный раствор, способный заполнять все пустоты между крупным заполнителем, тем самым, создавая плотную структуру двустадийного бетона.

### Литература

1. Abdelgader H.S. How to design concrete produced by a two-stage concreting method // Cement and Concrete Research. 1999. № 29(3). Pp. 331–337. DOI 10.1016/S0008-8846(98)00215-4
2. Fediuk R.S., Yevdokimova Y.G., Smoliakov A.K., Stoyushko N.Y., Lesovik V.S. Use of geonics scientific positions for designing of building composites for protective (fortification) structures. IOP Conference Series // Materials Science and Engineering. 2017. № 221. Pp. 012011.
3. O'Malley J., Abdelgader H.S. Investigation into viability of using two stage (preplaced aggregate) concrete in an Irish setting // Front. Archit. Civ. Eng. China. 2010. № 4(1). Pp. 127–132.
4. Fediuk R., Timokhin R., Mochalov A., Otsokov K., Lashina I. Performance properties of high-density impermeable cementitious paste // Journal of Materials in Civil Engineering. 2019. № 31(4).
5. Abdelgader H.S., Najjar M.F. Advances in concreting methods // Proceed. 1st Int. Conf. Sust. Built. Env. Infrastruct. Devel. Countr., Oran, Algeria. 2009. Pp. 315–324.
6. Abirami T., Loganaganandan M., Gunasekaran M., Fediuk R., Vickhram Sreekrishna R., Vignesh T., Kothandapani K.T. Experimental research on impact response of novel steel fibrous concretes under falling mass impact // Construction and Building Material. 2019. № 222. Pp. 447–457.
7. Loganina V., Skachkov Yu.P., Ryzhov A.D. Additive based on aluminosilicates for lime dry mortar mixes // IOP Conference Series: Mater. Sci. Eng. 2018. 441. 012028.
8. Свинцов А.П., Николенко Ю.В., Харун М.И., Казаков А.С. Влияние вязкости нефтепродуктов на деформативные свойства бетона // Инженерно-строительный журнал. 2014. № 7. С. 16–22.
9. Abdelgader H.S., Elgalhud A.A. Effect of grout proportions on strength of two-stage concrete // Struct. Concr. 2008. 9(3). Pp. 163–170.

10. Najjar M.F., Ahmed M.S., Mancef L.N. Critical overview of two-stage concrete: properties and applications // *Construction and Building Materials*. 2014. № 62. Pp. 47–58. DOI 10.1016/j.conbuildmat.2014.03.021
11. Volodchenko A.A., Lesovik V.S., Zagorodnjuk L.H., Volodchenko A.N. Influence of the inorganic modifier structure on structural composite properties // *Int. J. Appl. Eng. Res.* 2015. № 10(19). Pp. 40617–40622.
12. Ghasan Fahim Huseien, Abdul Rahman Mohd.Sam, Shah Kwok Wei, Asaad M.A., Tahir M.Md., Mirza J. Properties of ceramic tile waste based alkali-activated mortars incorporating GBFS and fly ash // *Construction and Building Materials*. 2019. № 214. Pp. 355–368. DOI: 10.1016/j.conbuildmat.2019.04.154
13. Abdelgader H.S., Górski J. Concrete repair using two-stage concrete method // *Materiały Budowlane*. 2015. № 8. Pp. 66–67. DOI: 10.15199/33.2015.08.17
14. Lesovik V.S., Alfimova N.I., Trunov, P.V. Reduction of energy consumption in manufacturing the fine ground cement // *Res. J. Appl. Sci.* 2014. № 9(11). Pp. 745–748.
15. Najjar M.F., Soliman A.M., Azabi T.M., Nehdi M.L. Green sidewalks using sustainable two-stage concrete // *Proceed. CSCE Annual Conf. 2016. Resilient Infrastructure*, London, Ontario, Canada.
16. Volodchenko A.A., Lesovik V.S., Volodchenko A.N., Zagorodnjuk L.H., Pukharenko Y.V. Composite performance improvement based on non-conventional natural and technogenic raw materials // *Int. J. Pharm. Technol.* 2016. № 8(3). Pp. 18856–18867.
17. Abdelgader H.S., Najjar M.F., Azabi T.M. Study of underwater concrete using two-stage (pre-placed aggregate) concrete in Libya // *J. Struct. Concr.* 2010. № 11 (3). Pp. 161–165.
18. Mosaberpanah M.A., Eren O. Effect of Different Ingredients of Ultra High Performance Asphalt Concrete Pavement on Modulus of Elasticity Using Response Surface Modelling // *Solid State Phenomena*. 2019. № 292. DOI: 10.4028/www.scientific.net/SSP.292.15
19. Dauji S., Bhargava K. Comparison of concrete strength from cube and core records by bootstrap // *J. Asian Concr. Fed.* 2014. № 4(1). Pp. 35–46.
20. ACI 304.1, Guide for the use of preplaced aggregate concrete for structural and mass concrete applications, American Concrete Institute, Farmington Hills, Michigan, USA. 2005. Pp. 19–24.
21. Klemm A.J., Sikora K.S. The effect of Superabsorbent Polymers (SAP) on microstructure and mechanical properties of fly ash cementitious mortars // *Construction and Building Materials*. 2013. № 49. Pp. 134–143.
22. Mohammadhosseini H., Awal A.S.M.A., Sam A.R.M. Mechanical and thermal properties of prepacked aggregate concrete // *Sadhana-Springer*. 2016. № 41(10). Pp. 1235–1244.
23. Ibrahim M., Issa M.A. Evaluation of chloride and water penetration in concrete with cement containing limestone and IPA // *Construction and Building Materials* 2016. № 129. Pp. 279–288.
24. Prentice D.P., Walkley B., Bernal S.A., Bankhead M., Hayes M., Provis J. Thermodynamic modelling of BFS-PC cements under temperature conditions relevant to the geological disposal of nuclear wastes // *Cement and Concrete Research*. 2019. № 119. Pp. 21–35. DOI: 10.1016/j.cemconres.2019.02.005
25. Morohashi N., Meyer C., Abdelgader H.S. Concrete with recycled aggregate produced by the two-stage method // *Concr. Plant Intnl.* 2013. № 4. Pp. 34–41.
26. Niyigena C., Amziane S., Chateaufort A. Assessing the impact of calculation methods on the variability of Young's modulus for hemp concrete material // *Construction and Building Materials*. 2018. № 198. Pp. 332–344.
27. Abdelgader H.S. Effect of the quantity of sand on the compressive strength of two-stage concrete // *Magazine of Concrete Research*. 1996. № 48(177). Pp. 353–360.
28. Choi W.-C., Picornell M., Hamoush S.A. Performance of 90-2019-old concrete in a historical structure // *Construction and Building Materials*. 2016. № 105. Pp. 595–602.
29. Abdelgader H.S., Ben-Zeitun A.E. Effect of grout proportions on tensile strength of two-stage concrete measured by split and double-punch tests // *Struct. Concr.* 2004. № 5(4). Pp. 173–177.
30. Macie Z., Skocek J., Bullerjahn F., Lothenbach B., Scrivener K.L., Ben Haha M. Early hydration of ye'elimite: Insights from thermodynamic modeling // *Cement and Concrete Research*. 2019. № 120. Pp. 152–163. DOI: 10.1016/j.cemconres.2019.03.024
31. Shamsuddoha Md., Hüskén G., Schmidt W., Kühne H.-C., Baeßler M. Ternary mix design of grout material for structural repair using statistical tools // *Construction and Building Materials*. 2018. № 189. Pp. 170–180.
32. Najjar M., Soliman A., Nehdi M. Two-stage concrete made with single, binary and ternary binders // *Mater. Struct. Concr. J.* 2014. № 62. Pp. 47–58.
33. Mariak A., Kurpińska M., Wilde K. Maturity curve for estimating the in-place strength of high performance concrete. 64 Scient. Conf. Committee Civ. Eng. Polish Acad. Sciences and the Science Committee of the Polish Assoc. Civ. Eng. (PZITB). 2019. KRYNICA. Pp. 1–7.
34. Horszczaruk E., Brzozowski P., Adamczewski G. Influence of Hydrostatic Pressure on Compressive Strength of Self-Consolidating Underwater Concrete. Fifth North Americ. Conf. Des. Use of Self-Consolid. Concr., Chicago. 2013.
35. Abdelgader H. S., Górski J., Khatib J., El-Baden A.S. Two-stage concrete: effect of silica fume and superplasticizers on strength // *Concr. Plant Precast Technol.*, 2016. № 82(3). Pp. 38–47.
36. Lukutsova N.P., Pykin A.A. Stability of nanodisperse additives based on metakaolin // *Glass and Ceramics*. 2015. № 71(11-12). Pp. 383–386.
37. Hunger M., Brouwers H.J.H. Flow analysis of water–powder mixtures: application to specific surface area and shape factor // *Cement and Concrete Composites*. 2009. № 31(1). Pp. 39–59.
38. Coe M., Pheeraphan T. Effect of sand, fly ash, and coarse aggregate gradation on preplaced aggregate concrete studied through factorial design // *Construction and Building Materials*. 2015. № 93. Pp. 812–821.
39. Yoon J.Y., Kim J.H., Hwang Y.Y., Shin D.K. Lightweight Concrete Produced Using a Two-Stage Casting // *Process, Mater.* 2015. № 8. Pp. 1384–1397. DOI: 10.3390/ma8041384
40. Najjar M.F. Innovating Two-Stage Concrete with Improved Rheological // *Mechanical and Durability Properties*, Electronic Thesis and Dissertation Repository. 2016. № 4118 [Электронный ресурс]. URL: <https://ir.lib.uwo.ca/etd/4118>
41. Lukutsova N., Kolomatskiy A., Pykin A., Nikolaenko A., Kalugin A., Tugicova M. Environmentally safe schungite-based nanodispersion additive to concrete // *Int. J. Appl. Eng. Res.* 2014. № 9(22). Pp. 15801.
42. Da Silva W.R., Stemberk P. Optimized fuzzy logic model for predicting selfcompacting concrete shrinkage // *Mechanika*. 2013. № 19(1). Pp. 67–72.

43. Najjar M., Soliman A., Nehdi M. Two-Stage Concrete Made With Single, Binary and Ternary Binders // Mater. Struct. 2016. № 49(1). Pp. 317–327.
44. Coo M, Pheeraphan T. Effect of sand, fly ash and limestone powder on preplaced aggregate concrete mechanical properties and reinforced beam shear capacity // Construction and Building Materials. 2016. № 120. Pp. 581–592. .
45. Nesvetavaev G.V., Koryanova Y.I., Zhilnikova T.N. Coefficients for calculation of deformation-strength characteristic of concrete for injection with two-stage expansion // Solid State Phenomena. 2018. № 284. Pp. 922–928
46. Kristowski A., Grzyl B., Kurpińska M., Pszczoła M. The rigid and flexible road pavements in terms of life cycle costs // Creative Construction Conference 2018, CCC 2018, 30 June – 3 July 2018, Ljubljana, Slovenia. Pp. 226–233. DOI 10.3311/CCC2018-030
47. Abdelgader H.S., Górski J. Influence of grout proportions on modulus of elasticity of two-stage concrete // Magazine of Concrete Research. 2002. № 4(5). Pp. 251–255.
48. Rajabi A.M., Omid M.F. Simple empirical formula to estimate the main geomechanical parameters of preplaced aggregate concrete and conventional concrete // Construction and Building Materials. 2017. № 146. Pp. 485–492, DOI 10.1016/j.conbuildmat.2017.04.089
49. Telford T. Condensed Silica Fume in Concrete. FIP Commission on Concrete, State of the Art Report. 1988.
50. Horszczaruk E., Sikora P., Cendrowski K., Mijowska E. The effect of elevated temperature on the properties of cement mortars containing nanosilica and heavyweight aggregates // Construction and Building Materials. 2017. № 137. Pp. 420–431.
51. Raposeiro da Silva P., de Brito J. Fresh-state Properties of Self-compacting Mortar and Concrete with Combined Use of Limestone Filler and Fly Ash // Mater. Res. 2015. № 18(5). DOI 10.1590/1516-1439.028715
52. ASTM C873, Standard test method for compressive strength of concrete cylinders cast in place in cylinder molds, American Society for Testing and Materials, Philadelphia, 9, USA. 2010.
53. ASTM C496/C496M, «Standard test method for splitting tensile strength of cylindrical concrete specimens», American Society for Testing and Materials, West Conshohocken, PA, USA. 2011.
54. ASTM C943, Standard practice for making test cylinders and prisms for determining strength and density of preplaced-aggregate concrete in the laboratory, American Society for Testing and Materials, West Conshohocken, PA, USA. 2010.
55. Najjar M.F., Soliman A.M., Nehdi M.L. Sustainable high-volume fly ash grouts for two-stage concrete // Proceed. CSCE Annual Conf.: Resilient Infrastructure. 2016. London, Ontario, Canada.
56. Omid M.F., Rajabi A.M., Abdelgader H.S., Kurpińska M., Wilde K. Effect of coarse grain aggregate on strength parameters of two-stage concrete // Materiały Budowlane. 2019 № 559. DOI: 10.15199/33.2019.03 [Электронный ресурс]. URL: <http://www.materialybudowlane.info.pl/pl/11885>
57. Клюев С.В., Клюев А.В., Ватин Н.И. Фибробетон для строительной индустрии // Инженерно-строительный журнал. 2018. № 8(84). С. 41–47.

#### **Контактные данные:**

*Хаким Абделгадер, +79502817945; эл. почта: hakimsa@poczta.onet.pl*

*Роман Сергеевич Федюк, +79502817945; эл. почта: roman44@yandex.ru*

*Марзена Курпинска, +79502817945; эл. почта: marzena.kurpinska@pg.edu.pl*

*Джамал Хатиб, +79502817945; эл. почта: j.khatib@bau.edu.ib*

*Гунасекаран Мурали, +919944224485; эл. почта: murali\_220984@yahoo.co.in*

*Андрей Вячеславович Баранов, +79502817945; эл. почта: de\_montgomery@mail.ru*

*Роман Андреевич Тимохин, +79502817945; эл. почта: gera210307@yandex.ru*

© Абделгадер Х., Федюк Р.С., Курпинска М., Хатиб Д., Мурали Г., Баранов А.В., Тимохин Р.А., 2019



DOI: 10.18720/MCE.89.4

## Nonlinear deformation and stability of geometrically exact elastic arches

V.V. Lalin, A.N. Dmitriev\*, S.F. Diakov

Peter the Great St. Petersburg Polytechnic University, St. Petersburg, Russia

**Ключевые слова:** stability of structures, buckling, geometrically exact theory, dead load, round arch, stiffness, stationary point, Lagrange functional

**Abstract.** In the present paper a plane round double-hinged arch under the potential dead load is investigated. To describe the stress-strain state and the equilibrium stability the geometrically exact theory is used. According to this theory every point of the bar has two translational degrees of freedom and one rotational, which is independent from the previous two. To solve the problem no displacements are simplified and all the stiffnesses are used: axial, shear and bending. Exact nonlinear differential equations are found for the static problem. A variational definition for the problem is defined as finding a stationary point of Lagrange functional. The match of the differential and variational formulations is shown. Exact stability equations accounting non-linear geometric deformations in pre-buckling state were worked out. The problem of the equilibrium stability of the round arch under the potential dead load was solved using the obtained equations regarding all the bar's stiffnesses. The characteristic transcendental equation and its asymptotic solution as simple formulas, suitable for practical application, were worked out. The comparison of described solution which regards all the bar's stiffnesses and classical solution, based on bending stiffness, was made.

### 1. Introduction

Arches are one of the most widespread structural systems. On the one hand, this is due to their architectural expression; on the other hand, they are efficient at mechanics due to their curvature which can neglect the effect of the bending moment. As a result, the arch can be rather flexible as the size of the cross section can be relatively small. That is why the problem of arch equilibrium stability is one of the main problems for engineers to consider.

Historically, the most popular problem in the theory of stability of arches is the problem of stability of round arch under the radial pressure. This implication is typical for different underground structures – tunnels, pipelines and hull ribs of the submarines. The solution for this problem for the semi-ring was derived according to the fact that the loads, despite the bending of the axis of the bar, maintain the line of action. Besides, lines of action don't move in case of buckling [1–4]:

$$q_T = 3 \frac{EI}{R^3}. \quad (1)$$

The solution for the problem of the stability of the plane arch under the radial pressure, when the load maintains the line of action, but the application points move with the axis of the arch were worked out by N.V. Kornoukhov [5] and A.N. Dinnik [6]. In case of the semi-ring the critical force is:

$$q_K = 3.27 \frac{EI}{R^3}. \quad (2)$$

---

Lalin, V.V., Dmitriev, A.N., Diakov, S.F. Nonlinear deformation and stability of geometrically exact elastic arches. Magazine of Civil Engineering. 2019. 89(5). Pp. 39–51. DOI: 10.18720/MCE.89.4

Лалин В.В., Дмитриев А.Н., Дьяков С.Ф. Геометрически нелинейное деформирование и устойчивость упругих арок // Инженерно-строительный журнал. 2019. № 5(89). С. 39–51. DOI: 10.18720/MCE.89.4



This open access article is licensed under CC BY 4.0 (<https://creativecommons.org/licenses/by/4.0/>)

In practice arches usually suffer different loads. A lot of problems were solved about the non-linear stability and the post-buckling deformation of round arches under the single force in the center [7–9]; under vertical or horizontal pressure, distributed on whole length [10–14] or located only on the part of the arch [15, 16]. Some other problems and their solutions can be found in the papers of V.N. Paimushin [17, 18], I.A. Karnovsky [19, 20], V.V. Galishnikova [21].

The critical force value is influenced not only by external loads but by the other parameters: flexibility of the supports, material properties and shape of the axis of the arch. The effect of the horizontal and vertical support stiffness on the stability of the round arch and frames was analyzed in [22, 23]. The effect of the physical properties, inconstant through the cross-section was analyzed with the help of functionally graded materials in [9, 14, 24, 25]. The problems of linear stability of plane parabolic arches can be found in [12, 13, 26]. Experimental researches of pre-buckling deformation, ultimate equilibrium and the failure behavior in case of buckling are described in [27–30].

Despite the big amount of analytical study, all the mentioned researches consider only the bending stiffness of the bar, and for this reason should be considered as approximate. There are no problem formulations and their solutions about the stability of arches, considering both axial and shear stiffness.

Variational method as the principle of virtual displacements is the most popular method to research the problems of stability [16–18, 31]. However, the variational definition for the problem as finding a stationary point of some functional was used only for straight bars [32], not for the arches. Note, that exact stability equations can be obtained from the second variation of the functional [31].

Thus, the purpose of this paper is to solve the problem of stability of plane double-hinged arch under the potential dead load regarding all the stiffnesses of the bar: axial, shear and bending by variational approach.

The aims of this paper are:

1. to work out a variational definition for the problem of deformation of the geometrical non-linear plane elastic round arch regarding axial, shear and bending stiffnesses as finding the stationary point of Lagrange functional;
2. to work out the stability equations as the result of the second variation of the Lagrange functional;
3. solving the problem of the stability of the arch with the help of the obtained equations under the potential dead load regarding all the stiffnesses of the bar: axial, shear and bending.
4. comparing the obtained solution with the Kornoukhov-Dinnik solution (2), where only bending stiffness was considered.

## 2. Methods

This paper is based on geometrically exact bar theory [32–37], whereby each point of the plane bar has two translational degrees of freedom – displacements  $u$ ,  $w$  and one rotational – angle  $\varphi$ , which is independent from the previous ones.

Consider a plane round double-hinged arch with radius  $R$  under the potential dead load: uniformly applied forces and moments. Each point of the arch can be described with the local trihedron  $(t, n, k)$ : tangent basis vector  $t$  is directed towards the increasing  $\theta$ , normal basic vector  $n$  is away from the center of curvature  $C$ . The direction of the basic binormal vector  $k$  can be found using the vectorial product  $t \times n = k$ . All the unknowns, describing the stress-strain state of the bar can be found via angular coordinate  $\theta$ ,  $0 \leq \theta \leq \Theta$ , where  $\Theta$  is the central angle (Figure 1).

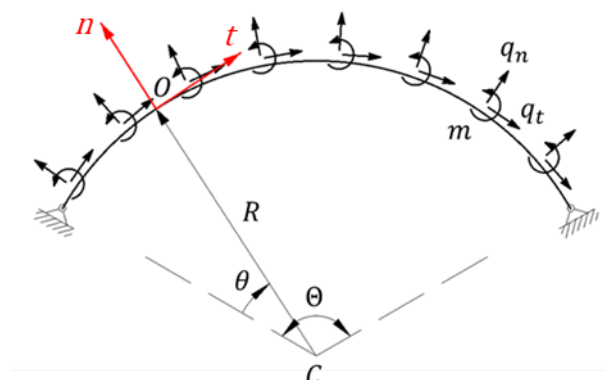


Figure 1. Arch state in basic condition (condition before deformation).

Definition of the problem of geometrically non-linear deformation of the round arch consists of three groups of differential equations: static (equilibrium equations), geometrical and physical. The equations for the static problem in the vector form were derived in [32–33]. The scalar form for the vector equations in the curvilinear coordinates will be derived below.

Equilibrium equations for the problem of the plane non-linear deformation of the arch are:

$$\begin{cases} (N \cos \varphi - Q \sin \varphi)' + (N \sin \varphi + Q \cos \varphi) + Rq_t = 0; \\ (N \sin \varphi + Q \cos \varphi)' - (N \cos \varphi - Q \sin \varphi) + Rq_n = 0; \\ M' + (u' + w + R)(N \sin \varphi + Q \cos \varphi) - (w' - u)(N \cos \varphi - Q \sin \varphi) + Rm = 0, \end{cases} \quad (3)$$

where  $N$  is axial force;

$Q$  is shear force;

$M$  is bending moment;

$q_t, q_n$  are projection of the distributed loads on the tangential and normal (radial) direction;

$m$  is distributed moment load;

$u, w$  are tangential and normal displacements;

$\varphi$  is rotating angle. Henceforward differentiation is made according to angle  $\theta( )' \equiv d( )/d\theta$ .

Geometrical equations for the plane problem are:

$$\begin{cases} \varepsilon = \frac{1}{R}(u' + w + R)\cos \varphi + \frac{1}{R}(w' - u)\sin \varphi - 1, \\ \gamma = -\frac{1}{R}(u' + w + R)\sin \varphi + \frac{1}{R}(w' - u)\cos \varphi, \\ \psi = \frac{1}{R}\varphi', \end{cases} \quad (4)$$

where  $\varepsilon, \gamma, \psi$  are axial, shear and bending deformations.

Physical equations for the linear elastic material are

$$N = k_1\varepsilon; \quad Q = k_2\gamma; \quad M = k_3\psi, \quad (5)$$

where  $k_1 = EA$  is axial stiffness;  $k_2 = GAk$  is shear stiffness;  $k_3 = EI$  is bending stiffness;  $E$  is Young's modulus;  $A$  is cross-section area of the bar;  $G$  is shear modulus;  $k$  is cross-section form coefficient;  $I$  is moment of inertia.

The equations (3)–(5) are the exact equations of geometrical non-linear round arch, taking into account all stiffnesses of round arch. To get the closed system on each end of the arch three boundary conditions are needed. For the double-hinged arch they are as follows:

$$\begin{aligned} \theta = 0: \quad u(0) = 0, \quad w(0) = 0, \quad M(0) = 0; \\ \theta = \Theta: \quad u(\Theta) = 0, \quad w(\Theta) = 0, \quad M(\Theta) = 0. \end{aligned} \quad (6)$$

### 3. Results and Discussion

#### 3.1. Variational formulation of non-linear static problem

Lagrange functional can be written as follows:

$$\mathcal{L}(u, w, \varphi) = R \int_0^\Theta \left[ \frac{1}{2} (k_1\varepsilon^2 + k_2\gamma^2 + k_3\psi^2) - q_t u - q_n w - m\varphi \right] d\theta. \quad (7)$$



To derive Euler equations for the variational problem of finding a stationary point of functional  $F_{ST}^* \rightarrow \text{STAT}$  in carrying out essential boundary conditions (12) the first variation of the stability functional should be computed:

$$\begin{aligned} \delta F_{ST}^*(u_v, w_v, \varphi_v) = & \int_0^{\Theta} \left( \delta u_v \left( -(N_v \cos \varphi - \varphi_v N \sin \varphi - Q_v \sin \varphi - \varphi_v Q \cos \varphi)' - \right. \right. \\ & - N_v \sin \varphi - \varphi_v N \cos \varphi - Q_v \cos \varphi + \varphi_v Q \sin \varphi) + \delta w_v \left( -(N_v \sin \varphi + \varphi_v N \cos \varphi + \right. \\ & + Q_v \cos \varphi - \varphi_v Q \sin \varphi)' + N_v \cos \varphi - \varphi_v N \sin \varphi - Q_v \sin \varphi - \varphi_v Q \cos \varphi) + \\ & + \delta \varphi_v \left( -M_v' - (u' + w + R) N_v \sin \varphi + (w' - u) N_v \cos \varphi - (u_v' + w_v) N \sin \varphi - \right. \\ & - \varphi_v (u' + w + R) N \cos \varphi + (w_v' - u_v) N \cos \varphi - \varphi_v (w' - u) N \sin \varphi - \\ & - (u' + w + R) Q_v \cos \varphi - (w' - u) Q_v \sin \varphi - (u_v' + w_v) Q \cos \varphi + \varphi_v (u' + w + R) Q \sin \varphi - \\ & - (w_v' - u_v) Q \sin \varphi - \varphi_v (w' - u) Q \cos \varphi) d\theta + \left[ \delta u_v (N_v \cos \varphi - \varphi_v N \sin \varphi - Q_v \sin \varphi - \right. \\ & \left. - \varphi_v Q \cos \varphi) + \delta w_v (N_v \sin \varphi + \varphi_v N \cos \varphi + Q_v \cos \varphi - \varphi_v Q \sin \varphi) + \delta \varphi_v M_v \right]_0^{\Theta}, \end{aligned} \quad (16)$$

where the following labels are introduced:

$$\begin{aligned} N_v &= k_1 \varepsilon_v, \quad Q_v = k_2 \gamma_v, \quad M_v = k_3 \psi_v; \\ \varepsilon_v &= \frac{1}{R} \left( (w_v' - u_v) \cos \varphi - \varphi_v (u' + w + R) \sin \varphi + (w_v' - u_v) \sin \varphi + \varphi_v (w' - u) \cos \varphi \right), \\ \gamma_v &= \frac{1}{R} \left( -(u_v' + w_v) \sin \varphi - \varphi_v (u' + w + R) \cos \varphi + (w_v' - u_v) \cos \varphi - \varphi_v (w' - u) \sin \varphi \right), \\ \psi_v &= \frac{1}{R} \varphi_v'. \end{aligned} \quad (17)$$

Euler equations resulting from the condition  $\delta F_{ST}^* = 0$  are the further equations:

$$\begin{aligned} & \varphi_v (N \cos \varphi - Q \sin \varphi) + (N_v \sin \varphi + Q_v \cos \varphi) - (\varphi_v (N \sin \varphi + Q \cos \varphi) - \\ & - (N_v \cos \varphi - Q_v \sin \varphi))' = 0; \\ & \varphi_v (N \sin \varphi + Q \cos \varphi) - (N_v \cos \varphi - Q_v \sin \varphi) + (\varphi_v (N \cos \varphi - Q \sin \varphi) + \\ & + (N_v \sin \varphi + Q_v \cos \varphi))' = 0; \\ & M_v' + (u_v' + w_v) (N \sin \varphi + Q \cos \varphi) - (w_v' - u_v) (N \cos \varphi - Q \sin \varphi) + \\ & + (u' + w + R) (\varphi_v (N \cos \varphi - Q \sin \varphi) + (N_v \sin \varphi + Q_v \cos \varphi)) + \\ & + (w' - u) (\varphi_v (N \sin \varphi + Q \cos \varphi) - (N_v \cos \varphi - Q_v \sin \varphi)) = 0. \end{aligned} \quad (18)$$

Expression (18) is the system of equations involving functions  $u_v, w_v, \varphi_v$ . Functions  $u, w, \varphi, N, Q, M$  are known and are the solution of nonlinear static problem, the stability of which is being researched.

Equations (18) are the exact stability equations of the elastic round arch under the potential dead load, taking into account all stiffnesses of round arch. To get these equations no hypothesis was made about the value of displacements and type of stress-strain state of the bar.

The natural boundary conditions can be derived from the terms outside the integral (16) regarding the essential boundary conditions (12):

$$M_v(\Theta) = 0, \quad M_v(0) = 0. \quad (19)$$

Thus, the formulation of the stability problem consists of stability equations (18) and six boundary conditions (12), (19). The exact solution for the problem of stability can be derived if the exact solution of the nonlinear static problem (3)–(6) is put in system (18). There are no exact analytical solutions for the nonlinear static problems of the curvilinear bars. That is why the solution of the stability problem is derived in a linearized formulation [31]. This means, that solution of the original static problem in linear formulation is put in system (18).

### 3.3. Solving the problem of arch equilibrium stability

Consider the problem of half ring equilibrium (an arch with central angle  $\Theta = \pi$ ) of radius  $R$ , under the dead radial pressure (Figure 2).

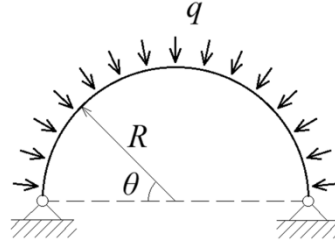


**Figure 2. Structural model of the half-ring under the radial pressure.**

Statically acceptable solution in linear formulation [19] can be written as follows:

$$N = -qR, \quad Q = 0, \quad M = 0. \quad (20)$$

As the physical equations (5) and functionals (7) and (15) are valid only for the elastic material, then the distributed pressure shouldn't outnumber the following values:

$$q \leq \frac{\sigma_y A}{R}, \quad (21)$$

where  $\sigma_y$  is elastic limit.

Substitution of the static solution (20) into stability equations (18) leads to the following system:

$$\begin{cases} (N\varphi_v + Q_v) + (N_v)' = 0; \\ -N_v + (N\varphi_v + Q_v)' = 0; \\ M_v' - N(w_v' - u_v) + R(N\varphi_v + Q_v) = 0, \end{cases} \quad (22)$$

where, according to the (17), are made the following labels:

$$N_v = \frac{k_1}{R}(u_v' + w_v), \quad Q_v = \frac{k_2}{R}(-R\varphi_v + (w_v' - u_v)), \quad M_v = \frac{k_3}{R}\varphi_v'.$$

The solution of the system (22) are the following functions:

$$\begin{aligned} u_v &= \frac{1}{2}GC_1 \cos \theta + \frac{1}{2}GC_1\theta \sin \theta + \frac{1}{2}GC_2\theta \cos \theta + HC_3 \cos \sqrt{A}\theta + HC_4 \sin \sqrt{A}\theta + \\ &\quad + C_5 \cos \theta + C_6 \sin \theta; \\ w_v &= -\frac{1}{2}GC_1\theta \cos \theta + \frac{R}{k_1}C_1 \sin \theta + \frac{R}{k_1}C_2 \cos \theta + \frac{1}{2}GC_2\theta \sin \theta - \frac{1}{2}GC_2 \cos \theta + \\ &\quad + \sqrt{A}HC_3 \sin \sqrt{A}\theta - \sqrt{A}HC_4 \cos \sqrt{A}\theta + C_5 \sin \theta - C_6 \cos \theta; \\ \varphi_v &= \frac{R}{k_3}HC_1 \cos \theta - \frac{R}{k_3}HC_2 \sin \theta + C_3 \cos \sqrt{A}\theta + C_4 \sin \sqrt{A}\theta, \end{aligned} \quad (23)$$

where  $C_i$  is integration constants and the following labels are used:

$$A = \left(1 + \frac{qR}{k_2}\right) \frac{qR^3}{k_3}, \quad H = \frac{\left(1 + \frac{qR}{k_2}\right)R}{\left(1 + \frac{qR}{k_2}\right) \frac{qR^3}{k_3} - 1}, \quad G = \left(\frac{1}{k_1} + \frac{1}{k_2} - H \left(1 + \frac{qR}{k_2}\right) \frac{R}{k_3}\right). \quad (24)$$

Boundary conditions (12), (19) lead to the system of linear equations involving integration constants. After the equivalent transformations it can be derived:

$$\begin{cases} GC_1 = 0; \\ \sqrt{AH} \sin(\sqrt{A}\pi) C_3 = 0; \\ \begin{cases} -H \frac{R}{k_3} C_2 + \sqrt{A} \sin(\sqrt{A}\pi) C_4 = 0; \\ -\frac{1}{2} G\pi \sqrt{A} \sin(\sqrt{A}\pi) C_2 + 2\sqrt{AH} \sin(\sqrt{A}\pi) (\cos(\sqrt{A}\pi) + 1) C_4 = 0. \end{cases} \end{cases} \quad (25)$$

According to the numerical test, a critical load, calculated from the first two equations of the set (25), outnumbers the critical load from the last system of two equations. Hence the transcendental equation relative to the minimal value of the critical load can be derived:

$$\sqrt{AH}^2 \frac{R}{k_3} (\cos(\sqrt{A}\pi) + 1) - \frac{\pi}{4} AG \sin(\sqrt{A}\pi) = 0, \quad (26)$$

Using the labels from (24) and trigonometric transformations, (26) can be rewritten:

$$\begin{aligned} & \operatorname{tg} \left( \frac{\pi}{2} \sqrt{\left(1 + \frac{qR}{k_2}\right) \frac{qR^3}{k_3}} \right) = \\ & = \frac{4}{\pi} \frac{\left(1 + \frac{qR}{k_2}\right)^2 \frac{R^2}{k_3}}{\sqrt{\left(1 + \frac{qR}{k_2}\right) \frac{qR^3}{k_3}} \left( \frac{1}{k_1} + \frac{1}{k_2} + \frac{\left(1 + \frac{qR}{k_2}\right)^2 \frac{R^2}{k_3}}{1 - \left(1 + \frac{qR}{k_2}\right) \frac{qR^3}{k_3}} \right) \left(1 - \left(1 + \frac{qR}{k_2}\right) \frac{qR^3}{k_3}\right)^2}. \end{aligned} \quad (27)$$

Transcendental equation (27) makes it possible to determine the value for the critical load  $q_{cr}$  for the circle arch under the dead pressure considering all the stiffnesses of the bar. Equation (27) can be solved numerically for any arch with any cross-section, though you can't get a general correlation between loading and bar stiffness. Moreover, it is very uncomfortable to use such an equation in practice. To get the simple form for the critical load an asymptotic solution for the equation (27) will be done.

Consider the labels for the non-dimensional values:

$$b = \sqrt{\frac{qR^3}{k_3}}, \quad \xi_1 = \frac{k_3}{k_2 R^2}, \quad \xi_2 = \frac{k_3}{k_1 R^2}. \quad (28)$$

For the cross-sections, widely used in practice, shear and axial stiffnesses are much more than bending stiffness, that is why  $\xi_1$ ,  $\xi_2$  can be considered as small parameters:  $\xi_1$ ,  $\xi_2 \ll 1$ .

According to (28), (27) can be written as follows:

$$\operatorname{tg} \left( \frac{\pi}{2} b \sqrt{1 + b^2 \xi_1} \right) = \frac{4}{\pi} \frac{(1 + b^2 \xi_1)^2}{b \sqrt{1 + b^2 \xi_1} \left( \xi_2 + \xi_1 + \frac{(1 + b^2 \xi_1)^2}{1 - (1 + b^2 \xi_1) b^2} \right) (1 - (1 + b^2 \xi_1) b^2)^2}. \quad (29)$$

The parameter  $\xi_2$  can be considered to be dependent on  $\xi_1$  through the  $k$  coefficient, where  $k$  is a certain constant value.

$$\xi_2 = \xi_1 k. \quad (30)$$

According to (30), (29) can be written as follows:

$$\operatorname{tg}\left(\frac{\pi}{2}b\sqrt{(1+b^2\xi_1)}\right) = \frac{4}{\pi} \frac{(1+b^2\xi_1)^2}{b\sqrt{(1+b^2\xi_1)}\left(\xi_1(k+1) + \frac{(1+b^2\xi_1)^2}{1-(1+b^2\xi_1)b^2}\right)\left(1-(1+b^2\xi_1)b^2\right)^2}. \quad (31)$$

The unknown  $b$  can be estimated as an asymptotic series with a small parameter  $\xi_1$ :

$$b = b_0 + b_1\xi_1 + b_2\xi_1^2 + \dots, \quad (32)$$

where  $b_0 = \sqrt{q_K R^3 / k_3}$  relates the value of the critical force  $q_K$  neglecting axial and shear yielding, i.e. when  $k_1 \rightarrow \infty, k_2 \rightarrow \infty$ , which is equivalent to  $\xi_2 \rightarrow 0, \xi_1 \rightarrow 0$ .

In fact, when  $\xi_1 \rightarrow 0, \xi_2 \rightarrow 0$ , (29) transforms into

$$\operatorname{tg}\left(\frac{\pi}{2}b_0\right) = \frac{4}{\pi} \frac{1}{b_0(1-b_0^2)}. \quad (33)$$

The minimal positive root of the transcendental equation (33) is  $b_0 \approx 1.80866$ . Using the first expression in (28) a Kornoukhov-Dinnik solution (2) can be derived:

$$q_{cr} = 1.80866^2 \frac{k_3}{R^3} \approx 3.27 \frac{k_3}{R^3}. \quad (34)$$

An approximate formula for the critical force can be derived by substitution of the asymptotic series with a small parameter (32) into the equation (31), expanding both parts of the equation into a series, setting coefficients of the same powers equal and considering only terms of the first order of smallness:

$$q_{cr} = q_K \left(1 - 0.223 \frac{q_K R}{k_1} - 1.223 \frac{q_K R}{k_2}\right). \quad (35)$$

The solution for the model neglecting axial stiffness (Timoshenko beam theory) can be obtained from the (35) by letting  $k_1 \rightarrow \infty$ .

$$q_{cr} = q_K \left(1 - 1.223 \frac{q_K R}{k_2}\right). \quad (36)$$

The solution for the model regarding only bending stiffness can be obtained from the (35) by letting  $k_1 \rightarrow \infty, k_2 \rightarrow \infty$ . In that case the Kornoukhov-Dinnik solution (2) is derived.

Using the value for the critical load from (27) or (35) the mode of buckling can be found:

$$\begin{cases} u_\theta = \frac{1}{2} G_{cr} C_2 \theta \cos \theta + H_{cr} C_4 \sin \sqrt{A_{cr}} \theta; \\ w_\theta = \frac{1}{2} G_{cr} C_2 \theta \sin \theta - \frac{1}{2} G_{cr} C_2 \cos \theta + \frac{R}{k_1} C_2 \cos \theta - \sqrt{A_{cr}} H_{cr} C_4 \cos \sqrt{A_{cr}} \theta; \\ \varphi_\theta = -H_{cr} \frac{R}{k_3} C_2 \sin \theta + C_4 \sin \sqrt{A_{cr}} \theta, \end{cases} \quad (37)$$

where  $A_{cr}, H_{cr}, G_{cr}$  are labels from (24), where the critical force value was substituted.

It is easy to prove, that each of the terms in (37) has no left-to-right symmetry, so the buckling mode is antisymmetry. This goes with the results of the experiments [38], shown in Figure 3.

The comparison of the numerical exact solution (27), asymptotic solutions (35), (36) and a Kornoukhov-Dinnik solution (2) can be made. Consider an arch with radius  $R = 12$  m, cross-section is a thin-walled tube with a thickness of 10 mm and a variety of diameters: from 355.6 mm till 1420 mm. Geometrical and stiffness values can be found in Table 1.

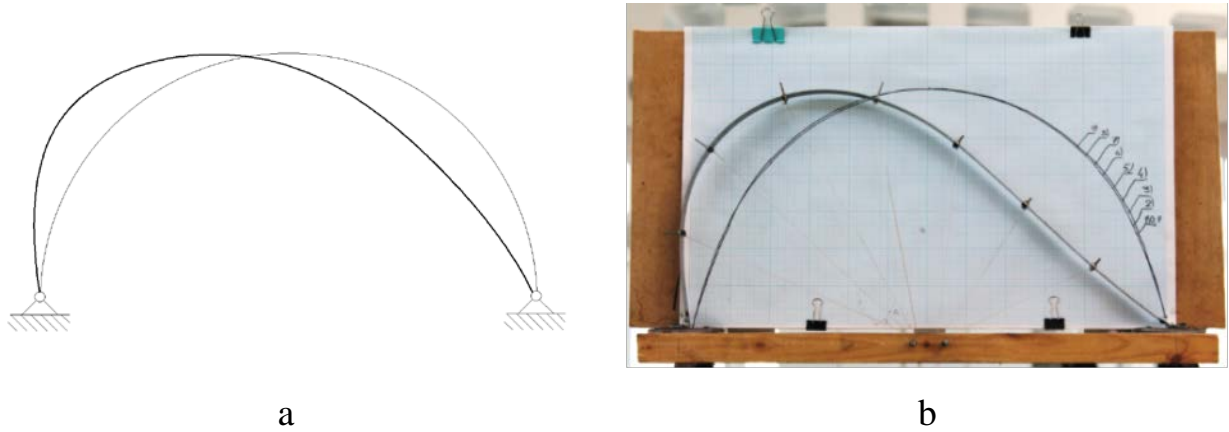


Figure 3. Buckling mode of the arch under the dead radial load: a – analytical model; b – experiment.

Table 1. Geometrical and stiffness values of the cross-section.

Cross-section	Outer diameter, [mm]	Cross-section area $A$ , [cm <sup>2</sup> ]	Moment of inertia $I$ , [m <sup>4</sup> ]	Axial stiffness $k_1 = EA$ , [N]	Shear stiffness $k_2 = GAk$ , [N]	Bending stiffness $k_3 = EI$ , [N·m <sup>2</sup> ]
355.6×10	355.60	108.57	1.62E-04	2.1714E+09	4.1758E+08	1.5698E+08
377×10	377.00	115.29	1.94E-04	2.3058E+09	4.4342E+08	1.9832E+08
406.4×10	406.40	124.53	2.45E-04	2.4906E+09	4.7896E+08	2.6780E+08
426×10	426.00	130.69	2.83E-04	2.6138E+09	5.0265E+08	3.2332E+08
478×10	478.00	147.02	4.03E-04	2.9404E+09	5.6546E+08	5.1252E+08
530×10	530.00	163.36	5.52E-04	3.2672E+09	6.2831E+08	7.7465E+08
630×10	630.00	194.77	9.36E-04	3.8954E+09	7.4912E+08	1.5465E+09
720×10	720.00	223.05	1.41E-03	4.4610E+09	8.5788E+08	2.6383E+09
820×10	820.00	254.46	2.09E-03	5.0892E+09	9.7869E+08	4.4387E+09
920×10	920.00	285.88	2.96E-03	5.7176E+09	1.0995E+09	7.0332E+09
1020×10	1020.00	317.29	4.05E-03	6.3458E+09	1.2203E+09	1.0627E+10
1120×10	1120.00	348.71	5.37E-03	6.9742E+09	1.3412E+09	1.5448E+10
1220×10	1220.00	380.12	6.96E-03	7.6024E+09	1.4620E+09	2.1749E+10
1420×10	1420.00	442.95	1.10E-02	8.8590E+09	1.7037E+09	3.9917E+10

Consider the non-dimensional values of critical forces (27), (35), (36) by dividing them by  $q_K$  and construct a plot (Figure 4). An equation (27) is solved using the iterative Newton’s method with the help of Wolfram Mathematica software.

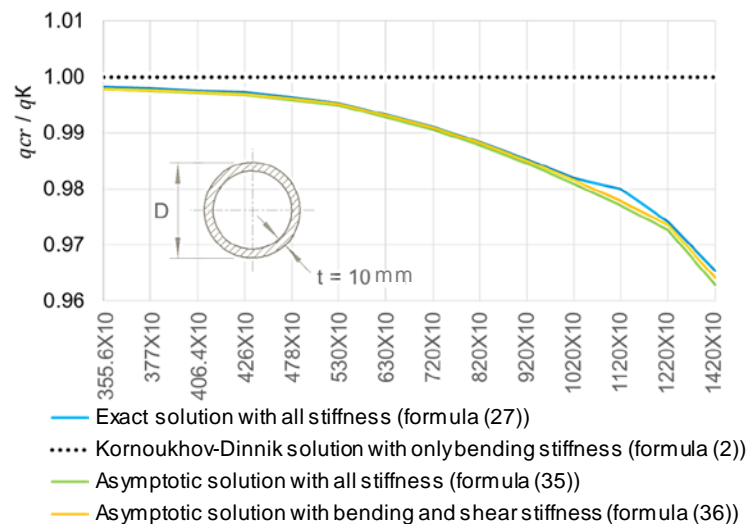


Figure 4. The comparison for the critical load values.

According to the comparison of the critical loads, the one, that considers all stiffnesses is tends to be less, than the one, that regards only bending stiffness. It is worthwhile noticing, that inaccuracy between the Kornoukhov-Dinnik solution (2) and transcendental equation (27) increases as the size of the cross-section grows. Critical loads, estimated using the asymptotic formulas (35) and (36) are always smaller, than the exact values, so they improve the margin of safety. Moreover, inaccuracy between the asymptotic formulas and the solution (27) is less than 0.3 %.

The results can be used in the analytical defining of the stress-strain state of structures, where tensile-compression and shear stiffnesses make a significant contribution. Such structures include masonry and concrete arches [39–42], curvilinear elements of dams [43, 44] and long-span steel roofs [45, 46].

## 4. Conclusions

1. An analytical model of a geometrical non-linear deformation and stability of the plane elastic round arch taking into account all stiffnesses was worked out. This model contains:

- 1.1. exact non-linear equilibrium equations;
- 1.2. variational formulation for the problem is defined as finding stationary point of Lagrange functional;
- 1.3. static stability functional;
- 1.4. exact stability equations.

2. Based on the derived equations the problem of the equilibrium stability of the round arch under the dead radial load was solved. The characteristic transcendental equation and its asymptotic solution as a number of simple formulas, suitable for practical application, were worked out.

3. The comparison of described solution which regards all the bar's stiffnesses and classical Kornoukhov-Dinnik solution based on bending stiffness, was made. It was shown, that considering axial and shear stiffnesses leads to decreasing the values of the critical forces.

## References

1. Timoshenko, S.P., Gere, G.M. Theory of Elastic Stability. 17th ed. McGraw-Hill International Book Company. New York, 1985. 541 p.
2. Eslami, M.R. Buckling and Postbuckling of Beams, Plates and Shells. 1st ed. Springer. New York, 2018. 588 p.
3. Farshad, M. Stability of Structures. 1st ed. Elsevier Science. New York, 1994. 425 p.
4. Simitses, G.J., Hodge, D.H. Fundamentals of Structural Stability. 1st ed. Elsevier Science. New York, 2006. 379 p.
5. Kornoukhov, N.V. Prochnost i ustoychivost sterzhnevyykh system [Strength and stability of rod systems]. Moscow: Gosstroyizdat, 1949. 376 p. (rus)
6. Dinnik, A.N. Ustoychivost arok [Stability of arches]. Moscow: Gostekhteorizdat, 1946. 128 p. (rus)
7. Pi, Y.L., Bradford, M.A. Non-linear buckling and postbuckling analysis of arches with unequal rotational end restraints under a central concentrated load. International Journal of Solids and Structures. 2012. 49(26). Pp. 3762–3773. DOI 10.1016/j.ijsolstr.2012.08.012.
8. Bradford, M.A., Uy, B., Pi, Y.-L. In-Plane Elastic Stability of Arches under a Central Concentrated Load. Journal of Engineering Mechanics. 2002. 128(7). Pp. 710–719. DOI 10.1061/(ASCE)0733-9399(2002)128:7(710)
9. Bateni, M., Eslami, M.R. Non-linear in-plane stability analysis of FGM circular shallow arches under central concentrated force. International Journal of Non-Linear Mechanics. 2014. No. 60. Pp. 58–69. DOI 10.1016/j.ijnonlinmec.2014.01.001
10. Pi, Y.L., Bradford, M.A., Uy, B. In-plane stability of arches. International Journal of Solids and Structures. 2002. 39(1). Pp. 105–125. DOI 10.1016/S0020-7683(01)00209-8
11. Pi, Y.L., Trahair, N.S. Non-linear buckling and postbuckling of elastic arches. Engineering Structures. 1998. 20(7). Pp. 571–579. DOI 10.1016/S0141-0296(97)00067-9
12. Cai, J., Feng, J. Buckling of parabolic shallow arches when support stiffens under compression. Mechanics Research Communications. 2010. 37(5). Pp. 467–471. DOI 10.1016/j.mechrescom.2010.05.004
13. Cai, J., Xu, Y., Feng, J., Zhang, J. In-Plane Elastic Buckling of Shallow Parabolic Arches under an External Load and Temperature Changes. Journal of Structural Engineering. 2012. 138(11). Pp. 1300–1309. DOI 10.1061/(ASCE)ST.1943-541X.0000570.
14. Bateni, M., Eslami, M.R. Non-linear in-plane stability analysis of FG circular shallow arches under uniform radial pressure. Thin-Walled Structures. 2015. No. 94. Pp. 302–313. DOI 10.1016/j.tws.2015.04.019
15. Lu, H., Liu, A., Pi, Y.L., Bradford, M.A., Fu, J., Huang, Y. Localized loading and nonlinear instability and post-instability of fixed arches. Thin-Walled Structures. 2018. No. 131. Pp. 165–178. DOI 10.1016/j.tws.2018.06.019
16. Xu, Y., Gui, X., Zhao, B., Zhou, R. In-Plane Elastic Stability of Arches under a Radial Concentrated Load. Engineering. 2014. 09(06). Pp. 572–583. DOI 10.4236/eng.2014.69058
17. Paimushin, V.N., Polyakova, N.V. The consistent equations of the theory of plane curvilinear rods for finite displacements and linearized problems of stability. Journal of Applied Mathematics and Mechanics. 2009. 73(2). Pp. 220–236. DOI 10.1016/j.jappmathmech.2009.04.012
18. Paimushin, V.N., Polyakova, N.V. The stability of a ring under the action of a linear torque, constant along the perimeter. Journal of Applied Mathematics and Mechanics. 2011. 75(6). Pp. 691–699. DOI 10.1016/j.jappmathmech.2012.01.009
19. Karnovsky, I.A. Theory of Arched Structures: Strength, Stability, Vibration. 1st ed. Springer. New York, 2012. DOI 10.1007/978-1-4614-0469-9
20. Karnovsky, I.A., Lebed, O. Advanced Methods of Structural Analysis. 1st ed. Springer. New York, 2010. DOI 10.1007/978-1-4419-1047-9

21. Galishnikova, V.V., Pahl, P.J. Analysis of frame buckling without sidesway classification. *Structural Mechanics of Engineering Constructions and Buildings*. 2018. 14(4). Pp. 299–312. DOI 10.22363/1815-5235-2018-14-4-299-312
22. Han, Q., Cheng, Y., Lu, Y., Li, T., Lu, P. Nonlinear buckling analysis of shallow arches with elastic horizontal supports. *Thin-Walled Structures*. 2016. No.109. Pp. 88–102. DOI 10.1016/j.tws.2016.09.016
23. Zhou, Y., Yi, Z., Stanciulescu, I. Nonlinear Buckling and Post-buckling of Shallow Arches with Vertical Elastic Supports. *Journal of Applied Mechanics*. 2019. 86(6). Pp. 1–16. DOI 10.1115/1.4042572
24. Ghayesh, M.H., Farokhi, H. Mechanics of tapered axially functionally graded shallow arches. *Composite Structures*. 2018. No. 188. Pp. 233–241. DOI 10.1016/j.compstruct.2017.11.017
25. Kiss, L.P. Nonlinear stability analysis of FGM shallow arches under an arbitrary concentrated radial force. *International Journal of Mechanics and Materials in Design*. 2019. No. 2. Pp. 1–18. DOI 10.1007/s10999-019-09460-2
26. Cai, J., Zhou, Y., Feng, J. Post-buckling behavior of a fixed arch for variable geometry structures. *Mechanics Research Communications*. 2013. No. 52. Pp. 74–80. DOI 10.1016/j.mechrescom.2013.07.002
27. Lu, Y., Cheng, Y., Han, Q. Experimental investigation into the in-plane buckling and ultimate resistance of circular steel arches with elastic horizontal and rotational end restraints. *Thin-Walled Structures*. 2017. No. 118. Pp. 164–180. DOI 10.1016/j.tws.2017.05.010
28. Guo, Y.L., Yuan, X., Bradford, M.A., Pi, Y.L., Chen, H. Strength design of pin-ended circular steel arches with welded hollow section accounting for web local buckling. *Thin-Walled Structures*. 2017. No. 115. Pp. 100–109. DOI 10.1016/j.tws.2017.02.010
29. Guo, Y.-L., Chen, H., Pi, Y.-L., Dou, C., Bradford, M.A. In-Plane Failure Mechanism and Strength of Pin-Ended Steel I-Section Circular Arches with Sinusoidal Corrugated Web. *Journal of Structural Engineering*. 2016. 142(2). Pp. 15–21. DOI 10.1061/(ASCE)ST.1943-541X.0001393
30. Guo, Y.L., Chen, H., Pi, Y.L. In-plane failure mechanisms and strength design of circular steel planar tubular Vierendeel truss arches. *Engineering Structures*. 2017. No. 151. Pp. 488–502. DOI 10.1016/j.engstruct.2017.08.055
31. Perelmuter, A.V., Slivker, V.I. *Handbook of Mechanical Stability in Engineering*. Vol. 1: General Theorems and Individual Members of Mechanical Systems. World Scientific. New York, 2013. DOI 10.1142/8372
32. Lalin, V.V., Rozin, L.A., Kushova, D.A. Variational functionals for two-dimensional equilibrium and stability problems of Cosserat-Timoshenko elastic rods. *Magazine of Civil Engineering*. 2013. 36(1). Pp. 87–96. DOI 10.5862/MCE.36.11 (rus)
33. Simo, J.C. A finite strain beam formulation. The three-dimensional dynamic problem. Part I. *Comput. Methods Appl. Mech. Eng.* 1985. 49(1). Pp. 55–70. DOI 10.1016/0045-7825(85)90050-7
34. Lalin, V.V., Zdanchuk, E.V., Kushova, D.A., Rozin, L.A. Variational formulations for non-linear problems with independent rotational degrees of freedom. *Magazine of Civil Engineering*. 2015. 56(04). Pp. 54–65. DOI 10.5862/MCE.56.7 (rus)
35. Lang, H., Linn, J., Arnold, M. Multi-body dynamics simulation of geometrically exact Cosserat rods. *Multibody System Dynamics*. 2011. 25(3). Pp. 285–312. DOI 10.1007/s11044-010-9223-x
36. Jelenić, G., Crisfield, M.A. Geometrically exact 3D beam theory: Implementation of a strain-invariant finite element for statics and dynamics. *Computer Methods in Applied Mechanics and Engineering*. 1999. 171(1–2). Pp. 141–171. DOI 10.1016/S0045-7825(98)00249-7
37. Gerstmayr, J., Shabana, A.A. Analysis of thin beams and cables using the absolute nodal co-ordinate formulation. *Nonlinear Dynamics*. 2006. 45(1–2). Pp. 109–130. DOI 10.1007/s11071-006-1856-1
38. Dmitriev, A.N., Semenov, A.A., Lalin, V.V. Stability of the equilibrium of elastic arches with a deformed axis. *Construction of Unique Buildings and Structures*. 2018. 2(67). Pp. 19–31. DOI 10.18720/CUBS.67.2 (rus)
39. Bepalov, V., Semenova, M. Influence of masonry adhesion on mechanical performance of arches-walls. *MATEC Web Conf.* 245 02002. 2018. DOI 10.1051/mateconf/201824502002
40. Kaldar-ool, A-Kh.B., Babanov, V.V., Allahverdiv, B.M., Saaya, S.S. Additional load on barrel vaults of architectural monuments. *Magazine of Civil Engineering*. 2018. 84(8). Pp. 15–28. DOI 10.18720/MCE.84.2.
41. Zubkov, S.V., Ulybin, A.V., Fedotov, S.D. Assessment of mechanical properties of brick masonry by flat-jack method. *Magazine of Civil Engineering*. 2015. 60(8). Pp. 20–29. DOI 10.18720/MCE.60.3.
42. Orlovich, R.B., Nowak, R., Vatin, N.I., Bepalov V.V. Natural oscillations of a rectangular plates with two adjacent edges clamped. *Magazine of Civil Engineering*. 2018. 82(6). Pp. 95–102. DOI 10.18720/MCE.82.9
43. Hirkovskis, A., Serdjusks, D., Goremikins, V., Pakrastins, L., Vatin, N.I. Behaviour analysis of load-bearing aluminium members. *Magazine of Civil Engineering*. 2015. 57(5). Pp. 86–96. DOI 10.5862/MCE.57.8
44. Gusevs, J., Serdjusks, D., Artebjakina, G.I., Afanasjeva, E.A., Goremikins, V. Behaviour of load-carrying members of velodromes' long-span steel roof. *Magazine of Civil Engineering*. 2016. 65(5). Pp. 3–16. DOI 10.5862/MCE.65.1
45. Eigenson, S.N., Korikhin, N.V., Golovin, A.I. Experimental investigation considering the stressed state of some essential constructions of large hydropower buildings. *Magazine of Civil Engineering*. 2014. 45(1). Pp. 59–70. DOI 10.5862/MCE.45.7
46. Kolosova, G.S., Lalin, V.V., Kolosova, A.V. The effect of construction joints and cracks on the stress-strain state of the arch-gravity dam. *Magazine of Civil Engineering*. 2013. 40(5). Pp. 76–85. DOI 10.5862/MCE.40.9

### Contacts:

Vladimir Lalin, +7(921)319-98-78; [vllalin@yandex.ru](mailto:vllalin@yandex.ru)  
 Andrey Dmitriev, +7(999)249-09-00; [dmitriefan@outlook.com](mailto:dmitriefan@outlook.com)  
 Stanislav Diakov, +7(921)300-89-17; [stass.f.dyakov@gmail.com](mailto:stass.f.dyakov@gmail.com)



DOI: 10.18720/MCE.89.4

## Геометрически нелинейное деформирование и устойчивость упругих арок

**В.В. Лалин, А.Н. Дмитриев\*, С.Ф. Дьяков**

*Санкт-Петербургский политехнический университет Петра Великого, Санкт-Петербург, Россия*

**Keywords:** устойчивость конструкций, потеря устойчивости, геометрически точная теория, «мертвая» нагрузка, круговая арка, жесткость, точка стационарности, функционал Лагранжа

**Аннотация.** В статье рассматривается плоская круговая двухшарнирная арка, нагруженная потенциальной «мертвой» нагрузкой. Для описания напряженно-деформированного состояния и устойчивости равновесия используется геометрически точная теория, в соответствии с которой каждая точка стержня имеет две трансляционные степени свободы и одну вращательную, не зависящую от трансляционных. Для получения решения не используются никакие упрощения о величинах перемещений и углов поворота, а также учитываются все жесткости стержня – продольная, сдвиговая и изгибная. Получены точные нелинейные дифференциальные уравнения статической задачи. Сформулирована вариационная постановка в виде задачи поиска точки стационарности функционала типа Лагранжа. Доказана эквивалентность дифференциальной и вариационной постановок. Получены точные уравнения устойчивости, учитывающие геометрически нелинейное деформирование в докритическом состоянии. На основе полученных уравнений решена задача устойчивости равновесия круговой арки при действии «мертвого» радиального давления с учетом всех жесткостей стержня. Получено характеристическое трансцендентное уравнение, а также асимптотическое решение этого уравнения в виде простых формул, пригодных для практического применения. Выполнено сравнение полученного решения, учитывающего все жесткости стержня, с классическим решением, учитывающим только изгибную жесткость.

### Литература

1. Timoshenko S.P., Gere G.M. Theory of Elastic Stability. 17th ed. McGraw-Hill International Book Company. New York, 1985. 541 p.
2. Eslami M.R. Buckling and Postbuckling of Beams // Plates and Shells. 1st ed. Springer. New York, 2018. 588 p.
3. Farshad M. Stability of Structures. 1st ed. Elsevier Science. New York, 1994. 425 p.
4. Simitses G.J., Hodge D.H. Fundamentals of Structural Stability. 1st ed. Elsevier Science. New York, 2006. 379 p.
5. Корнухов Н.В. Прочность и устойчивость стержневых систем. М.: Госстройиздат, 1949. 376 с.
6. Динник А.Н. Устойчивость арок. М.: Гостехтеориздат, 1946. 128 с.
7. Pi Y.L., Bradford M.A. Non-linear buckling and postbuckling analysis of arches with unequal rotational end restraints under a central concentrated load // International Journal of Solids and Structures. 2012. 26(49). Pp. 3762-3773.
8. Bradford M.A., Uy B., Pi Y.-L. In-Plane Elastic Stability of Arches under a Central Concentrated Load // Journal of Engineering Mechanics. 2002. No. 7 (128). Pp. 710–719. DOI 10.1061/(ASCE)0733-9399(2002)128:7(710)
9. Bateni M., Eslami M.R. Non-linear in-plane stability analysis of FGM circular shallow arches under central concentrated force // International Journal of Non-Linear Mechanics. 2014. No. 60. Pp. 58–69. DOI 10.1016/j.ijnonlinmec.2014.01.001
10. Pi Y.L., Bradford M.A., Uy B. In-plane stability of arches // International Journal of Solids and Structures. 2002. No. 1(39). Pp. 105–125. DOI 10.1016/S0020-7683(01)00209-8
11. Pi Y.L., Trahair N.S. Non-linear buckling and postbuckling of elastic arches // Engineering Structures. 1998. No. 7(20). Pp. 571–579. DOI 10.1016/S0141-0296(97)00067-9
12. Cai J., Feng J. Buckling of parabolic shallow arches when support stiffens under compression // Mechanics Research Communications. 2010. No. 5(37). Pp. 467–471. DOI 10.1016/j.mechrescom.2010.05.004
13. Cai J., Xu Y., Feng J., Zhang J. In-Plane Elastic Buckling of Shallow Parabolic Arches under an External Load and Temperature Changes // Journal of Structural Engineering. 2012. No. 11(138). Pp. 1300–1309. DOI 10.1061/(ASCE)ST.1943-541X.0000570.
14. Bateni M., Eslami M.R. Non-linear in-plane stability analysis of FG circular shallow arches under uniform radial pressure. Thin-Walled Structures. 2015. No. 94. Pp. 302–313. DOI 10.1016/j.tws.2015.04.019
15. Lu H., Liu A., Pi Y.L., Bradford M.A., Fu J., Huang, Y. Localized loading and nonlinear instability and post-instability of fixed arches // Thin-Walled Structures. 2018. No. 131. Pp. 165–178. DOI 10.1016/j.tws.2018.06.019
16. Xu Y., Gui X., Zhao B., Zhou R. In-Plane Elastic Stability of Arches under a Radial Concentrated Load // Engineering. 2014. No. 6(9). Pp. 572–583. DOI 10.4236/eng.2014.69058
17. Paimushin V.N., Polyakova N.V. The consistent equations of the theory of plane curvilinear rods for finite displacements and linearized problems of stability // Journal of Applied Mathematics and Mechanics. 2009. No. 2(73). Pp. 220–236. DOI 10.1016/j.jappmathmech.2009.04.012

18. Paimushin V.N., Polyakova N.V. The stability of a ring under the action of a linear torque, constant along the perimeter // Journal of Applied Mathematics and Mechanics. 2011. No. 6(75). Pp. 691–699. DOI 10.1016/j.jappmathmech.2012.01.009
19. Karnovsky I.A. Theory of Arched Structures: Strength, Stability, Vibration. 1st ed. Springer. New York, 2012. DOI 10.1007/978-1-4614-0469-9
20. Karnovsky I.A., Lebed O. Advanced Methods of Structural Analysis. 1st ed. Springer. New York, 2010. DOI 10.1007/978-1-4419-1047-9
21. Галишников В.В., Паль П.Я. Анализ устойчивости рам без учета классификации по возможности поперечных смещений // Строительная механика инженерных конструкций и сооружений. 2018. No. 4(14). С. 299–312. DOI: 10.22363/1815-5235-2018-14-4-299-312.
22. Han Q., Cheng Y., Lu Y., Li T., Lu P. Nonlinear buckling analysis of shallow arches with elastic horizontal supports // Thin-Walled Structures. 2016. No. 109. Pp. 88–102. DOI 10.1016/j.tws.2016.09.016
23. Zhou Y., Yi Z., Stanciulescu I. Nonlinear Buckling and Post-buckling of Shallow Arches with Vertical Elastic Supports // Journal of Applied Mechanics. 2019. No. 6(86). Pp. 1–16. DOI 10.1115/1.4042572
24. Ghayesh M.H., Farokhi H. Mechanics of tapered axially functionally graded shallow arches // Composite Structures. 2018. No. 188. Pp. 233–241. DOI 10.1016/j.compstruct.2017.11.017
25. Kiss L.P. Nonlinear stability analysis of FGM shallow arches under an arbitrary concentrated radial force // International Journal of Mechanics and Materials in Design. 2019. No. 2. Pp. 1–18. DOI 10.1007/s10999-019-09460-2
26. Cai J., Zhou Y., Feng J. Post-buckling behavior of a fixed arch for variable geometry structures // Mechanics Research Communications. 2013. No. 52. Pp. 74–80. DOI 10.1016/j.mechrescom.2013.07.002
27. Lu Y., Cheng Y., Han Q. Experimental investigation into the in-plane buckling and ultimate resistance of circular steel arches with elastic horizontal and rotational end restraints // Thin-Walled Structures. 2017. No. 118. Pp. 164–180. DOI 10.1016/j.tws.2017.05.010
28. Guo Y.L., Yuan X., Bradford M.A., Pi Y.L., Chen, H. Strength design of pin-ended circular steel arches with welded hollow section accounting for web local buckling // Thin-Walled Structures. 2017. No. 115. Pp. 100–109. DOI 10.1016/j.tws.2017.02.010
29. Guo Y.-L., Chen H., Pi Y.-L., Dou C., Bradford M.A. In-Plane Failure Mechanism and Strength of Pin-Ended Steel I-Section Circular Arches with Sinusoidal Corrugated Web // Journal of Structural Engineering. 2016. No. 2(142). Pp. 15–21. DOI 10.1061/(ASCE)ST.1943-541X.0001393
30. Guo, Y.L., Chen, H., Pi, Y.L. In-plane failure mechanisms and strength design of circular steel planar tubular Vierendeel truss arches // Engineering Structures. 2017. No. 151. Pp. 488–502. DOI 10.1016/j.engstruct.2017.08.055
31. Перельмутер А.В., Сливкер В.И. Устойчивость равновесия конструкций и родственные проблемы. Т. 1. Общие теоремы. Устойчивость отдельных элементов механических систем. М.: Изд-во СКАД СОФТ, 2010. 681 с.
32. Лалин В.В., Розин Л.А., Кушова Д.А. Вариационная постановка плоской задачи геометрически нелинейного деформирования и устойчивости упругих стержней // Инженерно-строительный журнал. 2013. № 1(36). С. 87–96. DOI 10.5862/MCE.36.11
33. Simo J.C. A finite strain beam formulation // The three-dimensional dynamic problem. Part I. Comput. Methods Appl. Mech. Eng. 1985. No. 1(49). Pp. 55–70. DOI 10.1016/0045-7825(85)90050-7
34. Лалин В.В., Зданчук Е.В., Кушова Д.А., Розин Л.А. Вариационные постановки нелинейных задач с независимыми вращательными степенями свободы // Инженерно-строительный журнал. 2015. № 4(56). С. 54–65. DOI 10.5862/MCE.56.7
35. Lang H., Linn J., Arnold M. Multi-body dynamics simulation of geometrically exact Cosserat rods // Multibody System Dynamics. 2011. No. 3(25). Pp. 285–312. DOI 10.1007/s11044-010-9223-x
36. Jelenić G., Crisfield M.A. Geometrically exact 3D beam theory: Implementation of a strain-invariant finite element for statics and dynamics // Computer Methods in Applied Mechanics and Engineering. 1999. No. 1–2(171). Pp. 141–171. DOI 10.1016/S0045-7825(98)00249-7
37. Gerstmayr J., Shabana A.A. Analysis of thin beams and cables using the absolute nodal co-ordinate formulation // Nonlinear Dynamics. 2006. No. 1–2(45). Pp. 109–130. DOI 10.1007/s11071-006-1856-1
38. Дмитриев А.Н., Семенов А.А., Лалин В.В. Устойчивость равновесия упругих арок с учетом искривления оси // Строительство уникальных зданий и сооружений. 2018. № 4(67). С. 19–31. DOI:10.18720/CUBS.67.2.
39. Bepalov V., Semenova M. Influence of masonry adhesion on mechanical performance of arches-walls // MATEC Web Conf. 245 02002. 2018. DOI 10.1051/mateconf/201824502002
40. Калдар-оол А.Б., Бабанов В.В., Аллахвердов Б.М., Саая С.С. Дополнительная нагрузка на коробовый свод в памятнике архитектуры // Инженерно-строительный журнал. 2018. № 84(8). С. 15–28. DOI:10.18720/MCE.84.2.
41. Зубков С.В., Улыбин А.В., Федотов С.Д. Исследование механических свойств кирпичной кладки методом плоских домкратов // Инженерно-строительный журнал. 2015. № 8(60). С. 20–29. DOI:10.5862/MCE.60.3.
42. Орлович Р.Б., Новак Р., Ватин Н.И., Беспалов В.В. Оценка прочности кирпичебетонных Прусских сводов // Инженерно-строительный журнал. 2018. № 6(82). С. 95–102. DOI:10.18720/MCE.82.9.
43. Хирковский А., Сердюк Д.О., Горемыкин В.В., Пакрастиньш Л., Ватин Н.И. Анализ работы несущих элементов из алюминиевых сплавов // Инженерно-строительный журнал. 2015. № 5(57). С. 86–96. DOI 10.5862/MCE.57.8
44. Гусев Е., Сердюк Д.О., Артебякина Г.И., Афанасьева Е.А., Горемыкин В.В. Behaviour of load-carrying members of velodromes' long-span steel roof // Инженерно-строительный журнал. 2016. № 5(65). С. 3–16. DOI:10.5862/MCE.65.1.
45. Эйгенсон С.Н., Корихин Н.В., Головин А.И. Экспериментальное исследование напряженного состояния некоторых ответственных конструкций крупных гидроэнергетических сооружений // Инженерно-строительный журнал. 2014. № 1(45). С. 59–70. DOI:10.5862/MCE.45.7.
46. Колосова Г.С., Лалин В.В., Колосова А.В. Влияние строительных швов и трещин на напряженно-деформированное состояние арочно-гравитационной плотины // Инженерно-строительный журнал. 2013. № 5(40). С. 76–85. DOI 10.5862/MCE.40.9

#### **Контактные данные:**

*Владимир Владимирович Лалин, +7(921)319-98-78; эл. почта: vllalin@yandex.ru*  
*Андрей Николаевич Дмитриев, +7(999)249-09-00; эл. почта: dmitriefan@outlook.com*  
*Станислав Федорович Дьяков, +7(921)300-89-17; эл. почта: stass.f.dyakov@gmail.com*



DOI: 10.18720/MCE.89.5

## Optimization of the structure and properties of foam-glass ceramics

**K.S. Ivanov**

*Earth Cryosphere Institute SB RAS, Tyumen, Russia*

**Keywords:** building material, thermal insulation, glass ceramics, silicates

**Abstract.** The basic properties of foam-glass ceramics — a porous inorganic material are optimized in the study. This material is used for thermal insulation of various engineering structures: foundations of buildings, roads and railways, pipelines, etc. The main raw material components of the material are sodium hydroxide and opal-cristobalite rocks: diatomite, tripoli, opoka. The mixture of components is subjected to firing and foams with the formation of a porous structure with vitreous and crystalline phases. A significant impact of two different ways of preparing the batch on the basic properties of the material was studied and analyzed. In the first method, the batch was obtained as a suspension with a high water content, which was subjected to mechanical activation in a vibratory mill. In the second method, the batch was obtained by pushing a mixture of components through calibrated holes with the help of a screw auger. Thus, the batch was an extruded tough-plastic granular mass with lower water content. As a result, the formation of a heterogeneous structure of the samples and the presence of dense non-foamed inclusions, leading to an increased average density of the material were established in the first method. The extruded batch in the second method was foamed more evenly without stratification; thereby the average density of the samples was reduced. An additional reduction in the average density of the samples by 17% due to the intensification of dissolution of silica during the autoclave treatment of extruded batch was observed. The extrusion method is recommended for the production of foam-glass ceramics in granular form, which contributes to the saving of expensive sodium hydroxide.

### 1. Introduction

Foam-glass ceramics is an inorganic insulating material of cellular structure. The advantages of foam-glass ceramics include the high prevalence of the raw material base — these are opal-cristobalite and zeolite-containing rocks [1, 2], low thermal conductivity, water resistance, non-flammability and also a wide scope of application. Foam-glass ceramics can be obtained both in block form (plates, shells, segments) and in the form of granules. The material can be used for thermal insulation of enclosing structures of residential and industrial buildings [3]. Another field of application for granulated foam-glass ceramics is the thermal insulation of foundations of engineering structures in areas with seasonal freezing of soils to protect against frost heaving. Such structures include: buildings with low-depth foundations, roads, railways, pipelines, etc. [4–5].

The disadvantages of the material include the need to use expensive sodium hydroxide, therefore reducing its content, taking into account the preservation of the functional properties of foam-glass ceramics, is an actual scientific and technical problem. Another limiting factor of industrial production of foam-glass ceramics is the lack of a unified technology of the material synthesis.

Opal-cristobalite rocks which include diatomite, tripoli, and flask are rich in amorphous forms of silica. The key process in the synthesis of foam-glass ceramics is the dissolution amorphous silica in the alkalis. The mixture of the rock and alkaline solution is subjected to firing and foams at a temperature of 800–900 °C. Foaming of the mixture during the physicochemical interaction in the system  $\text{SiO}_2\text{-Na}_2\text{O-H}_2\text{O}$  occurs in two stages. At the first stage, when components are mixed, the formation of hydrated alkali silicates occurs. At the second stage, during firing, the batch passes into the pyroplastic state with simultaneous dehydration of hydrated alkaline silicates and the subsequent polycondensation of silicon-oxygen anions [6–9]. As a result, a

---

Ivanov, K.S. Optimization of the structure and properties of foam-glass ceramics. Magazine of Civil Engineering. 2019. 89(5). Pp. 52–60. DOI: 10.18720/MCE.89.5

Иванов К.С. Оптимизация структуры и свойств пеностеклокерамики // Инженерно-строительный журнал. 2019. № 5(89). С. 52–60. DOI: 10.18720/MCE.89.5



This open access article is licensed under CC BY 4.0 (<https://creativecommons.org/licenses/by/4.0/>)

«silicate foam», containing both the vitreous phase and the crystalline phase, introduced with the insoluble residue of the opal-cristobalite rock, is formed.

The advantage of this method is the fact that an inorganic thermal insulation material is synthesized in one stage and the intermediate process of sintering the granular glass is excluded [10–12]. Unlike thermal insulation materials obtained by hot-foaming method [13, 14], commercial liquid glass is not used in described method. In addition, the usage of waste glass, that is necessary in classical foam-glass production [15, 16], is not required in foam-glass ceramics technology.

The methodology of mixing the opal-cristobalite rock and alkali can have a significant impact on the structure formation and functional properties of foam-glass ceramics. On the one hand, the mixing process should be accompanied by chemical interaction between the components with the formation of hydrated sodium silicates. On the other hand, opal-cristobalite rocks have a high adsorption capacity, which makes it difficult the batching process. Thus, it is obvious that the procedure of the preparing the mixture is a complex physicochemical process that has not been adequately covered in the scientific literature. For example, in studies of recent years, the methodology of mixing components is described insufficiently, but only their ratios are given [1, 6–8].

Taking into account the above features of mixing the components, the studies examined two different ways of the batching process. The first (wet method) consists in obtaining a suspension with a relatively high water content from milled opal-cristobalite rock, sodium hydroxide and water. It can be assumed that in the liquid phase a better quality of the reaction between sodium hydroxide and amorphous silica of opal cristobalite rock can be achieved. It should be noted that these batches in the form of liquid suspensions, are used in the preparation of various materials and binders and play a structure-forming role [17, 18]. The disadvantage of this method is the difficulty of further drying the batch before firing.

In the second embodiment, the continuous pushing of components through calibrated holes with the help of a screw auger, in one or more stages, is used (extrusion method). The process of interaction between sodium hydroxide solution and amorphous silica of the rock is intensified under the mechanical influence of the screw, resulting a tight-plastic batch with high homogeneity. Secondly, the processes of mixing components and granulation of the batch are combined in one operation. Compared to the wet method, the granulated mixture has a low water content, which simplifies its further drying, since in the wet method, the water content can reach 70 % or more, whereas in the extrusion method 16–18 %.

The purpose of the work was to study the influence of wet and extrusion methods of obtaining the batch on the structural features and basic properties of foam-glass ceramics.

## 2. Materials and experimental technique

### 2.1. Diatomite analysis

The opal-cristobalite rock was represented by diatomite with the following chemical composition, mas. %:  $\text{SiO}_2$  — 76.71,  $\text{Al}_2\text{O}_3$  — 7.33,  $\text{Fe}_2\text{O}_3$  — 2.43,  $\text{CaO}$  — 0.46,  $\text{MgO}$  — 0.93,  $\text{R}_2\text{O}$  — 1.24,  $\text{TiO}_2$  — 0.61,  $\text{SO}_3$  — 0.72, loss of ignition — 9.57. The diatomite was dried to constant weight at 100 °C, powdered using a ball mill and sifted through a sieve with a mesh size of 0.16 mm. The structure of diatomite was studied using a Jeol JSM-6510A scanning electron microscope (Japan) and a DRON-6 diffractometer (Russia), a wavelength of 0.179 nm, Cu K $\alpha$ -radiation, and a Fe-filter.

SEM image shown in Figure 1 suggests that diatomite is composed mainly of the remains of the shells of diatoms — fossilized algae, consisting of amorphous silica. The maximum size of shells is about 0.1 mm. A high content of the amorphous phase in the form of opal in the diatomite is indicated by the disperse reflex on the diffractogram of X-ray phase analysis in the range of angles of 18–26° (Figure 2a). The crystalline phases of diatomite were identified using the American Mineralogist Crystal Structure Database. The XRD pattern (Figure 2a) shows the presence of quartz (reflections at angles of 20.87°, 26.65°, 36.56°, 39.49°, 40.41° and 50.17°), montmorillonite (reflections at angles 19.60° and 34.67°), illite, having similar reflections to montmorillonite, as well as feldspar mineral albite (reflections at angles of 21.69° and 27.84°).

In order to quantify the content of soluble silica the diatomite was dissolved in NaOH solution with a concentration of 20 % in a mass ratio of solid and liquid phase equal to 1:3. To intensify the dissolution, the mixture was heated to a temperature of 90 °C and continuously stirred for 4 hours. By determining the concentration of  $\text{SiO}_2$  in the resulting suspension using the method [19], it was established that diatomite contains 44.6 % of soluble silica in its composition. The insoluble mass of diatomite (55.4 %) falls on the clay minerals, feldspar and organic impurities.

Figure 3a shows TG, DTG and DSC curves of thermal analysis of diatomite. The endothermic effect on the DSC curve in the range of 70–200 °C corresponds to the removal of physically bound (adsorption) water from the sample. The clay minerals of diatomite are dehydrated at 490 °C, which is confirmed by the corresponding peak on the DTG curve. The exothermic effect at a temperature of 350 °C can be explained by

the burning out of organic impurities. The last endothermic effect on the DSC curve at 870 °C is not associated with a change in the sample mass and characterizes the structural changes of montmorillonite and illite, which is confirmed by the thermal analysis of these minerals [20]. Thus, the main phases of diatomite are opal, in the form of alkali-soluble shells of diatoms, quartz and clay minerals. The identified phases are in accordance with the given above chemical composition of diatomite.

## 2.2. Batch preparation process

The mass ratio between diatomite and dry NaOH in the experiments was assumed to be 9.1. Theoretically, this gives a molar ratio between the soluble silica of diatomite and alkali (in terms of Na<sub>2</sub>O), equal to 5. In traditional liquid glass, this ratio, called the silicate module, is 3–4. A lower ratio, with the chosen methods of obtaining the material, is not economically justified. At a higher ratio the average density of foam-glass ceramics is decreased resulting in deteriorating its thermal insulation properties.

For comparison, in the studies of other authors, the mass ratio between diatomite and dry NaOH was taken to be 4.9 [6] and 4.0 [7], respectively, i.e. the mixture contained almost twice the amount of NaOH. Taking into account the chemical composition of diatomite and the accepted ratio between diatomite and NaOH, the theoretical total content of alkali oxides R<sub>2</sub>O (Na<sub>2</sub>O + K<sub>2</sub>O) in foam-glass ceramics should be 11 %. At the same time, the foamed glass obtained from glass waste by adding NaOH as a foaming agent contained about 19 % R<sub>2</sub>O in its chemical composition [16].

In the wet method of obtaining the batch diatomite, dry NaOH and water were taken in the weight proportion between the solid components and water equal to 1:2; the spreadability of the fluid batch according to Suttard viscometer was 80–90 mm. To intensify the interaction between diatomite and NaOH the batch was processed in a 300 ml vibratory mill, in which there were stainless steel balls with a diameter of 8 mm and a total weight of 250 g. The oscillation frequency, amplitude and duration of treatment were 1500 min<sup>-1</sup>, 2 mm and 15 min, respectively.

The extrusion method of batching consisted in the primary mixing of components by hand in a steel spherical bowl, until a press powder with a moisture content of 17 % was prepared. Next, the press powder was processed in a laboratory extruder with the screw parameters: diameter and a screw step of 80 mm, rotation speed of 45 min<sup>-1</sup>, maximum torque of 490 N·m. The granulating grid was made with 26 calibrated holes with a diameter of 5 mm. This parameter sets the diameter of the granules at the exit of the extruder and is the most optimal for the given parameters of the extruder. Under the influence of the screw, the mixture turned into a tight-plastic mass, which was pressed through the holes of the granulating grid as individual granules with a diameter of 5 mm, whose length was limited to 5–6 mm. To achieve the required plasticity, water was introduced into the mixture in the amount of 4–6 %.

The mixture was subjected to double extrusion, i.e. after the first passage through the granulating grid, it was returned to the extruder and extruded again. Increasing the rate of extrusion over two is impractical because of the sharp decrease in the plasticity of the batch due to the high adsorption properties of diatomite, which causes overheating and an emergency stop of the extruder. Mass homogeneity at single extrusion of the mixture was not provided. The average density of the raw grains obtained by the extrusion method was 1560–1630 kg/m<sup>3</sup>.

## 2.3. Samples Preparation Technique

The effect of the method of preparing the batch was evaluated after thermal foaming the samples according to their average density, porous structure and compressive strength. The main criterion was the average density that directly depends on NaOH consumption per unit volume of foam-glass ceramics. In addition, the value of average density affects the key characteristic of thermal insulation material – its thermal conductivity.

The mixture was subjected to drying to constant weight at 80 °C. Then the mixture was crushed to a fraction of 1–2.5 mm, poured into molds of heat-resistant steel and subjected to firing in a muffle furnace at 850 °C for 20 minutes. During firing, foaming and sintering of individual grains of the batch took place among themselves. Cooling of the molds took place together with the furnace, after which cubic samples with a rib length of 30 mm were cut out of the monolithic material. The average density of cubic samples was determined as the ratio of their mass to volume.

Depending on the processing method and the type of treatment, the batch was marked in accordance with Table 1. The W0 and E0 batches were foamed according to the above regime on a ceramic substrate, without pre-drying and grinding. In this case, the determination of the average density of the samples was carried out using the hydrostatic weighing method. In order to intensify the process of dissolution of silica and reduce the consumption of NaOH, the EAD batch was subjected to autoclave treatment at a water vapor pressure of 1.5 MPa for an hour and then dried and crushed.

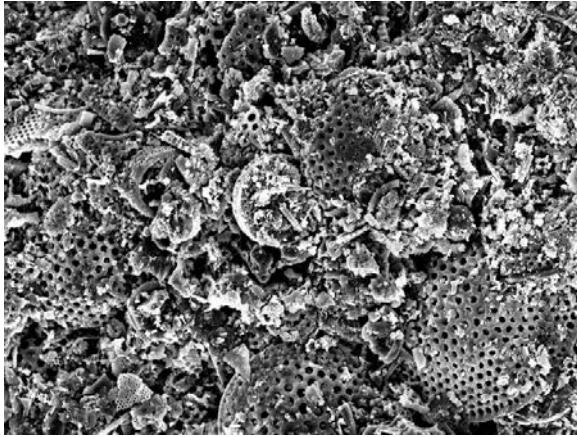


Figure 1. SEM image of diatomite, magnification x500.

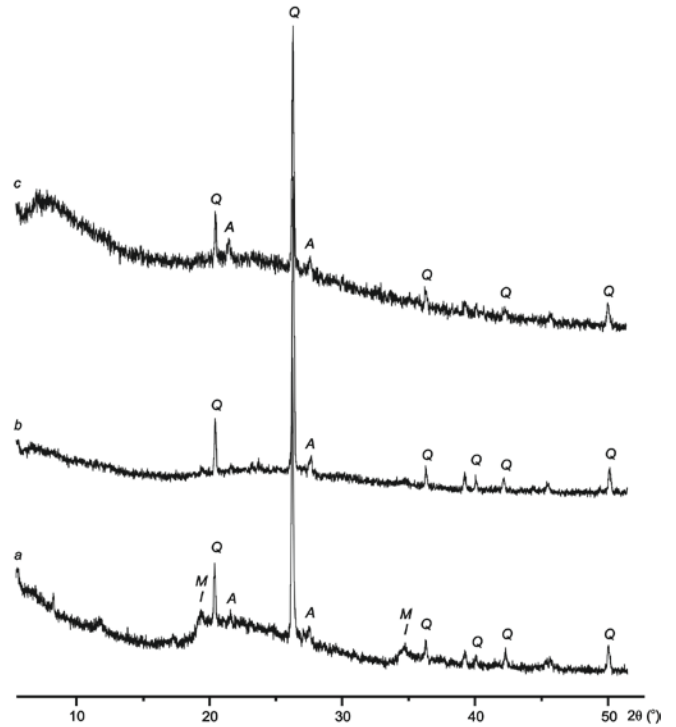


Figure 2. X-ray phase analysis: a – raw diatomite; b and c – batch WD heat treated at 100 and 800 °C respectively. A – albite, I – illite, M – ontmorillonite, Q – quartz.

### 3. Results and Discussion

To study the physicochemical processes during foam-glass ceramics firing thermal analysis of the WD batch (Table 1) was carried out (Figure 3b). Curves DTG and DSC shown in Figure 3b are characterized by endothermic effects in the form of a sharp peaks at 100 °C and a more extended effects (unlike the sample of raw diatomite in Figure 3a) in the range of 350–600 °C. In accordance with the TG curve, the second effect is accompanied by almost half of the total weight loss of the sample, which, apparently, is due to the dehydration of hydrated sodium silicates formed in the batch before. The last insignificant endothermic effect of the DSC curve at 760 °C in Figure 3b, is possibly associated with melting of the crystalline phase of  $\text{Na}_6\text{Si}_8\text{O}_{19}$ . The occurrence of this phase was diagnosed using X-ray phase and thermal analysis at heating commercial liquid glass to 750 °C, followed by decomposition of  $\text{Na}_6\text{Si}_8\text{O}_{19}$  at 800 °C and the formation of a melt [21].

Table 1. Marking of batch depending on processing method and type of further treatment.

No.	Method of batch processing		Type of batch treatment	
1	W0	Wet	No treatment	
2	WD		Drying and crushing	Firing on a ceramic substrate
3	E0		No treatment	
4	ED	Extrusion	Drying and crushing	Firing in a steel mold
5	EAD		Autoclave, drying and crushing	
6	EA		Autoclave and drying	

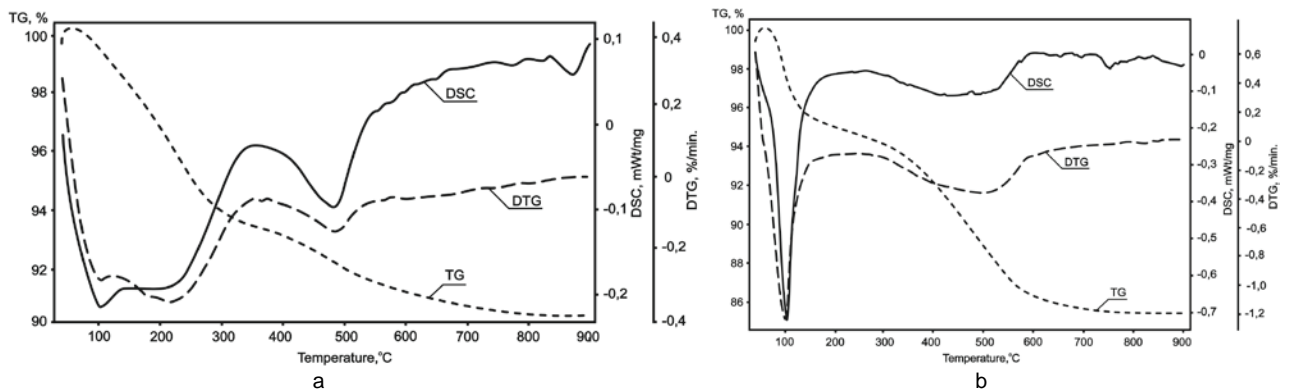


Figure 3. Results of thermal analysis: a — raw diatomite; b — batch WD.

X-ray phase analysis of the mixture depending on the heating temperature is presented in Figures 2b and 2c. The significant changes in crystalline component of diatomite under heat treatment of the batch WD are not seen in comparison with the diffraction pattern of raw diatomite: Figures 2b and 2a respectively. The disappearance of the amorphous gallo in the range of angles 18–26° after drying at 100 °C, which is typical for the dissolution of silica phases of diatomite under the influence of NaOH, is seen in Figure 2b. The diffractogram in Figure 2b is characterized by the disappearance of the peaks of montmorillonite and illite, the structure of which is subjected to a significant restructuring under the influence of alkalis [22]. The presence of a glass phase at 800 °C is confirmed by the formation of gallo in XRD pattern shown in Figure 2c at angles of 8–13°. The last is consistent with the data other authors who performed x-ray phase analysis of liquid glass at 800 °C [21]. Thus, at the batch firing, physically bound water is removed at 100 °C, then the process of dehydration of sodium silicates starts at 350 °C and continues until the melt is formed at 750 °C resulting in foaming the composition.

The structure of the samples fragment obtained from the batches W0 and WD is shown in Figures 4a and 4b respectively. The stratification in height of the sample W0 foamed in a liquid form on a ceramic substrate is seen in Figure 4a. The top of the sample is represented by a foamed mass with a characteristic glass luster, and in the lower part a dense mass of red color prevails, in appearance resembling ceramics, which is unacceptable in the technology of thermal insulation material.

In order to eliminate negative stratification during firing, the batch W0 was subjected to preliminary drying. Unlike the sample W0 in Figure 4a, an obvious delamination is not observed in a fragment of the foamed sample WD presented in Figure 4b. However, among the foamed particles up to 3 mm in size, there are dense ceramic inclusions of red color. The latter indicates that the liquid batch had already been separated during its drying and the grains of insoluble residue were distributed in the batch after its grinding that is seen in Figure 4b.

The average density of the samples obtained from the batches W0 and WD was 640 and 720 kg/m<sup>3</sup> respectively, which is a relatively high value for a thermal insulation material. Obtaining a more viscous batch with lower water content is impractical because of the difficulty of mixing, and therefore, further research was focused on the mechanized method of obtaining the batch using extrusion.

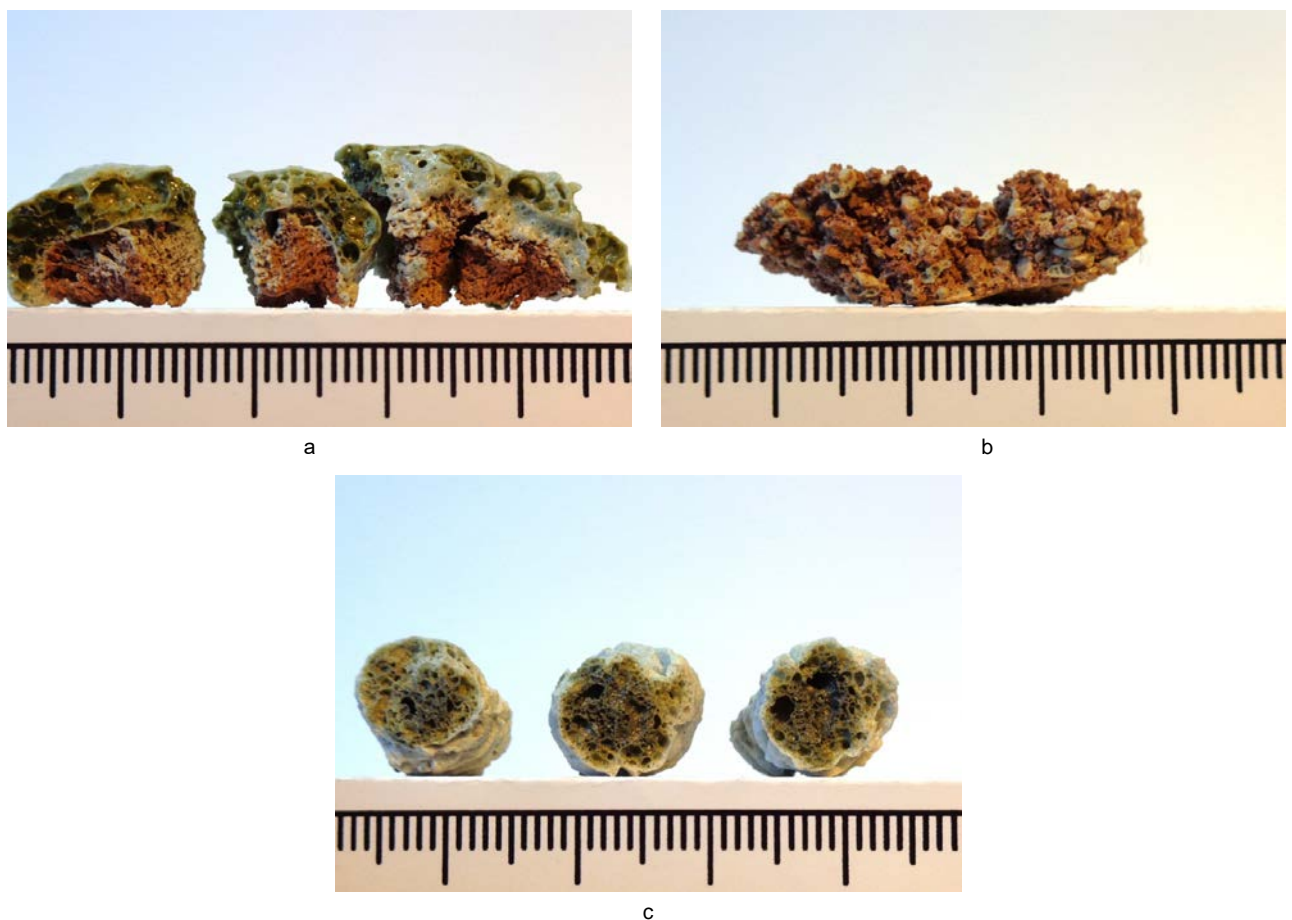


**Figure 4. Porous structure of foam-glass ceramics samples (scale is given in mm):  
a — batch W0; b — WD; c — E0.**

The porous structure of the foamed samples in the form of granules obtained from the batch E0 is shown in Figure 4c. In comparison with the batches W0 and WD (Figures 4a and 4b, respectively) pores are distributed throughout the volume and delamination is not seen (Figure 4c). Consequently, obtaining the batch

as a tight-plastic mass with a low water content contributes to the uniform foaming of foam glass-ceramic samples, while the insoluble residue of diatomite is distributed in the mixture without further separation during firing process. The average density of samples from the batch E0 is  $530 \text{ kg/m}^3$ , which is 1.2 and 1.7 times lower in comparison with the batches W0 and WD, respectively. The volume density of the granules, taking into account their average size of 10 mm, is  $290 \text{ kg/m}^3$ . The volume water absorption and compressive strength of granules in the cylinder determined according to Russian State Standard GOST 9758-2012 "Non-organic porous aggregates for construction work. Test methods" were 6 % and 1.8 MPa, respectively. Accordingly to these properties the granules can be used as insulating layers in various engineering structures: for example, to protect the soils of the roads foundations from seasonal freezing and frost heaving [4].

From the batches marked as ED and EAD, cubic samples of foam-glass ceramic with an average density of 540 and  $450 \text{ kg/m}^3$  and compressive strength of 7.4 and 3.4 MPa respectively, were obtained. Thus, the average density of the autoclave treated samples ED is decreased by about 17 %. The most likely explanation of the autoclave treatment effect is the formation of an additional amount of hydrated sodium silicates in the batch caused by intensification of the dissolving the silica phases. As a result, this can contribute to an increase in the amount of the liquid phase in the melt and give an additional amount of a pore-forming agent during the dehydration of sodium silicates.

In addition, due to the existence of known methods of hydrothermal synthesis of commercial zeolites from clays and alkalis [22], it is likely that they can be formed under the influence of pressure and steam. During firing, dehydration of artificial zeolites is likely, as a result they can participate in the process of foaming the material, reducing the average density. However, this is a theoretical assumption, since zeolites were not traced in XRD pattern of the batch WD (Figure 2b).

High glass phase content in the samples E0 is proved by a characteristic glass luster that observed in Figure 4c. Along with this, during firing, greenish color sometimes turning into black is seen in the samples W0 and E0 presented in Figures 4a and 4b respectively. The reason for this may be the formation of ferrous oxide as a result of the reduction of  $\text{Fe}_2\text{O}_3$ . The melting of the outer surface of the sample can prevent the penetration of oxygen and contribute to the creation of a reducing environment due to the organic compounds contained in diatomite [23].

The EA batch was foamed on a ceramic substrate and glass-ceramic samples in the form of granules were obtained. In accordance with Russian State Standard GOST 9758-2012, the samples had the following properties: an average grain size of 10 mm, a bulk density of  $250 \text{ kg/m}^3$ , a volume water absorption of 7 %, and a compressive strength in the cylinder of 1.5 MPa. Bulk density of EA samples was 14 % lower compared to the samples E0 due to the autoclave treatment. The thermal conductivity of 10 cm thick layer of granules, determined in accordance with the methodology of Russian State Standard GOST 7076-99 "Building materials and products. Method of determination of steady-state thermal conductivity and thermal resistance", was  $0.71 \text{ W/(m}\cdot\text{K)}$ .

Due to the presence of intergranular voids, granulated foam-glass ceramics from the batches E0 and EA have a significantly lower bulk density ( $290$  and  $250 \text{ kg/m}^3$ , respectively) compared to foam-glass ceramics, obtained in mold from the batches ED and EAD ( $540$  and  $450 \text{ kg/m}^3$ , respectively). Consequently, a larger volume of foam-glass ceramics in granular form is released that is economically justified, given the wide scope of this material [4]. In addition, due to intergranular voids and lower density of granulated foam-glass ceramics, there is a proportional decrease in the specific consumption of expensive NaOH per unit volume of material, compared to cubic samples synthesized in mold.

The samples properties can be compared with the results of other authors. Foam-glass ceramics was synthesized at a lower mass ratio between diatomite and NaOH equal to 4; cubic samples with an average density of  $200\text{--}220 \text{ kg/m}^3$  and compressive strength  $2.0\text{--}2.3 \text{ MPa}$  were obtained [7]. In this study the higher average density and compressive strength of cubic samples of  $450 \text{ kg/m}^3$  and 3.4 MPa, respectively, was caused by the higher mass ratio between diatomite and NaOH equal to 9.1. Thus, the extrusion method is preferable in obtaining granular foam-glass ceramics, since its bulk density is almost half the average density of cubic samples: 250 and  $450 \text{ kg/m}^3$ , respectively, i.e. a larger volume of material is released.

#### 4. Conclusion

1. The separation of the samples along with the formation of a porous structure on top and dense ceramics from below due to the high water content in the liquid batch of the wet method was observed. The samples with increased average density and non-uniform structure containing both foamed particles and more dense ceramic particles were obtained after pre-drying the liquid batch.

2. The batch with lower water content, obtained by the extrusion method, was foamed evenly, without stratification, thereby structure of foam-glass-ceramics was optimized and its average density reduced. An additional decrease in the average density of samples from 540 to  $450 \text{ kg/m}^3$  due to the activation of dissolving the diatomite silica phases during the autoclave treatment of the extruded batch was defined. The additional saving NaOH in proportion to the decrease in the average density of the material was achieved.

3. Combining the processes of mixing and granulation of the batch in a single operation is the advantage of the extrusion method in foam-glass ceramics technology. The maximum economic and technological efficiency of the extrusion method is achieved during obtaining granular foam-glass ceramics as a result of reducing the consumption of NaOH and bulk density due to the presence of intergranular voids. Using the extrusion method and autoclave treatment the samples of granulated foam-glass ceramics with a bulk density of 250 kg/m<sup>3</sup>, thermal conductivity of the granule layer of 0.71 W/(m·K) and compressive strength in the cylinder of 1.5 MPa were obtained.

### Acknowledgments

The work was carried out according to the scientific plan of Tyumen Scientific Center of the SB RAS: Priority direction IX.135. Programm IX.135.2. Project IX.135.2.4.

### References

1. Kazantseva, L.K., Rashchenko, S.V. Optimization of porous heat-insulating ceramics manufacturing from zeolitic rocks. *Ceramics International*. 2016. No. 42. Pp. 19250–19256. DOI: 10.1016/j.ceramint.2016.09.091.
2. Erofeev, V.T., Rodin, A.I., Kravchuk, A.S., Kaznacheev, S.V., Zaharova, E.A. Biostable silicic rock-based glass ceramic foams. *Magazine of Civil Engineering*. 2018. 84(8). Pp. 48–56. DOI: 10.18720/MCE.84.5.
3. Portnyagin, D.G. Improving the thermal performance of the building envelopes with the use of foam glass-ceramics. *Magazine of Civil Engineering*. 2015. 60(8). Pp. 56–67. DOI: 10.5862/MCE.60.7.
4. Ivanov, K.S. Granulated foam-glass ceramics for ground protection against freezing. *Magazine of Civil Engineering*. 2018. 79(3). Pp. 95–102. DOI: 10.18720/MCE.79.10.
5. Yatsenko, E.A., Goltsman, B.M., Ryabova, A.V. Complex protection of pipelines using silicate materials based on local raw materials of the far east. *Materials Science Forum*. 2019. Vol. 945. Pp. 46–52. DOI: 10.4028/www.scientific.net/MSF.945.46.
6. Senik, N.A., Meshkov, A.V., Vinitskiy, A.L., Vakalova, T.V., Vereshchagin, V.I. Polucheniye vysokoeffektivnogo teploizolyatsionnogo materiala na osnove diatomita putem nizektemperaturnogo vspenivaniya [Production of highly efficient thermal insulation material based on diatomite by low-temperature foaming]. *Tekhnika i tekhnologiya silikatov*. 2012. Vol. 19. No. 4. Pp. 6–12. (rus)
7. Kazantseva, L.K., Rashchenko, S.V. Chemical processes during energy-saving preparation of lightweight ceramics. *Journal of American Ceramics Society*. 2014. Vol. 97. Pp. 1743–1749. DOI: 10.1111/jace.12980.
8. Kazantseva, L.K., Zheleznov, D.V., Seretkin, Yu.V., Rashchenko, S.V. Formation of a pore-forming gas source by wetting natural aluminum-silicates with NaOH solution. *Glass and Ceramics*. 2013. Vol. 69. No. 9–10. Pp. 353–357. DOI: 10.1007/s10717-013-9478-9.
9. Ivanov, K.S. Study of sodium silicate system firing during glass ceramic foam preparation. *Refractories and Industrial Ceramics*. 2016. Vol. 56. No. 6. Pp. 621–625. DOI: 10.1007/s11148-016-9900-2.
10. Manevich, V.E., Subbotin, R.K., Nikiforov, E.A., Senik, N.A., Meshkov, A.V. Diatomite – siliceous material for the glass industry. *Glass and Ceramics*. 2012. Vol. 69. No. 5–6. Pp. 168–172. DOI: 10.1007/s10717-012-9438-9.
11. Vinitskiy, A.L., Ryabov, G.K., Senik, N.A., Meshkov, A.V., Korosteleva, Y.A., Fetyukhina, Y.G. Diatomit kak perspektivnoye syr'ye dlya polucheniya penostekla [Diatomite as a promising raw material for foamglass]. *Sovremennoye promyshlennoye i grazhdanskoye stroitelstvo*. 2012. Vol. 8. No. 2. Pp. 63–70. (rus)
12. Zhimalov, A.A., Bondareva, L.N., Igitkhanyan, Y.G., Ivashchenko, Y.G. Use of amorphous siliceous rocks – opokas to obtain foam glass with low foaming temperature. *Glass and Ceramics*. 2017. Vol. 74. No. 1–2. Pp. 13–15. DOI: 10.1007/s10717-017-9916-1.
13. Malyavskiy, N.I. Shchelochnosilikatnyye utepliteli. Svoystva i khimicheskiye osnovy proizvodstva [Alkaline silicate insulation. Properties and chemical bases of production]. *Rossiyskiy khimicheskiy zhurnal*. 2003. No. 4. Pp. 39–45. (rus)
14. Hesky, D., Aneziris, C.G., Gros, U., Horn, A. Water and waterglass mixtures for foam glass production. *Ceramics International*. 2015. No. 41. Pp. 12604–12613. DOI: 10.1016/j.ceramint.2015.06.088.
15. Fernandes, H.R., Tulyaganov, D.U., Ferreira, J.F. Preparation and characterization of foams from sheet glass and fly ash using carbonates as foaming agents. *Ceramics International*. 2009. No. 35. Pp. 229–235. DOI: 10.1016/j.ceramint.2007.10.019.
16. Da Silva, R.C., Kubaskia, E.T., Tenorio-Neto, E.T., Lima-Tenorio, M.K., Tebcherani, S.M. Foam glass using sodium hydroxide as foaming agent: Study on the reaction mechanism in soda-lime glass matrix. *Journal of Non-Crystalline Solids*. 2019. Vol. 511. Pp. 177–182. DOI: 10.1016/j.jnoncrysol.2019.02.003.
17. Ivanov, K.S., Korotkov, E.A. Effect of sodium silicate slurries on the properties of alkali-activated materials. *Inorganic Materials*. 2017. Vol. 53. No. 9. Pp. 973–979. DOI: 10.1134/S0020168517090096.
18. Ivashchenko, Y.G., Strakhov, A.V. Svoystva silikatnatriyevogo svyazuyushchego, poluchennogo na osnove silitsitovykh porod metodom gidrotermalnogo sinteza [Properties of silicate-sodium binder, obtained on the basis of silicite rocks by the method of hydrothermal synthesis]. *Vestnik Saratovskogo GTU*. 2010. Vol. 4. No. 1(49). Pp. 193–200. (rus)
19. Sokolovich, V.E. Rapid method of determining the modulus of sodium silicate solution. *Glass and Ceramics*. 1975. Vol. 32. No. 10. Pp. 707–708. DOI: 10.1007/BF00676879.
20. Grim, R.E. Rowland, R.A. Differential thermal analysis of clay minerals and other hydrous materials. Part 1. *American mineralogist*. 1942. Vol. 27. No. 11. Pp. 746–761.
21. Raghvan, S., Helfried, N. Phase evolution on heat treatment of sodium silicate water glass. *Journal of Non-Crystalline Solids*. 2008. Vol. 354. Pp. 896–900. DOI: 10.1016/j.jnoncrysol.2007.08.037.
22. Breck, D.W. *Zeolite Molecular Sieves: Structure, Chemistry and Use*. New York, 1973. 771 p.
23. Abdrakhimov, V.Z., Abdrakhimova, E.S. Combustion during firing heat insulation ceramic material based on waste fuel shale. *Refractories and Industrial Ceramics*. 2013. Vol. 54. No. 4. Pp. 299–303. DOI: 10.1007/s11148-013-9597-4.

### Contacts:

Konstantin Ivanov, +7(922)0424352; [sillicium@bk.ru](mailto:sillicium@bk.ru)



DOI: 10.18720/MCE.89.5

## Оптимизация структуры и свойств пеностеклокерамики

**К.С. Иванов**

*Институт криосферы Земли ТюмНЦ СО РАН,  
625000 г. Тюмень, ул. Малыгина, 85, а/я 1230*

**Ключевые слова:** строительный материал, теплоизоляция, пеностеклокерамика, силикаты

**Аннотация.** В исследованиях оптимизированы основные свойства пеностеклокерамики — пористого неорганического теплоизоляционного материала. Данный материал применяется для теплоизоляции различных инженерных сооружений: фундаментов, оснований автомобильных и железных дорог, трубопроводов и т.д. Основными сырьевыми составляющими материала являются гидроксид натрия и опал-кристобалитовые горные породы: диатомит, трепел, опока. Смесь компонентов подвергается обжигу и вспенивается с формированием пористой структуры, которая включает как стекловидную, так и кристаллическую фазы. В исследованиях проанализировано и установлено существенное влияние двух различных способов приготовления смеси компонентов на основные свойства материала. В первом способе шихта представляла собой суспензию с высоким содержанием воды, которая подвергалась механической активации в вибрационной мельнице. Во втором способе, шихта была получена экструзией, т.е. путём продавливания смеси компонентов через калиброванные отверстия с помощью шнека. Вследствие этого, шихта представляла собой гранулированную туго-пластичную массу с низким содержанием воды. В результате было установлено, что более высокое содержание воды в первом способе синтеза приводит к формированию неоднородной структуры образцов, их расслоению, наличию плотных не вспененных включений и повышенной средней плотности материала. Шихта, полученная экструзионным методом, вспенивается более равномерно, без расслоения, благодаря чему снижается средняя плотность пеностеклокерамики. Дополнительному снижению средней плотности образцов на 17 % способствует автоклавная обработка шихты, полученной экструзионным методом, за счёт активизации процесса растворения кремнезёма диатомита. Экструзионный метод рекомендован для получения пеностеклокерамики в гранулированном виде, что способствует экономии дорогостоящего гидроксида натрия.

### Литература

1. Kazantseva L.K., Rashchenko S.V. Optimization of porous heat-insulating ceramics manufacturing from zeolitic rocks // *Ceramics International*. 2016. № 42. Pp. 19250–19256. DOI: 10.1016/j.ceramint.2016.09.091.
2. Ерофеев В.Т., Родин А.И., Кравчук А.С., Казначеев С.В., Захарова Е.А. Биостойкие пеноситаллы на основе кремнеземсодержащих пород // *Инженерно-строительный журнал*. 2018. № 8(84). С. 48–56. DOI: 10.18720/MCE.84.5.
3. Портнягин Д.Г. Повышение теплозащиты узлов ограждающих конструкций зданий с применением пеностеклокристаллического материала // *Инженерно-строительный журнал*. 2015. № 8(60). С. 56–67. DOI: 10.5862/MCE.60.7.
4. Иванов К.С. Гранулированная пеностеклокерамика для защиты грунтов от сезонного промерзания и морозного пучения // *Инженерно-строительный журнал*. 2018. № 3(79). С. 95–102. DOI: 10.18720/MCE.79.10.
5. Yatsenko E.A., Goltsman B.M., Ryabova A.V. Complex protection of pipelines using silicate materials based on local raw materials of the far east // *Materials Science Forum*. 2019. Vol. 945. Pp. 46–52. DOI: 10.4028/www.scientific.net/MSF.945.46.
6. Сенник Н.А., Мешков А.В., Виноцкий А.Л., Вакалова Т.В., Верещагин В.И. Получение высокоэффективного теплоизоляционного материала на основе диатомита путём низкотемпературного вспенивания // *Техника и технология силикатов*. 2012. Т. 19. № 4. С. 6–12.
7. Kazantseva L.K., Rashchenko S.V. Chemical processes during energy-saving preparation of lightweight ceramics // *Journal of American Ceramic Society*. 2014. Vol. 97. Pp. 1743–1749. DOI: 10.1111/jace.12980.
8. Kazantseva L.K., Zhelezov D.V., Seretkin Y.V., Rashchenko S.V., Formation of a pore-forming gas source by wetting natural aluminum-silicates with NaOH solution // *Glass and Ceramics*. 2013. Vol. 69. № 9–10. Pp. 353–357. DOI: 10.1007/s10717-013-9478-9.
9. Ivanov K.S. Study of sodium silicate system firing during glass ceramic foam preparation // *Refractories and Industrial Ceramics*. 2016. Vol. 56. № 6. Pp. 621–625. DOI: 10.1007/s11148-016-9900-2.
10. Manevich V.E., Subbotin R.K., Nikiforov E.A., Senik N.A., Meshkov A.V. Diatomite – siliceous material for the glass industry // *Glass and Ceramics*. 2012. Vol. 69. № 5–6. Pp. 168–172. DOI: 10.1007/s10717-012-9438-9.
11. Виноцкий А.Л., Рябов Г.К., Сенник Н.А., Мешков А.В., Коростелёва Ю.А., Фетюхина Е.Г. Диатомит как перспективное сырьё для получения пеностекла // *Современное промышленное и гражданское строительство*. 2012. Т. 8. № 2. С. 63–70.

12. Zhimalov A.A., Bondareva L.N., Igithkanyan Y.G., Ivashchenko Y.G. Use of amorphous siliceous rocks – opokas to obtain foam glass with low foaming temperature // *Glass and Ceramics*. 2017. Vol. 74. № 1–2. Pp. 13–15. DOI: 10.1007/s10717-017-9916-1.
13. Малявский Н.И. Щелочносиликатные утеплители. Свойства и химические основы производства // *Российский химический журнал*. 2003. № 4. С. 39–45.
14. Hesky D., Aneziris C.G., Gros U., Horn A., Water and waterglass mixtures for foam glass production // *Ceramics International*. 2015. № 41. Pp. 12604–12613. DOI: 10.1016/j.ceramint.2015.06.088.
15. Fernandes H.R., Tulyaganov D.U., Ferreira J.F. Preparation and characterization of foams from sheet glass and fly ash using carbonates as foaming agents // *Ceramics International*. 2009. № 35. Pp. 229–235. DOI: 10.1016/j.ceramint.2007.10.019.
16. Da Silva R.C., Kubaskia E.T., Tenorio-Neto E.T., Lima-Tenorio M.K., Tebcherani S.M. Foam glass using sodium hydroxide as foaming agent: Study on the reaction mechanism in soda-lime glass matrix // *Journal of Non-Crystalline Solids*. 2019. Vol. 511. Pp. 177–182. DOI: 10.1016/j.jnoncrysol.2019.02.003.
17. Ivanov K.S., Korotkov E.A. Effect of sodium silicate slurries on the properties of alkali-activated materials // *Inorganic Materials*. 2017. Vol. 53. № 9. Pp. 973–979. DOI: 10.1134/S0020168517090096.
18. Иващенко Ю.Г., Страхов А.В. Свойства силикатнатриевого связующего, полученного на основе силицитовых пород методом гидротермального синтеза // *Вестник Саратовского ГТУ*. 2010. Т. 4. № 1(49). С. 193–200.
19. Sokolovich V.E. Rapid method of determining the modulus of sodium silicate solution // *Glass and Ceramics*. 1975. Vol. 32. № 10. Pp. 707–708. DOI: 10.1007/BF00676879.
20. Grim R.E. Rowland R.A. Differential thermal analysis of clay minerals and other hydrous materials. Part 1. // *American mineralogist*. 1942. Vol. 27. № 11. Pp. 746–761.
21. Raghvan S., Helfried N. Phase evolution on heat treatment of sodium silicate water glass // *Journal of Non-Crystalline Solids*. 2008. Vol. 354. Pp. 896–900. DOI: 10.1016/j.jnoncrysol.2007.08.037.
22. Breck D.W. *Zeolite Molecular Sieves: Structure, Chemistry and Use*. New York. 1973. 771 p.
23. Abdrakhimov V.Z., Abdrakhimova E.S. Combustion during firing heat insulation ceramic material based on waste fuel shale // *Refractories and Industrial Ceramics*. 2013. Vol. 54. № 4. Pp. 299–303. DOI: 10.1007/s11148-013-9597-4.

**Контактные данные:**

Константин Сергеевич Иванов, +7(922)0424352; эл. почта: [sillicium@bk.ru](mailto:sillicium@bk.ru)

© Иванов К.С., 2019



DOI: 10.18720/MCE.89.6

## Finite element model of Reisner's plates in stresses

**Yu. Ya. Tyukalov**

*Vyatka State University, Kirov, Russia*

**Keywords:** Reisner's plates, possible displacements, finite elements, bending plate

**Abstract.** A method for calculating bending plates by the finite element method based on Reisner's theory is proposed. The method is based on the fundamental principles of minimum of additional energy and possible displacements. For discretization of the subject area, arbitrary quadrangular finite elements are used. Over the area of the finite element, the moment fields and shear forces are approximated by constant functions that satisfy the differential equilibrium equations in the area of the finite element in the absence of a distributed load. Using the principle of possible displacements, algebraic equilibrium equations of the nodes of the finite element grid are compiled. In accordance with Reisner's theory, vertical displacements and angles of rotation of the middle surface of the plate are taken as nodal possible displacements as independent. The proposed method of calculation allows you to calculate both thick and thin plates. There is no effect of «locking» of the solution for thin plates, which is confirmed by calculations of rectangular plates with different support conditions of side and different ratios of thickness to plate sizes. The solutions obtained by the proposed method for plates of various shapes are compared with analytical solutions. Sufficiently fast convergence and accuracy of the proposed calculation method for both thick and thin plates is shown.

### 1. Introduction

Bending plates are one of the main elements of the supporting structures for various construction objects. Often in construction, for example as a foundation, thick reinforced concrete slabs are used. When calculating thick plates, it is necessary to consider, in addition to bending deformations, transverse shear deformations of sections, which can significantly affect the stress-strain state of the plate. The theory of bending plates, based on the hypothesis of direct normals, does not allow to consider shear deformations. Finite elements, developed based on the Kirchhoff theory, can be used only for the calculation of thin plates [1–2].

The Reisner's bending plate theory is widely used for calculating thick plates [3–4]. In contrast to the classical Kirchhoff theory, in Reisner's theory, the angles of rotation of the middle surface and vertical displacements are considered as independent variables. Such way makes it possible to lower the maximum order of derivatives in the strain energy functional and makes it possible to use first-order functions for approximating the displacement functions. As known, the direct use of Reisner's theory for constructing finite elements in displacements leads to the «locking» effect which consists in the impossibility of using these finite elements for calculating thin plates, which limits their applicability only to the area of thick plates. In order to overcome the «blocking» effect, various additional coordination of the finite element's unknowns is often used. For example, the hypothesis of direct normals is enforced gone at discrete points or high order shift theory is used [5–6]. The finite elements based on satisfying the hypothesis of direct normals in the middle of the sides of finite elements are widely used in software and demonstrate good accuracy.

Various variational principles are successfully used to solve the stability and dynamics problems of various structures, including plates of variable stiffness [7–8]. A detailed analysis of the applicability of variational principles to the solution of a wide range of problems of the theory of elasticity by the finite element method is performed in [9–10]. In these works, the formulations of the variational principles of Lagrange,

---

Tyukalov, Yu.Ya. Finite element model of Reisner's plates in stresses. Magazine of Civil Engineering. 2019. 89(5). Pp. 61–78. DOI: 10.18720/MCE.89.6

Тюкалов Ю.Я. Конечно-элементная модель в напряжениях для пластин Рейснера // Инженерно-строительный журнал. 2019. № 5(89). С. 61–78. DOI: 10.18720/MCE.89.6



This open access article is licensed under CC BY 4.0 (<https://creativecommons.org/licenses/by/4.0/>)

Castilian, Reisner are considered in detail and the relevance of obtaining a two-sided estimate of the obtained approximate solutions is noted.

When constructing analytical solutions of the problems of bending rectangular plates, high-order shear theories are applied. In this case, along the cross section the deformations change according to law different from linear principle [11–12]. To construct finite elements that consider shear deformations, the third-order shear theory is applied successfully [13–14]. In [14], quadrangular finite element is presented that has seven degrees of freedom at each node: three displacements of the middle surface along the axes of coordinates, two shear angles and two angles of rotation of the normals. Such an approach allows one to more accurately consider shear deformations, when the properties of the material are changing in different directions. In [15], an additional procedure is used to account for shear deformations in the finite elements already construct, which are used to calculate thin plates. Transverse shear deformations are calculated of based on the direct application of the equations of the three-dimensional theory of elasticity. To construct quadrangular finite element the Galerkin's method is used in a weak form [16]. Also, the Galerkin's method is used to construct triangular and quadrangular finite elements according to Reisner-Mindlin theory in [17]. In [18, 19], analytical solutions for rectangular plates, obtained based on Reisner's theory, are proposed.

Mixed and hybrid variational formulations are also used to construct finite elements of plates with allowance for shear deformations [20–23]. On the one hand, such formulations simplify the inclusion of shear deformations by using both displacements and shear forces and moments as unknowns, but, on the other hand, matching of displacements and forces is required to ensure convergence.

Thus, most of the developed methods for calculating plates with considering shearing deformations, in one form or another, are based either on approximations of displacement functions or on solving differential equations expressed in terms of displacement functions. In this case, stresses are determined as derivatives of displacements expressed by approximate functions, which leads to an inevitable loss of accuracy in their determination, although stresses are more important for assessing the strength of a structure. In addition, the accuracy of the solution depends on the selected finite element mesh and we cannot, in the general case for an arbitrary construction, determine the accuracy of the solution obtained. Therefore, it remains actual to build alternative models, to the finite element method in displacements, for considering shear deformations when calculating flexible plates based on Reisner's theory. If we have solutions obtained on an alternative basis, then by comparing two (or more) solutions we will be able to obtain a more reliable estimate of the accuracy of the solutions obtained.

The purpose of this work is to develop a method for calculating plates with considering to the shear deformations of Reisner's plates, which based on the functional of additional energy and the principle of possible displacements, as well as comparing the solutions obtained for plates of various shapes and with different supporting conditions with solutions obtained by other methods. Such an approach for solving the plane problem of the theory of elasticity is used in [24], for rod systems in [25–26] and for bendable plates in [27–28]. In [28], a method for calculating thick bent plates with allowance for shear deformations based on the extended Castiliano functional is proposed. As additional terms, using the Lagrange multipliers method, algebraic equilibrium equations of nodes, obtained using the principle of possible displacements, are added to the functional. Possible vertical displacements of nodes causing bending and possible vertical displacements of nodes causing shear are used separately. As a result of the calculation, the rotation angles for the nodes are not directly determined. In this work, as possible displacements, both possible displacements in the form of vertical displacements and rotation angles will be used. In this case, as a result of the calculation, we can obtain both the magnitudes of the vertical displacements and the magnitudes of the rotation angles, which is more convenient.

## 2. Methods

Solving the problems of plate bending we obtain based on the functional of additional energy for an isotropic plate (for simplicity, we assume that there are no specified displacements) considering the shear deformations:

$$\Pi^c = \frac{1}{2} \left( \frac{12}{E \cdot t^3} \right) \int (M_x^2 + M_y^2 - 2\nu M_x M_y + 2(1+\nu) M_{xy}^2) d\Omega + \frac{1}{2} \left( \frac{2k(1+\nu)}{E \cdot t} \right) \int (Q_x^2 + Q_y^2) d\Omega \rightarrow \min. \quad (1)$$

$E$  is the modulus of material elasticity;

$t$  is the plate thickness;

$\nu$  is Poisson's ratio;

$k = 6/5$  is coefficient considering the parabolic law of change of tangential stress across the plate thickness. The functional (1) is can written in matrix form that is more convenience for solving by the finite element method:

$$\Pi^c = \frac{1}{2} \int \{M\}^T [E]^{-1} \{M\} d\Omega + \frac{1}{2} \int \{Q\}^T [E_{sh}]^{-1} \{Q\} d\Omega \rightarrow \min. \quad (2)$$

In expression (2) the following notation is entered:

$$\{M\} = \begin{Bmatrix} M_x \\ M_y \\ M_{xy} \end{Bmatrix}, \quad \{Q\} = \begin{Bmatrix} Q_x \\ Q_y \end{Bmatrix}, \quad [E]^{-1} = \frac{12}{E \cdot t^3} \begin{bmatrix} 1 & -\nu & 0 \\ -\nu & 1 & 0 \\ 0 & 0 & 2(1+\nu) \end{bmatrix}, \quad [E_{sh}]^{-1} = \frac{12(1+\nu)}{5E \cdot t} \begin{bmatrix} 1 & 0 \\ 0 & 1 \end{bmatrix}. \quad (3)$$

In functional (2), the first addend is associated with the bending deformations of the plate, the second is due to shear deformations by transverse forces.

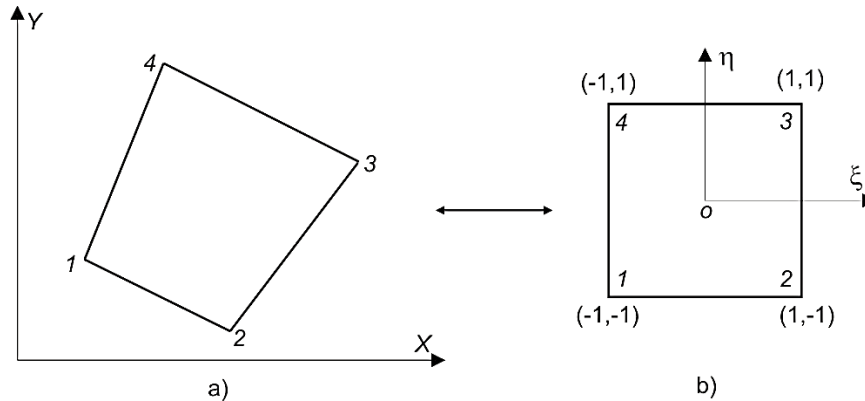


Figure 1. An arbitrary quadrangular finite element.

For discretization of the subject area, we use arbitrary quadrangular finite elements (Figure 1). Over the area of the finite element the moments and shear forces will be approximated by the constant functions. It is obvious that such functions satisfy differential equilibrium equations in the area of a finite element in the absence of distributed loads.

For the finite element  $k$  in the global coordinate system, we combine the unknown internal forces into the vector  $\{F_k\}$ , and shall denote the flexible matrix as  $[D_k]$ .

$$\{F_k\} = \begin{Bmatrix} M_{x,k} \\ M_{y,k} \\ M_{xy,k} \\ Q_{x,k} \\ Q_{y,k} \end{Bmatrix}, \quad [D_k] = A_k \begin{bmatrix} \frac{12}{E \cdot t^3} & \frac{-12 \cdot \nu}{E \cdot t^3} & 0 & 0 & 0 \\ \frac{-12 \cdot \nu}{E \cdot t^3} & \frac{12}{E \cdot t^3} & 0 & 0 & 0 \\ 0 & 0 & \frac{24(1+\nu)}{E \cdot t^3} & 0 & 0 \\ 0 & 0 & 0 & \frac{12(1+\nu)}{5 \cdot E \cdot t} & 0 \\ 0 & 0 & 0 & 0 & \frac{12(1+\nu)}{5 \cdot E \cdot t} \end{bmatrix}. \quad (4)$$

$A_k$  is the area of the finite element;

$n$  is number of finite elements. Then the expression of the functional (1) can be written in the following matrix form:

$$\Pi^c = \frac{1}{2} \sum_{k=1}^n \{F_k\}^T [D_k] \{F_k\} = \frac{1}{2} \{F\}^T [D] \{F\} \rightarrow \min; \quad (5)$$

$$[D] = \begin{bmatrix} [D_1] & & \\ & \ddots & \\ & & [D_n] \end{bmatrix}, \quad \{F\} = \begin{Bmatrix} \{F_1\} \\ \vdots \\ \{F_n\} \end{Bmatrix}. \quad (6)$$

In accordance with the principle of minimum of the additional energy, the functions for moments  $M_x$ ,  $M_y$ ,  $M_{xy}$  and shear forces  $Q_x$ ,  $Q_y$  must satisfy the corresponding differential equilibrium equations (7) and static boundary conditions.

$$\frac{\partial M_x}{\partial x} + \frac{\partial M_{xy}}{\partial y} - Q_x = 0, \quad \frac{\partial M_y}{\partial y} + \frac{\partial M_{xy}}{\partial x} - Q_y = 0, \quad \frac{\partial Q_x}{\partial x} + \frac{\partial Q_y}{\partial y} + q = 0. \quad (7)$$

Dividing the region of problem into finite elements and using approximations for internal efforts, then we shall obtain a finite-dimensional analog of the differential equations (7). For this we use the method of weighted residuals. Then for the first differential equation, we can write the following equations for the method of weighted residuals:

$$\int_{A_i} \left( \frac{\partial M_x}{\partial x} + \frac{\partial M_{xy}}{\partial y} - Q_x \right) \delta\theta_{x,i} dA = 0, \quad i = 1, 2, \dots, N. \quad (8)$$

$N$  is the number of nodes of the finite element grid;

$\delta\theta_{x,i}$  is weight functions;

$A_i$  is area of the region where the weight function is nonzero. We assume that the weight functions  $\delta\theta_{x,i}$  are nonzero only in the region of finite elements adjacent to the node  $i$  under consideration. Such weight functions can be called "local" or "finite". Using for (8) the integration procedure in parts, we obtain the following expression:

$$-\int_{A_i} \left( M_x \frac{\partial(\delta\theta_{x,i})}{\partial x} + M_{xy} \frac{\partial(\delta\theta_{x,i})}{\partial y} - Q_x \delta\theta_{x,i} \right) dA + \int_{A_i} \left( \frac{\partial(M_x \delta\theta_{x,i})}{\partial x} + \frac{\partial(M_{xy} \delta\theta_{x,i})}{\partial y} \right) dA = 0, \quad i = 1, 2, \dots, N. \quad (9)$$

The second integral in expression (9) can be transformed using the Gauss theorem [1] (integration by parts in the plane case) into the integral over the boundary of the region, then we get:

$$\int_{A_i} \left( M_x \frac{\partial(\delta\theta_{x,i})}{\partial x} + M_{xy} \frac{\partial(\delta\theta_{x,i})}{\partial y} - Q_x \delta\theta_{x,i} \right) dA - \int_{\Gamma_i} (M_x l_x + M_{xy} l_y) \delta\theta_{x,i} d\Gamma = 0, \quad i = 1, 2, \dots, N. \quad (10)$$

$\Gamma_i$  is the boundary of the area in which the weight function  $\delta\theta_{x,i}$  is nonzero;

$l_x, l_y$  are direction cosines of normal to the boundary of the region  $\Gamma_i$ . If we shall give the weight functions  $\delta\theta_{x,i}$  a physical meaning and take them in the form of possible angles of rotation along the  $X$  axis, then expression (10) coincides with the expression of the principle of possible displacements. The first integral in (10) is the work of internal forces on possible displacements, the second integral is the potential of external, given moments on the boundary. Bending and torsional moments perform work on the corresponding curvatures, and shear forces perform work on shear angles.

Performing similar transformations to the second and third equations (7), we obtain two more equilibrium equations:

$$\int_{A_i} \left( M_y \frac{\partial(\delta\theta_{y,i})}{\partial y} + M_{xy} \frac{\partial(\delta\theta_{y,i})}{\partial x} - Q_y \delta\theta_{y,i} \right) dA - \int_{\Gamma_i} (M_y l_y + M_{xy} l_x) \delta\theta_{y,i} d\Gamma = 0, \quad i = 1, 2, \dots, N. \quad (11)$$

$$\int_{A_i} \left( Q_x \frac{\partial(\delta w_i^{sh})}{\partial x} + Q_y \frac{\partial(\delta w_i^{sh})}{\partial y} \right) dA - \int_{\Gamma_i} (Q_x l_x + Q_y l_y) \delta w_i^{sh} d\Gamma - \int_{A_i} q \delta w_i^{sh} dA = 0, \quad i = 1, 2, \dots, N. \quad (12)$$

$\delta\theta_{y,i}$  is possible displacement (weight function) in the form of a rotation angle along the  $Y$  axis;

$\delta w_i^{sh}$  is possible displacement (weight function) in the form of a vertical displacement associated with a shear.

Thus, from differential equilibrium equations (7), for the Reissner plate, we obtained algebraic equilibrium equations (10)–(12) for nodes of the finite elements grid, which, when crushing the grid, will tend to differential equations. Note that expressions for derivatives of internal forces are not included in expressions (2), (10)–(12), so they can be accepted to be constant over the finite element region, and possible displacements can be taken as linear functions.

To build a solution, instead of the three differential equilibrium equations (7), having completed the transformations, we can get only two:

$$\frac{\partial^2 M_x}{\partial x^2} + 2 \frac{\partial^2 M_{xy}}{\partial x \partial y} + \frac{\partial^2 M_y}{\partial y^2} + q = 0, \quad \frac{\partial Q_x}{\partial x} + \frac{Q_y}{\partial y} + q = 0. \quad (13)$$

Obviously, the first equation is associated with bending deformations, and the second with shear deformations. For the second differential equation, algebraic equilibrium equations (12) are obtained above. For the first equation, we shall take the function  $\delta w_i^b$  as a weight function. Then we get

$$\int_{A_i} \left( \frac{\partial^2 M_x}{\partial x^2} + 2 \frac{\partial^2 M_{xy}}{\partial x \partial y} + \frac{\partial^2 M_y}{\partial y^2} + q \right) \delta w_i^b dA = 0, \quad i = 1, 2, \dots, N. \quad (14)$$

For the convenience of recording transformations, we introduce intermediate notation:

$$\delta \varphi_{x,i} = \frac{\partial w_i^b}{\partial x}, \quad \delta \varphi_{y,i} = \frac{\partial w_i^b}{\partial y}, \quad V_x = \frac{\partial M_x}{\partial x}, \quad V_y = \frac{\partial M_y}{\partial y}, \quad U_x = \frac{\partial M_{xy}}{\partial x}, \quad U_y = \frac{\partial M_{xy}}{\partial y}. \quad (15)$$

Using (15) we get

$$\int_{A_i} \left( \frac{\partial V_x}{\partial x} + \frac{\partial U_x}{\partial y} + \frac{\partial U_y}{\partial x} + \frac{\partial V_y}{\partial y} + q \right) \delta w_i^b dA = 0, \quad i = 1, 2, \dots, N. \quad (16)$$

Let us demonstrate the further transformations scheme by the example of the transformation of the first addend in (16). Using procedure of integration in parts we get:

$$I_1 = \int_{A_i} \frac{\partial V_x}{\partial x} \delta w_i^b dA = - \int_{A_i} V_x \frac{\partial (\delta w_i^b)}{\partial x} dA + \int_{A_i} \frac{\partial (V_x \delta w_i^b)}{\partial x} dA. \quad (17)$$

Next, using the Gauss theorem, we replace the second integral over the area by the integral along the boundary contour:

$$I_1 = - \int_{A_i} V_x \frac{\partial (\delta w_i^b)}{\partial x} dA + \int_{\Gamma_i} V_x l_x \delta w_i^b d\Gamma. \quad (18)$$

Using (15), we replace the variables again:

$$I_1 = - \int_{A_i} \frac{\partial M_x}{\partial x} \delta \varphi_{x,i} dA + \int_{\Gamma_i} \frac{\partial M_x}{\partial x} l_x \delta w_i^b d\Gamma. \quad (19)$$

To the first integral from (19), we also use integration by parts:

$$I_1 = \int_{A_i} M_x \frac{\partial (\delta \varphi_{x,i})}{\partial x} dA - \int_{A_i} \frac{\partial (M_x \delta \varphi_{x,i})}{\partial x} dA + \int_{\Gamma_i} \frac{\partial M_x}{\partial x} l_x \delta w_i^b d\Gamma. \quad (20)$$

Applying the Gauss theorem to the second integral, we finally get

$$I_1 = \int_{A_i} M_x \frac{\partial^2 (\delta w_i^b)}{\partial x^2} dA - \int_{\Gamma_i} M_x l_x \frac{\partial (\delta w_i^b)}{\partial x} d\Gamma + \int_{\Gamma_i} \frac{\partial M_x}{\partial x} l_x \delta w_i^b d\Gamma. \quad (21)$$

Using similar transformations for all terms and using the expression for the transverse forces from (7), we obtain the following expression for (16):

$$\int_{A_i} \left( M_x \frac{\partial^2 (\delta w_i^b)}{\partial x^2} + 2M_{xy} \frac{\partial^2 (\delta w_i^b)}{\partial x \partial y} + M_y \frac{\partial^2 (\delta w_i^b)}{\partial y^2} \right) dA - \int_{\Gamma_i} (M_x l_x + M_{xy} l_y) \frac{\partial (\delta w_i^b)}{\partial x} d\Gamma - \int_{\Gamma_i} (M_y l_y + M_{xy} l_x) \frac{\partial (\delta w_i^b)}{\partial y} d\Gamma + \int_{\Gamma_i} (Q_x l_x + Q_y l_y) \delta w_i^b d\Gamma + \int_{A_i} q \delta w_i^b dA = 0, \quad i = 1, 2, \dots, N. \quad (22)$$

Equations (22) are equilibrium equations for nodes on possible vertical displacements, causing flexural deformations. In [27, 28], equilibrium equations like (22) were used in constructing a solution for Kirchhoff plates, which based on the functional of additional energy. Linear functions were taken as possible displacements in the finite element region. Therefore, in the triangular finite elements, the first integral was zero. For the rectangular finite elements in the first integral, only the term associated with the torsional curvature was nonzero. The fourth integral is zero, both at the boundaries between the finite elements and at the outer boundaries. The fourth integral is the work of transverse forces normal to the boundary. Therefore, if the external boundary is free, then the transverse forces are zero. If there are no displacements at the border, then there is also zero the possible displacement. The second and third integrals in (22) are the work of moments at the angles of rotation along the normal to the sides of the finite elements. With linear possible displacements, these angles get fractures (breaks) and therefore the third and fourth integrals will not be equal to zero. In papers [27, 28] for triangular finite elements, these integrals were calculated using geometric constructions. Note that when using this approach to the solution, it is impossible to use the approximations of forces constant over the finite element region, since in this case the second and third integrals will be equal to zero.

Comparing the two options have considered above, we note that in the second version, the states of bending and shear are completely separated, and in the first version they are connected. But at the same time, it should be noted that the original differential equations equilibrium of are the same.

In this paper, we will use the first version of the equilibrium equations construction, based on three independent possible displacements. In accordance with the minimum of additional energy principle the functions of moments and shear forces must satisfy the corresponding differential equilibrium equations and static boundary conditions. Since, in the general case, it is almost impossible to select such functions, we shall act as follows. Using the possible displacements principle, we shall compose algebraic equilibrium equations for the nodes of the finite element grid. In this case, in accordance with Reissner's theory we shall take, as the nodal possible displacements, the vertical displacements and rotation angles of middle surface independently. Further, the resulting algebraic equilibrium equations will be added to the functional (5) using the Lagrange multipliers method. This ensures the equilibrium of the selected stress fields in a discrete sense (in nodes) and the solution can be obtained by minimizing the resulting extended functional. It should be noted that the number of equilibrium equations must be less than the total number of unknown nodal forces. Since the forces in the domain of finite elements are approximated by constant functions, then small grids are necessary for obtaining sufficiently accurate solutions, therefore the above requirement will be fulfilled. For example, in a 4x4 square grid, the number of unknown nodal forces will already be greater than the number of equilibrium equations, even if the superposed supports are not taken into account.

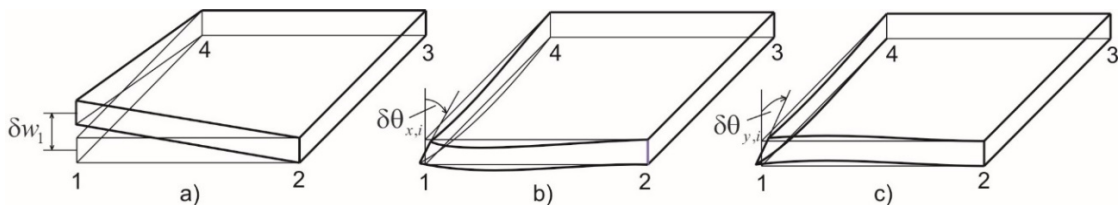


Figure 2. Possible displacements of the node 1 of finite element.

To get the solution, we use the well-known transformation of an arbitrary quadrilateral (Figure 1a) into the square element (Figure 1b). Such transformation can be written in the following form:

$$x = \sum_{i=1}^4 N_i(\xi, \eta) \cdot x_{i,k}, \quad y = \sum_{i=1}^4 N_i(\xi, \eta) \cdot y_{i,k}, \quad N_i(\xi, \eta) = \frac{1}{4} (1 + \xi_i \xi) (1 + \eta_i \eta). \quad (23)$$

$x_{i,k}, y_{i,k}$  are coordinates nodes of finite element  $k$  in the global coordinate system.

Displacements in the finite element area, caused by possible displacements of the node  $i$ , we shall express using the linear basis functions introduced above –  $N_i(\xi, \eta)$ :

$$\delta w = N_i(\xi, \eta)\delta w_i, \quad \delta \theta_x = N_i(\xi, \eta)\delta \theta_{x,i}, \quad \delta \theta_y = N_i(\xi, \eta)\delta \theta_{y,i}. \quad (24)$$

With the possible displacement  $\delta w_i = 1$  only shear deformations occur in the plate:

$$\delta \gamma_{xz} = \frac{\partial(\delta w)}{\partial x} = \frac{\partial N_i(\xi, \eta)}{\partial x}, \quad \delta \gamma_{yz} = \frac{\partial(\delta w)}{\partial y} = \frac{\partial N_i(\xi, \eta)}{\partial y}. \quad (25)$$

Then, the work of the internal forces of finite element  $k$  by possible displacement is expressed in the following form:

$$\delta U_{w_i,k} = Q_{x,k} \iint_{A_k} \delta \gamma_{xz} dA + Q_{y,k} \iint_{A_k} \delta \gamma_{yz} dA. \quad (26)$$

The work of external forces

$$\delta V_{w_i,k} = P_{z,i} + \iint_{A_r} N_i(\xi, \eta) \cdot q_{z,k} dA. \quad (27)$$

$P_{z,i}$  is force which concentrated in a node;

$q_{z,k}$  is load which is distributed over area of the finite element;

$A_k$  is area of the finite element. In accordance with the principle of possible displacements, we shall obtain the equilibrium equation for the node  $i$

$$\sum_{k \in \Xi_i} \delta U_{w_i,k} + \sum_{k \in \Xi_i} \delta V_{w_i,k} = 0. \quad (28)$$

$\Xi_i$  is the set of finite elements adjacent to the node  $i$ . Equations (28) for all nodes can be written in the following general matrix form:

$$\{C_{w,i}\}^T \{F_{w,i}\} + \bar{P}_i = 0, \quad i \in \Xi_w. \quad (29)$$

$\{C_{w,i}\}$  is vector containing the coefficients before unknown forces of finite elements in the equilibrium equation of the node  $i$ ;

$\{F_{w,i}\}$  is vector of unknown forces of finite elements adjacent to node  $i$ .

$\bar{P}_i$  is generalized force equal to the work of external forces;

$\Xi_w$  is set of nodes that have degree of freedom along the  $Z$  axis. The expressions for the elements of the vectors and the generalized forces will be given below.

With the possible displacement in the form of rotation angle along the  $X$  axis  $\delta \theta_{x,i} = 1$ , both bending and torsional deformations and shear deformations take place:

$$\delta \chi_{xx} = \frac{\partial(\delta \theta_x)}{\partial x} = \frac{\partial N_i(\xi, \eta)}{\partial x}, \quad \delta \chi_{xy} = \frac{\partial(\delta \theta_x)}{\partial y} = \frac{\partial N_i(\xi, \eta)}{\partial y}, \quad \delta \gamma_{xz} = -\delta \theta_x = -N_i(\xi, \eta). \quad (30)$$

In this case, the work of the internal forces for the finite element has the following form:

$$\delta U_{\theta_{x,i},k} = Q_{x,k} \iint_{A_k} \delta \gamma_{xz} dA + M_{x,k} \iint_{A_k} \delta \chi_{xx} dA + M_{xy,k} \iint_{A_k} \delta \chi_{xy} dA. \quad (31)$$

The work of external forces in the general case

$$\delta V_{\theta_{x,i},k} = M_{\theta_{x,i}} + \iint_{A_r} N_i(\xi, \eta) \cdot m_{\theta_{x,k}} dA. \quad (32)$$

$M_{\theta_x, i}$  is the moment of external forces concentrated in the node, which acting along the  $X$  axis; – acting along the  $X$  axis moment of external forces, which distributed over the finite element area;

$A_k$  is the area of the finite element. Equilibrium equation, like equation (29), will have the following form:

$$\{C_{\theta_x, i}\}^T \{F_{\theta_x, i}\} + \bar{M}_{x, i} = 0, \quad i \in \Xi_{\theta_x}. \quad (33)$$

$\{C_{\theta_x, i}\}$  is vector containing coefficients before unknown forces of finite elements in the equilibrium equation of the node  $i$ ;

$\{F_{\theta_x, i}\}$  is unknown forces vector for finite elements adjacent to node  $i$ .

$\bar{M}_{x, i}$  is generalized moment equal to the work of external forces;

$\Xi_{\theta_x}$  is nodes set, which have degrees of freedom in the form turn angles  $\theta_x$ .

For possible displacement, in the form a rotation angle along the  $Y$  axis  $\delta\theta_{y, i} = 1$ , such expressions are written similarly:

$$\delta\chi_{yy} = \frac{\partial(\delta\theta_y)}{\partial y} = \frac{\partial N_i(\xi, \eta)}{\partial y}, \quad \delta\chi_{xy} = \frac{\partial(\delta\theta_y)}{\partial x} = \frac{\partial N_i(\xi, \eta)}{\partial x}, \quad \delta\gamma_{yz} = -\delta\theta_y = -N_i(\xi, \eta). \quad (34)$$

$$\delta U_{\theta_{y, k}} = Q_{y, k} \iint_{A_k} \delta\gamma_{yz} dA + M_{y, k} \iint_{A_k} \delta\chi_{yy} dA + M_{xy, k} \iint_{A_k} \delta\chi_{xy} dA. \quad (35)$$

$$\delta V_{\theta_{y, k}} = M_{\theta_{y, i}} + \iint_{A_r} N_i(\xi, \eta) \cdot m_{\theta_{y, k}} dA. \quad (36)$$

$$\{C_{\theta_{y, i}}\}^T \{F_{\theta_{y, i}}\} + \bar{M}_{y, i} = 0, \quad i \in \Xi_{\theta_y}. \quad (37)$$

Using the Lagrange multipliers, equations (29), (33) and (37) we shall add to the functional (5). Then we get

$$\begin{aligned} \Pi^c = & \frac{1}{2} \{F\}^T [D] \{F\} + \sum_{i \in \Xi_w} w_i \left( \{C_{w, i}\}^T \{F_{w, i}\} + \bar{P}_i \right) + \\ & \sum_{i \in \Xi_{\theta_x}} \theta_{x, i} \left( \{C_{\theta_x, i}\}^T \{F_{\theta_x, i}\} + \bar{M}_{x, i} \right) + \sum_{i \in \Xi_{\theta_y}} \theta_{y, i} \left( \{C_{\theta_y, i}\}^T \{F_{\theta_y, i}\} + \bar{M}_{y, i} \right) \rightarrow \min. \end{aligned} \quad (38)$$

We introduce the notation for the nodal displacements global vector –  $\{W\}$ . The vector combines all unknown vertical displacement and rotation angles for the whole area:

$$\{W\} = (w_1 \quad \theta_{x, 2} \quad \theta_{y, 3} \quad \cdots \quad w_{m-2} \quad \theta_{x, m-1} \quad \theta_{y, m})^T.$$

Then, equating to zero the derivatives of the functional (38) with respect to the vectors  $\{W\}$  and  $\{F\}$ , we shall obtain the following linear algebraic equations system:

$$\begin{bmatrix} [D] & [L]^T \\ [L] & [0] \end{bmatrix} \begin{Bmatrix} \{F\} \\ \{W\} \end{Bmatrix} = \begin{Bmatrix} \{P\} \\ 0 \end{Bmatrix}. \quad (39)$$

The matrix  $[L]$  and vector  $\{P\}$  is formed from the coefficients of the equilibrium equations (29), (33) and (37).

The matrix  $[D]$  is block diagonal form and easily analytically invertible. Therefore, we can express the vector  $\{F\}$  from first matrix equation:

$$\{F\} = [D]^{-1} \{P\} - [D]^{-1} [L]^T \{W\} \quad (40)$$

Then we express the vector  $\{W\}$  from the second matrix equation

$$[K] \{W\} = [D]^{-1} \{P\}, \quad [K] = [L][D]^{-1}[L]^T. \quad (41)$$

Note that the matrix  $[K]$  has tape structure of nonzero elements.

Consider the matrix  $[L]$  formation algorithm for a plate represented by arbitrary quadrangular finite elements. For partial derivatives of the function  $N_i(\xi, \eta)$  of the finite element with the number  $k$ , the following expressions can be written:

$$\frac{\partial N_i}{\partial \xi} = \frac{\partial N_i}{\partial x} \frac{\partial x}{\partial \xi} + \frac{\partial N_i}{\partial y} \frac{\partial y}{\partial \xi}, \quad \frac{\partial N_i}{\partial \eta} = \frac{\partial N_i}{\partial x} \frac{\partial x}{\partial \eta} + \frac{\partial N_i}{\partial y} \frac{\partial y}{\partial \eta}. \quad (42)$$

Index  $i$  denotes the local number of a finite element node (Figure 1a). Equations (42) are written in the matrix form:

$$\begin{Bmatrix} \frac{\partial N_i}{\partial \xi} \\ \frac{\partial N_i}{\partial \eta} \end{Bmatrix} = \begin{bmatrix} \frac{\partial x}{\partial \xi} & \frac{\partial y}{\partial \xi} \\ \frac{\partial x}{\partial \eta} & \frac{\partial y}{\partial \eta} \end{bmatrix} \begin{Bmatrix} \frac{\partial N_i}{\partial x} \\ \frac{\partial N_i}{\partial y} \end{Bmatrix}, \quad [J] = \begin{bmatrix} \frac{\partial x}{\partial \xi} & \frac{\partial y}{\partial \xi} \\ \frac{\partial x}{\partial \eta} & \frac{\partial y}{\partial \eta} \end{bmatrix}. \quad (43)$$

Using relations (7), we obtain the expressions of the Jacobi  $[J]$  matrix's elements:

$$\begin{aligned} J_{11} &= \frac{\partial x}{\partial \xi} = \sum_{i=1}^4 \frac{\xi_i(1+\eta\eta_i)}{4} x_{i,k} = \frac{1}{4} [(1-\eta)(x_{2,k} - x_{1,k}) + (1+\eta)(x_{3,k} - x_{4,k})], \\ J_{12} &= \frac{\partial y}{\partial \xi} = \sum_{i=1}^4 \frac{\xi_i(1+\eta\eta_i)}{4} y_{i,k} = \frac{1}{4} [(1-\eta)(y_{2,k} - y_{1,k}) + (1+\eta)(y_{3,k} - y_{4,k})], \\ J_{21} &= \frac{\partial x}{\partial \eta} = \sum_{i=1}^4 \frac{\eta_i(1+\xi\xi_i)}{4} x_{i,k} = \frac{1}{4} [(1-\xi)(x_{4,k} - x_{1,k}) + (1+\xi)(x_{3,k} - x_{2,k})], \\ J_{22} &= \frac{\partial y}{\partial \eta} = \sum_{i=1}^4 \frac{\eta_i(1+\xi\xi_i)}{4} y_{i,k} = \frac{1}{4} [(1-\xi)(y_{4,k} - y_{1,k}) + (1+\xi)(y_{3,k} - y_{2,k})]. \end{aligned} \quad (44)$$

From relation (43), we can obtain the expressions for the necessary derivatives:

$$\begin{Bmatrix} \frac{\partial N_i}{\partial x} \\ \frac{\partial N_i}{\partial y} \end{Bmatrix} = [J]^{-1} \begin{Bmatrix} \frac{\partial N_i}{\partial \xi} \\ \frac{\partial N_i}{\partial \eta} \end{Bmatrix}, \quad [J]^{-1} = \begin{bmatrix} b_{11} & b_{12} \\ b_{21} & b_{22} \end{bmatrix}. \quad (45)$$

The elements of matrix  $[J]^{-1}$  have the following expressions:

$$\det J = J_{11}J_{22} - J_{12}J_{21}, \quad b_{11} = \frac{J_{22}}{\det J}, \quad b_{12} = \frac{-J_{12}}{\det J}, \quad b_{21} = \frac{-J_{21}}{\det J}, \quad b_{22} = \frac{J_{11}}{\det J}. \quad (46)$$

Using the expression (45) and (7), we shall get

$$\begin{aligned} \frac{\partial N_i}{\partial x} &= b_{11} \frac{\xi_i(1+\eta\eta_i)}{4} + b_{12} \frac{\eta_i(1+\xi\xi_i)}{4}, \\ \frac{\partial N_i}{\partial y} &= b_{21} \frac{\xi_i(1+\eta\eta_i)}{4} + b_{22} \frac{\eta_i(1+\xi\xi_i)}{4}. \end{aligned} \quad (47)$$

We shall get integrals on the area of arbitrary quadrilateral finite element, for function  $N_i(\xi, \eta)$  and its derivatives  $\frac{\partial N_i}{\partial x}$ ,  $\frac{\partial N_i}{\partial y}$ , using the integrals on area of square element.

$$\begin{aligned} c_{1i,k} &= \iint_{A_k} \frac{\partial N_i}{\partial x} dA = \frac{1}{4} \int_{-1}^1 \int_{-1}^1 (b_{11}\xi_i(1+\eta\eta_i) + b_{12}\eta_i(1+\xi\xi_i)) \det J d\xi d\eta, \\ c_{2i,k} &= \iint_{A_k} \frac{\partial N_i}{\partial y} dA = \frac{1}{4} \int_{-1}^1 \int_{-1}^1 (b_{21}\xi_i(1+\eta\eta_i) + b_{22}\eta_i(1+\xi\xi_i)) \det J d\xi d\eta, \\ c_{3i,k} &= \iint_{A_k} N_i dA = \frac{1}{4} \int_{-1}^1 \int_{-1}^1 (1+\xi\xi_i)(1+\eta\eta_i) \det J d\xi d\eta. \end{aligned} \quad (48)$$

Integrals (48) are calculated numerically using the four-point Gauss formula.

Using (48), we write the expressions (26), (31) and (35) for the possible displacements of the node  $i$  for the finite element with the number  $k$  in the following form:

$$\begin{aligned} \delta U_{w_i,k} &= Q_{x,k} c_{1i,k} + Q_{y,k} c_{2i,k}, \\ \delta U_{\theta_{xi},k} &= M_{x,k} c_{1i,k} + M_{xy,k} c_{2i,k} - Q_{x,k} c_{3i,k}, \\ \delta U_{\theta_{yi},k} &= M_{xy,k} c_{1i,k} + M_{y,k} c_{2i,k} - Q_{y,k} c_{3i,k}. \end{aligned} \tag{49}$$

We can introduce the vector –  $\{\delta U_{i,k}\} = \begin{Bmatrix} \delta U_{w_i,k} \\ \delta U_{\theta_{xi},k} \\ \delta U_{\theta_{yi},k} \end{Bmatrix}$ . Then

$$\{\delta U_{i,k}\} = [L_{i,k}] \{F_k\}, \quad [L_{i,k}] = \begin{bmatrix} 0 & 0 & 0 & c_{1i,k} & c_{2i,k} \\ c_{1i,k} & 0 & c_{2i,k} & -c_{3i,k} & 0 \\ 0 & c_{2i,k} & c_{1i,k} & 0 & -c_{3i,k} \end{bmatrix}. \tag{50}$$

From the matrices  $[L_{i,k}]$  formed for each finite elements nodes, in accordance with the numbering of the nodes and finite elements, the global matrix  $[L]$  is formed for whole system. If the boundary of the area is not parallel to one of the global axes, but lies at an angle  $\alpha$  to the  $X$  axis, then the matrix should be multiplied by the matrix of direction cosines:

$$[L_{i,k}^s] = [S][L_{i,k}], \quad [S] = \begin{bmatrix} 1 & 0 & 0 \\ 0 & \cos \alpha & \sin \alpha \\ 0 & -\sin \alpha & \cos \alpha \end{bmatrix}. \tag{51}$$

For the case of a load uniformly distributed on the finite element, the work of external forces on possible displacement is calculated by the following formula:

$$\delta V_{w_i,k} = \iint_{A_r} N_i(\xi, \eta) \cdot q_{z,k} dA = q_{z,k} c_{3i,k}. \tag{52}$$

### 3. Results and Discussion

It is well known that when using the theory of bending of Reissner plates for building finite elements in the form of the displacement's method, the so-called problem of "locking" the solution arises. "Locking" is that such finite elements are unsuitable for the calculation of thin plates. Therefore, as first example, we shall obtain solutions for rectangular plates with different ratios of the plate thickness to its dimensions and for different variants of supporting the sides (Figure 3).

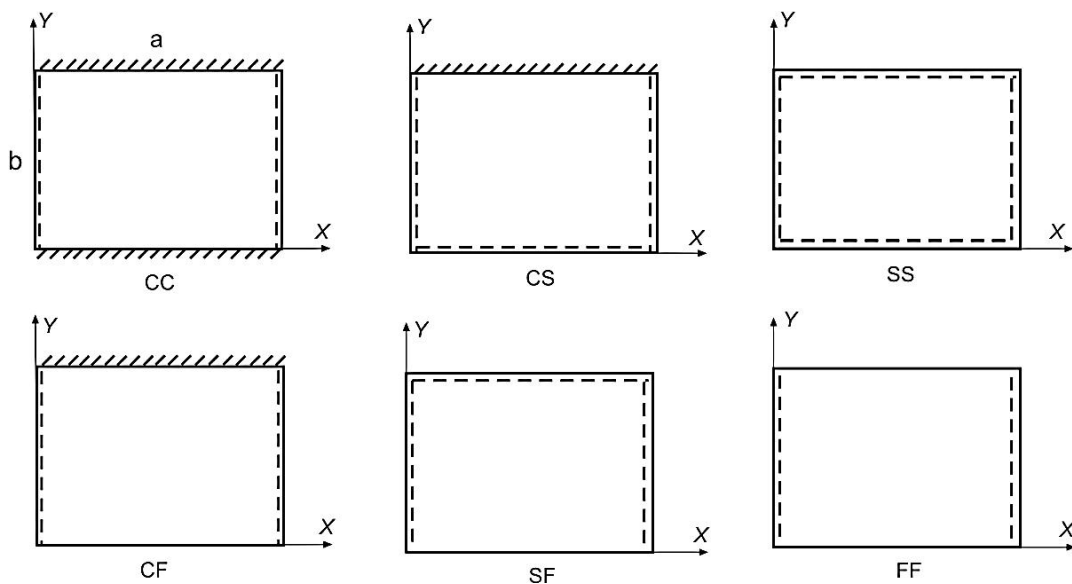


Figure 3. Conditions of support and the sizes of the sides of bending Levi's plates.

In Figure 3 dashed line and the letter S denotes a simply supported side, the oblique hatching and the letter C denotes a clamped side, and the letter F denotes the free side. Table 1 presents the results of calculations of the plate denoted SS, given in [11] for various theories, and the results obtained by the proposed method — SFEM. The lengths of the plate sides were taking equal to 3 m or 1.5 m. The side 3 m long was divided into 30 finite elements, and the side 1.5 m — into 16 elements. Poisson's ratio is  $\nu = 0.3$ . The load was taken evenly distributed over the plate area. The results of calculations in Table 1 are presented in dimensionless form:

$$\bar{w} = \frac{100D}{qa^4} w\left(\frac{a}{2}, \frac{b}{2}\right). \quad (53)$$

**Table 1. Displacement of the center of the plate under the action of a uniformly distributed load.**

a	b	t/a	Theory	Boundary conditions						
				CC	CS	SS	CF	SF	FF	
3	1.5	0.001	CRT	0.0163	0.0305	0.0633	0.1450	0.3810	1.3714	
			S-FSDT	0.0163	0.0305	0.0633	0.1450	0.3809	1.3713	
			[11]	0.0163	0.0305	0.0633	0.1450	0.3810	1.3714	
			<b>SFEM</b>	<b>0.0161</b>	<b>0.0303</b>	<b>0.0632</b>	<b>0.1449</b>	<b>0.3808</b>	<b>1.3688</b>	
		0.04	CRT	0.0178	0.0322	0.0647	0.1505	0.3880	1.3797	
			S-FSDT	0.0175	0.0318	0.0646	0.1476	0.3835	1.3770	
			[11]	0.0178	0.0322	0.0646	0.1504	0.3879	1.3795	
			<b>SFEM</b>	<b>0.0176</b>	<b>0.0320</b>	<b>0.0646</b>	<b>0.1503</b>	<b>0.3890</b>	<b>1.3769</b>	
		0.1	CRT	0.0256	0.0421	0.0725	0.1746	0.4111	1.4168	
			S-FSDT	0.0245	0.0386	0.0714	0.1614	0.3972	1.4070	
			[11]	0.0256	0.0407	0.0714	0.1721	0.4084	1.4130	
			<b>SFEM</b>	<b>0.0254</b>	<b>0.0405</b>	<b>0.0715</b>	<b>0.1721</b>	<b>0.4100</b>	<b>1.4103</b>	
	0.2	CRT	0.0524	0.0694	0.0958	0.2391	0.4688	1.5247		
		S-FSDT	0.0489	0.0630	0.0958	0.2105	0.4464	1.5141		
		[11]	0.0525	0.0695	0.0958	0.2395	0.4692	1.5248		
		<b>SFEM</b>	<b>0.0524</b>	<b>0.0695</b>	<b>0.0960</b>	<b>0.2396</b>	<b>0.4712</b>	<b>1.5220</b>		
	3	3	0.001	CRT	0.1917	0.2785	0.4062	0.5667	0.7931	1.3094
				S-FSDT	0.1917	0.2786	0.4062	0.5667	0.7931	1.3094
				[11]	0.1917	0.2786	0.4062	0.5667	0.7931	1.3094
				<b>SFEM</b>	<b>0.1916</b>	<b>0.2786</b>	<b>0.4063</b>	<b>0.5663</b>	<b>0.7924</b>	<b>1.3068</b>
			0.04	CRT	0.1965	0.2830	0.4096	0.5737	0.7981	1.3154
				S-FSDT	0.1955	0.2819	0.4096	0.5712	0.7975	1.3151
				[11]	0.1965	0.2830	0.4096	0.5737	0.7981	1.3154
				<b>SFEM</b>	<b>0.1964</b>	<b>0.2834</b>	<b>0.4107</b>	<b>0.5732</b>	<b>0.7983</b>	<b>1.3128</b>
0.1			CRT	0.2209	0.3059	0.4273	0.6065	0.8224	1.3459	
			S-FSDT	0.2128	0.2996	0.4273	0.5945	0.8208	1.3451	
			[11]	0.2209	0.3059	0.4273	0.6065	0.8224	1.3459	
			<b>SFEM</b>	<b>0.2209</b>	<b>0.3065</b>	<b>0.4289</b>	<b>0.6061</b>	<b>0.8230</b>	<b>1.3432</b>	
0.2		CRT	0.3021	0.3827	0.4904	0.7139	0.9072	1.4539		
		S-FSDT	0.2759	0.3827	0.4904	0.6777	0.9041	1.4523		
		[11]	0.3021	0.3827	0.4904	0.7139	0.9072	1.4539		
		<b>SFEM</b>	<b>0.3023</b>	<b>0.3837</b>	<b>0.4924</b>	<b>0.7135</b>	<b>0.9081</b>	<b>1.4512</b>		
1.5		3	0.001	CRT	0.8445	0.9270	1.0129	1.0605	1.1496	1.2887
				S-FSDT	0.8445	0.9270	1.0129	1.0605	1.1496	1.2887
				[11]	0.8445	0.9270	1.0129	1.0605	1.1496	1.2887
				<b>SFEM</b>	<b>0.8440</b>	<b>0.9256</b>	<b>1.0106</b>	<b>1.0564</b>	<b>1.1444</b>	<b>1.2804</b>
			0.04	CRT	0.8511	0.9330	1.0181	1.0664	1.1547	1.2938
				S-FSDT	0.8497	0.9322	1.0181	1.0660	1.1551	1.2944
				[11]	0.8511	0.9330	1.0181	1.0664	1.1547	1.2938
				<b>SFEM</b>	<b>0.8506</b>	<b>0.9323</b>	<b>1.0172</b>	<b>1.0623</b>	<b>1.1502</b>	<b>1.2855</b>
	0.1		CRT	0.8850	0.9637	1.0454	1.0981	1.1829	1.3228	
			S-FSDT	0.8770	0.9596	1.0454	1.0946	1.1837	1.3244	
			[11]	0.8850	0.9637	1.0454	1.0981	1.1829	1.3228	
			<b>SFEM</b>	<b>0.8845</b>	<b>0.9638</b>	<b>1.0420</b>	<b>1.0940</b>	<b>1.1791</b>	<b>1.3145</b>	
	0.2	CRT	1.0000	1.0704	1.1430	1.2090	1.2844	1.4283		
		S-FSDT	0.9746	1.0572	1.1430	1.1970	1.2861	1.4316		
		[11]	1.0000	1.0704	1.1430	1.2090	1.2844	1.4283		
		<b>SFEM</b>	<b>0.9998</b>	<b>1.0712</b>	<b>1.1446</b>	<b>1.2050</b>	<b>1.2812</b>	<b>1.4199</b>		

The results presented in Table 1 demonstrate good accuracy of the solution according to the proposed method, both for thin and thick plates. Thus, the proposed solution method is free from the so-called "locking" effect and can be used to calculate plates of any thickness.

To assess the accuracy of determining the bending moments, we consider the results of calculations of the SS plate for different aspect ratios. It is known that when the sides of plate are simply supported, the values of the bending moments don't depend on the plate thickness. Table 2 provides comparison of the values of moments in the center of the plate, obtained by the proposed method, with the results of analytical calculations according to the Kirchhoff theory [29]. The finite element grid was taken  $21 \times 21$ .

**Table 2. Moments in the center of the SS plate which loaded with a uniformly distributed load.**

$b/a$	$100M_x / qa^2$			$100M_y / qa^2$		
	$t/a = 0.001$	$t/a = 0.2$	Exact [29]	$t/a = 0.001$	$t/a = 0.2$	Exact [29]
1.0	4.79	4.84	4.79	4.79	4.84	4.79
1.1	5.55	5.60	5.54	4.93	4.98	4.93
1.2	6.27	6.33	6.27	5.01	5.06	5.01
1.3	6.94	7.00	6.94	5.03	5.08	5.03
1.4	7.55	7.62	7.55	5.02	5.07	5.02
1.5	8.11	8.19	8.12	4.98	5.03	4.98
1.6	8.62	8.69	8.62	4.93	4.98	4.92
1.7	9.08	9.15	9.08	4.86	4.90	4.86
1.8	9.48	9.56	9.48	4.78	4.83	4.79
1.9	9.85	9.92	9.85	4.71	4.75	4.71
2.0	10.17	10.24	10.17	4.63	4.67	4.64

Note that for thin plates, the proposed solution practically coincides with the analytical one, and for thick plates one, the resulting moments are more than analytical ones by about 1 %.

Also, the rate of the solution convergence by the proposed method was tested when was crushing the finite element grid. The test showed fast convergence of displacements for all considered variants of plates. In Figure 4 shows graphs of solutions convergence for two variants of square plates, depending on the number side's divisions.

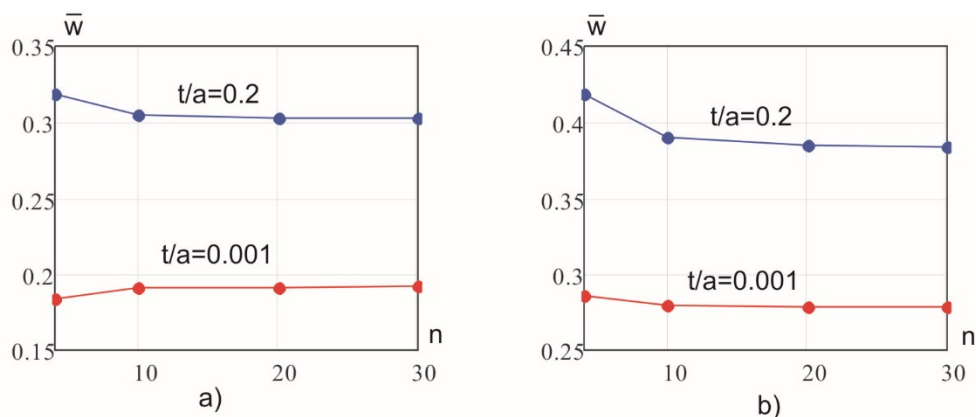


**Figure 4. Displacement the center of a square plate depending on the number of side divisions: a) SS plate; b) CS plate.**

In Figure 5 shows the graphs of the change in bending moments in the SS plate (Figure 3) for various sides ratios. The plate was crushed into 21 finite elements along each side. Therefore, the lengths of the finite element's sides were in the same ratio as the lengths of the plate sides. Bending moments are constant values in the finite element region and so more accurately model the value in the finite element centers. Therefore, to more accurately determine the value of the moment in the clamped side middle  $M_{y,2}$ , linear extrapolation was used according to the moment values in the two finite elements nearest to the boundary. Obviously, with an increase in the ratio of the finite element sides, the error in determining the moment on the clamped side also increases.

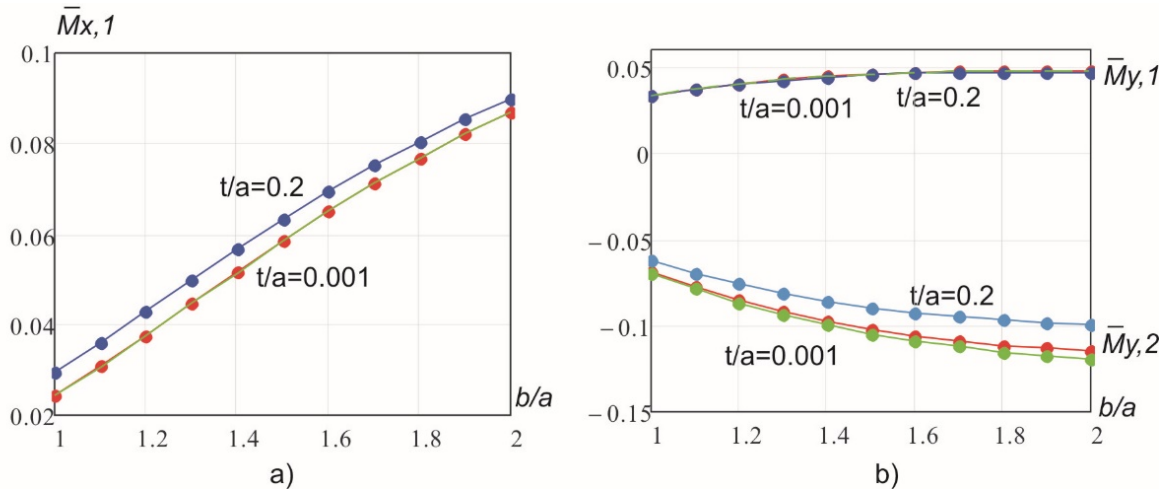


**Figure 5. Bending moments for a uniformly loaded square plate CC with different ratios of sides.**

$\bar{M}_{x,1} = M_{x,1}/qa^2$  and  $\bar{M}_{y,1} = M_{y,1}/qa^2$  are bending moments in the center of the plate;

$\bar{M}_{y,2} = M_{y,2}/qa^2$  is bending moment in the middle of the clamped side. Designations:

**Red line is  $t/a = 0.001$ ; Blue line is  $t/a = 0.2$ ; Green line is the solutions for the Kirchhoff plate [29].**

Graphs in Figure 5 shows the concurrence of the obtained moment values for thin plates with the analytical solution for Kirchhoff plates (the Green lines coincide with the Red lines). For thick plates (Blue line), only the moments  $\bar{M}_{y,1}$  coincide with the solution for Kirchhoff's plates (Figure 5b). The values of the moments  $\bar{M}_{x,1}$  and  $\bar{M}_{y,2}$  for thick plates differ by 10–20 % from the corresponding moments obtained for thin plates. For an additional estimation of the results accuracy obtained, square SS plate was calculated on the LIRA-SAPR program using volume finite elements. A quarter of the plate was divided into 12 elements in height and into 20 elements along the X and Y axes. A plate with thickness  $t = 0.6\text{m}$  was calculated. The dimensions of the plate quarter in plan are 1.5 m by 1.5 m. Poisson's ratio  $\nu = 0.3$ . Load is  $q = 10\text{ kN/m}^2$ . Modulus of elasticity is  $E = 10000\text{ kN/m}^2$ .

**Table 3. Stresses in a square SS plate – (Figure 2).**

Solution	Fiber of section	Center of the plate		Middle of the clamped side
		$ \sigma_{x,1} , \text{kN/m}^2$	$ \sigma_{y,1} , \text{kN/m}^2$	$ \sigma_{y,2} , \text{kN/m}^2$
LIRA-SAPR	top	41.85	43.39	88.11
	bottom	47.50	46.29	89.13
	mean value	44.68	44.84	88.62
SFEM		43.91	49.95	93.15
Kirchhoff's plate [29]		36.54	49.86	103.46

Comparison of the results presented in Table 3 shows that the stress values obtained for thick plate based on Reissner's theory agree well with the stress values obtained by solving three-dimensional elasticity theory problem. Stresses in the clamped side  $\sigma_{y,2}$  were determined using linear extrapolation from the values in the two finite elements nearest to the boundary. Also note that the displacements of the slab center, obtained by the LIRA-SAPR program, are 8.5 % more than the displacements obtained by the proposed method.

As next example the semiring was calculated on the acting of uniformly distributed load (Figure 6). The semiring has hinge supports along the lines DE and DB, and clamped support along the line EA. Line AB is the axis of symmetry, therefore, in the nodes lying on this line, the angles of rotation along the horizontal axis were excluded. In the calculations were taken the following data:  $E = 10000\text{ kN/m}^2$ ,  $\mu = 0.3$ ,  $t = 0.1\text{ m}$ ,  $q = 10\text{ kN/m}^2$ ,  $R = 6\text{ m}$ ,  $r = 3\text{ m}$ . In Figure 7 shows graphs of changes along the line AB: bending radial moments –  $\bar{M}_y$ ; moments directed perpendicular to the line AB –  $\bar{M}_x$  and vertical displacements  $\bar{w}$

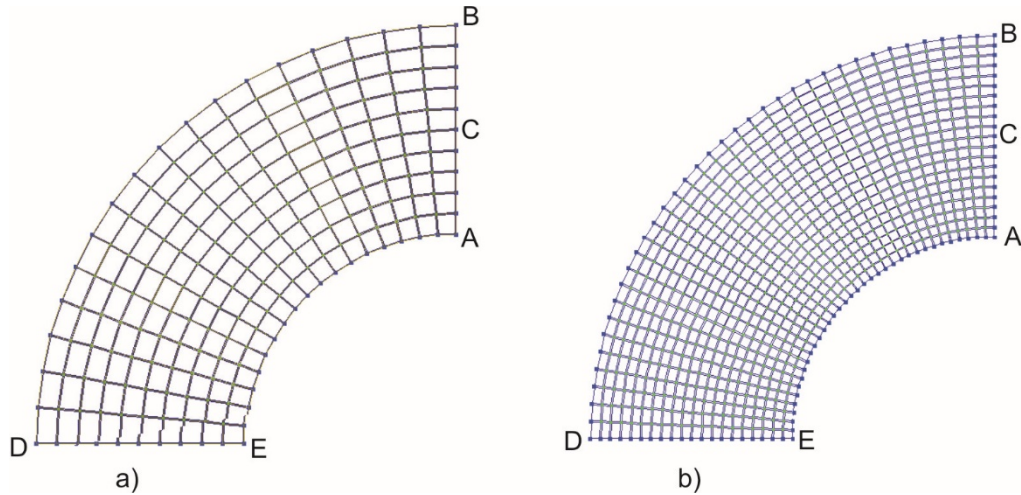


Figure 6. Finite element grids of the ring quarter.

$$\bar{w} = w \frac{1000D}{qR^4}, \bar{M}_x = \frac{M_x}{qR^2}, \bar{M}_y = \frac{M_y}{qR^2}. \tag{54}$$

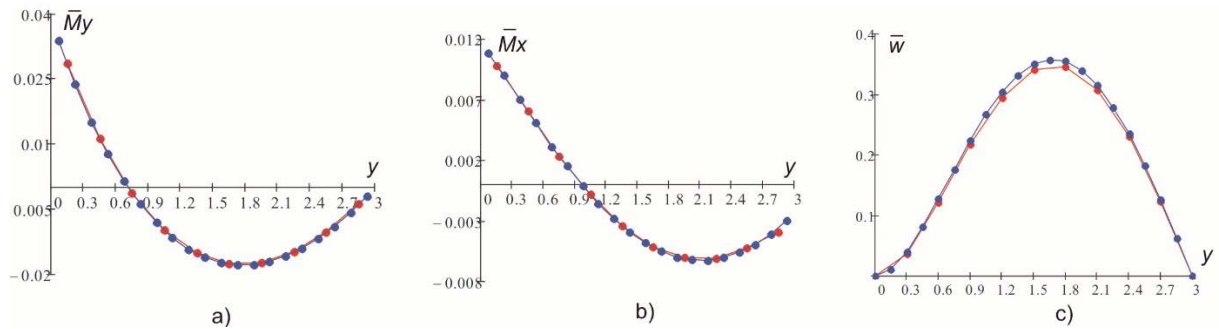


Figure 7. Bending moments and deflections of the semiring along the AB line: Red line is scheme in Figure 6a; Blue line is scheme in Figure 6b.

Table 4. Comparison of calculation results for the semiring with an analytical solution.

Solution	$\bar{w}_c$	$\bar{M}_{x,C}$	$\bar{M}_{y,C}$	$\bar{M}_{x,A}$	$\bar{M}_{y,A}$
SFEM (Figure 66)	0.357	0.0118	0.0387	-0.00436	-0.0167
Analytical [30]	0.358	0.0118	0.0393	-0.00439	-0.0168

The values of the moments at point C were determined as the middle value of moments in two finite elements adjacent to the point on both sides. The values of the moments at point A were determined by linear extrapolation from the values of moments in the two nearest finite elements. Graphs in Figure 7 illustrate the linear variation of moments near clamped side ( $y = 0$ ). Thus, the graphs in Figure 7 and the data in Table 4 show good convergence and accuracy of the proposed method and for this example.

In the following example we use the finite element in the form of a parallelogram which have maximum inner angle of 120 degrees. A skewed plate was calculated (Figure 8). For such plate the finite difference solution is given in [29].

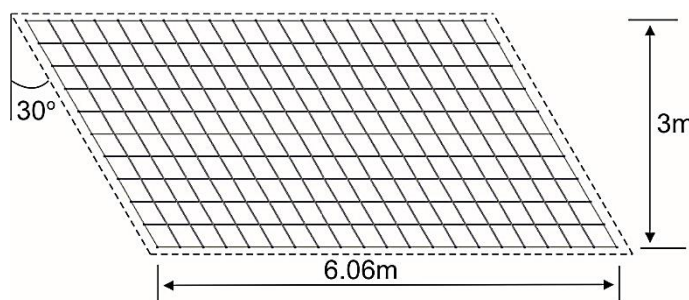


Figure 8. Skewed plate. Grid – 10x20 finite elements.

The following plate parameters were taken:  $E = 10^7$  kN/m<sup>2</sup>,  $\mu = 0.21$ ,  $t = 0.1$  m,  $q = 10$  kN/m<sup>2</sup>. Sizes of the plate are shown in Figure 8. Calculations were performed for two finite element grids: 10 by 20 elements (Figure 8) and 20 by 40 elements. In addition, for comparison, calculations of this plate were performed using the LIRA-SAPR program. All results are given in Table 5.

**Table 5. Displacements and bending moments in the center of the plate (Figure 8).**

Solution (grid)	$w$ , mm	$M_x$ , kN · m/m	$M_y$ , kN · m/m
SFEM (10×20)	9.074	3.371	8.635
SFEM (20×40)	9.187	3.437	8.780
LIRA-SAPR (10×20)	9.115	4.758	7.237
LIRA-SAPR (20×40)	9.149	4.828	7.347
Timoshenko [29]	9.719	–	8.712

The values of the bending moments in the plate center (for SFEM and for LIRA-SAPR) were determined as the middle value of moments in two elements adjacent to the center point on one half plate. Note that the moments in the two finite elements differ by about 5 percent. The bending moments obtained by the proposed method are close to the corresponding values given in [29], and the value of plate center displacement is less than the corresponding value given in [29] by about 6 %, but almost coincides with the value obtained using the LIRA-SAPR program. The results of the skew plate calculations show a good accuracy of the proposed method for calculating the Reissner's plates with using finite elements in the parallelogram form. Note that the plate under consideration is thin, but nevertheless the solution "locking" effect is absent, as well as for the plate in the semiring form from the previous example.

#### 4. Conclusion

1. A method for calculating of bending plates based on Reissner's theory by the finite element method is proposed. The method is based on the fundamental principles of additional energy minimum and possible displacements. The necessary relations for an arbitrary quadrangular finite element are obtained. Mathematically, the transition from differential equilibrium equations of bent plates to algebraic equilibrium equations for nodes of finite element grid.

2. The bending moments, torques and shear forces are constant in the finite element area, which is necessary condition for ensuring the solution convergence, when the mesh is crushed.

3. The proposed calculation method allows both thick and thin plates to be calculated. There is no effect of solution "locking" for thin plates, which is confirmed by rectangular plates calculations with different support conditions of side and different ratios of thickness to plate sizes.

4. Comparison of solutions obtained by the proposed method for plates of various shapes with analytical solutions shows fast convergence and proposed method accuracy of calculating both thick and thin plates.

#### References

- Gallager, R. Metod konechnykh elementov. Osnovy [Finite element method The basics]. Moskow: Mir, 1984. 428 p.(rus)
- Sekulovich, M. Metod konechnykh elementov [Finite element method]. Moskow: Stroyizdat, 1993. 664 p. (rus)
- Timoshenko, S.P., Voinovskiy-Kriger, S. Plastiny i obolochki [Plates and shells]. Moskow: Nauka, 1966. 636 p. (rus)
- Fallah, N. On the use of shape functions in the cell centered finite volume formulation for plate bending analysis based on Mindlin-Reissner plate theory. Computers & Structures. 2006. 84. Pp. 1664–1672.
- Katili, I., Batoz, J.L., Maknun, I.J., Hamdouni, A., Millet, O. The development of DKMQ plate bending element for thick to thin shell analysis based on the Naghdi/Reissner/Mindlin shell theory. Finite Elements in Analysis and Design. 2015. 100. Pp. 12–27.
- Khezri, M., Gharib, M., Rasmussen, K.J.R. A unified approach to meshless analysis of thin to moderately thick plates based on a shear-locking-free Mindlin theory formulation. Thin-Walled Structures. 2018. Pp. 161–179.
- Mirsaidov, M.M., Abdikarimov, R.A., Vatin, N.I., Zhgutov, V.M., Khodzhayev, D.A., Normuminov, B.A. Natural oscillations of a rectangular plates with two adjacent edges clamped. Magazine of Civil Engineering. 2018. 82(6). Pp. 112–126. doi: 10.18720/MCE.82.11
- Lalin, V.V., Rozin, L.A., Kushova, D.A. Variatsionnaya postanovka ploskoy zadachi geometricheski nelineynogo deformirovaniya i ustoychivosti uprugikh sterzhney [Variational statement of the plane problem of geometrically nonlinear deformation and stability of elastic rods]. Magazine of Civil Engineering. 2013. 36(1). Pp. 87–96. (rus) doi: 10.5862/MCE.36.11
- Rozin, L.A. Zadachi teorii uprugosti i chislennyye metody ikh resheniya [Problems of the theory of elasticity and numerical methods for their solution]. Sankt-Peterburg: SPbGTU, 1998. 532 p. (rus)
- Rozin, L.A. Metod konechnykh elementov v primenenii k uprugim sistemam [The finite element method as applied to elastic systems]. Moskow: Stroyizdat, 1977. 129 p. (rus)
- Park, M., Choi, D.-H. A two-variable first-order shear deformation theory considering in-plane rotation for bending, buckling and free vibration analysis of isotropic plates. Applied Mathematical Modelling. 2018. 61. Pp. 49–71.
- Kumara, R., Lala, A., Singhb, B.N., Singhc, J. New transverse shear deformation theory for bending analysis of FGM plate under patch load. Composite Structures. 2019. 208. Pp. 91–100.

13. Thai, H.-T., Choi, D.-H. Finite element formulation of various four unknown shear deformation theories for functionally graded plates. *Finite Elements in Analysis and Design*. 2013. 75. Pp. 50–61.
14. Doa, T.V., Nguyenb, D.K., Ducc, N.D., Doanc, D.H., Buie, T.Q. Analysis of bi-directional functionally graded plates by FEM and a new third-order shear deformation plate theory. *Thin-Walled Structures*. 2017. 119. Pp. 687–699.
15. Mulcahy, N.L., McGuckin, D.G. The addition of transverse shear flexibility to triangular thin plate elements. *Finite Elements in Analysis and Design*. 2012. 52. Pp. 23–30.
16. Karttunen, A.T., Hertenzen, R., Reddy, J.N., Romanoff, J. Shear deformable plate elements based on exact elasticity solution. *Computers & Structures*. 2018. 200. Pp. 21–31.
17. Duan, H., Ma, J. Continuous finite element methods for Reissner-Mindlin plate problem. *Acta Mathematica Scientia*. 2018. 38. Pp. 450–470.
18. Sukhoterina, M.V., Baryshnikov, S.O., Knysh, T.P. Stress-strain state of clamped rectangular Reissner plates. *Magazine of Civil Engineering*. 2017. 76(8). Pp. 225–240. doi: 10.18720/MCE.76.20
19. Sukhoterina, M.V., Baryshnikov, S.O., Potekhina, Ye.V. O raschetah plastin po sdvigovym teoriyam [About plate calculations based on shear theories]. *Vestnik gosudarstvennogo universiteta morskogo i rechnogo flota im. admirala, S.O. Makarova*. 2015. 30(2). Pp. 81–89. (rus)
20. Zenkour, A.M. Exact mixed-classical solutions for the bending analysis of shear deformable rectangular plates. *App. Math. Model.* 2003. 27. Pp. 515–534.
21. Erkmén, R.E. Shear deformable hybrid finite-element formulation for buckling analysis of thin-walled members. *Finite Elements in Analysis and Design*. 2014. 82. Pp. 32–45.
22. Özütok, A., Madenci, E. Static analysis of laminated composite beams based on higher-order shear deformation theory by using mixed-type finite element method. *International Journal of Mechanical Sciences*. 2017. 130. Pp. 234–243.
23. Senjanović, I., Vladimir, N., Hadžić, N. Modified Mindlin plate theory and shear locking free finite element formulation. *Mechanics Research Communications*. 2014. 55. Pp. 95–104.
24. Tyukalov, Yu.Ya. Finite element models in stresses for plane elasticity problems. *Magazine of Civil Engineering*. 2018. 77(1). Pp. 23–37. doi: 10.18720/MCE.77.3
25. Tyukalov, Yu.Ya. The functional of additional energy for stability analysis of spatial rod systems. *Magazine of Civil Engineering*. 2017. 70(2). Pp. 18–32. doi: 10.18720/MCE.70.3
26. Tyukalov, Yu.Ya. Stress finite element models for determining the frequencies of free oscillations. *Magazine of Civil Engineering*. 2016. 67(7). Pp. 39–54. doi: 10.5862/MCE.67.5
27. Tyukalov, Yu.Ya. Finite element models in stresses for bending plates. *Magazine of Civil Engineering*. 2018. 82(6). Pp. 170–190. doi: 10.18720/MCE.82.16
28. Tyukalov, Yu.Ya. Calculation method of bending plates with assuming shear deformations. *Magazine of Civil Engineering*. 2019. 85(1). Pp. 107–122. doi: 10.18720/MCE.85.9
29. Donnell, L.G. *Balki, plastiny i obolochki* [Beams, plates and shells]. Moscow: Nauka, 1982. 568 p. (rus)
30. Belkin, A.Ye., Gavryushin, S.S. *Raschet plastin metodom konechnykh elementov* [Plate calculation by finite element method]. Moscow: MGTU, 2008. 231 p. (rus)

### **Contacts:**

*Yury Tyukalov, +7(912)8218977; yutvgu@mail.ru*

© Tyukalov, Yu.Ya., 2019



DOI: 10.18720/MCE.89.6

## Конечно-элементная модель в напряжениях для пластин Рейсснера

**Ю.Я. Тюкалов**

*Вятский государственный университет, г. Киров, Россия*

**Ключевые слова:** пластины Рейсснера, возможные перемещения, конечные элементы, изгибаемые пластины

**Аннотация.** Предложена методика расчета изгибаемых пластин методом конечных элементов на основе теории Рейсснера. Метод основывается на фундаментальных принципах минимума дополнительной энергии и возможных перемещений. Для дискретизации предметной области используются произвольные четырехугольные конечные элементы. По области конечного элемента поля моментов и поперечных сил аппроксимируются постоянными функциями, которые удовлетворяют дифференциальным уравнениям равновесия в области конечного элемента при отсутствии распределенной нагрузки. Используя принцип возможных перемещений, составляются алгебраические уравнения равновесия узлов сетки конечных элементов. При этом, в соответствии с теорией Рейсснера, в качестве узловых возможных перемещений принимаются, независимо, вертикальные перемещения и углы поворота срединной поверхности пластины. Предлагаемый метод расчета позволяет рассчитывать как толстые, так и тонкие пластины. Эффект «заклинивания» решения для тонких пластин отсутствует, что подтверждено расчетами прямоугольных пластин с различными условиями опирания и различными отношениями толщины к размеру пластины. Сравниваются решения, полученные по предлагаемой методике для пластин различной формы, с аналитическими решениями. Показана достаточно быстрая сходимости и точность предлагаемой методики расчета как для толстых, так и для тонких пластин.

### Литература

1. Галлагер Р. Метод конечных элементов. Основы. М.: Мир, 1984. 428 с.
2. Секулович М. Метод конечных элементов. М.: Стройиздат, 1993. 664 с.
3. Тимошенко С.П., Войновский-Кригер С. Пластины и оболочки. М.: Наука, 1966. 636 с.
4. Fallah N. On the use of shape functions in the cell centered finite volume formulation for plate bending analysis based on Mindlin-Reissner plate theory // Computers & Structures. 2006. Vol. 84. Pp. 1664–1672.
5. Katili I., Batoz J.L., Maknun I.J., Hamdouni A., Millet O. The development of DKMQ plate bending element for thick to thin shell analysis based on the Naghdi/Reissner/Mindlin shell theory // Finite Elements in Analysis and Design. 2015. Vol. 100. Pp. 12–27.
6. Khezri M., Gharib M., Rasmussen K.J.R. A unified approach to meshless analysis of thin to moderately thick plates based on a shear-locking-free Mindlin theory formulation // Thin-Walled Structures, 2018. Pp. 161–179.
7. Мирсаидов М.М., Абдикаримов Р.А., Ватин Н.И., Жгутов В.М., Ходжаев Д.А., Нормуминов Б.А. Нелинейные параметрические колебания вязкоупругой пластинки переменной толщины // Инженерно-строительный журнал. 2018. № 6(82). С. 112–126. doi: 10.18720/MCE.82.11
8. Лалин В.В., Розин Л.А., Кушова Д.А. Вариационная постановка плоской задачи геометрически нелинейного деформирования и устойчивости упругих стержней // Инженерно-строительный журнал. 2013. № 1(36). С. 87–96. doi: 10.5862/MCE.36.11
9. Розин Л. А. Задачи теории упругости и численные методы их решения. СПб.: СПбГТУ, 1998. 532 с.
10. Розин Л.А. Метод конечных элементов в применении к упругим системам. М.: Стройиздат, 1977. 129 с.
11. Park M., Choi D.-H. A two-variable first-order shear deformation theory considering in-plane rotation for bending, buckling and free vibration analysis of isotropic plates // Applied Mathematical Modelling. 2018. Vol. 61. Pp. 49–71.
12. Kumara R., Lala A., Singhb B.N., Singhc J. New transverse shear deformation theory for bending analysis of FGM plate under patch load // Composite Structures. 2019. Vol. 208. Pp. 91–100.
13. Thai H.-T., Choi D.-H. Finite element formulation of various four unknown shear deformation theories for functionally graded plates // Finite Elements in Analysis and Design. 2013. Vol. 75. Pp. 50–61.
14. Doa T.V., Nguyenb D.K., Duc N.D., Doanc D.H., Buie T.Q. Analysis of bi-directional functionally graded plates by FEM and a new third-order shear deformation plate theory // Thin-Walled Structures. 2017. Vol. 119. Pp. 687–699.
15. Mulcahy N.L., McGuckin D.G. The addition of transverse shear flexibility to triangular thin plate elements // Finite Elements in Analysis and Design. 2012. Vol. 52. Pp. 23–30.

16. Karttunen A.T., Herten R., Reddy J.N., Romanoff J. Shear deformable plate elements based on exact elasticity solution // *Computers & Structures*. 2018. Vol. 200. Pp. 21–31.
17. Duan H., Ma J. Continuous finite element methods for Reissner-Mindlin plate problem // *Acta Mathematica Scientia*. 2018. Vol. 38. Pp. 450–470.
18. Сухотерин М.В., Барышников С.О., Кныш Т.П. Напряженно-деформированное состояние защемленной прямоугольной пластины Рейсснера // *Инженерно-строительный журнал*. 2017. № 8(76). С. 225–240. doi: 10.18720/MCE.76.20
19. Сухотерин М.В., Барышников С.О., Потехина Е.В. О расчетах пластин по сдвиговым теориям // *Вестник государственного университета морского и речного флота им. адмирала С.О. Макарова*. 2015. № 2 (30). С. 81–89.
20. Zenkour A.M. Exact mixed-classical solutions for the bending analysis of shear deformable rectangular plates // *App. Math. Model.* 2003. Vol. 27. Pp. 515–534.
21. Erkmen R.E. Shear deformable hybrid finite-element formulation for buckling analysis of thin-walled members // *Finite Elements in Analysis and Design*. 2014. Vol. 82. Pp. 32–45.
22. Özütok A., Madenci E. Static analysis of laminated composite beams based on higher-order shear deformation theory by using mixed-type finite element method // *International Journal of Mechanical Sciences*. 2017. Vol. 130. Pp. 234–243
23. Senjanović I., Vladimir N., Hadžić N. Modified Mindlin plate theory and shear locking free finite element formulation // *Mechanics Research Communications*. 2014. Vol. 55. Pp. 95–104.
24. Тюкалов Ю.Я. Конечно-элементные модели в напряжениях для задач плоской теории упругости // *Инженерно-строительный журнал*. 2018. № 1(77). С. 23–37. doi: 10.18720/MCE.77.3
25. Тюкалов Ю.Я. Функционал дополнительной энергии для анализа устойчивости пространственных стержневых систем // *Инженерно-строительный журнал*. 2017. № 2(70). С. 18–32. doi: 10.18720/MCE.70.3
26. Тюкалов Ю.Я. Определение частот свободных колебаний методом конечных элементов в напряжениях // *Инженерно-строительный журнал*. 2016. № 7(67). С. 39–54. doi: 10.5862/MCE.67.5
27. Тюкалов Ю.Я. Конечно элементные модели в напряжениях для изгибаемых пластин // *Инженерно-строительный журнал*. 2018. № 6(82). С. 170–190. doi: 10.18720/MCE.82.16
28. Тюкалов Ю.Я. Метод расчета изгибаемых плит с учетом деформаций сдвига // *Инженерно-строительный журнал*. 2019. № 1(85). С. 107–122. DOI: 10.18720/MCE.85.9
29. Доннелл Л.Г. Балки, пластины и оболочки. М.: Наука, 1982. 568 с.
30. Белкин А.Е., Гаврюшин С.С. Расчет пластин методом конечных элементов. М.: МГТУ, 2008. 231 с.

**Контактные данные:**

Юрий Яковлевич Тюкалов, +7(912)8218977; эл. почта: [yutvgu@mail.ru](mailto:yutvgu@mail.ru)

© Тюкалов Ю.Я., 2019



DOI: 10.18720/MCE.89.7

## Mixed finite-element method in V.I. Slivker's semi-shear thin-walled bar theory

V.V. Lalin, V.A. Rybakov\*, S.S. Ivanov, A.A. Azarov

Peter the Great St. Petersburg Polytechnic University, St. Petersburg, Russia

\* E-mail: fishermanoff@mail.ru

**Keywords:** mixed finite element method, thin-walled beam, Slivker's semi-shear theory, Reissner's functional

**Abstract.** Variational formulation of stability problems for thin-walled beams is presented. Geometrical stiffness matrix is derived from the stability functional. Shear deformation is taken into account by using V.I. Slivker's semi-shear theory of thin-walled bars. Quadratic Hermite polynomials were considered as approximation for all the internal forces and displacements functions. The exact analytical solutions to some particular eigenfrequency and stability problems for thin-walled beam are obtained. The effect of «spurious» frequencies in thin-walled beam spectrum is discussed. Comparison of the numerical results from the finite element methods is presented. Approximation by quadratic functions turns out to be faster in cases where the buckling has a flexural-torsional form.

### 1. Introduction

Classical finite element method (FEM) applied to structural mechanics has a serious drawback concerning accuracy of stress calculation. As displacements are the only unknown functions approximated by some polynomials, the process of evaluating stresses appears to be secondary to the main problem of solving system of linear equations. Due to the necessity of taking derivative, the degree of polynomials forming the Ritz sum in stress expression decreases which means that calculation precision suffers.

Thin-walled beam, because of its specific properties, has a unique internal force factor — bimoment, which in certain cases can cause large normal stresses in cross-section. In order to determine that stresses with good accuracy mixed FEM can be used.

The first mixed formulation in classic calculus of variations was presented by Hellinger. However, only after the work [1] by Reissner the mixed variational principle has become a common tool for variational formulations of problems in structural mechanics. The main property of the Reissner's functional is that it includes stress functions along with displacements, which gives an advantage of choosing the approximation functions for every unknown value independently.

The first theory of thin-walled beams of open cross-section was developed by Vlasov in [2], and since that work many researches have been devoted to the application of this theory to a variety of static and dynamic problems of thin-walled structures. The problem of free vibrations of thin-walled beam with open cross-section was solved in [3]. In this article, based on the solution of ordinary differential equations governing the static problem, stiffness and consistent mass matrixes were derived. In addition, some numerical experiments were carried out in order to prove sufficient accuracy of the lumped mass matrix formulation. In [4] another finite element model, based on Vlasov's theory, was introduced. In this work special attention was paid to the computational problems arising when coefficients of stiffness matrix vanish whilst compiling the global governing system of equations. The influence of boundary conditions on coupled vibrations of thin-walled bar was investigated. Galerkin's method was used for spectrum analysis in article [5], which showed sufficient accuracy of results even for the problems that do not have analytical solution. An anisotropic

---

Lalin, V.V., Rybakov, V.A., Ivanov, S.S., Azarov, A.A. Mixed finite-element method in V.I. Slivker's semi-shear thin-walled bar theory. Magazine of Civil Engineering. 2019. 89(5). Pp. 79–93. DOI: 10.18720/MCE.89.7

Лалин В.В., Рыбаков В.А., Иванов С.С., Азаров А.А. Смешанный метод конечных элементов в полусдвиговой теории тонкостенных стержней В.И. Сливкера // Инженерно-строительный журнал. 2019. № 5(89). С. 79–93. DOI: 10.18720/MCE.89.7



composite material of thin-walled bar considered by author has led to introduction of nonclassical parameters such as warping restraint, transverse shear flexibility and structural couplings.

In [6] author clarified Vlasov's equations of motion for thin-walled beams taking into account torsional shear deformation in middle surface. In addition, that paper introduced some experiments on thin-walled beam resonant frequency and verification with the theoretical results. Simply supported thin beams were numerically and empirically investigated in [7]. This work presented so-called "engineering" theory of bars based on analogy with elastic behavior of thin plates. Due to its relative simplicity, this theory could be applied in designing practice, although it is not valid for other boundary conditions. The method of trigonometric series used in this article to approximate stress function is suitable for finite element analysis as well.

The expressions describing thin-walled rod vibrations in [8] were presented as four partial, linear integro-differential equations. The complex formulation allowed to take into account the effect of longitudinal inertia and shear flexibility. Moreover, the application area of the generalized theory is not limited to open cross-section beams with uniform mechanical and geometrical properties. Vlasov's and Timoshenko's equations of motion for thin-walled beam appear to be special cases of this theory if relevant hypotheses are accepted.

The influence of shear deformation and rotational degree of freedom on thin-walled beam vibrations were considered in [9]. The governing equations were derived from Vlasov's theory but with some additional modifications concerning shear ductility. One advantage of the proposed theory is that it allows obtaining dynamic characteristics of beams made out of viscoelastic material.

One important type of load that could be applied to a thin-walled structure is an impact load. Mechanical behavior of thin-walled beam under such load was discussed in [10], where six differential equations of motion suitable for some particular dynamic problems were presented. For the case when the center of inertia coincides with the shear center approximate solution for engineering use was obtained.

Generally speaking, the problems of natural and forced oscillations of any structural element are more complex than corresponding static problem and that is why many different engineering techniques were presented by researchers in order to keep up with the growing tendency of high accuracy stress-strain calculations [11–17]. For example, method of additional energy functional, viscoelastic models for parametric nonlinear oscillation problems, response-spectra method for non-proportional damping systems.

The behavior of elastic stress waves in structural elements under dynamic impact, including seismic load, was discussed in [18–20]. In terms of mechanics, the main feature of the problems solved by the authors is the significant influence of forces of inertia applied to flexible bodies. This fact leads to increasing complexity of the governing equations due to their time-dependency and it should be considered whilst solving similar problems with thin-walled bars.

As FEM is discretization method, in most cases its result accuracy depends on the number of elements in specific model. For the vibration problem of thin-walled beam this drawback could be avoided by using dynamic stiffness method presented in [21]. The main idea of this method is to use frequency-dependent shape functions allowing to obtain vibration modes with a higher accuracy than with a classical way of approximation. In this paper it was shown that the curvature of thin-walled beam requires a denser finite element mesh, which makes dynamic stiffness method even more valuable for these kinds of problems.

In [22] mass matrix and stiffness matrix of thin-walled beam in non-shear theory were developed. In this work it was pointed out that FEM matrixes of vibrating rod do not consist of blocks corresponding to different types of deformation, in other words, bending and twisting problems of thin-walled beams are not independent and must be solved simultaneously.

One perspective theory of thin-walled beams of both open and closed cross-section is semi-shear Slivker's theory presented in [23]. The main idea of this theory is to split shear deformation on two groups: torsional and transverse (bending) shear. The last one is neglected just like in Euler-Bernoulli beam theory. Compared to non-shear Vlasov's one this theory has obvious advantage of improved accuracy achieved by shear accounting. Transverse shear neglecting in its turn simplifies governing equations considerably compared to other theories based on Timoshenko's beam model. The only drawback of this theory is more complicated process of sectorial properties calculation, which can be solved by using modern technical computing systems.

The first works devoted to Slivker's semi-shear theory combined with finite element method applied to structural mechanics were [24] and [25]. In this papers with the use of quadratic and linear approximations of twist angle and warping functions several stiffness matrixes of thin-walled beam elements were obtained. Presented numerical and analytical results could be applied for both open and closed cross-sections for rods with different boundary conditions. Moreover, the problem of finding internal forces in thin-walled beam under several types of load were solved in this works.

Fundamental research of all aspects of semi-shear theory in FEM implementation was presented in thesis [26]. The peculiarity of this work, among other things, is that it is supplied with the computer algorithm designed to solve static problems with thin-walled beams.

In work [27] constrained vibrations of thin walled-beams under impulse and short-term loads were discussed. The contact force parameters were determined by means of Hertz's theory, and derived integral equation is solved numerically by Euler's method. With the use of obtained results strength and stiffness of thin-walled beams under dynamic pressure could be determined.

Very important problem concerning thin-walled bars in FEM is connection between finite elements of different types. In [28] it was proposed to model the joints by classical shell elements, whereas the main parts of thin-walled bars are modeled by element with 7 degrees of freedom in each node.

Numerical analysis of spatial thin-walled bar system under torsional loads was carried out in [29, 30]. Specific properties of stiffness matrices of thin-walled rods with opened cross-section were shown and discussed. In addition, the influence of structural steel joints on warping of cross-section was examined.

The equations of motion in Timoshenko's, Vlasov's and Slivker's theories were obtained and compared with each other in work [31]. It was shown that semi-shear theory has an important property of revealing optical dispersion waves in thin-walled beams while the other two theories have only acoustic ones in corresponding spectrum. Optical part of frequencies comes from pure warping vibrations of thin-walled beam which do not show up when shear deformation is neglected. However, mass and stiffness matrixes obtained in this works have a good convergence only if quadratic and hyperbolic approximations are used.

Another work devoted to convergence problem of finite element models of thin-walled beams is [32]. In this article It was shown that linear approximation of both twist angle and warping functions gives a very poor convergence to analytical solutions. One way to improve convergence is to use a higher degree of approximation polynomial. Increasing finite elements mesh density could make numerical results more precise as well. However, this approach has a serious disadvantage of stiffness and mass matrixes enlargement leading to computational expenses. In addition, lack of accuracy problem when calculating stress values still remains.

A detailed review of analytical and numerical calculation methods for static, dynamic and stability problems of thin-walled beams was presented in [33]. Due to sufficient computational speed and simplicity of method implementation, FEM was proved to be one of the most perspective techniques for solving different thin-walled beam problems in structural mechanics. In addition, the mentioned article showed that semi-shear theory is the most versatile and mathematically straightforward theory among all the others.

The aim of this research is to construct a finite element model based on mixed variational formulation in order to improve convergence and provide an explicit way to calculate internal forces and stresses in thin-walled bar.

The main objectives of the research are:

1. Writing of the initial mixed functionals of thin-walled bar for static and dynamic problems within semi-shear theory.
2. Derivation of stiffness and mass matrixes with nodal forces vector for single finite element of thin-walled bar.
3. Assembly of global stiffness and mass matrixes with nodal forces vector. Construction of the governing equations of equilibrium and motion.
4. Solving of test static and dynamic problems by mixed FEM with comparison to classical method and analytical solution.

## 2. Methods

In order to obtain stiffness and mass matrixes based on mixed FEM we need write down Reissner-like functional (see [1]) for thin-walled beam taking into account shear deformation. For the sake of simplicity, we will consider only cross-sections with two symmetry axes. For static problems desired functional can be written as follows:

$$\Phi_{R,stat} = \int_L \left( \frac{M_x^2}{2GI_x} + \frac{B^2}{2EI_\omega} + \frac{M_\omega^2}{2GI_g} - M_x\theta' - B\beta' - M_\omega(\theta' - \beta) + m_x\theta + b_\omega\beta \right) dL, \quad (1)$$

here  $I_\omega$  is sectorial moment of inertia,  $\text{sm}^6$ ;

$I_x$  is pure torsional moment of inertia,  $\text{sm}^4$ ;

$I_g$  is constrained torsional moment of inertia,  $\text{sm}^4$  (see [26, 31]);

$E$  is elastic modulus, MPa;

$G$  is shear modulus, MPa;

$L$  is beam length, m;

$\theta$  is twist angle, rad;

$\beta$  is warping, rad/m;

$M_x$  is pure torque, N·m;

$M_\omega$  is constrained torque, N·m;

$B$  is bimoment, N·m<sup>2</sup>;

$m_x$  is distributed torque, N;

$b_\omega$  is distributed bimoment, N·m;

Similarly for the case of natural oscillations of thin-walled bar:

$$\Phi_{R,dyn} = \int_L \left( \frac{M_x^2}{2GI_x} + \frac{B^2}{2EI_\omega} + \frac{M_\omega^2}{2GI_g} - M_x \theta' - B \beta' - M_\omega (\theta' - \beta) + \frac{\rho \omega^2 I_r}{2} \theta^2 + \frac{\rho \omega^2 I_\omega}{2} \beta^2 \right) dL, \quad (2)$$

here  $\rho$  is material density, kg/m<sup>3</sup>;

$\omega$  is natural frequency, rad/s;

$I_r$  is polar moment of inertia, sm<sup>4</sup>;

In order to obtain stiffness and mass matrixes and force vector, one should define the shape functions for all the unknown values in functionals (1) and (2). From now on, we will use only linear approximation functions:

$$N_1(x) = \frac{x}{L}; \quad N_2(x) = 1 - \frac{x}{L}. \quad (3)$$

For each function  $f(x)$ :  $M_x(x)$ ,  $B(x)$ ,  $M_\omega(x)$ ,  $\theta(x)$ ,  $\beta(x)$  we can write:

$$f(x) = N_1(x) f_1 + N_2(x) f_2, \quad (3a)$$

here  $f_1, f_2$  are the values of function  $f(x)$  in the first and second node, respectively.

Substituting all the internal forces and displacements in (1) and (2) by their expressions in terms of shape functions and unknown nodal values (3a), we can use Hamilton's principle to obtain equations of equilibrium and motion. For convenience, we denote (4)–(7):

$$M = \begin{bmatrix} \frac{\rho L I_\omega}{3} & 0 & \frac{\rho L I_\omega}{6} & 0 \\ 0 & \frac{\rho L I_r}{3} & 0 & \frac{\rho L I_r}{6} \\ \frac{\rho L I_\omega}{6} & 0 & \frac{\rho L I_\omega}{3} & 0 \\ 0 & \frac{\rho L I_r}{6} & 0 & \frac{\rho L I_r}{3} \end{bmatrix}, \quad (4)$$

here  $M$  is mass matrix block;

$$F = \begin{bmatrix} \frac{L}{3EI_\omega} & 0 & 0 & \frac{L}{6EI_\omega} & 0 & 0 \\ 0 & \frac{L}{3GI_g} & 0 & 0 & \frac{L}{6GI_g} & 0 \\ 0 & 0 & \frac{L}{3GI_x} & 0 & 0 & \frac{L}{6GI_x} \\ \frac{L}{6EI_\omega} & 0 & 0 & \frac{L}{3EI_\omega} & 0 & 0 \\ 0 & \frac{L}{6GI_g} & 0 & 0 & \frac{L}{3GI_g} & 0 \\ 0 & 0 & \frac{L}{6GI_x} & 0 & 0 & \frac{L}{3GI_x} \end{bmatrix}, \quad (5)$$

here  $F$  is standard stiffness matrix block;

$$S = \begin{bmatrix} -\frac{1}{2} & 0 & \frac{1}{2} & 0 \\ -\frac{L}{3} & -\frac{1}{2} & -\frac{L}{6} & \frac{1}{2} \\ 0 & -\frac{1}{2} & 0 & \frac{1}{2} \\ -\frac{1}{2} & 0 & \frac{1}{2} & 0 \\ -\frac{L}{6} & -\frac{1}{2} & -\frac{L}{3} & \frac{1}{2} \\ 0 & -\frac{1}{2} & 0 & \frac{1}{2} \end{bmatrix}, \quad (6)$$

here  $S$  is mixed stiffness matrix block;

$$P = \begin{bmatrix} \frac{b_\omega L}{2} \\ \frac{m_x L}{2} \\ \frac{b_\omega L}{2} \\ \frac{m_x L}{2} \end{bmatrix}, \quad (7)$$

here  $P$  is nodal forces vector block;

Vector blocks of unknown nodal displacements and internal forces are denoted as follows (8)–(9):

$$W = \begin{bmatrix} \beta_1 \\ \theta_1 \\ \beta_2 \\ \theta_2 \end{bmatrix}, \quad (8)$$

here  $W$  is nodal displacements vector block;

$$V = \begin{bmatrix} B_1 \\ M_{\omega 1} \\ M_{x1} \\ B_2 \\ M_{\omega 2} \\ M_{x2} \end{bmatrix}, \quad (9)$$

here  $V$  is nodal internal forces vector block, index numbers 1 and 2 correspond to the first and second node of finite element, respectively;

With presented designations, functional (1) will look like:

$$\Phi_{R,stat} = \frac{1}{2} V^T FV - V^T SW + W^T P. \quad (9a)$$

Similarly, for expression (2):

$$\Phi_{R,dyn} = \frac{1}{2} V^T FV - V^T SW + \frac{1}{2} \omega^2 W^T MW. \quad (9b)$$

Hamilton's principle for functionals (9a) and (9b) can be written down as follows:

$$\frac{\partial \Phi_R}{\partial V} = 0; \quad \frac{\partial \Phi_R}{\partial W} = 0. \quad (9c)$$

Conditions (9c) yield the equations of equilibrium and motion of thin-walled bar. In case of static problem, governing system of linear equations will look like:

$$\begin{cases} S^T V = P, \\ -FV + SW = 0. \end{cases} \quad (10)$$

Likewise for natural vibrations of thin-walled bar:

$$\begin{cases} S^T V = \omega^2 MW, \\ -FV + SW = 0. \end{cases} \quad (11)$$

The first obtained system of equations can be written down in a more general way:

$$\begin{bmatrix} S^T & 0 \\ -F & S \end{bmatrix} \begin{bmatrix} V \\ W \end{bmatrix} = \begin{bmatrix} P \\ 0 \end{bmatrix}. \quad (12)$$

Corresponding matrix form of the second system of equations:

$$\left( \begin{bmatrix} S^T & 0 \\ -F & S \end{bmatrix} - \omega^2 \begin{bmatrix} 0 & M \\ 0 & 0 \end{bmatrix} \right) \begin{bmatrix} V \\ W \end{bmatrix} = \begin{bmatrix} 0 \\ 0 \end{bmatrix}. \quad (13)$$

Thereby, the governing systems of equations for static and dynamic problems of thin-walled beam were obtained.

Now we can introduce the vector of unknown values:

$$U_{element} = \begin{bmatrix} \beta_1 \\ \theta_1 \\ B_1 \\ M_{\omega 1} \\ M_{x1} \\ \beta_2 \\ \theta_2 \\ B_2 \\ M_{\omega 2} \\ M_{x2} \end{bmatrix}. \quad (14)$$

Corresponding stiffness matrix of thin-walled beam element will look like:

$$K_{element} = \begin{pmatrix} 0 & 0 & -\frac{1}{2} & -\frac{L}{3} & 0 & 0 & 0 & -\frac{1}{2} & -\frac{L}{6} & 0 \\ 0 & 0 & 0 & -\frac{1}{2} & -\frac{1}{2} & 0 & 0 & 0 & -\frac{1}{2} & -\frac{1}{2} \\ -\frac{1}{2} & 0 & \frac{-L}{3EI_{\omega}} & 0 & 0 & \frac{1}{2} & 0 & \frac{-L}{6EI_{\omega}} & 0 & 0 \\ -\frac{L}{3} & -\frac{1}{2} & 0 & \frac{-L}{3GI_g} & 0 & -\frac{L}{6} & \frac{1}{2} & 0 & \frac{-L}{6GI_g} & 0 \\ 0 & -\frac{1}{2} & 0 & 0 & \frac{-L}{3GI_x} & 0 & \frac{1}{2} & 0 & 0 & \frac{-L}{6GI_x} \\ 0 & 0 & \frac{1}{2} & -\frac{L}{6} & 0 & 0 & 0 & \frac{1}{2} & -\frac{L}{3} & 0 \\ 0 & 0 & 0 & \frac{1}{2} & \frac{1}{2} & 0 & 0 & 0 & \frac{1}{2} & \frac{1}{2} \\ -\frac{1}{2} & 0 & \frac{-L}{6EI_{\omega}} & 0 & 0 & \frac{1}{2} & 0 & \frac{-L}{3EI_{\omega}} & 0 & 0 \\ -\frac{L}{6} & -\frac{1}{2} & 0 & \frac{-L}{6GI_g} & 0 & -\frac{L}{3} & \frac{1}{2} & 0 & \frac{-L}{3GI_g} & 0 \\ 0 & -\frac{1}{2} & 0 & 0 & \frac{-L}{6GI_x} & 0 & \frac{1}{2} & 0 & 0 & \frac{-L}{3GI_x} \end{pmatrix}. \quad (15)$$

Similarly, the mass matrix of the element can be denoted as:

$$M_{element} = \begin{bmatrix} 0 & M \\ 0 & 0 \end{bmatrix}. \quad (15a)$$

Expressions (12) should be treated as a system of linear equations while (13) is classic eigenvalue problem.

In order to give formulas (12) and (13) more traditional FEM look we can do some mathematical transformations:

$$(S^T F^{-1} S)W = P, \quad (S^T F^{-1} S)W = \omega^2 M W. \quad (16)$$

We can denote:

$$K = (S^T F^{-1} S), \quad (17)$$

here  $K$  is shortened version of mixed stiffness matrix.

Therefore (16) will look like:

$$K W = P \quad (18)$$

and:

$$(K - \omega^2 M) W = 0. \quad (18a)$$

Expressions (18) and (18a) coincide with traditional FEM equations of linear statics and dynamics, but with stiffness matrix based on formula (17).

Obtained matrixes can be used to determine stress-strain state and natural frequencies of thin-walled beam with arbitrary boundary conditions and under any uniformly distributed load.

In order to get exact analytical solutions of static and dynamic problems we have to derive Euler equations using expressions (1) and (2).

In order to apply Hamilton's principle we need to calculate the following values for each function  $f(x)$ :  $M_x(x)$ ,  $B(x)$ ,  $M_\omega(x)$ ,  $\theta(x)$ ,  $\beta(x)$ :

$$\frac{\partial \Phi_R}{\partial f(x)} = 0. \quad (19)$$

For the static case expression (19) gives:

$$\begin{cases} M'_\omega + M'_x = -m_x, \\ B' + M_\omega = -b_\omega, \\ \frac{M_\omega}{G I_g} + \beta - \theta' = 0, \\ \frac{B}{E I_\omega} - \beta' = 0, \\ \frac{M_x}{G I_x} - \theta' = 0. \end{cases} \quad (19)$$

Similarly, for the case of natural vibrations:

$$\begin{cases} M'_\omega + M'_x = -\omega^2 \rho I_r \theta, \\ B' + M_\omega = -\omega^2 \rho I_\omega \beta, \\ \frac{M_\omega}{G I_g} + \beta - \theta' = 0, \\ \frac{B}{E I_\omega} - \beta' = 0, \\ \frac{M_x}{G I_x} - \theta' = 0. \end{cases} \quad (20)$$

Equations (19) and (20) will be used to obtain exact solutions of thin-walled beam problems in order to compare with numerical results.

### 3. Results and Discussion

Static analysis of thin-walled beam under uniformly distributed torque (Figure 1) will be carried out to examine accuracy of obtained equations (12).

The value of distributed torque  $m_x$  is 10 N·m.

Geometrical and mechanical characteristics of the beam are presented in Table 1:

**Table 1. Geometrical and mechanical properties of thin-walled beam.**

$E$ , Pa	$G$ , Pa	$I_x$ , m <sup>4</sup>	$I_\omega$ , m <sup>6</sup>	$A$ , m <sup>2</sup>	$L$ , m	$\rho$ , kg/m <sup>3</sup>	$I_r$ , m <sup>4</sup>	$I_g$ , m <sup>4</sup>
$2.06 \cdot 10^{11}$	$7.9 \cdot 10^{10}$	$1.11 \cdot 10^{-9}$	$1.48 \cdot 10^{-11}$	$3.51 \cdot 10^{-4}$	10.0	7850.0	$1.41 \cdot 10^{-7}$	$1.85 \cdot 10^{-7}$

Corresponding thin-walled cross-section is depicted on Figure 2.

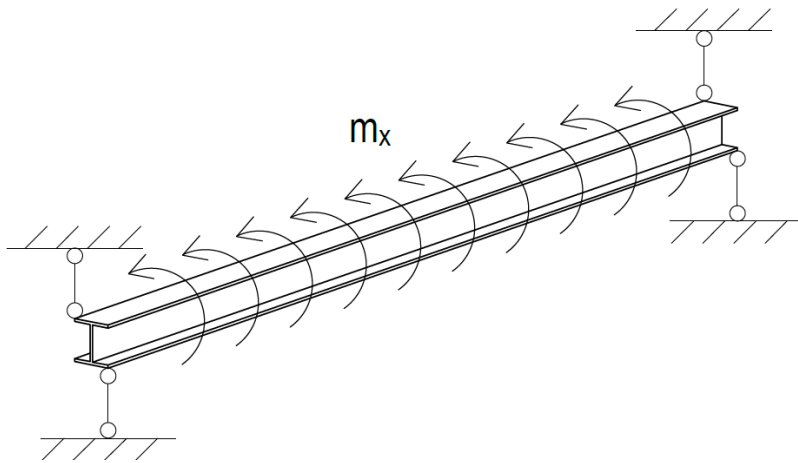


**Figure 1. Thin-walled beam under uniformly distributed torque.**

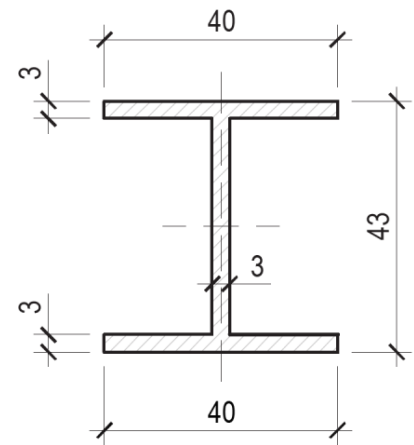


**Figure 2. Thin-walled cross-section (dimensions in cm).**

The exact analytical solution of equations (19) for the value of bimoment in cross-section of thin-walled beam with boundary conditions on Figure 1 can be written down as follows:

$$B_\omega(x) = \frac{m_x}{GI_x} \left[ \frac{ch\left(kx - \frac{kL}{2}\right)}{ch\left(\frac{kL}{2}\right)} - 1 \right] EI_\omega, \quad (21)$$

here

$$k = \sqrt{\frac{GI_x I_g}{(I_x + I_g) EI_\omega}}. \quad (22)$$

For example, we can calculate bimoment value in the middle of beam's span:

$$B_\omega\left(\frac{L}{2}\right) = \frac{m_x EI_\omega}{GI_x} \left[ \frac{1}{ch\left(\frac{kL}{2}\right)} - 1 \right]. \quad (23)$$

Substituting beam properties into (23) we can calculate bimoment, which equals 0.348 kN·m<sup>2</sup>

For the comparison of mixed and classical FEMs to be correct the finite element mesh of thin-walled beam must be chosen in the way that the number of unknown values for both methods approximately equaled to each other. For mixed FEM we have chosen 8 elements which corresponds to 45 unknown values, and for classical FEM – 21 elements (44 unknown values). The first method gives the value of bimoment 0.327 kN·m<sup>2</sup>, while the second one – 0.298 kN·m<sup>2</sup>.

It appears that mixed FEM has much more accurate results of internal force analysis of thin-walled beam compared to classical method. The relative errors can be calculated as follows:

$$\delta_{mixed} = \frac{B_{L/2}^{mixed} - B_{L/2}^{exact}}{B_{L/2}^{exact}} 100\% = \frac{0.327 - 0.348}{0.348} 100\% = -6.03\%,$$

$$\delta_{class} = \frac{B_{L/2}^{class} - B_{L/2}^{exact}}{B_{L/2}^{exact}} 100\% = \frac{0.298 - 0.348}{0.348} 100\% = -14.37\%.$$

here  $B_{L/2}^{mixed}$ ,  $B_{L/2}^{class}$ ,  $B_{L/2}^{exact}$  are bimoments calculated by mixed FEM, classical FEM and analytical formula (23), respectively.

Modal analysis of thin-walled beam depicted on Figure 3 will be carried out to examine convergence properties of (13).

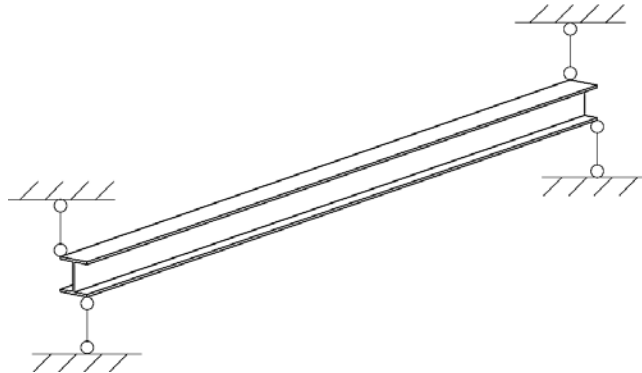


**Figure 3. Boundary conditions of thin-walled beam**

The exact analytical solution of equations (20) for the acoustic eigenfrequencies of thin-walled beam with boundary conditions on Figure 3 will look like:

$$\omega = \sqrt{\frac{\alpha_2 - \sqrt{\alpha_2^2 - 4\alpha_1\alpha_3}}{2\alpha_1}}, \quad (21)$$

here

$$\alpha_1 = \frac{\rho^2 I_r}{G I_g E}, \quad (22)$$

$$\alpha_2 = \frac{\rho \eta^2}{E} + \frac{\rho I_r \eta^2}{G I_g} + \frac{\rho I_r I_g}{(I_x + I_g) E I_\omega}, \quad (23)$$

$$\alpha_3 = \frac{G I_x I_g \eta^2}{(I_x + I_g) E I_\omega} + \eta^4, \quad (24)$$

$$\eta = \frac{\pi n}{L}, \quad n \in N. \quad (25)$$

Performing numerical calculations using expression (13) and matrixes (4)–(6) and (8)–(9) followed by determination of the exact solution for the first acoustic frequency by means of (21)–(25) we can draw Table 2:

**Table 2. Fundamental frequency by mixed FEM, classical FEM and analytical solution.**

Number of finite elements	2	4	8	16	32	64	128
Mixed FEM 1 <sup>st</sup> frequency, rad/s	291.01	135.84	94.81	89.57	88.60	88.47	88.47
Classical FEM 1 <sup>st</sup> frequency, rad/s	636.89	287.10	158.47	109.85	94.26	89.96	88.85
Exact 1 <sup>st</sup> frequency, rad/s				88.48			

Graphical visualization of the numerical results is presented on Figure 4.

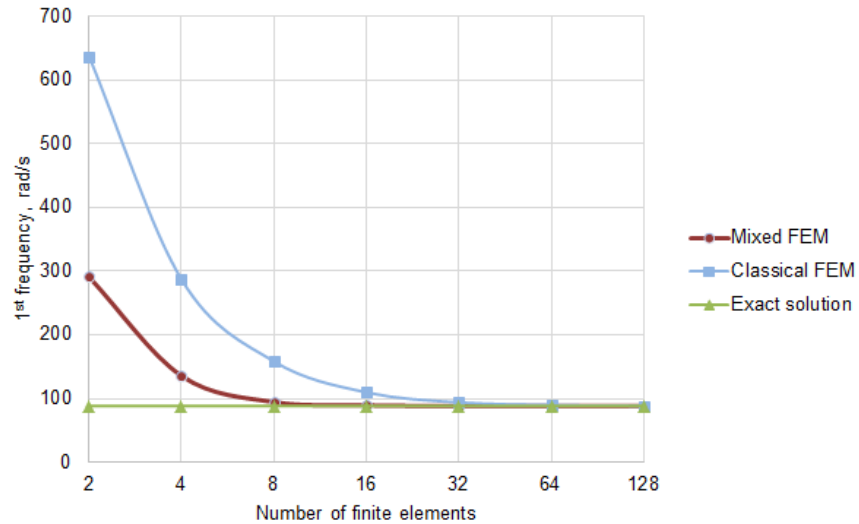


**Figure 4. Convergence of fundamental frequency by mixed and classical FEM to analytical solution.**

Table 2 and Figure 4 show that mixed FEM gives much more accurate value of the first eigenfrequency of thin-walled beam compared to classical FEM. For example, 16 finite elements produce only 1.23 % error:

$$\delta = \frac{\omega_1^{mixed} - \omega_1^{exact}}{\omega_1^{exact}} 100\% = \frac{89.57 - 88.48}{88.48} 100\% = 1.23\%.$$

While classical FEM with 16 elements gives 24.15 %:

$$\delta = \frac{\omega_1^{class} - \omega_1^{exact}}{\omega_1^{exact}} 100\% = \frac{109.85 - 88.48}{88.48} 100\% = 24.15\%,$$

here  $\omega_1^{mixed}$ ,  $\omega_1^{class}$ ,  $\omega_1^{exact}$  are fundamental frequencies calculated by mixed FEM, classical FEM and analytical formula (21), respectively.

Comparing these values to the results of work [31], where classical FEM with linear approximation and 32 finite elements has given an error of 23.3 % for similar eigenfrequency problem of thin-walled beam, we can see that developed mixed FEM model produces a much more precise outcome and has a better convergence.

The other important property of mixed FEM applied to dynamic problems of thin-walled beam is that the vibration modes include not only warping and twist angle functions, but internal torques and bimoment as well. The first mode shape of the examined beam with 16 finite elements is presented on Figures 5–9.

Besides the advantages of high accuracy of calculations and explicit output of internal forces, there is also one drawback concerning dynamic analysis of thin-walled beam using mixed FEM. If not only the fundamental mode shape is considered, the effect of “spurious” high frequencies in thin-walled beam spectrum occurs. In other words, the frequencies are not arranged in the ascending order if mixed FEM is used. For the examined beam with 16 finite elements, it appears that the third and seventh mode shapes are presented by high-frequency vibrations (Figures 10, 11).

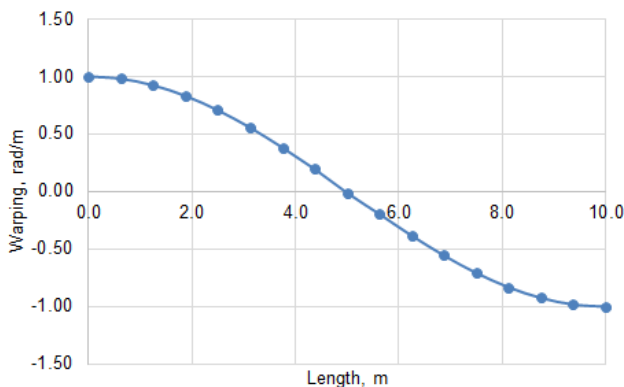


**Figure 5. The first warping mode of thin-walled beam.**

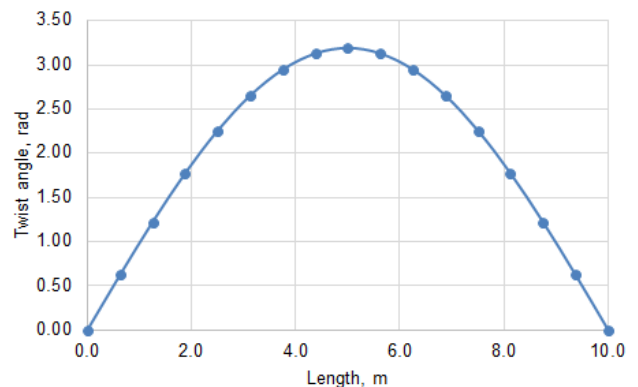


**Figure 6. The first twist angle mode of thin-walled beam.**

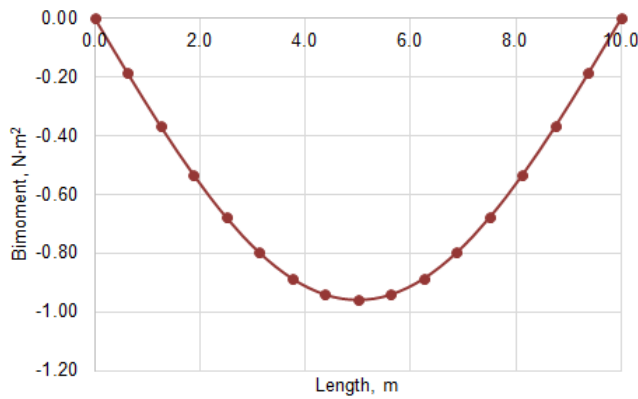


Figure 7. The first bimoment mode of thin-walled beam.

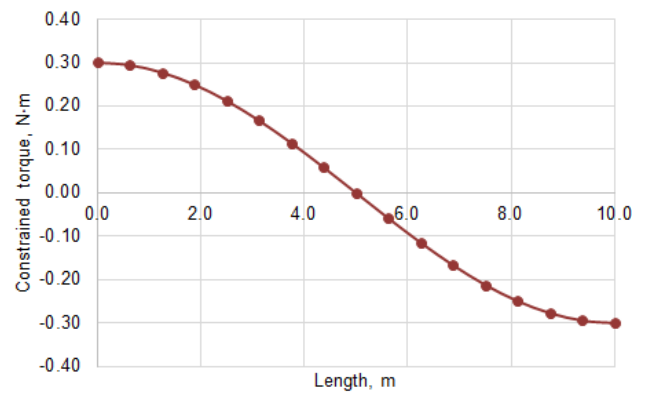


Figure 8. The first constrained torque mode of thin-walled beam.

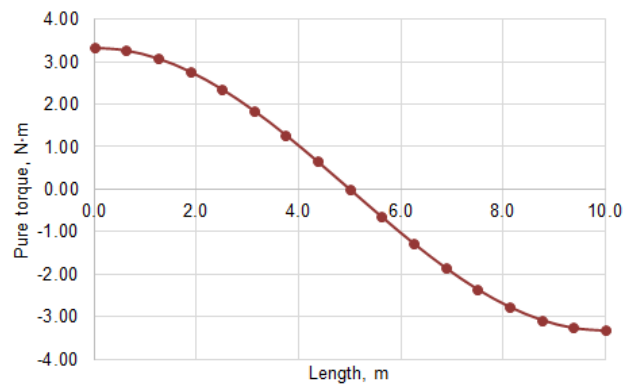


Figure 9. The first pure torque mode of thin-walled beam.

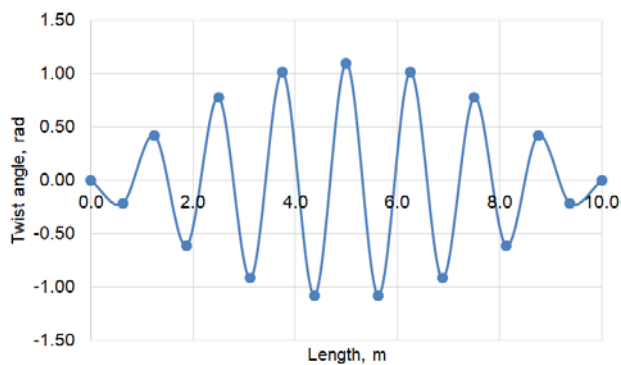


Figure 10. The 3<sup>rd</sup> twist angle mode of thin-walled beam.

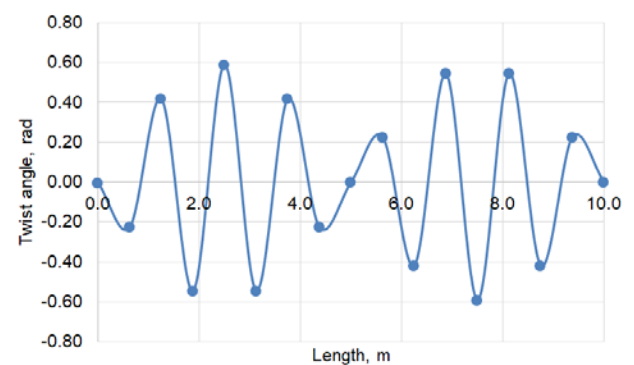


Figure 11. The 7<sup>th</sup> twist angle mode of thin-walled beam.

The presented effect can bring some difficulties in modal analysis of thin-walled beam as the “spurious” frequencies distort the spectrum, making it necessary to filter them out.

The observed problem could be easily solved in practical application by means of simple visual analysis of oscillation modes, since the “spurious” frequency can always be detected by many sign alterations of the corresponding mode.

It should be noted that the proposed model of thin-walled rod based on mixed formulation could be generalized for more complex spatial bar systems. Although, the matrix for transformation from local coordinate systems to the global one should in some way take into account the dependence between relative angle positions of rods and warping of cross-sections. At the present time, the problem of bimoment and warping “rotation” in nodal parts of thin-walled bar systems stays unresolved. This is very perspective scientific challenge and when some progress in this direction is achieved the results of the article could be applied to flat and spatial thin-walled bar systems.

## 4. Conclusions

Mixed variational formulation of static and dynamic problems of thin-walled bars has many advantages compared to classical approach. The main ones can be summarized as follows:

1. Mixed FEM gives more accurate results of stress analysis of thin-walled bar under static load. For example, the value of bimoment in the middle of the bar under uniform torque matches the analytical solution

with relative error of only 6.03 %, while classical FEM gives the tolerance of 14.37 %, whereas the number of unknown values is 45 and 44, respectively.

2. The internal forces evaluation proceeds simultaneously with the main operation of solving system of linear equations, which obviates the need to perform additional calculations.

3. Natural mode shapes and eigenfrequencies of thin-walled bar are determined with a higher accuracy, which allows to reduce the number of finite elements in the model. For example, the value of fundamental frequency of the examined bar with 16 finite elements matches the analytical solution with relative error of only 1.23 %, while classical FEM gives the tolerance of 24.15 %.

However, mixed FEM has a drawback of revealing “spurious” high-frequency vibration modes distorting spectrum of thin-walled beams.

## References

1. Reissner, E. On a variational theorem in elasticity. *J. Math. And Phys.* 1950. No. 29(2). Pp. 90–95.
2. Vlasov, V.Z. Thin-walled elastic beams. Israel Program for Scientific Translation. Jerusalem, 1961. 493 p.
3. Gabor, V. Free vibration of thin walled beams. *Mech. Eng.* 2004. No. 48(1). Pp. 99–110.
4. Chen, H.H., Hsiao, K.M. Quadruply coupled linear free vibrations of thin-walled beams with a generic open section. *Engineering Structures.* 2008. Vol. 30. No. 5. Pp. 1319–1334.
5. Kim, K.T. Free vibration of composite thin-walled beams with chordwise asymmetric closed cross-sections. *International Journal of Aerospace Engineering.* 2019. No. 10(1). Pp. 1–14.
6. Ambrosini, D. On free vibration of nonsymmetrical thin-walled beams. *Thin-Walled Structures.* 2009. Vol. 47. No. 7. Pp. 629–636.
7. Ren, Y., Cheng, W., Wang, Y., Wang, B. Analysis of flexural behavior of a simple supported thin beam under concentrated multiloading using trigonometric series method. *Thin-Walled Structures.* 2017. Vol. 120. Pp. 124–137.
8. Suryanarayan, S., Krishna Murty, A.V. Vibration of non-uniform thin-walled beams of arbitrary shape. *Zeitschrift für Angewandte Mathematik und Mechanik.* 1975. No. 55(3). Pp. 159–169.
9. Ambrosini, R.D., Riera, J.D., Danesi, R.F. Dynamic analysis of thin-walled and variable open section beams with shear flexibility. *International Journal for Numerical Methods in Engineering.* 1995. 38(17). Pp. 2867–2885.
10. Chefanova, E.V. *Dinamika tonkostennykh sterzhney pri deystvii udarnykh nagruzok [Dynamics of thin-walled rods under impact load].* PhD Thesis. Moscow, 2004. 129 p. (rus).
11. Tyukalov, Yu.Ya. Stress finite element models for determining the frequencies of free oscillations. *Magazine of Civil Engineering.* 2016. 67(7). Pp. 39–54. DOI: 10.5862/MCE.67.5.
12. Sergeev, O.A., Kiselev, V.G., Sergeeva, S.A. Optimal design of 3d frame structures taking into account the stress and multiple natural frequency constraints. *Magazine of Civil Engineering.* 2016. 61(1). Pp. 74–81. DOI: 10.5862/MCE.61.7.
13. Sukhoter, M.V., Baryshnikov, S.O., Knysh, T.P., Abdikarimov, R.A. Natural oscillations of a rectangular plates with two adjacent edges clamped. *Magazine of Civil Engineering.* 2018. 82(6). Pp. 81–94. DOI: 10.18720/MCE.82.8.
14. Mirsaidov, M.M., Abdikarimov, R.A., Vatin, N.I., Zhgutov, V.M., Khodzhaev, D.A., Normuminov, B.A. Nonlinear parametric oscillations of viscoelastic plate of variable thickness. *Magazine of Civil Engineering.* 2018. 82(6). Pp. 112–126. DOI: 10.18720/MCE.82.11.
15. Nesterova, O.P., Uzdin, A.M., Fedorova, M.Yu. Method for calculating strongly damped systems with non-proportional damping. *Magazine of Civil Engineering.* 2018. 81(5). Pp. 64–72. DOI: 10.18720/MCE.81.7.
16. Abdikarimov, R.A., Zhgutov, V.M. *Matematicheskiye modeli zadach nelineynoy dinamiki vyazkouprugikh ortotropnykh plastin i obolochek peremennoy tolshchiny [Mathematical models of nonlinear dynamics problems of viscoelastic orthotropic plates and shells of variable thickness].* *Magazine of Civil Engineering.* 2010. 16(6). Pp. 38–47. (rus).
17. Abdikarimov, R.A., Khodzhaev, D.A. Computer modelling of tasks in dynamics of viscoelastic thin-walled elements in structures of variable thickness. *Magazine of Civil Engineering.* 2014. 49(5). Pp. 83–94. DOI: 10.5862/MCE.49.9.
18. Taheri Fard, A.R., Taha, M.I., Hidayat, A. Evaluation of seismic analysis in diverse effect position of shear wall for reinforced concrete frame building. *Construction of Unique Buildings and Structures.* 2017. 62(11). Pp. 7–14. DOI: 10.18720/CUBS.62.1.
19. Belash, T.A., Rybakov, P.L. Buildings with suspended structures in seismic areas. *Magazine of Civil Engineering.* 2016. 65(5). Pp. 17–26. DOI: 10.5862/MCE.65.2.
20. Hashemi, E.S., Kheyroddin, A., Gerami, M. Probabilistic seismic assessment of concrete frame with mass irregularity. *Magazine of Civil Engineering.* 2018. 82(6). Pp. 49–59. DOI: 10.18720/MCE.82.5.
21. Leung, A.Y.T., Zhou, W.E. Dynamic stiffness analysis of curved thin-walled beams. *Shock and Vibration.* 1993. 1(1). Pp. 77–88.
22. Osokin, A.V. *Razvitiye metoda konechnykh elementov dlya rascheta sistem, vklyuchayushchikh tonkostennyye sterzhni otkrytogo profilya [Finite-element method development for calculation of systems with thin-walled rods of opened cross-section].* PhD Thesis. Moscow, 2010. 134 p. (rus).
23. Perelmuter, A.V., Slivker, V.I. *Handbook of mechanical stability in engineering (in 3 volumes): Vol. 1: General theorems and individual members of mechanical systems.* World Scientific Publishing Co. Singapore, 2013. 1656 p.
24. Lalin, V.V., Rybakov, V.A. The finite elements for design of building walling made of thin-walled beams. *Magazine of Civil Engineering.* 2011. 26(8). Pp. 69–80. DOI: 10.5862/MCE.26.11.
25. Lalin, V.V., Rybakov, V.A., Morozov, S.A. *The Finite Element Research for Calculation of Thin-Walled Bar Systems].* *Magazine of Civil Engineering.* 2012. 27(1). Pp. 53–73. DOI: 10.5862/MCE.27.7.
26. Rybakov, V.A. *Primeneniye polusdvigovoy teorii V.I. Slivkera dlya analiza napryazhenno-deformirovannogo sostoyaniya sistem tonkostennykh sterzhney [Application of semi-shear theory by V.I. Slivker for stress-strain analysis of systems with thin-walled rods].* PhD Thesis. Saint Petersburg, 2012. 184 p. (rus).
27. Aung, Z.L. *Povedeniye tonkostennykh sterzhney pri udarnykh nagruzkakh [Mechanical behavior of thin-walled rods under impact load].* PhD Thesis. Moscow, 2013. 117 p. (rus).
28. Chernov, S.A. *Modelirovaniye zadach dinamiki tonkostennoy sterzhnevoy sistemy [Modeling dynamic problems of thin-walled framework].* *Program products and systems.* 2014. 2(2). Pp. 171–176. (rus).

29. Tusnin, A.R. Chislennyy raschet konstruksiy iz tonkostennykh sterzhney otkrytogo profilya [Numerical calculation of opened thin-walled rod structures]. Moscow: ASV, 2009. 144 p. (rus).
30. Tusnin, A.R. Nesushchaya sposobnost dvutavrovoy balki pri deystvii krutyashchikh nagruzok [Bearing capacity of I-beam under torsional loads]. Construction and Specific Works in Civil Engineering. 2003. 2(2). Pp. 4–6. (rus).
31. Dyakov, S.F. Primeneniye polusdvigovoy teorii V.I. Slivkera k resheniyu zadach statiki i dinamiki tonkostennykh sterzhney [Application of semi-shear theory by V.I. Slivker to solve problems of statics and dynamics of thin-walled rods]. PhD Thesis. St. Petersburg, 2013. 147 p. (rus).
32. Rybakov, V.A., Dyakov, S.F., Sovetnikov, D.O., Azarov, A.A., Ivanov, S.S. Finite elements apparatus in thin-walled rods dynamics problems. MATEC Web of Conferences. 2018. Vol. 245. No. 08007. Pp. 1–8.
33. Sovetnikov, D., Azarov, A., Ivanov, S., Rybakov, V. Methods of calculation of thin-walled bars: statics, dynamics and stability. Alfabuild. 2018. 4(2). Pp. 7–33. (rus).

**Contacts:**

*Vladimir Lalin, +7(921)3199878; vllalin@yandex.ru*

*Vladimir Rybakov, +7(964)3312915; fishermanoff@mail.ru*

*Sergey Ivanov, +7(904)5567654; serzikserzik@gmail.com*

*Artur Azarov, +7(905)2705646; alexio009@mail.ru*

© Lalin, V.V., Rybakov, V.A., Ivanov, S.S., Azarov, A.A., 2019



DOI: 10.18720/MCE.89.7

## Смешанный метод конечных элементов в полусдвиговой теории тонкостенных стержней В.И. Сливкера

**В.В. Лалин, В.А. Рыбаков\*, С.С. Иванов, А.А. Азаров**

Санкт-Петербургский политехнический университет Петра Великого, Санкт-Петербург, Россия

\* E-mail: fishermanoff@mail.ru

**Ключевые слова:** смешанный метод конечных элементов, тонкостенный стержень, полусдвиговая теория Сливкера, функционал Рейсснера

**Аннотация.** Представлена вариационная постановка задач устойчивости тонкостенных стержней. Получена матрица геометрической жесткости конечного элемента на основе функционала устойчивости. С помощью полусдвиговой теории В.И. Сливкера произведен учет деформации сдвига в поперечном сечении тонкостенного стержня. В качестве аппроксимации искомых функций перемещений и внутренних усилий рассмотрены линейные полиномы Эрмита. Для некоторых частных задач тонкостенных стержней представлено точное аналитическое решение. Произведено численное сравнение результатов расчета методами конечных элементов. Аппроксимация квадратичными функциями оказывается быстрее в тех случаях, когда потеря устойчивости имеет изгибно-крутильную форму.

### Литература

1. Reissner E. On a variational theorem in elasticity // J. Math. And Phys. 1950. No. 29(2). Pp. 90–95.
2. Vlasov V.Z. Thin-walled elastic beams. Israel Program for Scientific Translation. Jerusalem, 1961. 493 p.
3. Gabor V. Free vibration of thin walled beams // Mech. Eng. 2004. No. 48(1). Pp. 99–110.
4. Chen H.H., Hsiao K.M. Quadruply coupled linear free vibrations of thin-walled beams with a generic open section // Engineering Structures. 2008. Vol. 30. No. 5. Pp. 1319–1334.
5. Kim K.T. Free vibration of composite thin-walled beams with chordwise asymmetric closed cross-sections // International Journal of Aerospace Engineering. 2019. No. 10(1). Pp. 1–14.
6. Ambrosini D. On free vibration of nonsymmetrical thin-walled beams // Thin-Walled Structures. 2009. Vol. 47. No. 7. Pp. 629–636.
7. Ren Y., Cheng W., Wang Y., Wang B. Analysis of flexural behavior of a simple supported thin beam under concentrated multiloading using trigonometric series method // Thin-Walled Structures. 2017. Vol. 120. Pp. 124–137.
8. Suryanarayan S., Krishna Murty A.V. Vibration of non-uniform thin-walled beams of arbitrary shape // Zeitschrift für Angewandte Mathematik und Mechanik. 1975. No. 55(3). Pp. 159–169.
9. Ambrosini R.D., Riera J.D., Danesi R.F. Dynamic analysis of thin-walled and variable open section beams with shear flexibility // International Journal for Numerical Methods in Engineering. 1995. 38(17). Pp. 2867–2885.
10. Чефанова Е.В. Динамика тонкостенных стержней при действии ударных нагрузок: дис. ... канд. техн. наук. М., 2004. 129 с.
11. Тюкалов Ю.Я. Определение частот свободных колебаний методом конечных элементов в напряжениях // Инженерно-строительный журнал. 2016. № 7(67). С. 39–54.
12. Сергеев О.А., Киселев В.Г., Сергеева С.А. Оптимальное проектирование рам с учетом ограничений по прочности и кратным частотам собственных колебаний // Инженерно-строительный журнал. 2016. № 1(61). С. 74–81.
13. Сухотерин М.В., Барышников С.О., Кныш Т.П., Абдикаримов Р.А. Собственные колебания прямоугольной пластины, защемленной по двум смежным краям // Инженерно-строительный журнал. 2018. № 6(82). С. 81–94.
14. Мирсаидов М.М., Абдикаримов Р.А., Ватин Н.И., Жгутов В.М., Ходжаев Д.А., Нормуминов Б.А. Нелинейные параметрические колебания вязкоупругой пластинки переменной толщины // Инженерно-строительный журнал. 2018. № 6(82). С. 112–126.
15. Нестерова О.П., Уздин А.М., Федорова М.Ю. Метод расчета сильно демпфированных систем с непропорциональным демпфированием // Инженерно-строительный журнал. 2018. № 5(81). С. 64–72.
16. Абдикаримов Р.А., Жгутов В.М. Математические модели задач нелинейной динамики вязкоупругих ортотропных пластин и оболочек переменной толщины // Инженерно-строительный журнал. 2010. № 6(16). С. 38–47.
17. Абдикаримов Р.А., Ходжаев Д.А. Компьютерное моделирование задач динамики вязкоупругих тонкостенных элементов конструкций переменной толщины // Инженерно-строительный журнал. 2014. № 5(49). С. 83–94.
18. Тахери Фард А.Р., Таха М.И., Хидаят А. Оценка сейсмического анализа в различных положениях воздействия сдвиговой стенки для железобетонного каркасного здания // Строительство уникальных зданий и сооружений. 2017. № 11(62). С. 7–14.
19. Белаш Т.А., Рыбаков П.Л. Здания с подвесными конструкциями в сейсмических районах // Инженерно-строительный журнал. 2016. № 5(65). С. 17–26.

20. Хашеми Е.С., Хайруддин А., Герами М. Конструктивно-технологические решения при регулировании стока атмосферных осадков // Инженерно-строительный журнал. 2018. № 6(82). С. 49–59.
21. Leung A.Y.T., Zhou W.E. Dynamic stiffness analysis of curved thin-walled beams // Shock and Vibration. 1993. No. 1(1). Pp. 77–88.
22. Осокин А.В. Развитие метода конечных элементов для расчета систем, включающих тонкостенные стержни открытого профиля: дис. ... канд. техн. наук. М., 2010. 134 с.
23. Perelmuter A.V., Slivker V.I. Handbook of mechanical stability in engineering (in 3 volumes): Vol. 1: General theorems and individual members of mechanical systems. World Scientific Publishing Co. Singapore, 2013. 1656 p.
24. Лалин В.В., Рыбаков В.А. Конечные элементы для расчета ограждающих конструкций из тонкостенных профилей // Инженерно-строительный журнал. 2011. № 8(26). С. 69–80.
25. Лалин В.В., Рыбаков В.А., Морозов С.А. Исследование конечных элементов для расчета тонкостенных стержневых систем // Инженерно-строительный журнал. 2012. № 1(27). С. 53–73.
26. Рыбаков В.А. Применение полусдвиговой теории В.И. Сливкера для анализа напряженно-деформированного состояния систем тонкостенных стержней: дис. ... канд. техн. наук. СПб., 2012. 184 с.
27. Аунг З.Л. Поведение тонкостенных стержней при ударных нагрузках: дис. ... канд. техн. наук. М., 2013. 117 с.
28. Чернов С.А. Моделирование задач динамики тонкостенной стержневой системы // Программные продукты и системы. 2014. № 2(2). С. 171–176.
29. Туснин А.Р. Численный расчёт конструкций из тонкостенных стержней открытого профиля. М.: Изд-во АСВ, 2009. 144 с.
30. Туснин А.Р. Несущая способность двутавровой балки при действии крутящих нагрузок // Монтажные и специальные работы в строительстве. 2003. № 2(2). С. 4–6.
31. Дьяков С.Ф. Применение полусдвиговой теории В.И. Сливкера к решению задач статики и динамики тонкостенных стержней: дис. ... канд. техн. наук. СПб., 2013. 147 с.
32. Rybakov V.A., Dyakov S.F., Sovetnikov D.O., Azarov A.A., Ivanov S.S. Finite elements apparatus in thin-walled rods dynamics problems // MATEC Web of Conferences. 2018. Vol. 245. No. 08007. Pp. 1–8.
33. Советников Д.О., Азаров А.А., Иванов С.С., Рыбаков В.А. Методы расчета тонкостенных стержней: статика, динамика, устойчивость // Alfabuild. 2018. № 2(4). С. 7–33.

**Контактные данные:**

*Владимир Владимирович Лалин, +7(921)3199878; эл. почта: vllalin@yandex.ru*

*Владимир Александрович Рыбаков, +7(964)3312915; эл. почта: fishermanoff@mail.ru*

*Сергей Сергеевич Иванов, +7(904)5567654; эл. почта: serzikserzik@gmail.com*

*Артур Александрович Азаров, +7(905)2705646; эл. почта: alexio009@mail.ru*

© Лалин В.В., Рыбаков В.А., Иванов С.С., Азаров А.А., 2019



DOI: 10.18720/MCE.89.8

## Strengthening of RC beams by ferrocement made with unconventional concrete

M.J. Miah<sup>a\*</sup>, M.S. Miah<sup>b</sup>, W.B. Alam<sup>c</sup>, F. Lo Monte<sup>d</sup>, Y. Li<sup>e</sup>

<sup>a</sup> University of Asia Pacific, Dhaka, Bangladesh

<sup>b</sup> Technische Universität Dresden — TU Dresden, Dresden, Germany

<sup>c</sup> University of Asia Pacific, Dhaka, Bangladesh

<sup>d</sup> Politecnico di Milano, Milano MI, Italy

<sup>e</sup> Nanyang Technological University, Singapore

\* E-mail: [jihad.miah@uap-bd.edu](mailto:jihad.miah@uap-bd.edu)

**Keywords:** unconventional concrete, bending, shear, ferrocement, retrofitting, deflection

**Abstract.** Some countries in South Asia has very limited availability of natural stones due to geological features, therefore, most of the concrete buildings of the past are made with burnt clay brick aggregates whose strength is rather low those are more vulnerable to collapse due to any extreme loads. However, ferrocement strengthening has several advantages such as good mechanical performance, cost-effectiveness, locally availability of the materials, and simplicity, this latter making available workmanship able to implement such technique (aspect which is very important in developing countries such as Bangladesh). Hence, the paper deals with the efficacy of ferrocement technique in improving the performance of reinforced concrete beams made in low-strength concrete (beam width 230 mm, height 230 mm, and length 2135 mm). The beams are made with unconventional concrete whose strength is about 12.5–13.0 MPa. The flexural tests are performed experimentally and numerically via the finite element software ABAQUS by considering the following loading configurations: (i) 2 point loads placed at L/3, (ii) 2 point loads are to the support, (iii) 2 point loads close to the mid-span, and (iv) 1 load next to the support and 1 load on the mid-span. The experimental results have shown that unsymmetrical loading decreases the overall load carrying capacity and increases the deformability due to the localization of the damage. The ferrocement beams reinforced by steel wire mesh exhibits high ultimate load carrying capacity and more ductile behavior. The outcome of this research can be used for future modeling and for the development of appropriate design guidelines on the strengthening of concrete structures dealing with different loading conditions.

### 1. Introduction

Structures very often struggle with extreme static and dynamic actions during their service life, this leading to increasing damage with time, depending on the load level and on the loading layout (compression or tension, shear or bending, etc.). Hence, different caution should be considered depending on the bearing element, namely columns, beams, arches, ceilings, due to the different stress state. In the particular case of beams, the mechanical behavior is generally driven by bending, with a more or less pronounced influence of shear action, this making the load-deflection ( $P - \Delta$ ) relationship a powerful tool to investigate their overall performance. Within this context, an open issue is represented by unconventional concrete (i.e., very low strength concrete made with burnt clay brick aggregate), widely used in several countries in South Asia, and not properly addressed in most of the design codes, even though they cover the design details for normal concrete.

Typically, beams' behavior is critical in the case of concentrated loads, due to the high stresses induced by shear in the disturbed zone, because of the interaction among global mechanisms and local strut-and-tie systems. The cracking patterns and the damage strongly depend on the loading configurations, influencing the flexural stiffness and, consequently, the deflection characteristics. For instance, concentrated loads on

---

Miah, M.J., Miah, M.S., Alam, W.B., Lo Monte, F., Li, Y. Strengthening of RC beams by ferrocement made with unconventional concrete. Magazine of Civil Engineering, 2019. 89(5). Pp. 94–105. DOI: 10.18720/MCE.89.8

Миах, М.Д., Миах М.С., Алам В.Б., Ло Монте Ф., Ли Й. Усиление железобетонных балок ферроцементом // Инженерно-строительный журнал. 2019. № 5(89). С. 94–105. DOI: 10.18720/MCE.89.8.



This open access article is licensed under CC BY 4.0 (<https://creativecommons.org/licenses/by/4.0/>)

beam may locally affect the shear or moment capacity of the beam and as a result damages or sudden collapse may occur leading to catastrophic losses, this being even more evident in the case of construction materials with low quality. In many developing countries such as Bangladesh, many structures have constructed with poor construction materials and unconventional concrete. Due to the aforementioned issue, retrofitting such structures is unavoidable. Since retrofitting solutions should represent a good compromise between effectiveness and cost, this study addresses the application to low strength concrete (LSC) structures of economical (no sophisticated technology is needed) retrofitting based on the use of ferrocement.

In existing literature, just a few works including retrofitting with LSC can be found, focusing on the effect of the type of loading (related to shear and bending stress concentration). Damage pattern as a function of load configuration is reported in [1]. Several works describe the finite element analysis and also the modeling technique for considering moving loads induced by wheels and lateral load distribution in I-girders of highway bridges [2, 3]. A simplified method for evaluating load carrying capacity of structure subjected to concentrated impact load with increasing loading rate has been implemented to evaluate the load carrying capacity of RC beams with reduced effective length [4].

Results from the literature addressing the flexural characteristics of T-beams and rectangular beams retrofitted with ferrocement at the tension side showed a significant improvement of the structural performance, with a delay of the first crack formation and an increase of the overall flexural stiffness [5, 6]. By using high-performance ferrocement strengthened with U-shaped steel mesh increases the flexural capacity of beams reducing the crack formation [7]. The bending performance of retrofitted RC beams have studied by using wire mesh-epoxy composite in [8], while an experimental investigation of strengthened RC beams with FRP strips and special resins is reported in [9]. Another method for enhancing the flexural capacity is to use layers of externally bonded wire mesh by using epoxy. In addition, cracking behavior and energy absorption capacity also increases [10]. Furthermore, to reduce the weight of the retrofitting system, investigations on the use of foamed blast furnace slag to replace sand in ferrocement is also conducted [11].

In order to enhance the shear strength, the use of wire mesh in web and flange region increases the shear capacity while limiting crack opening [12]. In addition, vertical and inclined plates using glass fiber reinforced or carbon fiber reinforced polymers (GFRP or CFRP, respectively), Kevlar fiber-reinforced plastic (KFRP) and steel plate have been previously investigated in several research works, showing benefits in shear behavior [13–16]. In a recent study, the behavior of square columns with ferrocement jacket shows an improvement in ductility under cyclic and axial loading [17, 18]. RC slabs and masonry walls retrofitted with ferrocement also showed improved behavior under different types of loading [19, 20]. In a previous study [21], ferrocement retrofitting proved to be rather economical and effective to enhance the performance of partially damaged flat-slab type structures. Additionally, the ferrocement is used to enhance the shear bond performance and excellent outcome has reported in [22]. In [23] the authors studied the shear behavior of beam by performing test experimentally and numerically. Further, bending behavior of ferrocement beams with lightweight cores and different types of mesh reinforcement have been investigated and authors reported that the ferrocement can be used for low cost structures. The superior performances of ferrocement beams have reported under flexural loadings in [25]. The ferrocement jacketing with diagonal reinforcements has been used to improve the structural behavior of internal joints in [26].

In order to better understand the experimental results, numerical simulations are essential, so to generalize the specific results obtained. Numerical study on the deflection behavior of retrofitted beams with Wire Mesh-Polyurethane Cement (WM-PUC), composite and near-surface-mounted (NSM) and fiber-reinforced polymer (FRP), namely NSM-FRP rods, show a good agreement with the experimental results [27, 28]. Similarly, finite element analysis on retrofitted beams with CFRP and FRP have also been conducted to monitor  $P - \Delta$  behavior, crack pattern, and failure mode [29, 30]. Concrete with polymer composite reinforcement (FRP) instead of steel one proved the benefits of FRP when existing gap minimization between the bars is crucial [31]. The use of multilayered glass fiber to enhance the shear capacity performance of short beam is studied in [32]. The main motivation behind this research is that just a few published researches focus on LSC. Hence, this research project has been launched to investigate the behavior of unretrofitted and retrofitted beams made with unconventional concrete (i.e., LSC).

The rest of the article is organized as follows: Section 2 describes the experimental method, including material properties, specimen detail, and test procedure. Section 3 presents the numerical investigations, including the modeling detail. Section 4 reports comparisons and discussion of the results. Finally, Section 5 includes a summary of the outcome of the study and future perspectives.

## 2. Experimental Method

### 2.1. Material properties

The first class burnt clay bricks (commonly used in Bangladesh) are used as coarse aggregates, while natural river sand (locally called Sylhet sand) passing a No. 4 sieve (4.75 mm), clean and free of any deleterious substance, and of fineness modulus and specific gravity 3.1 and 2.56, respectively is used as fine aggregate. The maximum and minimum size of coarse aggregates are 20 mm and 5 mm respectively and the grading of the coarse aggregates is controlled as reported in ASTM C33 [33]. The volumetric mix ratio (commonly practiced mix design in Bangladesh) of 1:2:4 (cement: fine aggregate: coarse aggregate) and water to cement ratio (by weight) of 0.45 are used for the concrete mix. Cement CEM II/B-M is used as a binder, with 65–79 % clinker and 21–35 % mineral admixture (fly ash and slag) including gypsum. In order to evaluate concrete compressive strength, cylindrical specimens ( $D \times L = 100 \times 200$  mm) are cast and demolded after 24 hours. Afterward, all concrete specimens are cured underwater ( $20 \pm 2$  °C) up to the day of the beam specimens tests (i.e., 28 days). Compressive tests are performed at 28 days according to ASTM C39 [34] by using a Universal Testing Machine (UTM). Deformation of the specimen is measured by means of two dial gauges to investigate the stress-strain law. The average compressive strength of concrete of four batches are, respectively, 12.3, 12.8, 13.0, and 13.3 MPa (average value of 12.9 MPa with a normalized standard deviation of 3.3 %).

### 2.2. Preparation of Specimens

#### 2.2.1 Preparation of Un-Retrofitted Beam Specimens

Four beams ( $230 \times 230 \times 2135$  mm) are cast to evaluate the flexural performances under four different loading conditions: (i) Reference, (ii) Combined, (iii) Shear, and (iv) Bending conditions. Reference, Combined, and Shear beams are provided with 2  $\varnothing$  16 mm mild steel bars as tension reinforcements at the bottom face, while Bending beam is fitted with 3  $\varnothing$  16 mm. In the upper face (compression zone), 2  $\varnothing$  16 mm bars are used for all the beams. Shear reinforcement consists of 10 mm bars @ 127 mm c/c (center to center). The reinforcements have the yield stress of 400 MPa and elastic modulus of 200 GPa. Detailing of reinforcement arrangements are shown in Figure 1. The clear cover for the reinforcements is 40 mm for all the beams. The flexural tests are carried out after 28 days of curing.

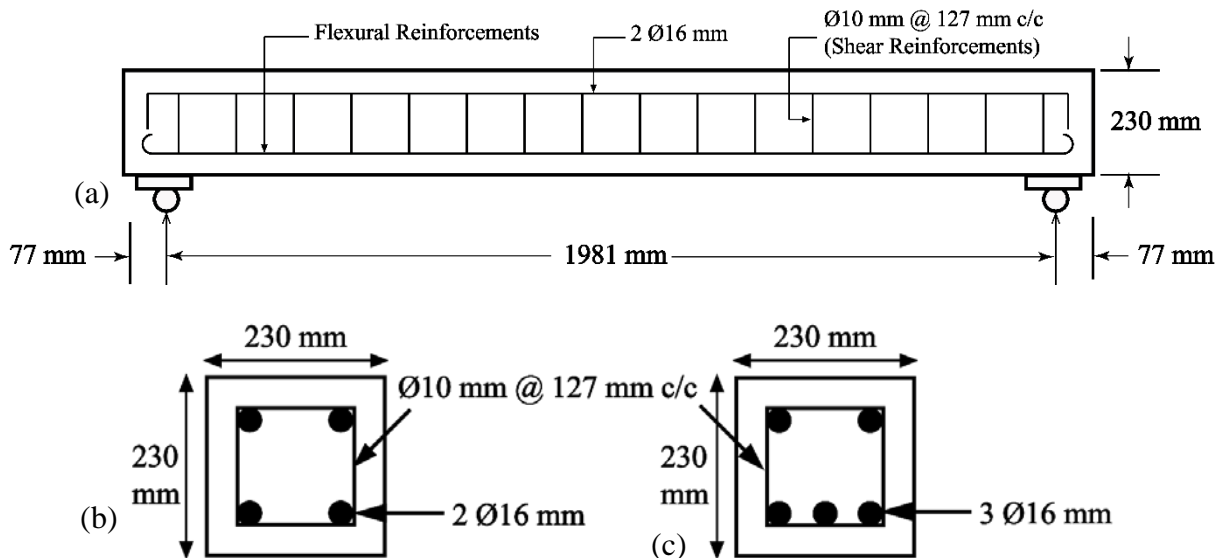


**Figure 1. Reinforcement detailing of beams: (a) longitudinal view; (b) cross-section of Reference case (URRC), Combined case (URCC), and Shear case (URSC); (c) cross-section of Bending case (URBC) respectively.**

#### 2.2.2 Preparation of Retrofitted Beam Specimens

Before retrofitting, one specimen of each case is first preloaded until both flexural and diagonal major cracks appear (Figure 2a). The loads that induced the major cracks are, respectively, 82.25 kN for Reference case, 59.05 kN for Combined case, 52.42 kN for Shear case, and 62.36 kN for Bending case. Preloading is conducted via a Universal Testing Machine (UTM) with a load capacity of 1000 kN. Afterward, damaged parts are removed by using chipping hammers. Great attention needs to be paid to not damaging the reinforcing bars. The surface is then cleaned to remove the dust using a brush and a vacuum cleaner for a better bond between the original concrete surface and the retrofitting layer. For retrofitting, square welded wire steel mesh (opening of 4 mm) available in local markets is used as reinforcing mesh (Figure 2b). In order to provide confinement, the beams are wrapped with a single layer of steel wire mesh around the beam surface. The average thickness of the ferrocement mortar is about 25 mm.



**Figure 2. Retrofitting via ferrocement technique: (a) partially damaged beam, (b) the wire-mesh around the partially damaged beam, and (c) retrofitted beam before the flexural test.**

The mortar for ferrocement is made with locally available ordinary Portland composite cement (CEM type II/B-M), natural river sand (Sylhet sand) with fineness modulus and specific gravity 3.1 and 2.56 respectively, and water. Sand to cement ratio by weight of 2 and water to cement ratio of 0.45 are used for the mortar mix. 25 mm thick mortar is poured around the beam specimens by hand plastering. During pouring, the mortar has forced through the steel wire mesh in order to avoid the formation of voids and to ensure good bond among mortar, wire mesh, and original concrete beam surface. Finally, the beams are covered with double layer wet burlap in the laboratory temperature of  $20 \pm 2$  °C in order to avoid evaporation of water from mortar and to continue hydration of cement so to guarantee better strength. After 28 days from the application of ferrocement, the beams are painted using white paint and grids are signed so that crack patterns could be easily observed during the testing process (Figure 2c). The flexural tests are performed after 28 days of curing.

### 2.2.3. Instrumentation and test setup

Four beams are cast to evaluate the flexural and shear performance of un-retrofitted and retrofitted beams under four different loading conditions. Beams are subjected to four-point incremental static loads with different positions of the loading points: (i) 2 point loads placed at  $L/3$  interval (Reference case), (ii) 2 point loads close to the support (Shear case), (iii) 2 point loads close to the mid-span (Bending case), and (iv) 1 load next to the support and 1 load on the mid-span (Combined case). More specifically, the Reference case, designated as URRC/WRRC (un-retrofitted/retrofitted Reference Case) is subjected to a uniformly spaced concentrated loads (660 mm). For the combined effect, designated with URCC/WRCC (un-retrofitted/retrofitted Combined Case), 1 load is applied at the mid-span and the other one at 305 mm from the support, so to have high bending and shear on the loaded zone. In order to observe the behavior under shear effect (URSC/WRSC, Shear Case), loads are placed at 305 mm from the support and at 530 mm from the first load (this distance has chosen due to the limitation of test setup dimension in the lab), so generating high shear concentration. Finally, in URBC/WRBC (Bending Case), both point loads are placed across mid-span at 305 mm apart from each other. Figure 3 illustrates the loading schemes.

In order to monitor the deformation, three dial gauges with an accuracy of  $10 \mu\text{m}$  are placed under the concrete beams in the steel loading frame (Figure 4). Gauge 2 is positioned at mid-span of the beam, while Gauge 1 and Gauge 3 are placed at 305 mm aside of Gauge 2. For the un-retrofitted beam tests, the beams are first loaded until major flexural and diagonal cracks appear. On the other hand, for the retrofitted beam tests, load is increased until

complete failure of the specimen. Propagation of cracks throughout the sides of the specimens are marked with black marker on the beams. Additionally, the failure patterns of the beams are also recorded.

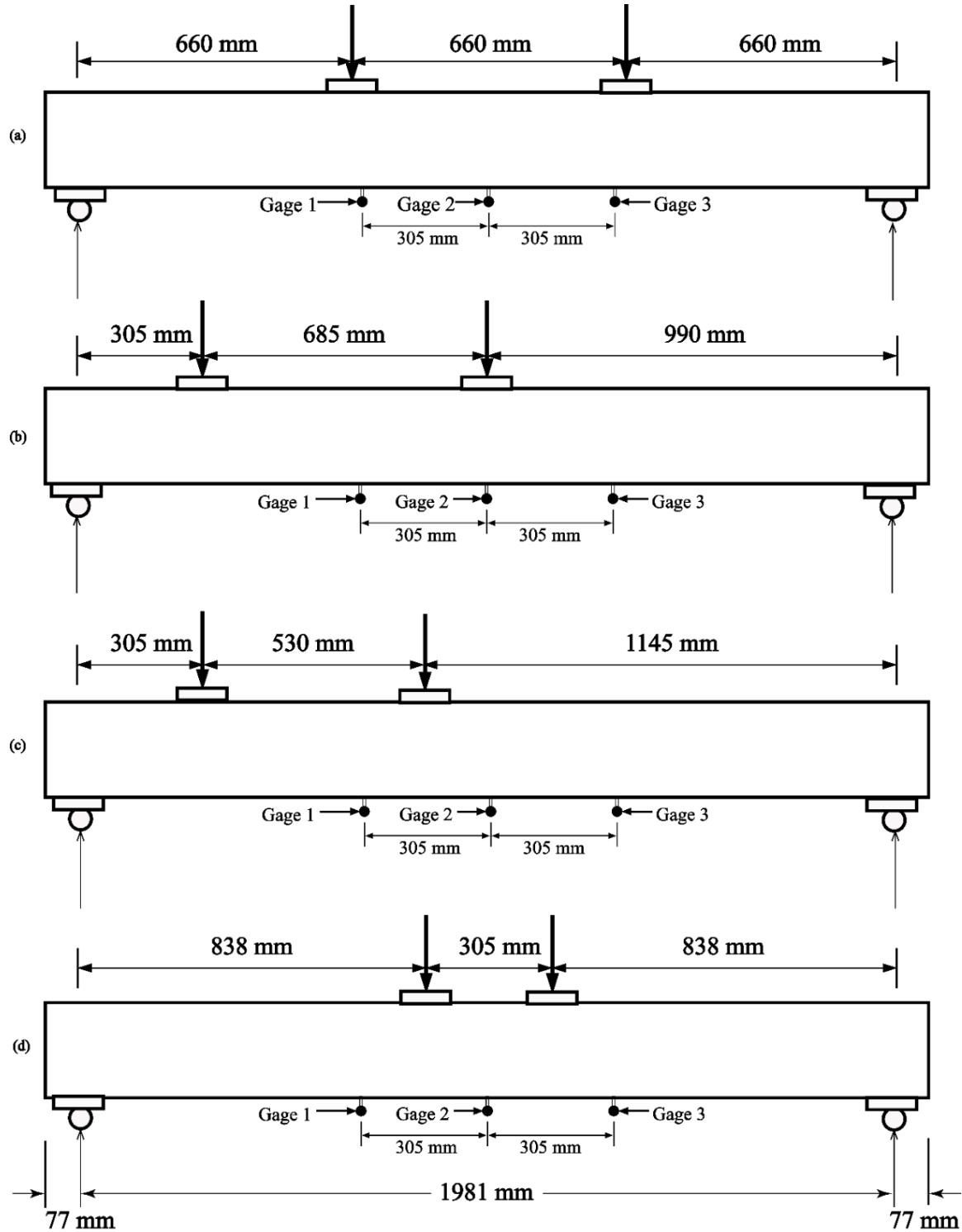


Figure 3. Schematic diagram of loading and gauge positions of the beams: (a) Reference case, (b) Combined case, (c) Shear case, and (d) Bending case respectively.



Figure 4. Beam test setup (left) and position of the dial gauges placed at steel loading frame (right).

### 3. Numerical Investigations

In order to better understand the experimental results, a three-dimensional nonlinear finite element model has been implemented to simulate the tests. The commercial software ABAQUS/Standard is used. All tests of un-retrofitted and retrofitted beams are presented in the followings.

#### 3.1. Geometry and Element Types

Three-dimensional solid elements are adopted with a mesh size of 15 mm for both concrete and steel rebar depicted in Figure 5. The outer ferrocement layer is modeled as three-dimensional solid element and the wire mesh is herein embedded. Supports and loading points are modeled using a discrete rigid restraint, since the relative positions of the nodes involved remain constant throughout the simulation [35].

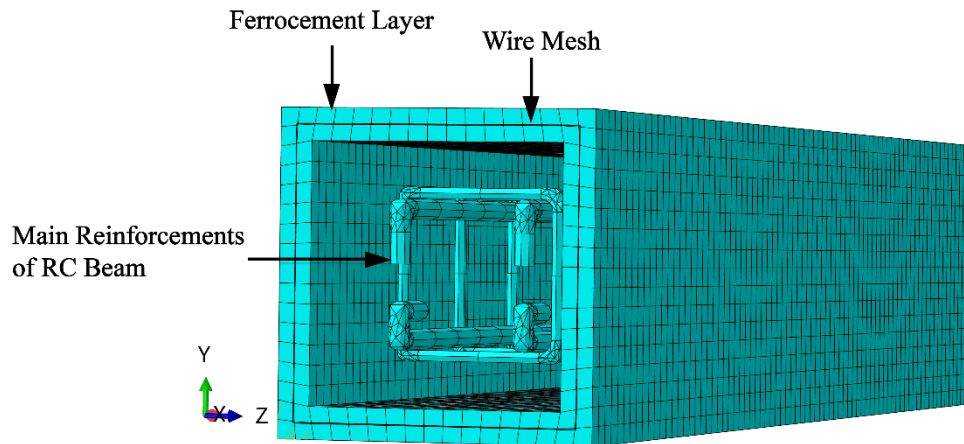


Figure 5. Numerical model in ABAQUS with the details of the retrofitted beam with embedded wire mesh inside the ferrocement layer.

#### 3.2. Material Modeling

Concrete Damaged Plasticity model for concrete is implemented in ABAQUS and the Standard analysis is performed. The aforementioned model describes the unrecoverable stiffness reduction due to cracking processes. Concrete strength values are obtained from laboratory tests (average  $f'_{c(28\text{ days})} = 12.9$  MPa). The behavior of the wire mesh is specified by an elastic-perfect plastic stress-strain model. For reinforcements, elastic modulus,  $E_s = 200$  GPa and yield stress,  $f_y = 400$  MPa are adopted. The Poisson's ratio for concrete and reinforcements are 0.2 and 0.3, respectively.

#### 3.3. Bond between Ferrocement Layer and Concrete Surface

To define the bond between ferrocement layer and concrete surface, a tie constraint (namely perfect bond) has been implemented for the whole simulation period. The wire mesh and the main reinforcements are bonded with an embedded constraint in the host region (mortar layer and concrete, respectively). In embedded constraint, the transitional Degree Of Freedoms (DOFs) of the embedded nodes become constrained to the interpolated value of the corresponding DOFs of the host element [28]. Perfect bond between concrete and steel is adopted, since reinforcement-to-concrete bond failure has not been observed experimentally.

#### 3.4. Boundary Condition and Solution Algorithm

Supports are placed at 77 mm from the edge of the beam. Two point loads on top of the beams are restricted to move in  $X$  (longitudinal) and  $Z$  (transverse) directions using displacement/rotation boundary conditions, and loads are applied in  $Y$  (vertical) direction.

## 4. Results and Discussion

In the followings, both experimental and numerical load-deflection ( $P-\Delta$ ) curves are shown for retrofitted and un-retrofitted beams (Reference, Combined, Shear, and Bending cases). The ultimate load carrying capacity, peak deflection, and failure pattern are also discussed herein.

### 4.1. Role of loading configuration on the $P-\Delta$ behavior of un-retrofitted beams

The load-deflection ( $P-\Delta$ ) curves at the three measuring points of un-retrofitted beams are represented in Figure 6. For the un-retrofitted beams, the loading is carried up to the formation of major cracks (e.g., flexural and diagonal). The Reference case (URRC) reached the load and deflection of 82.25 kN and 12.95 mm, respectively, which has been recorded at mid-span (gauge 2). Obviously, bending case (URBC) exhibited higher deflection than the URRC at similar load level due to the higher induced bending moment with respect to the other cases. It is also observed that the slope of the  $P-\Delta$  curve is lower for the unsymmetrical loading positions (e.g., Bending case and Combined case) than the symmetrical (Reference case) ones. Despite being subjected to different loading configurations, Bending case (URBC) and Combined case (URCC) has almost similar  $P-\Delta$  behavior, and their maximum deflection ranged from around 8 to 10 mm. On the other hand, for the Shear case (URSC), the final  $P-\Delta$  curve is significantly lower than the other cases. This behavior could be due to the development of high concentration of shear-induced damaged close to the support (damage localization). A thick crack is observed for Shear case close to the loading point at the end of the beam, while no similar cracking or damage has been observed for the other three cases.

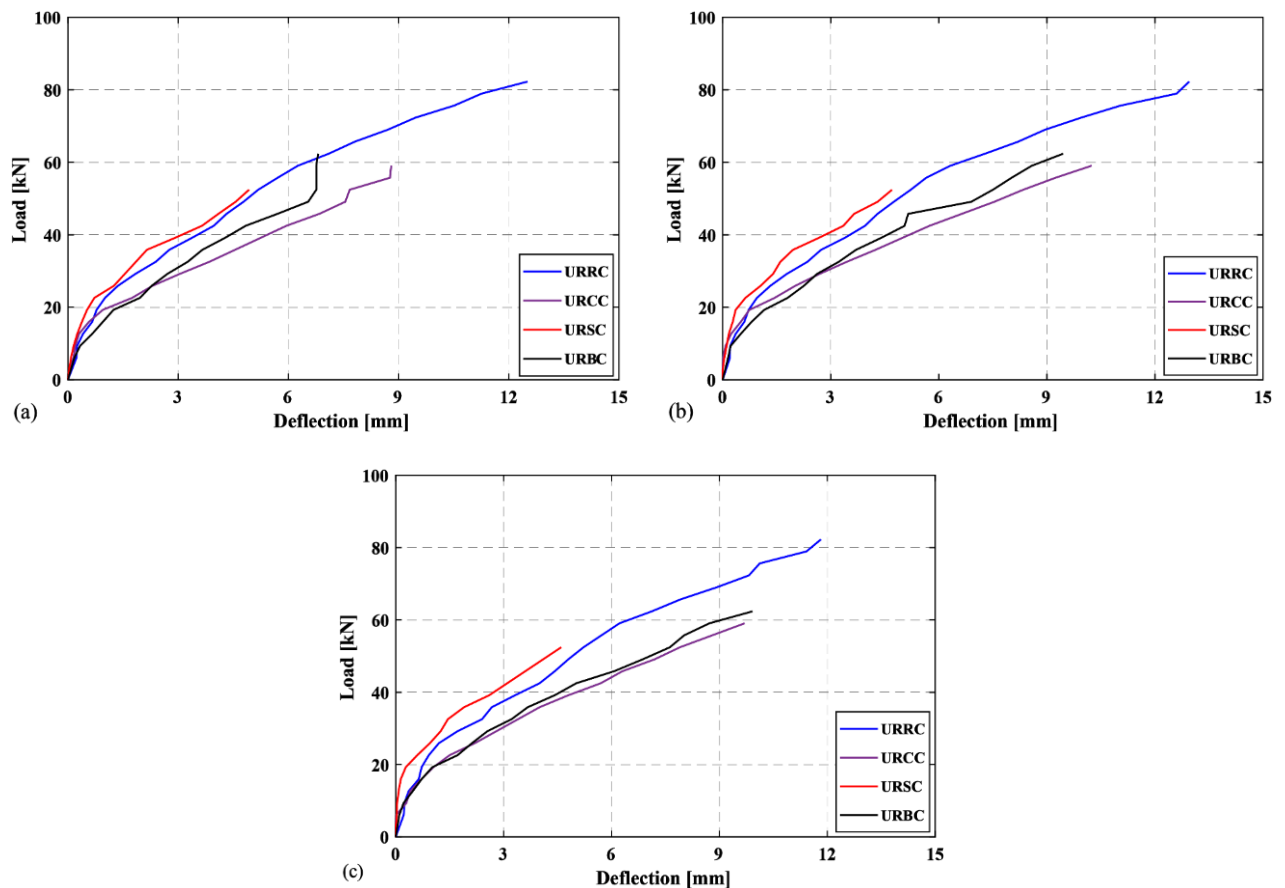
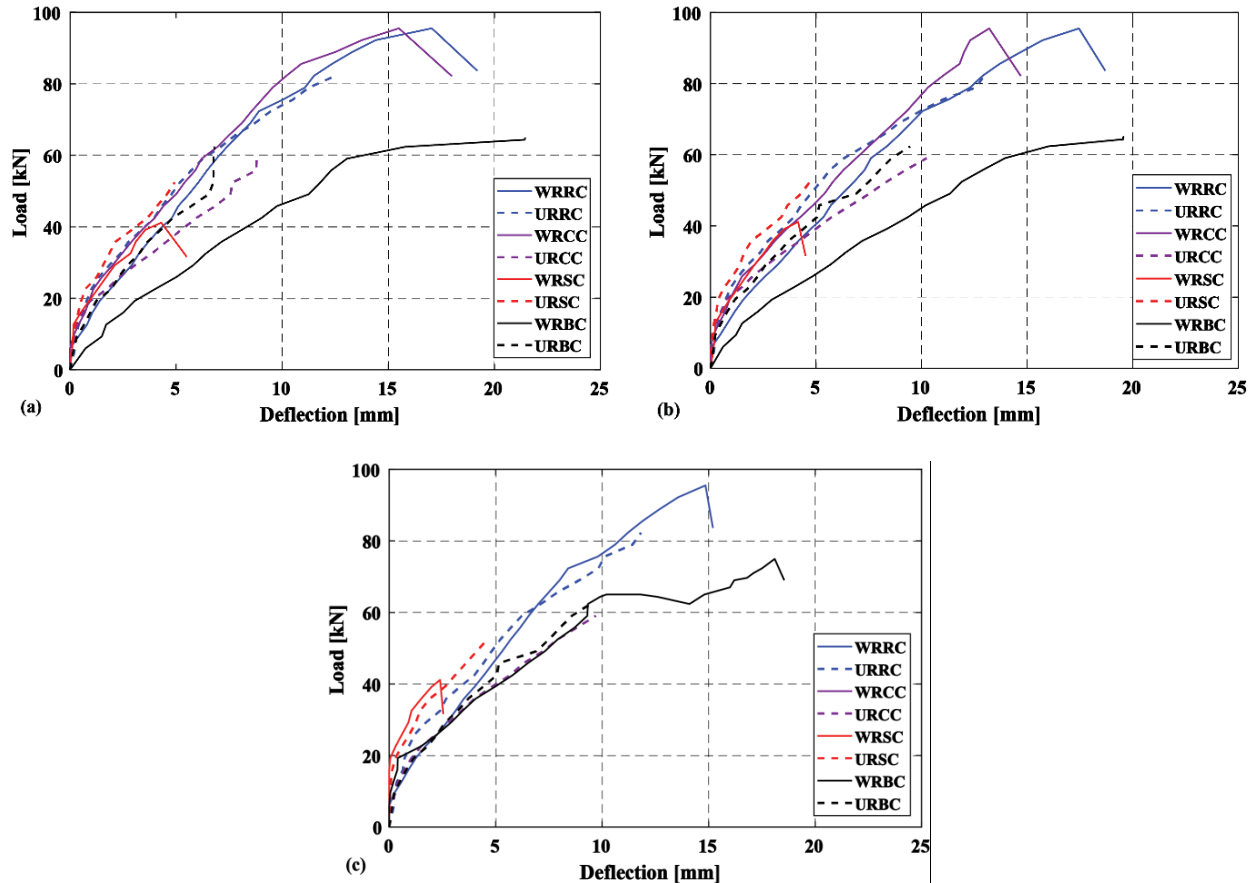


Figure 6.  $P-\Delta$  curves of un-retrofitted beams: (a) at 305 mm left from the midpoint (Gauge 1), (b) at midpoint (Gauge 2), and (c) at 305 mm right from the midpoint (Gauge 3) of the beam respectively.

### 4.2. Role of ferrocement technique on the $P-\Delta$ behavior of beams

Figure 7 shows  $P-\Delta$  curves for all the un-retrofitted (URRC, URCC, URSC, and URBC) and retrofitted (WRRC, WRCC, WRSC, and WRBC) beams. Except that for the Shear case, ferrocement beams exhibited an improvement, thanks to the partial prevention of crack propagation and to the additional tensile strength provided. As mentioned before, the Shear case beam was seriously damaged at the end of the first loading (before retrofitting) next to the support, thus making vain the following strengthening. In most of the cases, similar flexural behavior is observed between retrofitted and un-retrofitted beams in all the three measuring points. It is worth noting that, due to technical problems, the deflection at Gauge 3 of Combined case is not monitored.

It should be noted that retrofitting with ferrocement allowed to mostly recover the “virgin” stiffness of the beams, as shown by the very similar trends of  $P - \Delta$  curves at first loading (un-retrofitted specimens) and after damaging and retrofitting (retrofitted specimens). The overall response of the retrofitted beams demonstrated the benefit of using ferrocement technique for enhancing the flexural performance of partially damaged structures, for example, due to earthquake, wind load, blast and fire. This is in agreement with the results of previous tests on flat plate systems reported in [36]. Similar behavior is observed in the literature [5–7, 24]. It is also observed that the first crack is delayed in retrofitted beams with respect to the un-retrofitted beams.



**Figure 7. Comparison of  $P - \Delta$  behavior of un-retrofitted and retrofitted beams: (a) at 305 mm left from the midpoint (Gauge 1), (b) at midpoint (Gauge 2), and (c) at 305 mm right from the midpoint (Gauge 3) of the beams correspondingly.**

It can be noticed that the retrofitted Reference (WRRC) and Combined (WRCC) cases collapsed at almost the same load, despite the different loading configuration. However, the deflection of Combined case is significantly lower than the Reference case due to higher shear stress. Among all the cases, except Shear case (since it collapses earlier due to pre-damage of the beam), the Bending case showed the lowest load-bearing capacity due to the significantly higher bending moment with respect to the other three cases. However, ductility is significantly improved in most of the ferrocement beams. In general, it is observed that retrofitting with steel wire mesh combined with ferrocement improves the flexural behavior and load carrying capacity for the different loading configurations, by limiting the formation of cracks and micro-cracks. Thanks to the strengthening process, the wire mesh embedded in ferrocement provided an effective further contribution in tension, allowing an increase of the load-bearing capacity. A further benefit probably is the lateral confinement provided by the retrofitting, so limiting the propagation of cracks and improving the shear behavior close to the supports. Both Reference case and Combined case of retrofitted beams reached the maximum load of 95.5 kN and the retrofitted Bending case attained 75.0 kN.

#### 4.3. Failure pattern of the retrofitted beams

The cracking patterns of the retrofitted beams at failure is presented in Figure 8. The figure indicates that there is a significant difference in failure patterns depending on the loading configuration. In Reference and Combined cases, a marked distribution of cracks are observed all along the length showing a combination of bending and shear collapse, while in Shear and Bending cases the damage is concentrated at the support or in the mid-span, respectively, due to shear or bending-induced collapse. Ductile mode of failure is observed for Reference and Bending cases thanks to multiple cracking, while a brittle failure has seen for the Shear

case. As regards the retrofitting system, yielding of the steel wire mesh probably occurred before debonding between the steel wire mesh and original concrete surface, and then finally the retrofitted beam failed with significant higher deflection.

The numerical  $P - \Delta$  behavior of un-retrofitted beams is compared with the experimental results and presented in Figure 9 (a–d). The figure shows a rather good agreement between measured and predicted deflections for the four un-retrofitted beams, with just a slight underestimation of the initial stiffness.

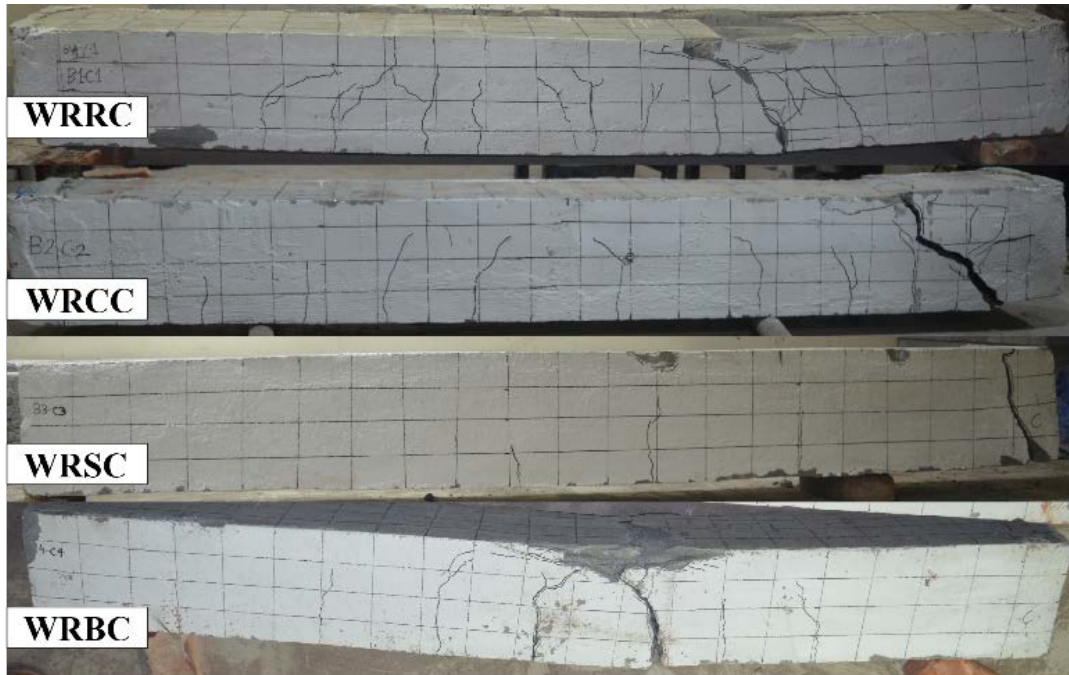


Figure 8. Crack pattern of the retrofitted beams tested in four different loading positions.

#### 4.4. Numerical $P - \Delta$ behavior

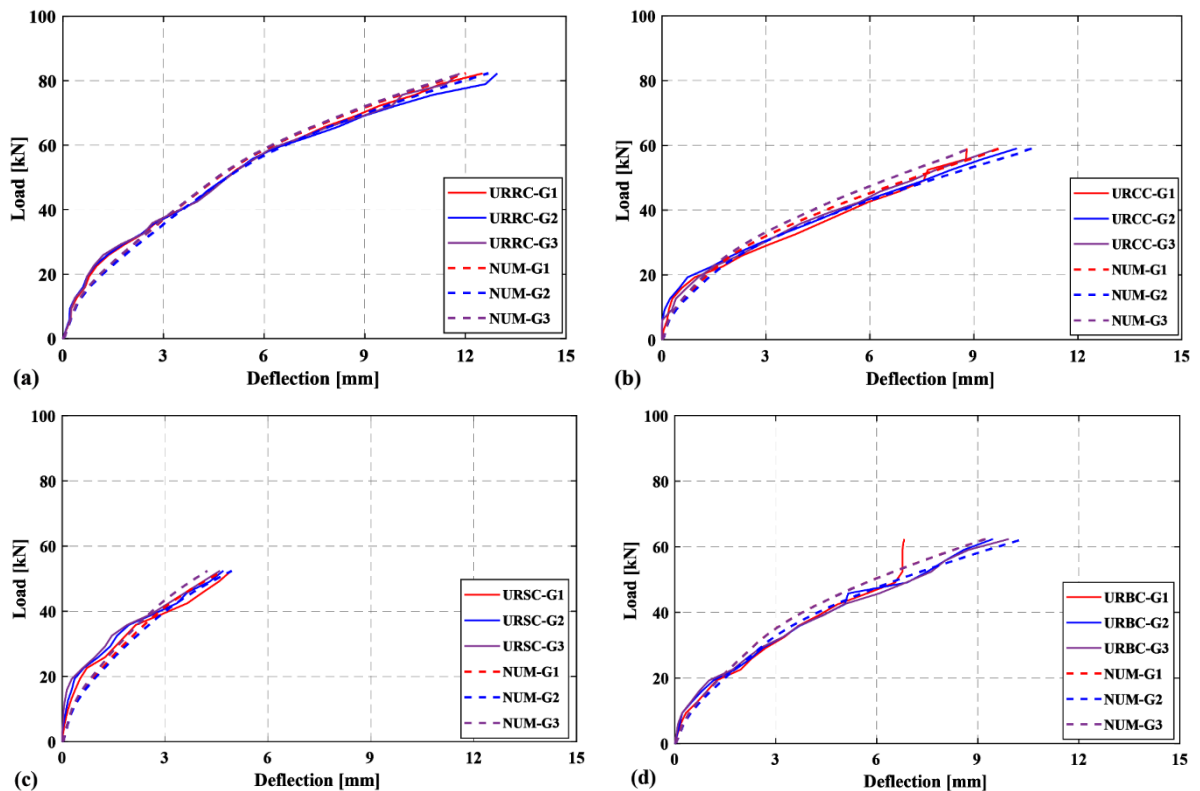


Figure 9. Comparison of experimental and numerical  $P - \Delta$  curves of un-retrofitted beams: (a) Reference case, (b) Combined case, (c) Shear case, and (d) Bending case respectively.

As concern the retrofitted beams, the numerical deflections calculated at three different positions are quite similar to the experimental results, especially for the Combined case (see Figure 10). The differences can be

ascribed to the fact that the partial damage of the beams before applying ferrocement is not taken into account in the numerical model. Probably, because of that reason, the numerical slope of the load-deflection curve is higher than the experimental curves. Furthermore, the ferrocement behavior is a bit more complicated than the RC beam due to different role of different materials such as steel wire mesh, reinforced concrete and cement mortar, in addition to steel-concrete bond stiffness. Finally, the plots of plastic strain distribution in the retrofitted beams are shown in Figure 11. As expected, except Shear case, the higher stain occurred near the mid-span (i.e., gauge G2) of the beam as observed in Figure 11. The rather good agreement between numerical and experimental results corroborate the idea that no significant debonding occurred at the ferrocement to beam interface.

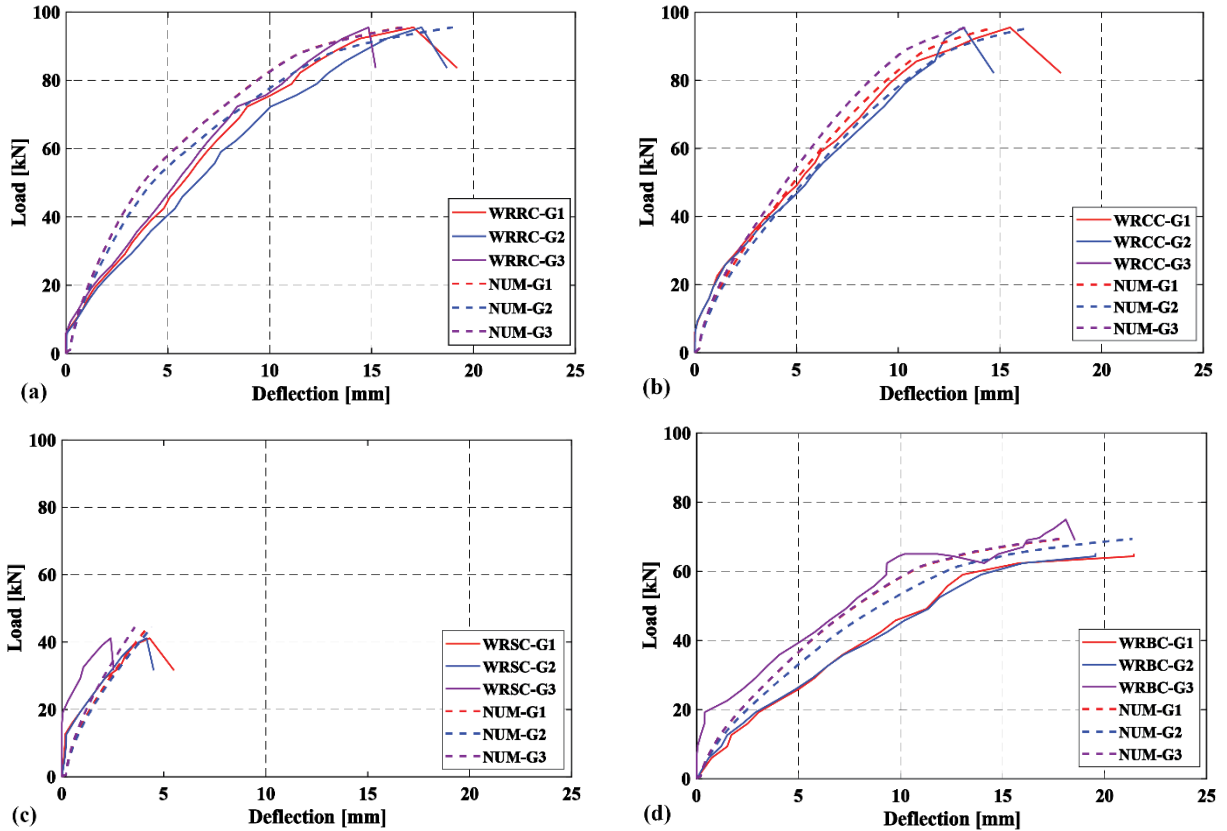


Figure 10. Comparison of experimental and numerical  $P - \Delta$  curves of beams: (a) Reference case, (b) Combined case, (c) Shear case, and (d) Bending case correspondingly.

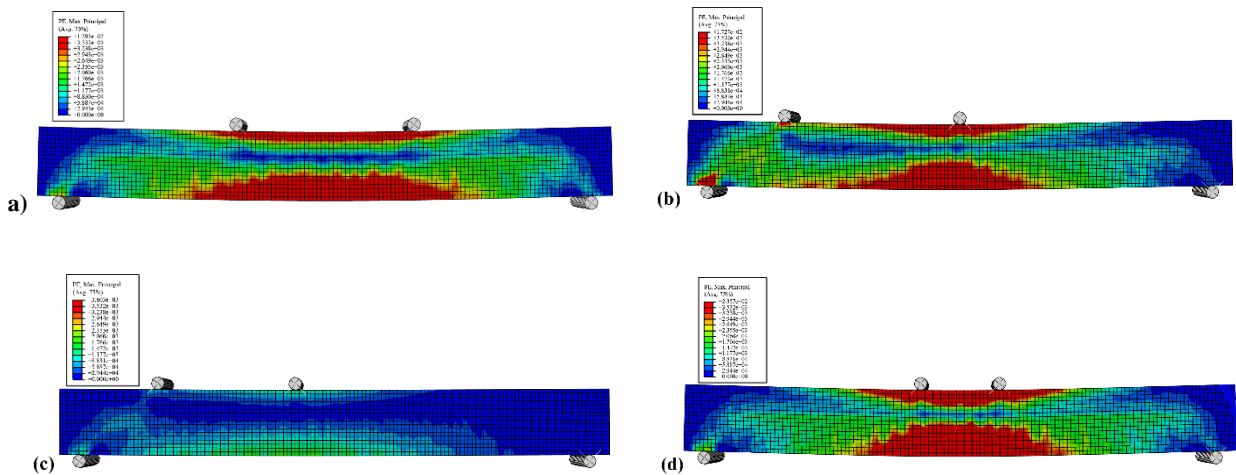


Figure 11. 3D image of plastic strain distribution in the retrofitted beams at the end of loading: (a) Reference case, (b) Combined case, (c) Shear case, and (d) Bending case respectively.

### 5. Conclusions

This study is carried out on RC un-retrofitted and retrofitted beams made with unconventional concrete (i.e., very low strength concrete – LSC at 28 days  $\approx 12.5-13.0$  MPa) under four-point incremental static loading. In order to gain a deeper understanding of the role of loading positions on the flexural performance of the beams, numerical simulations have been performed via the finite element software ABAQUS. Four-point

flexural tests are performed experimentally and numerically on both retrofitted and un-retrofitted beams with different loading positions: (i) 2 loads at  $L/3$  (Reference case), (ii) 2 loads close to the support (Shear case), (iii) 2 loads close to the mid-span (Bending case), and (iv) 1 load next to the support and 1 load on the mid-span (Combined case). The following conclusions can be drawn based on the results presented in this research work:

– The beams tested under unsymmetrical loading show a worse mechanical performance due to shear action. Among four cases, poor performance of RC beam is observed in Shear case which is associated to the formation of major crack at the end of the beam (shear failure).

– Ductile mode of failure is observed for the Reference and Bending cases in retrofitted beams, while a brittle failure has been seen for the Shear case due to severe cracking with damage localization occurred during the pre-cracking phase on the un-retrofitted beam.

– Numerical results of un-retrofitted and retrofitted tests are in quite good agreement with the experimental results. In numerical analyses retrofitting debonding is not considered, this corroborating the idea that ferrocement-to-beam bond has been effective.

– Ferrocement technique is cheap, sustainability, achievable with local materials and ordinary (namely, not specialized) workmanship, light in weight (i.e., lower self-weight, so reducing the increase of the permanent load on the structure to be retrofitted), and efficient in construction time. Therefore, it could be recommended to use ferrocement technique to strengthen existing structures made with low strength concrete to avoid sudden collapse due to extreme loading, such as earthquake.

Though a better performance of ferrocement retrofitted beams have been observed, it is essential to study other important issues, such as the bond between ferrocement and original concrete (i.e., ferrocement jacketing), the possible benefits in ductility brought in by adding different layer of wire mesh or by the introduction of steel or natural fibers in the mortar, the durability performance of ferrocement due to its lower net cover and the higher surface area of the reinforcement (i.e., higher risk of corrosion), the lower density of the mortar (i.e., higher penetration of water, higher corrosion) as well as dynamic and fire behavior. This is an ongoing research project where further work is planned in the direction of strengthening of beam-column structures made with low strength concrete subjected to gravitational loads or to extreme events such as earthquake or fire.

## 6. Acknowledgements

The authors have appreciated the financial support of the Department of Civil Engineering of University of Asia Pacific. Authors also acknowledge the assistance of the lab attendee and students of the aforementioned department.

### References

1. Raof, M., Lin, Z. Structural characteristics of RC beams with exposed main steel. In Proceedings of the Institution of Civil Engineers – Structures and Building. 1997. 122(1). Pp. 35–51.
2. Tarhini, K.M., Frederick, G.R. Wheel load distribution in I-girder highway bridges. Journal of Structural Engineering. 1992. 118(5). Pp. 1285–1294.
3. Tarhini, K.M., Frederick, G.R. Lateral load distribution in I-girder bridges. Computers & structures. 1995. 54(2). Pp. 351–354.
4. Cotsovos, D.M. A simplified approach for assessing the load-carrying capacity of reinforced concrete beams under concentrated load applied at high rates. International Journal of Impact Engineering. 2010. 37(8). Pp. 907–917.
5. Paramasivam, P.K., Ong, C.G., Lim, C.T.E. Ferrocement Laminates for Strengthening RC T-Beams. Cement & Concrete Composites. 1994. Vol. 16. Pp. 143–152.
6. Paramasivam, P., Lim, C.T.E., Ong, C.G. Strengthening of RC Beams with Ferrocement Laminates. Cement and Concrete Composites. 1998. Vol. 20. Pp. 53–65.
7. Liao, H.P., Fang, S.S. An experimental study on flexural behavior of reinforced concrete beams strengthened with high-performance ferrocement. Advanced Materials Research. 2011. Vol. 163. Pp. 3772–3776.
8. Qeshta, I.M., Shafiqh, P., Jumaat, M.Z. Flexural behaviour of RC beams strengthened with wire mesh-epoxy composite. Construction and Building Materials. 2015. Vol. 79. Pp. 104–114.
9. Gao, B., Kim, J.K., Leung, C.K. Experimental study on RC beams with FRP strips bonded with rubber modified resins. Composites Science and Technology. 2004. 64(16). Pp. 2557–2564.
10. Qeshta, I.M., Shafiqh, P., Jumaat, M.Z., Abdulla, A.I., Ibrahim, Z., Alengaram, U.J. The use of wire mesh-epoxy composite for enhancing the flexural performance of concrete beams. Materials & Design. 2014. Vol. 60. Pp. 250–259.
11. Desayi, P., Reddy, V. Strength of lightweight ferrocement in flexure. Cement and Concrete Composites. 1991. 13(1). Pp. 13–20.
12. Al-Sulaimani, G.J., Basunbul, I.A., Mousselhy, E.A. Shear behavior of ferrocement box beams. Cement and Concrete Composites. 1991. 13(1). Pp. 29–36.
13. Sundarraja, M.C., Rajamohan, S. Strengthening of RC beams in shear using GFRP inclined strips—An experimental study. Construction and building materials. 2009. 23(2). Pp. 856–864.
14. Obaidat, Y.T., Heyden, S., Dahlblom, O., Abu-Farsakh, G., Abdel-Jawad, Y. Retrofitting of reinforced concrete beams using composite laminates. Construction and Building Materials. 2011. 25(2). Pp. 591–597.

15. Alam, M.A., Hassan, A., Muda, Z.C. Development of kenaf fibre reinforced polymer laminate for shear strengthening of reinforced concrete beam. *Materials and Structures*. 2016. 49(3). Pp. 795–811.
16. Alam, M.A., Jabbar, A.S.A., Jumaat, M.Z., Mustapha, K.N. Effective Method of Repairing RC Beam Using Externally Bonded Steel Plate. *Applied Mechanics and Materials*. 2014. Vol. 567. Pp. 399–404.
17. Takiguchi, K. An investigation into the behavior and strength of reinforced concrete columns strengthened with ferrocement jackets. *Cement and Concrete Composites*. 2003. 25(2). Pp. 233–242.
18. Kaish, A.B.M.A., Alam, M.R., Jamil, M., Zain, M.F.M., Wahed, M.A. Improved ferrocement jacketing for restrengthening of square RC short column. *Construction and Building Materials*. 2012. Vol. 36. Pp. 228–237.
19. Hago, A.W., Al-Jabri, K.S., Alnuaimi, A.S., Al-Moqbali, H., Al-Kubaisy, M.A. Ultimate and service behavior of ferrocement roof slab panels. *Construction and Building Materials*. 2005. 19(1). Pp. 31–37.
20. Ashraf, M., Khan, A.N., Naseer, A., Ali, Q., Alam, B. Seismic behavior of unreinforced and confined brick masonry walls before and after ferrocement overlay retrofitting. *International Journal of Architectural Heritage*. 2012. 6(6). Pp. 665–688.
21. Miah, M.S., Miah, M.J., Hossain, M.M., Paul, S.C. Seismic Retrofit of Flat Plate and Flat Slabs Using Ferrocement, Proceedings of 5th International Congress on Technology Engineering and Science, Kuala Lumpur, Malaysia. 2018. Pp. 317–326.
22. Li, B., Lam, E.S.S. Influence of interfacial characteristics on the shear bond behaviour between concrete and ferrocement. *Construction and Building Materials*. 2018. Vol. 176. Pp. 462–469.
23. El-Sayed, T.A., Erfan, A.M. Improving shear strength of beams using ferrocement composite. *Construction and Building Materials*. 2018. Vol. 172. Pp. 608–617.
24. Shaaban, I.G., Shaheen, Y.B., Elsayed, E.L., Kamal, O.A., Adesina, P.A. Flexural characteristics of lightweight ferrocement beams with various types of core materials and mesh reinforcement. *Construction and Building Materials*. 2018. Vol. 171. Pp. 802–816.
25. Shaaban, I.G., Shaheen, Y.B.I., Elsayed, E.L., Kamal, O.A., Adesina, P.A. Flexural behaviour and theoretical prediction of lightweight ferrocement composite beams. *Case Studies in Construction Materials*. 2018. Vol. 9. e00204.
26. Li, B., Lam, E.S.S., Wu, B., Wang, Y.Y. Experimental investigation on reinforced concrete interior beam–column joints rehabilitated by ferrocement jackets. *Engineering Structures*. 2013. Vol. 56. Pp. 897–909.
27. Zhang, K., Sun, Q. The use of Wire Mesh-Polyurethane Cement (WM-PUC) composite to strengthen RC T-beams under flexure. *Journal of Building Engineering*. 2018. Vol. 15. Pp. 122–136.
28. Hawileh, R.A. Nonlinear finite element modeling of RC beams strengthened with NSM FRP rods. *Construction and Building Materials*. 2012. 27(1). Pp. 461–471.
29. Obaidat, Y.T., Heyden, S., Dahlblom, O. The effect of CFRP and CFRP/concrete interface models when modelling retrofitted RC beams with FEM. *Composite Structures*. 2010. 92(6). Pp. 1391–1398.
30. Kishi, N., Zhang, G., Mikami, H. Numerical cracking and debonding analysis of RC beams reinforced with FRP sheet. *Journal of Composites for Construction*. 2005. 9(6). Pp. 507–514.
31. Gizdatullin, G.A., Khusainov, R.R., Khozin, V.G., Krasnikova, N.M. Strength and deformability of concrete structures reinforced with fibre-reinforced polymer bars. *Magazine of Civil Engineering*. 2016. 62(2). Pp. 32–41. DOI:10.5862/MCE.62.4
32. Boldyreva, A.A., Yarunicheva, Y.A., Dernakova, A.V., Ivashov, I.I. The strength of the polymer composite (fiberglass) with interlaminar shear. *Magazine of Civil Engineering*. 2016. Vol. 62. No. 2. Pp. 42–50. DOI: 10.5862/MCE.62.5
33. ASTM C33, Standard Specification for Concrete Aggregates. ASTM International, West Conshohocken, PA, USA, 2003. 11 p.
34. ASTM C39, Standard Test Method for Compressive Strength of Cylindrical Concrete Specimens. ASTM Standard, West Conshohocken, PA, USA, 2005. 16 p.
35. ABAQUS. ABAQUS/standard version 6.10 user's manuals: volumes I-III, Hibbitt, Karlsson, and Sorenson, Inc., Pawtucket (RI), 2010.
36. Miah, M.S., Miah, M.J., Hossain, M.M., Paul, S.C. Nonlinear Seismic Response of Flat Plate Systems made with Ultra Low Strength Concrete. *Global Science and Technology Journal*. 2018. 6(2). Pp. 35–46.

### **Contacts:**

*Md Jihad Miah, +880258157091; jihad.miah@uap-bd.edu*

*Mohammad Shamim Miah, +4917632415430; mohammad\_shamim.miah@tu-dresden.de*

*Walid Bin Alam, +8801682077158; walidbin.alam40@gmail.com*

*Francesco Lo Monte, +393331845409; francesco.lo@polimi.it*

*Ye Li, +6583586646; LIYE0006@e.ntu.edu.sg*

© Miah, M.J., Miah, M.S., Alam, W.B., Lo Monte, F., Li, Y., 2019



DOI: 10.18720/MCE.89.9

## Water permeation simulation of autoclaved aerated concrete blocks using the Lattice Boltzmann method

F. Jun\*, Y. Yue, Y. JiaBin

School of Civil Engineering and Architecture, Zhejiang Sci-Tech University, Hangzhou, China

\* E-mail: [fujun@zstu.edu.cn](mailto:fujun@zstu.edu.cn)

**Keywords:** autoclaved aerated concrete block, LBM, penetration, flow simulation, MATLAB

**Abstract.** In this paper, the Lattice Boltzmann Method (LBM) is used to simulate the seepage field of autoclaved aerated concrete blocks. The macroscopic permeability coefficients of aerated blocks are obtained. The complex flow characteristics of the internal flow field are revealed. A stochastic four-parameter growth method (QSGS) based on the distribution probability of initial growth nuclei and porosity is proposed. A meso-model of the real pore structure of aerated blocks is established. The influence of initial inlet pressure and model porosity on the permeability of aerated block is analyzed by numerical calculation of the permeability development process of aerated block. The results show that the two-dimensional meso-model close to the real pore structure of aerated block can be constructed by the stochastic four-parameter growth method; the water permeability coefficient of aerated block calculated by the LBM numerical method is in good agreement with the experimental results; under certain conditions, the linear relationship between the permeability coefficient of autoclaved aerated concrete block and its porosity satisfies the requirement of practical engineering application. It has certain guiding significance for practical engineering application.

### 1. Introduction

Autoclaved aerated concrete blocks are some of the most widely used new wall materials. They have a porosity of 65–80 % and the advantages of being light weight, fire resistant, heat preserving and convenient in terms of construction [1–3]. However, in bad weather conditions, rainwater easily enters the interior of the wall from the pore isotonic passage, which causes a decline in thermal insulation performance and durability of the wall. Thus, the leakage of the wall cannot be ignored [4]. Currently, few studies have been conducted on the permeability of autoclaved aerated concrete blocks and on seepage simulation methods at the mesoscopic level. Because micro-factors such as pore structure and pore distribution of aerated blocks can reflect the macro-properties of aerated blocks and affect their macro-permeability, studying the permeability of autoclaved aerated concrete blocks at the micro-level is of great theoretical value [5–6].

As a highly efficient fluid dynamics simulation method, the lattice Boltzmann method (LBM) is widely used in the field of porous media seepage because of its powerful boundary processing and excellent parallel computing capabilities. Hazlett [7] simulated a multiphase flow inside the pores of porous media successfully based on the LBM. Degruyter et al. Reconstructed volcanic pumice using synchronous accelerated computed tomography (CT) imaging technology while studying the relationship between the porosity and permeability of volcanic pumice using the LBM method [8]. Qian [9] used a single relaxation incompressible LBM model to simulate a flow field in a two-dimensional porous media model at the mesoscopic level, which verified the accuracy of Darcy's law, and proposed an efficient and simple permeability calculation method. Luo [10] used the LBM to simulate fluid flow in random porous media and tested Darcy's law. Li [11] constructed a porous media model based on the quartet structure generation set (QSGS) and then calculated the permeability of porous media using an LBM program compiled by MATLAB software.

---

Jun, F., Yue, Y., JiaBin, Y. Water Permeation Simulation of Autoclaved Aerated Concrete Blocks using the Lattice Boltzmann Method. Magazine of Civil Engineering. 2019. 89(5). Pp. 106–114. DOI: 10.18720/MCE.89.9

Джун Ф., Юэ Ф., Джабин Й. Моделирование водопроницаемости газобетонных блоков методом решёточных уравнений Больцмана // Инженерно-строительный журнал. 2019. № 5(89). С. 106–104. DOI: 10.18720/MCE.89.9



This open access article is licensed under CC BY 4.0 (<https://creativecommons.org/licenses/by/4.0/>)

The key to successfully simulating the water infiltration process of autoclaved aerated concrete blocks is to describe quantitatively the pore structure characteristics using appropriate methods [1–4]. In 2007, the QSGS proposed by Wang et al. [15] was shown to solve the aforementioned problems effectively. The solid phase growth process effectively considers the solid particle size, random distribution of the solid phase, and statistical properties of the model. When the parameters are adjusted, a mesoscopic model closer to a real aerated block can be obtained, and the reconstructed mesoscopic model of an aerated block can be combined with the LBM to make the calculation more efficient.

A QSGS combined with the LBM can simulate the water infiltration process effectively in autoclaved aerated concrete blocks. Therefore, a simple and efficient QSGS is proposed in this study. Then, based on the LBM, the infiltration process in the two-dimensional micro-model of the aerated block is accurately revealed by numerical calculation, and the influence of the initial inlet pressure and model porosity on the permeability coefficient of the model is analyzed. The linear relationship between the permeability coefficient and porosity of autoclaved aerated concrete blocks is finally established.

## 2. Methods

### 2.1. Lattice Boltzmann method model

The macroscopic motion of fluid can be simulated by solving the Boltzmann equation numerically. The Boltzmann equation can be expressed as

$$\frac{\partial f}{\partial t} + c \cdot \nabla f = -\frac{1}{\tau} [f - f^{\text{eq}}], \quad (1)$$

where  $f = f(r, c, t)$  represents the number of molecules in the unit volume at a speed of  $c \sim c + dc$  at a time of  $t$  and position of  $r$ ;

$\tau$  denotes the relaxation factor;

$f^{\text{eq}}$  represents the equilibrium distribution function.

The most representative two-dimensional square lattice D2Q9 model in LBM is applied. According to the discrete velocity distribution of mesh and fluid particles, each fluid particle has nine moving directions (including the static state of particles). The corresponding velocity in each direction can be expressed as [16]

$$e_i = \begin{cases} (0, 0) & \dots i = 0, \\ c \left( \cos \left[ (i-1) \frac{\pi}{2} \right], \sin \left[ (i-1) \frac{\pi}{2} \right] \right) & \dots i = 1, 2, 3, 4, \\ \sqrt{2}c \left( \cos \left[ (2i-1) \frac{\pi}{4} \right], \sin \left[ (2i-1) \frac{\pi}{4} \right] \right) & \dots i = 5, 6, 7, 8, \end{cases} \quad (2)$$

where  $c$  represents the lattice velocity with  $c = \delta_x / \delta_t$ ,  $\delta_x$  represents the grid step size, and  $\delta_t$  represents the time step. Then (1) can be discretized into

$$f_i(\mathbf{x} + \mathbf{e}_i \Delta t, t + \Delta t) - f_i(\mathbf{x}, t) = -\frac{1}{\tau} [f_i(\mathbf{x}, t) - f_i^{\text{eq}}(\mathbf{x}, t)]. \quad (3)$$

The equilibrium distribution function is expressed as [16]

$$f_i^{\text{eq}} = \omega_i \rho \left[ 1 + \frac{3}{c_s^2} (\mathbf{e}_i \cdot \mathbf{u}) + \frac{9}{2c_s^4} (\mathbf{e}_i \cdot \mathbf{u})^2 - \frac{3}{2c_s^2} u^2 \right] \quad (4)$$

where  $\rho$  represents the macroscopic density of fluid;

$\mathbf{u}$  represents the macroscopic velocity;

$c_s = \frac{c}{\sqrt{3}}$  represents the base lattice velocity;

$\omega_i$  represents the weight coefficient.

$$\omega_i = \begin{cases} 4/9 & \dots i = 0, \\ 1/9 & \dots i = 1, 2, 3, 4, \\ 1/36 & \dots i = 5, 6, 7, 8. \end{cases} \quad (5)$$

According to the law of conservation of mass and momentum, the macro-density of fluid can be expressed by the sum of distribution functions in each grid node, and the macro-velocity of fluid can be expressed by the product of the micro-velocity per unit mass and distribution function in the direction of the lattice, which can be represented as  $\rho\mathbf{u}$ . Therefore, the distribution function of particles satisfies the following equation [17]:

$$\rho = \sum_i f_i, \quad \rho\mathbf{u} = \sum_i f_i \mathbf{e}_i. \tag{6}$$

By the Chapman–Enskog expansion [18] of the evolution equation, the macroscopic Navier–Stokes equation corresponding to the single relaxation model can then be obtained:

$$\partial_t \rho + \nabla \cdot (\rho\mathbf{u}) = 0; \tag{7}$$

$$\partial_t (\rho\mathbf{u}) + \nabla \cdot (\rho\mathbf{u}\mathbf{u}) = -\nabla p + \nabla \cdot [\rho\nu(\nabla\mathbf{u} + (\nabla\mathbf{u})^T)], \tag{8}$$

where  $p = \rho c_s^2$  and  $\nu = c_s^2 \left( \tau - \frac{1}{2} \right) \Delta t$  represents kinematic viscosity.

### 2.2. Boundary condition

The seepage process of water in an aeration block is limited by the solid wall. When the LBM is used to simulate the seepage process of the aeration block, appropriate boundary conditions must be selected to deal with all the points on the wall. The standard rebound and periodic boundary treatment schemes are adopted in this study. For the collision between solid skeleton and fluid particles, the rebound treatment which is called the standard rebound scheme in LBM, is typically used (Figure 1).

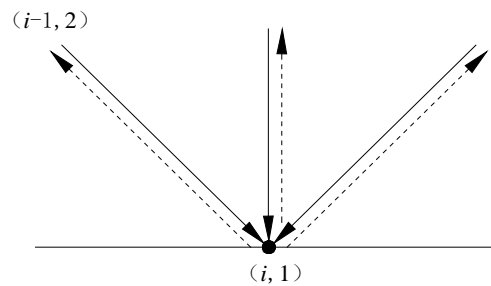


Figure 1. Label bounce format.

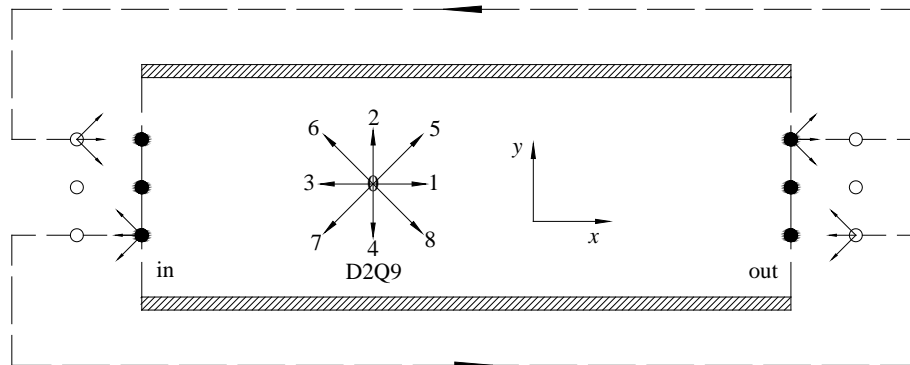


Figure 2. Periodic boundary format.

If the flow field is periodic in space or infinite in one direction, the periodic boundary treatment scheme [19] can be used at the corresponding boundary. A schematic diagram of the periodic boundary treatment scheme (Figure 2) shows that solid and hollow circles represent fluid and virtual fluid nodes, respectively. The periodic boundary processing format can be expressed as

$$\begin{cases} f_{1,5,8}(0, j) = f_{1,5,8}(N_x, j), \\ f_{3,6,7}(N_x + 1, j) = f_{3,6,7}(1, j), \end{cases} \tag{9}$$

where  $f_{1,5,8}(0, j)$  and  $f_{3,6,7}(N_x + 1, j)$  represent distribution functions on the  $(0, j)$  and  $(N_x + 1, j)$  nodes, respectively;

$f_{1,5,8}(N_x, j)$  and  $f_{3,6,7}(1, j)$  represent distribution functions on the  $(N_x, j)$  and  $(1, j)$  nodes, respectively.

### 2.3. Calculation of permeability coefficient

When fluid flows inside a porous medium, both the flow rate and Reynolds number are low ( $Re < 10$ ). The permeability of the porous medium can be obtained by Darcy's theorem, which can be expressed as [20]

$$\bar{u} = \frac{k}{\mu} \cdot \frac{\Delta P}{L}, \quad (10)$$

where  $\bar{u}$  denotes the average velocity;

$\mu$  is the kinematic viscosity coefficient of fluid;

$k$  represents permeability;

$L$  denotes the permeation path of fluid in porous media;

$\Delta P$  is the pressure loss value of flow.

With the introduction of  $K = \frac{k \rho g}{\mu}$ , the permeability coefficient of the porous medium at a low flow rate can be obtained as follows:

$$K = \frac{\bar{u} \rho g L}{\Delta P}. \quad (11)$$

## 3. Results and Discussion

### 3.1. Construction of two-dimensional meso-model of an aeration block

The development route of water infiltration in a block is not a straight line, but rather constitutes multiple lines and directions. It is assumed that the fluid can flow only in the effective pore, and the distribution of the effective pore is interlaced and does not overlap along the height direction of the aeration block. In other words, the pore corresponding to the upper pore is randomly distributed in the next section.

An autoclaved aerated concrete block has many irregular pore distributions with different shapes. The length direction of the autoclaved aerated concrete block wall has a fatal research value as compared to the width direction. Therefore, a stochastic four-parameter growth method was used in this study to reconstruct a two-dimensional mesoscopic equivalent model of an aerated block by adjusting the initial growth core distribution probability and porosity. The solid phase of the aerated block is the growth phase, the pore phase is the non-growth phase, and the initial phase in the model area is the pore. Several growth phases are randomly distributed within the scope of the model, and they then grow in all directions with a set probability. The growth stops when the porosity of the model reaches the set porosity. The concrete reconstruction steps are described as follows:

1. In the model range, the solid phase growth nuclei are randomly arranged with probability  $P_{cd}$ , which is less than the volume fraction (porosity  $n$ ) of the growth phase;
2. Each growth nucleus grows to its adjacent point with a preset probability  $P_i$ , and its growth direction is  $i$ ,  $i = 1, 2, 3, \dots, 8$ , as shown in Figure 3;
3. Repeat Step 2 until the growth phase reaches its preset volume fraction (porosity  $n$ );
4. The growth nucleus stops growing and the porous medium is reconstructed.

The stochastic four-parameter growth method is a traditional and widely used method for constructing porous media. However, under the premise of known permeability coefficient of porous media, few studies on the application of the equivalent model for constructing porous media by adjusting parameters have been reported. In this study, the sizes of solid particles, the random distribution of solid phases, and the statistical characteristics of the model were all controlled by adjusting the four parameters of initial growth probability ( $P_{cd}$ ), growth probability in all directions ( $P_i$ ), growth probability in the  $i$  direction ( $P^{(im)}$ ), and model porosity ( $n$ ). The reconstructed aerated block mesoscopic model more closely resembles a real aerated block, and a prerequisite is provided for studying the impermeability of the aerated block and its internal water infiltration process.

### 3.2. Simulation calculation and analysis

#### 3.2.1. Determining simulation parameters

The mesh size selected in this simulation was  $100 \times 100$ , the porosity of the model was  $n = 70\%$ ,  $Re = 10$ , and the micro-model of the aeration block is shown in Figure 4. The upper and lower boundaries of the model were established as impermeable boundaries, and the standard rebound scheme was applied. The left and right boundaries were established as the entrance and exit of the flow field, respectively, and the periodic boundary was adopted. The pore and solid boundary adopted the standard rebound scheme. Water flowed into the model from the inlet at different pressures and flowed from left to right as driven by the pressure differential.

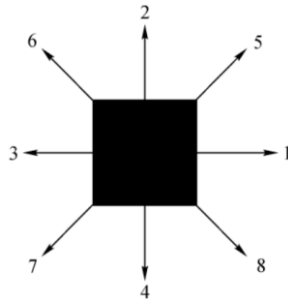


**Figure 3. Growth direction of the two-dimensional QSGS growth phase.**

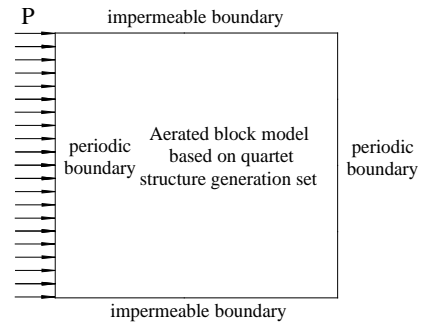


**Figure 4. Aerated block penetration model.**

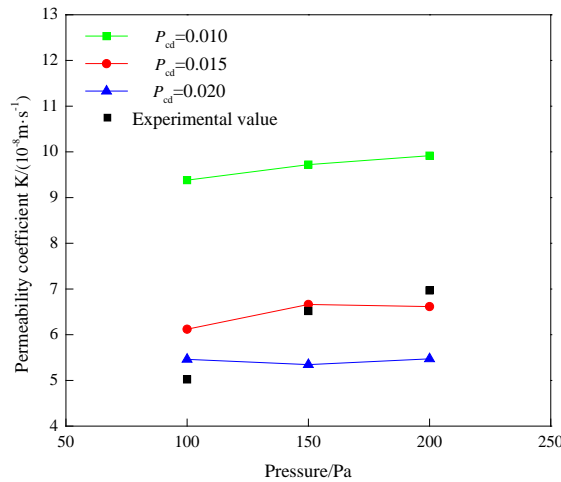


**Figure 5. Permeability coefficient measured by an LBM simulation and experiment.**

Figure 5 shows a comparison of the permeability coefficient of the A3.5 and B06 autoclaved aerated concrete blocks ( $n = 70\%$ ) measured using the Darcy method with an LBM simulation value. It should be pointed out that the simulated values of permeability coefficients are discrete to some extent. Because the aeration block model must be reconstructed prior to each permeability simulation, a difference of pore volume, quantity, and connectivity in the different models is the results and thus a discretization of simulated values of permeability coefficients appears. Figure 5 shows that when the inlet water pressure was 150 Pa and the mesh size was  $100 \times 100$ , the average permeability coefficient of the two-dimensional mesoscopic model reconstructed by  $P_{cd} = 0.015$  was  $K = 6.662 \times 10^{-8}$  m/s, whereas the permeability coefficient of the aerator block obtained by the experiment under 150 Pa water pressure was  $K = 6.517 \times 10^{-8}$  m/s. Figure 5 clearly shows that our numerical simulation results match those of the previous real test [21] very well, where the error range was within 2.2%. Therefore, our numerical accuracy is reliable. The results show that when the inlet water pressure was 150 Pa and mesh size was  $100 \times 100$ , the two-dimensional mesoscopic model reconstructed by  $P_{cd} = 0.015$  proved reliable for studying the water infiltration process and law at work inside the aerator block.

### 3.2.2. Relationship between the size of solid particles and permeability coefficient of the model

An autoclaved aerated concrete block is a kind of porous silicate masonry material made by internal gas generation. Therefore, the volume of its internal solid aggregate is different [22]. Large solid particles have smaller specific surface areas, but their pore size is usually greater than those of small solid particles. To study the effect of solid particle size on the permeability coefficient of aerator, different initial growth nucleus distribution probabilities were selected to reconstruct aerator models with different solid particle sizes and to simulate permeability.

Taking the porosity  $n = 70\%$  as an example, a two-dimensional micro-model of aerated blocks grown isotropically with initial growth nucleus distribution probabilities of  $P_{cd} = 0.01, 0.015$  and  $0.02$  is presented in Figure 6.

Figures 6 and 7 clearly show that with a decrease in the initial growth nucleus distribution probability, the volume of solid particles increases, the connectivity of the model improves, and the permeability coefficient increases.

### 3.2.3. Relationship between porosity of aerated block and its permeability coefficient

As a porous material, the macroscopic permeability of an autoclaved aerated concrete block is usually related to its porosity [23–24]. However, due to the limitation of the test period and engineering environment, a direct test method is not suitable for a field test of the permeability coefficient of an aerated block.

Accordingly, this study examined the relationship between the porosity and permeability coefficient of an aerated block to characterize the permeability coefficient by porosity of the aerated block and in turn reflect its permeability resistance.

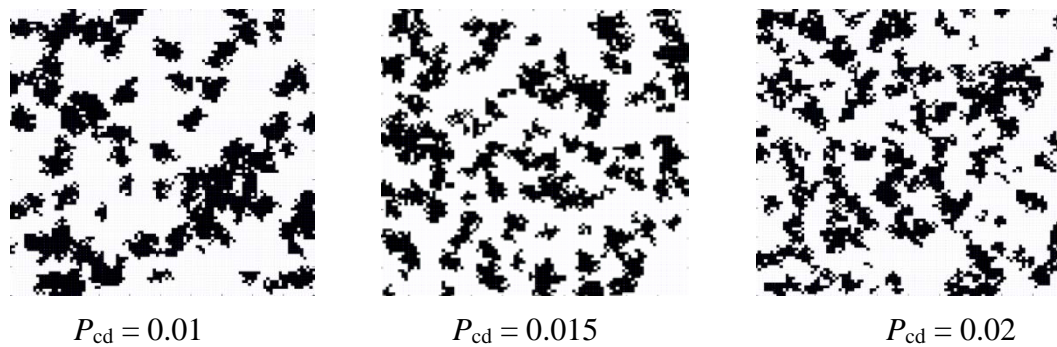


**Figure 6. Reconstructed two-dimensional mesoscopic model.**

Based on an LBM numerical calculation, the relationship between the porosity and permeability coefficient of an autoclaved aerated concrete block in a two-dimensional mesoscopic model was established in this study. Figure 8 shows the relationship between the porosity and permeability of a two-dimensional mesoscopic model of an autoclaved aerated concrete block. Figure 8 shows that the permeability coefficient of the model increases with an increase in its porosity. The relationship between the porosity and permeability coefficient of the model is linear and can be expressed as follows

$$K = 67.65n - 41.04, \quad (12)$$

where  $K$  represents the water permeability coefficient of the autoclaved aerated concrete block (unit:  $10^{-8}$  m/s) and  $n$  represents its porosity.

Because the porosity of autoclaved aerated concrete blocks is generally in the range of 65–80 %, and the model porosity is also in this range when conducting a permeability simulation, the linear relationship between the porosity and permeability coefficient of aerated blocks is satisfied only when the porosity is in the range of 65–80 %.

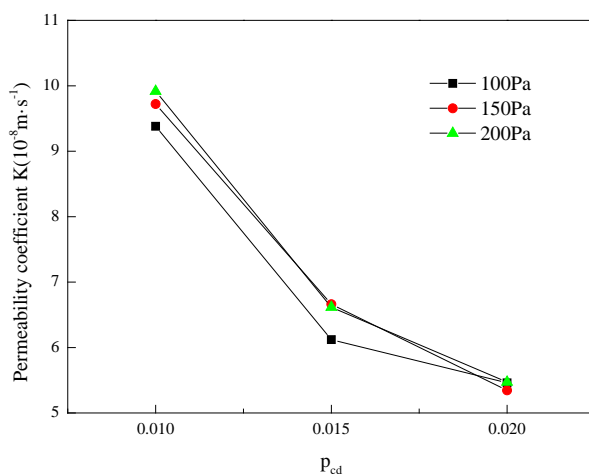


**Figure 7. Relationship between solid particle size and model permeability coefficient.**

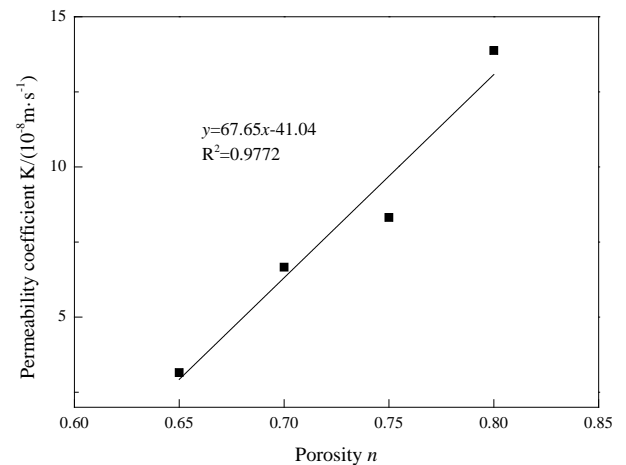
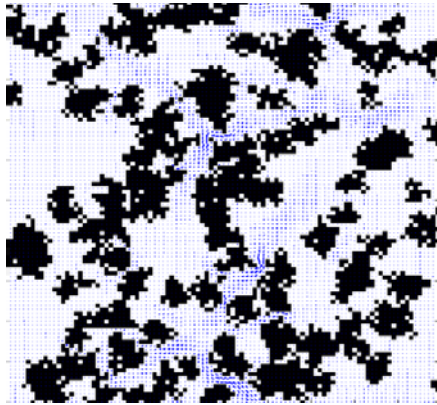


**Figure 8. Relationship between porosity and permeability coefficient of the aerated block.**

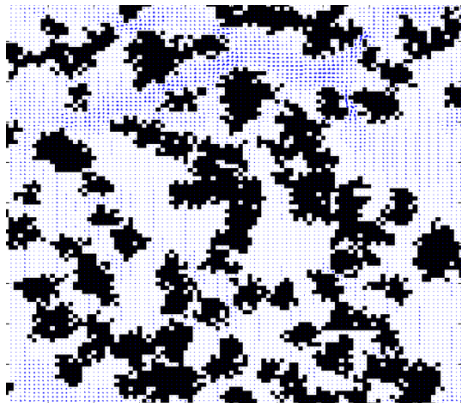
### 3.3. Analysis of water permeation process

To study further the water infiltration internal flow characteristics of the real pore structure of the aerated block, the water infiltration process of the two-dimensional mesoscopic model with porosities of 65, 70, and 75 % was calculated by LBM numerical values.

Figures 9–14 are the velocity vector and velocity distribution vectographs of the reconstructed two-dimensional mesoscopic model under a constant inlet water pressure ( $P = 150$  Pa) with a mesh size of  $100 \times 100$ . These figures below show that at the initial stage of the pressure flow into the model ( $1000 \delta_t$ ), the flow velocity is distributed, but the flow direction basically follows the rule of «large pore inflow area». When the seepage is stable, the distribution of the flow velocity tends to be stable and, in the whole model, presents an obvious law, that is, the flow velocity in the through channel is greater. Simultaneously, several stable seepage channels are formed, namely, the «dominant channels» of seepage, and these «dominant channels» are mainly located in areas with good connectivity. In practical engineering, these «dominant passages» may be the easily seepage points on the wall. Therefore, studying the formation law and location of these passages to judge the seepage law of the wall and conducting the work of leakage prevention and repair of the wall have obvious engineering significance.

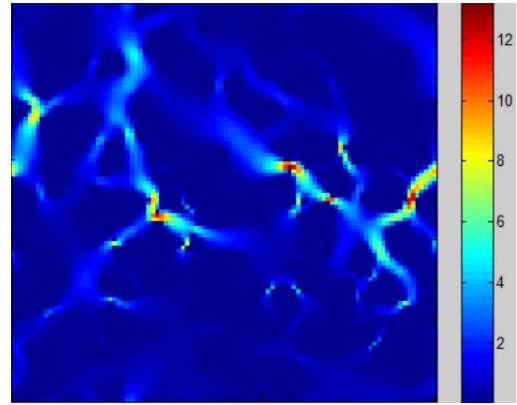


(a) Velocity vectograph at  $1000 \delta_t$



(b) Velocity vectograph of steady flow

**Figure 9. Velocity vectograph in aerated block ( $n = 65\%$ ).**

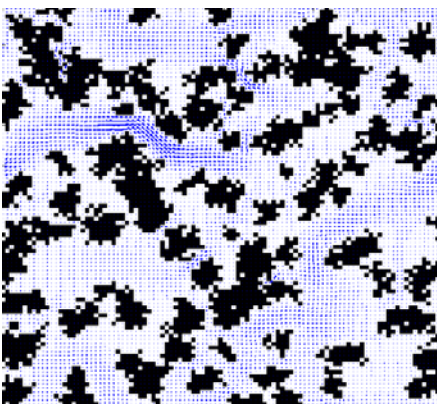


(a) Velocity distribution at  $1000 \delta_t$

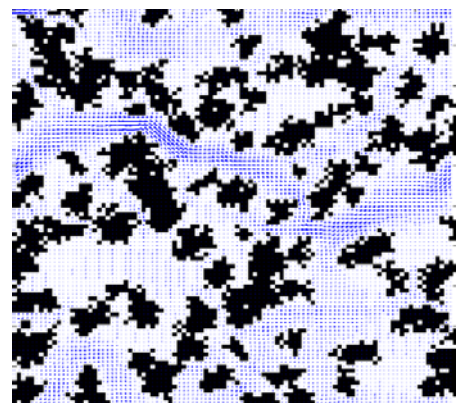


(b) Velocity distribution of steady flow

**Figure 10. Velocity distribution in aerated block ( $n = 65\%$ ).**

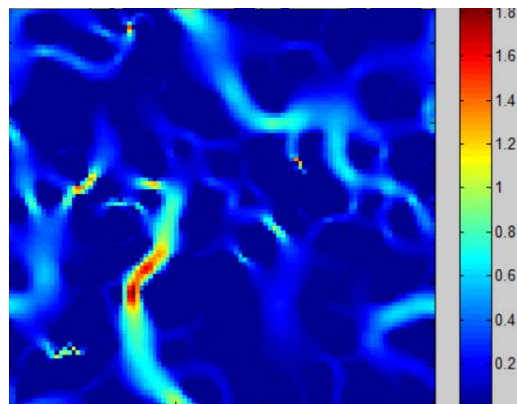


(a) Velocity vectograph at  $1000 \delta_t$

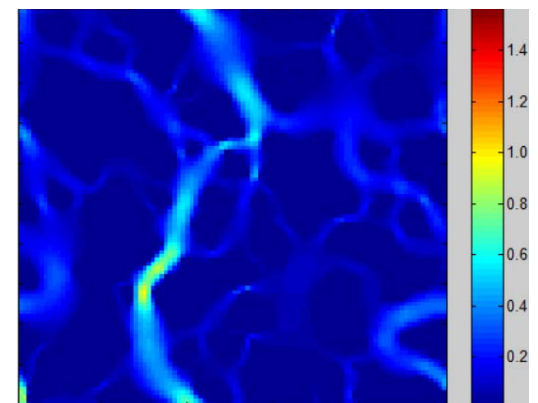


(b) Velocity vectograph of steady flow

**Figure 11. Velocity vectograph in aerated block ( $n = 70\%$ ).**

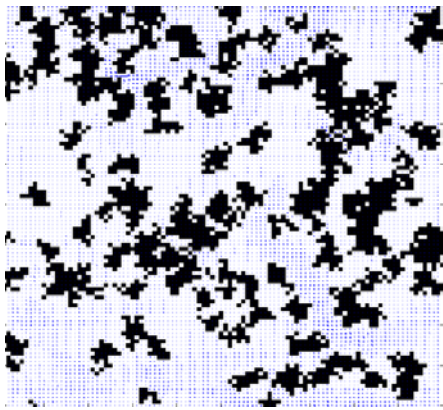
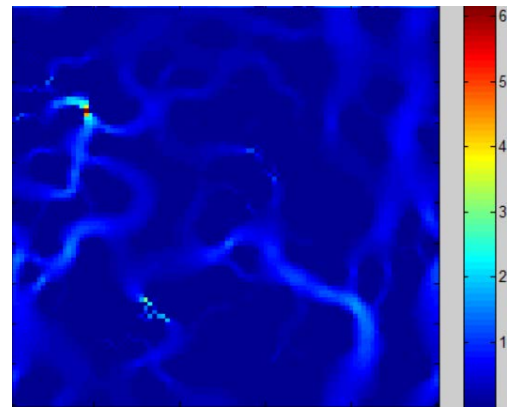
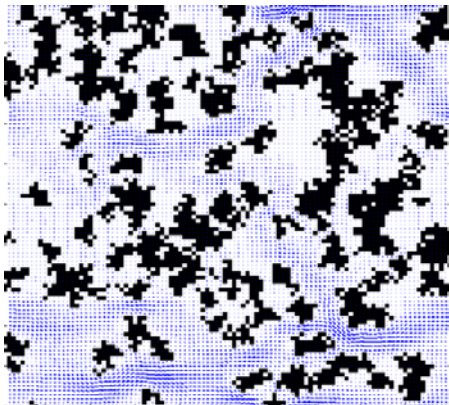


(a) Velocity distribution at  $1000 \delta_t$

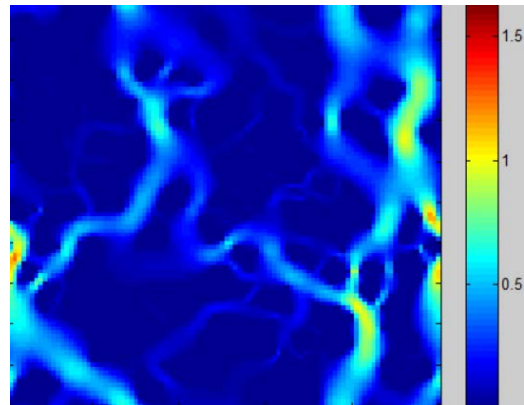


(b) Velocity distribution of steady flow

**Figure 12. Velocity distribution in aerated block ( $n = 70\%$ ).**

(a) Velocity vectograph at  $1000\delta_t$ (a) Velocity distribution at  $1000\delta_t$ 

(b) Velocity vectograph of steady flow



(b) Velocity distribution of steady flow

**Figure 13. Velocity vectograph  
in aerated block ( $n = 75\%$ ).**

**Figure 14. Velocity distribution  
in aerated block ( $n = 75\%$ ).**

#### 4. Conclusion

Based on the LBM, a stochastic porous medium model was used to simulate the water infiltration process inside an autoclaved aerated concrete block. The following are the conclusions derived from this study:

1. When the micro-model of an autoclaved aerated concrete block was reconstructed by the QSGS, the pore structure of the model could be controlled by adjusting the porosity and initial growth nucleus distribution probability, and a two-dimensional micro-model resembling a real aerated block could be established.
2. When the inlet water pressure was 150 Pa and mesh size was  $100 \times 100$ , the permeability coefficient of the reconstructed two-dimensional mesoscopic model resembled that of the autoclaved aerated concrete block obtained from the experiment.
3. When the porosity of the two-dimensional mesoscopic model was in the range of 65–80 %, its permeability coefficient increased with increased porosity and effectively satisfied the linear relationship.
4. The water infiltration process inside the aerator block was shown to have an effective relationship with its pore connectivity. The water flow mainly flowed to the well-connected pore channel, and the flow velocity was greater in the through channel.

#### 5. Acknowledgements

The authors would like to thank the Zhejiang Basic Public Welfare Research Project (LGF8E080016) and China Association for Engineering Construction Standardization for supporting this research project.

#### References

1. Jerman, M., Keppert, M., Vyborny, J., Cerny, R. Hygric, thermal and durability properties of autoclaved aerated concrete. *Construction and Building Materials*. 2013. Vol. 41. Pp. 352–359.
2. Schoendube, T., Rashid, S., Carrigan, S., Schoch, T., Kornadt, O. Autoclaved aerated concrete: Influence of heat storage capacity on thermal performance and thermal comfort. *Mauerwerk*. 2018. 22(5). Pp. 297–304.
3. Pukhkal, V.A., Mottaeva, A.B. FEM modeling of external walls made of autoclaved aerated concrete blocks. *Magazine of Civil Engineering*. 2018. 81(5). Pp. 203–212.

4. Pilon, B.S., Tyner, J.S., Yoder, D.C., Buchanan, J.R. The effect of pervious concrete on water quality parameters: a case study. *Water*. 2019. 11(2).
5. Fu, J., Zhou, Q.S., Ye, J.B. Summary of test methods for wall impermeability and design of test equipment. *Wall Materials Innovation & Energy Saving in Buildings*. 2017. No. 12. Pp. 30–34. (Chinese).
6. Wang, H., Su, Y., Zhao Z., Wang W., Sheng G., Zhan S. Apparent permeability model for shale oil transport through elliptic nanopores considering wall-oil interaction. *Journal of Petroleum Science and Engineering*. 2019. Vol. 176. Pp. 1041–1052.
7. Hazlett. Simulation of capillary-dominated displacements in microtomographic images of reservoir rocks. *TransPorousMedia*. 1995. No. 20. Pp. 21–35.
8. Degruyter, W., Burgisser, A., Bachmann, O., Malaspina, O. Synchrotron X-ray microtomography and lattice Boltzmann simulations of gas flow through volcanic pumices. *Geosphere*. 2010. 6(6). Pp. 470–481.
9. Qian, J.Y., Li, Q., Xuan, Y.M., Yu, K. Application of Lattice-Boltzmann Scheme on Determining Flow Parameters of Porous Media. *Journal of Engineering Thermophysics*. 2004. 25(4). Pp. 655–657. (Chinese).
10. Luo, Z.X., Qiu, Y.J., Yu, H.Q. Computational Modeling of Flows in Random Porous Media using Lattice Boltzmann Method. *Journal of Southwest Jiaotong University*. 2014. 49(1). Pp. 93–96. (Chinese).
11. Li, J.Z., Zhao, Z.G., Tan, Y.L., Yang, Z.L., Song, L.L. Method of LBM for Isotropy Porous Medium of Permeability Calculation. *Coal Technology*. 2015. 34(8). Pp. 138–140. (Chinese).
12. Cui, G.Z., Shen, L.F., Wang, Z.L. Numerical simulation of mesoscopic seepage field of soil CT scanned slice based on lattice Boltzmann method. *Rock and Soil Mechanics*. 2016. 37(5). Pp. 1497–1502.
13. Shen, L.F., Wang, Z.L., Li, S.J. Numerical simulation for mesoscopic seepage field of soil based on lattice Boltzmann method at Rev scale. *Rock and Soil Mechanics*. 2015. 36. Pp. 689–694.
14. Fan, H., Zheng, H. MRT-LBM-based numerical simulation of seepage flow through fractal fracture networks. *Science China-Technological Sciences*. 2013. 56(12). Pp. 3115–3122.
15. Wang, M., Pan, N. Numerical analyses of effective dielectric constant of multiphase micro-porous media. *Journal of Applied Physics*. 2007. 101(11). Pp. 114102-1–114120-8.
16. Qian, Y.H., Humieres, D.D., Lallemand, P. Lattice BGK models for navier-stokes equation. *Europhysics Letters*. 1992. 17(6). Pp. 479–484.
17. Akai, T., Bijeljic, B., Blunt, M.J. Wetting boundary condition for the color-gradient lattice Boltzmann method: Validation with analytical and experimental data. *Advances in Water Resources*. 2018. Vol. 116. Pp. 56–66.
18. Chapman, S., Cowling, T.G. *The mathematical theory of nonuniform gases: an account of the kinetic theory of viscosity, thermal conduction and diffusion in gases*. 3rd ed. Cambridge: Cambridge University Press. 1970.
19. Stobiac, V., Tanguy, P.A., Bertrand, F. Boundary conditions for the lattice Boltzmann method in the case of viscous mixing flows. *Computers & Fluids*. 2013. Vol. 73. Pp. 145–161.
20. Chai, Z.H., Guo, Z.L., Shi, B.C. Prediction of permeability in porous media with multi-relaxation-time lattice Boltzmann method. *Journal of Engineering Thermophysics*. 2010. No. 1. Pp. 107–109. (Chinese)
21. Zhou, Q.S. Study on permeability of autoclaved aerated concrete block and the wall. Hangzhou: Zhejiang Sci-Tech University. 2018. (Chinese)
22. Korniyenko, S.V., Vatin, N.I., Gorshkov, A.S. Thermophysical field testing of residential buildings made of autoclaved aerated concrete blocks. *Magazine of Civil Engineering*. 2016. 64(4). Pp. 10–25. DOI: 10.5862/MCE.64.2
23. Fedosov, S.V., Romyantseva, V.E., Krasilnikov, I.V., Konovalova, V.S., Evsyakov, A.S. Mathematical modeling of the colmatation of concrete pores during corrosion. *Magazine of Civil Engineering*. 2018. 83(7). Pp. 198–207. doi: 10.18720/MCE.83.18
24. Zhu, M.G., Wang, H., Liu, L.L., Ji, R., Wang, X.D. Preparation and characterization of permeable bricks from gangue and tailings. *Construction and Building Materials*. 2017. Vol. 148. Pp. 484–491.

### **Contacts:**

*Fu Jun*, 13588717727; [fujun@zstu.edu.cn](mailto:fujun@zstu.edu.cn)

*Yu Yue*, +8617364522496; [2206105018@qq.com](mailto:2206105018@qq.com)

*Ye JiaBin*, 15757124083; [1640092012@qq.com](mailto:1640092012@qq.com)

© Jun, F., Yue, Y., JiaBin, Y., 2019



DOI: 10.18720/MCE.89.10

## Coordinate functions quadratic approximation in V.I. Slivker's semi-shear stability theory

**V.A. Rybakov, V.V. Lalin, S.S. Ivanov, A.A. Azarov\***

*Peter the Great St. Petersburg Polytechnic University, St. Petersburg, Russia*

\* E-mail: [alexio009@mail.ru](mailto:alexio009@mail.ru)

**Keywords:** thin-walled bars, Slivker's semi-shear theory, stability theory, stability functional, Hermite polynomial, coordinate functions

**Abstract.** The loss of bearing capacity of some compressed self-framing metal structures elements occurs with a general buckling and for some of them there is no analytical solution. That is why consideration of the problem variational statement and its numerical solution is particular interesting. In this study, the stiffness and geometric stiffness matrices were obtained for Hermite polynomials quadratic variation that approximate the functions of the twist angle and deplanation functions. The dependences of the critical load on the number of finite elements for different geometric and kinematic boundary conditions are obtained. The inconsistency of the approximation by forms linear functions is shown in comparison with the quadratic approximation, which turns out to be optimal. The reason is that it almost immediately reaches the exact analytical solution, with a flexural-torsional form of buckling. For a purely torsional or flexural form of buckling, it is shown that functions of the twist angle and deplanation functions approximation for different Hermite polynomials does not give faster convergence.

### 1. Introduction

The evaluation of the building structures reliability is the main task in civil engineering. So, in [1] authors considered the applying of probabilistic method for bearing capacity criterion estimation. Planar frame rod model was presented in [2–3]. They determined forces equations in the most compressed elements, depending upon the amount of panels in grid. This has enabled elements strength [4] and general stability determination. However, this kind of Self-framing metal application in frame constructions must have a strict evidence. So in [5] they showed the benefits of using Self-framing metal for pitched roofs major repairs.

In [6] they analyzed buckling modes depending on various cases of the rod stress state and its geometrical and physical characteristics. Stability losses bending modes of axially-loaded bars depend on the face sections stiffness correlation. After the study of flexural-torsional stability losses modes of the non-axially compressed, variable stiffness, constant chords width I-shaped bars the following was found. Bending modes for bars with any unilateral end-point eccentricity combination and same chords slopes are not differ significantly; they might be taken to be equal. However, torsional modes are very different, they depend on the chords slopes. The study of bending-torsional buckling modes of variable stiffness non-axially compressed I-shaped beams which have different chords width and high, showed: modes depend on chord slope and narrowing combination. Constraint of warping impact on the critical force and the buckling mode. In [7], the deformation calculation and eccentric stability with eccentricity around two axes, compressed combined section bars, taking into account the warping links, were investigated. This study is based on the equations proposed by E.A. Beilin. The differential equations system solution by combining exact integration methods with the Bubnov-Galerkin's method with exact satisfaction of different boundary conditions shows us the reason to use a Self-framing metal bar compressed with a biaxial eccentricity. It is confirmed that in the particular case of the cross section geometry and the application of a longitudinal load, a bifurcation of the equilibrium modes is possible and the problem of compression with biaxial eccentricity in general form is not bifurcation. The problem of deformation and calculation for the arbitrary profile bar stability of with warping

Rybakov, V.A., Lalin, V.V., Ivanov, S.S., Azarov, A.A. Coordinate functions quadratic approximation in V.I. Slivker's semi-shear stability theory. Magazine of Civil Engineering. 2019. 89(5). Pp. 115–128. DOI: 10.18720/MCE.89.10

Рыбаков В.А., Лалин В.В., Иванов С.С., Азаров А.А. Квадратичная аппроксимация функций форм в полусдвиговой теории устойчивости В.И. Сливкера // Инженерно-строительный журнал. 2019. № 5(89). С. 115–128. DOI: 10.18720/MCE.89.10



bonds distributed along the length is investigated, and a change in displacements and forces is revealed depending on the compliance of the warping links. A natural study of combined profile warping connections bars constrained torsion was carried out. The difference between experiment and the analytical solution is 16 %. Methods for approximating the local and general buckling modes and cross section stability, with perforations, were provided in [8–9]. According to the results, the total loss of stability of elements with holes can be approximated by applying a "weighted-average" approach in determining the geometric characteristics of the section. The loss of the local shape of the stability of elements with holes is approximated using careful modifications of the models of the end strips of the cross section. Since the hole effect is different, in each case of buckling new model is required. In [10], the stability of the cross-sectional shape depending on the load is investigated using the example of monosymmetric I-beams. According to the results, the nature of buckling changes with a change in the length of the monosymmetric I-beam. In [11–12], the features of determining the bearing capacity of Self-framing metal structures are considered using the North American design standards and Eurocode 3. A loss of local stability in the both standards is taken into account equally, by the effective cross section. These standards are based on the methods for determining the parts of the section that are turned off from work because of the secondary buckling.

Works on numerical methods for calculating Self-framing metal bars.

The practical contribution was made in the works [13–15], where, based on the core model of calculation, analytical solutions for the displacement functions and internal force factors according to the semi-shear theory by V.I. Slivker were given. Solutions are given for three most popular structures that are often encountered in practice with kinematic boundary conditions given in the paper, i.e. practically determine the field of the stress-strain state (SSS). Finite elements of three types are constructed for the numerical solution of the constrained torsion of Self-framing metal bars problem in a variation formulation using the Ritz method with approximating polynomials of the chosen order according to V.I. Slivker's semi-shear theory. Iterative calculations were carried out, and then recommendations were given on choosing the sizes of finite elements depending on the type of the finite element and its interpolation polynomials. A database was created for correlation of the open and / or closed profile form for displacement and internal force factors.

The system of equations of the dynamics [16] of a Self-framing metal bar for the theory by V.I. Slivker was derived. In this system: one equation describes only longitudinal vibrations, while the remaining system of joint equations describes flexural-torsional warping oscillations. The dispersion dependences and phase velocities of torsional-warping waves in bisymmetric. Self-framing metal bar was analyzed according to the theory by V.I. Slivker. As a consequence, it was possible to conclude about the second optical dispersion branch, which, according to analysis of the eigenmodes of oscillations, corresponds to high-frequency warping oscillations. The formula was obtained that approximates the frequency of warping oscillations and the formula that determines the lowest frequency. Also matrices of masses were agreed, which differ in the type of displacement functions approximation, the twist angle functions of the warping measures for solving static problems with any kinematic boundary conditions. It certainly has great practical use. The automated algorithm has been developed for solving the spatial structures of Self-framing metal elements of both a closed and open profile in a dynamic formulation.

In the paper [17–18], stiffness matrices for various types of approximation of displacement functions with different numbers of freedom degrees of finite elements were determined. The greatest value in the operation of structures is the justification for taking into account nodal stiffness, compliance, or taking into account initial imperfections when calculating Self-framing metal bars for strength and stability. For example, [19] is about taking into account the initial imperfections of tubular nodal on their bearing capacity. The results showed the possibility of neglecting the negative effects caused by geometric imperfections during the operation of the structure. Influence of knot stiffness on the Self-framing metal rods stability were considered in [20]. The influence of the torsional stiffness of the beam-wall connection and the dependence of these characteristics on the number of floors of the rack were noted. In fact, the nodal mates of crossbars with columns occupy some intermediate value, which has a certain compliance, the magnitude of which is influenced by the constructive nodal solution. The work [21] shows the need to use the scheme with nodes that perceive some of the bending moments.

In [22], the bifurcation stability problem was solved numerically, much of which was written on solving it, including [23–25], a thin-walled rod on the Vlasov's theory and analytically on the Euler's theory. A significant difference was revealed in the value of the critical load according to two theories, a greater value is obtained by numerical calculation using the V.Z. Vlasov's no-slip theory.

In [26] they consider the stability of straightened from the plane thin-walled cold-formed beams with two types of finite element models. They took into account the geometric nonlinearity and material properties which were built in the ABAQUS software package. Model with two elements: two beams, through panels and hot-rolled pipes. Model with one element: one beam, and the other component, which was designed using the appropriate boundary conditions. It was found that the results for the two models are similar, but the simplified model is certainly computationally more attractive. It was also found that strain hardening does not affect the behavior of cold-formed beams.

This research is a continuation of the work [27] on the application of the finite element method in solving problems of stability of thin-walled rods according to the semi-shear theory by V.I. Slivker [23, 24].

A stiffness matrix and a geometric stiffness matrix for a quadratic approximation of the torsion functions and the warping measure were obtained in this research. Several problems with different forms of buckling are considered, the problem domain is defined in which approximation of torsion functions and warping measures by quadratic functions are faster than approximation by linear Hermite polynomials used in [27].

## 2. Methods

Equilibrium stability functional of a squeezed-curved thin-walled rod according to a semi-shear theory by V.I. Slivker [27]:

$$S = \frac{1}{2} \int_0^L [GI_x \theta'^2 + GI_\beta (\theta' - \beta)^2 + EI_z \eta''^2 + EI_y \zeta''^2 + EI_\omega \beta'^2 + K \theta'^2 + N(\eta'^2 + \zeta'^2) + 2(M_\eta \eta'' - M_\zeta \zeta'') \theta] dx. \quad (1)$$

A detailed description of the functional integrand is presented in the previous article [27]:

Consider the  $i$ -th finite element of a thin-walled rod:

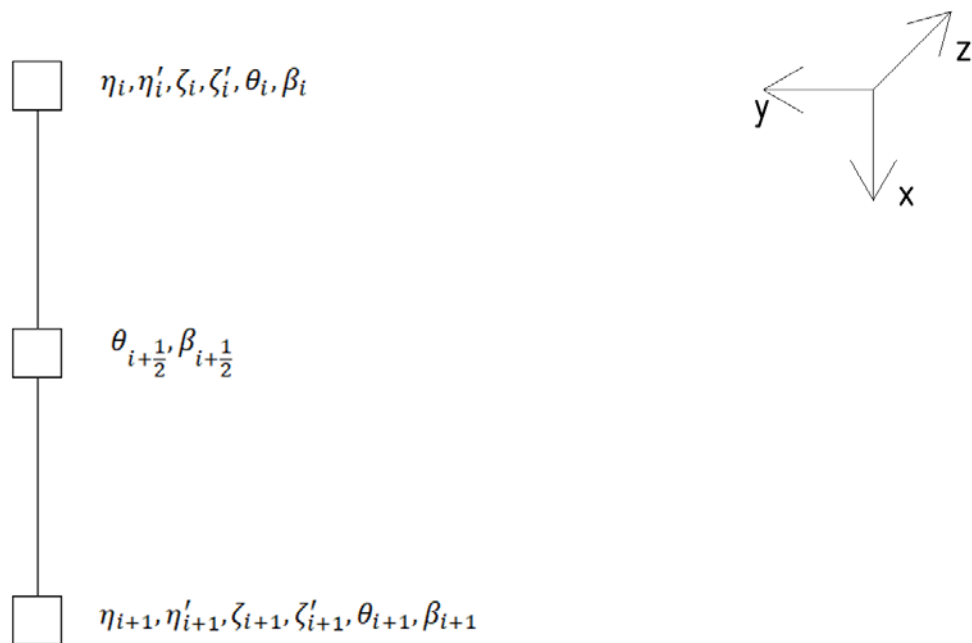


**Figure 1. Finite element with 14 degrees of freedom.**

Nodal displacements of a single finite element column:

$$U = \left( \eta_i \quad \eta'_i \quad \zeta_i \quad \zeta'_i \quad \theta_i \quad \beta_i \quad \theta_{i+1/2} \quad \beta_{i+1/2} \quad \eta_{i+1} \quad \eta'_{i+1} \quad \zeta_{i+1} \quad \zeta'_{i+1} \quad \theta_{i+1} \quad \beta_{i+1} \right)^T, \quad (2)$$

where  $\eta$  is bending center movement along  $Y$ ;

$\eta'$  is rotation angle about the axis  $Z$ ;

$\zeta$  is bending center movement along  $Z$ ;

$\zeta'$  is rotation angle about the axis  $Y$ ;

$\theta$  is torsion angle;

$\beta$  is warping measure in the corresponding nodes.

We write the functional V.I. Slivker in the matrix form, the process is given in [27]:

$$\begin{aligned}
S = & \frac{1}{2} \int_0^L \{ GI_x [U_\theta]^T [H']_{\theta\beta}^T [H']_{\theta\beta} [U_\theta] + GI_\beta [U_{\theta\beta}]^T [\Phi]^T [\Phi] [U_{\theta\beta}] + \\
& + EI_z [U_\eta]^T [H'']_{\eta\zeta}^T [H'']_{\eta\zeta} [U_\eta] + EI_y [U_\zeta]^T [H'']_{\eta\zeta}^T [H'']_{\eta\zeta} [U_\zeta] + \\
& + EI_\omega [U_\beta]^T [H']_{\theta\beta}^T [H']_{\theta\beta} [U_\beta] - P[(r_p^2 + e_z b_z + e_y b_y + \omega_A b_\omega) [U_\theta]^T [H']_{\theta\beta}^T \\
& [H']_{\theta\beta} [U_\theta] + [U_\eta]^T [H']_{\eta\zeta}^T [H']_{\eta\zeta} [U_\eta] + [U_\zeta]^T [H']_{\eta\zeta}^T [H']_{\eta\zeta} [U_\zeta] + \\
& + (e_z - z_p) ([U_\eta]^T [H'']_{\eta\zeta}^T [H]_{\theta\beta} [U_\theta] + [U_\theta]^T [H]_{\theta\beta}^T [H'']_{\eta\zeta} [U_\eta] - \\
& - (e_y - y_p) ([U_\zeta]^T [H'']_{\eta\zeta}^T [H]_{\theta\beta} [U_\theta] + [U_\theta]^T [H]_{\theta\beta}^T [H'']_{\eta\zeta} [U_\zeta]) ] dx
\end{aligned} \quad (3)$$

The columns of the nodal values of the transverse displacements are formed from the same elements as in our previous work [27]:

$$[U_\eta] = (\eta_i \quad \eta'_i \quad \eta_{i+1} \quad \eta'_{i+1})^T; \quad (4)$$

$$[U_\zeta] = (\xi_i \quad \xi'_i \quad \xi_{i+1} \quad \xi'_{i+1})^T. \quad (5)$$

Columns made up of twist angles and warping measures have a different look - they are added to an intermediate value in the middle of the finite element.

$$[U_\theta] = \left( \theta_i \quad \theta_{i+\frac{1}{2}} \quad \theta_{i+1} \right)^T; \quad (6)$$

$$[U_\beta] = \left( \beta_i \quad \beta_{i+\frac{1}{2}} \quad \beta_{i+1} \right)^T; \quad (7)$$

$$[U_{\theta\beta}] = \left( \theta_i \quad \beta_i \quad \theta_{i+\frac{1}{2}} \quad \beta_{i+\frac{1}{2}} \quad \theta_{i+1} \quad \beta_{i+1} \right)^T. \quad (8)$$

Hermite polynomials for the functions of transverse displacements are assumed to be similar to our previous work [27]:

$$H_1 = \frac{2}{l^3} x^3 - \frac{3}{l^2} x^2 + 1; \quad H_2 = \frac{x^3}{l^2} - \frac{2}{l} x^2 + x; \quad H_3 = -\frac{2}{l^3} x^3 + \frac{3}{l^2} x^2; \quad H_4 = \frac{x^3}{l^2} - \frac{1}{l} x^2. \quad (9)$$

The strings composed of the given Hermite polynomials looks like:

$$[H']_{\eta\xi} = \left( \frac{dH_1}{dx} \quad \frac{dH_2}{dx} \quad \frac{dH_3}{dx} \quad \frac{dH_4}{dx} \right); \quad (10)$$

$$[H'']_{\eta\xi} = \left( \frac{d^2H_1}{dx^2} \quad \frac{d^2H_2}{dx^2} \quad \frac{d^2H_3}{dx^2} \quad \frac{d^2H_4}{dx^2} \right). \quad (11)$$

The Hermite polynomials for the torsion and warping functions in this paper will be quadratic [27]:

$$H_5 = 1 - \frac{3x}{l} + \frac{2x^2}{l^2}; \quad H_6 = \frac{4x}{l} - \frac{4x^2}{l^2}; \quad H_7 = -\frac{x}{l} + \frac{2x^2}{l^2} \quad (12)$$

and the corresponding lines are denoted as:

$$[H]_{\theta\beta} = (H_5 \quad H_6 \quad H_7); \quad (13)$$

$$[H']_{\theta\beta} = \left( \frac{dH_5}{dx} \quad \frac{dH_6}{dx} \quad \frac{dH_7}{dx} \right); \quad (14)$$

$$[\Phi] = \left( \frac{dH_5}{dx} \quad -H_5 \quad \frac{dH_6}{dx} \quad -H_6 \quad \frac{dH_7}{dx} \quad -H_7 \right). \quad (15)$$

Calculating the integrals in (3) by grouping them in accordance with the vector of nodal displacements (2), we get:

$$S = \frac{1}{2} [U]^T ([K] - P[G])[U]. \quad (16)$$

$P$  is concentrated load applied at the end of the rod along the  $x$  axis at an arbitrary section point with coordinates  $(e_y, e_z)$ , matrixes  $[K]$  and  $[G]$  consist of matrices blocks, which we numbered in accordance with the numbering of nodes of a finite element (Figure 1):

$$[K] = \begin{pmatrix} [K_{i,i}] & [K_{i,i+1}] \\ [K_{i+1,i}] & [K_{i+1,i+1}] \end{pmatrix}, \quad [G] = \begin{pmatrix} [G_{i,i}] & [G_{i,i+1}] \\ [G_{i+1,i}] & [G_{i+1,i+1}] \end{pmatrix}, \quad (17)$$

where

$$K_{i,i} = \begin{pmatrix} \frac{12}{l^3} EI_z & \frac{6}{l^2} EI_z & 0 & 0 & 0 & 0 & 0 & 0 \\ \frac{6}{l^2} EI_z & \frac{4}{l} EI_z & 0 & 0 & 0 & 0 & 0 & 0 \\ 0 & 0 & \frac{12}{l^3} EI_y & \frac{6}{l^2} EI_y & 0 & 0 & 0 & 0 \\ 0 & 0 & \frac{6}{l^2} EI_y & \frac{4}{l} EI_y & 0 & 0 & 0 & 0 \\ 0 & 0 & 0 & 0 & \frac{7}{3l} GI_x + \frac{7}{3l} GI_\beta & -\frac{1}{2} GI_\beta & -\frac{8}{3l} GI_x - \frac{8}{3l} GI_\beta \\ 0 & 0 & 0 & 0 & -\frac{1}{2} GI_\beta & \frac{2l}{15} GI_\beta + \frac{7}{3l} EI_\omega & \frac{2}{3} GI_\beta \\ 0 & 0 & 0 & 0 & -\frac{8}{3l} GI_x - \frac{8}{3l} GI_\beta & \frac{2}{3} GI_\beta & \frac{16}{3l} GI_x + \frac{16}{3l} GI_\beta \end{pmatrix};$$

$$K_{i,i+1} = \begin{pmatrix} 0 & -\frac{12}{l^3} EI_z & \frac{6}{l^2} EI_z & 0 & 0 & 0 & 0 & 0 \\ 0 & -\frac{6}{l^2} EI_z & \frac{2}{l} EI_z & 0 & 0 & 0 & 0 & 0 \\ 0 & 0 & 0 & -\frac{12}{l^3} EI_y & \frac{6}{l^2} EI_y & 0 & 0 & 0 \\ 0 & 0 & 0 & -\frac{6}{l^2} EI_y & \frac{2}{l} EI_y & 0 & 0 & 0 \\ -\frac{2}{3} GI_\beta & 0 & 0 & 0 & 0 & 0 & \frac{1}{3l} (GI_x + GI_\beta) & \frac{1}{6} GI_\beta \\ -\frac{8}{3l} EI_\omega + \frac{l}{15} GI_\beta & 0 & 0 & 0 & 0 & 0 & -\frac{1}{6} GI_\beta & -\frac{l}{30} GI_\beta + \frac{1}{3l} EI_\omega \\ 0 & 0 & 0 & 0 & 0 & 0 & -\frac{8}{3l} EI_\omega - \frac{8}{3l} EI_\beta & -\frac{2}{3} GI_\beta \end{pmatrix};$$

$$K_{i+1,i+1} = \begin{pmatrix} \frac{16}{3l}EI_{\omega} + \frac{8l}{15}GI_{\beta} & 0 & 0 & 0 & 0 & \frac{2}{3}GI_{\beta} & -\frac{8}{3l}EI_{\omega} + \frac{l}{15}GI_{\beta} \\ 0 & \frac{12}{l^3}EI_z & -\frac{6}{l^2}EI_z & 0 & 0 & 0 & 0 \\ 0 & -\frac{6}{l^2}EI_z & \frac{4}{l}EI_z & 0 & 0 & 0 & 0 \\ 0 & 0 & 0 & \frac{12}{l^3}EI_y & -\frac{6}{l^2}EI_y & 0 & 0 \\ 0 & 0 & 0 & -\frac{6}{l^2}EI_y & \frac{4}{l}EI_y & 0 & 0 \\ \frac{2}{3}GI_{\beta} & 0 & 0 & 0 & 0 & \frac{7}{3l}(GI_x + GI_{\beta}) & \frac{1}{2}GI_{\beta} \\ -\frac{8}{3l}EI_{\omega} + \frac{l}{15}GI_{\beta} & 0 & 0 & 0 & 0 & \frac{1}{2}GI_{\beta} & \frac{2l}{15}GI_{\beta} + \frac{7}{3l}EI_{\omega} \end{pmatrix};$$

$$G_{i,i} = \begin{pmatrix} \frac{6}{5l} & \frac{1}{10} & 0 & 0 & -\frac{(e_z - z_p)}{l} & 0 & 0 \\ \frac{1}{10} & \frac{2l}{15} & 0 & 0 & -\frac{2}{3}e_z + \frac{2}{3}z_p & 0 & -\frac{2}{3}e_z + \frac{2}{3}z_p \\ 0 & 0 & \frac{6}{5l} & \frac{1}{10} & \frac{(e_y - y_p)}{l} & 0 & 0 \\ 0 & 0 & \frac{1}{10} & \frac{2l}{15} & \frac{2}{3}e_y - \frac{2}{3}y_p & 0 & \frac{2}{3}e_y - \frac{2}{3}y_p \\ -\frac{(e_z - z_p)}{l} & -\frac{2}{3}e_z + \frac{2}{3}z_p & \frac{(e_y - y_p)}{l} & \frac{2}{3}e_y - \frac{2}{3}y_p & \frac{7}{3l}c & 0 & -\frac{16}{6l}c \\ 0 & 0 & 0 & 0 & 0 & 0 & 0 \\ 0 & -\frac{2}{3}e_z + \frac{2}{3}z_p & 0 & \frac{2}{3}e_y - \frac{2}{3}y_p & -\frac{16}{6l}c & 0 & \frac{16}{6l}c \end{pmatrix};$$

$$G_{i,i+1} = \begin{pmatrix} 0 & -\frac{6}{5l} & \frac{1}{10} & 0 & 0 & \frac{(e_z - z_p)}{l} & 0 \\ 0 & -\frac{1}{10} & -\frac{l}{30} & 0 & 0 & \frac{(e_z - z_p)}{3} & 0 \\ 0 & 0 & 0 & -\frac{6}{5l} & \frac{1}{10} & -\frac{(e_y - y_p)}{l} & 0 \\ 0 & 0 & 0 & -\frac{1}{10} & -\frac{l}{30} & -\frac{(e_y - y_p)}{3} & 0 \\ 0 & \frac{(e_z - z_p)}{l} & -\frac{(e_z - z_p)}{3} & -\frac{(e_y - y_p)}{l} & \frac{(e_y - y_p)}{3} & \frac{2c}{6l} & 0 \\ 0 & 0 & 0 & 0 & 0 & 0 & 0 \\ 0 & 0 & \frac{2(e_z - z_p)}{3} & 0 & -\frac{2(e_y - y_p)}{3} & \frac{16c}{6l} & 0 \end{pmatrix};$$

$$G_{i+1,i+1} = \begin{pmatrix} 0 & 0 & 0 & 0 & 0 & 0 & 0 \\ 0 & \frac{6}{5l} & -\frac{1}{10} & 0 & 0 & -\frac{(e_z - z_p)}{l} & 0 \\ 0 & -\frac{1}{10} & \frac{2l}{15} & 0 & 0 & \frac{2}{3}e_z - \frac{2}{3}z_p & 0 \\ 0 & 0 & 0 & \frac{6}{5l} & -\frac{1}{10} & \frac{(e_y - y_p)}{l} & 0 \\ 0 & 0 & 0 & -\frac{1}{10} & \frac{2l}{15} & -\frac{2}{3}e_y + \frac{2}{3}y_p & 0 \\ 0 & -\frac{(e_z - z_p)}{l} & \frac{2}{3}e_z - \frac{2}{3}z_p & \frac{(e_y - y_p)}{l} & -\frac{2}{3}e_y + \frac{2}{3}y_p & \frac{7c}{3l} & 0 \\ 0 & 0 & 0 & 0 & 0 & 0 & 0 \end{pmatrix};$$

$$c = (r_p^2 + e_z b_z + e_y b_y + \omega_A b_\omega). \tag{18}$$

Matrices  $[K]$  and  $[G]$  are symmetric therefore equalities (19) are fulfilled:

$$[K_{i,i+1}] = [K_{i+1,i}]^T; \quad [G_{i,i+1}] = [G_{i+1,i}]^T. \tag{19}$$

### 3. Results and Discussion

For the numerical solution of the problem, we consider a thin-walled rods of open profile (warped (Figure 2) and non-warped (Figure 3)) and closed profile (Figure 4). Rod length  $L_1 = 5$  m for profile 1 and rod length  $L_{2,3} = 3$  m for profiles 2 and 3.

Kinematic boundary conditions:

In the first case:  $\eta_1 = \zeta_1 = \theta_1 = \eta_n = \zeta_n = \theta_n = 0$  (hinge support, prohibitive translational motion (non-axial longitudinal rods) и rotational motion relative to the rods longitudinal axis;

In the second case:  $\eta_1 = \eta'_1 = \zeta_1 = \zeta'_1 = \theta_1 = \beta_1 = 0$  (hard pinch at one end).

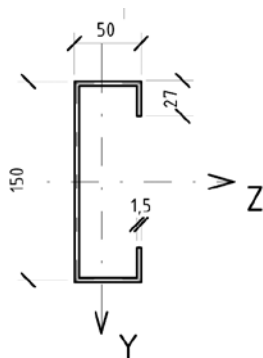


Figure 2. Shape 1.

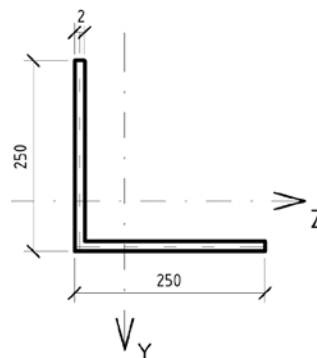


Figure 3. Shape 2.

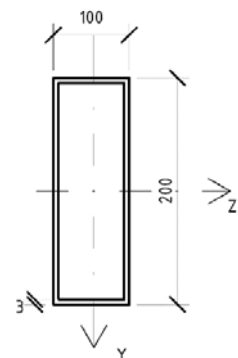


Figure 4. Shape 3.

Rod material - steel C245:

Physical characteristics of steel C245:  $E = 20600$  kN/cm<sup>2</sup>,  $G = 7920$  kN/cm<sup>2</sup>.

Table 1. Geometric characteristics of the rod section.

$I_z$	$I_y$	$I_x$	$I_\omega$	$I_\beta$	$e_z$	$e_y$	$z_p$	$y_p$	$b_\omega$	$b_z$	$b_y$	$r_p^2$
cm <sup>4</sup>	cm <sup>4</sup>	cm <sup>4</sup>	cm <sup>6</sup>	cm <sup>4</sup>	cm	cm	cm	cm	cm	cm	cm	cm <sup>2</sup>
18.767	152.964	0.034	1137	203	0	0	-2.8	0	0	8.253	0	45.5
651	651	0.133	0	0	0	0	0	0	0	0	0	130
947	324	745	1553	78	0	0	0	0	0	0	0	72

Solve the basic resolving stability equation for compressed rods:

$$\det([K] - P[G]) = 0. \quad (20)$$

Determine the smallest solution that corresponds to the critical force for the given number of FE and for given kinematic boundary conditions. The tables below compare the results obtained in the numerical solution of problems with different types of approximation to each other. The numerical solutions are compared with analytical solutions. Numerical solutions for linear approximation are obtained based on the results in [27].

**Table. 2 Magnitude of critical forces  $P^{ij}$  ( $i$  – shape,  $j$  – anchor) for two types of approximation of the functions of the twist angle and the  $\theta$  and  $\beta$  deplanation with a different number of FE.**

	2	4	8	16	32	64
$P_{lin}^{11}$ [27], kN	15.373	15.250	15.180	14.955	14.378	13.636
$P_{quad}^{11}$ , kN	13.548	13.154	13.065	13.044	13.0413	13.039
Analytical solutions $P^{11}$ , kN						
$P_{Euler}^{an}$ , kN				15.247		
$P_{Vlasov}^{an}$ , kN				13.039		
$P_{lin}^{12}$ [27], kN	3.817	3.815	3.813	3.808	3.797	3.785
$P_{quad}^{12}$ , kN	3.788	3.780	3.778	3.777	3.777	3.777
Analytical solutions $P^{12}$ , kN						
$P_{Euler}^{an}$ , kN				3.811		
$P_{Vlasov}^{an}$ , kN				3.777		
$P_{lin}^{21(22)}$ [27], kN				8.1028		
$P_{quad}^{21(22)}$ , kN						
Analytical solutions $P^{21(22)}$ , kN						
$P_{Euler}^{an}$ , kN				1469.146		
$P_{Vlasov}^{an}$ , kN				8.1028		
$P_{lin}^{32}$ [27], kN	183.076	182.988	182.983	182.983	182.983	182.983
$P_{quad}^{32}$ , kN	183.076	182.988	182.983	182.983	182.983	182.983
Analytical solutions $P^{32}$ , kN						
$P_{Euler}^{an}$ , kN				182.983		
$P_{Vlasov}^{an}$ , kN						
$P_{lin}^{31}$ [27], kN	737.436	732.305	731.954	731.931	731.930	731.930
$P_{quad}^{31}$ , kN	737.436	732.305	731.954	731.931	731.930	731.930
Analytical solutions $P^{31}$ , kN						
$P_{Euler}^{an}$ , kN				731.930		
$P_{Vlasov}^{an}$ , kN						

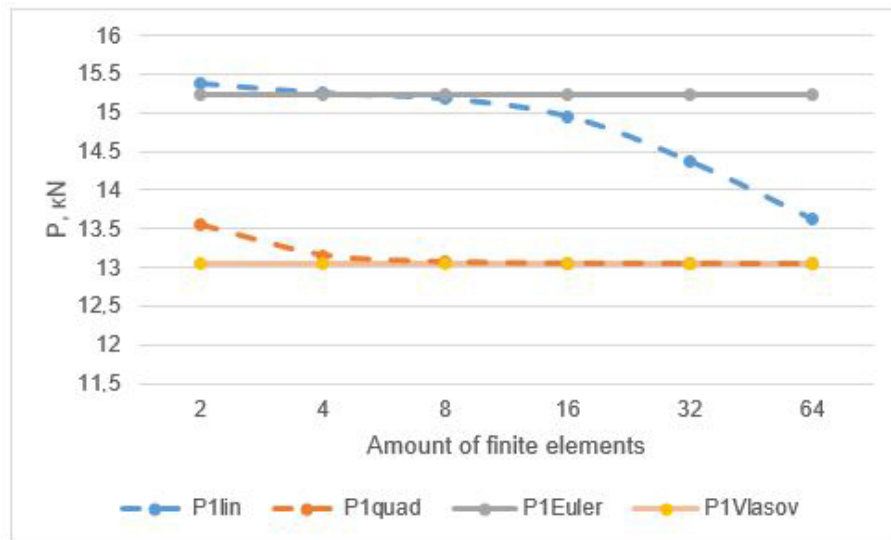


Figure 5. Graph of  $P_{11}$  versus the number of finite elements and the type of approximation of functions  $\theta$  and  $\beta$ .

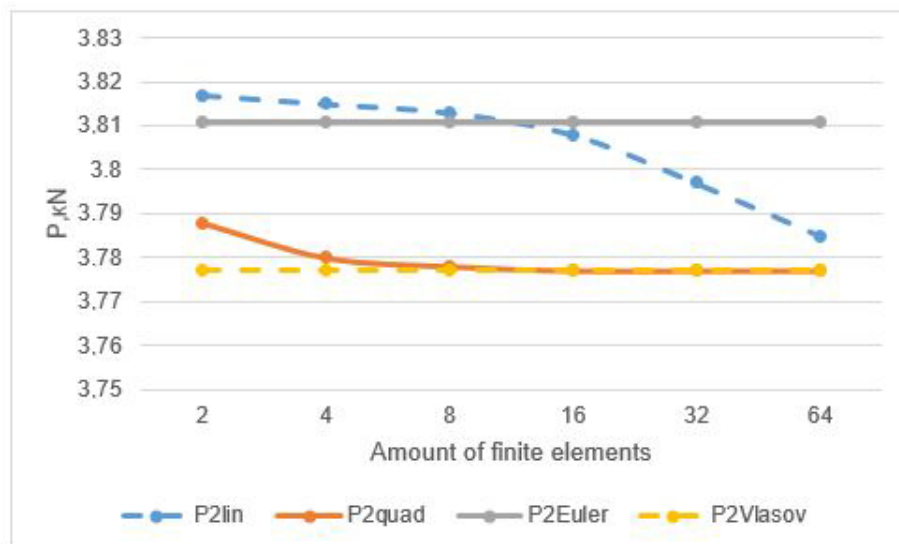


Figure 6. Graph of  $P_{12}$  versus the number of finite elements and the type of approximation of functions  $\theta$  and  $\beta$ .

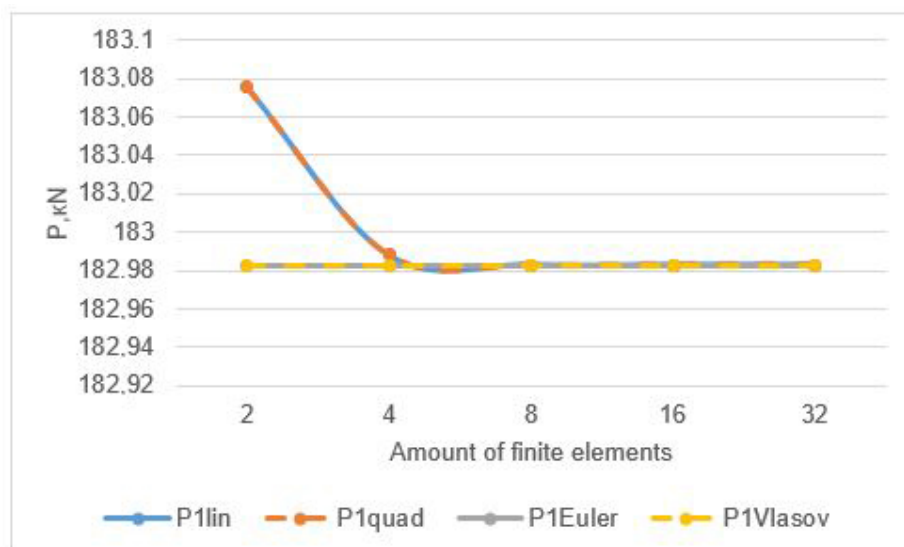
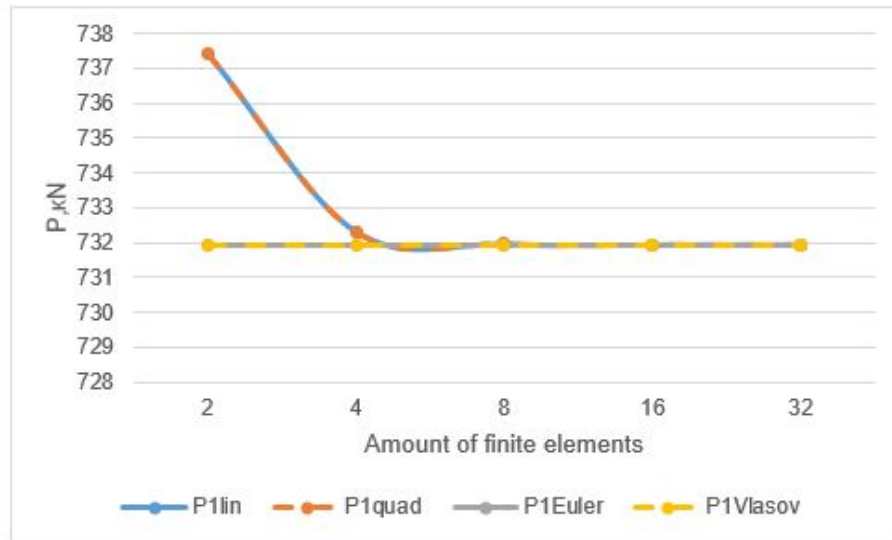


Figure 7. Graph of  $P_{32}$  versus the number of finite elements and the type of approximation of the functions  $\theta$  and  $\beta$ .



**Figure 8. Graph of  $P_{31}$  versus the number of finite elements and the type of approximation of the functions  $\theta$  and  $\beta$ .**

Determination of the critical force of a hinge-supported [28] rod having a profile 1:

$$(P_z - P)(P_y - P)(P_\omega - P) \cdot r_p^2 - y_p^2 \cdot P^2 \cdot (P_z - P) - z_p^2 \cdot P^2 \cdot (P_y - P) = 0, \quad (21)$$

where

$$P_z = \frac{\pi^2}{L^2} \cdot EI_z = 15.262 \text{ kN}; \quad P_y = \frac{\pi^2}{L^2} \cdot EI_y = 124.273 \text{ kN}; \quad P_\omega = \frac{\frac{\pi^2}{L^2} \cdot EI_\omega + GI_x}{r_p^2} = 26.220 \text{ kN}; \quad (22)$$

$r_p, y_p, z_p$  are polar radius of inertia relative to the center of the bend and coordinates of the center of the bend

From (21)  $P_{\min} = 13.039 \text{ kN}$ .

The critical forces obtained in the calculation of thin-walled rods having a profile of 1 under two types of kinematic boundary conditions correspond to the flexural-torsional form of buckling. Approximation by quadratic functions turns out to be faster in cases where the buckling has a flexural-torsional form. At 2 finite elements, the quadratic approximation reaches a value more precisely than at 64 finite elements, the linear approximation.

Analyzing the results of calculating the L-profile, we conclude that the values of the critical forces obtained by linear and quadratic approximations coincide in magnitude with the analytical value according to Vlasov [24] under any kinematic boundary conditions. The shape of the loss of stability in such a profile and at such geometric dimensions is a purely torsional (Figure 9). The value of the critical force according to Euler corresponds to the bending form of buckling and is given for reference.

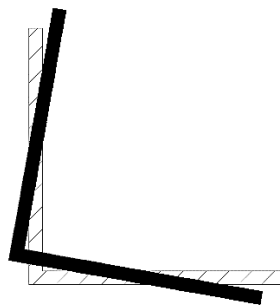


**Figure 9. Purely torsional form of stability loss of the rod(L-section).**

According to the results obtained, it is clear that the form of buckling of the box-shaped profile is purely bending. The order of approximation of the functions of the torsion forms and measures of deplanation is unimportant.

The critical load values were also compared with the Euler buckling loads. The results showed that taking warping into account reduces the critical load for the open cross sections (C-section, L-section) but doesn't have a significant impact on the closed cross-section (rectangular pipe).

The problem of spatial problems for systems of thin-walled rods has not been solved to date, and therefore the results obtained today cannot extend to spatial and even planar problems. However, as soon as the problem of turning the deplanation and bimoment measures is resolved, the results presented in the article will automatically be transferred to thin-walled rod systems.

#### 4. Conclusions

1. A geometric stiffness matrix of a thin-walled rod was obtained for a cubic approximation of the functions of transverse displacements and quadratic approximation of the torsion functions and deplanation.

2. With the help of the constructed matrix, using FEM the critical load was determined for the bar with both ends pinned and different types of the cross section (C-section, L-section and the rectangular pipe).

3. The critical load values were also compared with the Euler buckling loads. The results showed that taking warping into account reduces the critical load for the open cross sections (C-section, L-section) but doesn't have a significant impact on the closed cross-section (rectangular pipe).

4. Approximation by quadratic functions turns out to be faster in cases where the buckling has a flexural-torsional form. At 2 finite elements, the quadratic approximation reaches a value more precisely than at 64 finite elements, the linear approximation. In cases where the form of buckling is purely torsional or flexural, there are no advantages in no approximation method.

5. The constructed geometrical stiffness matrix is acceptable to solve buckling problems of the thin-walled bars for both open and closed cross sections.

#### References

- Pichugin, S.F. Reliability estimation of industrial building structures. Magazine of Civil Engineering. 2018. 83(7). Pp. 24–37. DOI: 10.18720/MCE.83.3.
- Kirsanov, M.N. Analytical calculation of the frame with an arbitrary number of panels. Magazine of Civil Engineering. 2018. 82(6). Pp. 127–135. DOI: 10.18720/MCE.82.12.
- Kirsanov, M.N. Installation diagram of the lattice truss with an arbitrary number of panels. Magazine of Civil Engineering. 2018. 81(5). Pp. 174–182. DOI: 10.18720/MCE.81.17.
- Trubina, D., Abdulaev, D., Pichugin, E., Rybakov, V., Garifullin, M., Sokolova, O. Comparison of the Bearing Capacity of LST- Profile Depending on the Thickness of its Elements. Applied Mechanics and Materials. 2015. Vol. 725–726. Pp. 752–757.
- Rybakov, V.A., Gamayunova, O.S. The stress-strain state of frame constructions elements from thin-walled cores. Construction of Unique Buildings and Structures. 2013. No. 7(12). Pp. 79–123.
- Askinazi, V.Yu. Prostranstvennaya ustoychivost stalnykh ramnykh konstruktivnykh peremennoy zhestkosti [Spatial stability of elements of steel frame structures of variable stiffness]. Doctorial Thesis. SPb., 2017. (rus)
- Belyy, A.G. Deformatsionnyy raschet i ustoychivost tonkostennykh prizmaticheskikh sterzhney proizvolnogo profilya szhatykh s dvukhosnym ekstsentsirizetom [Deformation calculation and stability of thin-walled prismatic rods in a compression profile compressed with a biaxial eccentricity]. PhD Thesis. SPb.: SPbGASU, 2000. 114 p. (rus)
- Moen, C.D., Schafer, B.W. Elastic buckling of cold-formed steel columns and beams with holes. Engineering Structures. 2009. Vol. 31. No. 12. Pp. 2812–2824.
- Vieira, R., Virtuoso, F., Pereira, E. Buckling of thin-walled structures through a higher order beam model. Computers & Structures. 2017. Vol. 180. Pp. 104–116.
- Samanta, A., Kumar, A. Distortional buckling in monosymmetric I-beams. Thin-walled structures. 2006. Vol. 44. No. 1. Pp. 51–56.
- Tuyev, D.S., Umnova, O.V. Vliyaniye mestnoy poteri ustoychivosti na nesushchuyu sposobnost lsk profilya [The effect of local buckling on the load-carrying capacity of a profile sheet]. In the collection: New information technologies in science. Collection of articles of the international scientific-practical conference. 2016. Pp. 177–184. (rus)
- Trubina, D.A., Kononova, L.A., Kaurov, A.A., Pichugin, Y.D., Abdulaev, D.A. Local buckling of steel cold-formed profiles under transverse bending. Construction of Unique Buildings and Structures. 2014. 19(4). (rus)
- Trouncer, A.N., Rasmussen, K.J.R. Flexural-torsional buckling of ultra light-gauge steel storage rack uprights. Thin-Walled Structures. 2014. Vol. 81. Pp. 159–174.
- Sastry, S.Y.B., Krishna, Y., Koduganti, A. Flexural buckling analysis of thin walled lipped channel cross section beams with variable geometry. International Journal of Innovative Research in Science. Engineering and Technology. 2014. Vol. 3. No. 6. Pp. 13484–13494.
- Rybakov, V.A. Primeneniye polusdvigovoy teorii V.I. Slivkera dlya analiza napryazhenno-deformirovannogo sostoyaniya sistem tonkostennykh sterzhney [Application of the semi-shear theory V.I. Slivker for the analysis of the stress-strain state of systems of thin-walled rods]. Phd Thesis. SPb., 2012. 184 p. (rus)
- Dyakov, S.F. Primeneniye polusdvigovoy teorii V.I. Slivkera k resheniyu zadach statiki i dinamiki tonkostennykh sterzhney [Application of the semi-shear theory V.I. Slivker to solve problems of statics and dynamics of thin-walled rods]. PhD Thesis. SPb., 2013. 147 p. (rus)
- Lalin, V., Rybakov, V., Sergey, A. The finite elements for design of frame of thin-walled beams. Applied Mechanics and Materials. 2014. Vol. 578–579. Pp. 858–863.
- Tyukalov, Yu.Ya. Refined finite element of rods for stability calculation. Magazine of Civil Engineering. 2018. 79(3). Pp. 54–65. DOI: 10.18720/MCE.79.6.

19. Garifullin, M., Bronzova, M., Heinisuo, M., Mela, K., Pajunen, S. Cold-formed RHS T joints with initial geometrical imperfections. Magazine of Civil Engineering. 2018. 80(4). Pp. 81–94. DOI: 10.18720/MCE.80.8 (rus)
20. Atavin, I.V., Melnikov, B.E., Semenov, A.S., Chernysheva, N.V., Yakovleva, E.L. Influence of stiffness of node on stability and strength of thin-walled structure. Magazine of Civil Engineering. 2018. 8(4). Pp. 48–61. DOI: 10.18720/MCE.80.5
21. Tusnina, V.M. Semi-rigid steel beam-to-column connections. Magazine of Civil Engineering. 2017. No. 5. Pp. 25–39. DOI: 10.18720/MCE.73.3.
22. Marchenko, T.V., Bannikov, D.O. Sopostavitelnyy analiz form poteri ustoychivosti tonkostennykh sterzhneykh elementov [Comparative analysis of the forms of buckling of thin-walled core elements]. Steel Construction. 2009. Vol. 15. No. 3. Pp. 177–188. (rus)
23. Perelmuter, A.V., Slivker, V.I. Structural equilibrium stability and related problems. Vol. 1. SCAD SOFT, 2007. 670 p. (rus)
24. Slivker, V.I. Structural mechanics. Variational basis. ASV, 2005. 736 p. (rus)
25. Perelmuter, A.V., Slivker, V.I. Design models of structures and the possibility of their analysis. Kiev: Steel, 2002. 600 p. (rus)
26. Haidarali, M.R., Nethercot, D.A. Finite element modelling of cold-formed steel beams under local buckling or combined local/distortional buckling. Thin-Walled Structures. 2011. Vol. 49. No. 12. Pp. 1554–1562.
27. Lalin, V.V., Rybakov, V.A., Dyakov, S.F., Kudinov, V.V., Orlova, Ye.S. Polusdvigovaya teoriya V.I. Slivkera v zadachakh ustoychivosti tonkostennykh sterzhney. Inzhenerno-stroitelnyy zhurnal. 2019. No. 3(87). Pp. 66–79. DOI: 10.18720/MCE.87.6
28. Vlasov, V.Z. Thin-walled elastic rods. Fizmatgis, 1959. 574 p.

**Contacts:**

*Vladimir Rybakov, +7(964)3312915; fishermanoff@mail.ru*

*Vladimir Lalin, +7(921)3199878; vllalin@yandex.ru*

*Sergey Ivanov, +7(904)5567654; serzikserzik@gmail.com*

*Artur Azarov, +7(905)2705646; alexio009@mail.ru*

© Rybakov, V.A., Lalin, V.V., Ivanov, S.S., Azarov, A.A., 2019



DOI: 10.18720/MCE.89.10

## Квадратичная аппроксимация функций форм в полусдвиговой теории устойчивости В.И. Сливкера

**В.А. Рыбаков, В.В. Лалин, С.С. Иванов, А.А. Азаров\***

*Санкт-Петербургский политехнический университет Петра Великого, Санкт-Петербург, Россия*

\* E-mail: [alexio009@mail.ru](mailto:alexio009@mail.ru)

**Ключевые слова:** тонкостенные стержни, полусдвиговая теория Сливкера, теория устойчивости, функционал устойчивости, полиномы Эрмита, функции формы

**Аннотация.** Поскольку потеря несущей способности некоторых сжатых элементов конструкций из ЛСТК происходит при общей потере устойчивости и для некоторых из них нет аналитического решения, представляется особо интересным рассмотрение вариационной постановки задачи и численное ее решение. В данном исследовании были получены матрицы жесткости и геометрической жесткости при квадратичной вариации полиномов Эрмита, аппроксимирующих функции угла закручивания и депланации. Получены зависимости критической нагрузки от количества КЭ для разных геометрических и кинематических граничных условий. Показана несостоятельность аппроксимации линейными функциями форм по сравнению с квадратичной аппроксимацией, которая оказывается оптимальной, так как практически сразу достигает точного аналитического решения, при изгибно-крутильной форме потери устойчивости. Для чисто крутильной или изгибной формы потери устойчивости показано, что аппроксимация функций угла закручивания и депланации при различных полиномах Эрмита не дает более быстрой сходимости.

### Литература

1. Пичугин С.Ф. Оценка надежности конструкций промышленных зданий // Инженерно-строительный журнал. 2018. № 7(83). С. 24–37. DOI: 10.18720/MCE.83.3.
2. Кирсанов М.Н. Аналитический расчет рамы с произвольным числом панелей // Инженерно-строительный журнал. 2018. № 6(82). С. 127–135. DOI: 10.18720/MCE.82.12.
3. Кирсанов М.Н. Монтажная схема решетчатой фермы с произвольным числом панелей // Инженерно-строительный журнал. 2018. № 5(81). С. 174–182. DOI: 10.18720/MCE.81.17.
4. Trubina D., Abdulaev D., Pichugin E., Rybakov V., Garifullin M., Sokolova O. Comparison of the Bearing Capacity of LST- Profile Depending on the Thickness of its Elements // Applied Mechanics and Materials. 2015. Vol. 725-726. Pp. 752–757.
5. Рыбаков В.А., Гамаюнова О.С. Напряженно-деформированное состояние элементов каркасных сооружений из тонкостенных стержней // Строительство уникальных зданий и сооружений. 2013. № 7(12). С. 79–123.
6. Аскинази В.Ю. Пространственная устойчивость элементов стальных рамных конструкций переменной жесткости: автореф. дис. ... канд. техн. наук. СПб., 2017.
7. Белый А.Г. Деформационный расчет и устойчивость тонкостенных призматических стержней произвольного профиля сжатых с двухосным эксцентриситетом: автореф. дис. ... канд. техн. наук. СПб.: СПбГАСУ, 2000. 114 с.
8. Moen C.D., Schafer B.W. Elastic buckling of cold-formed steel columns and beams with holes // Engineering Structures. 2009. Vol. 31. No. 12. Pp. 2812–2824.
9. Vieira R., Virtuoso F., Pereira E. Buckling of thin-walled structures through a higher order beam model // Computers & Structures. 2017. Vol. 180. Pp. 104–116.
10. Samanta A., Kumar A. Distortional buckling in monosymmetric I-beams // Thin-walled structures. 2006. Vol. 44. No. 1. Pp. 51–56.
11. Туев Д.С., Умнова О.В. Влияние местной потери устойчивости на несущую способность лстк профиля // Новые информационные технологии в науке: сб. статей Междунар. науч.-практ. конф.. 2016. С. 177–184.
12. Туев Д.С., Умнова О.В. Влияние местной потери устойчивости на несущую способность лстк профиля // Новые информационные технологии в науке: сб. статей Междунар. науч.-практ. конф., 2016. С. 177–184.
13. Trouncer A.N., Rasmussen K.J.R. Flexural-torsional buckling of ultra light-gauge steel storage rack uprights // Thin-Walled Structures. 2014. Vol. 81. Pp. 159–174.
14. Sastry S.Y.B., Krishna Y., Koduganti A. Flexural buckling analysis of thin walled lipped channel cross section beams with variable geometry // International Journal of Innovative Research in Science, Engineering and Technology. 2014. Vol. 3. No. 6. Pp. 13484–13494.
15. Рыбаков В.А. Применение полусдвиговой теории В.И. Сливкера для анализа напряженно-деформированного состояния систем тонкостенных стержней: дис. ... канд. техн. наук. СПб., 2012. 184 с.

16. Дьяков С.Ф. Применение полусдвиговой теории В.И. Сливкера к решению задач статики и динамики тонкостенных стержней: дис. ... канд. техн. наук. СПб., 2013. 147 с.
17. Lalin V., Rybakov V., Sergey A. The finite elements for design of frame of thin-walled beams // Applied Mechanics and Materials. 2014. Vol. 578-579. Pp. 858–863.
18. Тюкалов Ю.Я. Улучшенный стержневой конечный элемент для решения задач устойчивости // Инженерно-строительный журнал. 2018. № 3(79). С. 54–65. DOI: 10.18720/MCE.79.6.
19. Гарифуллин М.Р., Бронзова М.К., Хейнисуо М., Мэла К., Паюнен С. Сварные узлы холодногнутой труб прямоугольного сечения с начальными несовершенствами // Инженерно-строительный журнал. 2018. № 4(80). С. 81–94. DOI: 10.18720/MCE.80.8.
20. Атавин И.В., Мелников Б.Е., Семенов А.С., Чернышева Н.В., Яковлева Е.Л. Влияние жесткости узловых соединений на устойчивость и прочность тонкостенных конструкций // Инженерно-строительный журнал. 2018. 8(4). С. 48–61. DOI: 10.18720/MCE.80.5
21. Туснина В.М. Податливые соединения стальных балок с колоннами // Инженерно-строительный журнал. 2017. № 5(73). С. 25–39. DOI: 10.18720/MCE.73.3.
22. Марченко Т.В., Банников Д.О. Сопоставительный анализ форм потери устойчивости тонкостенных стержневых элементов // Металлические конструкции. 2009. Т. 15. № 3. С. 177–188.
23. Перельмутер А.В., Сливкер В.И. Устойчивость равновесия конструкций и родственные проблемы. Т. 1. М.: Изд-во СКАД СОФТ, 2007. 670 с.
24. Сливкер В.И. Строительная механика. Вариационные основы.: Изд-во АСВ, 2005. 736 с
25. Перельмутер А.В., Сливкер В.И. Расчетные модели сооружений и возможность их анализа. Киев: Изд-во Сталь, 2005. 600 с.
26. Naidarali M.R., Nethercot D.A. Finite element modelling of cold-formed steel beams under local buckling or combined local distortional buckling // Thin-Walled Structures. 2011. Vol. 49. No. 12. Pp. 1554–1562.
27. Лалин В.В., Рыбаков В.А., Дьяков С.Ф., Кудинов В.В., Орлова Е.С. Полусдвиговая теория В.И. Сливкера в задачах устойчивости тонкостенных стержней // Инженерно-строительный журнал. 2019. № 3(87). С. 66–79. DOI: 10.18720/MCE.87.6
28. Власов В.З. Тонкостенные упругие стержни. М.: Физматлит, 1959. 574 с.

**Контактные данные:**

*Владимир Александрович Рыбаков, +7(964)3312915; эл. почта: fishermanoff@mail.ru*

*Владимир Владимирович Лалин, +7(921)3199878; эл. почта: vllalin@yandex.ru*

*Сергей Сергеевич Иванов, +7(904)5567654; эл. почта: serzikserzik@gmail.com*

*Артур Александрович Азаров, +7(905)2705646; эл. почта: alexio009@mail.ru*

© Рыбаков В.А., Лалин В.В., Иванов С.С., Азаров А.А., 2019



DOI: 10.18720/MCE.89.11

## Method of forecasting the strength and thermal sensitive asphalt concrete

**S.Yu. Shekhovtsova<sup>a\*</sup>, E.V. Korolev<sup>a</sup>, S.S. Inozemtcev, J. Yu<sup>b</sup>, H. Yu<sup>b</sup>**

<sup>a</sup> National Research Moscow State Civil Engineering University, Moscow, Russia

<sup>b</sup> South China University of Technology, Guangzhou, China

\* E-mail: [SHehovtsovaSYU@mgsu.ru](mailto:SHehovtsovaSYU@mgsu.ru)

**Keywords:** pavement, asphalt concret, bitumen, interphase layer, rheology, extensive and intensive factors, strength, thermal sensitive

**Abstract.** A distinctive feature of composites is the manifestation of a synergistic effect due to the interaction of contacting substances at the interphase layer, and their intensity of interaction affects the volume properties of the composites. A study of the interphase layer of bitumen was carried out on the surface of the mineral powder. The proposed method according to the results of rheological tests allows calculating the thickness of the boundary layer in the binary system “asphalt – dispersed phase”. The dependence of the road composite strength on the layer thickness of structured asphalt is established: the strength of the composite increases with increasing thickness of the bitumen layer. Method of assessing the impact on the structural-sensitive properties of the composite extensive factor  $m$  – indicator reflecting the influence of the interface area and intensive factor  $n$  – indicator reflecting the influence of physicochemical effects at the interface is proposed. The extensive factor has a greater effect on the properties of SMA-20 with a quartz filler  $m/n > 2$ . There is a higher rate of decrease in the intensity of physicochemical interactions at the interface of the «oil bitumen-silica filler» phase as compared with the extensive factor. The different nature of the effect of temperature on the extensive and intensive factors is observed for SMA-20 with diatomite: as temperature increases, the factor  $m$  increases, whereas the opposite effect is observed for factor  $n$ . It indicates a positive effect of the specific surface of diatomite on the temperature properties of asphalt concrete.

### 1. Introduction

The purpose of actual research in the field of road construction is to establishing the processes of structure formation of materials at the micro level and the nanolevel. Bitumen is a microheterogeneous system consisting of complex structural units (size from 20 to 60 nm), which form a special structure with the addition of filler in the asphalt concrete composition [1]. Bituminous components adsorbed on the surface of the aggregate form bituminous films, which leads to the strong bonds formation in the structure of asphalt concrete. Basically oriented layers of bitumen are formed due to physical sorption.

General provisions on the relationship of the filler particle size and the dispersed bitumen system are considered in the work [2]. However, to determine the thickness of the films that form on the surface of the filler is not possible. It is known that the bitumen viscosity in the solvation shell (which is called «structured bitumen») is several orders of magnitude higher than the bulk bitumen viscosity. One of the first methods for determination of solvation shell thickness was proposed in [3]. The method is based on the classical model [4] for the viscosity of medium with non-interacting solid spherical particles. While such a model is only appropriate for diluted systems [5]. Methods of calculating the bitumen film thickness in asphalt concrete are proposed [6–9]. But the proposed methods allow to calculating of the relative values of bitumen film the thickness and do

---

Shekhovtsova, S.Yu., Korolev, E.V., Inozemtcev, S.S., Yu, J., Yu, H. Method of forecasting the strength and thermal sensitive asphalt concrete. Magazine of Civil Engineering. 2019. 89(5). Pp. 129–140. DOI: 10.18720/MCE.89.11

Шеховцова С.Ю., Королев Е.В., Иноземцев С.С., Ю Д., Ю Х. Методика прогнозирования прочности и термочувствительности асфальтобетона // Инженерно-строительный журнал. 2019. № 5(89). С. 129–140. DOI: 10.18720/MCE.89.11



not allow to calculating of the quantitative value of the adsorbed bitumen, on the value of which the asphalt concrete strength depends.

A feature of composites is the manifestation of a synergistic effect due to the interaction of contacting substances at the interface [10]. Often this interaction results in the formation of a layer with altered properties. It has been shown in the A.I. Rusanov's works [11, 12] that the investigated property of the dispersion medium varies with the layer thickness  $h$  according to the law:

$$\delta F = \frac{A}{h^3},$$

where  $A$  is a constant, which, depending on the intensity of the interaction at the interface, can be not only positive values, but also of negative ones; the “ $\delta$ ” sign means a relative change in property.

In [13], it was shown that the interaction intensity at the border of chapter can also affect the bulk properties of composites, and in [14] a method is proposed for estimating the level of layer strength change based on concentration dependencies of the composite strength. The importance this layer for the composite properties was emphasized by some researchers by the introduction of a separate name — “film phase” [15–17]. As a rule, an increase in the content of the film phase results in an increase in the indicators of the composite structural-sensitive properties [19–21]. Matrix material lack, which is accompanied by an increase in porosity and the formation of aggregates — particles of the dispersed phase not wetted by the matrix material — the composite strength is decreased with a formal increase in the concentration of the film phase [22–24].

There are no method of forecasting the strength and thermal sensitive asphalt concrete. In this work developing a quantitative assessment influence on the structural-sensitive properties of the composite extensive (an indicator characterizing at the border chapter of phases area) and intensive (an indicator characterizing the influence of physicochemical effects at the border chapter of phases) factors and establishing the mathematical dependence of the thickness structured bitumen layer with the road composite strength is relevant objective.

## 2. Method and Materials

The mineral fillers considered in the study are distinguished by their mineral composition and physico-mechanical properties. The filler from dolomite MP-1, diatomite of the Inzensky deposit, ground quartz sand  $S_u = 1000 \text{ m}^2/\text{kg}$  were considered. Mineral powder MP-1 meets the requirements of Russian state standard 52129-2003 “Mineral powder for asphalt and organic mixtures. Technical conditions”. Diatomite is a sedimentary rock with a highly porous structure formed by the shells (skeletons) of extinct diatoms, which mainly consist of silica hydrates with watering varying degrees. The chemical composition of mineral powders is presented in Table 1.

**Table 1. The chemical composition of mineral powders.**

Mineral material	Content, % by weight							
	SiO <sub>2</sub>	Al <sub>2</sub> O <sub>3</sub>	Fe <sub>2</sub> O <sub>3</sub>	CaO	MgO	CaCO <sub>3</sub> +MgCO <sub>3</sub>	SO <sub>3</sub>	LOI
MP-1	7.70	0.34	1.12	–	–	90.30	–	–
Diatomite	82.30	5.19	2.32	0.59	1.76	–	0.57	7.27
Quartz filler	98.72	0.67	0.07	0.33	0.21	–	–	–

The main physic-mechanical properties of mineral powders are presented in Table 2.

**Table 2. Physic-mechanical properties of mineral powders.**

Name of the indicator	Quartz filler	MP-1	Diatomite
Grain composition, % by weight smaller			
1.25 mm	100	100	100
0.315 mm	100	99.3	100
0.071 mm	95.2	75.5	97.7
Specific surface area, m <sup>2</sup> /kg	1002	461	1113
True density, g/cm <sup>3</sup>	2.73	2.82	2.11

In the course of work construction bitumen BND 60/90 produced by MOSCOW REFINERY with a softening temperature of 51 °C and a brittleness temperature of –20 °C was used.

The specific surface area and porosity of the mineral powders were determined by nitrogen adsorption at –196 °C according to the Brunauer-Emmett-Teller model (BET) using the pore structure analyzer NOVA 2200e Quantochrome.

The rheological properties of bitumen-mineral mixtures were estimated by viscosity at temperatures of 120, 130, 140 and 150 °C, which was determined using a rotary viscometer MCR 101, Anton Paar with a measuring cell – coaxial cylinders with a constant shear rate of 20 s<sup>-1</sup>.

Asphalt concrete strength indicators were determined on Samples-cylinders with a diameter and height of 71.7 mm made of crushed stone-mastic asphalt concrete mix SMA-20, corresponding to the requirements of Russian state standard 31015-2002.

The strength of asphalt concrete samples was determined under uniaxial compression at a speed of 3 mm/min at a temperature of 0, 20, 50 °C.

A experimental set and analytical methods has been used in work for quantifying the impact on the structural-sensitive properties of a composite of extensive and intensive factors, calculating the bitumen thickness on the surface of the mineral filler, for establishing a relationship describing the dependence of the thickness structured bitumen layer on the strength of the road composite.

### 3. Results and Discussion

It is obvious that the film phase content will depend on the area of the phase boundary and the intensity of interaction at this boundary. Formally, these factors influence on the composite property can be written as follows:

$$F = k_{geom} k_{fm} I_{geom}^m I_{fm}^n, \quad (1)$$

where  $I_{geom}$  is value characterizing the influence of the extensive factor;

$I_{fm}$  is value characterizing the influence of the intensive factor;

$k_i$  is conversion factors resulting in the units of measurement of the property under investigation  $F$ ;

$m$  and  $n$  are exponents characterizing the intensity of the influence of the factor.

To exclude additional studies related to the search for values  $k_i$ , the relative changes in properties should be analyzed:

$$\frac{F}{F_0} = \left( \frac{I_{geom}}{I_{geom,0}} \right)^m \left( \frac{I_{fm}}{I_{fm,0}} \right)^n \quad (2)$$

(here, the subscript "0" denotes the initial parameters).

An important condition for the application this approach is the choice of quantities that characterize the considered extensive ( $I_{geom}$ ) and intensive ( $I_{fm}$ ) factors. The extensive factor is related to the area of the phase interface and can be represented as a ratio:

$$\frac{I_{geom}}{I_{geom,0}} = \frac{S_f}{S_{f,0}}, \quad (3)$$

and the intensive factor is characterized by the intensity of the physicochemical interaction at the border of chapter and, following the work of A.I. Rusanov, can be estimated by the thickness of the layer  $h$ :

$$\frac{I_{fm}}{I_{fm,0}} = \frac{h_{fm}}{h_{fm,0}}, \quad (4)$$

where  $S_f$  is the area of the phase boundary «matrix material – dispersed phase»;

$h_{fm}$  is the layer thickness of the matrix substance located at the phases border and having properties which differ from similar ones in volume.

Hence the following relationship:

$$\frac{F}{F_0} = \left( \frac{S_f}{S_{f,0}} \right)^m \left( \frac{h_{fm}}{h_{fm,0}} \right)^n. \quad (5)$$

Calculation  $S_f$  by granulometric data is easy:

$$S_f = \sum_j S_{u,j} m_j, \quad (6)$$

where  $S_{u,j}$ ,  $m_j$  specific surface area and content  $j$ -th fraction of the dispersed phase.

Determination of  $h_{fm}$  is impossible to calculate (especially for complex molecular systems) and is an individual task. Several techniques for determining the thickness of the boundary layer are presented in [11]. It is advisable to apply the rheological method for dispersed systems «bitumen – dispersed phase». It is necessary to assume that an interphase layer is formed on the surface of the particles, consisting of the adsorption and kinetic layers: the kinetic layer characterizes the influence of the particle shape and viscosity of the dispersion medium, and the adsorption layer only the physicochemical dispersed phase activity.

Determining the interfacial layer thickness at the interface of the «bitumen – mineral powder» was carried out according to the method described in [25, 26] the volumetric degree range of mineral filling has been established by this method, at which A. Einstein law is fulfilled, and there is a possibility of calculation for the interfacial layer thickness. The volume content of the dispersed phase is formally increased by  $\Delta\varphi$ , when such a layer is formed. The equation of A. Einstein is represented as:

$$\eta_{ek} = \eta_o \left[ 1 + \alpha_o (\varphi_o + \Delta\varphi) \right] \text{ or } \eta_{ek} = \eta_u + \alpha_o \eta_o \Delta\varphi, \quad (7)$$

where  $\eta_u = \eta_o \left[ 1 + \alpha_o \varphi_o \right]$  is A. Einstein's equation [26];

$\eta_o$  is viscosity of the dispersion environment;

$\alpha_o$  is spherical particle shape factor ( $\alpha_o = 2.5$ );

$\varphi_o$  is filler volume share.

The increment of the filler volume share is equal to:

$$\Delta\varphi = \frac{\eta_{ek}(\varphi_o) - \eta_u}{\varphi_o \alpha_o}, \quad (8)$$

Hence the following relationship:

$$\varphi_i = N_f \frac{\pi}{6} d_f^3 \text{ and } N_f = N_{f,o}$$

we will have:

$$\Delta\varphi = \varphi_o \left[ \left( \frac{d_f}{d_{f,o}} \right)^3 - 1 \right].$$

Interfacial layer thickness is determined by replacing  $d_f = d_{f,o} + 2h$  and  $d_f = 6 / S_u \rho_f$ :

$$h = \frac{3}{S_u \rho_f} \left( \sqrt[3]{\frac{\eta_{ek}(\varphi_o) - \eta_o}{\varphi_o \alpha_o \eta_o} + 1} - 1 \right), \quad (9)$$

where  $\rho_f$  is dispersed phase material density;

$S_u$  is specific surface area of the dispersed phase.

Similarly, when taking into account the influence of the particle shape and the adsorption layer on the values of the coefficient  $\alpha$  ( $\alpha > \alpha_o$ ):

$$\left( \frac{d_f}{d_{f,o}} \right)^3 = \frac{1}{\alpha \varphi_o} \left( \frac{\eta_{ek}(\varphi_o)}{\eta_o} - 1 \right).$$

From here:

$$h = \frac{3}{S_u \rho_f} \left( \sqrt[3]{\frac{\eta_{ek}(\varphi_o)}{\eta_o} - 1} - 1 \right), \quad (10)$$

The similar formula is proposed in [12]:

$$h = \frac{10^4}{\rho_f S_u} \left( \frac{\alpha}{\alpha_m} - 1 \right), \quad (11)$$

where  $\alpha_m$  is coefficients calculated, respectively, on the basis of measuring the dispersed system viscosity under investigation and the model system “filler – environment”, in which the environment does not form at all or forms a solvation shell with negligible thickness on the surface.

The disadvantage of the presented technique is the assumption that the layers formation in different dispersion environments is identical, that is, the comparison in the system behavior is not carried out with the ideal system described by A. Einstein's equation, but with some model system. In addition, certain difficulties arise in the selection of a model dispersion environments (in this case, it is necessary to have an environment with a similar dependence of viscosity in the temperature range under study and lyophobic to the surface mineral component). The implementation of the specified requirements for the dispersion model environment allows to calculating thickness values of the adsorption layer of the dispersion environment.

When using formulas (9) and (10) with the assumption

$$h_a = h - h_k$$

( $h_a$  – absorption layer thickness;  $h_k$  – kinetic layer thickness):

$$h_a = \frac{3}{S_u \rho_f} \left( \sqrt[3]{\frac{\eta_{ek}(\varphi_o) - \eta_o}{\varphi_o \alpha_o \eta_o} + 1} - \sqrt[3]{\frac{\eta'_{ek}(\varphi_o) - \eta'_o}{\varphi_o \alpha_o \eta'_o} + 1} \right); \quad (12)$$

$$h_a = \frac{3}{S_u \rho_f} \left( \sqrt[3]{\frac{1}{\alpha \varphi_o} \left( \frac{\eta_{ek}(\varphi_o)}{\eta_o} - 1 \right)} - \sqrt[3]{\frac{1}{\alpha' \varphi_o} \left( \frac{\eta'_{ek}(\varphi_o)}{\eta'_o} - 1 \right)} \right), \quad (13)$$

where the index “ ’ ” is used for a model system.

The elimination of this deficiency of the method [25] is possible by the following way. The kinetic layer depends mainly on the dispersion environment viscosity and the particles shape of the dispersed phase. Clearly, dispersion environment viscosity decreases, when the temperature increases. When in the model system  $\eta_o \rightarrow 0$  (or for a multicomponent dispersion environment  $\eta_o \rightarrow \eta_{o,\min}$ , hence  $\eta_{o,\min}$  is viscosity of the highly mobile component) the kinetic layer thickness is  $h_k \rightarrow 0$ .

A. Einstein equation is being implemented in the range of the dispersed phase volume content  $\varphi$  [0; 0.05]; therefore, in the work [13], the calculation of layer thicknesses has been carried out with a volume filling degree of 2 %. As dispersed phases was considered mineral powder, the properties of which are presented in Table 3.

**Table 3. Mineral fillers properties.**

Parameters	Requirements of Russian state standard	Quartz filler	Limestone	Diatomite
Grading, % by weight less				
1.25 mm	Not less 100	100	100	100
0.315 mm	Not less 100	100	99	100
0.071 mm	From 70 to 80	95	76	98
Surface area, m <sup>2</sup> /kg	Not standardized	1002	461	1113
True density, g/cm <sup>3</sup>	Not standardized	2.73	2.82	2.11

The considered mineral powders differ in the specific surface area of the particles, which characterizes the potential area of the interface between the phases and bitumen, along which the physico-chemical interaction processes take place. The dispersed phase type and temperature also affect the system viscosity (Figure 1).

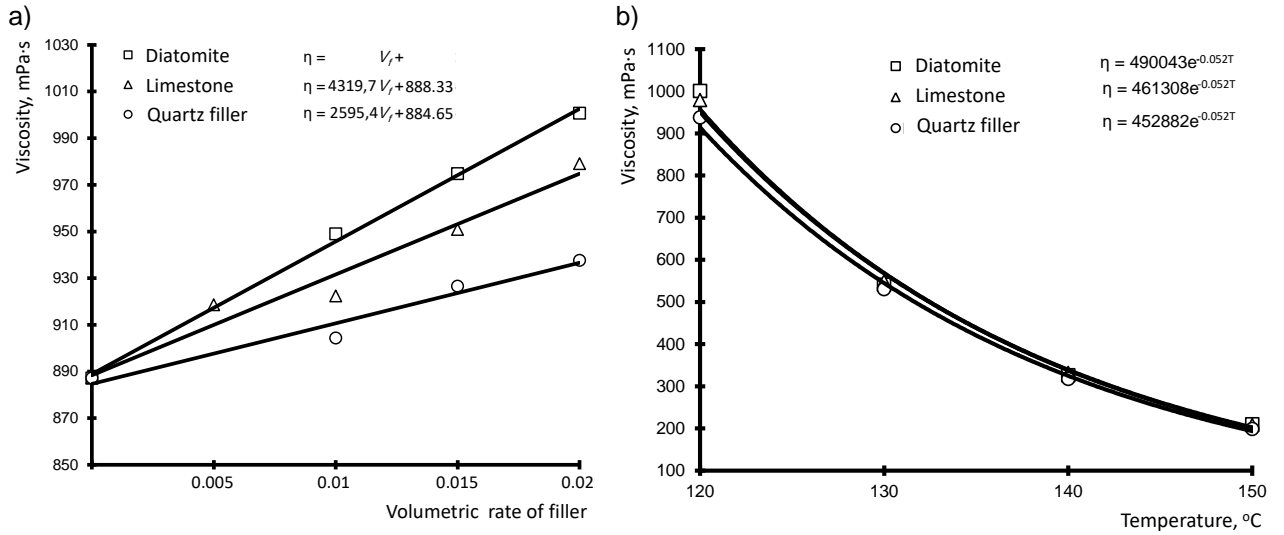


**Figure 1. Dependence of the dispersion system viscosity:**  
**a – from the degree of filling (at  $T = 120\text{ }^{\circ}\text{C}$ ); b – from temperature (at  $\phi = 0.02$ ).**

The equation of viscosity as a function of the degree of volumetric rate the approximation is:  $y = kx + b$  or according to A. Einstein equation  $\eta = \alpha\eta_0\phi + \eta_0$ , hence  $k = \alpha\eta_0$  and  $b = \eta_0$ , therefore, the angular coefficient characterizing the effect of the dispersed phase is equal to  $\alpha = k/b$ . The values of the coefficients are presented in Table 4.

**Table 4. The coefficients values of the equations of the viscosity of the dispersed system “bitumen-mineral powder” from the filling degree.**

Coefficient	Temperature, °C	Filler		
		Limestone	Diatomite	Quartz filler
$k$	120	4319.70	5252.90	2595.40
$b$		888.30	897.56	884.60
$\alpha$		4.86	5.85	2.93
$k$	130	2109.20	1585.30	1294.10
$b$		506.20	510.15	504.62
$\alpha$		4.17	3.11	2.56
$k$	140	1222.20	867.95	588.50
$b$		307.00	308.39	305.90
$\alpha$		3.98	2.81	1.92
$k$	150	687.60	775.50	305.94
$b$		194.50	195.36	193.88
$\alpha$		3.54	3.97	1.58

According to the obtained experimental dependences of the viscosity of the dispersed system “bitumen – mineral powder”, the calculations of layer thicknesses was make: by formulas (9) and (10) – total thickness, and by formulas (12) and (13) – adsorption layer (when conducting the experiment with dispersed the system “castor oil – mineral powder” selected the temperature at which the viscosity of castor oil would correspond to the viscosity of the melt of bitumen) (Tables 5 and 6).

**Table 5. The bitumen layers thickness on the surface of the mineral filler (at  $\alpha_0 = 2.5$ ).**

Filler	Total interfacial layer thickness by the formula (9)			
	120 °C	130 °C	140 °C	150 °C
Limestone	2.690	1.510	1.080	0.192
Diatomite	0.595	-1.708	-2.127	-1.342
Quartz filler	0.777	-0.037	-0.847	-1.661
Filler	Total interfacial layer thickness by the formula (12)			
	120 °C	130 °C	140 °C	150 °C
Limestone	2.690	1.510	1.080	0.192
Diatomite	0.732	-1.572	-1.991	-1.205
Quartz filler	0.790	-0.025	-0.834	-1.649

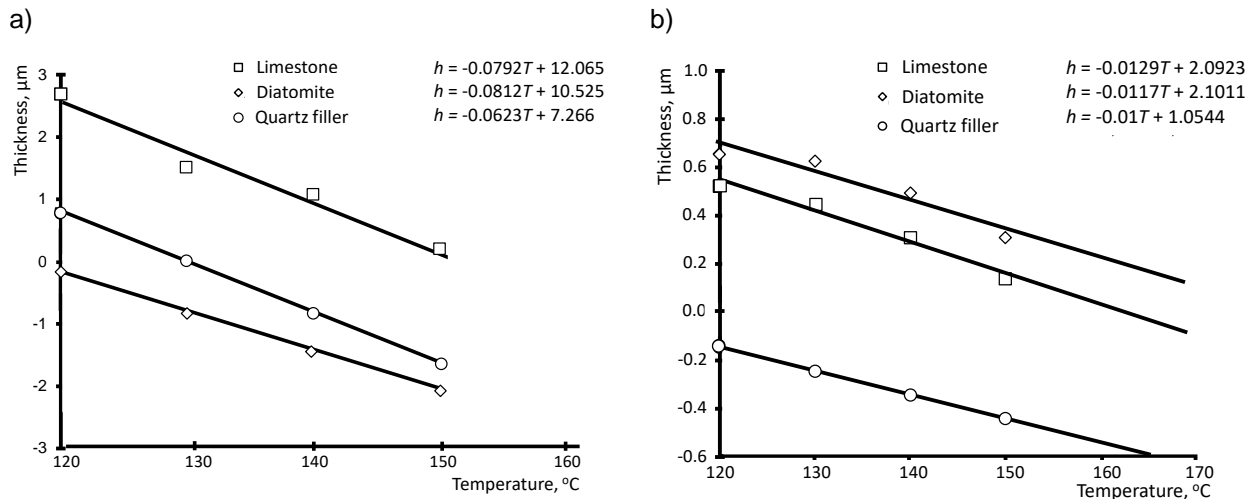
**Table 6. Thickness of the bitumen layer on the surface of the mineral filler (particle shape factor  $\alpha$ ).**

Filler	Total interfacial layer thickness by the formula (10)			
	120 °C	130 °C	140 °C	150 °C
Limestone	0.488	0.413	0.272	0.106
Diatomite	0.387	0.656	0.525	0.041
Quartz filler	-0.185	-0.285	-0.385	-0.485

Filler	Total interfacial layer thickness by the formula (13)			
	120 °C	130 °C	140 °C	150 °C
Limestone	0.522	0.447	0.306	0.140
Diatomite	0.656	0.625	0.494	0.309
Quartz filler	-0.145	-0.245	-0.345	-0.445

Analysis of the thicknesses calculation results of the bitumen layers shows for ideal system (A. Einstein's equation) and the model system that for some powders the thickness values have negative values. This fact is physically absurd, since this is possible only when the filler is dissolved. Negative thicknesses actually indicate the absence of a bitumen layer on the surface of the mineral component (both of the adsorption layer and the kinetic layer).



**Figure 2. Dependence of the thickness of the adsorption layer of bitumen on temperature: a – at  $\alpha = \alpha_0$ ; b – at  $\alpha = \alpha$  (Table 2).**

For determination of the bitumen layer thickness, it is important to determine the temperature at which the kinetic layer thickness is small ( $h_k \rightarrow 0$ ). For it is necessary to determine the minimum bitumen viscosity; under the condition that bitumen is multi-component, is assumed that low viscosity oils provide the minimum viscosity of the bitumen. In this case, as the model of oil, we take the castor oil viscosity (Figure 2). The minimum castor oil viscosity is observed at a temperature 140 °C:  $\eta_{o,\min} = 5.34$  mPa·s. The temperature at which the bitumen has  $\eta_{o,\min}$ , total  $T^* = 220$  °C (the calculation was made according to the formula:  $T^* = \ln(a/\eta_{o,\min})/b$ , hence  $a, b$  are empirical dependency coefficients  $\eta_o = f(T)$  (Figure 2).

Data analysis Figure 2 shows that at a temperature  $T^*$  the bitumen layers thicknesses on the mineral fillers have negative values. This means that no adsorption bitumen layer of significant (definable rheological method) thickness is formed on the surface of the studied mineral components [27].

Estimated temperatures of melts of dispersed systems at which  $h_a(T) = 0$  are presented down. The data allow placing of the investigated fillers in a row according to the temperature “sensitivity”, assessed by  $dh_a/dT$ : Diatomite (169 °C) > limestone (145 °C) > Quartz filler (101 °C). Moreover  $T^* > 140$  °C for the fillers studied (with the exception of quartz filler). It indicates that physico-chemical activity of the filler need to take into account during the asphalt concrete mix preparation and the temperature “sensitivity” – during for compacting the mixture.

Figures 3 show that  $T^* > 140$  °C for the fillers studied (with the exception of quartz filler). It indicates that physico-chemical activity of the filler need to take into account during the asphalt concrete mix preparation and the temperature “sensitivity” – during for compacting the mixture.

Obtained results and data from [28, 29] show a good convergence and reproducibility of the proposed method for determining the structured bitumen thickness and the physico-chemical activity of the mineral filler.

To determine the influence of the considered extensive (which is related to the area at the border chapter of phases; the exponent is  $m$ ) and intensive (which is related to the intensity of the physico-chemical interaction at the border chapter of phases; the exponent is  $n$ ) for this necessary research on the structure-sensitive properties. In accordance with [13], the strength of the composite refers to such properties. Studies were performed by using crushed stone mastic asphalt SMA-20, corresponding to the requirements of Russian state standard 31015-2002 (Table 7).

**Table 7. Stone mastic asphalt SMA-20 properties.**

Indicator name	Requirements of Russian state standard 31015-2002	Actual properties values		
		Limestone	Diatomite	Quartz filler
Compressive Strength, MPa				
( $R_{20}$ ) at temperature 20 °C	more 2.2	3.84	5.16	2.62
( $R_{50}$ ) at temperature 50 °C	more 0.65	0.96	2.14	0.67
( $R_0$ ) at temperature 0 °C	not standardized	7.19	5.99	5.42

SMA-20 with limestone powder was control asphalt concrete ( $F_0$  depending on (2)).

The data in Figure 2b and Table 7 allow us to make the relationship between the structured bitumen layer thickness and the composite strength. Figure 3 show: asphalt concrete strength increase when thickness  $h_a$  increase. This dependence has an asymptotic character:

$$h_b \geq \frac{Vb}{\sum m_i S_n i} \tag{14}$$

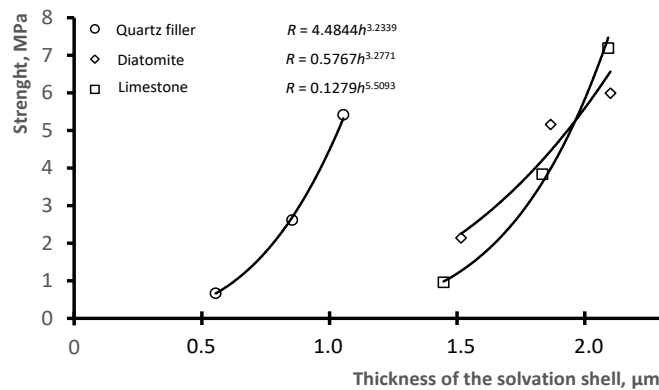


**Figure 3. Dependence of asphalt concrete strength on the structured bitumen thickness.**

Using  $R(f) = f(h)$  turn out:

$$R(h) = R_{\max} \left( \frac{h}{h_{\max}} \right)^b$$

The presented dependence has a limited scope. It needs verification not only at the top boundary ( $R_{\max}$ ,  $h_{\max}$ ), but also at the bottom boundary ( $R_{\min}$ ,  $h_{\min}$ ).

The results of the calculation of the exponents  $n$  and  $m$  of dependence (2) are presented in Table 8.

**Table 8. Value  $n$  and  $m$  calculated according to the formula (2).**

Temperature range, °C	The intensity of the influence of parameters			
	Diatomite		Quartz filler	
	$m$	$n$	$m$	$n$
0...20	0.32	35.34	1.07	0.46
20...50	0.86	17.63	0.77	-0.12

The data from Table 8 show that the main contribution to the concrete structure formation is made by the intensive factor  $n$  in SMA-20 with Diatomite, which is responsible for the physical-mechanical interaction of the mineral powder at the border chapter of phases, characterized by the structured bitumen thickness. The main influence on the structure and properties of SMA-20 with quartz filler is exerted by the extensive factor  $m$ , which characterizes the influence at the border chapter of phases area.

## 4. Conclusion

1. Method for calculating of the bitumen layer thickness on the surface of the mineral powders using by the rheological tests results is proposed.

2. A mathematical relationship between the structured bitumen layer thickness and the road composite strength are established: an increase in the bitumen layer thickness on the surface of the mineral powder leads to an increase in the composite strength.

3. Method for the quantitative assessment of the influence on the structural-sensitive properties of the composite extensive (an indicator characterizing at the border chapter of phases area) and intensive factors are proposed (an indicator characterizing the influence of physico-chemical effects at the border chapter of phases).

4. The extensive factor has a greater effect on the properties of SMA-20 with a quartz filler ( $m/n > 2$ ). There is a higher rate of decrease in the intensity of physicochemical interactions at the interface of the "oil bitumen-silica filler" phase (index  $m$ ) as compared with the extensive factor (index  $n$ ). The different nature of the temperature effect on the extensive and intensive factors is observed for SMA-20 with diatomite: as temperature increased, the factor  $m$  is increased, whereas the opposite effect is observed for factor  $n$ . It indicates a positive effect of the specific diatomite surface on the temperature asphalt concrete properties. From here follows a technological decision to increase the specific surface area ( $S_{sp}$ ) of the diatomite powder used. The latter was realized by treating diatomite powder with a nanoscale modifier, which provided an increase in  $S_{sp}$  in 2.08 times. In [13], it was shown that the use of this nano-modified diatomite powder provided an increase in all indicators of asphalt concrete properties.

## References

- Guo, M., Tan, Y., Wang, L., Hou, Y. A state-of-the-art review on interfacial behavior between asphalt binder and mineral aggregate. *Front. Struct. Civ. Eng.* 2018. 12(2). Pp. 248–259.
- Korolev, E.V., Tarasov, R.V., Makarova, L.V., Smirnov, V.A. Model research of bitumen composition with nanoscale structural units. *Contemporary engineering sciences.* 2015. 8(9–12). Pp. 393–399.
- Diab, A., Eneib, M. Investigating influence of mineral filler at asphalt mixture and mastic scales. *International Journal of Pavement Research and Technology.* 2018. 11(3). Pp. 213–224.
- Macías-Salinas, R., Flores-Granados, M.A., Díaz-Cruz, M., García-Sánchez, F. Modeling the dynamic viscosity of associating and polar fluids via the use of density scaling. *Fluid Phase Equilibria.* 2018. Vol. 458. Pp. 16–29.
- Pal, R. *Fundamental Rheology of Disperse Systems Based on Single-Particle Mechanics.* Fluids. 2016. Vol. 1. No. 4. 40.
- Radovskiy, B. Analytical Formulas for Film Thickness in Compacted Asphalt Mixture. *Transportation Research Record.* 2003. No. 1829. Pp. 26–32.
- Zhang, M., Heitzman, M., Smith, A.E. Improving hot mix asphalt production using computer simulation and real time optimization. *Journal of Computing in Civil Engineering.* 2014. 28(3). 04014011.
- Radovskiy, B. Analytical Formulas for Film Thickness in Compacted Asphalt Mixture. *Transportation Research Record 1829, TRB, National Research Council, Washington, D.C., 2003. Pp. 26–32.*
- Heitzman, M., Michael, A. Development of new film thickness models for hot mix asphalt. *Retrospective Theses and Dissertations.* 2005. 1737.
- Garkina, I.A., Danilov, A.M. *Mathematical Methods of System Analysis in Construction Materials.* IOP Conf. Series: Materials Science and Engineering. 2017. Vol. 245. 062014.
- Rusanov, A.I. *Termodinamicheskiye osnovy mekhanokhimii [Thermodynamic principles of mechanochemistry].* SPb.: Science. 2006. 221 p. (rus)
- Rusanov, A.I. *Fazovyie ravnovesiya i poverkhnostnyye yavleniya [Phase equilibria and surface phenomena].* SPb.: Chemistry. 1967. 388 p. (rus)
- Korolev, E.V., Inozemtcev, S.S., Smirnov, V.A. Nanomodified bitumen composites: solvation and rheology. *Advanced Materials, Structures and Mechanical Engineering Proceedings of the International Conference on Advanced Materials, Structures and Mechanical Engineering.* 2016. Pp. 393–398.
- Korolev, E.V., Bazhenov, Yu.M., Albasov, A.I. *Radiatsionno-zashchitnyye i khimicheski stoykiye sernyye stroitelnyye materialy [Radiation-protective and chemically resistant sulfur building materials].* Penza, Orenburg: IPK OGU. 2010. 364 p.
- Jahromi, S.G., Khodaii, A. Effects of nanoclay on rheological properties of bitumen binder. *Construction and building materials.* 2009. 23(8). Pp. 2894–2904.
- Poulikakosa, L.D., Tiwari, M.K., Partla, M.N. Analysis of failure mechanism of bitumen films. *Fuel.* 2013. Vol. 106. Pp. 437–447.
- Sengoz, B., Agar, E. Effect of asphalt film thickness on the moisture sensitivity characteristics of hot-mix asphalt. *Building and Environment.* 2007. 42(10). Pp. 3621–3628.
- Tao, Y.Y., Yu, J.Y., Li, B., Feng, P.C. Effect of different montmorillonites on rheological properties of bitumen/clay nanocomposites. *Journal of Central South University of Technology.* 2008. 15(1). Pp. 172–175.
- Hafeez, I., Hussain, J., Riaz, K., Khitab, A., Hussain, S., Zaidi, B., Farooqi, U., Hayat, A., Ahmed, I., Asif, A. Influence of Time and Temperature on Asphalt Binders Rheological Properties. *Life Science Journal.* 2013. 20(5). Pp. 355–365.
- Islam, M.R., Tarefder, R.A. Determining thermal properties of asphalt concrete using field data and laboratory testing. *Construction and Building Materials.* 2014. Vol. 67. Part B. Pp. 297–306.
- Markanday, S.S., Stastna, J., Polacco, G., Filippi, S., Kazatchkov, I., Zanzotto, L. Rheology of bitumen modified by EVA-organoclay nanocomposites. *Journal of Applied Polymer Science.* 2010. 118(1). Pp. 557–565.

22. Yangming, G., Yuqing, Z., Fan, G., Tao, X., Hao, W. Impact of minerals and water on bitumen-mineral adhesion and debonding behaviours using molecular dynamics simulations. *Construction and Building Materials*. 2018. Vol. 171. Pp. 214–222.
23. Meng, G., Amit, B., Yiqiu, T. Effect of mineral fillers adsorption on rheological and chemical properties of asphalt binder. *Construction and Building Materials*. 2017. Vol. 141. Pp. 152–159.
24. Keith, E. Ensley Multilayer adsorption with molecular orientation of asphalt on mineral aggregate and other substrates. *Journal of Applied Chemistry and Biotechnology banner*. 2007. 25 (9). Pp. 671–682.
25. Inozemtcev, S.S., Korolev, E.V. Interaction process on the phases interface «bitumen – dispersed phase from cement stone». *Magazine of Civil Engineering*. 2018. 82(6). Pp. 60–67.
26. Einstein, A. A new determination of molecular dimensions. *Annalen der Physik*. 1906. 19(4). Pp. 289–306.
27. Willenbacher, N., Georgieva, K. Rheology of Disperse Systems. *Nature*. 1957. No. 180. Pp. 957–959.
28. Mwanza, A., Hao, P., Wang, H. Effects of Type and Content of Mineral Fillers on the Consistency Properties of Asphalt Mastic. *Journal of Testing and Evaluation*. 2012. 40(7). 20120140.
29. Wei, J., Yue, H., Aimin, S. A review of eco-friendly functional road materials. *Construction and Building Materials*. 2018. Vol. 191. Pp. 1082–1092.

**Contacts:**

*Svetlana Shekhovtsova, +7(980)3749704; SHehovtsovaSYU@mgsu.ru*

*Evgenyi Korolev, +7(499)1880400; korolev@nocnt.tu*

*Sergei Inozemtcev, +7(985)2505866; inozemtcevss@mgsu.ru*

*Jiangmiao Yu, 18898837614; yujm@scut.edu.cn*

*Huayang Yu, 18898837614; huayangyu@scut.edu.cn*

© Shekhovtsova, S.Yu., Korolev, E.V., Inozemtcev, S.S., Yu, J., Yu, H., 2019



DOI: 10.18720/MCE.85.11

## Методика прогнозирования прочности и термочувствительности асфальтобетона

**С.Ю. Шеховцова<sup>a\*</sup>, Е.В. Королев<sup>a</sup>, С.С. Иноземцев<sup>a</sup>, Д. Ю<sup>b</sup>, Х. Ю<sup>b</sup>**

<sup>a</sup> *Национальный исследовательский Московский государственный строительный университет, г. Москва, Россия*

<sup>b</sup> *Южно-Китайский Технологический университет, г. Гуанчжоу, Китай*

\* *E-mail: SShehovtsovaSYU@mgsu.ru*

**Ключевые слова:** дорожное покрытие, асфальтобетон, битум, межфазный слой, реология, экстенсивный и интенсивный факторы, прочность, термочувствительность

**Аннотация.** Отличительной особенностью композитов является проявление синергетического эффекта вследствие взаимодействия контактирующих веществ на границе раздела фаз, а их интенсивность взаимодействия влияет на объемные свойства композитов. В работе произведено исследование межфазного слоя битума на поверхности минерального порошка. Предложена методика позволяющая, по результатам реологических испытаний, рассчитать толщину граничного слоя в бинарной системе «нефтяной битум – дисперсная фаза». Установлена взаимосвязь, описывающая зависимость толщины слоя структурированного нефтяного битума с прочностью дорожного композита: увеличение толщины слоя битума на поверхности минерального порошка приводит к увеличению прочности композита. Предложена методика для количественной оценки влияния на структурно-чувствительные свойства композита экстенсивного фактора  $m$  – показателя, характеризующего влияние площади границы раздела фаз и интенсивного фактора  $n$  – показателя, характеризующего влияние физико-химического воздействия на границе раздела фаз. Установлено, что для щебеночно-мастичного асфальтобетона ЦМА-20, изготовленного с применением кварцевого наполнителя более существенное влияние оказывает экстенсивный фактор  $m/n > 2$ . Также для него характерна более высокая скорость снижения интенсивности физико-химических взаимодействий на границе раздела фаз «нефтяной битум-кварцевый наполнитель» по сравнению с экстенсивным фактором. Для ЦМА-20, приготовленного с применением диатомита, установлено отличное от симбатного снижения факторов  $n$  и  $m$  с ростом температуры, установлен различный характер влияния температуры на экстенсивный и интенсивный факторы: при ее увеличении фактор  $m$  увеличивается, тогда, как для фактора  $n$  наблюдается противоположное влияние. Это свидетельствует о положительном влиянии удельной поверхности диатомита на температурные свойства асфальтобетона.

### Литература

1. Guo M., Tan Y., Wang L., Hou Y. A state-of-the-art review on interfacial behavior between asphalt binder and mineral aggregate // Front. Struct. Civ. Eng. 2018. Vol. 12. No. 2. Pp. 248–259.
2. Korolev E.V., Tarasov R.V., Makarova L.V., Smirnov V.A. Model research of bitumen composition with nanoscale structural units // Contemporary engineering sciences. 2015. Vol. 8. No. 9–12. Pp. 393–399.
3. Diab A., Enieb M. Investigating influence of mineral filler at asphalt mixture and mastic scales // International Journal of Pavement Research and Technology. 2018. Vol. 11. No. 3. Pp. 213–224.
4. Macías-Salinas R., Flores-Granados M.A., Díaz-Cruz M., García-Sánchez F. Modeling the dynamic viscosity of associating and polar fluids via the use of density scaling // Fluid Phase Equilibria. 2018. Vol. 458. Pp. 16–29.
5. Pal R. Fundamental Rheology of Disperse Systems Based on Single-Particle Mechanics // Fluids. 2016. Vol. 1. No. 4. 40.
6. Radovskiy B. Analytical Formulas for Film Thickness in Compacted Asphalt Mixture // Transportation Research Record. 2003. No. 1829. Pp. 26–32.
7. Zhang M., Heitzman M., Smith A.E. Improving hot mix asphalt production using computer simulation and real time optimization // Journal of Computing in Civil Engineering. 2014. Vol. 28. No. 3. 04014011.
8. Radovskiy B. Analytical Formulas for Film Thickness in Compacted Asphalt Mixture // Transportation Research Record 1829, TRB, National Research Council, Washington, D.C., 2003. Pp. 26–32.
9. Heitzman M., Michael A. Development of new film thickness models for hot mix asphalt. Retrospective Theses and Dissertations. 2005. 1737.

10. Garkina I.A., Danilov A.M. Mathematical Methods of System Analysis in Construction Materials // IOP Conf. Series: Materials Science and Engineering. 2017. Vol. 245. 062014.
11. Rusanov A.I. Termodinamicheskiye osnovy mekhanokhimii [Thermodynamic principles of mechanochemistry]. SPb.: Science. 2006. 221 p. (rus)
12. Rusanov A.I. Fazovyye ravnovesiya i poverkhnostnyye yavleniya [Phase equilibria and surface phenomena]. SPb.: Chemistry. 1967. 388 p. (rus)
13. Korolev E.V., Inozemtcev S.S., Smirnov V.A. Nanomodified bitumen composites: solvation and rheology. Advanced Materials, Structures and Mechanical Engineering Proceedings of the International Conference on Advanced Materials, Structures and Mechanical Engineering. 2016. Pp. 393–398.
14. Korolev E.V., Bazhenov Yu.M., Albakasov A.I. Radiatsionno-zashchitnyye i khimicheski stoykiye sernyye stroitelnyye materialy [Radiation-protective and chemically resistant sulfur building materials]. Penza, Orenburg: IPK OGU. 2010. 364 p.
15. Jahromi S.G., Khodaii, A. Effects of nanoclay on rheological properties of bitumen binder // Construction and building materials. 2009. Vol. 23. No. 8. Pp. 2894–2904.
16. Poulikakosa L.D., Tiwari M.K., Partla M.N. Analysis of failure mechanism of bitumen films // Fuel. 2013. Vol. 106. Pp. 437–447.
17. Sengoz B., Agar E. Effect of asphalt film thickness on the moisture sensitivity characteristics of hot-mix asphalt // Building and Environment. 2007. Vol. 42. No. 10. Pp. 3621–3628.
18. Tao Y.Y., Yu J.Y., Li B., Feng P.C. Effect of different montmorillonites on rheological properties of bitumen/clay nanocomposites // Journal of Central South University of Technology. 2008. Vol. 15. No. 1. Pp. 172–175.
19. Hafeez I., Hussain J., Riaz K., Khitab A., Hussain S., Zaidi B., Farooqi U., Hayat A., Ahmed I., Asif A. Influence of Time and Temperature on Asphalt Binders Rheological Properties // Life Science Journal. 2013. Vol. 20. No. 5. Pp. 355–365.
20. Islam M.R., Tarefder R.A. Determining thermal properties of asphalt concrete using field data and laboratory testing // Construction and Building Materials. 2014. Vol. 67. Part B. Pp. 297–306.
21. Markanday S.S., Stastna J., Polacco G., Filippi S., Kazatchkov I., Zanzotto L. Rheology of bitumen modified by EVA-organoclay nanocomposites // Journal of Applied Polymer Science. 2010. Vol. 118. No. 1. Pp. 557–565.
22. Yangming G., Yuqing Z., Fan G., Tao X., Hao W. Impact of minerals and water on bitumen-mineral adhesion and debonding behaviours using molecular dynamics simulations // Construction and Building Materials. 2018. Vol. 171. Pp. 214–222.
23. Meng G., Amit B., Yiqiu T. Effect of mineral fillers adsorption on rheological and chemical properties of asphalt binder // Construction and Building Materials. 2017. Vol. 141. Pp. 152–159.
24. Keith E. Ensley Multilayer adsorption with molecular orientation of asphalt on mineral aggregate and other substrates // Journal of Applied Chemistry and Biotechnology banner. 2007. Vol. 25. No. 9. Pp. 671–682.
25. Inozemtcev S.S., Korolev E.V. Interaction process on the phases interface «bitumen – dispersed phase from cement stone» // Magazine of Civil Engineering. 2018. Vol. 82. No. 6. Pp. 60–67.
26. Einstein A. A new determination of molecular dimensions // Annalen der Physik. 1906. Vol. 19. No. 4. Pp. 289–306.
27. Willenbacher N., Georgieva K. Rheology of Disperse Systems // Nature. 1957. No. 180. Pp. 957–959.
28. Mwanza A., Hao P., Wang H. Effects of Type and Content of Mineral Fillers on the Consistency Properties of Asphalt Mastic // Journal of Testing and Evaluation. 2012. Vol. 40. No. 7. 20120140.
29. Wei J., Yue H., Aimin S. A review of eco-friendly functional road materials // Construction and Building Materials. 2018. Vol. 191. Pp. 1082–1092.

#### **Контактные данные:**

*Светлана Юрьевна Шеховцова, +7(980)3749704; эл. почта: SHehovtsovaSYU@mgsu.ru*

*Евгений Валерьевич Королев, +7(499)1880400; эл. почта: korolev@nocnt.tu*

*Сергей Сергеевич Иноземцев, +7(985)2505866; эл. почта: inozemtcevss@mgsu.ru*

*Джунанжмиао Ю, 18898837614; эл. почта: yujm@scut.edu.cn*

*Хуаяне Ю, 18898837614; эл. почта: huayangyu@scut.edu.cn*

© Шеховцова С.Ю., Королев Е.В., Иноземцев С.С., Ю. Д., Ю. Х., 2019



DOI: 10.18720/MCE.89.12

## The effect of design on interaction of foundation slabs with the base

**S.V. Ikonin, A.V. Sukhoterin\***

*Voronezh State Technical University, Voronezh, Russia*

\* E-mail: [asuhoterin@list.ru](mailto:asuhoterin@list.ru)

**Keywords:** Experimental studies, systems with controlled properties, slab foundations, hinged beams

**Abstract.** The paper suggests advanced trend in reduction of materials consumption for the base slabs owing to their design. As an example, the stress and strain state of the models of solid slabs and slabs with controlled forces interacting with sand base, are addressed in the paper. The models were loaded by static system of concentrated vertical forces. Stress and strain state of the models was assessed by the results of laboratory tray experiments with strain measurement and by the data of numeric calculations by finite element method with application of Coulomb-Mohr soil model. Based on the comparison of obtained results, it is demonstrated that the slab with controlled forces has advantages over a solid slab. For example, owing to the control of forces, it becomes possible to avoid alternation in bending moments diagram, flatten the values of support bending moments for intermediate supports and achieve more smooth deflection of the slab, thus creating prerequisites for significant reduction of materials consumption. Apart from this, it was established that experimental values of bending moments and slab deflection are qualitatively consistent with numerical prediction, while the finite element calculation gives slightly inflated absolute values as compared to the experiment results. The results of the studies may appear useful in the design of base slabs for supports of overhead roads, trestlework along with industrial civil buildings and frame type structures with regular grids of columns.

### 1. Introduction

Solid reinforced concrete slab foundations on soil base are widely used in foundation engineering. The basic advantage of this type of foundations is their ability to distribute significant external loads from buildings and structures on a large contact area with the base. This feature enables us to use upper soil layers with low strength deformation characteristic and soil masses with complex bedding of engineering and geological elements as bases. Apart from this, ease of manufacture and no need for backfilling and under-floor waterproofing in underground part of buildings and structures are deemed the advantages of slab foundations.

The shortcoming of the foundation structure discussed in this paper is high materials' output ratio, mainly related to the cost of steel used for reinforcement. The article addresses the aspect of reducing the materials output ratio and improving the technical-economic and performance indicators of foundation slabs.

Analysis of the existing sources show that the materials output ratio for the slab foundation structure can be reduced due to the use of refined calculation models namely, calculation of slab foundations in «superstructure-foundation-base» system with account of non-linear properties of soil base and foundation material. Such approaches are outlined in papers [1-16].

Recently, the base-foundation systems with controlled properties have been widely used in foundation engineering. Their use provides for generation of a set deflected mode at the design and construction phases to improve technical-economic and performance indicators of the bases and foundations.

The aforementioned systems with controlled properties are being implemented due to design solutions related to targeted change of the base and foundation stiffness. Such design solutions are described in papers [17-28].

---

Ikonin, S.V., Sukhoterin, A.V. The effect of design on interaction of foundation slabs with the base. Magazine of Civil Engineering. 2019. 89(5). Pp. 141–155. DOI: 10.18720/MCE.89.12

Иконин С.В., Сухотерин А.В. Влияние конструктивного исполнения на взаимодействие фундаментных плит с основанием // Инженерно-строительный журнал. 2019. № 5(89). С. 141–155. DOI: 10.18720/MCE.89.12



This open access article is licensed under CC BY 4.0 (<https://creativecommons.org/licenses/by/4.0/>)

The research results published by the authors in this article are related to this subject and are elaboration of paper [29].

## 2. Methods

The key goal of this paper is to research on the deflected mode of foundation slab structure with controlled forces on specially developed scale model, along with performance evaluation of foundation slab structure with controlled forces.

The following tasks were identified to attain the goal:

- Experimental and numerical studies of a scale model of foundation slab structure with controlled forces;
- Analysis of deflected mode of foundation slab structure with controlled forces;
- Establishing the qualitative and quantitative patterns based on experimental and numerical studies;
- Efficiency evaluation of the foundation slab structure by comparison of calculation results for the proposed structure of foundation slab with controlled forces against a solid foundation slab.

### 2.1. Description of tested models

As part of the experiment, scale models of foundation slab with controlled forces and solid foundation slab were tested.

The model of foundation slab with controlled forces comprises five separate sections with dimensions in the plane 200x200 mm interconnected with hinged units (Figures 1–3). Foundation model is made of sheet steel S245, 5 mm thick.

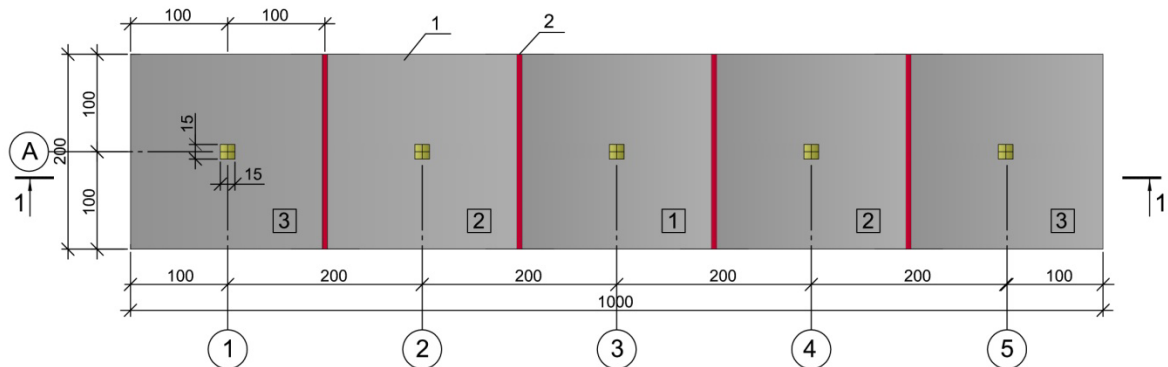


Figure 1. Design of foundation slab with controlled forces, plan:  
1 – separate slab section; 2 – hinged unit.

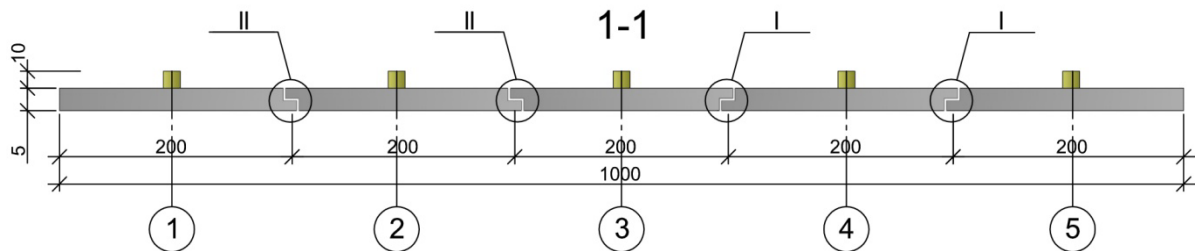


Figure 2. Design of foundation slab with controlled forces, cross-section 1-1:  
I, II – hinged units.

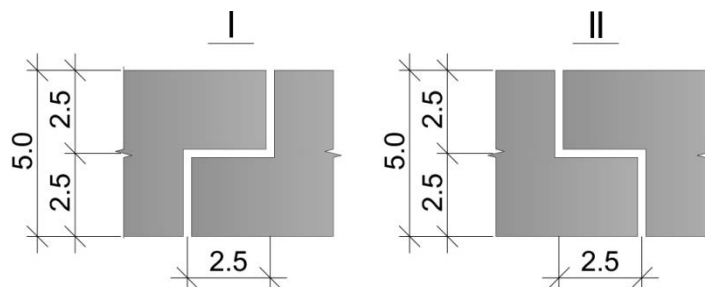


Figure 3. Hinged units I, II.

The proposed hinged unit provides for reciprocal turn of two adjacent sections of foundation slab relative to each other, thus creating a hinge effect to its work. Moreover, joint work of adjacent parts of the foundation slab in vertical direction is provided for.

According to paper [29] such design solution provides for unloading of foundation slab cross-sections both in spans and under the columns while retaining the foundation distribution capacity.

The model of a solid foundation slab dimensions in the plane are 200x1000 mm, made of sheet steel S245, 5 mm thick (Figure 4).

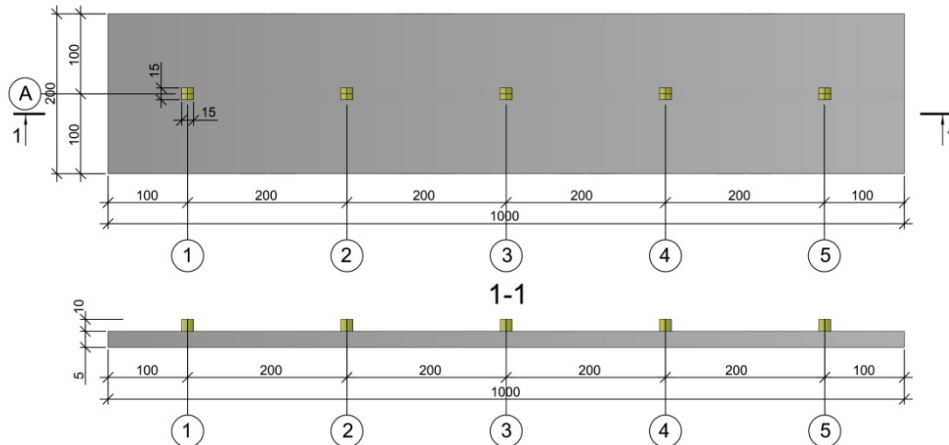


Figure 4. Design of a solid foundation slab, plane, cross-section 1-1.

### 2.2. Experiment method

Experimental studies were carried out in the center of collective use named after professor Yu. M. Borisov of Voronezh State Technical University.

As part of the experiment, it was required to identify the actual distribution of forces in the models and the foundation settlement.

In the course of foundation models' tests, the following data were recorded at each loading stage: the actual applied loads, relative deformations in characteristic points of the model and foundation settlement.

To determine the relative deformations in characteristic points of foundation models, a tensometric complex, comprising an instrumentation amplifier, connection blocks, resistance strain gauges and personal computer with specialized software, was used.

To measure the longitudinal and lateral deformations, strain gauges with the base of 20 mm were pasted on the foundation models. Foundation settlement was measured with Maximov flexometers with scale interval of 0.1 mm. Schemes of strain gauges' pasting and installation of Maximov flexometers are given on Figure 5.

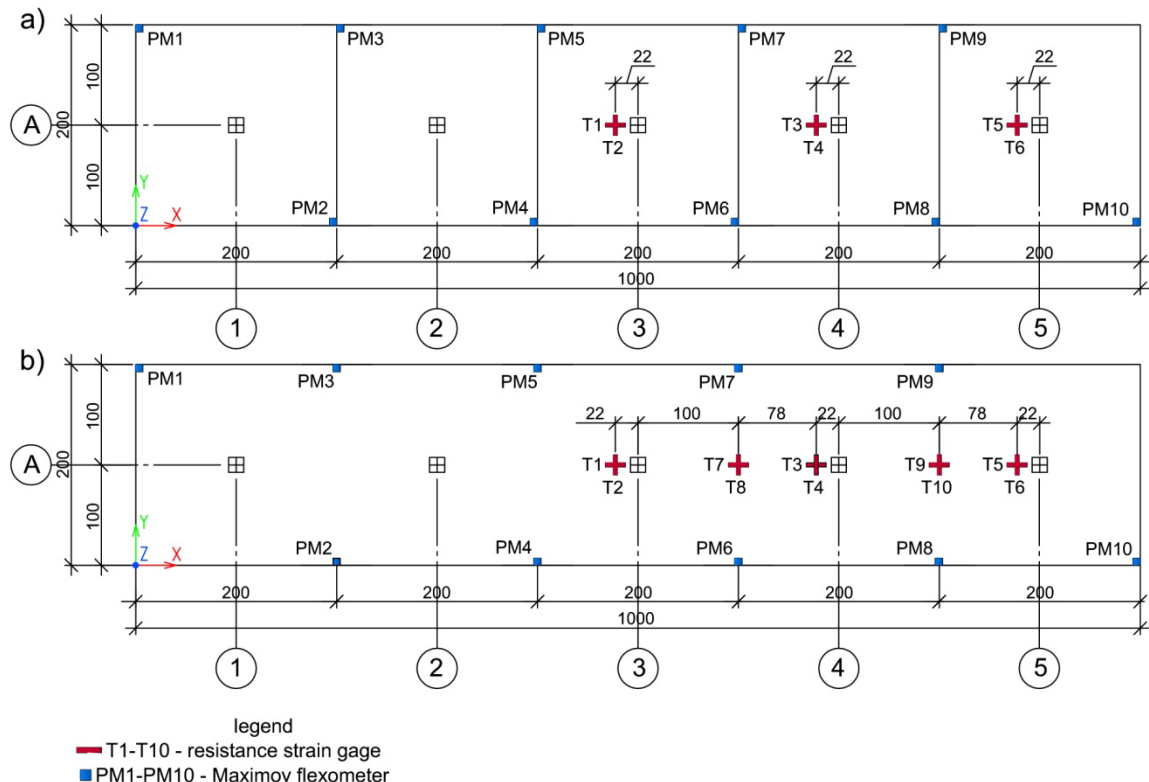


Figure 5. Schemes of strain gauges' pasting and installation of Maximov flexometers: a) Model of foundation slab with controlled forces; b) Model of solid foundation slab.

The models were loaded stage-wise by installation with hydraulic jacks. The loads were controlled by force-measuring sensors and dynamometers. The maximal load and the number of loading stages were determined on the basis of preliminary calculations. Each loading stage was sustained till conventional stabilization.

Validity of the test results is ensured by tensometric complex registered in the State Registry of Measurement Instruments (RF SRMI), pre-calibration of dynamometers on calibrated pressure equipment (INSTRON (USA) model 5982), use of materials for the models conforming with the effective codes and standards.

Basic parameters of experimental installation are presented in Table 1 below.

**Table 1. Basic parameters of experimental installation.**

General view of experimental installation



Equipment used:

1. A rig for testing the soils and foundation models in special arrangement
2. Strain gauge equipment:
  - Amplifiers MGCplus and QuantumX;
  - Communication processor CP42 with Ethernet and USB-interface
  - Measurement module DC;
  - Multimode amplifier 8-channel
  - CATMAN-AP software
3. Force-measuring tensoresistive sensors C6A 200 kN
4. Resistance strain gauges with the base of 20 mm KF 5P1-20-120-A12 according to Specifications 3.06 7710-0001-93
5. Lifting jacks, weight-carrying 5 tons
6. Dynamometers, brands: DOSM-3-1 ultimate load 1t, DOSM-3-5 ultimate load 5t;
7. Maximov flexometers with scale interval of 0.1 mm.

Schemes of models' loading:

1. The models' loads were incremented
2. Each load increment was retained till conventional stabilization of 0.1 mm over the last 15 minutes of observation
3. The following load increments were assumed:
  - For intermediate supports – 0.5 kN;
  - For end supports – 0.25 kN;
4. Maximum load:
  - For intermediate supports – 4.0 kN;
  - For end supports – 2.0 kN.

Base characteristics:

1. The base is represented by homogeneous layer of sand of average size and density with the following physical and mechanical characteristics:

$$1. \rho = 1.72 \text{ g/cm}^3, W = 2.4 \%, \varphi = 36^\circ, C = 1.6 \text{ kPa}, E = 21.8 \text{ MPa}, \nu = 0.3$$

2. Deformation characteristics of the base are determined by the stamping tests.



### 3. Results and Discussion

As a result of tests, we have obtained data arrays for each load increment characterizing the relative deformations of models in places of resistance strain gauges installation, and model base settlement in points of flexometers' string fixture. The total amount of processed and analyzed data characterizing the relative deformations comes up to approximately 90000 for each foundation model.

Experimented foundation models are classified as thin plates [30]. Therefore, thin plate theory equations were used to determine the internal forces by tensometry data: (1), (2):

$$M_x = -D \cdot \left( \frac{\partial^2 W}{\partial x^2} + \mu \frac{\partial^2 W}{\partial y^2} \right) = \frac{D}{z} \cdot (\varepsilon_x + \nu \cdot \varepsilon_y); \quad (1)$$

$$M_y = -D \cdot \left( \frac{\partial^2 W}{\partial y^2} + \mu \frac{\partial^2 W}{\partial x^2} \right) = \frac{D}{z} \cdot (\varepsilon_y + \nu \cdot \varepsilon_x), \quad (2)$$

where  $M_x$ ,  $M_y$  are bending moments in  $x$  and  $y$  direction;

$\varepsilon_x$ ,  $\varepsilon_y$  are relative deformations in  $x$  and  $y$  directions;

$$D = \frac{Eh^3}{12(1-\nu^2)} \text{ is cylindrical rigidity;}$$

$E$  is modulus of elasticity for plate material;

$\nu$  is Poisson ratio,

$h$  is plate thickness;

$z$  is distance to neutral plane of the plate.

Based on the results of a series of experiments, we obtained averaged values of relative deformations and forces in characteristic points. Averaged results are given for the final load increment corresponding to the load of 4 kN for intermediate supports and 2 kN for the end supports. The results are presented below in Tables 2 and 3.

**Table 2. Tensometry results.**

Relative deformations	Solid foundation slab				Foundation slab with controlled forces			
	Experiment 1	Experiment 2	Experiment 3	$\bar{\varepsilon}$	Experiment 1	Experiment 2	Experiment 3	$\bar{\varepsilon}$
$\varepsilon_{t1}$ $\mu\text{m/m}$	117.379	114.262	180.512	137.384	369.671	305.898	242.824	306.131
$\varepsilon_{t2}$ $\mu\text{m/m}$	608.991	400.236	577.123	528.783	467.436	348.594	293.983	370.004
$\varepsilon_{t3}$ $\mu\text{m/m}$	242.76	311.815	378.614	311.063	231.02	282.628	310.105	274.584
$\varepsilon_{t4}$ $\mu\text{m/m}$	579.472	476.83	661.339	572.547	461.628	260.000	334.828	352.152
$\varepsilon_{t5}$ $\mu\text{m/m}$	17.340	79.611	131.482	76.144	174.119	78.606	118.842	128.069
$\varepsilon_{t6}$ $\mu\text{m/m}$	189.61	219.539	300.405	236.518	189.612	133.934	215.273	236.519
$\varepsilon_{t7}$ $\mu\text{m/m}$	-158.770	-187.952	-200.144	-182.289	-	-	-	-
$\varepsilon_{t8}$ $\mu\text{m/m}$	351.166	167.079	468.945	329.063	-	-	-	-
$\varepsilon_{t9}$ $\mu\text{m/m}$	-234.175	-158.978	-33.445	-142.199	-	-	-	-
$\varepsilon_{t10}$ $\mu\text{m/m}$	260.785	119.855	63.734	148.125	-	-	-	-

**Table 3. Summary of experiment results.**

	Solid foundation slab				Foundation slab with controlled forces			
	Experiment 1	Experiment 2	Experiment 3	$\bar{n}$	Experiment 1	Experiment 2	Experiment 3	$\bar{n}$
$M_x$ , kN·m (axial section 3)	0.283	0.221	0.334	0.279	0.481	0.387	0.312	0.393
$M_y$ , kN·m (axial section 3)	0.608	0.410	0.595	0.538	0.545	0.415	0.346	0.435
$M_x$ , kN·m (axial section 4)	0.393	0.429	0.544	0.455	0.346	0.340	0.387	0.358
$M_y$ , kN·m (axial section 4)	0.615	0.538	0.731	0.628	0.501	0.325	0.404	0.410
$M_x$ , kN·m (axial section 5)	0.070	0.137	0.209	0.139	0.216	0.112	0.173	0.167
$M_y$ , kN·m (axial section 5)	0.184	0.230	0.321	0.245	0.222	0.149	0.237	0.203
$M_x$ , kN·m (section between axes 3-4)	-0.050	-0.130	-0.056	-0.079	-	-	-	-
$M_y$ , kN·m (section between axes 3-4)	0.286	0.104	0.386	0.259	-	-	-	-
$M_x$ , kN·m (section between axes 4-5)	-0.147	-0.116	-0.014	-0.092	-	-	-	-
$M_y$ , kN·m (section between axes 4-5)	0.180	0.068	0.051	0.010	-	-	-	-
Average settlement by indications of flexometers: PM4, PM5, PM 6, PM7, mm	0.74	0.46	0.72	0.64	0.69	0.50	0.57	0.59
Average settlement by indications of flexometers: PM2, PM3, PM8, PM9, mm	0.54	0.59	0.71	0.61	0.41	0.59	0.52	0.51
Average settlement by indications of flexometers: PM1, PM10, mm	0.17	0.30	0.27	0.25	0.32	0.25	0.6	0.39

Based on the data of Table 3, we plotted the bending moments' and settlement diagrams for the foundation models under review (Figure 6).

Experiment results show that availability of hinged nodes changes the diagrams of bending moments for foundation slabs in a positive way. Comparison of the diagrams shows that the proposed design solution ensures unloading of foundation slab section in each span, in locations of maximal span bending moments, and excluding the sign difference in bending moments'  $M_x$  diagram.

It should be noted that in foundation slab with controlled forces, the non-uniformity distribution of bending moments in foundation slab with controlled forces is less expressed, which will have positive effect on reinforcement. The values of support moments differ:

- for bending moments  $M_x$  in solid foundation slab by 38.7 %;
- for bending moments  $M_x$  in foundation slab with controlled forces by 8.91 %;
- for bending moments  $M_y$  in solid foundation slab by 14.33 %;
- for bending moments  $M_y$  in foundation slab with controlled forces by 5.74 %;

The advantage is that the settlement line in the foundation slab with controlled forces is smoother, which in its turn will have positive affect on distribution of forces in superstructure components.

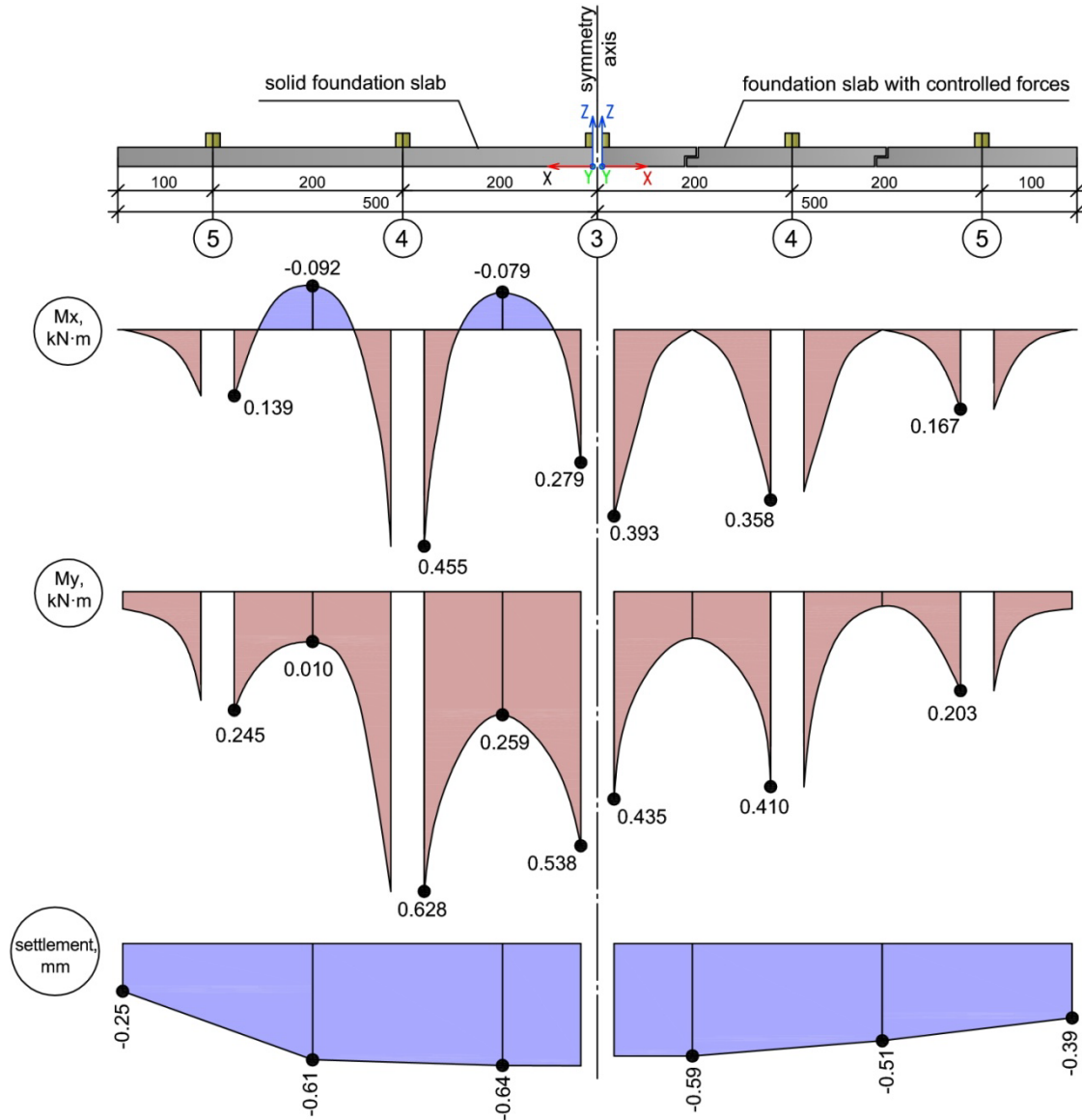


**Figure 6. Diagrams of bending moments and settlement for foundation models under review, based on the results of experimental studies.**

For the purpose of comparison with experimental results, we made a series of comparative FEM calculations. Calculation of “base-foundation” system was carried out in a software complex MIDAS GTS NX.

The following types of finite elements were used for modeling the “base-foundation” system:

- For soil mass – volume elements of “Solid” type (with three translational degrees of freedom in the nodes)
- For foundation – plate elements of the “Shell” type (with three translational and two rotational degrees of freedom in the nodes).

To create a hinged effect for two adjacent sections of a foundation slab, the “Add End Release (Shell)” function was applied enabling control of the amount of freedom degrees in the plate elements’ nodes.

Elastic perfect-plastic Mohr-Coulomb model was used as soil calculation model.

This model is widely used for modeling non-linear behavior of soil and demonstrates reliable results in solution of geotechnical tasks. It accounts for basic properties of soil, such as elastic behavior at small loads, degradation of material rigidity in case of destruction, destruction criterion and possibility of elastic unloading after the flow. Mohr-Coulomb strength criterion takes the form given below:

$$\sigma_1 - \sigma_3 = (\sigma_1 + \sigma_3) \cdot \sin \varphi + 2 \cdot C \cdot \cos \varphi, \quad (3)$$

where  $\sigma_1$ ,  $\sigma_3$  are principal stresses;

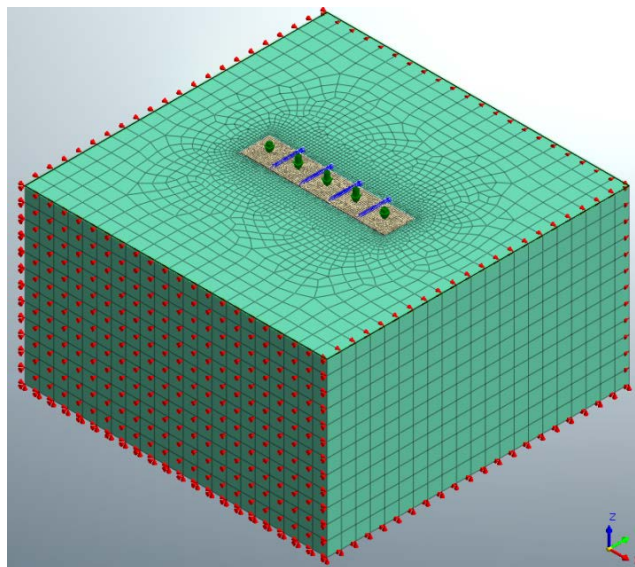
$\varphi$  is angle of internal friction;

$C$  is cohesion.

The remaining parameters of the «base-foundation» system are presented in Table 4 below.

**Table 4. Initial data of the “base-foundation” system.**

General view of “base-foundation” calculation scheme



Foundation characteristics

**Solid foundation slab model:**

1. Geometric dimensions in a plane 200×1000 mm
2. Foundation slab thickness  $h = 5$  mm
3. Material: steel S245,  $E = 2.06 \cdot 10^8$  kN/m<sup>2</sup>,  $R_y = 240$  mPa
4. Load on the foundation slab:
  - intermediate supports is 4.0 kN
  - end supports is 2.0 kN.

**Model of foundation slab with controlled forces:**

1. Comprises five separate sections with geometric dimensions in a plane 200×200 mm
2. Foundation slab thickness  $h = 5$  mm
3. Material: steel S245,  $E = 2.06 \cdot 10^8$  kN/m<sup>2</sup>,  $R_y = 240$  mPa
4. Load on the foundation slab:
  - intermediate supports is 4.0 kN
  - end supports is 2.0 kN.

Base characteristics

The base is represented by homogeneous layer of sand of average size and density with the following physical and mechanical characteristics:  $\rho = 1.72$  g/cm<sup>3</sup>,  $W = 2.4$  %,  $\varphi = 36^\circ$ ,  $C = 1.6$  kPa,  $E = 21.8$  mPa,  $\nu = 0.3$ .

Based on calculation results for two options of foundation slabs, we obtained isofields of bending moments, shears and settlements presented on Figures 7–12 as appropriate. The graphical materials presented on Figures 7–12 are summarized in Table 5.

In Table 5 the values of bending moments in places of resistance strain gauges installation are given in numerator, and maximal support bending moments are given in denominator.

A bar chart (Figure 13) based on the data of Table 5 reflects distribution of forces for the reviewed foundation models in FEM calculation and experiment.

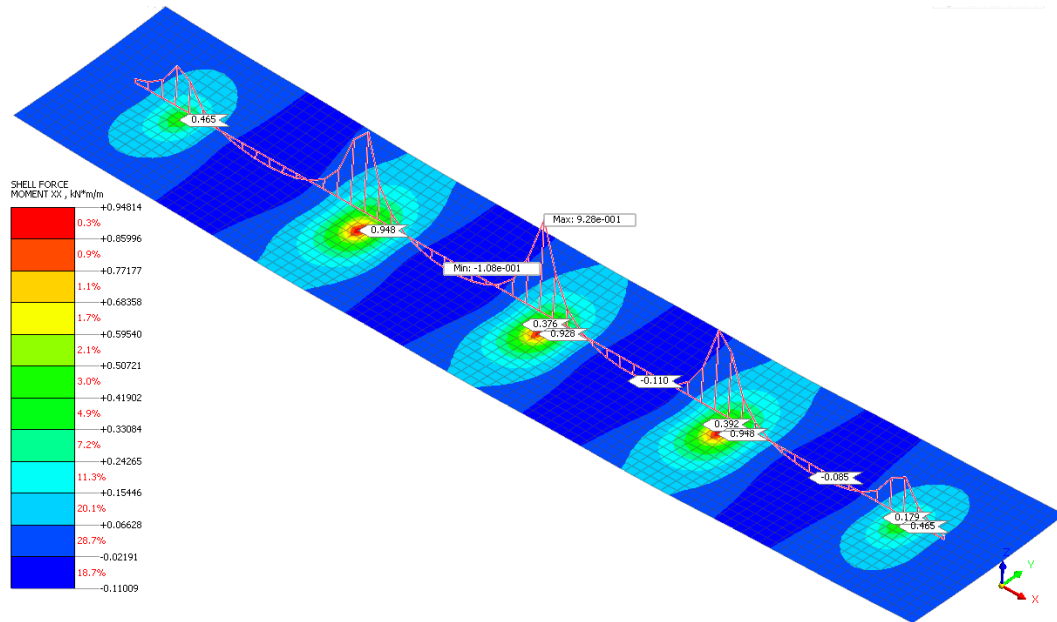


Figure 7. Isofields of bending moments  $M_x$  (kN-m) for solid foundation slab model.

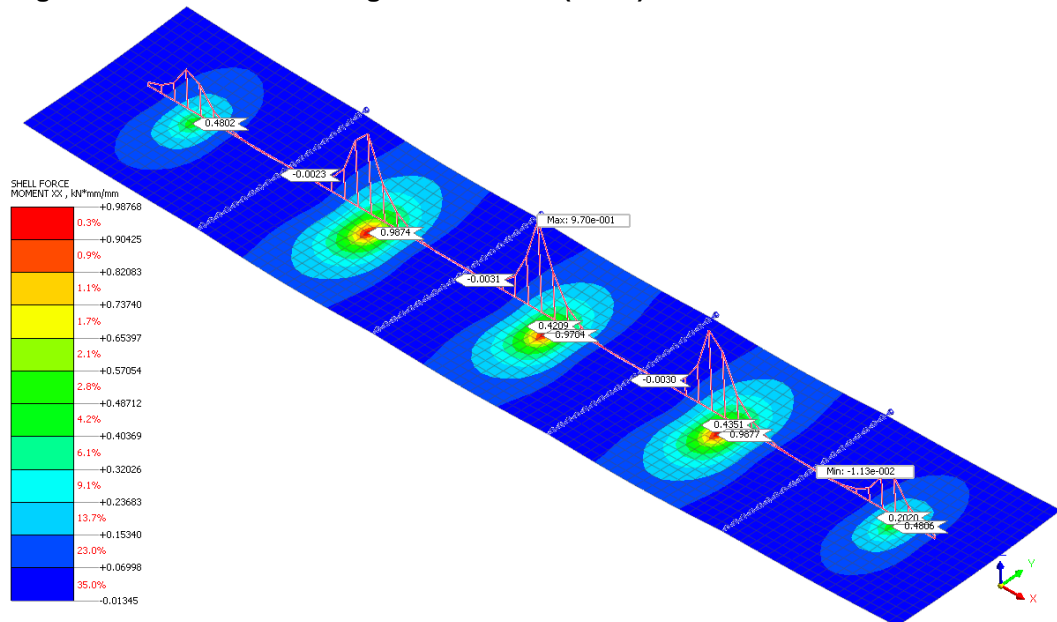


Figure 8. Isofields of bending moments  $M_x$  (kN-m) for foundation slab model with controlled forces.

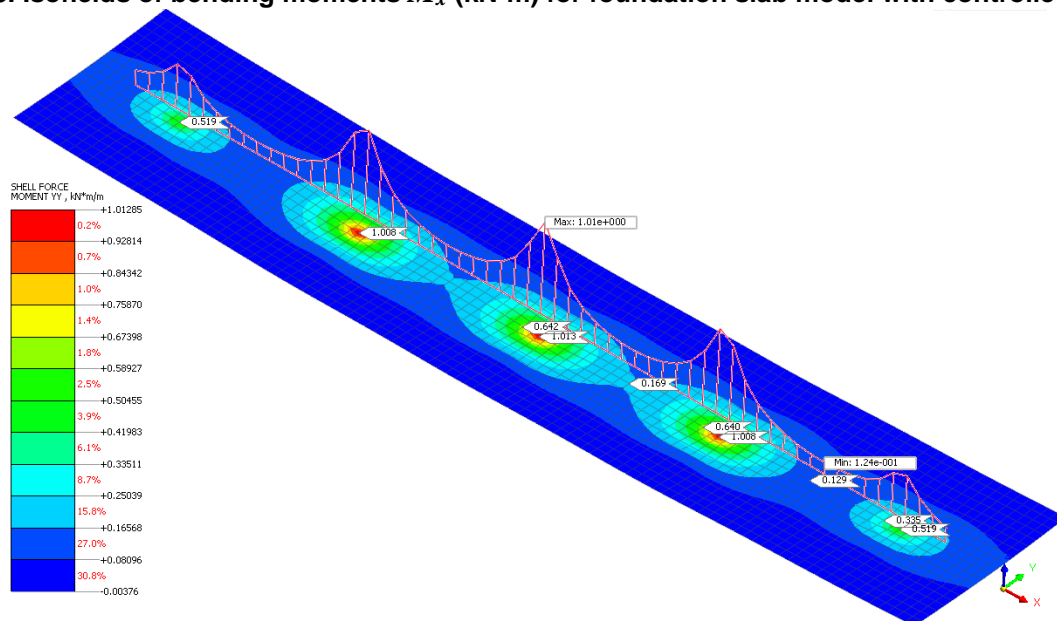


Figure 9. Isofields of bending moments  $M_y$  (kN-m) for solid foundation slab model.

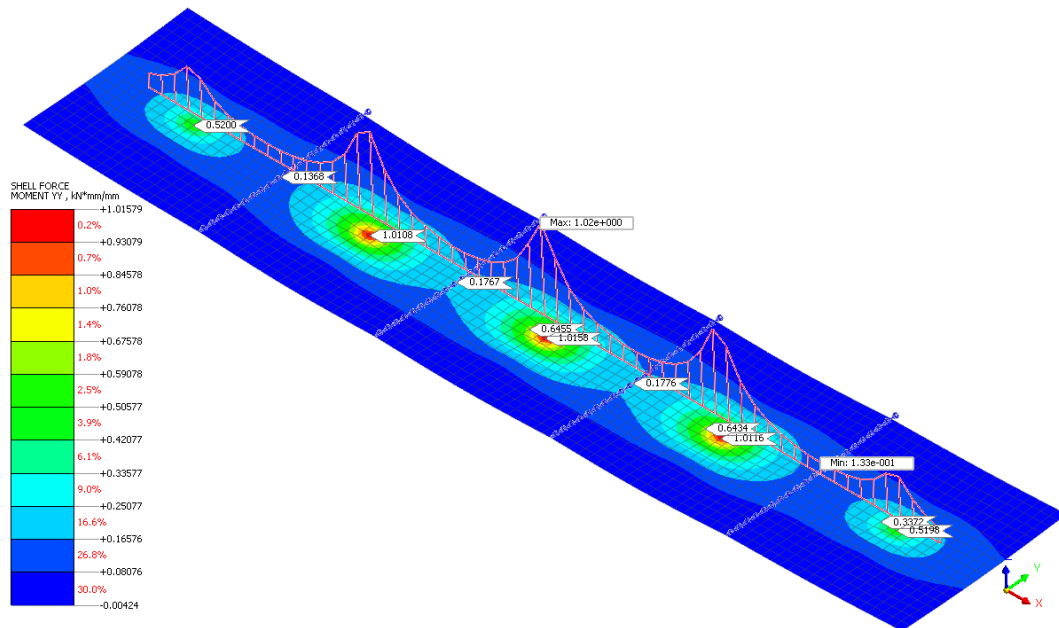


Figure 10. Isofields of bending moments  $M_y$  (kN·m) for foundation slab model with controlled forces.

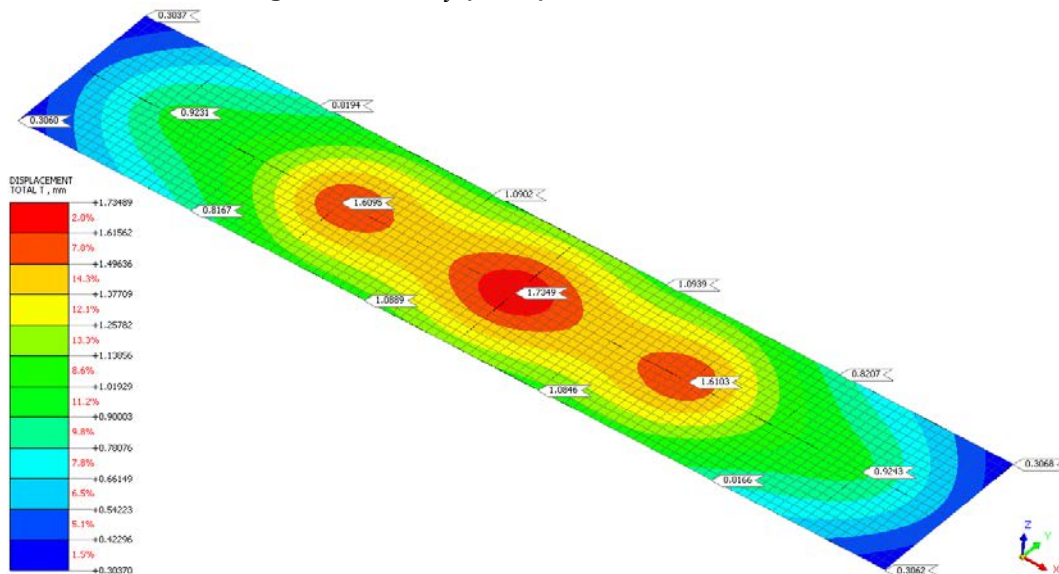


Figure 11. Base settlement (mm) for solid foundation slab model.

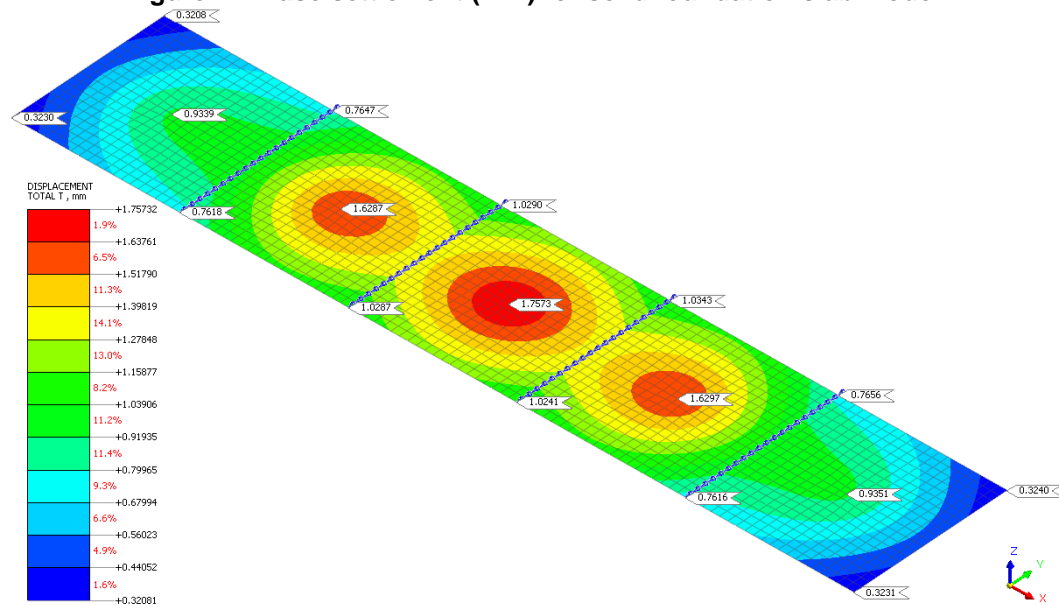
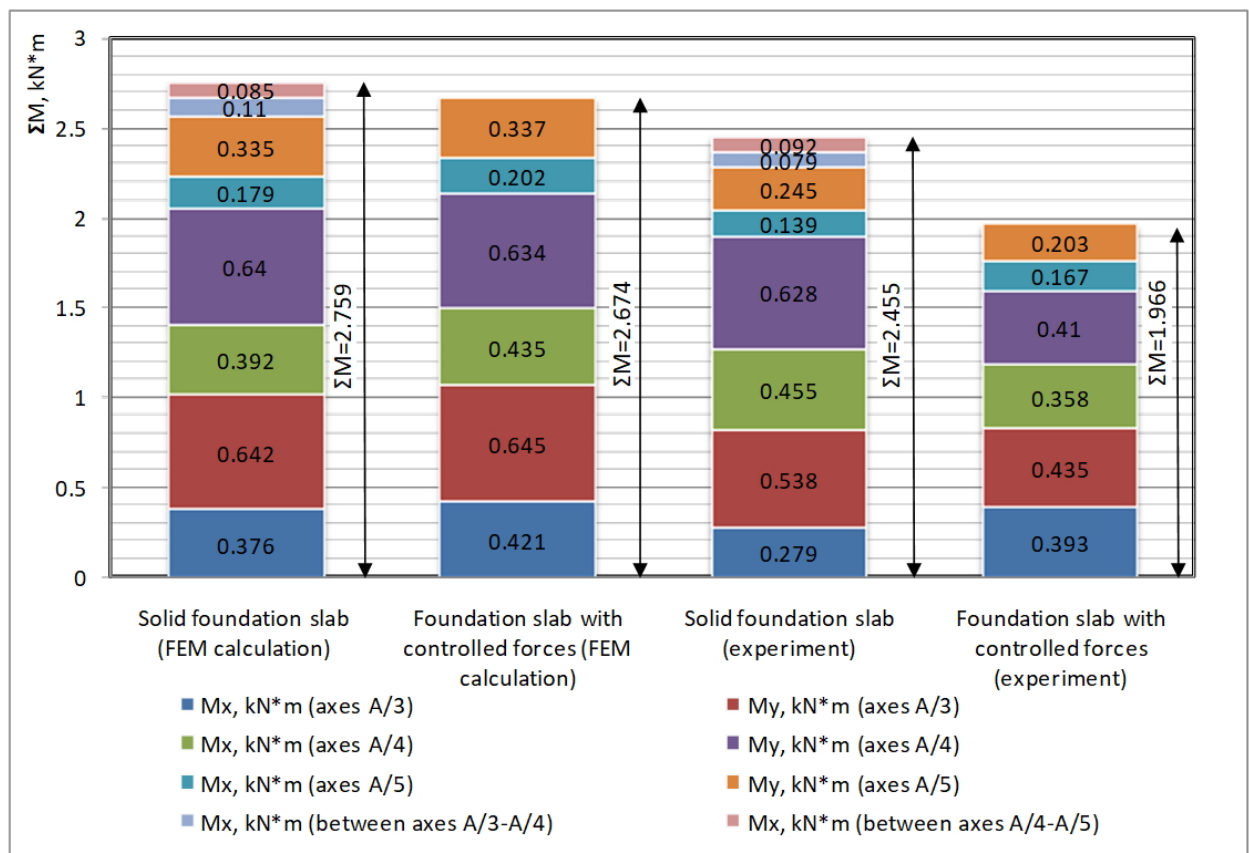


Figure 12. Base settlement (mm) for foundation slab model with controlled forces.

**Table 5. Summary of FEM calculations and experiment for foundation models under review.**

Compared parameters	FEM calculation results		Experiment results	
	Solid foundation slab	Foundation slab with controlled forces	Solid foundation slab	Foundation slab with controlled forces
M <sub>x</sub> , kN·m (axis 3)	<u>0.376</u> 0.928	<u>0.421</u> 0.970	0.279	0.393
M <sub>y</sub> , kN·m (axis 3)	<u>0.642</u> 1.013	<u>0.645</u> 1.016	0.538	0.435
M <sub>x</sub> , kN·m (axis 4)	<u>0.392</u> 0.948	<u>0.435</u> 0.988	0.455	0.358
M <sub>y</sub> , kN·m (axis 4)	<u>0.640</u> 1.008	<u>0.634</u> 1.012	0.628	0.410
M <sub>x</sub> , kN·m (axis 5)	<u>0.179</u> 0.465	<u>0.202</u> 0.481	0.139	0.167
M <sub>y</sub> , kN·m (axis 5)	<u>0.335</u> 0.519	<u>0.337</u> 0.520	0.245	0.203
M <sub>x</sub> , kN·m (between axes 3-4)	-0.110	-0.003	-0.079	-
M <sub>y</sub> , kN·m (between axes 3-4)	0.169	0.178	0.259	-
M <sub>x</sub> , kN·m (between axes 4-5)	-0.085	-0.002	-0.092	-
M <sub>y</sub> , kN·m (between axes 4-5)	0.129	0.137	0.010	-
Settlement in placements of PM4, PM5, PM6, PM7, mm	1.09	1.03	0.64	0.59
Settlement in placements of PM2, PM3, PM8, PM9, mm	0.82	0.76	0.61	0.51
Settlement in placements of PM1, PM10, mm	0.31	0.32	0.25	0.39



**Figure 13. Bar chart of compared values of bending moments in characteristic points (in places of resistance strain gauges installation) for the reviewed foundation models.**

Comparison of experimental and numerical results showed their qualitative and quantitative convergence for considered foundation models which is the evidence of correctness of the results obtained. Moreover, it is worth mentioning that the results of the studies are consistent with the results of the earlier publications [17–19].

#### 4. Conclusions

Based on the analysis of obtained data, we may come to the following conclusions:

1. Analysis of the results of experiment and numerical calculations showed qualitative and quantitative convergence of the results for the considered foundation models.
2. According to the results of the experiment in a continuous slab there is more uneven distribution of the values of the reference bending moments in comparison with numerical calculations.
3. Due to the hinged nodes, it is possible to change the nature of the bending moments' diagram, namely:
  - get rid of bending moments in the spots of maximal span bending moments
  - get rid of difference of signs of the bending moments' diagram
  - flatten the values of support bending moments for intermediate supports
4. Base settlements for the considered foundations do not have any significant difference in experiment and numeric calculations. However, it should be noted that according to the experiment results, the settlement line in the foundation slab with controlled forces is smoother, which will have a beneficial effect on distribution of forces in superstructure components.
5. Foundation slabs with controlled forces do not require reinforcement of the upper slab zone, and there is no need for mounting the structural anti-settlement reinforcement, as the sizes of sections for standard column meshes 6×6 and 6×9 m are small. Hence, mounting of supporting reinforcement frames for the upper mesh, due to the absence of the latter, is not needed, which considerably optimizes steel consumption per 1 m<sup>3</sup> of concrete for the proposed structure.
6. Use of foundation slab structure with controlled forces reduces the steel consumption for reinforcement, improves technical, economical and performance indicators, while retaining the basic favorable properties of solid slab foundations. The aforementioned factors enabled obtaining two patents of the Russian Federation for invention:
  - “Design of foundation slab with controlled forces” No. 2641356 [31];
  - “Hinged node for foundation slab with controlled forces” No. 2641357 [32].

#### References

1. Shmatkov, S.B., Kreilis, Y.V. Nonlinear analytical model of the 'foundation slab-soil base' system. 1989. Soil Mechanics and Foundation Engineering. 26(1). Pp. 31–33. DOI: 10.1007/BF02306234
2. Andreev, V.I., Barmenkova, E.V., Matveeva, A.V. On the Nonlinear Effect of Joint Work of the Basis, Foundation Slab and the Structure. 2011. Advanced Materials Research. No. 250–253. Pp. 3591–3594. DOI: 10.4028/www.scientific.net/AMR.250-253.3591
3. Dutta, S.C., Roy, R.A. A critical review on idealization and modeling for interaction among soil–foundation–structure system. Computers & Structures. 2002. 80(20–21). Pp. 1579–1594. DOI: 10.1016/S0045-7949(02)00115-3
4. Fiedler, J., Koudelka, T. Numerical modeling of foundation slab with concentrated load. Pollack Periodica. 2016. 11(3). Pp. 119–129. DOI: 10.1556/606.2016.11.3.11
5. Buchta, V., Janulikova, M., Fojtik, R. Experimental Tests of Reinforced Concrete Foundation Slab. Procedia Engineering. 2015. 114. Pp. 530–537. DOI: 10.1016/j.proeng.2015.08.102
6. Buchta, V., Fojtik, R., Hurta, J. Experimental load tests of reinforced concrete slab. Jurnal Teknologi. 2016. 78(5–5). Pp. 93–97. DOI: 10.11113/jt.v78.8624
7. Vallabhan, C.V.Girija, Das, Y.C. A refined model for beams on elastic foundations. International Journal of Solids and Structures. 1991. 27(5). Pp. 629–637. DOI: 10.1016/0020-7683(91)90217-4
8. Werkle, H., Slongo, L. Modellierung des Baugrunds bei der Finite-Element-Berechnung von Bodenplatten. 2018. Bautechnik. 95(9). Pp. 607–619. DOI: 10.1002/bate.201800041
9. Vaskova, A., Cajka, R. Interaction of nonlinear numerical model of SFRC slab and nonlinear numerical subsoil model. International Journal of GEOMATE. 2018. 47(15). Pp. 103–110. DOI: 10.21660/2018.47.3576
10. Loukidis, D., Tamiolakis, G.-P. Spatial distribution of Winkler spring stiffness for rectangular mat foundation analysis. Engineering Structures. 2017. No. 153. Pp. 443–459. DOI: 10.1016/J.ENGSTRUCT.2017.10.001
11. Mohyla, M., Vojtasik, K., Stolarik, M., Pinka, M., Lahuta, H. Experimentally measurement and analysis of stress under foundation slab. International Journal of GEOMATE. 2017. 35(13). Pp. 128–135. DOI: 10.21660/2017.35.6694
12. Ter-Martirosyan, Z., Ter-Martirosyan, A., Luzin, I. Settlement of a foundation slab, non-uniform in depth. MATEC Web of Conferences. 2017. 117(00166). Pp. 1–7. DOI: 10.1051/mateconf/201711700166
13. Kabantsev, O., Perelmuter A. Modeling Transition in Design Model when Analyzing Specific Behaviors of Structures. Procedia Engineering. 2013. No. 57. Pp. 479–488. DOI: 10.1016/J.PROENG.2013.04.062

14. Gorbunov-Passadov, M.I., Malikova, T.A., Solomin, V.I. Raschet konstruktsey na uprugom osnovanii [Calculation of structures on elastic foundation]. Moscow: Stroyizdat, 1984. 679 p. (rus)
15. Zhemochkin, B.N., Sinityn, A.P. Prakticheskiye metody rascheta fundamentnykh balok i plit na uprugom osnovanii [Practical methods for calculation of foundation beams and slabs on elastic foundation]. Moscow: Gosstroyizdat, 1962. 239 p. (rus)
16. Simvulidi, I.A. Raschet inzhenernykh konstruktsey na uprugom osnovanii [Calculation of engineering structures on elastic basement]. Moscow: Vysshaya shkola, 1978. 480 p. (rus)
17. Simvulidi, I.A. Sostavnyye balki na uprugom osnovanii [Compound beams on elastic foundation]. Moscow: Vysshaya shkola, 1961. 204 p. (rus)
18. Bosakov, S.V., Zinevich, S.I., Kozunova, O.V. Sticheskiy raschet sharnirno-soyedinennykh balok na uprugom osnovanii [Static design of hinged beams on elastic base]. Minsk: Izd-vo BNTU, 2018. Geotekhnika Belarusi: nauka i praktika. Minsk: Izd-vo BNTU. Pp. 82–91 [Online]. URL: <https://rep.bntu.by/handle/data/48484> (date of application: 30.03.2019). (rus)
19. Turabov, Kh.Sh., Eshbayeva, Z.N. Raschet dvukh balok, lezhashchikh na uprugom neodnorodnom osnovanii pri deystvii proizvolnoy raspredelennoy nagruzki [Calculation of two beams lying on elastic non-uniform base exposed to random distributed loads]. 2017. Molodoy Uchenyy. No. 6. Pp. 90–95 [Online]. URL: <https://moluch.ru/archive/140/39337/> (date of application: 30.03.2019). (rus)
20. Kiselev, N., Pronozin, Y., Stepanov, M., Bartolomey, L., Keck, D. Theoretical and Experimental Substantiation for Applicability of a Damping Layer in a Foundation Slab Placed on Soil Bed. MATEC Web of Conferences. 2016. 73(01017). P. 10. DOI: 10.1051/mateconf/20167301017
21. Iarkin, V., Kukhar, H. Regulation forces in slab foundation in the process construction of the building. 2016. Modern Industrial and Civil Construction. 12(3). Pp. 119–126 [Online]. URL: [http://donnasa.ru/publish\\_house/journals/spgs/2016-3/03\\_iarkin\\_kukhar.pdf](http://donnasa.ru/publish_house/journals/spgs/2016-3/03_iarkin_kukhar.pdf) (date of application: 30.03.2019).
22. Pronozin, Ya.A., Yepifantseva, L.R., Stepanov, M.A., Chikishev, V.M. Geotekhnicheskiy monitoring stroitelstva zhilogo doma na lentochno-obolocheynykh fundamentakh v gorode Tyumeni [Geotechnical Monitoring of Construction of a Residential Building on Strip-Shell Foundations in the City of Tyumen]. Industrial and Civil Engineering. 2017. No. 10. Pp. 59–66 [Online]. URL: <http://pgs1923.ru/english/eindex.htm> (date of application: 30.03.2019). (rus)
23. Nazarimofrad, E., Barkhordar, A. Buckling analysis of orthotropic rectangular plate resting on Pasternak elastic foundation under biaxial in-plane loading. Mechanics of Advanced Materials and Structures. 2016. 23(10). Pp. 1144–1148. DOI: 10.1080/15376494.2015.1059528
24. Cajka, R., Mynarcik, P., Labudkova, J. Experimental measurement of soil-prestressed foundation interaction. 2016. International Journal of GEOMATE. 22(10). Pp. 2101–2108 [Online]. URL: <http://dSPACE.vsb.cz/handle/10084/111836> (date of application: 30.03.2019).
25. Čajka, R., Vaskova, J. Fibre Concrete Foundation Slab Experiment and FEM Analysis. Key Engineering Materials. 2014. No. 627. Pp. 441–444. DOI: 10.4028/www.scientific.net/KEM.627.441
26. Mynarcik, P., Labudkova, J., Koktan, J. Experimental and numerical analysis of interaction between subsoil and post-ensoned slab-on-ground. Jurnal Teknologi. 2016. 78(5–4). Pp. 23–27. DOI: 10.11113/jt.v78.8530
27. Goncharov, B., Galimurova, O., Gareeva, N.B., Bashlykov, A.V. Estimation of bearing capacity and settlement of shell foundations on tamped beds. Soil Mechanics and Foundation Engineering. 2011. 48(2). Pp. 62–66. DOI: 10.1007/s11204-011-9130-z
28. Shulyatyev, S.O., Shulyatyev, O.A., Fedorovskiy, V.G. Sposob regulirovaniya neravnomernykh osadok mnogoetazhnogo zdaniya s plitnym ili plitno-svaynym fundamentom [Method of regulation of differential settlements of multi-storied building with raft or piled-raft foundation]. Patent Russia No. 2520751, 2014 [Online]. URL: [http://www1.fips.ru/Archive/PAT/2014FULL/2014.06.27/INDEX\\_RU.HTM](http://www1.fips.ru/Archive/PAT/2014FULL/2014.06.27/INDEX_RU.HTM) (date of application: 30.03.2019). (rus)
29. Ikonin, S.V., Sukhoterin, A.V. Design of the foundation slab with controlled forces. Magazine of Civil Engineering. 2015. 55(3). Pp. 10–20. DOI: 10.5862/MCE.55.2
30. Timoshenko, S.P., Woinowsky-Krieger, S. Theory of plates and shells. McGraw-hill. 1959. 575 p.
31. Ikonin, S.V., Sukhoterin, A.V. Konstruktsiya fundamentnoy plity s reguliruyemyimi usilyami [Design of foundation slab with adjustable forces]. Patent Russia No. 2641356, 2018. [http://www1.fips.ru/wps/portal/ofic\\_pub\\_ru/#page=document&type=doc&tab=IZPM&id=26C4A975-56E7-4808-B493-81699286BB92](http://www1.fips.ru/wps/portal/ofic_pub_ru/#page=document&type=doc&tab=IZPM&id=26C4A975-56E7-4808-B493-81699286BB92) (date of application: 30.03.2019). (rus)
32. Ikonin, S.V., Sukhoterin, A.V. Uzel sharnirnogo deystviya dlya fundamentnoy plity s reguliruyemyimi usilyami [Hinge action unit for foundation slab with adjustable forces]. Patent Russia No. 2641357, 2018 [Online]. URL: [http://www1.fips.ru/wps/portal/ofic\\_pub\\_ru/#page=document&type=doc&tab=IZPM&id=6ACCE6B5-9AC9-4393-BA30-62A0B8651530](http://www1.fips.ru/wps/portal/ofic_pub_ru/#page=document&type=doc&tab=IZPM&id=6ACCE6B5-9AC9-4393-BA30-62A0B8651530) (date of application: 30.03.2019). (rus)

### Contacts:

*Sergey Ikonin, +7(4732)558328; эл. почта: fornag@inbox.ru*

*Andrey Sukhoterin, +7(952)5529563; эл. почта: asukhoterin@list.ru*



DOI: 10.18720/MCE.85.12

## Влияние конструктивного исполнения на взаимодействие фундаментных плит с основанием

**С.В. Иконин, А.В. Сухотерин\***

*Воронежский государственный технический университет, г. Воронеж, Россия*

\* E-mail: [asuhoterin@list.ru](mailto:asuhoterin@list.ru)

**Ключевые слова:** экспериментальные исследования, системы с регулируемыми свойствами, плитные фундаменты, узел шарнирного действия

**Аннотация.** Предложено перспективное направление по снижению материалоемкости фундаментных плит за счет конструктивного исполнения. В качестве примера рассмотрено напряженно-деформированное состояние моделей сплошной плиты и плиты с регулируемыми усилиями при взаимодействии с песчаным основанием. Нагружение моделей осуществлялось статической системой сосредоточенных вертикальных сил. Напряженно-деформированное состояние моделей оценивалось по результатам лабораторных лотковых опытов с применением тензометрии и данным численных расчетов методом конечных элементов с использованием модели грунта Кулона-Мора. На основе сопоставления полученных результатов показано, что плита с регулируемыми усилиями имеет преимущества по сравнению со сплошной плитой. Например, за счет регулирования усилий удается избавиться от знакопеременности в эпюре изгибающих моментов, выровнять значения опорных изгибающих моментов для промежуточных опор, добиться более плавного прогиба плиты, следовательно создаются предпосылки для существенного снижения материалоемкости. Кроме того, установлено, что экспериментальные значения изгибающих моментов и прогибов плит качественно согласуются с численным прогнозом. При этом конечно-элементный расчет дает несколько завышенные абсолютные значения величин по сравнению с экспериментом. Результаты исследований могут быть полезны при проектировании фундаментных плит под опоры путепроводов, эстакад, а также промышленно-гражданские здания и сооружения каркасного типа с регулярной сеткой колонн.

### Литература

1. Shmatkov S.B., Kreilis Y. V. Nonlinear analytical model of the «foundation slab-soil base» system // Soil Mech. Found. Eng. Kluwer Academic Publishers-Plenum Publishers. 1989. Vol. 26. No. 1. Pp. 31–33.
2. Andreev V.I., Barmenkova E.V., Matveeva A.V. On the Nonlinear Effect of Joint Work of the Basis, Foundation Slab and the Structure // Adv. Mater. Res. Trans Tech Publications. 2011. Vol. 250–253. Pp. 3591–3594.
3. Dutta S.C., Roy R.A. A critical review on idealization and modeling for interaction among soil–foundation–structure system // Comput. Struct. 2002. Vol. 80. No. 20–21. Pp. 1579–1594.
4. Fiedler J., Koudelka T. Numerical modeling of foundation slab with concentrated load // Pollack Period. 2016. Vol. 11. No. 3. Pp. 119–129.
5. Buchta V., Janulikova M., Fojtik R. Experimental Tests of Reinforced Concrete Foundation Slab // Procedia Eng. 2015. Vol. 114. Pp. 530–537.
6. Buchta V., Fojtik R., Hurta J. Experimental load tests of reinforced concrete slab // J. Teknol. 2016. Vol. 78. No. 5–5. Pp. 93–97.
7. Vallabhan C.V.Girija, Das Y.C. A refined model for beams on elastic foundations // Int. J. Solids Struct. Pergamon. 1991. Vol. 27. No. 5. Pp. 629–637.
8. Werkle H., Slongo L. Modellierung des Baugrunds bei der Finite-Element-Berechnung von Bodenplatten // Bautechnik. John Wiley & Sons, Ltd. 2018. Vol. 95. No. 9. Pp. 607–619.
9. Vaskova A., Cajka R. Interaction of nonlinear numerical model of SFRC slab and nonlinear numerical subsoil model // Int. J. GEOMATE. 2018. Vol. 15. No. 47. Pp. 103–110.
10. Loukidis D., Tamiolakis G.-P. Spatial distribution of Winkler spring stiffness for rectangular mat foundation analysis // Eng. Struct. Elsevier. 2017. Vol. 153. Pp. 443–459.
11. Mohyla M. et al. Experimentally measurement and analysis of stress under foundation slab // Int. J. GEOMATE. 2017. Vol. 13. No. 35. Pp. 128–135.
12. Ter-Martirosyan Z., Ter-Martirosyan A., Luzin I. Settlement of a foundation slab, non-uniform in depth // MATEC Web Conf. / ed. Jemioł S. et al. EDP Sciences. 2017. Vol. 117. No. 00166. Pp. 1–7.
13. Kabantsev O., Perelmutter A. Modeling Transition in Design Model when Analyzing Specific Behaviors of Structures // Procedia Eng. Elsevier. 2013. Vol. 57. Pp. 479–488.

14. Горбунов-Пассадов М.И., Маликова Т.А., Соломин В.И. Расчет конструкций на упругом основании. М.: Стройиздат, 1984. 679 с.
15. Жемочкин Б.Н., Сеницын А.П. Практические методы расчёта фундаментных балок и плит на упругом основании. М.: Госстройиздат, 1962. 239 с.
16. Симвулиди И.А. Расчёт инженерных конструкций на упругом основании. М.: Высшая школа, 1978. 480 с.
17. Симвулиди И.А. Составные балки на упругом основании. М.: Высшая школа, 1961. 204 с.
18. Босаков С.В., Зиневич С.И., Козунова О.В. Статический расчет шарнирно-соединенных балок на упругом основании. Минск: Изд-во БНТУ // Геотехника Беларуси: наука и практика. Минск: Изд-во БНТУ, 2018. С. 82–91.
19. Турабов Х.Ш., Эшбаева З.Н. Расчет двух балок, лежащих на упругом неоднородном основании при действии произвольной распределенной нагрузки // Молодой ученый. 2017. № 6. С. 90–95.
20. Kiselev N. et al. Theoretical and Experimental Substantiation for Applicability of a Damping Layer in a Foundation Slab Placed on Soil Bed // MATEC Web Conf. EDP Sciences. 2016. Vol. 73. No. 01017. Pp. 1–10.
21. Iarkin V., Kukhar N. Regulation forces in slab foundation in the process construction of the building // Mod. Ind. Civ. Constr. 2016. Vol. 12. No. 3. Pp. 119–126.
22. Пронозин Я.А. и др. Геотехнический мониторинг строительства жилого дома на ленточно-оболочечных фундаментах в городе Тюмени // Промышленное и гражданское строительство. 2017. № 10. С. 59–66.
23. Nazariomofrad E., Barkhordar A. Buckling analysis of orthotropic rectangular plate resting on Pasternak elastic foundation under biaxial in-plane loading // Mech. Adv. Mater. Struct. Taylor & Francis. 2016. Vol. 23. No. 10. Pp. 1144–1148.
24. Cajka R., Mynarcik P., Labudkova J. Experimental measurement of soil-prestressed foundation interaction // Int. J. GEOMATE. The Geomate International Society. 2016. Vol. 10. No. 22. Pp. 2101–2108.
25. Cajka R., Vaskova J. Fibre Concrete Foundation Slab Experiment and FEM Analysis // Key Eng. Mater. Trans Tech Publications. 2014. Vol. 627. Pp. 441–444.
26. Mynarcik P., Labudkova J., Koktan J. Experimental and numerical analysis of interaction between subsoil and post-ensioned slab-on-ground // J. Teknol. 2016. Vol. 78. No. 5–4. Pp. 23–27.
27. Goncharov B. et al. Estimation of bearing capacity and settlement of shell foundations on tamped beds // Soil Mech. Found. Eng. Springer US. 2011. Vol. 48. No. 2. Pp. 62–66.
28. Пат. 2520751 Российская Федерация, МПК E02D 35/00 (2006.01). Способ регулирования неравномерных осадок многоэтажного здания с плитным или плитно-свайным фундаментом / Шулятьев С.О., Шулятьев О.А., Федоровский В.Г.; заявитель и патентообладатель Открытое акционерное общество «Научно-исследовательский центр «Строительство» ОАО «НИЦ «Строительство» (RU). № 2012156715/03; заявл. 26.12.2012; опубл. 27.06.2014, Бюл. № 18. 10 с.
29. Иконин С.В., Сухотерин А.В. Конструкция фундаментной плиты с регулируемыми усилиями // Инженерно-строительный журнал. 2015. № 3(55). С. 10–20. DOI: 10.5862/MCE.55.2.
30. Timoshenko S.P., Woinowsky-Krieger S. Theory of plates and shells. McGraw-hill, 1959. 575 p.
31. Пат. 2641356 Российская Федерация, МПК E02D 27/01 (2006.01). Конструкция фундаментной плиты с регулируемыми усилиями / Иконин С.В., Сухотерин А.В.; заявитель и патентообладатель Воронежский государственный технический университет (RU). № 2016122012; заявл. 02.06.2016; опубл. 17.01.2018, Бюл. № 2. 6 с.
32. Пат. 2641357 Российская Федерация, МПК E02D 27/01 (2006.01). Узел шарнирного действия для фундаментной плиты с регулируемыми усилиями / Иконин С.В., Сухотерин А.В.; заявитель и патентообладатель Воронежский государственный технический университет (RU). № 2016121982; заявл. 02.06.2016; опубл. 17.01.2018, Бюл. № 2. 11 с.

### **Контактные данные:**

*Сергей Вячеславович Иконин, +7(4732)558328; эл. почта: fornag@inbox.ru*

*Андрей Владимирович Сухотерин, +7(952)5529563; эл. почта: asuhoterin@list.ru*



DOI: 10.18720/MCE.89.13

## Temperature regime during the construction massive concrete with pipe cooling

C.T. Nguyen<sup>a\*</sup>, N.A. Aniskin<sup>a</sup>

<sup>a</sup> National Research Moscow State Civil Engineering University, Moscow, Russia

\* E-mail: [ntchuc.mta198@gmail.com](mailto:ntchuc.mta198@gmail.com)

**Keywords:** temperature field, exothermic heating, maximum temperature, temperature difference, cracking, pipe cooling system, massive concrete

**Abstract.** Pipe cooling is one of the effective measures in order to reduce the exothermic heating of massive concrete structures. In this paper, analyzing the influence parameters of the pipe cooling system on the temperature regime and the thermal stress state in mass concrete to be built. The concrete mass was considered as a pillar with dimensions in plan (10×10) m and a final height of 30.0 m. The effect of the following parameters was investigated: the height of the concrete column from the elevation of the foundation is used for the cooling pipe system; the step of cooling pipe system according to the height and width of the concrete block; the temperature of water supplied to the pipe cooling system. Then, numerical studies were carried out by using the Midas civil software package based on the finite element method in order to solve the temperature problem and determine the thermal stress state of the block. From that will be collected the numerical results from pictures of changes in the temperature regime and the thermally stressed state in mass concrete during construction. The influence of each of those factors is considered in order to evaluate the change in temperature regime and thermal stress of the concrete mass. So, the results obtained are of practical importance and can be used to assign parameters of the pipe cooling system.

### 1. Introduction

As is known, due to the process of cement hydration heat during construction of massive concrete structures is the temperature at the center of mass concrete significantly increased. At «an early age» concrete this heating causes free expansion of plastic material [1]. The surface of mass concrete under the influence of ambient temperature is cooled faster at the center of mass concrete. As a result, there is a significant temperature difference between the center and the surface of the mass concrete [2, 3]. In that case, if concrete enough strength, its deformability is limited, and the temperature drop causes tensile thermal stresses. This is likely to occur in the contact area between the concrete and foundation [4]. When these tensile stresses exceed the tensile strength of the concrete, thermal cracks are formed. To prevent thermal cracking of massive concrete during construction, thermal stress and temperature difference to be controlled is necessary [5].

There are methods and measures to control the temperature regime of the mass concrete during construction period [6, 7]. One of the most effective methods reduced the maximum temperature of the mass concrete in the process of its construction is applied by pipe cooling system. This method is typically used for large-scale concrete structures such as dams, massive foundations and bridge supports, etc. In fact, advantages include the innermost heated parts of the mass concrete structures are exposed to the cooling pipe. In addition, it is possible to control the maximum temperature by changing the operation of the cooling pipe system. This method allows to quickly reducing the maximum temperature in a mass concrete to the desired values at an early age. Hence, in order to achieve effective cooling, the pipes cooling systems are designed parameters exactly during the operation period. It is important to choose the material and diameter of the cooling pipes, cooling height, the distance between pipes, cooling temperature control, the start time and the end of the cooling system, etc [8].

---

Nguyen, C.T., Aniskin, N.A. Temperature regime during the construction massive concrete with pipe cooling. Magazine of Civil Engineering. 2019. 89(5). Pp. 156–166. DOI: 10.18720/MCE.89.13

Нгуен Ч.Ч., Анискин Н.А. Температурный режим возводимого бетонного массива с трубным охлаждением // Инженерно-строительный журнал. 2019. № 5(89). С. 156–166. DOI: 10.18720/MCE.89.13



This open access article is licensed under CC BY 4.0 (<https://creativecommons.org/licenses/by/4.0/>)

For the first time, the pipe cooling system was applied in the construction by American Hoover Dam in 1933 [9]. For examples of the later were applied of pipe cooling system can be observed such as during the construction of the Xiang Hong Dian dam in China (1955), the Bureyskaya hydroelectric power in Russia (1978), the Seo-He Bridge in Korea (2000), Tuyen Quang dam in Vietnam (2002), Dagangshan dam in China (2013), etc [10–15].

This paper presents the temperature regime during the construction of massive concrete with varying the parameters of the pipe cooling system. The analysis of the influence of the height of the pipe cooling, the distance between pipes, and the temperature of the cooling water on the temperature field and the thermal stress of the concrete during construction. The construction of mass concrete in this study with dimensions 10×20×30 m was considered. The research results can be applied in the design of mass concrete structures with the optimal parameters of the pipe cooling system in order to reduce thermal stress and improving the thermal crack in a mass concrete at an early age.

## 2. Materials and methods

The temperature field in a mass concrete with the cooling pipe systems is determined based on solving two differential equations Fourier according to the principle of energy balance [16]. One of them is the basic equation of the theory of thermal conductivity, taking into account the release of heat due to cement hydration is expressed as:

$$k_c \nabla^2 T_c + Q_h = \rho_c c_c \frac{\partial T_c}{\partial t}, \quad (1)$$

where  $T_c$  is the temperature of concrete at age  $t$  days (°C);

$k_c$  is the thermal conductivity of concrete (W/m·°C);

$Q_h$  is the heat of hydration (W/m<sup>3</sup>);

$c_c$  is the specific heat of concrete (kJ/kg·°C);

$\rho_c$  is the mass density of concrete (kg/m<sup>3</sup>);

$t$  is time (day).

The second equation takes into account the heat exchange between the pipe cooling system and the concrete is expressed as:

$$\rho_w c_w \left( \frac{\partial T_w}{\partial t} + \vec{u} \nabla T_w \right) = k_w \nabla^2 T_w, \quad (2)$$

where  $T_w$  is the temperature of water at age  $t$  days (°C);

$k_w$  is the thermal conductivity of water, (W/m·°C);

$c_w$  is the specific heat of water (kJ/kg·°C);

$\rho_w$  is the mass density of water (kg/m<sup>3</sup>).

These Fourier equations (1) and (2) can be solved by using initial, boundary conditions and a given graph of cement heat release during the hydration of cement [17, 18].

The formation of the temperature regime in a mass concrete not only depends on exothermic heating due hydration of cement but also on many other factors. The process of developing a temperature regime in a mass concrete is influenced by changes in environmental temperature such as convection and radiation.

Convection at the boundary of the concrete with ambient air is expressed using Newton's law. He shows that the rate of heat loss of the body is proportional to the temperature difference between the body in mass concrete and its surroundings. The boundary condition of convection is given by equation (3) [19–21]:

$$q_{\text{convect}} = h_c (T_c - T_{\text{air}}), \quad (3)$$

where  $T_c$  is the temperature of the body of concrete (°C);

$T_{\text{air}}$  is the air temperature (°C);

$h_c$  is the convection coefficient of concrete surface with ambient air (W/m<sup>2</sup>·°C).

The main complication in solving this problem is to take into account the removal of heat released as a result of exothermic be moved in the pipe system with water. Figure 1 shows a diagram of the interaction

of mass concrete with cooling pipe system. Due to the absorption of heat from the concrete in during cement hydration, the water temperature will gradually increase and its heat absorbing capacity will decrease because to the decreasing temperature difference between the concrete and the water. Heat transfer between the concrete and the water can be considered using Newton's law of convective heat transfer (2) [22].

The heat transfer from concrete through a small section of the cooling pipe with a flow rate of  $q$  during a small time interval  $dt$  was considered is shown in Figure 1. The amount of heat transferred from mass concrete to water through the inner surface of the pipe along the length of the pipe from the inlet to the outlet can be written as:

$$dQ_1 = \iint 2\pi r_0 dl Q_{c \rightarrow w} dt = -\lambda_c \iint \frac{\partial T_c}{\partial n} dl dt, \quad (4)$$

where  $Q_{c \rightarrow w}$  is the amount of heat transferred from concrete to water;

$r_0$  is the radius of the cooling pipe;

$\lambda_c \partial T / \partial n$  is the specific heat flow at the border of concrete – water pipe;

$n$  is the normal to the inner surface of the pipe.

The heat energy entering through the inlet and outlet sections of the cooling system pipe by the equations (5), (6).

$$dQ_{\text{inlet}} = \rho_w c_w q T_{\text{inlet}} dt, \quad (5)$$

$$dQ_{\text{outlet}} = \rho_w c_w q T_{\text{outlet}} dt, \quad (6)$$

Using the condition of heat equilibrium by assumption water is incompressible and, therefore, there are no change in the internal energy of water is given by equation (7).

$$dQ_{\text{outlet}} = dQ_{\text{inlet}} + dQ_1. \quad (7)$$

After substitution (5) and (6) into (7), it is possible to obtain the change in water temperature when passing through mass concrete  $\Delta T$  is given by equation (8).

$$\Delta T = T_{\text{outlet}} - T_{\text{inlet}} = dQ_1 = \frac{2\pi r_0 \lambda_c}{\rho_w c_w q} \iint \frac{\partial T_c}{\partial n} dl dt, \quad (8)$$

The given mathematical dependencies are incorporated into the algorithm for the numerical solution of the temperature problem of the mass concrete with the cooling pipe system by Midas civil software [23]. This complex was used for research in this work. In this study, three-dimensional finite-element models of the "Midas civil" were used both in order to solve the temperature field and thermal stress in a mass concrete with a cooling pipe system.

### 3. Results and Discussion

#### 3.1. Object of study

In this paper, was analyzed the influence of the parameters of the pipe cooling system on the temperature field and the thermal stress state in a mass concrete during the construction period. The dimensions of massive concrete as column shape with a size 10x20x30 m are considered. Taking advantage of the axial symmetry of the concrete block, 1/2 of the concrete block model has been divided into finite element mesh. The temperature field and thermal stress of points were considered (Figure 2). The concrete block was placed by ten lifts (each lift is 3 m thick) and construction schedule according to the thick of 0.3 m/day. Thus, the total time of construction of the concrete column was considered about 100 days. In the calculations, the following values of temperature are assumed: ambient temperature – 26.5 °C; temperature of foundation – 20 °C, the initial temperature of the concrete – 30 °C.

In the paper, the cement used has the maximum heat generation cement (389 kJ/kg), which is classified as large-heat cement. Most of the heat from the cement hydration process (up to 90% of the total heat) is released in the first 6 days after concreting. The maximum heat release rate of cement occurs in the first days after the laying of concrete and is approximately 200 kJ/kg.day. In this case, the highest intensity of heat release is on the first day [24].

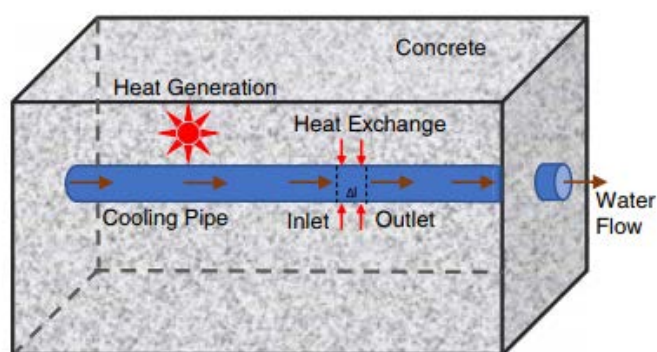


**Figure 1. Scheme of interaction of concrete with the cooling pipe system.**

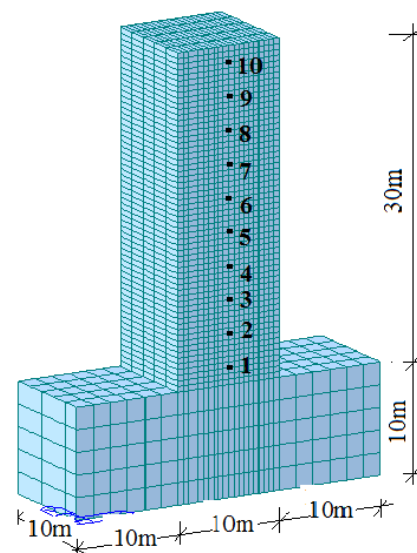


**Figure 2. Finite element discretization of the concrete block.**

The thermophysical characteristics of the concrete and the foundation were used in the numerical analysis and are shown in Table 1. The parameters and properties of the pipe cooling system are shown in Table 2.

**Table 1. Thermophysical characteristics of the materials in the model.**

Parameters	Concrete	Foundation
The coefficient of thermal conductivity (W/(m.°C))	2.65	1.98
Specific heat (kJ/kg.°C)	0.95	0.85
Density of the material (kg/m <sup>3</sup> )	2400	1800
The coefficient of convective heat transfer (W/m <sup>2</sup> .°C)	12.0	13.5
Modulus of elasticity (N/m <sup>2</sup> )	$2.7 \times 10^{10}$	$1.8 \times 10^{10}$
The coefficient of linear expansion (1/°C)	$1 \times 10^{-5}$	$1 \times 10^{-5}$
Poisson's ratio	0.20	0.28
Cement content (kg/m <sup>3</sup> )	289	–
Maximum heat release during hydration of cement (kJ/kg)	389	–

**Table 2. Characteristics of the pipe cooling system.**

Parameters	The pipe cooling
Heat transfer coefficient on the border with concrete (W/(m <sup>2</sup> .°C))	282
Specific heat (kJ/kg.°C)	4.2
The coefficient of thermal conductivity W(m.°C)	0.64
Volume (m <sup>3</sup> /h)	1.08
The water velocity in the pipe (m/s)	0.6
The water temperature in pipe (°C)	10÷20
Water density (kg/m <sup>3</sup> )	1000
Section area (m <sup>2</sup> )	0.00008
Diameter of pipe (m)	0.0254
Cooling duration (days)	7

There are many parameters and properties of the cooling pipe system effects on the temperature field and the thermal stress in a mass concrete during construction [25–27]. In this paper, the influence of the following parameters was studied:

- The height of the concrete column from the level of the foundation is used for the cooling pipe system.
- The step of cooling pipe system according to the height and width of the concrete block.
- The temperature of the water is supplied to the cooling pipe system.

### 3.2. Research results

As a result of the numerical simulation in during construction of concrete block by using software Midas civil has been obtained the temperature regime and thermal stress in a concrete block at different points in time during its construction. The most dangerous from the point of view about the capacity for work in the mass concrete is the values of the greatest tensile stresses. The study results show changes largest tensile stresses arising in the concrete block at the corresponding points in the period considered. For each point, the thermal stress was appeared at a certain time and in a certain direction are given in Figures 3–5.

#### Influence of the height of the pipe cooling zone on the thermal stress of the massive concrete.

The ratio of the height of the pipe cooling zone ( $b$ ) to the total height of concrete column ( $H$ ) changed and was taken to be equal to the following values  $b/H = 0.1, 0.2, 0.3, 0.4, 0.5$ . The pipe distance according to the height and width of the concrete block is  $1.5 \times 1.5$  m. Vertical layout schematic of the cooling water pipe is shown in Figure 3a. The number of layers of concrete laid from the foundation using a pipe cooling system varied from 1 to 5, which corresponds to a change in the ratio of  $b/H$ . The temperature of the cooling water entering the pipe cooling system was adopted  $t_w = 15$  °C. Time operation of the pipe cooling system after laying each layer of concreting was taken to be 7 days. The results of calculations of the distribution of the maximum thermal stress over the height of the concrete massif for the considered variants of the  $b/H$  are given in Figure 3b. For comparison with the cases of using the cooling pipe system, stress distribution in the concrete block without the cooling pipe system have been analyzed.

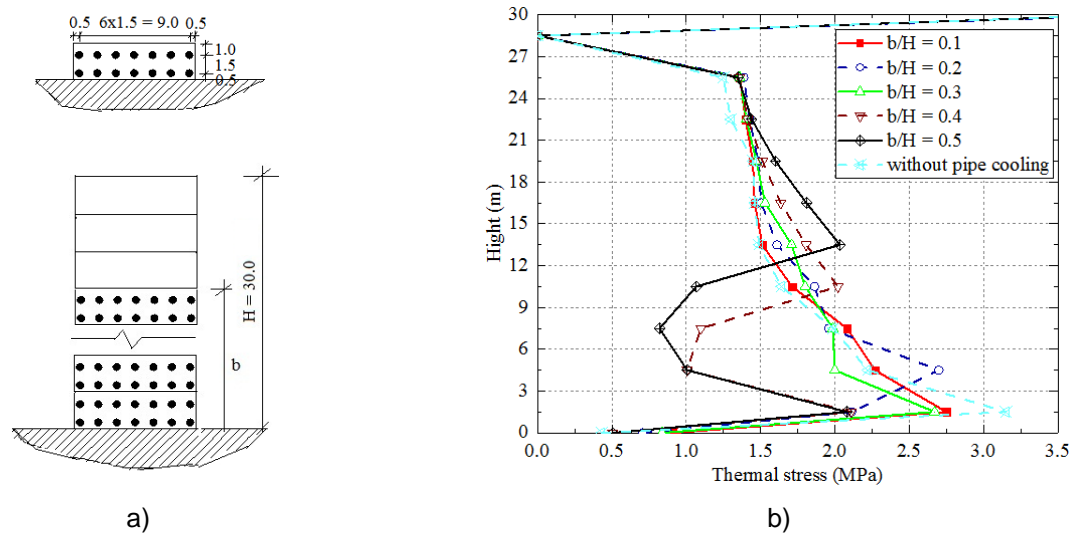


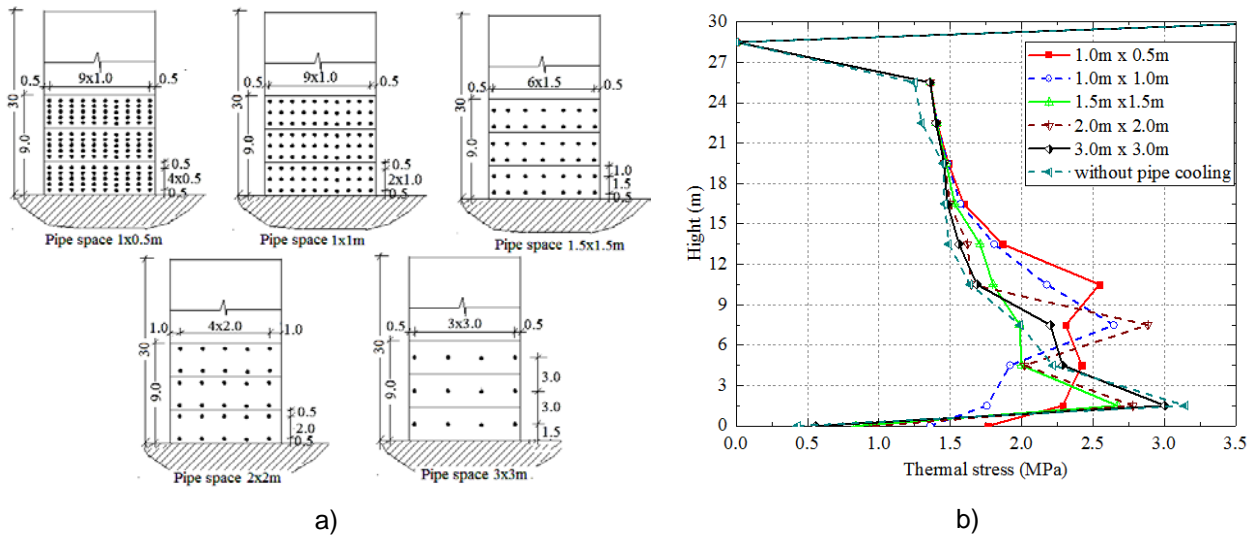
**Figure 3. Influence of the height of the pipe cooling zone on the thermal stress of the massive concrete: a) the layout of pipe cooling system; b) maximum thermal stress at the center of mass concrete with a different cooling height.**

As clearly observed in Figure 3b, we can give the following analysis. The thermally stressed state of concrete blocks for all variants is characterized by maximum tensile stresses in the contact zone. The maximum thermal stress depending on the height of the zone using the cooling pipe system. Thermal stress are 2.75, 2.70, 2.67, 2.11, 2.08 MPa, respectively when height of the cooling system zone  $b/H = 0.1, 0.2, 0.3, 0.4, 0.5$ . When the height of the pipe cooling zone increases, the maximum tensile thermal stress is reduced. Besides that, for comparison with the cases of using the cooling pipe system, the maximum tensile thermal stress when concrete block without cooling pipe system is 3.2 MPa is shown in Figure 3b. Furthermore, it is also possible to note that changes in the distribution of thermal stress on the height of the concrete column are presented in Figure 3b. So, when the height of the pipe cooling zone is 15.0 m ( $b/H = 0.5$ ) in the lower part of the column (the zone from the level of 3.0 m to the level of 12.0 m from the foundation), the thermal stress decreases and has a minimum thermal stress value of 0.78 MPa at the level of 7.5 m from the foundation. From the calculation results show that when the selected height of the pipe cooling zone reasonable, it is possible to reduce tensile stresses in the concrete mass and to obtain a favorable distribution of thermal stresses.

**The influence of the pipe spaces on the thermal stress in mass concrete.** The following cases of distances between pipes were considered (the first digit is the distance between pipes in the horizontal direction, the second is in the vertical): 1.0x0.5 m, 1.0x1.0 m, 1.5x0.5 m, 2.0x2.0 m, 3.0x3.0 m. The schemes of these cases are shown in Figure 4a. The height of the cooling zone in these calculations was assumed to be constant at 9 m ( $b/H = 0.3$ ). The water temperature in the pipes at the entrance to the system is  $t_w = 15$  °C. The duration of the cooling system after each layer concreting is 7 days.

Some results of the calculations obtained are shown in Figure 4b, which shows the distribution of maximum thermal stress along the height of the concrete column (at the points in the center of the concrete block is shown in Figure 2). It can be seen that thermal stress changes depending on the distances between the pipes of the cooling system (with cases are shown in Figure 4a – 1.0x0.5 m, 1.0x1.0 m, 1.5x1.5 m, 2.0x2.0 m and 3.0x3.0 m). It is clear that in terms of the above five different distances between the pipes, the maximum tensile stress of the concrete are 2.55, 2.65, 2.67, 2.88 and 3.00 MPa respectively is shown in Figure 4b.

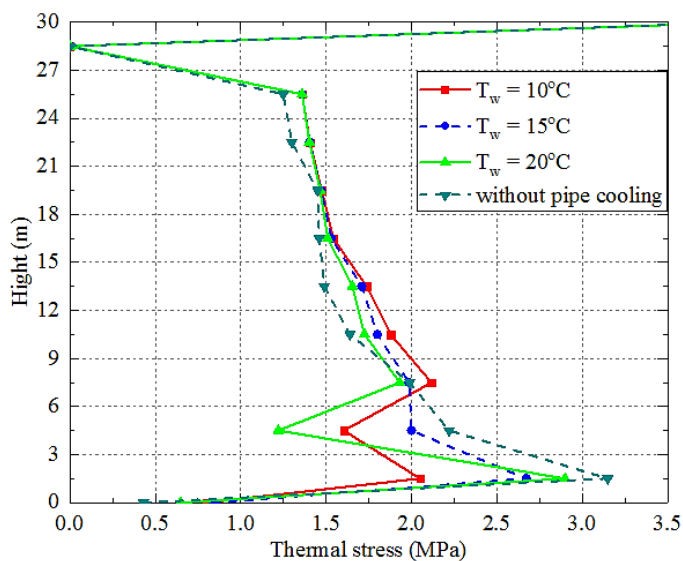
Research shows that when the most common pipe space (the case with the pipe space of 1.0 x 0.5 m), the maximum thermal stress of 2.55 MPa was obtained at the level of 10.5 m from the foundation (the area near the contact boundary between the concrete cooling zone and the layer on the concrete without the cooling pipe system). Figure 4b shows that the area near contact with the foundation, thermal stress is reduced to 2.30 MPa at 1.5 m from the foundation. Along the axis of the concrete block, when the distance of points from the foundation increases then the thermal stress decreases, as can be seen in Figure 4b.



**Figure 4. a – The layout of pipe cooling system with different distance between pipes; b – The effect of the distance between the cooling system pipe on the maximum thermal stress state of the concrete mass during construction.**

In the case of the concrete block without pipe cooling system the maximum tensile thermal stress of 3.2 MPa was obtained at a height of 1.5 m from the foundation. Obviously, the correct choice of the step between the cooling pipes will help prevent necessary crack formation and economic efficiency.

**Influence temperature of water in pipes on the thermal stress state in a mass concrete.** In these studies, the height of the pipe cooling zone is  $b/H = 0.30$ , the pipe distance is 1.5x1.5 m. The cooling duration after laying each 3 m layer of concreting was taken to be 7 days. In this paper, the temperature parameters of the cooling pipe system are assumed to vary from 10 to 20 °C.



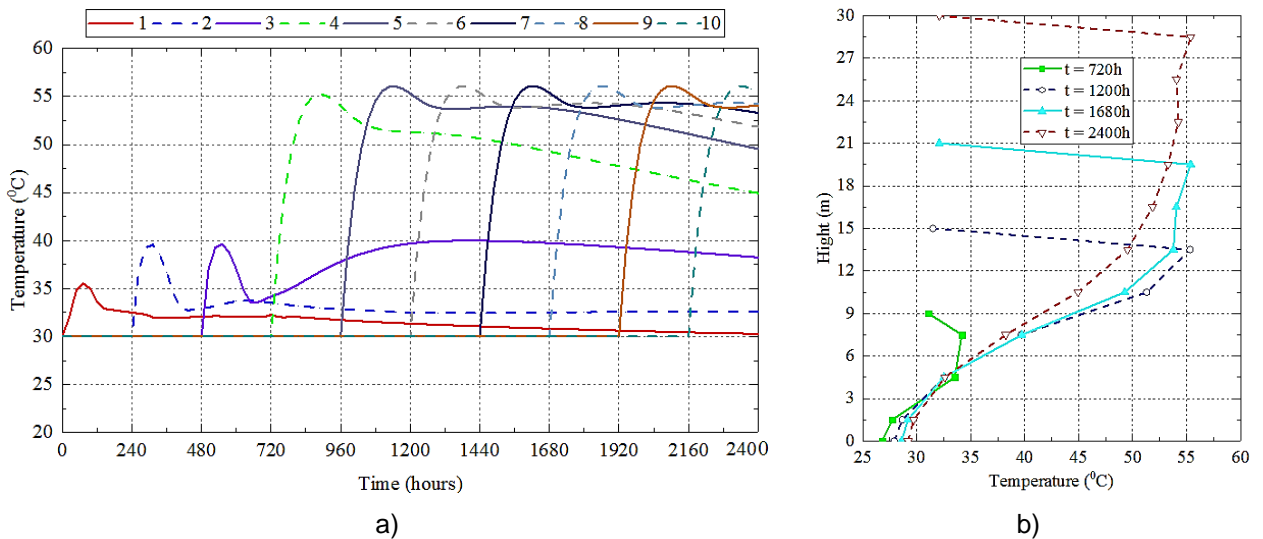
**Figure 5. Distribution of horizontal thermal stress along the height of the concrete column for different values of temperature of water in pipes.**

Figure 5 shows that maximum thermal stress distribution at the center section of the concrete column (at points 1–10 in Figure 2). The maximum thermal stress are 2.12, 2.67, 2.90 MPa respectively when the temperature of water in pipes 10, 15, 20 °C.

It should be noted that the use of cooling pipes can also have negative effects such as significant temperature difference, large local tensile stresses may occur around the cooling pipe. In order to avoid this, it is necessary to limit the minimum values of water temperature.

The temperature regime and the thermal stress in a concrete block with pipe cooling during construction were calculated with average values of the parameters of the cooling pipe system:  $b/H = 0.3$ , the pipe distance is  $1.5 \times 1.5$  m and water temperature in pipes  $t_w = 15$  °C. The results of these numerical calculations are presented in Figures 6–8.

The temperature of all the nodal points (10 nodes in Figure 2) changes over time during the construction of a concrete block are presented in Figure 6a. Analyzing the results it can be noted that the nodes 1, 2 and 3, which located in the zone of pipe cooling, the maximum temperature is significantly reduced: 36 °C (node 1) and 40 °C (nodes 2, 3) at the moment of time about 70 hours after corresponding to each layer of concrete. Besides that, the nodes (4–10) in the concrete block, the maximum temperature is reached about (55–56) °C at the time after 160 hours each of the concrete pours.



**Figure 6. Temperature regime of the concrete mass during construction: a – the graph changes the temperature of the nodes (1–10) in the mass concrete over time; b – the graph changes the temperature along the height of the concrete mass at different times.**

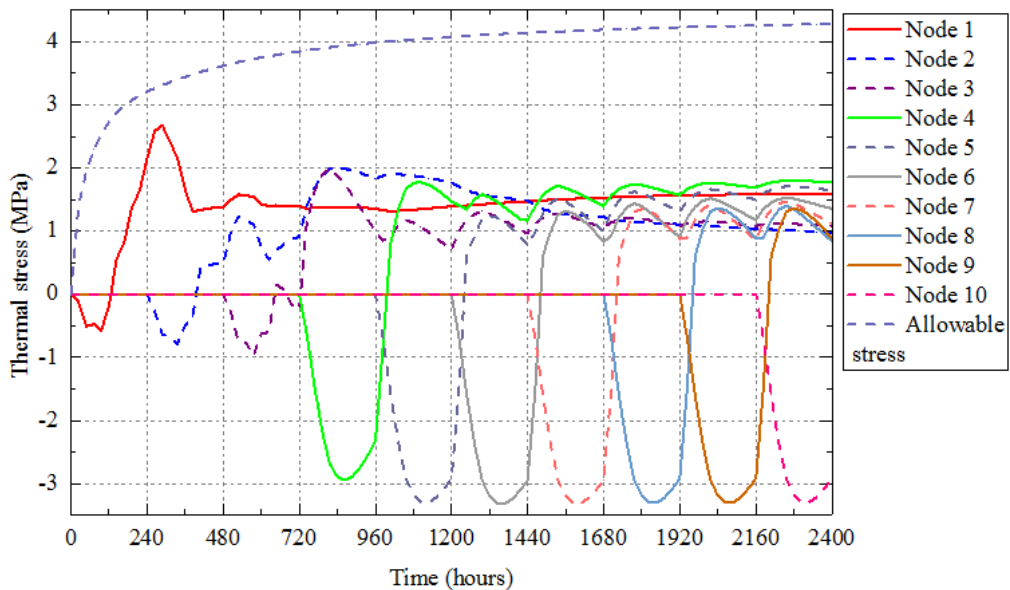


**Figure 7. The graph of the maximum thermal stress changes at the nodes (1–10) in the mass concrete over time, MPa.**

Figure 6b presents the results of temperature field changes at 10 nodes (see Figure 2) along the axis of the concrete block during construction. At elevation 9 m from the foundation, the maximum temperature is about 34 °C after 720 hours of pour concrete mixture. The maximum temperature in the concrete block is reduced when using the cooling pipe system. Besides, when concrete placing by large thickness without cooling pipe system, the maximum temperature in the concrete block is about 56.5 °C is shown in Figure 6a. Thus, the concrete block with the cooling pipe system has significantly reduced the risk of cracking in the mass concrete.

Furthermore, it can be noted that due hydration of cement raises the temperature at the center of each of the concrete pours, creating a temperature difference between the center and the surface of the concrete block reaching (22–24) °C, which induces a risk of through cracking at an early age.

The results of the calculation of thermal stresses at nodes along the axis of the concrete block are shown in Figure 7. The formation of cracks in mass concrete is possible when the maximum tensile stress exceeds the allowable tensile stress value. Allowable tensile stress is determined depending on the type of concrete and time. The graph of change of this tensile stress value in time is presented in Figure 7. For the considered problem, the maximum tensile stresses are observed near the base of the concrete block (node 1). However, the thermal tensile stress of node 1  $\sigma = 2.67$  MPa is lower than the allowable value (about 3.2 MPa), so thermal cracks do not occur in the concrete block during construction.

## 4. Conclusions

Based on the results of the study lead to the following conclusions:

1. The cooling pipe system was applied in the during construction of the mass concrete can significantly reduce the maximum temperature due to increased temperature of the cement hydration process and reduce the risk of thermal cracks.

2. When the mass concrete was applied to the pipe cooling system during construction, in order to obtain the optimal result for control the temperature field and economic efficiency, it is necessary to correctly assign the parameters of the cooling system such as the height of the pipe cooling zone, the distance between pipes and the temperature of water in pipes.

## References

- Krat, T.Yu., Rukavishnikova, T.N. Assessment of temperature regime and thermal stress state of concrete blocks under different conditions concreting. News VNIIG 2007. 248. Pp. 77–85.
- Bushmanova, A.V., Videnkov, N.V., Semenov, K.V., Barabanshchikov, Yu.G., Dernakova, A.V., Korovina, V.K. The thermo-stressed state in massive concrete structures. Magazine of Civil Engineering. 2017. 71(3). Pp. 51–60. DOI: 10.18720/MCE.71.6.
- Struchkova, A.Y., Barabanshchikov, Yu.G., Semenov, K.S., Shaibakova, A.A. Heat dissipation of cement and calculation of crack resistance of concrete massifs. Magazine of Civil Engineering. 2017. 78(2). Pp. 128–135. DOI: 10.18720/MCE.78.10
- Teleshev, V.I. Foundations and Methods of Concrete Dam Design and Construction in Severe Climatic Conditions. Doctoral Thesis. 2003, St. Peterburg: SPbGPU Publ. 217 p
- Aniskin, N.A., Nguyen, Hoang. Predicting crack formation in solid concrete dams in severe climatic conditions during construction period. Vestnik MGSU. 2014. Vol. 8. Pp. 165–178. DOI: 10.22227/1997-0935.2014.8.165-178
- Bushmanova, A.V., Barabanshchikov, Yu.G., Semenov, K.V., Struchkova, A.Ya., Manovitsky, S.S. Thermal cracking resistance in massive foundation slabs in the building period. Magazine of Civil Engineering. 2017. 76(8). Pp. 193–200. DOI: 10.18720/MCE.76.17
- Aurich, M., Filho, A.C., Bittencourt, T.N., Shah, S.P. Finite element analysis of concrete cracking at early age. Civil and Environmental Engineering. 2011. 37(5). Pp. 459–473. DOI: 10.12989/sem.2011.37.5.459
- Liu, X.-H., Duan, Y., Zhou, W., Chang, X. Modeling the piped water cooling of a concrete dam using the heat-fluid coupling method. Journal of Engineering Mechanics. 2013. 139(9). Pp. 1278–1289. DOI: 10.1061/(ASCE)EM.1943-7889.0000532
- Chen, S.-H., Su, P., Shahrour, I. Composite element algorithm for the thermal analysis of mass concrete Simulation of cooling pipes. International Journal of Numerical Methods for Heat & Fluid Flow. 2011. 21(4). Pp. 434–447 [Online]. URL: <https://doi.org/10.1108/09615531111123100>
- Ginzburg, S.M., Rukavishnikova, T.N., Shinker, N.Ya. Simulation models for assessing the temperature regime of a concrete dam on the example of the Bureyskaya HPP. News VNIIG. 2002. 241. Pp. 173–178.
- Khoa, H.N., Cong, V.C. Analyzing temperature field and thermal stress in massive concrete by finite element method. Journal of Science and Technology building. 2012. 14(12). Pp. 17–27.
- Li, C., Li, Y. Optimization of cooling pipes inside mass concrete bridge pile cap. The 2nd World Conference on Humanities and Social Sciences (WCHSS 2017). 2017. Pp. 25–30. DOI: 10.25236/wchss.2017.05
- Liu, X.-H., Zhang, C., Chang, X., Zou, W., Cheng, Y., Duan, Y. Precise simulation analysis of the thermal field in mass concrete with a pipe water cooling system. Applied Thermal Engineering. 2015. Vol. 78. Pp. 449–459 [Online]. URL: <https://doi.org/10.1016/j.applthermaleng.2014.12.050>
- Qiu, Y., Zhan, G. Stress and damage in concrete induced by pipe cooling at mesoscopic scale. Advances in Mechanical Engineering. 2017. 9(2). Pp. 1–17 [Online]. URL: <https://doi.org/10.1177/1687814017690509>
- Hong, Y.-X., Chen, W., Lin, J., Gong, J., Cheng, H.-D. Thermal field in water pipe cooling concrete hydrostructures simulated with singular boundary method. Water Science and Engineering. 2017. 10(2). Pp. 107–114 [Online]. URL: <https://doi.org/10.1016/j.wse.2017.06.004>

16. Myers, T.G., Fowkes, N.D., Ballim, Y. Modeling the cooling of concrete by piped water. *Journal of engineering mechanics*. 2009. 135(12). Pp. 1375–1383 [Online]. URL: [https://doi.org/10.1061/\(ASCE\)EM.1943-7889.0000046](https://doi.org/10.1061/(ASCE)EM.1943-7889.0000046)
17. Aniskin, N.A., Chuc, N.T. The thermal stress of roller-compacted concrete dams during construction. *MATEC Web of Conferences* 196, 04059(2018). 2018. Vol. 196. 8 p. [Online]. URL: <https://doi.org/10.1051/mateconf/201819604059>
18. Semenov, K.V., Konstantinov, I.A., Savchenko, A.V., Kokoreva, K.A., Nesterov, A.A. The effect of temperature influence in calculations of a thermostressed state of discretely increased concrete bodies. *Construction of Unique Buildings and Structures*. 2015. 32(5). Pp. 18–28.
19. Aniskin, N.A., Chuc, N.T. Temperature regime of massive concrete dams in the zone of contact with the base. *IOP Conf. Series: Materials Science and Engineering*. 2018. Vol. 365. 10 p. [Online]. URL: <https://doi.org/10.1088/1757-899X/365/4/042083>
20. Aniskin, N., Chuc, N.T., Long, H.Q. Influence of size and construction schedule of massive concrete structures on its temperature regime. *MATEC Web of Conferences*. 2018. Vol. 251. 8 p. [Online]. URL: <https://doi.org/10.1051/mateconf/201825102014>
21. Bennet, K., Nageswara, R.B., Dodagoudar, G.R. Early-age temperature distribution in a massive concrete foundation. *Global Colloquium in Recent Advancement and Effectual Researches in Engineering, Science and Technology (RAEREST 2016)*. 2016. Vol. 125. Pp. 107–114 [Online]. URL: <https://doi.org/10.1016/j.protcy.2016.08.087>
22. Singh, P.R., Rai, D.C. Effect of piped water cooling on thermal stress in mass concrete at early ages. *Journal of Engineering Mechanics*. 2018. 144(3). 11 p. [Online]. URL: [https://doi.org/10.1061/\(ASCE\)EM.1943-7889.0001418](https://doi.org/10.1061/(ASCE)EM.1943-7889.0001418)
23. Ding, J., Chen, S. Simulation and feedback analysis of the temperature field in massive concrete structures containing cooling pipes. *Applied Thermal Engineering*. 2013. 61(2). Pp. 554–562 [Online]. URL: <https://doi.org/10.1016/j.applthermaleng.2013.08.029>
24. Rasskazov, L.N., Orekhov, V.G., Aniskin, N.A. et al. Hydraulic structures. In 2 vol. Moscow, 2011. 535 p.
25. Japan Concrete Institute. Guidelines for control of cracking of mass concrete. Japan. 2016. 302 p.
26. Do, T., Lawrence, A., Tia, M., Bergin, M. Importance of insulation at the bottom of mass concrete placed on soil with high groundwater. *Transportation Research Record Journal of the Transportation Research Board*. 2013. 2342(1). Pp. 113-120 [Online]. URL: <https://doi.org/10.3141/2342-14>
27. Korotchenko, I.A., Ivanov, E.N., Manovitsky, S.S., Borisova, V.A., Semenov, K.V., Barabanshchikov Yu.G. Deformation of concrete creep in the thermal stress state calculation of massive concrete and reinforced concrete structures. *Magazine of Civil Engineering*. 2017. 69(1). Pp. 56–63. DOI: 10.18720/MCE.69.5.

**Contacts:**

*Chuc Nguyen, +7(966)3319199; ntchuc.mta198@gmail.com*

*Nikolay Aniskin, +7(910)4377227; nikolai\_aniskin@mail.ru*



DOI: 10.18720/MCE.89.13

## Температурный режим возводимого бетонного массива с трубным охлаждением

Ч.Ч. Нгуен<sup>а\*</sup>, Н.А. Анискин<sup>а</sup>

<sup>а</sup> Национальный исследовательский Московский государственный строительный университет, г. Москва, Россия

\* E-mail: [ntchuc.mta198@gmail.com](mailto:ntchuc.mta198@gmail.com)

**Ключевые слова:** температурный режим, экзотермический нагрев, максимальная температура, перепад температуры, трещинообразование, трубное охлаждение, массивный бетон

**Аннотация.** Трубное охлаждение является одним из эффективных мероприятий по снижению экзотермического нагрева массивных бетонных конструкций. В данной работе выполнен анализ влияния параметров системы трубного охлаждения на температурный режим и термонапряженное состояние возводимого бетонного массива. Бетонный массив рассматривался в виде столба с размерами в плане (10×10) м и окончательной высотой 30,0 м. Исследовалось влияние следующих параметров: высоты зоны бетонного столба от отметки основания, где используется система трубного охлаждения; шаг труб системы охлаждения по высоте и ширине бетонного массива; температура подаваемой в систему трубного охлаждения воды. Были проведены численные исследования с использованием программного комплекса «Midas civil» на основе метода конечных элементов как при решении температурной задачи, так и при определении термонапряженного состояния массива. В результате численных исследований получены картины изменения температурного режима и термонапряженного состояния бетонного массива в процессе его возведения. Проведена оценка влияния каждого из рассмотренных факторов на изменение температуры и температурных напряжений бетонного массива. Полученные результаты имеют практическое значение и могут быть использованы при назначении параметров системы трубного охлаждения.

### Литература

1. Крат Т.Ю., Рукавишникова Т.Н. Оценка температурного режима и термонапряженного состояния блоков водослива при различных условиях бетонирования // Известия ВНИИГ. 2007. Т. 248. С. 77–85.
2. Бушманова А.В., Виденков Н.В., Семенов К.В., Барабанщиков Ю.Г., Дернакова А.В., Коровина В.К. Термонапряженное состояние массивных бетонных конструкций // Инженерно-строительный журнал. 2017. № 3(71). С. 51–60. DOI: 10.18720/MCE.71.6.
3. Стручкова А.Я., Барабанщиков Ю.Г., Семенов К.В., Шайбакова А.А. Тепловыделение цемента и расчеты трещиностойкости бетонных массивов // Инженерно-строительный журнал. 2017. № 2(78). С. 128–135. DOI: 10.18720/MCE.78.10
4. Телешев В.И. Основы и методы проектирования и возведения бетонных плотин в особо суровых климатических условиях : дис. ... д-ра техн. наук. СПб.: СПбГПУ, 2003. 217 с.
5. Анискин Н.А., Нгуен Хоанг. Прогноз трещинообразования бетонных массивных плотин при возведении в суровых климатических условиях // Вестник МГСУ. 2014. Т. 8. С. 165–178. DOI: 10.22227/1997-0935.2014.8.165-178
6. Бушманова А.В., Барабанщиков Ю.Г., Семенов К.В., Стручкова А.Я., Мановицкий С.С. Термическая трещиностойкость массивных фундаментных плит в строительный период // Инженерно-строительный журнал. 2017. № 8(76). С. 193–200. DOI: 10.18720/MCE.76.17
7. Aurich M., Filho A.C., Bittencourt T.N., Shah S.P. Finite element analysis of concrete cracking at early age // Civil and Environmental Engineering. 2011. Vol. 37(5). Pp. 459–473. DOI: 10.12989/sem.2011.37.5.459
8. Liu X.-H., Duan Y., Zhou W., Chang X. Modeling the piped water cooling of a concrete dam using the heat-fluid coupling method // Journal of Engineering Mechanics. 2013. Vol. 139(9). Pp. 1278–1289. DOI: 10.1061/(ASCE)EM.1943-7889.0000532
9. Chen S.-H., Su P., Shahrour I. Composite element algorithm for the thermal analysis of mass concrete Simulation of cooling pipes // International Journal of Numerical Methods for Heat & Fluid Flow. 2011. Vol. 21. № 4. Pp. 434–447 [Электронный ресурс]. URL: <https://doi.org/10.1108/09615531111123100>
10. Гинзбург С.М., Рукавишникова Т.Н., Шейнкер Н.Я. Имитационные модели для оценки температурного режима бетонной плотины на примере Бурейской ГЭС // Известия ВНИИГ 2002. Т. 241. С. 173–178.
11. Khoa H.N, Cong V.C. Analyzing temperature field and thermal stress in massive concrete by finite element method // Journal of Science and Technology building. 2012. 14(12). Pp. 17–27.

12. Li C., Li Y. Optimization of cooling pipes inside mass concrete bridge pile cap // The 2nd World Conference on Humanities and Social Sciences (WCHSS 2017). 2017. Pp. 25–30. DOI: 10.25236/wchss.2017.05
13. Liu X.-H., Zhang C., Chang X., Zou W., Cheng Y., Duan Y. Precise simulation analysis of the thermal field in mass concrete with a pipe water cooling system // Applied Thermal Engineering. 2015. Vol. 78. Pp. 449–459 [Электронный ресурс]. URL: <https://doi.org/10.1016/j.applthermaleng.2014.12.050>
14. Qiu Y., Zhan G. Stress and damage in concrete induced by pipe cooling at mesoscopic scale // Advances in Mechanical Engineering. 2017. Vol. 9. № 2. Pp. 1–17 [Электронный ресурс]. URL: <https://doi.org/10.1177/1687814017690509>
15. Hong Y.-X., Chen W., Lin J., Gong J., Cheng H.-D. Thermal field in water pipe cooling concrete hydrostructures simulated with singular boundary method // Water Science and Engineering. 2017. Vol. 10. № 2. Pp. 107–114 [Электронный ресурс]. URL: <https://doi.org/10.1016/j.wse.2017.06.004>
16. Myers T.G., Fowkes N.D., Ballim Y. Modeling the cooling of concrete by piped water // Journal of engineering mechanics. 2009. Vol. 135. № 12. Pp. 1375–1383 [Электронный ресурс]. URL: [https://doi.org/10.1061/\(ASCE\)EM.1943-7889.0000046](https://doi.org/10.1061/(ASCE)EM.1943-7889.0000046)
17. Aniskin N.A., Chuc N.T. The thermal stress of roller-compacted concrete dams during construction // MATEC Web of Conferences 196, 04059(2018). 2018. Vol. 196. 8 p. [Электронный ресурс]. URL: <https://doi.org/10.1051/mateconf/201819604059>
18. Семенов К.В., Константинов И.А., Савченко А.В., Кокорева К.А., Нестеров А.А. Эффект температурного воздействия в расчетах термонапряженного состояния дискретно наращиваемых бетонных тел // Строительство уникальных зданий и сооружений. 2015. № 5(32). С. 18–28.
19. Aniskin N.A., Chuc N.T. Temperature regime of massive concrete dams in the zone of contact with the base. IOP Conf. Series // Materials Science and Engineering. 2018. Vol. 365. 10 p. [Электронный ресурс]. URL: <https://doi.org/10.1088/1757-899X/365/4/042083>
20. Aniskin N., Chuc N.T., Long H.Q. Influence of size and construction schedule of massive concrete structures on its temperature regime // MATEC Web of Conferences. 2018. Vol. 251. 8 p. [Электронный ресурс]. URL: <https://doi.org/10.1051/mateconf/201825102014>
21. Bennet K., Nageswara R.B., Dodagoudar G.R. Early-age temperature distribution in a massive concrete foundation // Global Colloquium in Recent Advancement and Effectual Researches in Engineering, Science and Technology (RAEREST 2016). 2016. Vol. 125. Pp. 107–114 [Электронный ресурс]. URL: <https://doi.org/10.1016/j.protcy.2016.08.087>
22. Singh P.R., Rai D.C. Effect of piped water cooling on thermal stress in mass concrete at early ages // Journal of Engineering Mechanics. 2018. Vol. 144. № 3. 11 p. [Электронный ресурс]. URL: [https://doi.org/10.1061/\(ASCE\)EM.1943-7889.0001418](https://doi.org/10.1061/(ASCE)EM.1943-7889.0001418)
23. Ding J., Chen S. Simulation and feedback analysis of the temperature field in massive concrete structures containing cooling pipes // Applied Thermal Engineering. 2013. Vol. 61. № 2. Pp. 554–562 [Электронный ресурс]. URL: <https://doi.org/10.1016/j.applthermaleng.2013.08.029>
24. Рассказов Л.Н., Орехов В.Г., Анискин Н.А. и др. Гидротехнические сооружения. В 2-х т. М., 2011. 535 с.
25. Japan Concrete Institute. Guidelines for control of cracking of mass concrete. Japan, 2016. 302 p.
26. Do T., Lawrence A., Tia M., Bergin M. Importance of insulation at the bottom of mass concrete placed on soil with high groundwater // Transportation Research Record Journal of the Transportation Research Board. 2013. Vol. 2342. № 1. Pp. 113–120 [Электронный ресурс]. URL: <https://doi.org/10.3141/2342-14>
27. Коротченко И.А., Иванов Э.Н., Мановицкий С.С., Борисова В.А., Семенов К.В., Барабанщиков Ю.Г. Деформации ползучести бетона в расчетах термонапряженного состояния массивных бетонных и железобетонных конструкций // Инженерно-строительный журнал. 2017. № 1(69). С. 56–63. DOI: 10.18720/MCE.69.5

**Контактные данные:**

*Нгуен Чонг Чык, +7(966)3319199; эл. почта: ntchuc.mta198@gmail.com*

*Николай Алексеевич Анискин, +7(910)4377227; эл. почта: nikolai\_aniskin@mail.ru*



DOI: 10.18720/MCE.89.14

## Modelling of contact interaction of structures with the base under dynamic loading

**A.A. Lukashevich**

*St. Petersburg State University of Architecture and Civil Engineering, St. Petersburg, Russia*

*E-mail: aaluk@bk.ru*

**Keywords:** structure, base, contact interaction, unilateral constraints, dynamic loading, discrete model, finite element method

**Abstract.** Constructively nonlinear problems with unilateral constraints are frequent in the calculation of various structures. At the same time, certain difficulties cause problems with the contact friction, as well as with the dynamic action of the load. In such cases, the contact problem becomes more complicated in terms of mathematics and its numerical solution becomes more complicated as well. This article is devoted to the construction of calculation models and methods for solving problems with non-ideal unilateral constraints under dynamic loading. As a result, a numerical algorithm has been developed based on the finite element model of contact and the step-by-step analysis method, which allows simultaneous integration of the motion equations and the realization of contact conditions with Coulomb friction. At the same time, to comply with the limitations under the conditions of ultimate friction-sliding, the method of compensating loads is applied. Using the proposed approach, numerical solutions of some problems of contact of a structure with a base have been obtained and analyzed. The reliability of the calculation results is confirmed by comparing them with the solution obtained by the alternative iteration algorithm. It can be concluded that the step-by-step analysis algorithm is more efficient in terms of computation time, showing satisfactory convergence, stability, and accuracy of the solution in a fairly wide range of time integration steps.

### 1. Introduction

Problems with unilateral constraints and friction between contacting surfaces are often encountered in the calculation of various types of structures. The solution of such problems under the action of static loads and different contact conditions was considered in some works [1–12]. At the same time, it is quite typical when it is necessary to take into account the dynamic loads on the structure [13–15].

When solving constructively nonlinear contact problems, both iterative (successive approximations) and incremental (step-by-step) methods are used. In particular, for the numerical solution of the dynamic contact problem, the variant of the iterative Schwartz method (with the finite-element discretization of the problem) is proposed in works [16, 17]. In works [18, 19] the iterative algorithm of the speeds correction of the Udzawa type is used for the finite-difference discrete model. In works [20–22] different versions of the method of iterations on the ultimate friction forces are applied on the basis of variational formulations of contact problems. As mentioned in these and other works, the application of the method of successive approximations allows one to build effective iterative algorithms that have a computational stability and guarantee the fulfillment of contact conditions for ideal unilateral constraints. However, the fulfillment of friction-sliding conditions on the contact here has certain difficulties and cannot always be realized.

In [23, 24], to fulfill the contact conditions, the weak formulation in the form of an elliptic quasi-variational inequality is used. The numerical solution of the variational problem is based on the finite element method and the implicit time integration scheme. The construction of various schemes for the numerical integration of the equations of motion is considered in works [25, 26]. In the first work the Lagrange multipliers and the minimum work principle are used at each time step, in the second one, the non-convex linear

---

Lukashevich, A.A. Modelling of contact interaction of structures with the base under dynamic loading. Magazine of Civil Engineering. 2019. 89(5). Pp. 167–178. DOI: 10.18720/MCE.89.14

Лукашевич А.А. Моделирование контактного взаимодействия конструкций с основанием при динамическом нагружении // Инженерно-строительный журнал. 2019. № 5(89). С. 167–178. DOI: 10.18720/MCE.89.14



This open access article is licensed under CC BY 4.0 (<https://creativecommons.org/licenses/by/4.0/>)

complementarity problem is solved at each step. The advantage of the step-by-step methods is that the solution of the contact problem can be obtained at any time point and at any stage of dynamic impact by using them. At the same time, there is an opportunity to satisfy the friction-sliding conditions more precisely, since the solution of the problem taking friction into account depends on the history of structure loading [1, 2]. The constructive nonlinearity in the case of dynamic loading will be manifested in the change of the working schemes of the structure in time – switching on and off unilateral constraints, both in normal and tangential direction. It is assumed that between two consecutive events on the contact, i.e. within the limits of each fixed working scheme, the character of the structure deformation is linear.

This paper is devoted to the development of a numerical model and algorithm for solving contact problems with unilateral constraints and friction under the dynamic load action. The immediate solution of the dynamic contact problem is made on the basis of time discretization using the direct schemes of integration of the equations of motion [27]. After each time step, the boundary conditions on the contact are checked. If within a certain step  $\Delta t$  there is a change of the working scheme, the time point of changing of the contact state (occurrence of the next event) is determined by the means of the step-by-time analysis of the contact state with the use of appropriate approximating expressions for displacements, speeds and accelerations on the time interval  $\Delta t$ . In this case, the integration step size is corrected and the current step is recalculated. As a result, a new state of contact is established at the given time point and, thus, the current working scheme of the structure is changed [7, 10]. Based on the step-by-step analysis of the dynamic loading process, the given approach has a clear physical nature and makes it possible to track the current state of the calculated system at any time point.

## 2. Methods

Let's consider the dynamic problem of interaction of linearly elastic bodies  $V^+$  and  $V^-$ , which may be, for example, the structure and base, with contacting surfaces,  $S_c^+$  and  $S_c^-$  correspondingly. To calculate this system we use a discrete computational model FEM, for which the following matrix equation of motion with initial conditions is true [27]:

$$[M]\{\ddot{U}^{t+\Delta t}\} + [C]\{\dot{U}^{t+\Delta t}\} + [K]\{U^{t+\Delta t}\} = \{P^{t+\Delta t}\}; \quad \{U\}|_{t=0} = \{U_0\}, \quad \{\dot{U}\}|_{t=0} = \{\dot{U}_0\}. \quad (1)$$

Taking into account that the displacement at time point  $t + \Delta t$  can be represented as  $U^{t+\Delta t} = U^t + \Delta U^{t+\Delta t}$ , let us convert equation (1) in the form that allows the solution of a constructively nonlinear dynamic contact problem to be reduced to the solution of the sequence of linear dynamic problems on the basis of step-by-step on time analysis of the contact state [28]:

$$[M]\{\ddot{U}^{t+\Delta t}\} + [C]\{\dot{U}^{t+\Delta t}\} + [K]\{\Delta U^{t+\Delta t}\} = \{P^{t+\Delta t}\} - [K]\{U^t\}; \quad \{U\}|_{t=0} = \{U_0\}, \quad \{\dot{U}\}|_{t=0} = \{\dot{U}_0\}. \quad (2)$$

Here  $[M]$ ,  $[C]$  and  $[K]$  are the mass, damping, and stiffness matrices of the finite element system respectively, at the same time, the proportional damping model is adopted  $[C] = \alpha[M] + \beta[\dot{M}]$ ;  $\{U^{t+\Delta t}\}$ ,  $\{\dot{U}^{t+\Delta t}\}$ ,  $\{\ddot{U}^{t+\Delta t}\}$  and  $\{P^{t+\Delta t}\}$  are the vectors of nodal displacements, speeds, accelerations, and the external nodal load at time point  $t + \Delta t$ ;  $\{\Delta U^{t+\Delta t}\}$  is the vector of displacements increment at step  $\Delta t$ . In addition, on the part of the outer boundaries  $S_g^\pm$ , for  $V^+$  and  $V^-$  correspondingly, boundary conditions on the forces, and on  $S_u^\pm$  – in the displacements should be given. It is assumed that at the initial time  $t = 0$  the vectors of displacements, speeds and accelerations are given and it is necessary to find a solution (2) during the time interval from 0 to some value  $T$ .

For the numerical integration of the motion equations (2), the implicit Newmark finite difference scheme is used, which is based on the assumption of a linear change of accelerations in the  $\Delta t$  interval. In this case, the following dependencies between the increments of displacements, speeds and accelerations for the time point  $t + \Delta t$  are used:

$$\ddot{U}^{t+\Delta t} = \frac{1}{\alpha(\Delta t)^2} (\Delta U^{t+\Delta t} - \Delta t \dot{U}^t) - \left( \frac{1}{2\alpha} - 1 \right) \ddot{U}^t; \quad \dot{U}^{t+\Delta t} = \dot{U}^t + \left( (1-\beta)\ddot{U}^t + \beta\ddot{U}^{t+\Delta t} \right) \Delta t. \quad (3)$$

Here  $\alpha$  and  $\beta$  are the parameters determining the accuracy and stability of integration [27]. Let us take  $\alpha = 1/4$ ,  $\beta = 1/2$ , which correspond to the case of the constant average acceleration at each of the intervals  $\Delta t$ . In this case, the Newmark integration scheme for linear problems is unconditionally stable, i.e. the solution does not grow indefinitely at large values of the step  $\Delta t$ .

Substituting the expression (3) in the equation (2), thereby excluding  $\ddot{U}^{t+\Delta t}$  and  $\dot{U}^{t+\Delta t}$  from the number of unknown ones, after simple transformations, we obtain the following matrix equation to determine  $\Delta U^{t+\Delta t}$ :

$$[\widehat{K}] \{ \Delta U^{t+\Delta t} \} = \{ \widehat{P}^{t+\Delta t} \}, \quad (4)$$

where  $\{ \widehat{P}^{t+\Delta t} \} = \{ P^{t+\Delta t} \} + [M] (\alpha_2 \{ \dot{U}^t \} + \alpha_3 \{ \ddot{U}^t \}) + [C] (\alpha_4 \{ \dot{U}^t \} + \alpha_5 \{ \ddot{U}^t \}) - [K] \{ U^t \}$ ;  $[\widehat{K}] = [K] + \alpha_0 [M] + \alpha_1 [C]$ . The coefficients  $\alpha_0 - \alpha_5$  depend on the step  $\Delta t$  and the parameters  $\alpha$  and  $\beta$ :

$$\alpha_0 = \frac{1}{\alpha(\Delta t)^2}; \quad \alpha_1 = \frac{\beta}{\alpha \Delta t}; \quad \alpha_2 = \frac{1}{\alpha \Delta t}; \quad \alpha_3 = \frac{1}{2\alpha} - 1; \quad \alpha_4 = \frac{\beta}{\alpha} - 1; \quad \alpha_5 = \frac{\beta \Delta t}{2\alpha} - \Delta t.$$

The system of algebraic equations (4) is solved by the LDLT factorization method, taking into account the sparsity of the symmetric matrix  $[\widehat{K}]$  and its variable profile. After finding  $\Delta U^{t+\Delta t}$  and, correspondingly,  $U^{t+\Delta t}$  for the calculation of accelerations  $\ddot{U}^{t+\Delta t}$  and speeds  $\dot{U}^{t+\Delta t}$ , equations (3) are used. In their turn, at any time point  $t'$  within the interval  $\Delta t$  ( $t \leq t' \leq t + \Delta t$ ), the values of accelerations  $\ddot{U}(t')$ , speeds  $\dot{U}(t')$  and displacements  $U(t')$  can be calculated with by the following formulas:

$$\begin{aligned} \ddot{U}(t') &= \ddot{U}^t + \frac{(t' - t)}{\Delta t} (\ddot{U}^{t+\Delta t} - \ddot{U}^t); \quad \dot{U}(t') = \dot{U}^t + \frac{(t' - t)}{2} (\ddot{U}^t + \ddot{U}^{t+\Delta t}); \\ U(t') &= U^t + (t' - t) \dot{U}^t + \frac{(t' - t)^2}{4} (\ddot{U}^t + \ddot{U}^{t+\Delta t}). \end{aligned} \quad (5)$$

The first of the equations (5), according to the Newmark scheme, expresses the linear law of change of acceleration on the interval  $\Delta t$ , the second and third ones are obtained from the expressions (3) with the value substitutions  $\alpha = 1/4$ ,  $\beta = 1/2$ , and the replacement of the value  $t + \Delta t$  by the value  $t'$ .

Furthermore, when taking into account unilateral constraint with Coulomb friction in addition to the initial conditions at  $t = 0$  and boundary conditions on  $S_g^\pm$ ,  $S_u^\pm$ , the conditions on the contacting surfaces  $S_c^\pm$  should be satisfied. The contact interaction will be modeled using frame-rod contact finite elements (CFE) [4, 10]. The CFE data provide a discrete contact between the nodes of the finite element grid located on the boundary surfaces of the contacting bodies.

Let us write conditions on the contact in terms of forces and displacements for each discrete unilateral constraint  $k$  (i.e. the  $k$  CFE), for the time point  $t$ :

$$u_{nk}^t \geq 0; \quad N_k^t \leq 0; \quad u_{nk}^t N_k^t = 0, \quad k \in S_c; \quad (6)$$

$$|T_k^t| \leq |T_{Uk}^t|; \quad T_k^t \dot{u}_{\tau k}^t \geq 0; \quad (T_k^t - T_{Uk}^t) \dot{u}_{\tau k}^t = 0, \quad k \in S_c. \quad (7)$$

Here  $u_{nk}^t$ ,  $u_{\tau k}^t$  are mutual displacements of the opposite nodes for unilateral constraint  $k$  in the normal and tangential direction;  $\dot{u}_{\tau k}^t = \partial u_{\tau k}^t / \partial t$  is the speed of mutual tangential displacement on the contact  $k$ ;  $N_k^t$ ,  $T_k^t$  are contact forces in the normal and tangential direction (forces in  $k$  CFE);  $T_{Uk}^t = -f_k N_k^t$  is ultimate Coulomb friction force for the contact  $k$ ;  $f_k \geq 0$  is the coefficient of friction-sliding.

The last of the conditions (6) means that upon contact  $u_{nk}^t = 0$ ,  $N_k^t < 0$ ; upon separation  $u_{nk}^t > 0$ ,  $N_k^t = 0$ . The last two conditions (7) establish the correspondence between the speeds of the mutual slippage

of the opposite nodes on the contact  $k$  and the magnitude of the force  $T_k^t$  at the time point  $t$ . Under the conditions  $\dot{u}_{\tau k}^t = 0$  and  $|T_k^t| < |T_{Uk}^t|$  there is a state of clutching (pre-ultimate friction); when  $\dot{u}_{\tau k}^t \neq 0$ ,  $|T_k^t| = |T_{Uk}^t|$  is the state of slippage, while the direction of the slip rate is in line with the direction of the shear force. Changing the current state, namely the moment of transition from one state to another, is an event – correspondingly, it will be the events of slippage, clutch, separation (switching off unilateral constraint), or contact (switching on it).

Let's briefly discuss the sequence of actions implementing a step-by-step algorithm for solving the dynamic problem with unilateral constraints and Coulomb friction. The General case is considered when the normal forces of interaction and, accordingly, the ultimate friction forces on the contact change in the process of dynamic loading, i.e. in time, as it often occurs in practical tasks.

It is believed that at the current time point  $t$  the state on the contact is known. The values of mutual displacements  $u_{nk}^t$ ,  $u_{\tau k}^t$ , speed  $\dot{u}_{\tau k}^t$  and contact forces  $N_k^t$ ,  $T_k^t$ ,  $T_{Uk}^t$  are determined for each unilateral constraint  $k$ . Let part of the constraints ( $k \in S_{1c}$ ) be in the state of clutching, the other part ( $k \in S_{2c}$ ) — in the state of contact with the slip and, finally, the third part ( $k \in S_{3c}$ ) — in the state of separation,  $S_c = S_{1c} \cup S_{2c} \cup S_{3c}$ . At the beginning of the calculation, at  $t = 0$ , the displacements, as well as the speeds and accelerations, are assumed to be zero.

1. The current time step  $\Delta t$  is performed, in the process of calculation its value can be changed in accordance with the established moment of occurrence of the next events on the contact. From the solution (4), the increments  $\Delta u_{nk}^{t+\Delta t}$ ,  $\Delta u_{\tau k}^{t+\Delta t}$ , then the values of displacements  $u_{nk}^{t+\Delta t}$ ,  $u_{\tau k}^{t+\Delta t}$ , speeds  $\dot{u}_{\tau k}^{t+\Delta t}$ , and contact forces  $N_k^{t+\Delta t}$ ,  $T_k^{t+\Delta t}$ ,  $T_{Uk}^{t+\Delta t}$  for the time point  $t + \Delta t$  are determined.

2. The traversal of all discrete constraints is performed, therewith for each constraint  $k$  there is (within the current step  $\Delta t$ ) the time point  $\hat{t}_k$  of occurrence of the next, i.e. the closest in the time event. The expression for determining the time point of slippage for the constraint  $k$  that was previously in the state of the clutching has the following form:

$$\hat{t}_k = t + \Delta t \left( \frac{T_{Uk}^t - T_k^t}{(T_k^{t+\Delta t} - T_k^t) - (T_{Uk}^{t+\Delta t} - T_{Uk}^t)} \right), \quad k \in S_{1c}. \quad (8)$$

The time point of clutch for the constraint  $k$  that was previously in the state of the sliding

$$\hat{t}_k = t + \Delta t \left( \frac{-\dot{u}_{\tau k}^t}{\dot{u}_{\tau k}^{t+\Delta t} - \dot{u}_{\tau k}^t} \right), \quad k \in S_{2c}. \quad (9)$$

The time point of separation or contact for the constraint  $k$  that, respectively, was previously in the state of the contact or separation

$$\hat{t}_k = t + \Delta t \left( \frac{-N_k^t}{N_k^{t+\Delta t} - N_k^t} \right), \quad k \in S_{1c}, S_{2c}; \quad \hat{t}_k = t + \Delta t \left( \frac{-u_{nk}^t}{u_{nk}^{t+\Delta t} - u_{nk}^t} \right), \quad k \in S_{3c}. \quad (10)$$

Since the change of displacements, speeds, and, therefore, forces, within the step  $\Delta t$  does not actually follow the linear law, then, additionally, using the expressions (4), an iterative refinement of the time point  $\hat{t}_k$  can be performed, the time consumption increases slightly in this case [28].

3. Of all the values  $\hat{t}_i$  having been found using the formulas (7) and being in the interval  $(t, t + \Delta t)$ , the smallest one corresponding to the moment of occurrence of the nearest time event on the contact is selected:  $\hat{t} = \min(\hat{t}_k)$ ,  $k \in S_c$ . In case  $\hat{t} > t + \Delta t$  the next basic integration step  $\Delta t$  is executed, i.e. transition to p.1 is performed.

4. In case  $t < \hat{t} < t + \Delta t$  — the recalculation of updated in such a way step with value  $\Delta \hat{t} = \hat{t} - t$  is performed. Herewith, the method of compensating loads is applied to comply with the conditions of the ultimate

friction [10, 28]. Changing of the ultimate friction forces on the contact is taken into account by the application of compensating forces to the opposite nodes

$$\widehat{F}_{\tau k} = -\Delta \widehat{T}_{Uk} = -\frac{\Delta t}{\Delta t} (T_{Uk}^{t+\Delta t} - T_{Uk}^t), \quad k \in S_{2c}. \quad (11)$$

The value of the transverse force on the contact  $k$  is corrected by the same quantity:  $T_k^{\hat{t}} = T_k^t + \Delta \widehat{T}_{Uk}$ .

As a result of the step recalculation, the values of displacements, speeds and forces on the contact in the time point  $\hat{t}$  are determined. The conditions of the expected event are checked; in case of slippage it will be a condition  $T_k^{\hat{t}} = T_{Uk}^{\hat{t}}$ ; in case of clutching —  $\dot{u}_{\tau k}^{\hat{t}} = 0$ , in case of detachment —  $N_k^{\hat{t}} = 0$ , in case of contact —  $u_{nk}^{\hat{t}} = 0$ . If the corresponding condition does not work, the time point  $\hat{t}$  should be updated once again but in the interval  $(t, \hat{t})$  or  $(\hat{t}, t+\Delta t)$ .

5. In case of occurrence of the next on time event on the corresponding support the state of contact changes — thereby the current working scheme of the construction changes too. Therewith the results of the recalculated step are considered final for the time point  $\hat{t}$ . Then all the above actions are repeated, but for the next integration step  $\Delta t$ .

The given algorithm is implemented by the author in the computer program [29]. The program is intended for doing numerical research and comparative analysis of various models of contact interaction of the deformable systems, methods and algorithms of their calculation. For the purpose of comparative evaluation of the results obtained, the program also implements the well-known methods for calculating systems with unilateral constraints and friction, in particular, the method of iterations on ultimate friction forces [21, 22].

Let us demonstrate the considered approach using the example of calculation of a plane framed system, which, for example, can simulate a pipeline section with a difference of relief under dynamic loading (Figure 1, a). It is considered that the system is fixed from lateral displacements, i.e. from the  $xy$  plane. On the rigid supports  $k = 1, 2$  the conditions of Coulomb friction-sliding with the possibility of separation on the contact operate. The structure is in the state of rest, then a horizontal impulse load  $P(t)$  is applied at the left end. The law of change of the pulse has a triangular shape with the duration of 0.1 s, the amplitude of 100 kN (Figure 1, b).

The longitudinal stiffness of the rods  $EA = 9 \cdot 10^6$  kN, bending stiffness  $EI = 2 \cdot 10^6$  kN·m<sup>2</sup>, the linear mass  $m = 0.4$  t/m. The damping matrix here simplistically computed as  $[C] = \alpha \cdot [M]$ , the damping coefficients were taken to be the following:  $\alpha = 0.2\omega_1$ ,  $\beta = 0$ . Contact interaction was modelled with frame-rod CEF [4, 10], connecting the support nodes of the framed system with fixed supports.

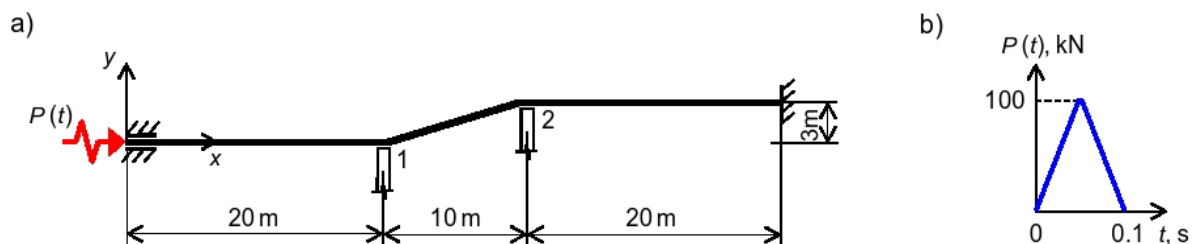


Figure 1. Framed system under the action of pulsed load  $P(t)$ .

At the initial time point  $t = 0$  on all supports the clutch state was set. The normal forces of interaction  $N_k^0$  on the contact of the structure nodes with the corresponding supports were taken to be equal to the reactions from the own weight of the structure. In the future, as a result of the action of the dynamic load, slippage, and the subsequent clutch on the contact is possible, as well as the switching off (separation) and the switching on of unilateral constraints during the considered time period. At the same time, due to the geometry of the framed system, the normal forces of interaction  $N_k^0$  also change over time.

The next was the problem of interaction of the water-tight slab of the dam with ground base at hydrodynamic effect of the water flow discharged from the headwater of the dam. The calculation scheme of the slab (Figure 2) corresponds to one of the objects of the Volzhsky hydroelectric complex. The purpose of

the calculations was to assess the impact of the pulsating component of water pressure in the discharge flow for the contact interaction of the water-tight slab of the dam with the base ground. The criterion condition for determining the ultimate values for the slab thickness in this case is to prevent the slippage or separation of the slab from the ground base.

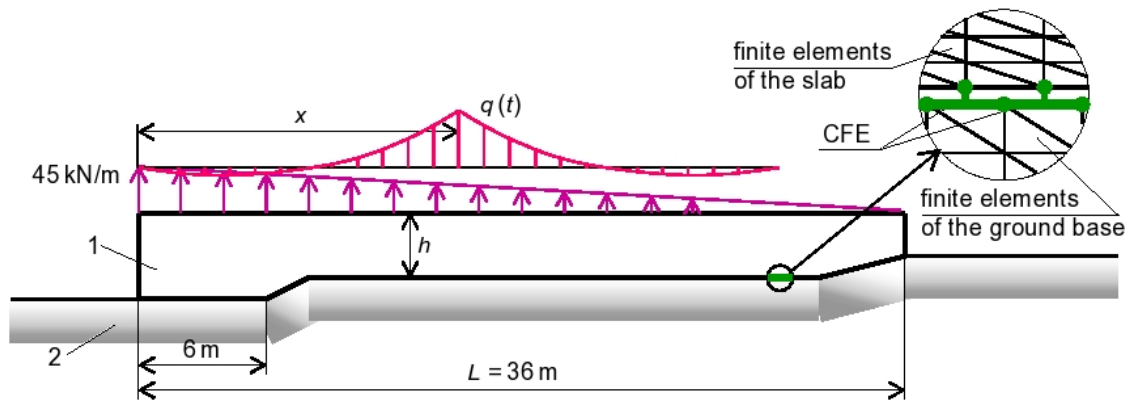


Figure 2. Scheme of the water-tight slab and applied loads.

The calculation took into account loads stipulated by the own weight of the slab, the hydrodynamic acting from the water flow, the filtration backpressure. The following characteristics of the slab material were taken: volume weight  $24 \text{ kN/m}^3$ , modulus of elasticity  $E_1 = 40000 \text{ MPa}$ , Poisson's ratio  $\nu_1 = 0.2$ . The considered area of the ground base was  $64 \times 20 \text{ m}$ , volume weight  $18 \text{ kN/m}^3$ , modulus of elasticity and Poisson's ratio  $E_2 = 600 \text{ MPa}$ ,  $\nu_2 = 0.25$ , the friction coefficient  $f = 0.31$ .

The pulsating component of the water pressure in the discharge flow was taken into account as a dynamic impulse load. The amplitude of the pulsating pressure  $q$  and the correlation of its distribution over the slab surface, depending on the position of the pulse center, were taken into account according to the recommendations from [30]. Taking into consideration the demonstration nature of the calculation, the accounting for damping is performed using a simplified scheme — similar to the previous example.

To study the dependence of the solution on the characteristics of the hydrodynamic acting, the behavior of the water-tight slab at different positions of the impulse on the slab ( $x/l$ ), likewise at its different directions and duration of the action was calculated.

### 3. Results and Discussion

#### 3.1. The problem of interaction of the framed system with rigid supports

The numerical solution of the considered problem, both by the proposed and, for comparative evaluation, by an alternative method, was carried out using the computer program [29]. The purpose of the calculations was to estimate the effect of the friction coefficient (the value  $f$  in the calculations varied from 0 to 1.5) on the behavior of the framed structure under dynamic loading. Figures 3 and 4 shows the horizontal and vertical displacements of the frame on one of the supports depending on the time at different values of the coefficient  $f$ , the integration step here was taken 0.0002 s.

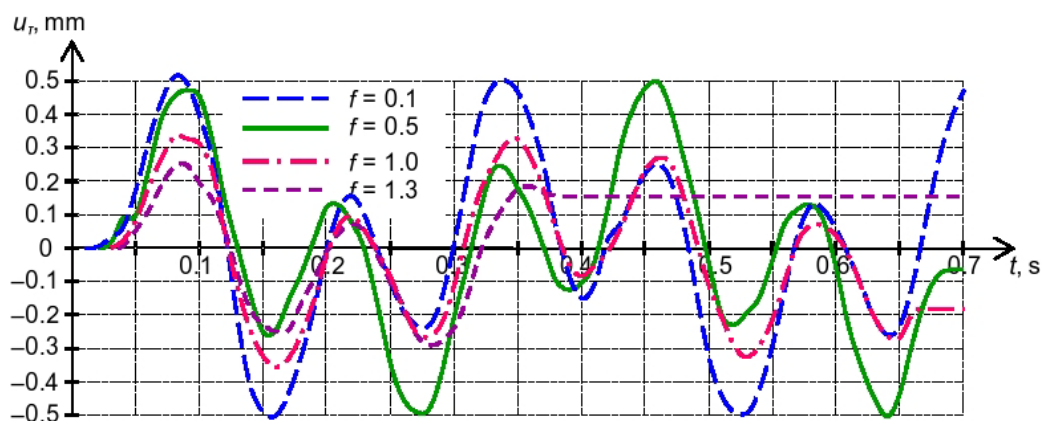


Figure 3. Horizontal displacements (slippage) on support 1 depending on time.

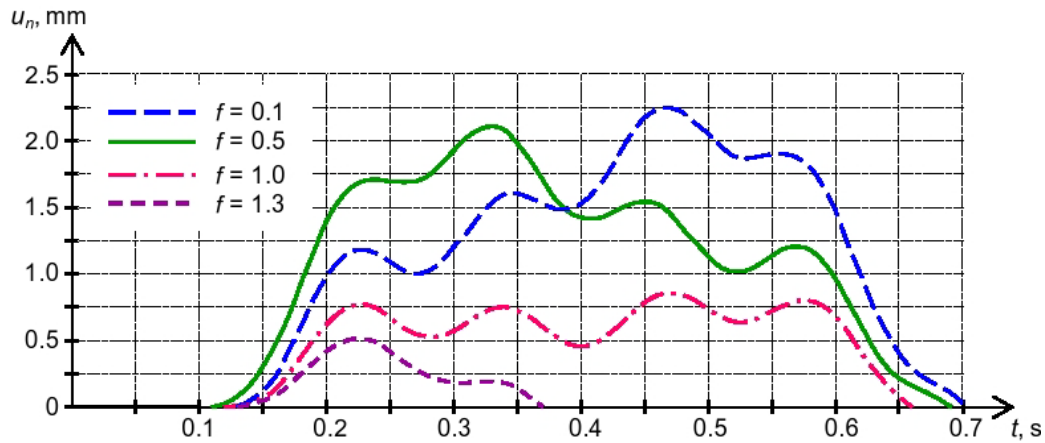


Figure 4. Vertical displacements (separation) on support 1 depending on time.

Figure 5 represents the dependencies between the amplitude values of the horizontal (slippage)  $u_\tau$  and vertical (separation)  $u_n$  displacements on the supports and the specified values of the friction coefficients  $f$  on the contact.

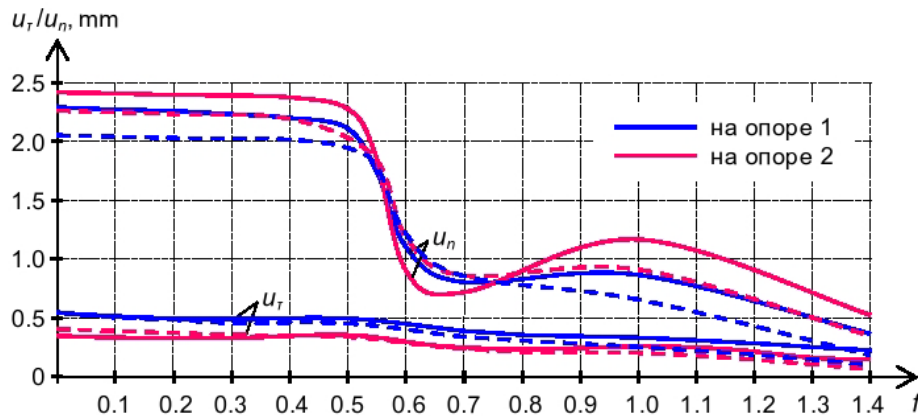


Figure 5. Amplitude values of displacements  $u_\tau$  and  $u_n$  on supports at different values of friction coefficient  $f$ .

The reliability of the obtained results is confirmed by the software check of the fulfillment of the equilibrium conditions and the compatibility of the system deformations after each time step. Besides, for the comparative evaluation of the results, the calculation of system was performed using an alternative algorithm where the contact conditions at each time step are realized by means of the method of iterations on ultimate friction forces (Figure 5 shows this solution by dotted line). As it can be seen, the results of the calculations by the proposed and alternative methods correspond each other, however, the algorithm of iterations on the ultimate forces requires much more calculation time (for the considered problem almost twice).

From the given graphs (Figures 3–5) it follows, that with an increase in the coefficient  $f$ , the separation of the structure from the supports as a result of the dynamic loading decreases significantly. Moreover, in the example considered here, there is a certain threshold value of the coefficient  $f$  (0.6–0.7), where the effect of contact friction on the value of maximum separation is extreme.

In order to study the dependence of the solution on the value of the integration step over time, the behavior of the framed structure for different values of  $\Delta t$  in the range from 0.0001 to 0.0064 s, with the successive doubling of the step length, was calculated. The comparison of the obtained results allows us to conclude that the proposed numerical approach shows satisfactory internal convergence in a rather wide range of integration steps on time. Thus, the values of horizontal and vertical displacements on the supports do not differ much when assigning the basic step in the range from 0.0001 to 0.0008 s. With a further increase in  $\Delta t$ , there is some deterioration in the convergence, especially at large values of the friction coefficient.

Note that, in the general case, the choice of the optimal integration step is a rather complex problem [27]. In this regard, basing on conducted numerical studies, it can be recommended to choose the value of the basic integration step in such a way that when it is increased, for example, twice, the change in the results does not exceed some specified error of calculation.

### 3.2. The problem of interaction of the water-fight slab with ground

As the results of the calculations show, the possible separation of the water-fight slab from the ground base in all cases occurs only at its edges (first from the left edge). The moment of separation depends on the position and direction of the impulse of pressure. The most dangerous, from the point of view of the separation slab from the base, is the pressure pulsation with the pulse duration of from 0.46 s (at the location of the pulse closer to the edges of the slab) to 0.5 s (for the middle of the slab). Figure 6 shows the change of contact stresses on the left edge of the slab base in time – to the moment of separation of the sole from the base. Here  $t/T_{imp}$  is the ratio of the current time  $t$  to the duration of the impulse of pressure  $T_{imp}$ ,  $x/L$  is the ratio of the  $x$  coordinate that defines the position of the impulse at the water-fight slab, to the slab length  $L$ . The slab thickness in these cases was taken to be slightly less than the ultimate values for separation  $h_{pr}$ .

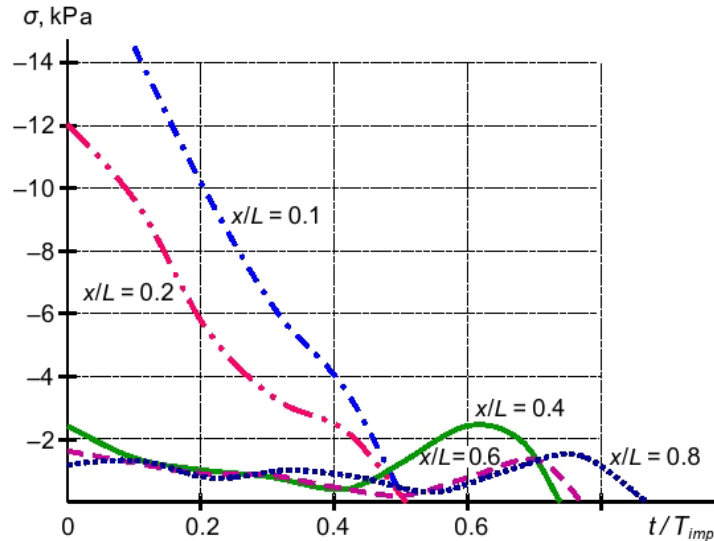


**Figure 6. Contact stresses on the left edge of the slab base before the moment of separation.**

Figures 7 and 8 demonstrate the deformed pattern of the slab-base system at the moment of maximum slab separation from the ground base. Here the slab thickness  $h = 2.5$  m – less than the ultimate one by separation, pulse position  $x/L = 0.4$ . Yellow and light blue points-markers indicate the zones of slippage or separation of the slab from the base.

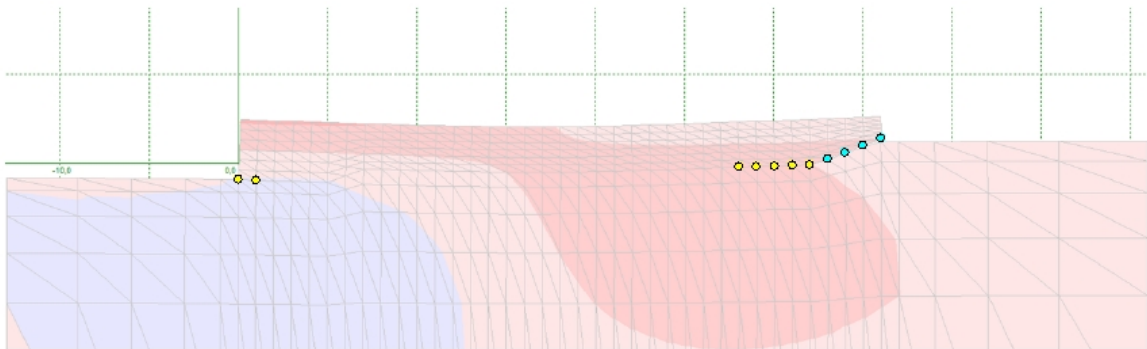


**Figure 7. Isopleth of horizontal displacements of the slab on the base.**

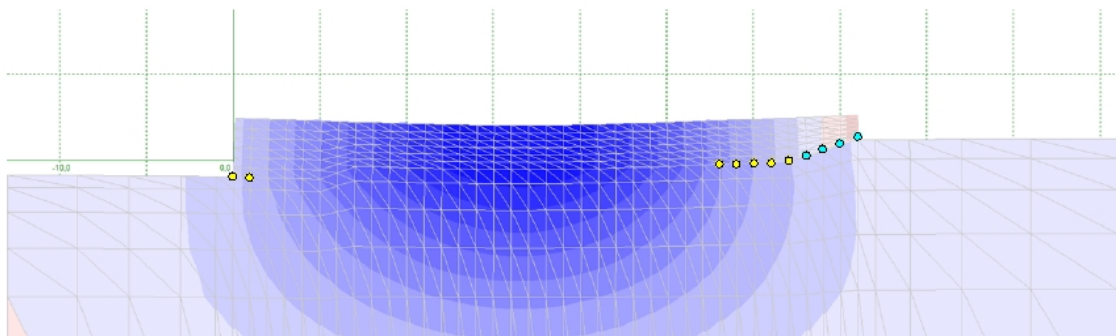


**Figure 8. Isopleth of vertical displacements of the slab on the base.**

Using numerical experiments, dependencies for the ultimate values of the water-fight slab thickness on the pulse position on it have been obtained (Figure 9). A solid line shows the envelope relative values of slab thickness, satisfying the condition its non-separation and shear from the base. Here  $h_{cr} = 3.48$  m is the critical depth corresponding to the design specific discharge of water. The dotted line corresponds to the ultimate slab thickness when only static loads are applied – pressure deficit and own weight of the slab. The given dependence can serve as a guide in the appointment of the thickness of the water-fight slab on the condition of preventing its slippage and separation from the ground base – you can take  $h = h_{cr}$ .

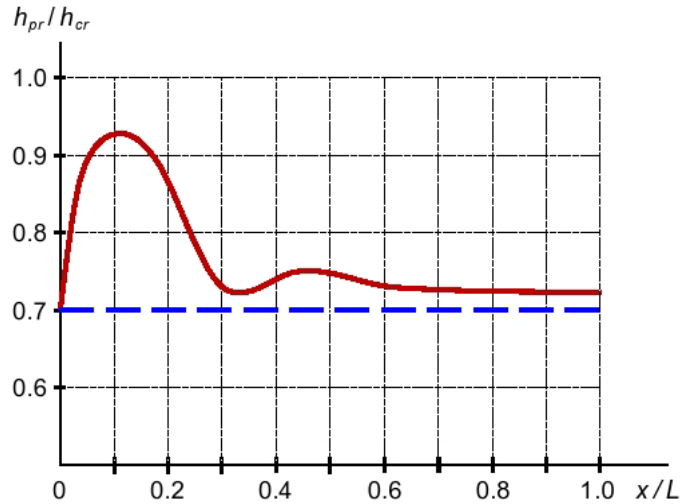


Figure 9. Dependence of the maximum slab thickness  $h_{pr}$  on the pulse position  $x / l$ .

#### 4. Conclusion

1. The problem of the contact interaction of elastically deformable systems under dynamic loading is considered in the article. To solve it, we propose the numerical algorithm combining in one step-by-step process with the integration of the equations of motion with step-by-time analysis of the contact state. For more accurate compliance with the limitations under the conditions of ultimate friction-sliding, the method of compensating loads has been applied.

2. The basis of the above algorithm is a step-by-step analysis method that has a clear physical interpretation. It is shown that this approach provides the possibility of analyzing the contact interaction of structures with the base under dynamic loading and has the advantage in cases when the solution of the problem depends on the history of loading, in particular, when accounting for friction-sliding in unilateral constraints.

3. The discrete calculation model of the FEM is used, upon that for the modeling of unilateral constraints with Coulomb friction, the contact finite elements in the form of frame-rod system has been used. The CFE data providing a discrete contact between the boundary surfaces of the interacting elastic bodies, allows you to determine the forces and displacements in the contact zone with the same and high accuracy, to apply an inconsistent finite element grids, to take the physical and geometric properties of the contact seam into account.

4. The carried out of test calculations allow us to conclude about the efficiency and reliability of the proposed algorithm, taking into account the complicated contact conditions and dynamic loading, which are essential for solving applied problems of structural mechanics. The comparison with the well-known algorithm of iterations on ultimate forces shows in our case a significant saving of calculation time. Using the analysis of the calculation results of the water-fight slab, proposals concerning the constructive solutions of the considered structure, taking into account the nature and position of the dynamic loads acting on it, were made.

5. In conclusion, we note that the account of complicated conditions of contact interaction contributes to the approximation of the calculation scheme to the real working conditions of structure and, thus, allows us getting more accurate and complete information about its strength and reliability.

#### References

1. Laursen, T.A. Computational Contact and Impact Mechanics. Berlin-Heidelberg: Springer, 2002. 454 p.
2. Wriggers, P. Computational Contact Mechanics. Berlin-Heidelberg: Springer, 2006. 521 p.
3. Laursen, T., Yang, B. A contact searching algorithm including bounding volume trees applied to finite sliding mortar formulations. Computational Mechanics. 2008. No. 41. Pp. 189–205.

4. Bukhartsev, V.N., Lukashevich, A.A. Stability assessment of a structure subject to asymmetric load application on a rock-free bed. *Power Technology and Engineering*. Springer New York Consultants Bureau. 2012. Vol. 45. No. 5. Pp. 346–350.
5. Wriggers, P., Schroder, J., Schwarz, A. A finite element method for contact using a third medium. *Computational Mechanics*. 2013. No. 52(4). Pp. 837–847.
6. Kolosova, G.S., Lalin, V.V., Kolosova, A.V. The effect of construction joints and cracks on the stress-strain state of the arch-gravity dam. *Magazine of Civil Engineering*. 2013. 40(5). Pp. 76–85. (rus) doi: 10.5862/MCE.40.9
7. Lukashevich A.A. Computational solution of contact problems with unilateral constraints and friction by step-by-step analysis. *Advanced Materials Research*. 2014. Vol. 941–944. Pp. 2264–2267.
8. Barboteu, M., Danan, D., Sofonea, M. Analysis of a contact problem with normal damped response and unilateral constraint. *Journal of Applied Mathematics and Mechanics*. 2016. 96(4). Pp. 408–428.
9. Wriggers, P., Rust, W.T., Reddy, B.D. A virtual element method for contact. *Computational Mechanics*. 2016. 58(6). Pp. 1039–1050.
10. Lukashevich, A.A. Computational modelling of stiffness and strength properties of the contact seam. *Magazine of Civil Engineering*. 2018. 81(5). Pp. 149–159. doi: 10.18720/MCE.81.15
11. Ignatyev, A.V., Ignatyev, V.A., Gamzatova, E.A. Analysis of bending plates with unilateral constraints through the finite element method in the form the of classical mixed method. *Izvestiya vuzov. Stroitelstvo*. 2018. No. 8. Pp. 5–14. (rus)
12. Lukashevich, A.A., Lukashevich, N.K., Timohina, E.I. Modelling of contact interaction with allowance for nonlinear. *IOP Conference Series: Materials Science and Engineering*. 2018. Vol. 463. No. 042054.
13. Albert, Y.U., Dolgaya, A.A. Ivanova, T.V. et al. Seismic input models for tuned mass damper designing. *Magazine of Civil Engineering*. 2017. 76(8). Pp. 98–105. doi: 10.18720/MCE.76.9.
14. Smirnov, V.N., Shestakova, E.B., Chizhov, S.V. et al. Dynamic interaction of high-speed trains with span structures and flexible support. *Magazine of Civil Engineering*. 2017. 76(8). Pp. 115–129. doi: 10.18720/MCE.76.11.
15. Tusnin, A. Dynamic factors in case of damaging continuous beam supports. *Magazine of Civil Engineering*. 2018. 78(2). Pp. 47–64. doi: 10.18720/MCE.78.4
16. Galanin, M.P., Lukin, V.V., Rodin, A.S., Stankevich, I.V. Application of the schwarz alternating method for simulating the contact interaction of a system of bodies. *Computational Mathematics and Mathematical Physics*. 2015. 55(8). Pp. 1393–1406.
17. Galanin, M.P., Lukin, V.V., Rodin, A.S. Use of various versions of Schwarz method for solving the problem of contact interaction of elastic bodies. *IOP Conf. Series: Journal of Physics: Conf. Series*. 2018. Vol. 991. No. 012021.
18. Bychek, O.V., Sadovskii, V.M. On the investigation of the dynamic contact interaction of deformable bodies. *Journal of Applied Mechanics and Technical Physics*. 1998. 39(4). Pp. 628–633.
19. Annin, B.D., Sadovskaya, O.V., Sadovskii, V.M. Dynamic contact problems of elastoplasticity. *Voprosy Materialovedeniya*. 2003. 33(1). Pp. 426–434.
20. Wriggers, P., Nackenhorst, U. *Analysis and Simulation of Contact Problems*. Berlin-Heidelberg: Springer, 2006. 394 p.
21. Kravchuk, A.S. Variatsionnyy metod v kontaktnykh zadachakh. *Sostoyaniye problemy, napravleniya razvitiya* [The variational method in contact problems. The present state of the problem and trends in its development]. *Journal of Applied Mathematics and Mechanics*. 2009. 73(3). Pp. 492–502. (rus)
22. Sofonea, M., Souleiman, Y. Analysis of a sliding frictional contact problem with unilateral constraint. *Mathematics and Mechanics of Solids*. 2017. No. 22. Pp. 324–342.
23. Barboteu, M., Danan, D. Analysis of a dynamic viscoelastic contact problem with normal compliance, normal damped response, and nonmonotone slip rate dependent friction. *Advances in Mathematical Physics*. 2016. No. 1. Pp. 1–15.
24. Barboteu, M., Cheng, X., Sofonea, M. Analysis of a contact problem with unilateral constraint and slip-dependent friction. *Mathematics and Mechanics of Solids*. 2016. No. 21. Pp. 791–811.
25. Barauskas, R. Dynamic analysis of structures with unilateral constraints: Numerical integration and reduction of structural equations. *International Journal for Numerical Methods in Engineering*. 1994. 37(2). Pp. 323–342.
26. Liolios A., Liolios K., Iossifidou K. et al. A numerical approach to the dynamic unilateral contact problem of soil-pile interaction under instabilizing and environmental effects // *Numerical Methods and Applications*, 6th International Conference, NMA 2006, Borovets, Bulgaria, August 20–24. Berlin; New York: Springer, 2007. Pp. 646–651.
27. Bathe, K.-J., Wilson, E.L. *Numerical methods in finite element analysis*. Englewood Cliffs: Prentice Hall, 1976. 544 p.
28. Lukashevich A.A., Rozin L.A. Numerical decision of problems of structural mechanics with nonideal unilateral constraints. *Applied Mechanics and Materials*. *Advances in Civil and Industrial Engineering IV*. 2014. Vol. 580–583. Pp. 2932–2935.
29. Lukashevich, A.A. Programma resheniya zadach kontaktnogo vzaimodeystviya s uchetom odnostoronnih svyazey i treniya metodom konechnykh elementov [The program for solving contact interaction problems taking into account unilateral constraints and friction by the finite element method]. *Svidetelstvo o gosudarstvennoy registracii programmy dlya EVM № 2008610113. Zaregistrirovano v Reestre programm dlya EVM. Federalnaya sluzhba po intellektualnoj sobstvennosti, patentam i tovarnym znakam RF, 2008. 1 p. (rus)*
30. Lappo, D.D., Veksler, A.B. et al. *Gidravlicheskie raschety vodosbrosnyh gidrotekhnicheskikh sooruzhenij: Spravochnoe posobie* [Hydraulic calculations of spillway hydraulic structures: Reference manual]. Moscow: Ergoatomizdat, 1988. 624 p. (rus)

### **Contacts:**

*Anatoliy Lukashevich, +7(911)8212553; aaluk@bk.ru*

© Lukashevich, A.A., 2019



DOI: 10.18720/MCE.85.14

## Моделирование контактного взаимодействия конструкций с основанием при динамическом нагружении

**А.А. Лукашевич\***

Санкт-Петербургский государственный архитектурно-строительный университет,  
Санкт-Петербург, Россия

\* E-mail: [aaluk@bk.ru](mailto:aaluk@bk.ru)

**Ключевые слова:** конструкция, основание, контактное взаимодействие, односторонние связи, динамическое нагружение, дискретная модель, метод конечных элементов

**Аннотация.** Конструктивно нелинейные задачи с односторонними связями часто встречаются при расчете различного рода конструкций и сооружений. При этом определенные трудности в решении представляют задачи при учете трения на контакте, а также при динамическом действии нагрузки. В этих случаях контактная задача усложняется в математическом отношении и усложняется ее численное решение. Настоящая статья посвящена построению расчетных моделей и методов решения задач с неидеальными односторонними связями при динамическом нагружении. На основе конечно-элементной модели контакта и метода пошагового анализа разработан численный алгоритм, позволяющий выполнять одновременно интегрирование уравнений движения и реализацию контактных условий с трением Кулона. Для соблюдения ограничений в условиях по предельному трению-скольжению применен способ компенсирующих нагрузок. С помощью предложенного подхода получены и проанализированы численные решения некоторых задач контакта сооружения с основанием. Достоверность результатов проведенных расчетов подтверждается сопоставлением их с решением, полученным альтернативным итерационным методом. При этом алгоритм пошагового анализа является более эффективным по времени вычислений, показывая удовлетворительную сходимость, устойчивость и точность решения в достаточно широком диапазоне шагов интегрирования по времени.

### Литература

1. Laursen T.A. Computational Contact and Impact Mechanics. Berlin-Heidelberg: Springer, 2002. 454 p.
2. Wriggers P. Computational Contact Mechanics. Berlin-Heidelberg: Springer, 2006. 521 p.
3. Laursen T., Yang B. A contact searching algorithm including bounding volume trees applied to finite sliding mortar formulations // Computational Mechanics. 2008. No. 41. Pp. 189–205.
4. Bukhartsev V.N., Lukashovich A.A. Stability assessment of a structure subject to asymmetric load application on a rock-free bed // Power Technology and Engineering. Springer New York Consultants Bureau. 2012. Vol. 45. No. 5. Pp. 346–350.
5. Wriggers P., Schroder J., Schwarz A. A finite element method for contact using a third medium // Computational Mechanics. 2013. No. 52(4). Pp. 837–847.
6. Колосова Г.С., Лалин В.В., Колосова А.В. Влияние строительных швов и трещин на напряженно-деформированное состояние арочно-гравитационной плотины // Инженерно-строительный журнал. 2013. № 5(40). С. 76–85. doi: 10.5862/MCE.40.9
7. Lukashovich A.A. Computational solution of contact problems with unilateral constraints and friction by step-by-step analysis // Advanced Materials Research. 2014. Vol. 941–944. Pp. 2264–2267.
8. Barboteu M., Danan D., Sofonea M. Analysis of a contact problem with normal damped response and unilateral constraint // Journal of Applied Mathematics and Mechanics. 2016. Vol. 96. No. 4. Pp. 408–428.
9. Wriggers P., Rust W.T., Reddy B.D. A virtual element method for contact // Computational Mechanics. 2016. No. 58(6). Pp. 1039–1050.
10. Лукашевич А.А. Численное моделирование жесткостных и прочностных свойств контактного шва // Инженерно-строительный журнал. 2018. № 5(81). С. 149–159. doi: 10.18720/MCE.81.15
11. Игнатьев А.В., Игнатьев В.А., Гамзатова Е.А. Анализ изгибаемых пластинок с односторонними связями по методу конечных элементов в форме классического смешанного метода // Изв. Вузов. Строительство. 2018. № 8. С. 5–14.
12. Lukashovich A.A., Lukashovich N.K., Timohina E.I. Modelling of contact interaction with allowance for nonlinear // IOP Conference Series: Materials Science and Engineering. 2018. Vol. 463. No. 042054.
13. Альберт И.У., Долгая А.А., Иванова Т.В. и др. Расчетное сейсмическое воздействие для сооружения с динамическим гасителем колебаний // Инженерно-строительный журнал. 2017. № 8(76). С. 98–105. doi: 10.18720/MCE.76.9.

14. Смирнов В.Н., Шестакова Е.Б., Чижов С.В. и др. Динамическое взаимодействие высокоскоростных поездов с пролетными строениями и гибкими опорами // Инженерно-строительный журнал. 2017. № 8(76). С. 115–129. doi: 10.18720/MCE.76.11
15. Туснин А.Р. Коэффициенты динамичности при повреждении опор неразрезных балок // Инженерно-строительный журнал. 2018. № 2(78). С. 47–64. doi: 10.18720/MCE.78.4
16. Galanin M.P., Lukin V.V., Rodin A.S., Stankevich I.V. Application of the Schwarz alternating method for simulating the contact interaction of a system of bodies // Computational Mathematics and Mathematical Physics. 2015. Vol. 55. No. 8. Pp. 1393–1406.
17. Galanin M.P., Lukin V.V., Rodin A.S. Use of various versions of Schwarz method for solving the problem of contact interaction of elastic bodies // IOP Conf. Series: Journal of Physics: Conf. Series. 2018. Vol. 991. No. 012021.
18. Bychek O.V., Sadovskii V.M. On the investigation of the dynamic contact interaction of deformable bodies // Journal of Applied Mechanics and Technical Physics. 1998. Vol. 39. No. 4. Pp. 628–633.
19. Аннин Б.Д., Садовская О.В., Садовский В.М. Динамические контактные задачи теории упругости и пластичности // Вопросы материаловедения. 2003. № 1(33). С. 426–434.
20. Wriggers P., Nackenhorst U. Analysis and Simulation of Contact Problems. Berlin-Heidelberg: Springer, 2006. 394 p.
21. Кравчук А.С. Вариационный метод в контактных задачах. Состояние проблемы, направления развития // Прикладная математика и механика. 2009. Т. 73. № 3. С. 492–502.
22. Sofonea M., Souleiman Y. Analysis of a sliding frictional contact problem with unilateral constraint // Mathematics and Mechanics of Solids. 2017. No. 22. Pp. 324–342.
23. Barboteu M., Danan D. Analysis of a dynamic viscoelastic contact problem with normal compliance, normal damped response, and nonmonotone slip rate dependent friction // Advances in Mathematical Physics. 2016. No. 1. Pp. 1–15.
24. Barboteu M., Cheng X., Sofonea M. Analysis of a contact problem with unilateral constraint and slip-dependent friction // Mathematics and Mechanics of Solids. 2016. No. 21. Pp. 791–811.
25. Barauskas R. Dynamic analysis of structures with unilateral constraints: Numerical integration and reduction of structural equations // International Journal for Numerical Methods in Engineering. 1994. No. 37(2). Pp. 323–342.
26. Liolios A., Liolios K., Iossifidou K. et al. A numerical approach to the dynamic unilateral contact problem of soil-pile interaction under instabilizing and environmental effects // Numerical Methods and Applications, 6th International Conference, NMA 2006, Borovets, Bulgaria, August 20–24. Berlin; New York: Springer, 2007. Pp. 646–651.
27. Bathe K.-J., Wilson E.L. Numerical methods in finite element analysis. Englewood Cliffs: Prentice Hall, 1976. 544 p.
28. Lukashевич А.А., Розин Л.А. Numerical decision of problems of structural mechanics with nonideal unilateral constraints // Applied Mechanics and Materials. Advances in Civil and Industrial Engineering IV. 2014. Vol. 580–583. Pp. 2932–2935.
29. Лукашевич А.А. Программа решения задач контактного взаимодействия с учетом односторонних связей и трения методом конечных элементов. Свидетельство о государственной регистрации программы для ЭВМ № 2008610113. Зарегистрировано в Реестре программ для ЭВМ // Федеральная служба по интеллектуальной собственности, патентам и товарным знакам РФ, 2008. 1 с.
30. Лаппо Д.Д., Векслер А.Б. и др. Гидравлические расчеты водосбросных гидротехнических сооружений: Справочное пособие. М.: Энергоатомиздат, 1988. 624 с.

### **Контактные данные:**

*Анатолий Анатольевич Лукашевич, +7(911)8212553; эл. почта: aaluk@bk.ru*

© Лукашевич А.А., 2019



DOI: 10.18720/MCE.89.15

## Physical and mechanical properties of cement stone with superabsorbent polyacrylate solutions

**A.S. Inozemtcev\*, E.V. Korolev, T.Q. Duong**

*National Research Moscow State Civil Engineering University, Moscow, Russia*

\* E-mail: [InozemtcevAS@mgsu.ru](mailto:InozemtcevAS@mgsu.ru)

**Keywords:** super-absorbent polymer, mechanical properties, compressive strength, internal curing, hardening, pore structure, shrinkage

**Abstract.** The 3D-technology is becoming widespread in construction. Thus, the development of mixtures with the indifferent set of properties to the influence of the environment is actual. The intensive setting and hardening of cement composites in aggressive conditions require finding solutions to ensure the internal curing of concrete. One of the ways to ensure the internal curing of cement composites can be the using of special superabsorbent polymers (SAP). The formation in the structure of the mixture of thin films of polyacrylate SAP with a delayed polymerization of acrylic acids will provide the reserve of water in the system for hydration. Wherein the mobility of the mixture and strength of composite does not get lost in contrast to the granular SAP. The determination of the influence of the SAP components "Renovir-hydrogel" on the physical and mechanical properties of the cement stone is the main aim of this study. Standard test methods in accordance with Russian state standards for average density and total pore volume, EN 196-1 for kinetics of hardening are used in the work. It has been shown that the super absorbent polymer solutions with a controlled polymerization process can be used in cement composites to control water balance. The investigated SAP solutions allow increasing the average density and compressive strength of cement stone. The admixture of the SAP solutions in the studied range of variable factors leads to an increase in the strength of cement stone by 29.5%. An experimental statistical model describing the dependence of the compressive strength on the amount of catalyst and the ratio of water to polymer part was obtained. This allows for achieving the required characteristics of the composite.

### 1. Introduction

The development of mixtures with a set of properties that are indifferent to the influence of the environment during the setting and hardening of the binder is relevant due to wide adoption of 3D-printers in construction [1-3]. Intensive water loss from cement compositions proceeds during the layer-by-layer printing process. This leads to an imbalance of fluid in the volume, lack of water for hydration, high shrinkage, decrease of density and strength. Therefore, the saving of water in the building "inks" is important throughout the full period of hardening in natural conditions.

One of the ways to ensure the internal curing of cement composites, by analogy with porous aggregate saturated with water in lightweight concrete, can be the use of special highly absorbent granular polymers. Superabsorbent polymers (SAP) are obtained from acrylic acid, its salts and derivatives, polymerized in solution or suspension. Polyacrylates have a high absorption capacity and therefore the field of application is very wide in various industries including construction [4]. Most SAPs are produced in the form of granules or fibers of micrometric size.

Today, experience in the use of SAP in cement systems has been gained in world practice due to the positive effect on reducing of shrinkage. The effectiveness of superabsorbent polymers as a component for

---

Inozemtcev, A.S., Korolev, E.V., Duong, T.Q. Physical and mechanical properties of cement stone with superabsorbent polyacrylate solutions. Magazine of Civil Engineering. 2019. 89(5). Pp. 179–186.  
DOI: 10.18720/MCE.89.15

Иноземцев А.С., Королев Е.В., Зьонг Т. Физико-механические свойства цементного камня с раствором суперабсорбирующих полиакрилатов // Инженерно-строительный журнал. 2019. № 5(89). С. 179–186.  
DOI: 10.18720/MCE.89.15



the internal curing of concrete is shown in [5]. The decreasing of autogenous shrinkage of concrete from 500 to 120  $\mu\text{m}/\text{m}$  with the admixture of SAP was shown. The similar positive effect – reducing shrinkage on drying (by 12.6%) and autogenous shrinkage (by 15.5 %) of self-leveling mortars is described in [4]. Such a shrink-inhibiting effect is most significant at the age of 28 days.

The authors [6, 7] investigated the effect of differently dispersed SAPs on the reduction of plastic shrinkage of cement systems (fractions 0...200  $\mu\text{m}$  and 200...500  $\mu\text{m}$ ) in different heat and humidity conditions. Longitudinal deformations for compositions with a dispersion of SAP less than 200  $\mu\text{m}$  and 200...500  $\mu\text{m}$  have decreased by 20 and 17 %, respectively.

In accordance with [6], an increasing in the content of superabsorbent polymers in cement mortar lead to the decreasing of the tensile and compression strength by 20.5 and 25.8 %, respectively. This is explained by the changing of porosity [11] which is additionally formed after the desorption of SAP (Figure 1).

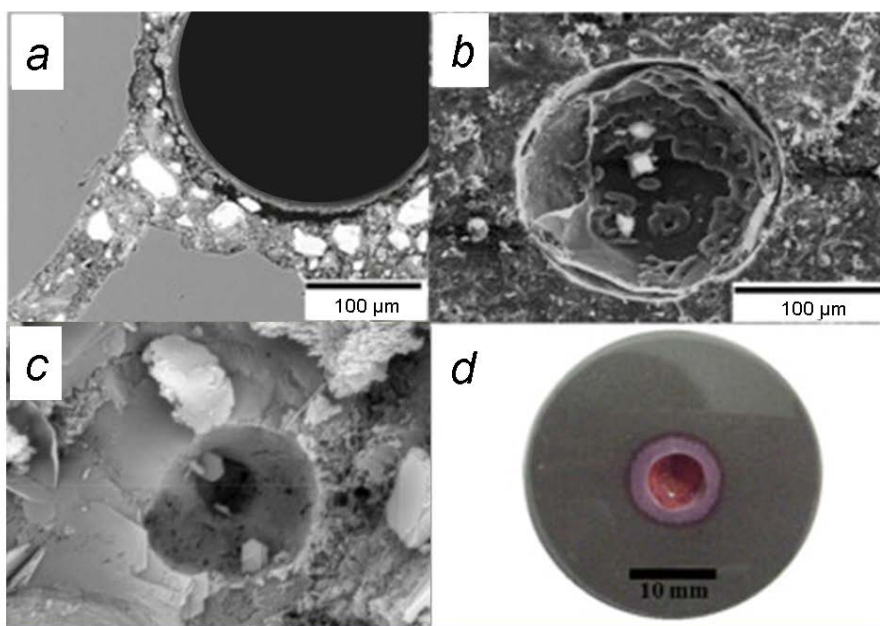


**Figure 1. Structure of cement mortar [6] (c) and a, b, d [11].**

In [10], it was shown that the introduction of SAP in cement composites does not lead to a significant changes in flexural strength at the age of 28 days. However, cement stone samples containing SAPs show an insignificant increasing in flexural strength by 9.05 and 2.91 %, for a particle size of < 200  $\mu\text{m}$  and fraction 200...500 microns, respectively, just in the early stages of hardening (3 days) [9]. A negative trend is observed in the later periods (28 days). Flexural strength decreases by 25.4 and 37.2 % and compressive strength by 13.6 and 21.8 % for SAP granules with a size of less than 200 microns and fraction 200...500 microns, respectively. In this case, the particle size of the SAP is essential. Large SAP granules have the greater reduction in the strength of the cement stone.

Studies of the SAP with different average particles size (from 324 to 1065  $\mu\text{m}$ ), density of anionic groups and crosslinking density from acrylic acid and acrylamide [9, 13] show a significant decreasing of compressive strength of mixtures with very high density of anionic functional groups. In this case, the desorption of water from the SAP occurs prematurely. This leads to an excess of water and forms additional porosity. A small decreasing or saving of strength is observed in cement mixtures with SAP with a lower concentration of anions.

The authors [14] based on the analysis of the effect of SAP on the mechanical properties of concrete at the age of 28 days conclude about an unambiguous negative influence. Compressive strength by 8...35 % under high humidity hardening and 28 % in conditions of low humidity is reduced. The tests of the samples that have been hardened under sealed conditions show inconsistent results For example, the flexural strength is decreased by 33 % [15] or increased by 7 % for different compositions, but the compressive strength is decreased by 10...13 % [16].

Thus, the use of superabsorbent polymers in cement composites is characterized by both positive and negative effects. On the one side, the use of SAP is justified by the positive effect of reducing shrinkage. On the other side the granular polymer requires pre-saturation (up to 30 minutes) to ensure sufficient mobility of the cement mixture and is in the composite structure as a source of additional pores, reducing mechanical properties. The desorption kinetics of SAP provides the most important for increasing efficiency. Water migration should be carried out in sufficient quantities from polyacrylates to the cement system in sufficient

quantities, and not the other way around. The properties of polymer cross-linking, the shape and size of the granules, and the properties of the sorbate are important factors for controlling the desorption process [9].

Based on the above analysis, the following hypothesis can be formulated: the forming of thin films of polyacrylates in the structure of the cement materials by delayed polymerization of acrylic acids in water solution provide the water reserve for internal curing without the loss of mobility of the mixture and strength properties of the composite. This is especially actual to develop recipes of building «inks» for 3D-printers [17–20].

## 2. Materials and Methods

In this paper the effect of the “Renovir-hydrogel” superabsorbent polymer on the properties of cement stone was investigated. The SAP solution is obtained by mixing water ( $W$ ) with the three components of the polymer part ( $\Sigma A = A_1 + A_2 + A_3$ ) and catalyst ( $B$ ). The component “ $A_1$ ” is acrylic acid (propenoic acid  $\text{CH}_2=\text{CH}-\text{COOH}$ ) or salt (sodium polyacrylate  $[-\text{CH}_2-\text{CH}(\text{COONa})-]_n$ ). The component “ $A_2$ ” is a crosslinking agent in which poly-saturated compounds are widely used. The component “ $A_3$ ” is an initiator from peroxides, hydroperoxides, hydrogen peroxide, persulfates, azo compounds or redox systems. Varying the concentrations of each component allows to control the polymerization process and form a different degree of crosslinking and polymerization speed. Main characteristics of the “Renovir-hydrogel” superabsorbent polymer are presented in [21].

The determination of the influence of the SAP components “Renovir-hydrogel” (Table 1) on the physical and mechanical properties of the cement stone is the main aim of this study. The study was carried out in the framework of a full two-factor experiment. The amount of catalyst  $B/A_1$  ( $X_1$ ) and the ratio of water to polymer part  $W/\Sigma A$  ( $X_2$ ) were chosen as factors. The average density and compressive strength were used as controlled indicators.

**Table 1. Compositions of superabsorbent polymer solutions “Renovir-hydrogel”.**

No	Composition	Amount, %			Factors	
		$\Sigma A$	$B$	$W$	$X_1$	$X_2$
1	C-0.003/5.0	16.67	0.042	83.29	0.003	5.0
2	C-0.009/5.0	16.44	1.390	82.71	0.009	5.0
3	C-0.003/8.5	10.44	0.880	88.68	0.009	8.5
4	C-0.009/8.5	10.53	0.027	89.44	0.003	8.5

The Portland cement CEM I 42.5 produced by “Stone Flower” was used to prepare a series of cement test samples with W/C-ratio 0.3. The SAP solutions were used as water in the cement mixtures. The control composition (C-0/0) was prepared without a solution of SAP. Hardening of the samples was carried out in normal conditions. The average density and total pore volume were determined by methods in accordance with regulatory and technical documents Russian State Standards GOST 12730.1-78 and GOST 12730.4-78. The average density was determined by the ratio of the mass and volume of the samples, and the true density by the pycnometric method. Six cubic-samples 50 mm in each series were tested to compressive strength according to EN 196-1 at the age of 7; 14; 21 and 28 days. The tests were carried out using static loading by the servo-hydraulic press «Advantest 9».

The study was performed by equipment from the Head Regional Shared Research Facilities of the Moscow State University of Civil Engineering. Technical specifications of the equipment are available on [22].

## 3. Results and Discussion

Cement pastes with SAP visually were not characterized by differences in workability unlike the control composition. Presumably, the process of SAP polymerization in the selected range of components is begun after the formation of samples. This provided a delay in the water sorption by SAP and in the deterioration of workability pastes. Previously [23], the studies of the polymer solutions “Renovir-hydrogel” were carried out by NMR-relaxometry method. The start and end times of polymerization of this SAP were established for studied concentrations. According to this study, the period of viability of the polymer solutions “Renovir-hydrogel” is from 14.2 to 105.2 minutes. That is, the limiting time of preservation of viscosity sufficient for technological operations exceeds 10 minutes before each of the mixtures was formed.

Analysis of the kinetics of setting and hardening of Portland cement with the addition of acrylate allows to estimate its impact on the process of structure formation of cement stone in time. The kinetics of the compressive strength of the cement stone with the hydrogel solutions of different composition were obtained in this study (Figure 2).

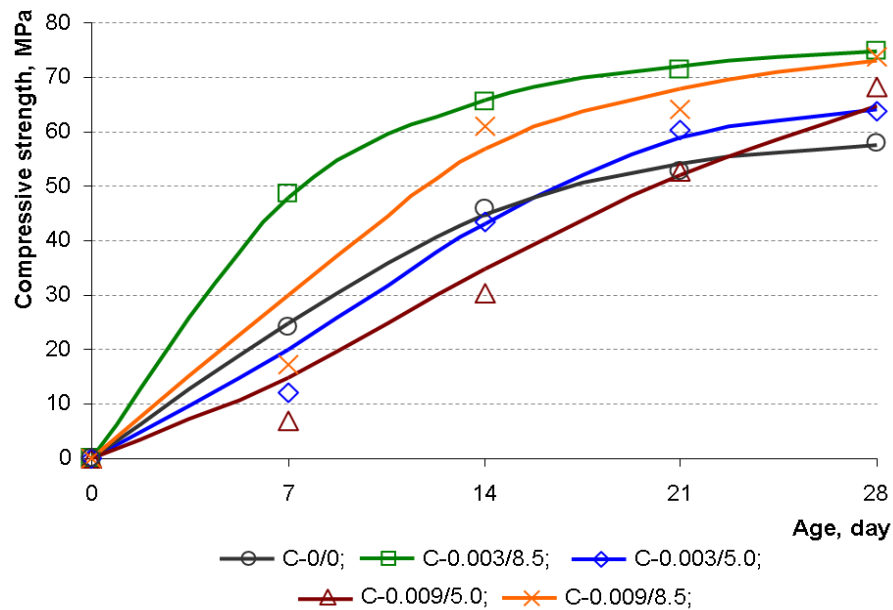


**Figure 2. Kinetics of hardening cement stone with SAP.**

The obtained results show that the cement stone modified by solution of the acrylate superabsorbent polymer is characterized by greater strength at the age of 28 days by 10.2 ... 29.5 % than the composition with water (Table 2). However, the different effect of the ratio  $W/\Sigma A$  and  $B/A_1$  on the strength in the early periods of hardening is shown in Figure 2. It can be noted that the compositions with the amount of polymer  $W/\Sigma A = 8.5$  (regardless of the amount of catalyst) are characterized by faster hardening kinetics than the control composition. At the same time the cement stone where the ratio of water to polymer part is equal to 5.0 has less strength than the control composition at the age of up to 14 days. This indicates an excess of polymer in the composition, which has a negative impact on the structure formation of cement stone.

**Table 2. Rheological properties of cement pastes and physical-mechanical properties of cement stone with SAP at the age of 28 days.**

No	Composition	$\rho$ , kg/m <sup>3</sup>	$S_\rho$ , %	$P$ , %	$S_P$ , %	$R_{com}$ , MPa	$S_R$ , %
0	C-0/0	2065	0.93	8.0	2.33	58.0	4.24
1	C-0.003/5.0	2100	0.30	3.5	3.13	63.9	3.22
2	C-0.009/5.0	2070	0.60	3.8	3.27	64.2	4.26
3	C-0.003/8.5	2135	0.79	3.3	2.61	75.1	4.13
4	C-0.009/8.5	2095	0.57	3.5	3.55	73.7	3.72

Notes:  $\rho$  is average density;  $P$  is total pore volume;  $R_{com}$  is compressive strength;  $S_\rho$ ,  $S_P$ ,  $S_R$  are standard deviations for average density, total pore volume and compressive strength respectively.

The studies have allowed to establish an experimental equation for estimation of the dependence of the compressive strength on selected prescription factors:

$$Y = 69.23 - 0.275X_1 + 5.175X_2.$$

The analysis of the structural parameters of the cement stone in the Table 2 show that an increase in the amount of catalyst to 0.009 leads to a slight decrease in the average density and an increase in the porosity of the cement stone due to the faster polymerization process of acrylate. In the initial period of preparation of the mixture due to absorption, the polymer reduces the amount of free water in the system and impairs mobility and workability. Delayed polymerization is achieved with a smaller amount of catalyst. In this case the polymer does not interfere the distribution of water in the volume and performs an absorbing function after molding the product. This has a positive effect on the compaction of the mixture and on the hydration of Portland cement, which provides a lower porosity of cement stone (more than 2 times) (Table 3). The introduction of the SAP solutions in the studied range of variable factors leads to an increase in the strength of cement stone by 10.2...29.5 %.

Thus, it was shown that the using of water solutions of acrylic acids with controlled polymerization does not lead to the loss of the strength of the cement stone. The studied SAP solutions allow to delay the absorption of water from the cement mixture in contrast to the granulated SAP. Obviously, additional studies are required to determine the action mechanism of SAP solution on the process of structure formation of cement stone and to establish the dependences of influence of prescription and technological factors on the deformation properties.

**Table 3. Changes of properties of cement pastes and cement stone compared with the control composition (C-0/0).**

No	Composition	$\rho$ , %	$P$ , %	$R_{com}$ , %
1	C-0.003/5.0	+1.7	-56.3	+10.2
2	C-0.009/5.0	+0.3	-52.5	+10.7
3	C-0.003/8.5	+3.4	-58.8	+29.5
4	C-0.009/8.5	+1.5	-56.3	+27.1

Note. «+» or «-» show an increase or decrease in the indicator.

The results show that the introduction of polymer solutions with controlled polymerization in cement compositions provides an increase in compressive strength from 58.0 to 63.9...75.1 MPa in contrast to the using of granulated SAP when compressive strength is decreased by 8...35 % [4, 6, 12].

Positive world experience in the use of granulated SAP for reducing shrinkage and the results of this study suggest the effectiveness of using SAP solutions with controlled polymerization in cement systems hardening in bad conditions. Such a solution may have further development and practical application in 3D-printing technology, where extruded concrete structures are subject to intensive moisture loss.

## 4. Conclusions

Based on this research the following conclusions were made:

1. The formulated hypothesis is confirmed in this paper. It has been shown that the super absorbent polymer solutions with a controlled polymerization process can be used in cement composites to control water balance for improving physical and mechanical properties.

2. An experimental equation for estimation of the dependence of the compressive strength on the amount of catalyst and the ratio of water to polymer part was obtained.

3. The investigated SAP solutions allow to increase the average density and compressive strength of cement stone. The introduction of the SAP solutions (for studied range of variable factors) leads to decrease the porosity from 8 to 3.3...3.5 % and increase the compressive strength of cement stone from 58.0 to 63.9...75.1 MPa or by 10.2 ... 29.5 % in comparison with the composition without SAP.

## Acknowledgement

The work was carried out within the framework of the agreement No 14.583.21.0072 on granting subsidies for the implementation of the federal target program «Research and development in priority areas for the development of the scientific and technological complex of Russia for 2014-2020» (project identifier - RFMEFI58318X0072) with the financial support from the Ministry of Education and Science of the Russian Federation.

## References

1. Buswell, R.A., Silva Leal de, W.R., Jones, S.Z., Dirrenberger, J. 3D printing using concrete extrusion: A roadmap for research. *Cement and Concrete Research*. 2018. 112. Pp. 37–49.
2. Pustovgar, A.P., Adamtsevich, A.O., Volkov, A.A. Technology and organization of additive construction. *Industrial and Civil Engineering*. 2018. 9. Pp. 12–20.
3. Inozemtcev, A.S., Korolev, E.V., Duong, T.Q. Analysis of existing technological solutions of 3D-printing in construction. *Vestnik MGSU*. 2018. 13 (7 (118)). Pp. 863–876. (rus)
4. Meshcherin, V. The use of superabsorbent polymers (SAP) as an additive to concrete. *Concrete and Reinforced Concrete*. 2017. 16(1). Pp. 8–13. (rus)
5. Klemm, A.J., Almeida, F.S.R., Sikora, K.S. The use of superabsorbent polymers (SAP) in binders based on multicomponent cements. *CPI – Concrete Plant International*. 2016. 4. Pp. 44–52. (rus)
6. Yang, J., Liu, L., Liao, Q., Wu, J., Zhang, L. Effect of superabsorbent polymers on the drying and autogenous shrinkage properties of self-leveling mortar. *Construction and Building Materials*. 2019. 201(20). Pp. 401–407.
7. Popov, D.Yu., Lesovik, V.S., Meshcherin, V.S. Effect of superabsorbent polymers on plastic shrinkage of cement stone. *Bulletin of Belgorod State Technological University to the V.G. Shukhov*. 2016. 11. Pp. 6–12. (rus)
8. Popov, D.Y. Improving the efficiency of textile concrete. *Belgorod: BGTU*, 2018. (rus)
9. Schröfl, Ch., Mechtcherine, V., Gorges, M. Relation between the molecular structure and the efficiency of superabsorbent polymers (SAP) as concrete admixture to mitigate autogenous shrinkage. *Cement and Concrete Research*. 2012. 42 (6). Pp. 865–873.
10. Senff, L., Modolo, R.C.E., Ascensao, G., Hotza, D., Labrincha, J.A. Development of mortars containing superabsorbent polymer. *Construction and Building Materials*. 2015. 95. Pp. 575–584.
11. Yang, J., Wang, F., He, X., Su, Y. Pore structure of affected zone around saturated and large superabsorbent polymers in cement paste. *Cement and Concrete Composites*. 2019. 97. Pp. 54–67.
12. Wang, F., Yang, J., Hu, S., Li, X., Cheng, H. Influence of superabsorbent polymers on the surrounding cement paste. *Cement and Concrete Research*. 2016. 81. Pp. 112–121.
13. Liu, H., Bu, Y., Sanjayan, J.G., Nazari, A., Shen, Zh. Suitability of polyacrylamide superabsorbent polymers as the internal curing agent of well cement. *Construction and Building Materials*. 2016. 112. Pp. 253–260.

14. Mechtcherine, V., Reinhardt, H.-W. Application of Superabsorbent Polymers (SAP) in Concrete Construction. Paris, 2012.
15. Igarashi, S.-I., Watanabe, A. Experimental study on prevention of autogenous deformation by internal curing using super-absorbent polymer particles. RILEM Proc. PRO. 2006. 52. Pp. 77–86.
16. Lura, P., Durand, F., Loukili, A., Kovler, K., Jensen, O.M. Compressive strength of cement pastes and mortars with superabsorbent polymers. RILEM Proc. PRO. 2006. 52. Pp. 117–126.
17. Grakhov, V.P., Mokhnachev, S.A., Borozdov, O.V. The impact of the development of 3D-technology on the construction economy. Basic research. 2014. 11–12. Pp. 2673–2676. (rus)
18. Inozemtcev, A.S., Duong, T.Q. Technical and economic efficiency of materials using 3D-printing in construction on the example of high-strength lightweight fiber-reinforced concrete. E3S Web of Conferences. 2019. 97. Pp. 02010.
19. Schutter, G.De, Lesage, K., Mechtcherine, V., Nerella, V.N., Habert, G., Agusti-Juan, I. Vision of 3D printing with concrete — Technical, economic and environmental potentials. Cement and Concrete Research. 2018. 112. Pp. 25–36.
20. Damme, H.V. Concrete material science: Past, present, and future innovations. Cement and Concrete Research. 2018. 112. Pp. 5–24.
21. RENOVIR HydroGel. [Online]. System requirements: AdobeAcrobatReader [Online]. URL: <http://www.renovir.ru/produkcziya/gidroizolyacziya/ximicheskaya-otsechnaya-gidroizolyacziya/renovir-gidrogel.html> (date of application: 01.06.2019).
22. SEC «Nanomaterials and nanotechnology» – Equipment. [Online]. System requirements: AdobeAcrobatReader [Online]. URL: <http://www.nocnt.ru/oborudovanie> (date of application: 01.06.2019).
23. Inozemtcev, A.S., Korolev, E.V., Duong, T.Q. Selection of a superabsorbent polymer hydrogel for cement systems. 2019. 7. Pp. 46–52.

**Contacts:**

*Aleksandr Inozemtcev, +7(499)1880400; InozemtcevAS@mgsu.ru*

*Evgeniy Korolev, +7(499)1880400; info@nocnt.ru*

*Thanh Qui Duong, +8(499)1880400; quiduongthanh@gmail.com*

© Inozemtcev, A.S., Korolev, E.V., Duong, T.Q., 2019



DOI: 10.18720/MCE.85.15

## Физико-механические свойства цементного камня с раствором суперабсорбирующих полиакрилатов

**А.С. Иноземцев\*, Е.В. Королев, Т. Зьонг**

*Национальный исследовательский Московский государственный строительный университет, г. Москва, Россия*

\* E-mail: [InozemcevAS@mgsu.ru](mailto:InozemcevAS@mgsu.ru)

**Ключевые слова:** суперабсорбирующий полимер, механические свойства, прочность при сжатии, внутренний уход, твердение, усадка

**Аннотация.** В связи с распространением 3D-принтеров актуальным является разработка рецептур, обладающих индифферентным к влиянию окружающей среды набором свойств в период схватывания и твердения вяжущего. Гидратация цементных композитов в агрессивных условиях требует поиска решений, обеспечивающих внутренний уход за бетоном. Одним из таких способов может быть использование специальных высокопоглощающих или суперабсорбирующих полимеров (САП). В отличие от традиционного введения гранулированных САП, формирование в структуре цементного композита тонких пленок полиакрилатов с отложенной полимеризацией акриловых кислот в водном растворе обеспечивает систему резервом воды для внутреннего ухода за процессами гидратации без потери подвижности смеси, способствуя снижению усадочных деформаций при сохранении прочностных свойств композита. Целью исследования является установление влияния соотношения компонентов в составе САП «Реновир-гидрогель» на физико-механические свойства цементного камня. В работе использованы стандартизированные методы испытаний в соответствии с ГОСТ с применением современного оборудования и инструментов. Установлено, что использование растворов САП с управляемым процессом полимеризации способствует увеличению средней плотности и прочности цементного камня. В исследуемом диапазоне варьируемых факторов введение раствора САП приводит к повышению прочности цементного камня до 29.5 %. Получена экспериментально-статистическая модель, описывающая зависимость предела прочности при сжатии от количества катализатора и отношения воды к полимерной части для обеспечения требуемых характеристик композита.

### Литература

1. Buswell R.A., Silva Leal de W.R., Jones S.Z., Dirrenberger J. 3D printing using concrete extrusion: A roadmap for research // *Cement and Concrete Research*. 2018. 112. Pp. 37–49.
2. Pustovgar A.P., Adamtsevich A.O., Volkov A.A. Technology and organization of additive construction. *Industrial and Civil Engineering*. 2018. 9. Pp. 12–20.
3. Inozemtcev A.S., Korolev E.V., Duong T.Q. Analysis of existing technological solutions of 3D-printing in construction // *Vestnik MGSU*. 2018. 13 (7 (118)). Pp. 863–876.
4. Meshcherin V. The use of superabsorbent polymers (SAP) as an additive to concrete // *Concrete and Reinforced Concrete*. 2017. 1 (16). Pp. 8–13.
5. Klemm A.J., Almeida F.S.R., Sikora K.S. The use of superabsorbent polymers (SAP) in binders based on multicomponent cements // *CPI – Concrete Plant International*. 2016. 4. Pp. 44–52.
6. Yang J., Liu L., Liao Q., Wu J., Zhang L. Effect of superabsorbent polymers on the drying and autogenous shrinkage properties of self-leveling mortar // *Construction and Building Materials*. 2019. 201 (20). Pp. 401–407.
7. Popov D.Yu., Lesovik V.S., Meshcherin V.S. Effect of superabsorbent polymers on plastic shrinkage of cement stone // *Bulletin of Belgorod State Technological University to the V.G. Shukhov*. 2016. 11. Pp. 6–12.
8. Popov D.Y. Improving the efficiency of textile concrete. Belgorod: BGTU, 2018.
9. Schröfl Ch., Mechtcherine V., Gorges M. Relation between the molecular structure and the efficiency of superabsorbent polymers (SAP) as concrete admixture to mitigate autogenous shrinkage // *Cement and Concrete Research*. 2012. 42 (6). Pp. 865–873.
10. Senff L., Modolo R.C.E., Ascensao G., Hotza D., Labrincha J.A. Development of mortars containing superabsorbent polymer // *Construction and Building Materials*. 2015. 95. Pp. 575–584.
11. Yang J., Wang F., He X., Su Y. Pore structure of affected zone around saturated and large superabsorbent polymers in cement paste // *Cement and Concrete Composites*. 2019. 97. Pp. 54–67.
12. Wang F., Yang J., Hu S., Li X., Cheng, H. Influence of superabsorbent polymers on the surrounding cement paste // *Cement and Concrete Research*. 2016. 81. Pp. 112–121.

13. Liu H., Bu Y., Sanjayan J.G., Nazari A., Shen Zh. Suitability of polyacrylamide superabsorbent polymers as the internal curing agent of well cement // *Construction and Building Materials*. 2016. 112. Pp. 253–260.
14. Mechtcherine V., Reinhardt H.-W. *Application of Superabsorbent Polymers (SAP) in Concrete Construction*. Paris, 2012.
15. Igarashi S.-I., Watanabe A. Experimental study on prevention of autogenous deformation by internal curing using super-absorbent polymer particles // *RILEM Proc. PRO*. 2006. 52. Pp. 77–86.
16. Lura P., Durand F., Loukili A., Kovler K., Jensen O.M. Compressive strength of cement pastes and mortars with superabsorbent polymers // *RILEM Proc. PRO*. 2006. 52. Pp. 117–126.
17. Grakhov V.P., Mokhnachev S.A., Borozdov O.V. The impact of the development of 3D-technology on the construction economy // *Basic research*. 2014. 11–12. Pp. 2673–2676.
18. Inozemtcev A.S., Duong T.Q. Technical and economic efficiency of materials using 3D-printing in construction on the example of high-strength lightweight fiber-reinforced concrete // *E3S Web of Conferences*. 2019. 97. Pp. 02010.
19. Schutter G.De, Lesage K., Mechtcherine V., Nerella V.N., Habert G., Agusti-Juan I. Vision of 3D printing with concrete — Technical, economic and environmental potentials // *Cement and Concrete Research*. 2018. 112. Pp. 25–36.
20. Damme H.V. Concrete material science: Past, present, and future innovations // *Cement and Concrete Research*. 2018. 112. Pp. 5–24.
21. RENOVIR HydroGel. [Электронный ресурс]. System requirements: AdobeAcrobatReader. URL: <http://www.renovir.ru/produkciya/gidroizolyacziya/ximicheskaya-otsechnaya-gidroizolyacziya/renovir-gidrogel.html> (дата обращения: 01.06.2019).
22. SEC «Nanomaterials and nanotechnology» – Equipment [Электронный ресурс]. System requirements: AdobeAcrobatReader. URL: <http://www.nocnt.ru/oborudovanie> (дата обращения: 01.06.2019).
23. Inozemtcev A.S., Korolev E.V., Duong T.Q. Selection of a superabsorbent polymer hydrogel for cement systems. 2019. 7. Pp. 46–52.

**Контактные данные:**

*Александр Сергеевич Иноземцев, +7(499)1880400; эл. почта: InozemtcevAS@mgsu.ru*

*Евгений Валерьевич Королев, +7(499)1880400; эл. почта: info@nocnt.ru*

*Тхань Куй Зыонг, +7(499)1880400; эл. почта: quiduongthanh@gmail.com*

© Иноземцев А.С., Королев Е.В., Зыонг Т., 2019



**ПОЛИТЕХ**  
Санкт-Петербургский  
политехнический университет  
Петра Великого

Инженерно-строительный институт  
Центр дополнительных профессиональных программ

195251, г. Санкт-Петербург, Политехническая ул., 29,  
тел/факс: 552-94-60, [www.stroikursi.spbstu.ru](http://www.stroikursi.spbstu.ru),  
[stroikursi@mail.ru](mailto:stroikursi@mail.ru)

Приглашает специалистов проектных и строительных организаций,  
не имеющих базового профильного высшего образования  
на курсы профессиональной переподготовки (от 500 часов)  
по направлению «Строительство» по программам:

**П-01 «Промышленное и гражданское строительство»**

Программа включает учебные разделы:

- Основы строительного дела
- Инженерное оборудование зданий и сооружений
- Технология и контроль качества строительства
- Основы проектирования зданий и сооружений
- Автоматизация проектных работ с использованием AutoCAD
- Автоматизация сметного дела в строительстве
- Управление строительной организацией
- Управление инвестиционно-строительными проектами. Выполнение функций технического заказчика

**П-02 «Экономика и управление в строительстве»**

Программа включает учебные разделы:

- Основы строительного дела
- Инженерное оборудование зданий и сооружений
- Технология и контроль качества строительства
- Управление инвестиционно-строительными проектами. Выполнение функций технического заказчика и генерального подрядчика
- Управление строительной организацией
- Экономика и ценообразование в строительстве
- Управление строительной организацией
- Организация, управление и планирование в строительстве
- Автоматизация сметного дела в строительстве

**П-03 «Инженерные системы зданий и сооружений»**

Программа включает учебные разделы:

- Основы механики жидкости и газа
- Инженерное оборудование зданий и сооружений
- Проектирование, монтаж и эксплуатация систем вентиляции и кондиционирования
- Проектирование, монтаж и эксплуатация систем отопления и теплоснабжения
- Проектирование, монтаж и эксплуатация систем водоснабжения и водоотведения
- Автоматизация проектных работ с использованием AutoCAD
- Электроснабжение и электрооборудование объектов

**П-04 «Проектирование и конструирование зданий и сооружений»**

Программа включает учебные разделы:

- Основы сопротивления материалов и механики стержневых систем
- Проектирование и расчет оснований и фундаментов зданий и сооружений
- Проектирование и расчет железобетонных конструкций
- Проектирование и расчет металлических конструкций
- Проектирование зданий и сооружений с использованием AutoCAD
- Расчет строительных конструкций с использованием SCAD Office

**П-05 «Контроль качества строительства»**

Программа включает учебные разделы:

- Основы строительного дела
- Инженерное оборудование зданий и сооружений
- Технология и контроль качества строительства
- Проектирование и расчет железобетонных конструкций
- Проектирование и расчет металлических конструкций
- Обследование строительных конструкций зданий и сооружений
- Выполнение функций технического заказчика и генерального подрядчика

По окончании курса слушателю выдается диплом о профессиональной переподготовке  
установленного образца, дающий право на ведение профессиональной деятельности

